AD-A223 025

NUMERICAL SOLUTIONS FOR A CYLINDRICAL

LASER DIFFUSER FLOWFIELD

DISSERTATION

James A. Horkovich
Lieutenant Colonel, USAF

AFIT/DS/ENY/90-3

DTIC

1990

90 06 20 061

AFIT/DS/ENY/90-3

NUMERICAL SOLUTIONS FOR A CYLINDRICAL

LASER DIFFUSER FLOWFIELD

DISSERTATION

Presented to the Faculty of the School of Engineering

of the Air Force Institute of Technology

Air University

In Partial Fulfillment of the

Requirements for the Degree of

Doctor of Philosophy

James A. Horkovich, B. S., M. S.

Lieutenant Colonel, USAF

June 1990

Approved for public release; distribution unlimited

NUMERICAL SOLUTIONS FOR

A CYLINDRICAL LASER

DIFFUSER FLOWFIELD

by

James A. Horkovich, B.S., M.S.
Lt Col, USAF

Approved:

(signature)   24th Aug 90

Chairman

(signature)   24 May 90

(signature) Gerald G Hasen   24 May 90

(signature)   24 May 90

(signature)   24 May 90

Accepted:

(signature) Robert A Calor   8 June 90

CONTENTS

ACKNOWLEDGEMENTS

I wish to express my love and deep gratitude to my wife, Betsy, for her encouragement, patience, and understanding.

I dedicate this effort to the loving memory of my mother, Amelia Rauba Horkovich Patti, who taught me at a very young age that one of the finest endeavors man can aspire to is the application of the mind for the expansion of knowledge.

James A. Horkovich

May 1990

LIST OF FIGURES

LIST OF TABLES

NOTATION

Symbols

A^+ Sublayer thickness parameter, eqn 5-2.

C Constant used to obtain exponentially stretched mesh.

C_A Adaptive mesh constant.

C_f Local skin friction coefficient, $2\tau_w/\rho_\infty u_\infty^2$.

C_p Specific heat at constant pressure.

C_v Specific heat at constant volume.

c Speed of sound, $\sqrt{\gamma RT}$.

E Error vector.

e Energy, $C_v T + (u^2 + v^2)/2$.

F Flux vector, eqn 2-28.

F_D Damping vector, eqn 3-29.

f Primitive flow variable ρ, u, v, or T.

G Flux vector, eqn 2-28.

G_D Damping vector, eqn 3-

H Flux vector, eqn 2-28.

H_o Total Enthalpy, $C_p T + (u^2 + v^2)/2$.

i Index for grid points in the axial direction.

IL Total number of grid points in the axial direction.

JL Total number of grid points in the radial direction.

j Index for grid points in the radial direction.

j_o Exponent parameter equal to 0 or 1 for two-dimensional or axisymmetric flow, respectively.

k_1 von Karman constant, eqn 5-2.

k_2 Clauser constant, eqn 5-3.

k	Thermal conductivity.
L	Length scale.
L_m	Length scale used to generate stretched mesh.
L_η, L_ξ	MacCormack difference operators in the η and ξ directions.
ℓ	Prandtl turbulent mixing length.
M	Mach number, $(u^2 + v^2)^{1/2}/c$.
P	Static pressure.
P_p	Pitot pressure (stagnation value).
P_s	Pitot static pressure.
Pr	Prandtl number, $\mu C_p/k$.
$\vec{q}$	Heat flux vector.
$\dot{q}_x$, $\dot{q}_r$	Heat flux in the axial and radial directions.
R	Gas constant for air.
Re	Reynolds number, $\rho(u^2 + v^2)^{1/2}L/\mu$.
r, y	Spatial coordinate normal to source nozzle centerline (parallel to diffuser wall).
S	Fluid stress tensor that includes pressure and viscous forces.
T	Absolute temperature.
T_0	Stagnation temperature.
t	Time.
t_{ch}	Characteristic time, eqn 3-35.
U	Conservative flow variable vector, eqn 2-28.
$\vec{u}$	Velocity vector.
u	Velocity component along the x axis.
u_{ch}	Characteristic velocity, eqn 3-35.

u^+ Nondimensional velocity component, $u/(\tau_w/\rho)^{1/2}$.

V Volume.

v Velocity component along the r axis.

x Spatial coordinate parallel to the nozzle centerline.

y Spatial coordinate normal to the x axis in a two-dimensional flow.

y^+ Nondimensional height, $y(\tau_w/\rho)^{1/2}/\nu$.

GREEK SYMBOLS:

α_η, α_ξ Damping coefficients in the η and ξ directions.

γ Ratio of specific heats, C_p/C_v.

δ Momentum boundary layer thickness.

δ^* Momentum boundary layer displacement thickness.

δ_{ij} Kronecker delta, equal to 0 if $i \neq j$ or equal to 1 if $i=j$.

η Transformed coordinate normal to source nozzle centerline (parallel to diffuser wall).

ξ Transformed coordinate normal to diffuser wall.

λ Viscosity diffusion coefficient, eqn 2-37.

λ_I Left running characteristic line.

μ Absolute viscosity coefficient.

ν Kinematic viscosity, μ/ρ.

ξ Transformed coordinate parallel to the nozzle centerline.

ρ Fluid density.

Δ Designates a finite difference when used as a prefix.

σ Normal stress on an element of fluid, eqn 2-29 - 2-31.

τ_{xr} Shear stress, eqn 2-32.

ω Vorticity.

SUBSCRIPTS:

aw   Adiabatic wall.

e   Evaluated at the edge of the boundary layer.

i,j   Grid point indices.

i,j   Indicial notation, chapter 2.

n   Normal to the diffuser wall

s   Tangential to the diffuser wall

t   Turbulent flow.

o   Stagnation value.

∞ Evaluated in the external freestream.

SUPERSCRIPTS:

n Evaluated at known time, $n\Delta t$.

$n+\frac{1}{2}$ Evaluated at intermediate predictor time level, $(n+\frac{1}{2})\Delta t$.

$n+1$ Evaluated at new corrector time level, $(n+1)\Delta t$.

o   Evaluated at time level $t=0$.

OTHER NOTATION:

$(\bar{\bar{\;}})$ Denotes a two-dimensional matrix.

$(\bar{\;})$ Denotes time averaged values, chapter 2.

$(\;)'$ Denotes unsteady values due to turbulence, chapter 2.

Abbreviations

D   Diffuser (cross-sectional) diameter (along x-axis).

Dstar   Momentum boundary layer kinematic displacement thickness.

EPB   Basic eddy viscosity; refers to the value determined by application of the basic Cebici-Smith turbulence model.

EPM   Modified eddy viscosity; refers to the value determined by application of the modified Cebici-Smith turbulence model.

EPR   Ratio of modified to basic eddy viscosity.

NSR   Normal Shock Recovery; used in conjunction with a percentage, such as 60% NSR; refers to 60 percent normal shock recovery total pressure as measured by a pitot probe (stagnation pressure behind a normal shock at the stated Mach number).

PPI   Total (stagnation) pitot pressure.

PW   Static pressure on diffuser wall.

PCL   Static pressure along diffuser line of symmetry.

R   Diffuser length (along r, or y axis).

RBD   Total length of baseline diffuser.

R_{de} Location of diffuser entrance referenced to source nozzle centerline.

R/R_{de} Ratio of distance through diffuser in streamwise direction; measured from source nozzle centerline.

RHOV   Streamwise component of specific momentum (r, or y-direction) as in Figure 63.

RUINF   Core flow average streamwise specific momentum, as used in Figure 63.

SDL   Supersonic Diffusion Laser.

SPOS   Shock Position; location of core flow normal shock stated as a percentage of distance from the diffuser entrance to the diffuser exit (measured along the r, or y, axis).

TCL   Static absolute temperature along diffuser line of symmetry.

U   Value of streamwise velocity, as used in the ratio U/UINF, Figure 30.

UINF   Flowfield average streamwise velocity, defined by eqn 6-2.

wbb   wall bank blower.

Xlt   Total x-length in the physical domain (half of the diffuser diameter) measured along the x-axis.

Ylt   Total y (r) length of the diffuser, measured from the y (r) location of the diffuser entrance to the y (r) location of the diffuser exit.

ABSTRACT

Numerical solution to the diffusion of a supersonic flow through a cylindrical laser diffuser is approached by incorporating a modified two-layer Cebici-Smith algebraic eddy viscosity turbulence model into the compressible Navier-Stokes equations. The standard algebraic constants are made functions of the local adverse pressure gradient based on experimental values obtained in the research of Jobe, Hankey, Laderman, Sturek, and Waltrup and Schetz. This modification allows solution of the Navier-Stokes equations by MacCormack's time-splitting explicit numerical scheme for selected experimental flow conditions. This effort represents the first full Navier-Stokes solution that has accurately simulated the viscous-inviscid interactions present in a supersonic axisymmetric diffuser. Numerous previous attempts required artificial and arbitrary numerical control of the wall boundary layers to achieve convergence.

The experimental tests used as a basis for the computational solutions were conducted at a diffuser entrance unit Reynolds number of 1.6 million per foot. Inflow to the diffuser was provided by ten Mach 2.5 primary nozzles plus two Mach 4.0 bank blowers (wall boundary layer flow energizers). Computations were performed for diffuser exit pressures representing 60 percent and 47 percent of normal shock recovery pressure. When the turbulence model was properly modified to accommodate the physics of flows with strong adverse pressure gradients, the numerical solution successfully reproduced all of the essential flow features including boundary layers, location and size of wall separation regions, location of the core flow normal shock, and the persistence of source nozzle flow interactions through several streamwise turnback shocks. Comparison with

experimentally obtained wall pressure data is acceptable; the only notable discrepancy occurs in the lambda shock impingement region where the numerical solution fails to accurately reproduce the intrinsic physics of the flowfield. Convergence to stable numerical solutions was not achieved using the basic Cebici-Smith model; eddy viscosity "stiffening" was required in the presence of adverse pressure gradients.

The required modifications to the basic Cebici-Smith two-layer algebraic eddy viscosity turbulence model are extremely sensitive to the von Karman universal mixing length constant, the sublayer thickness parameter, the Clauser outer region constant, and to the downstream location in the diffuser duct at which these modifications are implemented. Length scale determination in the large separation/recirculation zones present downstream of the lambda shock impingement also has a significant influence on the accuracy of the numerical solution.

Diffuser performance is shown to be constrained by source nozzle mixing losses, duct length, and the requirement for wall boundary layer energization if the design requires a relatively short duct. The numerical solutions confirmed Neumann and Lustwerk's experimental conclusions regarding minimum diffuser duct length if no wall boundary layer energization is employed.

CHAPTER I

INTRODUCTION

1.1 BACKGROUND

Within the past fifteen years, considerable attention has been focused on the chemical laser, in particular the supersonic diffusion laser (SDL) (1,2,3,4). In a typical SDL, a plenum gas mixture composed of hydrogen flouride (HF), flourine (F), and helium (He) diluent is expanded rapidly through an array of supersonic nozzles. At the exit of the nozzles, the following exothermic reaction (among others) occurs:

$$F + H_2 \rightarrow HF(v) + H \ , \quad \Delta H = 31.6 \text{ kcal/mole} \tag{1-1}$$
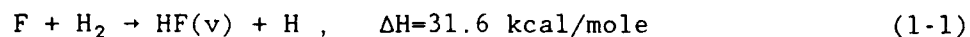
producing a vibrational (v) population inversion in HF. It is from the subsequent vibrational-energy redistribution of HF(v) that laser energy can be extracted.

In a SDL, the fluid dynamics are generally complex because of significant viscous interactions (2). Nozzle geometries introduce important inviscid considerations. Major inviscid/viscous considerations arise from the mixing of flow from numerous source nozzles, diffuser wall boundary-layer effects, and shock interation effects. Linear diffusers designed to overcome these complexities have been extremely long and heavy.

The design emphasis for such SDLs has focused quite naturally on the development of high powered, compact systems. Geometrically cylindrical designs evolved as one method of achieving compactness, giving them significant size and weight advantages over two-dimensional geometries when scaled up to achieve significant laser power output levels. In a radial (cylindrical) SDL, the fuel mixture is expanded radially from a cylindrical

1

plenum through an array of axisymmetric nozzles (Fig. 1). In the HF SDL mentioned earlier, the rapid expansion serves to "freeze" the concentration of monatomic flourine, F, inhibiting its recombination as F_2 while providing a low pressure and density conducive to effective lasing (1). The flow mixes with gas injected from the nozzle trailing edges, creating an annular axisymmetric lasing zone downstream of the nozzle exits. The laser energy is then extracted optically along the direction of the axis of the mechanism (Fig. 2). This nature of chemical laser systems requires establishment of a stable shock-free supersonic flow field in the optical tunnel (Figure 3) for optimum energy extraction. The supersonic flow from the source nozzles must be brought to ambient (subsonic) exhaust conditions with minimum losses to optimize performance of the system. Thus, the handling of the system of shock waves to decelerate the flow is a critical design issue. The efficiency of this process is usually quoted as a percentage of normal shock recovery (NSR) pressure.

The cylindrical laser configuration was first investigated by AVCO (5). This investigation included an analytical and a cold-flow subscale experimental determination of the stability of the supersonic radial flow shock system. (Cold-flow refers to a nonreacting flow field; i.e., the chemical kinetics of the species reactions, such as the recombination of monatomic fluorine, F, into F_2 are "switched off," resulting in no heat release (6). A hot-flow refers to a reacting flow field with fully coupled chemical kinetics resulting in heat release from the recombination of monatomic fluorine, F, into F_2). The configuration studied had no diffuser; instead an attempt was made to establish a stable cylindrical normal shock
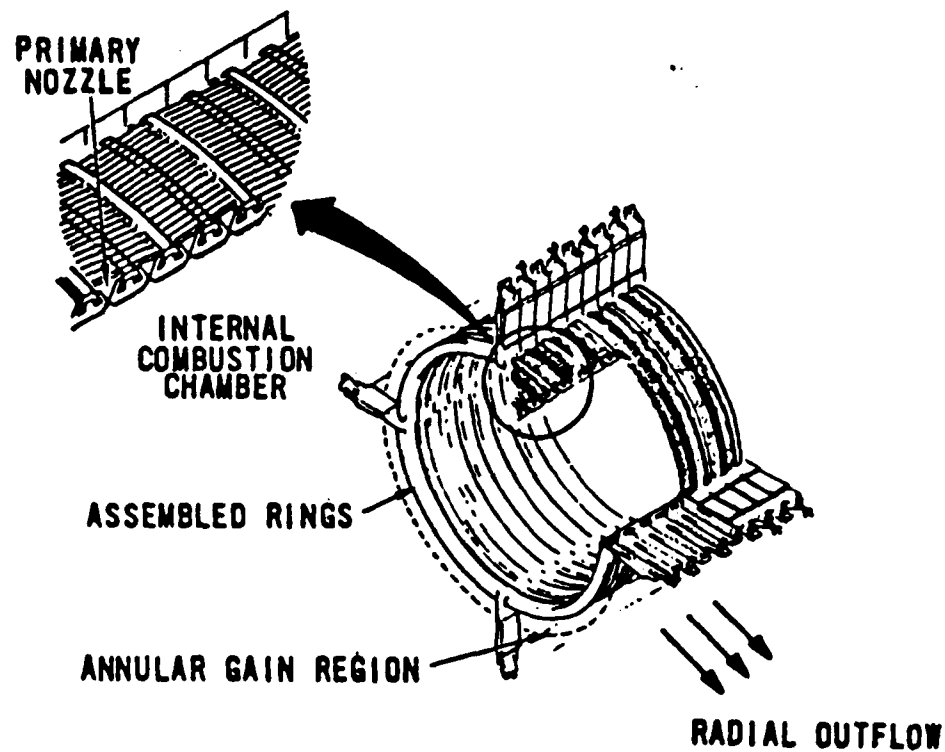
Fig. 1. Radial SDL Schematic.
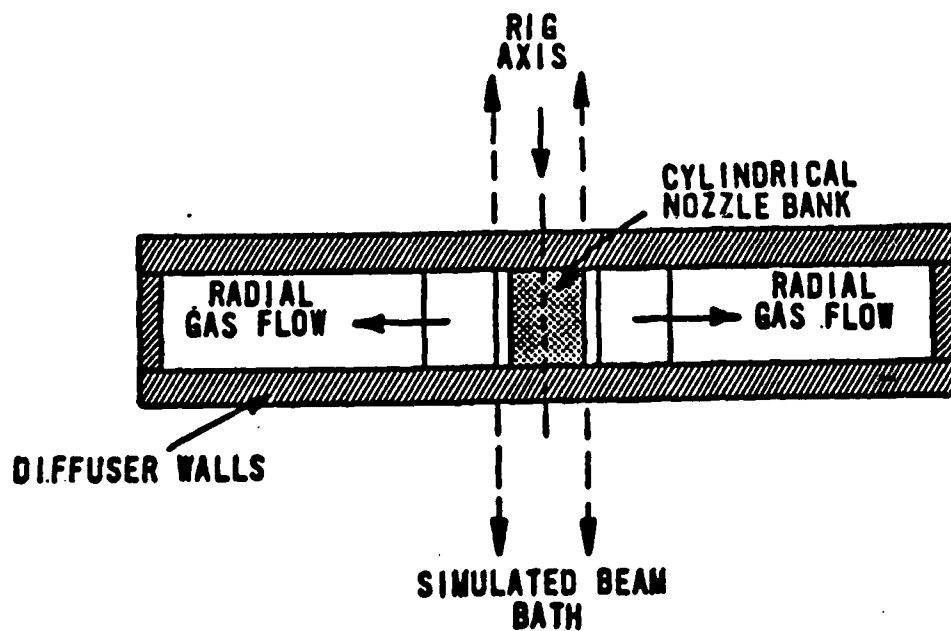
Fig. 2. Radial SDL Cross-Section.

3

CYLINDRICAL NORMAL SHOCK CONFIGURATION
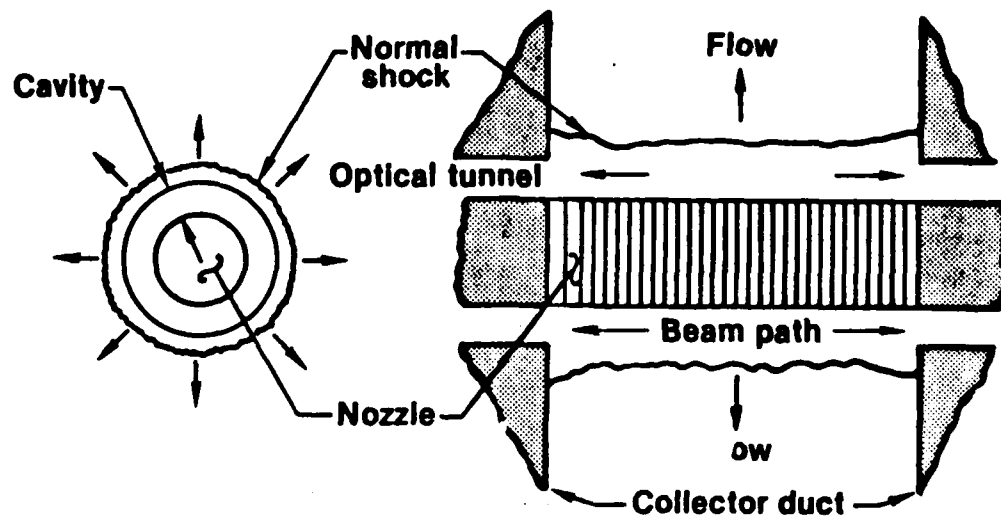
Figure 3. Cylindrical Normal Shock Configuration

4

system (also known as a barrel shock) downstream of the cavity region (Fig. 3). While the theoretical analysis (5) predicted that such a shock system could be established, experimentally it was found that the boundary layer separated and altered the cavity region flow field such that practical stable operation was impossible.

Ortwerth, et al. (7), recognized the need of a diffuser for cylindrical source flow nozzles to control the boundary layers and to provide gradual diffusion of the wake regions. Their experimental results indicated that a functional (operatable) shock-free supersonic optical cavity condition was achieved by using a twenty-four vaned passage diffuser. This work utilized source flow hardware which had a relatively low length-to-diameter ratio. The resulting diffuser passages were of low aspect ratio (less than unity) and consequently end-wall boundary layer control was not needed to achieve the reported 67 percent of normal shock pressure recovery.

Research conducted by Howard and Hasinger (8) at the Air Force Flight Dynamics Laboratory confirmed the need for a diffuser in experiments with both low (0.69) and high (2.85) values of nozzle length-to-diameter ratio. Further experimental results (9,10) indicate that the highest level of diffuser performance (80 percent of normal shock pressure recovery) was achieved by employing a contraction section at the diffuser entrance along with end-wall boundary layer energization. This is consistent with well established supersonic wind tunnel diffuser design criteria (11). Although this design is the most effective method to eliminate start/unstart hysteresis and achieve high diffuser performance, it may not provide optimum system performance due to adverse characteristics of such a contraction on the low Mach and Reynolds number supersonic reacting flow field present in chemical laser systems (12).

5

In 1982, Zumpano and Guile of the United Technologies Research Corporation (UTRC) began an experimental program to evaluate various diffuser configurations. Their approach (12) recognized that the fundamental problems associated with flow diffusion processes in radial flow diffusers are divided into two categories; those associated with boundary layers and those associated with core flow diffusion. Their experiment (13) utilized a one-fifth scale radial cold-flow diffuser (the scale is referenced to the USAF LS-14 chemical laser design). A baseline vaned diffuser configuration was used to conduct parametric evaluations of various diffuser configurations (including a vaneless diffuser) and boundary layer control techniques. Previous UTRC experimental work had shown good agreement between subscale cold-flow experiments and the limited amount of hot-flow diffuser performance data available (14); reported results (15) have shown that temperature distributions are affected the most and velocity distributions the least by the chemical energy heat release present in hot flows.

The cost of parametric experimental research is steadily increasing. Any technique which can reduce the requirement for exhaustive experimental work will result in significant savings of both time and resources. As more advanced computers are developed, the cost of numerical analyses are decreasing and the size and complexity of the problems tackled continues to expand. Numerous research papers have reported that boundary layer and shear layer growth, areas of separated flow, and shock wave formation and interactions can be analyzed using computational techniques validated by comparison with experimental data. Unlike experimental testing, computational analysis is not necessarily restricted by experimental Reynolds number or reacting flow temperature or chemical safety

restrictions. Computational fluid mechanics shows great promise as a technique that can have significant impact on the design of internal flow passages, employing advanced digital computers to simulate the diffuser flowfields at projected operating conditions, but have not yet been validated.

Due to the extremely specialized nature of cylindrical supersonic diffusion lasers, little emphasis has been focused on computational techniques in this area. However, there has been considerable work accomplished with more generic internal flow/nozzle/inlet/diffuser geometries. In 1974, Johnson and Wu (15:i) stated that "no systematic study of wind tunnel diffusers has been found." A search of the relevant technical literature still supports that comment. The bulk of design and performance knowledge has been built empirically over the years since Neumann and Lustwerk's 1947 paper (11).

From a computational standpoint, there are few significant differences between a supersonic wind tunnel diffuser, a supersonic engine inlet/diffuser, and a cylindrical laser diffuser. One difference is that the terminal shock in the cylindrical laser diffuser occurs at considerably higher Mach numbers than in inlets. Another is that wind tunnel diffusers and engine inlets/nozzles/diffusers feature relatively uniform core flow regions, while the nature of energy generation in a cylindrical laser requires the mixing of supersonic flows from numerous nozzles across the inflow region. A final, notable difference stems from the extremely low pressures (around 10 torr) necessary for chemical laser energy production resulting in relatively low diffuser entrance Reynolds numbers, whereas engine inlet/diffuser flows characteristically exhibit high Reynolds numbers. Numerical simulation of complex supersonic diffusion laser

7

flowfields must therefore encompass core flow mixing, inviscid/viscous shock-boundary layer interactions and the resulting large regions of separation and recirculation. Most of all, it must allow for dynamic time-variant analyses of rapid shock motion in the diffuser in response to changes in exit plane back-pressure conditions.

Steady transonic flow in nozzles has received considerable attention and theoretical treatment (16; 17:180-214; 18:131-207; 19:79-85). Messiter and Adamson (20:97-108) presented systematic solutions for inviscid flows with a shock in a nozzle, employing methods of matched asymptotic expansions. The same approach was used to study unsteady two-dimensional transonic flows in which large amplitude shock motion was allowed (21;1240-1247) and the boundary layers were included (22). Liou (23) continued this matched-asymptotic expansion approach with steady transonic flow in two-dimensional and annular diffusers, allowing for the possibility of shock-induced separation in the case of sufficiently strong shocks under the assumption that the separation bubble size was no larger than the boundary layer thickness.

Buggeln, et al. (24) utilized a consistently-split linearized block implicit technique to solve the finite difference analogs to the set of governing partial differential equations for a three-dimensional viscous supersonic flow through an inlet. They stated that "although use of the full three-dimensional Navier-Stokes equations would provide the necessary generality to predict the flow field in an inlet, the required computer run time and storage indicate that such a procedure should be used only if no suitable alternative exists." Their procedure solved the parabolized Navier-Stokes equations obtained by making the following fundamental assumptions: the streamwise or primary flow direction can be identified and

8

in that direction all diffusion terms can be neglected. The accuracy of these approximations depends on several factors, including the geometry, the coordinate system, and the characteristic Reynolds number of the flow. Neglecting streamwise diffusion is obviously invalid in the presence of large streamwise recirculation zones. Results of their computations gave good agreement with experimentally measured pressure values along the surfaces of the Mach number 3.0 inlet for the cases where the reduced form of the Navier-Stokes equations applied.

Liu, et al. (25) continued the effort to study terminal shock type flows in various flight regimes occurring in a diffuser/inlet model. Employing a mixing-length turbulence closure model, their numerical scheme was also based on a linearized block implicit approach and carried out numerous high Reynolds number calculations, including supersonic flow with a terminal shock. Their numerical results compared well with corresponding experimental wall static pressure data. These authors also extended their effort (26) to include shock tracking adaptive grid schemes. Additionally, calculations were carried out to study the dynamic response of shock waves occurring in a transonic inlet to externally imposed back pressure oscillations.

Concurrently, Talcott and Kumar (27) employed both MacCormack's explicit and implicit-explicit (28,29) methods with an algebraic, two-layer eddy viscosity turbulence model, to study the flow through three inlet/ diffuser configurations with terminal shock systems. In their numerical result, the use of bleed was required to stabilize the shock location. They also commented that the fully explicit method required too many time steps to converge due to the large regions of subsonic flow and the highly refined grid used near the solid boundaries to resolve the viscous effects.

Knight (30) had also employed MacCormack's explicit algorithm with the two-layer equilibrium turbulent eddy viscosity model of Cebici-Smith (31,32) to model the flowfields of two-dimensional high speed inlets. His work verified the ability of a compressible Navier-Stokes code with a coordinate transformation package to qualitatively predict the complex phenomenon of realistic high speed inlets. This research was consistent with the aforementioned efforts in studying relatively high Reynolds number flows with relatively low terminal shock Mach numbers (<2.5).

Hsieh, et al. (33) solved the Navier-Stokes equations implicitly, employing a more complex k-ω equation eddy viscosity model for turbulence closure, to study the response of a two-dimensional ramjet inlet to high-amplitude pressure fluctuations and the attendant large flow separation regions. Maximum terminal shock Mach number was approximately 1.6.

All of these previous efforts demonstrated that reasonable solutions to the governing Navier-Stokes equations could be obtained for high Reynolds number, relatively low terminal shock Mach number (<2.5) flows. Recent interest in hypersonic engine inlet performance has resulted in an extension of the methodology to high Mach number flow domains. Rose (34) used MacCormack's algorithm in computational simulations of a Mach 5 inlet configuration. Reddy, Benson, and Weir (35) validated a time-marching full Navier-Stokes code employing a Baldwin-Lomax (36) algebraic turbulence model for a Mach 5 inlet. Solutions have not been achieved for the low Reynolds number, high terminal shock Mach number (>2.5) cases involving cross-flow mixing characteristic of radial supersonic diffusion lasers (12). Some numerical research (3,4,6,37,38) has been done to study flow behavior from the source nozzles through the optical cavity, but these efforts have not been successfully extended through the length of the diffuser.

Additionally, the majority of this work has dealt with the laminar flow from a single nozzle or laminar mixing from two nozzles (6). Hasen (39) attempted numerical solutions to the unsteady Navier-Stokes equations for flow through a two-dimensional, supersonic laser diffuser channel in 1982 and 1983, concurrent with the beginning of this research. His simulation assumed uniform diffuser inflow conditions and achieved stable solutions only by artificially "freezing" the eddy viscosity turbulence models. He concluded that the Baldwin-Lomax turbulence model (36) caused dynamic flow effects in the boundary layer - shock interaction zone which prevented a steady, stable two-dimensional solution. A full Navier-Stokes solution for interactions of multiple source flow nozzles, inviscid/viscous shock-boundary layer interactions at high terminal shock Mach numbers, and the resulting large separation and recirculation regions is necessary to simulate SDL diffuser performance.

1.2 RESEARCH OBJECTIVES

The primary objective of this research is the development of a numerical method capable of accurately predicting cold flow radial SDL flowfields that contain highly viscous regions, core flow mixing, and complex shock structures. Vaneless axisymmetric diffusers will be studied as they are also the focus of current experimental research efforts. The experimental data of Zumpano, Guile, Haas, and Sobel (13), is the validating basis for this research effort. Data in this reference is for diffuser entrance flow at a mean Mach number of 2.55 at a unit Reynolds number of 1.63 million per foot with terminal shock Mach numbers in the range above 3.5. The vaneless diffuser geometric configuration is shown schematically in Figures 4 and 5. Figure 6 provides a photograph of the experimental source nozzle array. Figure 7 provides a schematic of the source nozzle

11

assemble and diffuser entrance. Turbulence modeling and outflow boundary conditions (the flow downstream of the terminal shock is subsonic and therefore the outflow boundary affects the flow throughout the diffuser) will be concentrated on in the present investigation in order to achieve the desired goal of validating an accurate predictive technique for radial SDL diffuser performance.

SCHEMATIC DRAWING OF BASELINE DIFFUSER CONFIGURATION

DIMENSIONS IN CENTIMETERS

VIEWED ALONG SIMULATED BEAM PATH
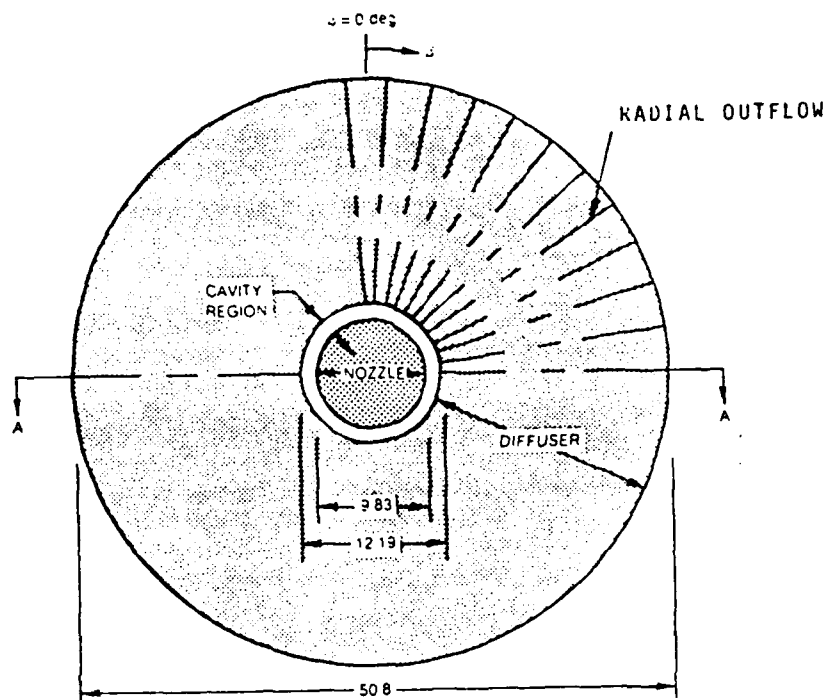
Figure 4a   Schematic Drawing of Baseline Diffuser Configuration, Viewed Along Simulated Beam Path.

SECTIONAL VIEW AA
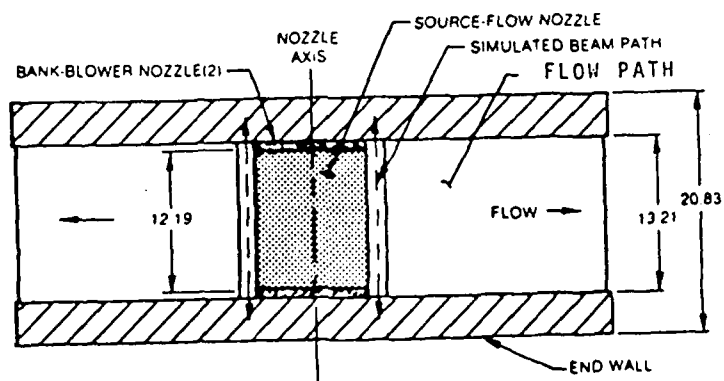
Figure 4b   Schematic Drawing of Baseline Diffuser Configuration, Sectional View AA.

VANELESS DIFFUSER CONFIGURATION
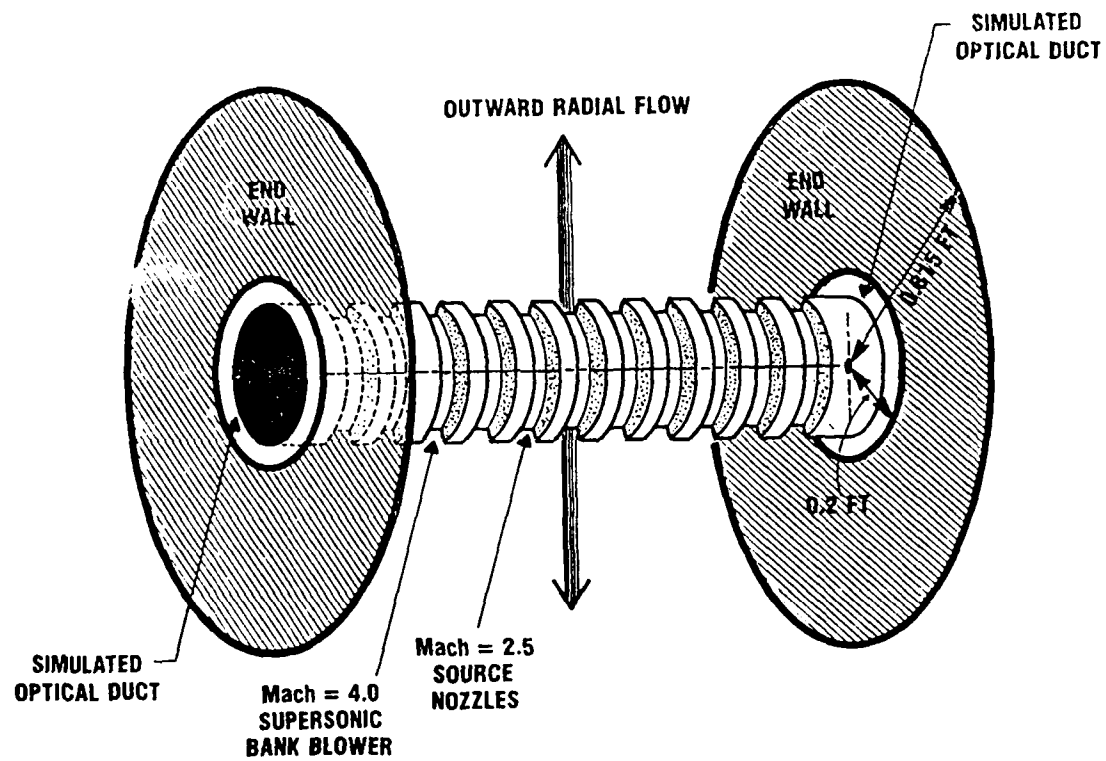
Figure 5. Three-Dimensional Schematic Drawing of
Diffuser/Nozzle Configuration
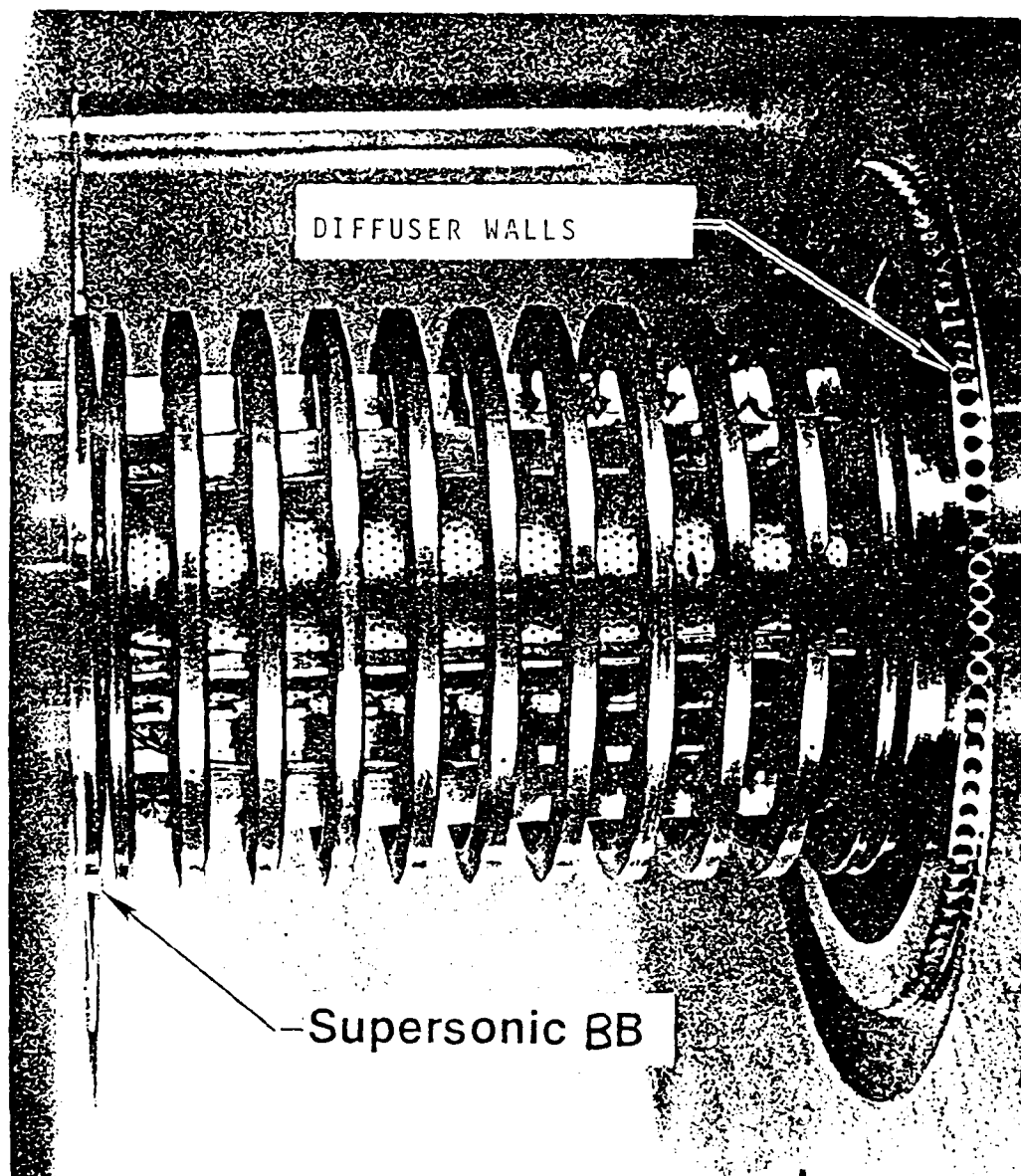
Figure 6. Photograph of Experimental Nozzle Array (Ref. 13)

Diffuser Line of Symmetry

—14.7 cm—

PARALLEL SIDE
WALLS

FLOW

OPTICAL CAVITY

PURGE FLOW

SUPERSONIC
BANK
BLOWER

10 SUPERSONIC NOZZLES

SUPERSONIC
BANK
BLOWER

source nozzle
centerline

Figure 7   Cross-Sectional Schematic Drawing of
Diffuser/Nozzle Configuration.

16

CHAPTER II

MATHEMATICAL DESCRIPTION OF THE FLOW STRUCTURE

2.1 GOVERNING EQUATIONS

The Navier-Stokes equations are the governing equations for flows containing the shock and viscous phenomena of interest. These equations are the conservation equations for mass, momentum, and energy. The gasses involved are assumed to be single component, have constant specific heats, and obey the calorically perfect gas equation of state:

$$P = \rho RT \qquad (2\text{-}1)$$

The Eulerian formulation is usually applied to the problem of interest in computational fluid mechanics. This method involves a fixed control volume that is specified relative to a given coordinate system. Properties of the fluid are then specified as functions of both time and space. The conservation equations are derived by using this frame of reference.
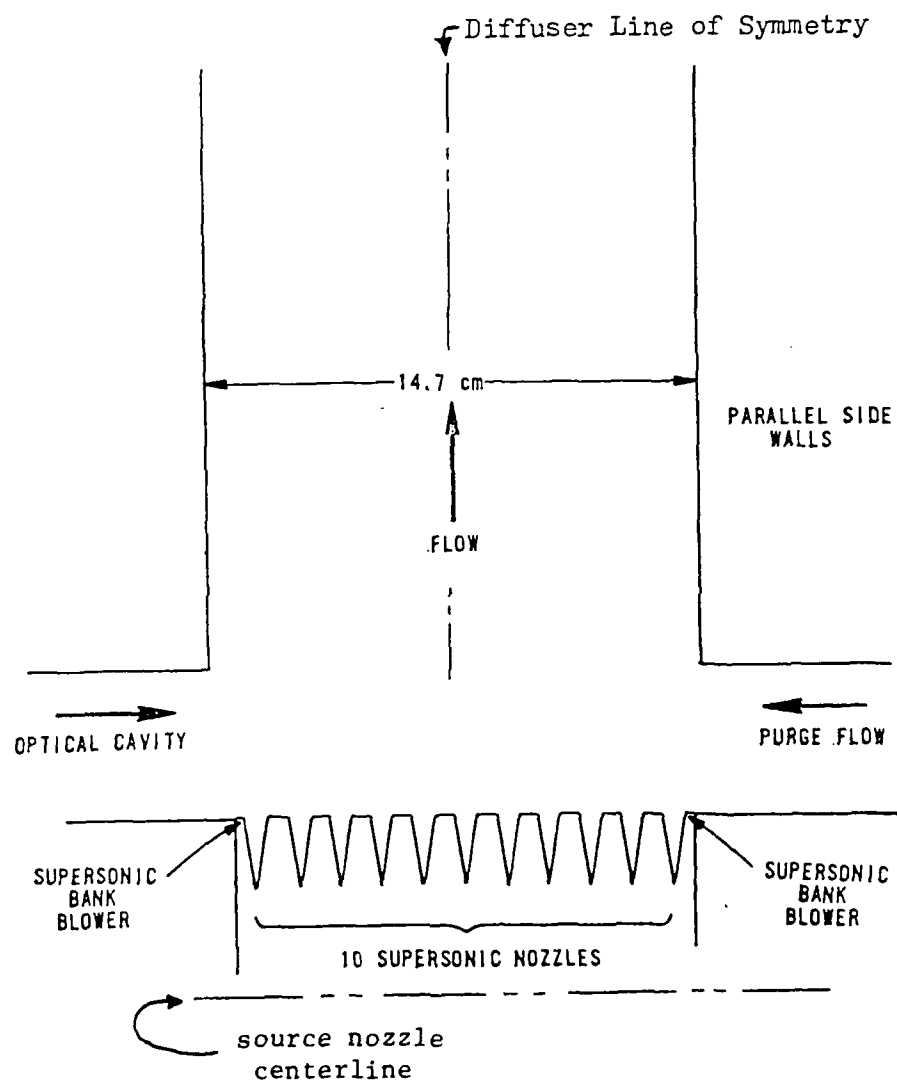
CONSERVATION OF MASS

For a given system in which matter is neither created or destroyed, the law of mass conservation can be written as

$$\iiint_V (\frac{\partial \rho}{\partial t} + \nabla \cdot \rho \vec{u}) \, dV = 0 \qquad (2\text{-}2)$$

where V is an arbitrary volume fixed in space.

CONSERVATION OF MOMENTUM

For a given system, the law of momentum conservation states that the rate of change of momentum is equal to the sum of the external forces acting on the control volume. If body forces are neglected, this law can be written as:

17

$$\iiint\limits_{V} [\frac{\partial(\rho\vec{u})}{\partial t} + \nabla \cdot (\rho\vec{u})\ \vec{u}]\ dV = \iiint\limits_{V} (\nabla \cdot \bar{\bar{S}})\ dV \qquad (2\text{-}3)$$

The variable $\bar{\bar{S}}$ denotes a stress tensor involving pressure and viscous forces which act on the fluid.

CONSERVATION OF ENERGY

The law of conservation of energy states that for a given system which does not contain any internal heat sources, the rate of change of the total energy of the system is equal to the rate at which heat is added into the system plus the rate at which work is done on the system by viscous and pressure forces. This can be stated as

$$\iiint\limits_{V} [\frac{\partial(\rho e)}{\partial t} + \nabla \cdot (\rho e)\ \vec{u}]\ dV = \iiint\limits_{V} (\nabla \cdot \vec{u} \cdot \bar{\bar{S}} - \nabla \cdot \vec{q})\ dV \qquad (2\text{-}4)$$

Since these conservation equations are valid for any arbitrary volume V; by the limiting process of infinitessimal control volumes:

$$\frac{\partial\rho}{\partial t} + \nabla \cdot \rho\vec{u} = 0 \qquad (2\text{-}5)$$

$$\frac{\partial(\rho\vec{u})}{\partial t} + \nabla \cdot (\rho\vec{u})\ \vec{u} - \nabla \cdot \bar{\bar{S}} = 0 \qquad (2\text{-}6)$$

$$\frac{\partial(\rho e)}{\partial t} + \nabla \cdot (\rho e)\ \vec{u} + \nabla \cdot \vec{q} - \nabla \cdot (\vec{u} \cdot \bar{\bar{S}}) = 0 \qquad (2\text{-}7)$$

It should be noted that these equations are written in conservative form where, for the two-dimensional and axisymmetric flows of interest, the applicable dependent variables are ρ, ρu, ρv, and ρe. As shown by Roache (40), finite differencing approximations derived from this conservative form allows the finite difference equations to preserve the Gauss divergence property of the continuum equations. This form allows a balance between the flux quantities and accumulation rates for a small control volume. Roache

18

also states that the Rankine-Hugoniot shock relations were derived using the conservative form. Thus, shock jump conditions are automatically satisfied, since some conservative variables are continuous across the shock and need no special treatment because of discontinuities. This approach is known as shock capturing or shock smearing. The conservation form of the equations then allows the finite difference formulation to satisfy the physical laws across a control surface, not merely in some discrete limit as Δx, Δy, and Δt approach zero. Since the flowfields of interest are turbulent, the solution of the conservation equations must take into account the effects of the random fluctuations of the dependent variables inherent to turbulent flows. In accounting for these effects, a temporal averaging process will decompose the dependent variables into mass averaged variables (41,42). The usual conventions of a repeated subscript indicating summation over the entire range of indices and a comma representing partial differentiation will be used to make the equations compact. Cartesian tensors are used to allow working directly with the physical components, while still being applicable to the 2-D and axisymmetric cases of interest. The conservation equations (2-5) through (2-7) can then be written as:

$$\rho,_t + (\rho u_j),_j = 0 \qquad (2\text{-}8)$$

$$(\rho u_i),_t + (\rho u_i u_j + \delta_{ij} P - \tau_{ij}),_j = 0 \qquad (2\text{-}9)$$

$$(\rho e),_t + (\rho e u_j + \dot{q}_j - u_i \tau_{ij}),_j = 0 \qquad (2\text{-}10)$$

where the stress tensor S_{ij} has been expanded in the form:

$$S_{ij} = - P\delta_{ij} + \tau_{ij} \qquad (2\text{-}11)$$

19

The dependent variables in the conservation equations can be expanded into the following form:

$$u = \bar{u} + u' \tag{2-12a}$$

$$v = \bar{v} + v' \tag{2-12b}$$

$$P = \bar{P} + P' \tag{2-12c}$$

$$\rho = \bar{\rho} + \rho' \tag{2-12d}$$

$$e = \bar{e} + e' \tag{2-12e}$$

In these expansions the barred variables represent time averaging over a time interval that is long compared to turbulent eddy fluctuations, yet small compared to macroscopic flow changes. The primed variables represent fluctuations due to the turbulent nature of the flow. As discussed by Chapman (43), this time averaging approach is valid since the frequencies of most unsteady flows of interest are a factor of 10 to 100 below the mean frequency of turbulent eddies.

If the dependent variables u, v, and e are mass averaged, and ρ and P are mean (time averaged) state variables, then the conservation equations can be written in the form of mean flow equations as:

$$\bar{\rho}_{,t} + (\bar{\rho}\bar{u}_j)_{,j} = 0 \tag{2-13}$$

$$(\bar{\rho}\bar{u}_i)_{,t} + [(\bar{\rho}\bar{u}_i\bar{u}_j) + \bar{P}\delta_{ij} - (\bar{\tau}_{ij} - \overline{\rho u_i' u_j'})]_{,j} = 0 \tag{2-14}$$

$$(\bar{\rho}\bar{e})_{,t} + [\bar{\rho}\bar{e}\bar{u}_j + \bar{q}_j + \overline{\rho u_j' e'} - \bar{u}_i(\bar{\tau}_{ij} - \overline{\rho u_i' u_j'})]_{,j} = 0 \tag{2-15}$$

where a higher order mean energy dissipation term in u_i' has been neglected in the energy equation (2-15).

The term $[-\bar{\rho}\overline{u_i' u_j'}]$ is known as the Reynolds stress. It represents a momentum transfer caused by turbulent fluctuations present in the flowfield. This stress term can be written as an apparent stress caused by the turbulent nature of the flow:

$$\tau_{ij}\Big|_{turb} = -\bar{\rho}\overline{u_i' u_j'} \tag{2-16}$$

The mean stress term can be expanded into its dilutational and roational components as:

$$\bar{\tau}_{ij} = \lambda \bar{u}_{k,k} \delta_{ij} + \mu (\bar{u}_{i,j} + \bar{u}_{j,i}) \tag{2-17}$$

Assuming isotropy, the turbulent stress term can then be approximated in analogous form as:

$$\tau_{ij}\Big|_{turb} = \lambda_t \bar{u}_{k,k} \delta_{ij} + \epsilon (\bar{u}_{i,j} + \bar{u}_{j,i}) \tag{2-18}$$

where λ_t and ϵ are the turbulent viscosity coefficients of the flow. The coefficient ϵ is known as the eddy viscosity, and is analagous to the molecular viscosity coefficient μ. However, λ_t and ϵ are more a property of the flow dynamics, whereas μ is only a property of the fluid. Combining the mean and turbulent stress terms, an overall stress term can be written as:

$$\tau_{ij}\Big|_{total} = (\lambda + \lambda_t) \bar{u}_{k,k} \delta_{ij} + (\mu + \epsilon) (\bar{u}_{i,j} + \bar{u}_{j,i}) \tag{2-19}$$

In the energy equation an additional unsteady term appears. This term is by nature an apparent heat flux caused by the fluctuations inherent to turbulent flow and can be written as:

$$\bar{q}_j\Big|_{turb} = \bar{\rho}\overline{u_j' e'} \tag{2-20}$$

21

If the heat flux term $\bar{q}_j$ is defined by the Fourier's law of heat transfer:

$$\bar{q}_j = -k\tilde{T},_j = -(C_P\mu/Pr)\;\tilde{T},_j \tag{2-21}$$

then by the former analogy $\bar{q}_j\big|_{turb}$ can be written as:

$$\bar{q}_j\big|_{turb} = -(C_P\epsilon/Pr_t)\;\tilde{T},_j \tag{2-22}$$

where again ϵ is the eddy viscosity coefficient, and Pr_t is the turbulent Prandtl number of the flow. Combining these two heat fluxes, a total heat flux can be written as:

$$\bar{q}_{j\;total} = -C_P\;(\mu/Pr + \epsilon/Pr_t)\;\tilde{T},_j \tag{2-23}$$

The mean conservation equation equations can then be written in the following form, where the overbars on the terms are dropped for convenience, and where the values of the shear stresses and heat fluxes are the total values (42):

$$\rho,_t + (\rho u_j),_j = 0 \tag{2-24}$$

$$(\rho u_i),_t + [(\rho u_i)u_j + P\delta_{ij} - \tau_{ij}],_j = 0 \tag{2-25}$$

$$(\rho e),_t + [(\rho e)u_j + \dot{q}_j - u_i\;\tau_{ij}],_j = 0 \tag{2-26}$$

Since the flowfields of interest are either two-dimensional or axisymmetric in nature, the mean conservation equations can be written in the following compact vector form:

$$\frac{\partial U}{\partial t} + \frac{\partial F}{\partial X} + \frac{1}{r^{j_\circ}}\frac{\partial(r^{j_\circ}G)}{\partial r} = j_\circ \cdot \frac{H}{r^{j_\circ}} \tag{2-27}$$

where $j_0 = 0$ or 1 for either the two-dimensional or axisymmetric case, respectively, and

$$U = \begin{pmatrix} \rho \\ \rho u \\ \rho v \\ \rho e \end{pmatrix} \qquad ; \qquad F = \begin{pmatrix} \rho u \\ \rho u^2 - \sigma_{xx} \\ \rho uv - \tau_{xr} \\ \rho ue - q_x - u\sigma_{xx} - v\tau_{xr} \end{pmatrix}$$

(2-28)

$$G = \begin{pmatrix} \rho v \\ \rho uv - \tau_{xr} \\ \rho v^2 - \sigma_{rr} \\ \rho ve - q_r - u\tau_{xr} - v\sigma_{rr} \end{pmatrix} \qquad ; \qquad H = \begin{pmatrix} 0 \\ 0 \\ -\sigma_H \\ 0 \end{pmatrix}$$

where

$$\sigma_{xx} = -P + (\lambda + \lambda_t) \ \text{div} \ \vec{V} + 2(\mu + \epsilon) \ \frac{\partial u}{\partial x} \tag{2-29}$$

$$\sigma_{rr} = -P + (\lambda + \lambda_t) \ \text{div} \ \vec{V} + 2(\mu + \epsilon) \ \frac{\partial v}{\partial r} \tag{2-30}$$

$$\sigma_H = -P + (\lambda + \lambda_t) \ \text{div} \ \vec{V} + 2(\mu + \epsilon) \ \frac{v}{r} \tag{2-31}$$

$$\tau_{xr} = (\mu + \epsilon) \ (\frac{\partial u}{\partial r} + \frac{\partial v}{\partial x}) \tag{2-32}$$

$$q_x = -C_P \ (\frac{\mu}{Pr} + \frac{\epsilon}{Pr_t}) \ \frac{\partial T}{\partial x} \tag{2-33}$$

$$q_r = -C_P \ (\frac{\mu}{Pr} + \frac{\epsilon}{Pr_t}) \ \frac{\partial T}{\partial r} \tag{2-34}$$

and

$$\text{div} \ \vec{V} = \frac{\partial u}{\partial x} + \frac{\partial v}{\partial r} + j_0 \ \frac{v}{r} \tag{2-35}$$

The coefficient of viscosity μ for air can be assumed to vary according to Sutherland's law (41):

$$\mu = (2.27 \cdot 10^{-8})T^{1.5}/(T + 198.6) \ (lbf - sec/ft^4) \tag{2-36}$$

23

The second coefficient of viscosity is assumed to be given by the Stokes Hypothesis (44):

$$(\lambda + \lambda_t) = -2/3 \; (\mu + \epsilon) \tag{2-37}$$

The governing equations for the problem of interest now consist of the four conservation equations in flux vector form (eq. 2-27) with four unknown dependent variables ρ, ρu, ρv, and ρe. The perfect gas law is used to define the pressure in terms of these conservative variables, and a model of eddy viscosity must be introduced to accomplish the "turbulent closure."

For numerical computation in a transformed (ξ, η) Cartesian plane, the matrix form of the conservation equations (2-27) can be written as:

$$\frac{\partial U}{\partial t} + [\xi_x \frac{\partial F}{\partial \xi} + \frac{1}{r^{j_\circ}} \xi_r \frac{\partial (r^{j_\circ} G)}{\partial \xi}]$$

$$+ [\eta_x \frac{\partial F}{\partial \eta} + \frac{1}{r^{j_\circ}} \eta_r \frac{\partial (r^{j_\circ} G)}{\partial \eta}] = j_\circ \frac{H}{r^{j_\circ}} \tag{2-38}$$

where ξ and η are now the independent variables, and the transformation metrics ξ_x, ξ_r, η_x, and η_r are obtained numerically from a mapping procedure. Equation (2-38) is actually in chain-rule conservation form due to the varying coefficients in front of the derivatives, and also due to the source term in the axisymmetric case.

2.2 BOUNDARY AND INITIAL CONDITIONS

Boundary and initial conditions must be specified to determine a unique solution of the conservation equations that govern the flowfields of interest. These conditions must be carefully specified, since many flow features such as shock waves, boundary layers, and recirculation are uniquely determined by the boundary conditions. For the solution of an axisymmetric supersonic flowfield through a diffuser, the domain of interest

24
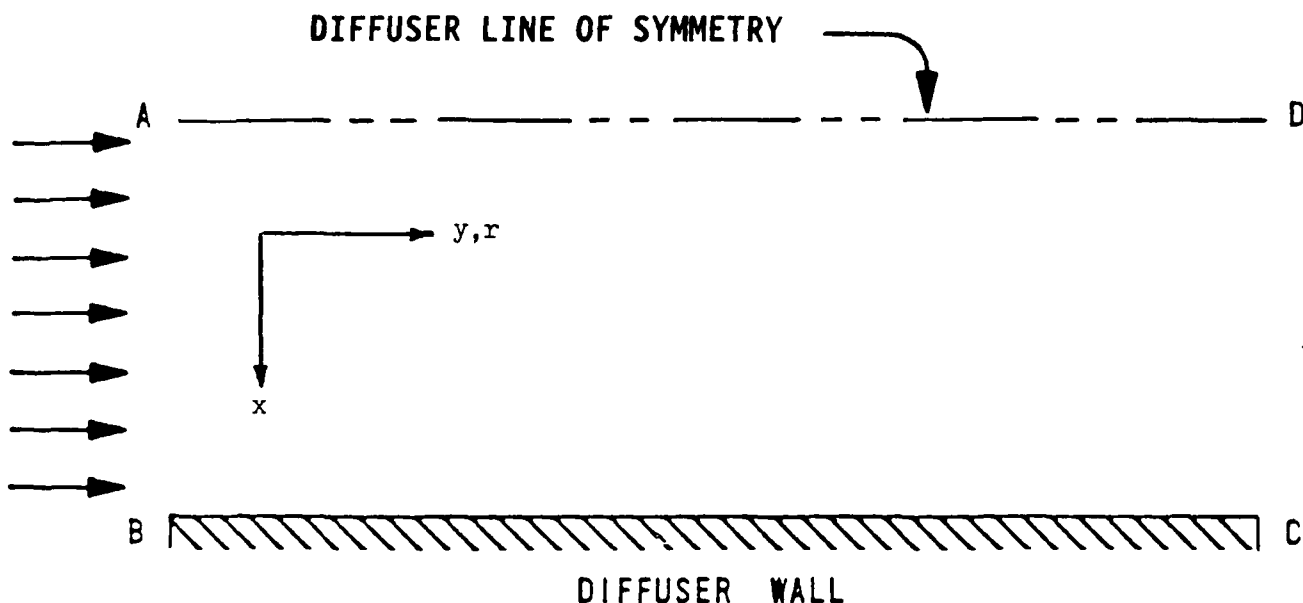
Figure 8. Computational Domain

can be defined as shown in Figure 8. Only one-half of the total diffuser

flowfield needs to be considered due to the axis of symmetry on the diffuser

centerline. The specific boundary conditions pertinent to this problem will

be described in the remainder of this chapter.

THE UPSTREAM BOUNDARY

Inflow conditions on the upstream diffuser boundary (AB) are completely

specified by interpolation of experimental data. Velocity, pressure, and

temperature profiles known experimentally from the data of Zumpano (12) on

this boundary fix ρ, ρu, ρv, and ρe for the problem solution.

THE DOWNSTREAM BOUNDARY

The downstream boundary (CD) is unique in that although the exit plane

back-pressure is known, no rigorous assumptions can be made about either the

variables or their gradients across the entire span of the boundary unless

the boundary is placed a great distance downstream. However, this would

25

dramatically increase the size of the domain and the required computational time. In this case a no change condition

$$\frac{\partial f}{\partial y}\bigg|_{CD} = 0 \qquad (2\text{-}40)$$

can be assumed, where f denotes the primitive variables ρ, u, v, and T. However, for the case under study the downstream boundary is fairly close to the inflow boundary, at the very least a gradient in velocity in the radial direction must exist. In this case, an extrapolation method can be reasonably applied. One such method is to assume that outside of the boundary-layer region along the diffuser wall, pressure can be specified along the outflow boundary and gradients in the remaining variables based on the conservation laws and geometry are appropriate. This condition is reasonable if the gradients at this boundary are not severe, as would be true if a strong shock wave exits the boundary. Inside the boundary-layer region no conditions may be specified or the problem will be over specified.

THE LINE OF SYMMETRY

The boundary (AD) is a line of symmetry with no mass or energy flux across it. Therefore physics dictates the following boundary conditions:

$$u\bigg|_{AD} = 0 \qquad (2\text{-}41)$$

$$\frac{\partial \rho}{\partial x}\bigg|_{AD} = 0 \qquad (2\text{-}42)$$

$$\frac{\partial v}{\partial x}\bigg|_{AD} = 0 \qquad (2\text{-}43)$$

$$\frac{\partial T}{\partial x}\bigg|_{AD} = 0 \qquad (2\text{-}44)$$

DIFFUSER WALLS

The diffuser walls (BC) are considered to be no-slip, impermeable boundaries. This assumption gives the conditions that:

$$u\Big|_{wall} = 0 \tag{2-45a}$$

$$v\Big|_{wall} = 0 \tag{2-45b}$$

Since the stainless steel diffuser walls consist of material with a thermal conductivity much greater than that of the contained fluid, the diffuser walls are assumed to be at a constant temperature:

$$T\Big|_{wall} = constant \tag{2-46}$$

This wall temperature can be easily determined as the adiabatic wall temperature achieved across the turbulent boundary layer. It is defined by the expression:

$$T_{aw} = T_\infty(1 + Pr^{1/3}(\frac{\gamma-1}{2}) M_\infty^2) \tag{2-47}$$

The pressure on the diffuser wall is unknown, but it can be approximated by applying the degenerate form of the appropriate normal momentum equation along the surface to obtain the following:

$$\frac{\partial p}{\partial n}\Big|_{wall} = \frac{\partial \tau_{sn}}{\partial s}\Big|_{wall} \tag{2-48}$$

In this expression n is the direction normal to the wall surface, and s is the direction parallel to the surface.

INITIAL CONDITIONS

Since the governing equations contain time dependent terms, initial conditions must be specified before the solution process can begin. The specification of these initial conditions is somewhat arbitrary in nature, although steep gradients must be avoided to prevent numerical divergence during the solution process. Since there is a significant portion of supersonic flow, the incoming flow profiles will have a significant effect on the solution in the whole computational domain. Given the extreme complexity of the inflow profile, an initial guess as to the solution based on a one-dimensional inviscid normal shock analysis for a uniform flow at an average of the inflow Mach number profile was imposed on the core flow. This was patched to an asymptotic initial guess for the nature of the boundary layer with the constraint that no pressure gradient exist across the interface between the boundary-layer and the wall energizer flow, and likewide between the wall energizer flow and the core flow. Details are discussed in the section on initial condition implementation of Chapter IV.

CHAPTER III

NUMERICAL PROCEDURE

The numerical procedure consists of solving the governing equations with applicable boundary and initial conditions through the use of appropriate finite difference techniques on a high-speed computer. This procedure can be broken down into several elements which include the computational domain, the finite difference algorithm, and the respective convergence criteria. Each of these areas will be discussed in this chapter.

3.1 COORDINATE SYSTEM

DOMAIN OF COMPUTATION

The physical domain of computation consists of a rectangular area defined by orthogonal coordinates (x,r) as shown in Figure 9. The mesh consists of IL points on the x axis and JL points on the r axis, where IL and JL are dependent on the extent of the physical domain.

MESH STRETCHING

In order to obtain an accurate numerical solution of a viscous flowfield, the mesh spacing must be much finer in areas containing relatively high gradients of the flow properties such as velocity, density, and temperature. In the diffuser, these high gradient areas include the boundary layers on the diffuser walls and the shear layer present due to the application of a bank blower to energize the boundary layer, as well as at the location of the normal shock/viscous interactions. This stretching is accomplished through the use of a patched exponential stretching scheme of the following form:

29
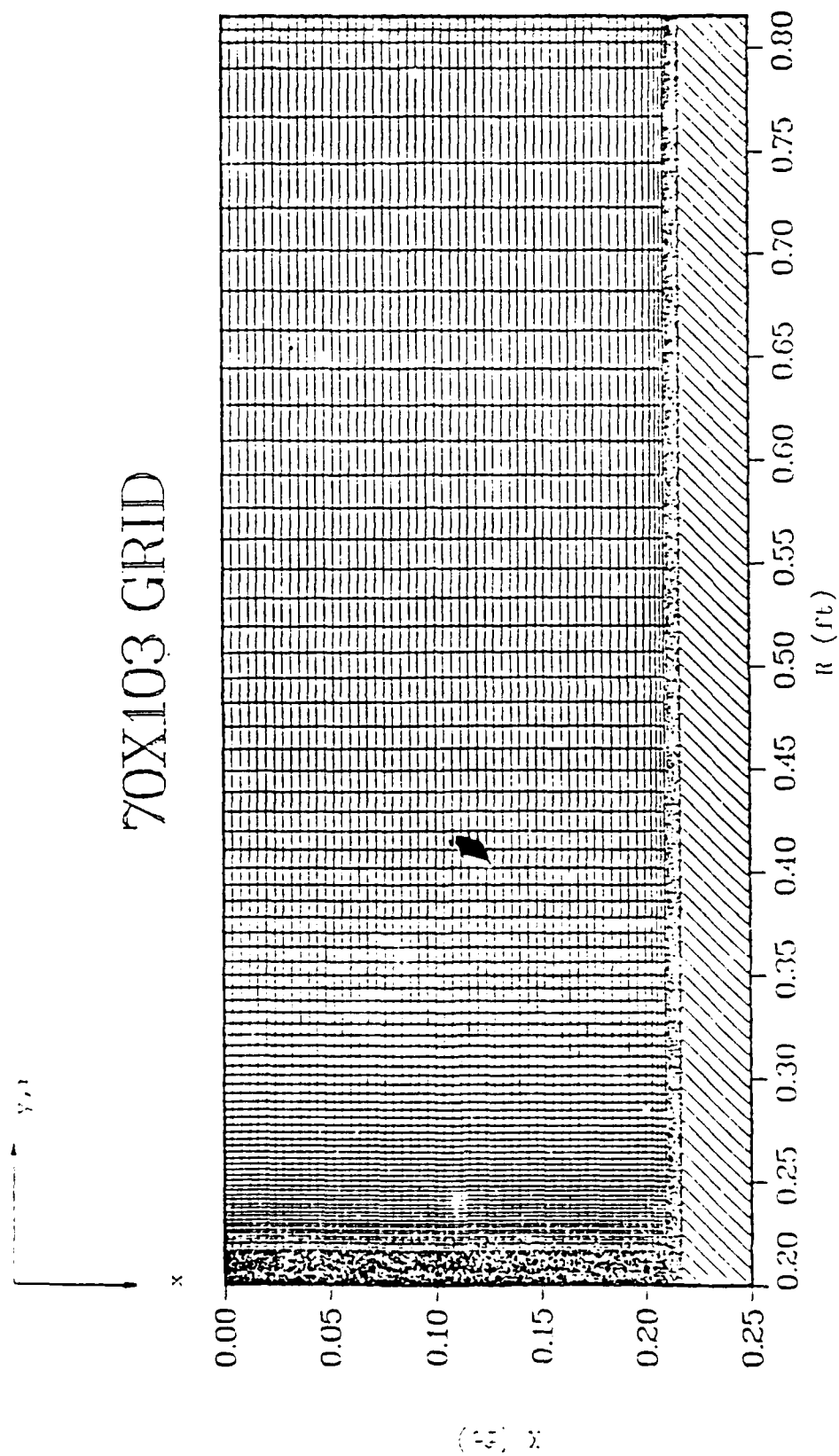
Figure 9. Computational Grid.

$$x(i) = L_m \frac{(e^{C\xi(i)} - 1)}{(e^C - 1)} \qquad\qquad \text{for } i = 1,N \qquad (3\text{-}1)$$

where L_m and ξ are defined as shown in Figure 10. The constant C is determined by the minimum spacing Δx_{min} desired for the mesh next to the wall boundary. The selection of Δx_{min} was based on analysis of the boundary-layer thickness along the diffuser wall to ensure that at least one grid point was located within the viscous (or laminar) sublayer (45). Applying the desired Δx_{min} to equation (3-1) gives

$$C = \frac{1}{\Delta\xi} \, Log_e \, (1 + \frac{\Delta x_{min}}{L_m} \, (e^C - 1) \qquad\qquad (3\text{-}2)$$

The value of C is then obtained throught the use of an iterative Aitken extrapolation technique (46).

This mesh stretching procedure is applied in the x-direction away from the diffuser wall where the major boundary layer/bank blower effects are present. Twenty points are applied in this region. From that point a uniform grid is employed in the x-direction to resolve the approximate sine wave profile of the incoming flow generated by the supersonic source nozzles. A total of fifty grid points are employed; ten for each of the five nozzles in the half plane of the diffuser flowfield up to the line of symmetry. This relatively coarse grid spacing was deemed sufficiently accurate to resolve critical flow behavior (47,48) while maintaining computational efficiency.

The exponential mesh stretching procedure is also employed in the radial direction to provide maximum resolution of the nozzle mixing interactions and strong shock/viscous interactions located not far downstream of the entrance to the diffuser.

31

COORDINATE TRANSFORMATION

The physical domain, as shown in Figure 9, is mapped to a unit square in the computational plane as shown in Figure 11. The constant ξ lines are aligned parallel to the line of symmetry and the constant η lines are in the direction normal to the line of symmetry. The numerical algorithm operates on this coordinate system using the transformed conservation equations (2-38). Care must be taken in generating the physical mesh so that smoothness of the transformation coefficients (ξ_x, ξ_r, η_x, and η_r) is retained in order to reduce numerical errors caused by the numerical approximation of these coefficients in the mesh configuration. In this application, the grids employed were purely rectangular, so both ξ_r and η_x were equal to zero.
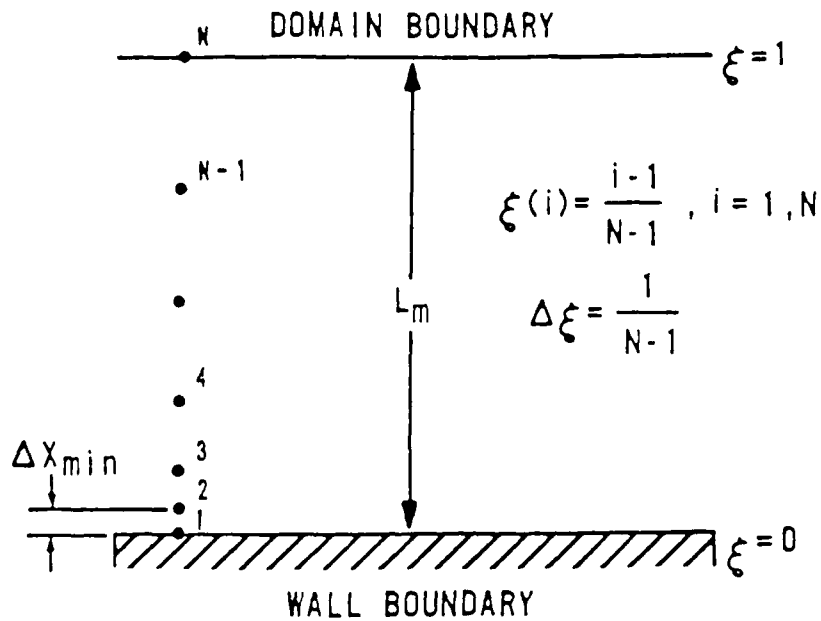
Figure 10. Exponentially Stretched Mesh Schematic.

32
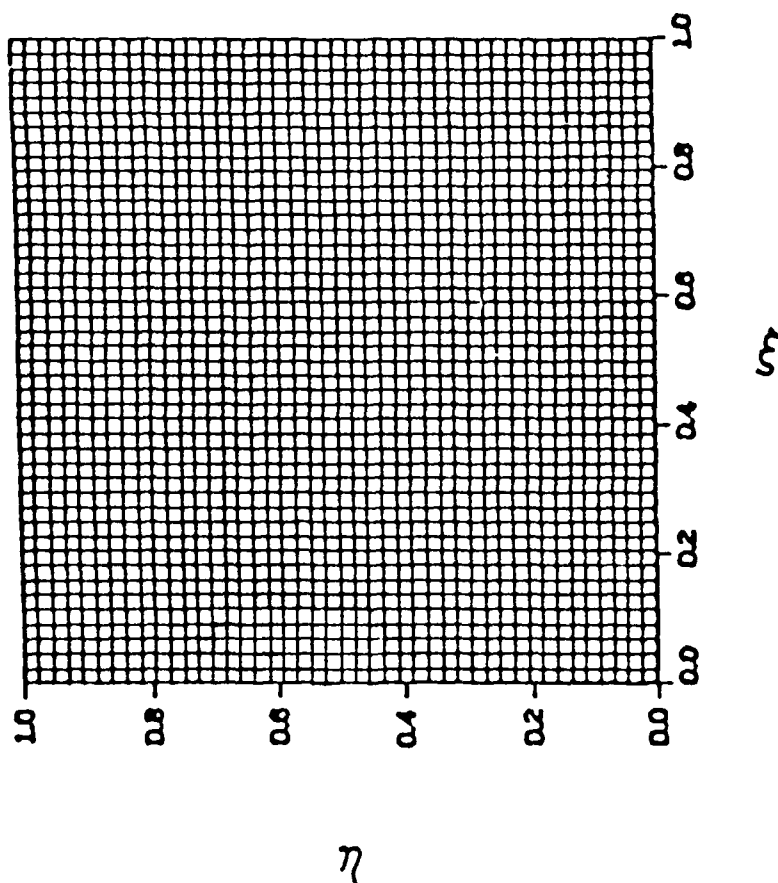
Figure 11. Computational Mesh in the Transformed Plane.

3.2 SOLUTION ALGORITHM

MACCORMACK'S METHOD

The chain-rule conservative form of the axisymmetric, time-dependent Navier-Stokes equations (eqn. 2-38) is solved using MacCormack's explicit finite-difference method (49). This algorithm is a Lax-Wendroff type differencing scheme of second order accuracy which utilizes time-splitting and two step predictor-corrector techniques. MacCormack's algorithm was chosen for application to the diffuser problem because of its previous success in computing inviscid/viscous interacting flows with shock waves, its stability in supersonic flow, and its computational efficiency achieved by time-splitting the finite difference operators (50, 51, and 52).

The computational solution is advanced in time by applying a numerical operator to the solution of the flowfield at time t. This can be written as:

$$U(\xi, \eta, t + \Delta t) = L(\Delta t) \cdot U(\xi, \eta, t) \qquad (3-3)$$

where $L(\Delta t)$ is the two-dimensional numerical operator representing MacCormack's algorithm acting on the transformed conservation equations. Through the use of a time-splitting technique, this two-dimensional operator $L(\Delta t)$ is separated into two one-dimensional sweep operators in the ξ and η directions. The operator $L_\xi(\Delta t)$ denotes the solution of the equation:

$$\frac{\partial U}{\partial t} + \xi_x \frac{\partial F}{\partial \xi} + \frac{1}{r^{j_\circ}} \xi_r \frac{\partial(r^{j_\circ}G)}{\partial \xi} = 0 \qquad (3-4)$$

in the ξ direction by time increment Δt seconds. Similarly, the operator $L_\eta(\Delta t)$ represents the solution of

$$\frac{\partial U}{\partial t} + \eta_x \frac{\partial F}{\partial \eta} + \frac{1}{r^{j_\circ}} \eta_r \frac{\partial(r^{j_\circ}G)}{\partial \eta} = j_\circ \frac{H}{r^{j_\circ}} \qquad (3-5)$$

34

in the η direction by a time increment of Δt seconds. The dependent
variable vector $U(\xi, \eta, t)$ can then be advanced in time as

$$U(\xi, \eta, t + \Delta t) = [L_{\xi}^{M/2}(\Delta t/M) \cdot L_{\eta}(\Delta t) \cdot L_{\xi}^{M/2}(\Delta t/M)] \cdot U(\xi, \eta, t) \quad (3\text{-}6)$$

with $\quad \Delta t = \Delta t_{\xi} \quad$ if $\quad \Delta t_{\xi} < \Delta t_{\eta}$

or as

$$U(\xi, \eta, t + \Delta t) = [L_{\eta}^{N/2}(\Delta t/N) \cdot L_{\xi}(\Delta t) \cdot L_{\eta}^{N/2}(\Delta t/N)] \cdot U(\xi, \eta, t) \quad (3\text{-}7)$$

with $\quad \Delta t = \Delta t_{\eta} \quad$ if $\quad \Delta t_{\eta} < \Delta t_{\xi}$

In these equations M and N are the smallest integers of the quotients
$(\Delta t_{\eta}/\Delta t_{\xi})$ and $(\Delta t_{\xi}/\Delta t_{\eta})$, respectively, and Δt_{ξ} and Δt_{η} are the maximum
allowable time steps in the ξ and η directions as determined by the Courant-
Friedrichs-Lewy (CFL) limit discussed in the next section on stability. The
values of M and N are usually equal to two for the grid distribution used in
the solution of the diffuser problem. This sets up a truly alternating
direction sweep procedure that is desirable when gradients exist in more
than one direction.

The finite-difference forms of the sweep operators consist of a
predictor-corrector procedure, which increases the accuracy of the time-
dependent term evaluations. This method utilizes one-sided differencing in
the direction of the sweep, but central differencing in the direction
perpendicular to the sweeping coordinate. At the completion of the
predictor-corrector process, this method is equivalent to a second-order
central differencing scheme in two dimensions.

The ξ sweep operator, $L_{\xi}(\Delta t)$, represents the following numerical
procedure. A predicted intermediate value is computed by the expression:

$$U_{i,j}^{n+1/2} = U_{i,j}^n - \frac{\Delta t}{\Delta \xi}[(\xi_x)_{i,j} \ (F_{i,j}^n - F_{i-1,j}^n)$$

$$+ \frac{1}{r_{i,j}^{j_\circ}} \ (\xi_r)_{i,j} \ (r_{i,j}^{j_\circ} \ G_{i,j}^n - r_{i-1,j}^{j_\circ} \ G_{i-1,j}^n)] \qquad (3\text{-}8)$$

where $U_{i,j}^n$ is the known value at time t, and $U_{i,j}^{n+1/2}$ is the intermediate

predictor value. The actual computed value at time $(t + \Delta t)$ is then

calculated by applying the following corrector algorithm:

$$U_{i,j}^{n+1} = 1/2 \left\{ U_{i,j}^n + U_{i,j}^{n+1/2} - \frac{\Delta t}{\Delta \xi}[(\xi_x)_{i,j} \ (F_{i+1,j}^{n+1/2} - F_{i,j}^{n+1/2}) \right.$$

$$\left. + \frac{1}{r_{i,j}^{j_\circ}} \ (\xi_r)_{i,j} \ (r_{i+1,j}^{j_\circ} \ G_{i+1,j}^{n+1/2} - r_{i,j}^{j_\circ} \ G_{i,j}^{n+1/2})] \right\} \qquad (3\text{-}9)$$

In this ξ sweep predictor-corrector algorithm, the matrices F and G are

functions of the following difference quotients:

$$F_{i,j}^m \ , \ G_{i,j}^m = f(U_{i,j}^m, \ \frac{U_{i+1,j}^m - U_{i,j}^m}{\Delta \xi}, \ \frac{U_{i,j+1}^m - U_{i,j-1}^m}{2\Delta \eta}) \qquad (3\text{-}10)$$

This scheme can be depicted graphically as shown in Figure 12.

The $L_\eta(\Delta t)$ numerical sweep operator is formulated in a similar manner.

The intermediate predictor value is given by the expression:

$$U_{i,j}^{n+1/2} = U_{i,j}^n - \frac{\Delta t}{\Delta \eta}[(\eta_x)_{i,j} \ (F_{i,j}^n - F_{i,j-1}^n)$$

$$+ \frac{1}{r_{i,j}^{j_\circ}} \ (\eta_r)_{i,j} \ (r_{i,j}^{j_\circ} \ G_{i,j}^n - r_{i,j-1}^{j_\circ} \ G_{i,j-1}^n)] + \frac{j_\circ \ \Delta t \ H_{i,j}^n}{r^{j_\circ}} \qquad (3\text{-}11)$$
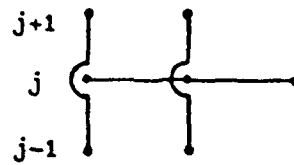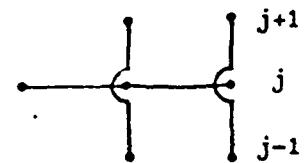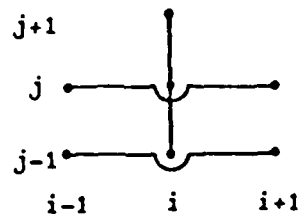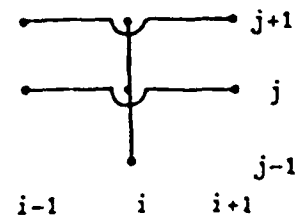
Figure 12. Graphical Representation of the Numerical Sweep Operators.

The corrector value at time $(t + \Delta t)$ is then given by:

$$U_{i,j}^{n+1} = 1/2 \left\{ U_{i,j}^{n} + U_{i,j}^{n+1/2} - \frac{\Delta t}{\Delta \eta} [(\eta_x)_{i,j} (F_{i,j+1}^{n+1/2} - F_{i,j}^{n+1/2}) \right.$$

$$\left. + \frac{1}{r_{i,j}^{j_\circ}} (\eta_r)_{i,j} (r_{i,j+1}^{j_\circ} G_{i,j+1}^{n+1/2} - r_{i,j}^{j_\circ} G_{i,j}^{n+1/2})] + \frac{j_\circ \Delta t H_{i,j}^{n+1/2}}{r^{j_\circ}} \right\} \quad (3\text{-}12)$$

The matrices F and G are now functions of the following difference quotients:

$$F_{i,j}^{m}, G_{i,j}^{m} = f(U_{i,j}^{m}, \frac{U_{i+1,j}^{m} - U_{i-1,j}^{m}}{2\Delta\xi}, \frac{U_{i,j+1}^{m} - U_{i,j}^{m}}{\Delta\eta}) \quad (3\text{-}13)$$

This scheme is also depicted graphically in figure 9.

The MacCormack algorithm satisfies the requirements of stability, consistency, and accuracy if the following conditions are met: It is stable if the time step limit satisfies the CFL stability condition given in the next section. It is consistent if the sum of the time steps for each of the sweep operators is equal, and the algorithm is second-order accurate in space and time if the sequence of sweep operators is symmetric.

STABILITY CONDITION

Although the stability of the finite difference equations cannot be analyzed when applied to the complete set of Navier-Stokes equations, MacCormack and Baldwin (53) have shown that considerable insight can be gained by separately analyzing the inviscid, diffusion, and mixed derivative parts of these equations. Stability criteria are determined by calculating the eigenvalues of the associated amplification matrix for each part. If this eigenvalue procedure is applied to the inviscid terms of the Navier-Stokes equations for flow in a Cartesian coordinate system, the following stability conditions emerge:

38

$$\Delta t_x \leq \frac{\Delta x}{|u| + c} \qquad (3\text{-}14)$$

and

$$\Delta t_r \leq \frac{\Delta r}{|v| + c} \qquad (3\text{-}15)$$

where c is the local speed of sound. Consideration of only the diffusive terms which contain $\frac{\partial^2 U}{\partial x^2}$ and $\frac{\partial^2 U}{\partial r^2}$ in the complete Navier-Stokes equations gives the following conditions:

$$\Delta t_x \leq 1/2 \; \frac{\Delta x^2}{\frac{\gamma}{\rho} \left(\frac{\mu}{Pr} + \frac{\epsilon}{Pr_t}\right)} \qquad (3\text{-}16)$$

and

$$\Delta t_r \leq 1/2 \; \frac{\Delta r^2}{\frac{\gamma}{\rho} \left(\frac{\mu}{Pr} + \frac{\epsilon}{Pr_t}\right)} \qquad (3\text{-}17)$$

Finally, analysis of the mixed derivative terms found in the Navier-Stokes equations gives the following conditions:

$$\Delta t_x = \Delta t_r \leq \frac{\Delta x \; \Delta r}{\frac{1}{\rho} \left[-(\lambda + \lambda_t)(\mu + \epsilon)\right]^{1/2}} \qquad (3\text{-}18)$$

For the finite difference equations applied to the complete set of Navier-Stokes equations, the stability criteria can then be estimated as (53):

$$\Delta t \leq \min_{i,j} (\Delta t_x, \; \Delta t_r) \qquad (3\text{-}19)$$

where

$$\Delta t_x \leq \frac{\Delta x}{|u| + c + \frac{1}{\rho} \left(\frac{2\gamma}{\Delta x} \left(\frac{\mu}{Pr} + \frac{\epsilon}{Pr_t}\right) + \frac{1}{\Delta r} \left[-(\lambda + \lambda_t)(\mu + \epsilon)\right]^{1/2} \right)} \qquad (3\text{-}20)$$

and

$$\Delta t_r \leq \frac{\Delta r}{|v| + c + \frac{1}{\rho} \left(\frac{2\gamma}{\Delta r} \left(\frac{\mu}{Pr} + \frac{\epsilon}{Pr_t}\right) + \frac{1}{\Delta x} \left[-(\lambda + \lambda_t)(\mu + \epsilon)\right]^{1/2} \right)} \qquad (3\text{-}21)$$

For the present non-Cartesian diffuser flow cases that were computed, the maximum time step was calculated as:

$$\Delta t = \underset{i,j}{\text{minimum}} \ (\Delta t_\xi, \ \Delta t_\eta) \qquad (3\text{-}22)$$

where

$$\Delta t_\xi \le \frac{\Delta S_\xi}{|u_\xi| + c + \frac{1}{\rho} \{ \frac{2\gamma}{\Delta S_\xi} (\frac{\mu}{Pr} + \frac{\epsilon}{Pr_t}) + \frac{1}{\Delta S_\eta} [-(\lambda + \lambda_t)(\mu + \epsilon)]^{1/2} \}} \qquad (3\text{-}23)$$

and

$$\Delta t_\eta \le \frac{\Delta S_\eta}{|u_\eta| + c + \frac{1}{\rho} \{ \frac{2\gamma}{\Delta S_\eta} (\frac{\mu}{Pr} + \frac{\epsilon}{Pr_t}) + \frac{1}{\Delta S_\eta} [-(\lambda + \lambda_t)(\mu + \epsilon)]^{1/2} \}} \qquad (3\text{-}24)$$

where

$$\Delta S_\xi = [(x_{i,j} - x_{i-1,j})^2 + (r_{i,j} - r_{i-1,j})^2]^{1/2} \qquad (3\text{-}25)$$

$$\Delta S_\eta = [(x_{i,j} - x_{i,j-1})^2 + (r_{i,j} - r_{i,j-1})^2]^{1/2} \qquad (3\text{-}26)$$

$$u_\xi = \text{Maximum} \ (u_{i,j}, \ v_{i,j}, \ u_{i-1,j}, \ v_{i-1,j}) \qquad (3\text{-}27)$$

$$u_\eta = \text{Maximum} \ (u_{i,j}, \ v_{i,j}, \ u_{i,j-1}, \ v_{i,j-1}) \qquad (3\text{-}28)$$

The actual time step used in the numerical procedure was less than this theoretically estimated maximum. Factors varying between 0.30 and 0.90 were used during the computations.

NUMERICAL DAMPING

The computation of strong shocks imbedded in a flowfield can often cause numerical oscillations (40) which may lead to program failure due to physically unrealistic values of computed pressure, density or temperature. These oscillations are caused by numerical truncation errors and can sometimes be reduced by refining the grid in the areas of shock locations. However, this can be impractical when the oscillations are of a transient

40

nature caused by computational start-up or re-start procedures, or where the shock location varies for different experimental cases and mesh refinement for each individual case is undesirable. Additionally, accommodation of these effects requires extremely small time steps. In this situation, a fourth order pressure-gradient damping procedure as introduced by MacCormack and Baldwin (53) can be applied to damp the numerical oscillations and avoid program failure.

This numerical damping scheme is applied in both the ξ and η directional sweeps. In the ξ numerical sweep, damping is implemented by replacing $F_{ii,j}$ by $(F_{ii,j} + F_{D_{ii,j}})$ and $G_{ii,j}$ by $(G_{ii,j} + G_{D_{ii,j}})$ in equation (3-4). The predictor and corrector sweeps in this case are represented by ii = i and ii = i+1, respectively. The damping terms F_D and G_D are in the following form:

$$F_{D_{ii,j}} = \alpha_\xi \ (|u_{ii,j}| + c_{ii,j}) \ \frac{|P_{i+1,j} - 2P_{i,j} + P_{i-1,j}|}{(P_{i+1,j} + 2P_{i,j} + P_{i-1,j})}$$
$$\cdot \ (U_{i+1,j} - U_{i,j}) \qquad\qquad (3\text{-}29)$$

and:

$$G_{D_{ii,j}} = \alpha_\eta \ (|v_{ii,j}| + c_{ii,j}) \ \frac{|P_{ii,j+1} - 2P_{ii,j} + P_{ii,j-1}|}{(P_{ii,j+1} + 2P_{ii,j} + P_{ii,j-1})}$$
$$\cdot \ (U_{ii,j+1} - U_{ii,j-1}) \cdot r_{ii,j}^{j_o} \qquad (3\text{-}30)$$

In the η sweep, a similar procedure is implemented by replacing $F_{i,jj}$ by $(F_{i,jj} + F_{D_{i,jj}})$ and $G_{i,jj}$ by $(G_{i,jj} + G_{D_{i,jj}})$ where

$$F_{D_{i,jj}} = \alpha_\xi \ (|u_{i,jj}| + c_{i,jj}) \ \frac{|P_{i+1,jj} - 2P_{i,jj} + P_{i-1,jj}|}{(P_{i+1,jj} + 2P_{i,jj} + P_{i-1,jj})}$$

41

$$\cdot \ (U_{i+1,jj} - U_{i-1,jj}) \tag{3-31}$$

and

$$G_{D_{i,jj}} - \alpha_\eta \ (|v_{i,jj}| + c_{i,jj}) \ \frac{|P_{i,j+1} - 2P_{i,j} + P_{i,j-1}|}{(P_{i,j+1} + 2P_{i,j} + P_{i,j-1})}$$

$$\cdot \ (U_{i,j+1} - U_{i,j}) \cdot r_{i,jj}^{j \circ} \tag{3-32}$$

In this case the predictor and corrector sweeps are represented by $jj = j$ and $jj = j+1$, respectively. For both sweeps α_ξ and α_η are damping constants where normally

$$\alpha_\xi - \alpha_\eta \tag{3-33}$$

and the values typically range from 0.5 to 3.0 (54).

This damping procedure produces fourth order viscosity like terms of the form

$$\alpha_\xi \ \Delta t \ \Delta\xi^3 \ \frac{\partial}{\partial\xi} \ [\frac{|u|+c}{4P} \ \left|\frac{\partial^2 P}{\partial\xi^2}\right| \ \frac{\partial U}{\partial\xi}] + \alpha_\eta \ \Delta t \ \Delta\eta^3 \ \frac{\partial}{\partial\eta} \ [\frac{|v|+c}{4P} \ \left|\frac{\partial^2 P}{\partial\eta^2}\right| \ \frac{\partial U}{\partial\eta}] \tag{3-34}$$

which are added to the difference equations. The magnitude of these damping terms is proportional to the second derivative of pressure and is significant only in regions of pressure oscillation where the truncation error is already adversely affecting the solution (55,56).

3.3 CONVERGENCE CRITERIA

Convergence, as applied in this section, refers to iteration convergence as opposed to truncation convergence, which involves the convergence of the solution of the FDE to the solution of the PDE as Δx, Δr, and $\Delta t \rightarrow 0$. Iteration convergence refers to the arrival at a steady-state solution to the discretized Navier-Stokes equations within some acceptable tolerance through the use of an iterative process. As stated by Roache (40), there are no definitive criteria for iteration convergence. A

somewhat subjective judgement of convergence must be made based upon an examination of the iterative behavior of the solution flow variables. Different flow variables, as well as variables at different locations, converge at different rates. If the slowest converging variable in the flow-field is known, it should be the most closely examined for convergence.

In this case of a supersonic diffuser, all of the flow variables vary radially along the length of the diffuser duct. Attention could be focused on a physical variable, such as pressure, at a particular point in the flow field. However, a clearer picture of convergence for this case may be obtained by monitoring the location of the shock (as defined by the radial position along the centerline where the Mach number equals unity - the sonic line location at the centerline). The location of the core flow normal shock will be dependent upon the behavior of the other flow variables, which will vary as disturbances traverse the flow field. A characteristic time for a disturbance to cross the flowfield may be defined by:

$$t_{ch} = L/u_{ch} \qquad\qquad (3-35)$$

where L is the length of the flowfield in the direction parallel to the characteristic velocity u_{ch}. Since the diffuser problem involves mixed supersonic and subsonic flow, and the inflow is further complicated by the approximately sinusoidal profile of the flow variables, a precise definition of the characteristic velocity and thus the time for a disturbance to traverse the entire flowfield is difficult.

Since the core flow in the diffuser is high Reynolds number flow, the advective terms in the conservation equations dominate the viscous diffusion terms. Focusing attention on the line of symmetry of the diffuser duct, the

characteristic time for a fine mesh grid (Fig. 13) can be approximated by the summation

$$t_{ch} = 2 \sum_{j=1}^{JLM} \frac{y_{j+1} - y_j}{v_{j+1} + v_j} \qquad (3\text{-}36)$$

$$JLM = JL - 1$$

where JL is the total number of grid points in the radial (flow) direction. Thus, the characteristic time varies considerably depending on the desired exit conditions (percent of normal shock recovery pressure) and the initial conditions, and has to be computed along with the other flow variables.

line of symmetry

grid points .	.	.	.	.	.	.	. . . .	.	.
j	1	2	3	4	5	6	7	JLM	JL
v_j	v_1	v_2	v_3	v_4	v_5	v_6	v_7	v_{JLM}	v_{JL}
y_j	y_1	y_2	y_3	y_4	y_5	y_6	y_7	y_{JLM}	y_{JL}

$$L_1 = y_2 - y_1$$

$$\Delta t_1 \simeq \frac{L_1}{(v_2 + v_1)/2} = \frac{2(y_2 - y_1)}{v_2 + v_1}$$

$$t_{ch} = \sum_N t_N$$

Figure 13. Characteristic Time Calculation.
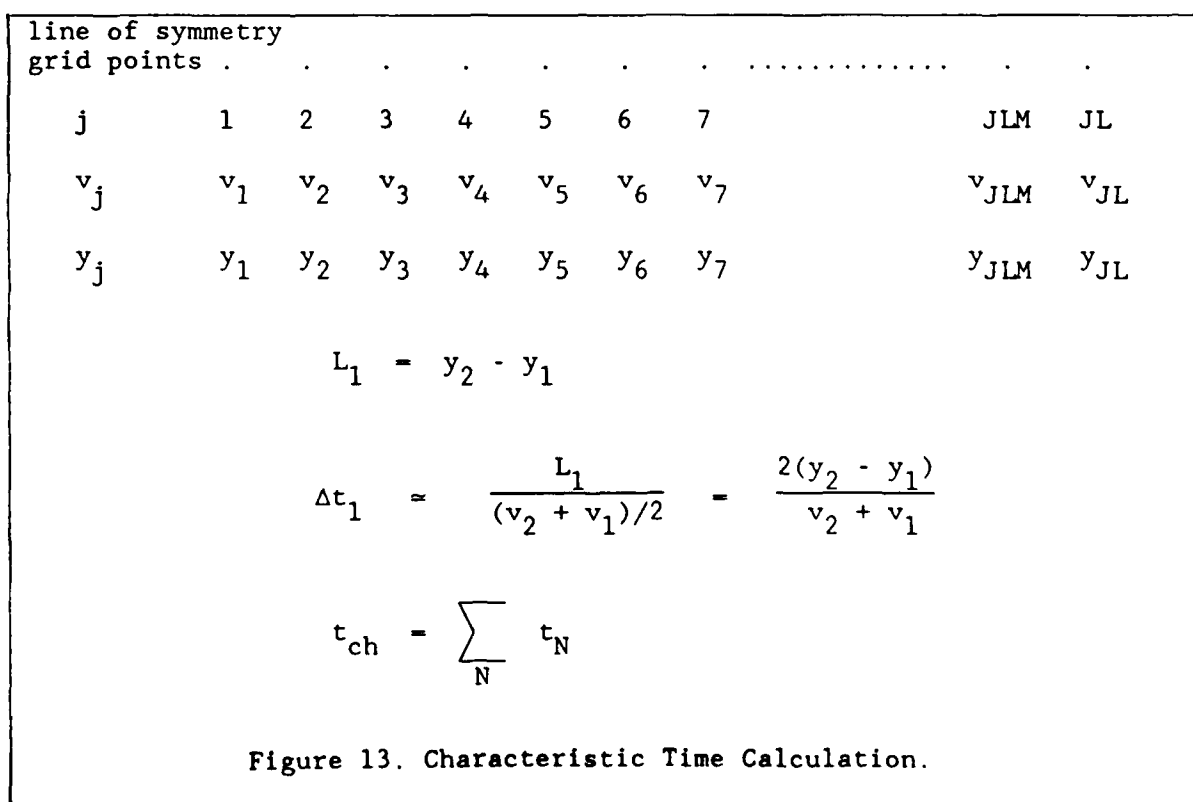
The convergence criteria were then established by the following procedure. The numerical solution was either initially started, or restarted from the previous case. As the solution converged, shock position on the line of symmetry was monitored until it varied less than ±1 percent for one characteristic time period. At the end of this characteristic time period the solution was stopped as convergence was considered to be achieved. Visual comparison of Mach number contours, line of symmetry pressure and temperature, and wall pressure profiles confirmed the convergence of the solution using this procedure. A sample convergence time history plot is shown in Figure 14.

CONVERGENCE TIME HISTORY 60%NSR
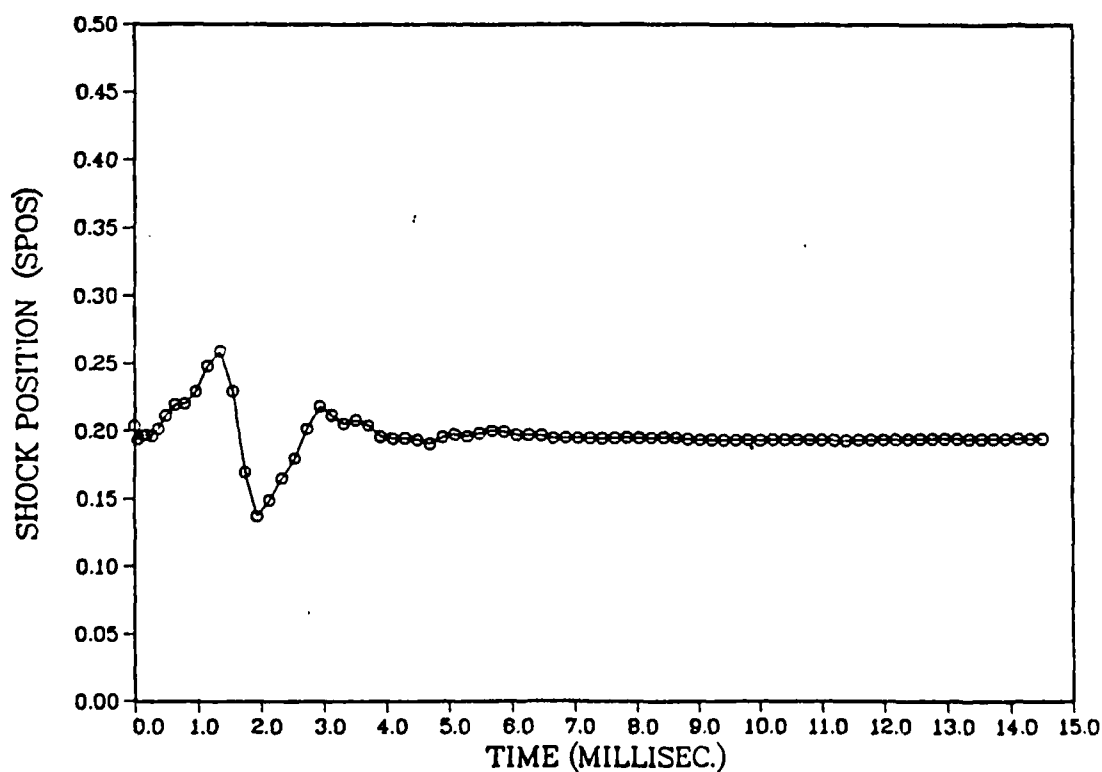
Figure 14. Sample Convergence Time History.

CHAPTER IV

BOUNDARY AND INITIAL CONDITION IMPLEMENTATION

As in Chapter II, boundary and initial conditions must be prescribed in order to solve the conservation equations that govern the flowfield. Values of the dependent variables for points on the the boundaries of the computational domain must be specified in order for the numerical operators to solve the flowfield correctly. This section presents the numerical formulation of the boundary and initial conditions used for the solution of the supersonic diffuser. The conditions were presented in a mathematical context in Chapter II.

4.1 THE UPSTREAM BOUNDARY

The flow properties on the up-cream boundary (AB of Figure 8) are held fixed for the duration of the computational solution. The values of these properties were developed from the experimental data of Zumpano, et al. (13), and include both the core flow values from the source flow nozzles as well as the flow conditions within the supersonic ink blower.

4.2 THE DOWNSTREAM BOUNDARY

The downstream boundary (CD) is placed at the exit of the diffuser, where only small gradients in the flow variables are expected to exist due to the geometric expansion of the area available to the flow. The flow exiting this boundary should be subsonic. This boundary condition is the most critical, for it dictates the behavior of the entire flow field. Because of the experimental set-up (13), the values of the flow variables can only be approximated at this boundary. Therefore, the conservative flow variables are set using a first-order, zero gradient condition, modified to

account for the geometric area increase between points (I,JL) and (I,JL-1) as follows:

$$\rho_{I,JL} = \rho_{I,JL-1} \tag{4-1a}$$

$$(\rho u)_{I,JL} = (\rho u)_{I,JL-1} \tag{4-1b}$$

$$(\rho v)_{I,JL} = (\rho v)_{I,JL-1} \cdot \frac{y(I,JL-1)}{y(I,JL)} \tag{4-1c}$$

$$(\rho e)_{I,JL} = (\rho e)_{I,JL-1} \tag{4-1d}$$

The exit pressure is then imposed for all points across the outflow boundary outside of the boundary layer. This is done by deriving u, v, and T from the conservative variables, and then using the imposed exit pressure to calculate new values of the conservative variables for the next iteration of the numerical solution.

4.3 THE LINE OF SYMMETRY

The boundary AD in Figure 8 is a line of symmetry with no mass or energy flux across it. A first-order, zero-gradient condition is therefore applied at the points on this boundary. Thus,

$$\rho_{IL,J} = \rho_{IL-1,J} \tag{4-2a}$$

$$(\rho u)_{IL,J} = 0.0 \tag{4-2b}$$

$$(\rho v)_{IL,J} = (\rho v)_{IL-1,J} \tag{4-2c}$$

$$(\rho e)_{IL,J} = (\rho e)_{IL-1,J} \tag{4-2d}$$

4.4 THE DIFFUSER WALLS

The diffuser walls (BC in Figure 8) are treated as no-slip, impermeable boundaries. The no-slip condition is imposed as follows:

$$(\rho u)_{1,j} = 0.0 \tag{4-3a}$$

$$(\rho v)_{1,j} = 0.0 \tag{4-3b}$$

47

As discussed in Chapter II, a constant wall temperature is imposed on the diffuser walls. This condition is applied simply as:

$$T_{1,j} = T_W \qquad \text{for} \qquad 1 < j \leq JL \qquad (4\text{-}4)$$

The density at the wall is derived from the assumption of zero pressure gradient across the boundary layer at the wall:

$$\frac{\partial p}{\partial \xi} = 0 \qquad (4\text{-}5)$$

where ξ is the direction normal to the wall. This boundary condition on the pressure is approximate, but due to the extremely close spacing of the grid points in the x-direction for this application, the additional terms arising from the derivative of the wall shear were assumed to have a negligible effect on the value of the wall pressure (39). Thus,

$$P_{1,J} = P_{2,j} \qquad (4\text{-}6a)$$

$$P_{1,J} = \rho_{1,J} \cdot R \cdot T_W \qquad (4\text{-}6b)$$

$$P_{2,J} = \rho_{2,J} \cdot R \cdot T_{2,J} \qquad (4\text{-}6c)$$

$$T_{2,J} = \frac{\dfrac{(\rho e)_{2,J}}{\rho_{2,J}} - 1/2 \ (u_{2,J}^2 + v_{2,J}^2)}{C_V} \qquad (4\text{-}6d)$$

$$\rho_{1,J} = \frac{\rho_{2,J} \cdot T_{2,J}}{T_W} \qquad (4\text{-}6e)$$

$$\rho_{1,J} = \frac{\rho_{2,J} \cdot \dfrac{(\rho e)_{2,J}}{\rho_{2,J}} - 1/2 \ (u_{2,J}^2 + v_{2,J}^2)}{(C_V \cdot T_W)} \qquad (4\text{-}6f)$$

4.5 INITIAL CONDITIONS

As discussed in Chapter II, initial values of the conservative variables must be imposed over the computational domain. The incoming flow variables are fixed in time, and vary nearly sinusoidally across the diffuser inlet. An average of those variables is used to compute a one-dimensional inviscid normal shock solution to the flow through the diffuser, subject to the constraint of conservation of mass. This one-dimensional solution is then imposed on the flow field as the starting condition.

Once an initial case of the supersonic laser diffuser had numerically converged to a valid solution, each succeeding case was initialized by imposing new downstream pressure constraints or eddy viscosity turbulence models on the preceeding converged solution. This allowed the new solutions to converge to steady state at a much greater rate.

CHAPTER V

TURBULENCE MODELING

The experimental tests used as a basis for the computational solutions were conducted at a diffuser entrance unit Reynolds number of 1.63 million per foot, or a Reynolds number based on diffuser entrance height of 788,400. Given the inflow from ten Mach 2.5 (nominal) nozzles plus two Mach 4.0 (nominal) bank blowers, a complex interacting flow field exists where several turnback shocks are encountered before the flow enters the diffuser. The condition of the flow at the diffuser entrance is thus determined to be turbulent (44).

Exact simulation of the dynamics of turbulence for practical applications (such as this complex flowfield) is unattainable (57). The turbulent nature of such a flow can be approximated in the computational solution by a variety of closure models ranging from locally dependent algebraic models to the more complex higher-order models such as the turbulent kinetic energy and Reynolds-Stress models (57, 58, 59, 60). In all cases the objective of the turbulence model is to relate known mean-flow variables to the unknown Reynolds stresses of the turbulence. Although the higher order methods can account for the time history of the turbulence in a flow, they require that accurate initial profiles of the turbulent shear stress be known or reliably calculated (61). If this initial condition cannot be described accurately, then this type of prediction method cannot be effectively utilized. Since this proved to be the case for the diffuser problem under consideration, modeling through eddy viscosity concepts was deemed appropriate (57). Therefore, locally dependent eddy viscosity models were carefully applied over the computational domain.

50

5.1 BOUNDARY-LAYER MODEL

A dominating flow feature is the boundary layer along the diffuser walls. Separation of this wall boundary layer is the primary influencing factor on whether the diffuser flow will remain "started" (i.e., if the shock system remains stable outside of the optical cavity region) or if too large a separation region will cause the flow to choke and "unstart." Since predicted boundary layer thicknesses are at least an order of magnitude smaller than the diffuser diameter, a two-dimensional turbulence model was selected as sufficient for the axisymmetric cases (57). The eddy viscosity model applied in this region is a modified two layer Cebeci-Smith model (31). The Cebeci-Smith model was selected rather than the Baldwin-Lomax model (62) based on Hasen's (39) experience and Visbal and Knight's (63) conclusion that the Baldwin-Lomax model was not suitable for the determination of the length scale when strong shock-induced separations are present. Recent work (64) supports the selection of the Cebeci-Smith model for the diffuser flow calculation.

The inner layer of this model accounts primarily for the laminar sublayer and the law-of-the-wall region adjacent to the wall, with the outer layer accounting for the remainder of the boundary layer region (the law-of-the-wake region.

The expression for the inner model is based on Prandtl's mixing-length theory, which can be written as (in the coordinate system of the diffuser problem):

$$\epsilon_\iota = \rho \ell_\iota^2 \left| \frac{\partial v_t}{\partial x_n} \right| \tag{5-1}$$

51

where v_t is the local tangential velocity parallel to the wall surface, and x_n is the normal distance measured from the wall. The mixing length in this model is adapted from Van Driest's sublayer model (65), and is expressed as:

$$\ell_{\iota} = k_1 \, x_n \, (1 - e^{\frac{-x_n\sqrt{\rho\tau_w}}{A^+\mu}}) \qquad (5\text{-}2)$$

The basic Cebeci-Smith model assumes a zero gradient pressure condition (the flat plate condition, $dp/dx = 0$), but can be modified to account for a pressure gradient in the direction parallel to the wall within the sublayer. Such a modification was employed and is discussed in a later section of this chapter.

The outer region eddy viscosity model consists of a Clauser-type displacement thickness model defined by the equation:

$$\epsilon_0 = k_2 \, \rho v_e \delta^* \qquad (5\text{-}3)$$

where v_e is the appropriate tangential velocity at the boundary layer edge and

$$\delta^* = \int_0^\delta (1 - \frac{v}{v_e}) \, dx_n \qquad (5\text{-}4)$$

is the kinematic displacement thickness (31). The term displacement thickness is to be taken as kinematic displacement thickness throughout this text.

The inner and outer regions of each boundary layer are defined by the requirement that the eddy viscosity remain a continuous function across the entire layer (31, 44). This is accomplished by applying the inner model outward from the wall until $\epsilon_{\iota} = \epsilon_0$ at a value x_c. The outer model is then

52

applied from x_c outward across the remainder of the the flowfield in the boundary layer region. Figure 15 shows a typical eddy viscosity profile across this region.

The above constants k_1, A^+, and k_2, known as the von Karman constant, the sublayer thickness, and the Clauser constant, conventionally have values of 0.4, 26, and 0.0168, respectively (31, 62). Modification of these constants to account for the effect of an adverse pressure gradient will be discussed later in this chapter.

The expression for the outer region eddy viscosity model (eqn. 5-3) usually contains a modification, Klebanoff's (65) intermittancy factor (γ), to approximate transition out of the boundary-layer region and into the free stream flow. It is based on Klebanoff's experimental observation (66) that as the free stream is approached, the turbulence becomes intermittent; that is, for only a fraction of the time γ is the flow turbulent. For the diffuser flowfield herein examined, such intermittancy is inappropriate. This modification was therefore not applied and the outer region eddy viscosity was calculated as a "constant" throughout the core flow region to approximate the effects of the turbulent mixing from the source flow nozzles.

5.2 THE CORE FLOW REGION

Since the core flow region entrance Re = 1.63 million per foot and this region is subject to the flow disturbances from the mixing of ten supersonic Mach 2.5 (nominal) nozzles and the attendant turnback shocks as that flow crosses the optical cavity region before entering the diffuser, this flow is considered to be fully turbulent in its nature. To satisfy the need for a continuous turbulent eddy viscosity profile across the flow from the
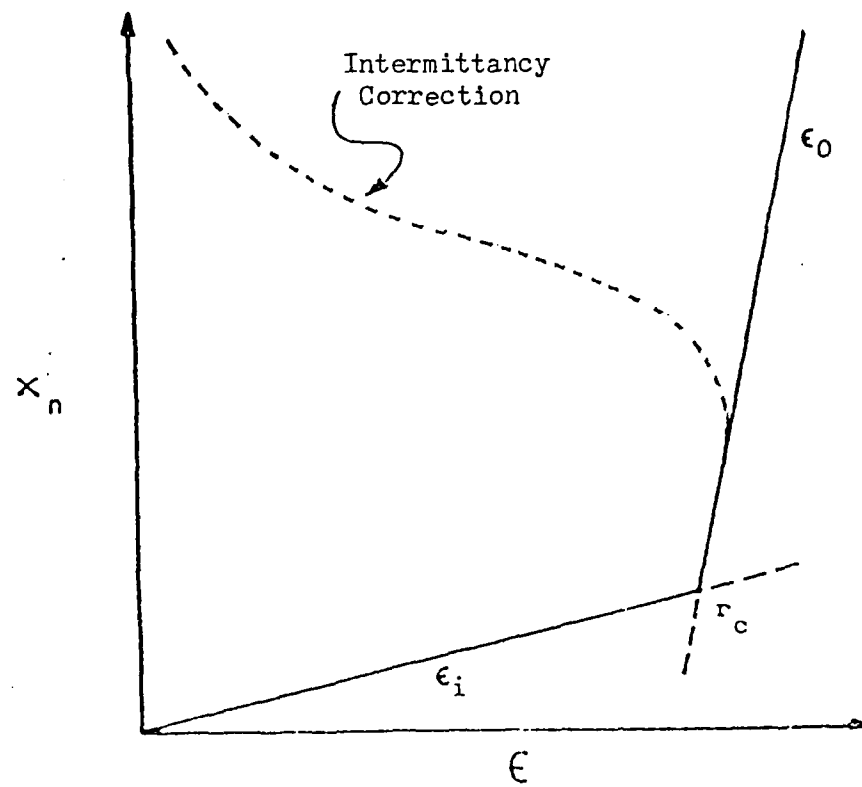
Figure 15. Eddy Viscosity Distribution Across a Boundary Layer

boundary layer to the flow centerline, the outer region boundary layer eddy viscosity model was applied in this region also. This mixing length formulation was used to approximate the effects of the shear layer thickness from the nozzle wakes which are of the same order of magnitude as the turbulent boundary layer kinematic displacement thickness δ^*.

5.3 ADVERSE PRESSURE GRADIENT MODIFICATIONS

Algebraic eddy viscosity models with fixed values for the von Karman constant (k_1), the Clauser constant (k_2), and the sublayer thickness parameter (A^+) are known to be inadequate for computing flows with adverse pressure gradients such as those in diffusers (39). However, it may be some time before higher-order turbulence models are sufficiently developed to be more accurate and reliable than this simpler model for engineering purposes (67). Additionally, the computational resources required for the use of higher-order models often prohibit their use for all but relatively simple flowfields. The flowfields of this investigation are very complex due to the supersonic mixing of the flows from ten nozzles and two wall mounted bank blowers (flow energizers).

Cebeci described (68) his modification to the basic Cebeci-Smith model for flows with adverse pressure gradient. He concluded that only the outer region is affected. He presented the modified outer region eddy viscosity model in the form:

$$\epsilon_{m_0} = \alpha \int_0^\infty (u_e - u) \, dy \qquad (5\text{-}5)$$

where

$$\alpha = \frac{.0168}{F^{2.5}} \qquad (5\text{-}6)$$

55

with

$$
F = \begin{cases} \dfrac{6}{[1 + 2R_t (2 - R_t)]} & ; & R_t \leq 1.0 \\[2ex] \dfrac{1 + R_t}{R_t} & ; & R_t \geq 1.0 \end{cases} \tag{5-7}
$$

where, with w denoting wall conditions

$$
R_t = \frac{\mu_w \left(\dfrac{\partial u}{\partial y}\right)_w}{\left[\epsilon_m \left(\dfrac{\partial u}{\partial y}\right)\right]_{max}} \tag{5-8}
$$

where $\epsilon_m = \epsilon_{m_\iota}$

This argument results in values of α (k_2, the Clauser constant) always less than .0168. Therefore, the value of ϵ_{m_0} obtained is lower than that for the non-adverse pressure gradient case, and a less "stiff" turbulence model results.

Jobe and Hankey (67) investigated the range of usefulness of the two-layer algebraic eddy viscosity model. Numerical solutions of the turbulent boundary-layer equations were compared with the experimental data of Laderman (69), Sturek (70), and Waltrup and Schetz (71), with the objective of increasing the accuracy of the two-layer eddy viscosity model for flows encountering constant adverse pressure gradients by adjusting the three constants (k_1, k_2, and A^+) contained therein. Variation of these universal constants from their conventional values in the algebraic eddy viscosity models has been suspected for some time (69 - 75) for flows with pressure gradient. Values from 0.35 to 0.75, increasing with increasingly adverse pressure gradients, have been reported (69 - 71) for the universal mixing

length constant (k_1), conventionally set at 0.4 in the wall region. Correlations and equations depending upon the pressure gradient have also been given for the inner region damping constant, A^+, and Clauser's constant, k_2, that appears in the outer region viscosity model.

Jobe and Hankey's analysis (67) concluded that the inner region reacts immediately, through the constants k_1 and A^+, to an imposed adverse pressure gradient, while the outer layer alone requires a lag equation (varying with streamwise distance and variation in the magnitude of the pressure gradient), to permit the constant k_2 to attain its maximum value. Their computations showed that $k_1 = 0.65$, and that A^+ increases immediately upon entering the region of adverse pressure gradient.

For the present numerical experiment, a simple model for the variation of k_2 with adverse pressure gradient was developed by plotting the experimental values of k_2 obtained by Laderman, Sturek, and Waltrup and Schetz as a function of pressure gradient (Figure 16). Simple linear regression techniques yielded the value of the slope for the change of k_2 versus nondimensionalized pressure gradient as $k_{s_p} = 0.015$. The increase in k_2 from one streamwise location to the next could then be written as:

$$k_{2_j} = k_{2_{j-1}} + k_{s_p} \cdot P_{grad_j} \cdot (y_j - y_{j-1}) \qquad (5\text{-}9)$$

where

$$P_{grad_j} = \frac{(P_{w_j} - P_{w_{j-1}}) / P_\infty}{(y_j - y_{j-1}) / y_\ell} \qquad (5\text{-}10)$$

Thus k_2 was allowed to increase above its equilibrium value in a manner that varies with both pressure gradient and streamwise distance.
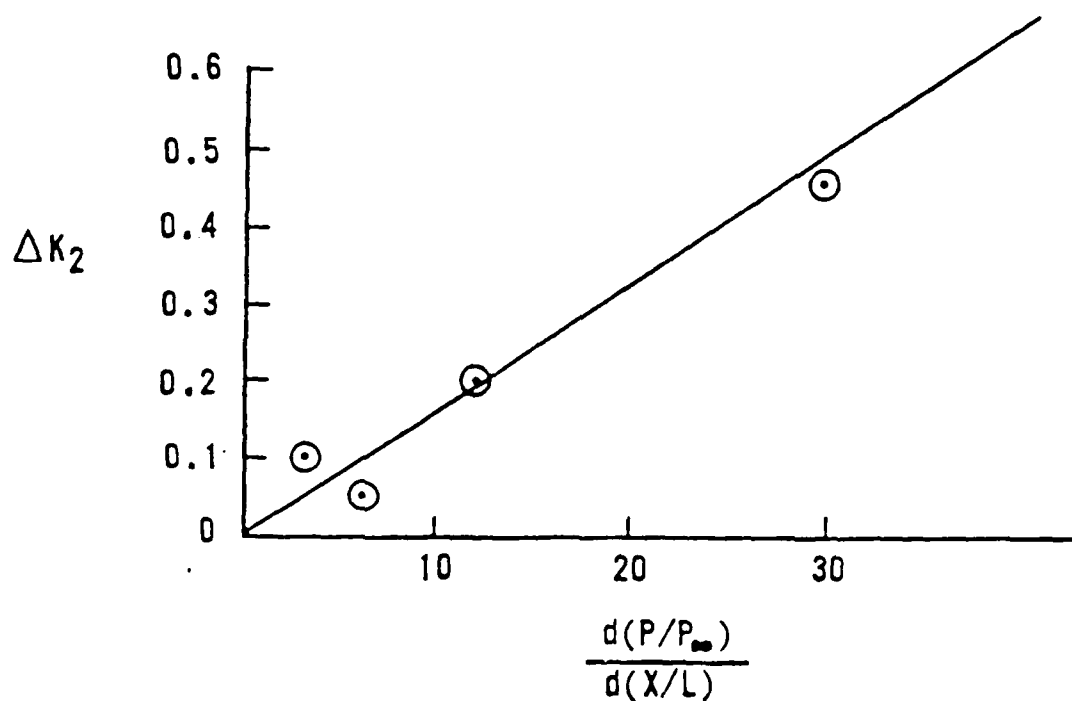
Figure 16. Variation in Clauser's Constant (k_2) With Nondimensionalized Adverse Pressure Gradient. Experimental data of Laderman (69), Sturek (70), and Waltrup and Schetz (71).

CHAPTER VI

NUMERICAL RESULTS

This chapter will discuss the numerical results of the computational solutions using the algorithm, boundary conditions, and turbulence modeling techniques detailed in previous chapters. The first section will discuss the experimental cases taken as the basis for comparison with the numerical solutions. The next section discusses details involved in the actual computational procedure. The last section covers the comparison between the experimental and computational solutions.

6.1 EXPERIMENTAL DATA BASE

As outlined in Chapter 1, the data from Zumpano, et al. (13), is used as the experimental basis for this research effort. The supersonic fields of flow generated experimentally contain both the highly viscous flow regions along the diffuser walls as well as shock structures ranging from weak reflected shock waves to the strong core flow normal shock formation. Wall pressure measurements and Schlieren photographs are the basis for experimental versus computational comparisons.

TEST APPARATUS AND FLOW CONDITIONS

The radial-flow diffuser test rig was described in Figures 4 through 7. The walls of the diffuser were instrumented with static pressure taps to obtain wall pressure data. Additionally, a pitot-static probe was employed to obtain the data to characterize the flowfield at the entrance to the diffuser.

Plots of diffuser entrance Mach number (M), static pressure (p_s), and total pressure (p_p) are shown in Figure 17.

DIFFUSER
ENTRANCE FLOWFIELD
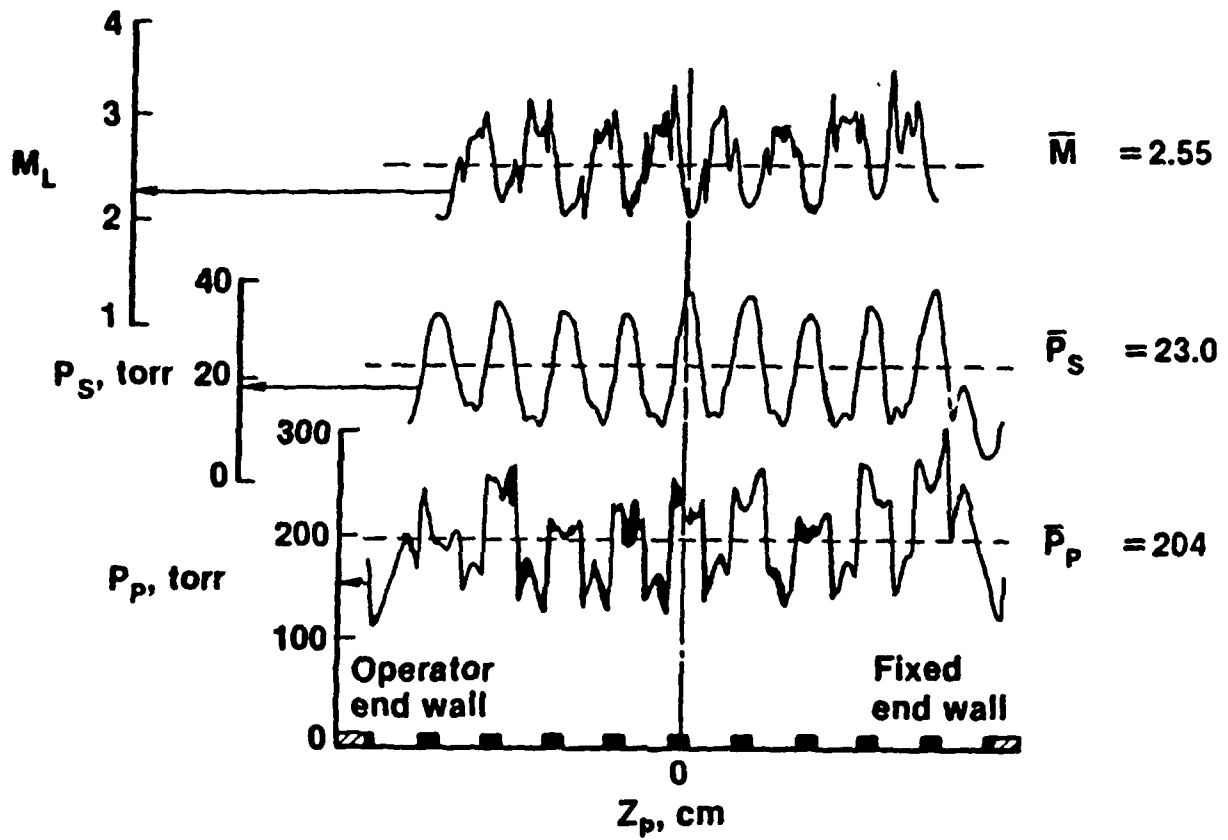
Figure 17. Experimental Diffuser Entrance Flowfield Conditions;
Mach Number, Static Pressure, Stagnation Pitot
Pressure (Ref. 13).

Digitally tabulated data obtained across the diffuser entrance provided the boundary condition information at the entrance to the computational grid, and is provided in detail in Appendix B. The nominal core flow diffuser entry conditions are summarized in Table I.

TABLE I

Nominal Core Flow Diffuser Entry Conditions

$\bar{M} = 2.55$

$\bar{P}_s = 23.0$ torr $= 64.1$ psf

$\bar{P}_p = 204.0$ torr $= 568.1$ psf

$T_0 = 530.0$ R $= 294.0$ K

$\bar{T}_{inlet} = 230.4$ R

$\dot{w}_{core} = 2.260$ kg/sec $= .155$ slugs/sec

In the UTRC experiment, both back (exhaust) pressure and bank blower flow rate were varied. Bank blowers are essentially devices that provide higher energy flow along the diffuser walls than in the core flow to control the amount of boundary layer separation. Too large a wall boundary layer

separation region will cause the diffuser core flow to unstart; i.e., the normal shock in the core flow region becomes unstable and travels upstream to the diffuser inlet and into the laser optical cavity. Such an event is catastrophic to laser device operation as it not only spoils the optical purity required for efficient laser resonator operation but it also poses an extreme physical hazard to the laser nozzle hardware: in early laser device experiments such unstarts have resulted in source nozzle melting due to the heat transfer that occurs when the normal shock hits the nozzle blades. One of the goals of the UTRC experimental study was to determine the necessity of supersonic bank blowers for successful diffuser operation, since they are somewhat inefficient if a significant percentage of the core mass flow is required to sufficiently energize the wall boundary layers. Based on experimental data (13) three bank blower cases were selected for continued experiment: (1) zero bank blower flow; (2) bank blower flow at 10 percent of the core mass flow rate; and (3) bank blower flow at 20 percent of the core mass flow rate (which experimentally turned out to be .195 rather than .20 of the core mass flow rate). These supersonic bank blowers provided this flow at a nozzle exit Mach number of 4.0. As seen in Figure 18, it was determined that bank blower flow of greater than 10 percent of the core flow was required in order to obtain a started core flow.

Figure 19 summarizes the experimental diffuser performance (as determined by the normal shock position in the core flow measured from schlieren photographs) for the 20 percent bank blower cases (13). Normalized (r/r_{de}) position of the normal shock is presented as a function of the back pressure (diffuser exit pressure), expressed as a fraction of
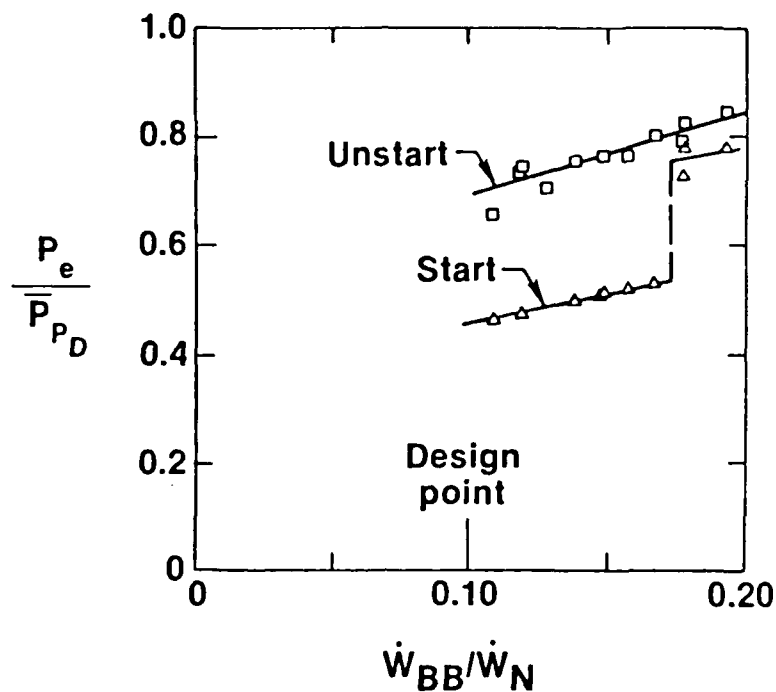
Figure 18. Vaneless Diffuser Experimental Performance (Ref. 13)
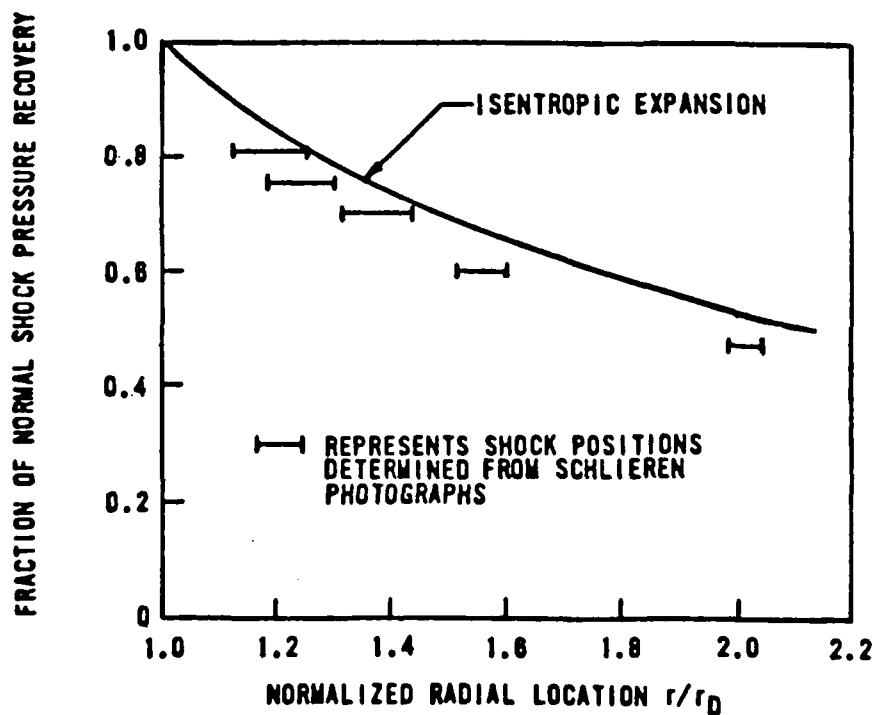
Figure 19. Cylindrical Vaneless Diffuser Performance;
Experimental Shock Positions Compared With One-
Dimensional Isentropic Expansion to Inviscid
Normal Shock Condition (Ref. 13).

63

Table II

SUMMARY OF NUMERICAL CASES

CASE	BASIC FLOW CONDITION	DIFFUSER CONFIGURATION	EXIT PRESSURE	WALL PLANE ENERGIZATION	TURBULENCE MODEL	RESULTS
1a	Uniform Core Inflow @$\bar{M}$=2.5	Standard UTRC	60% NSR	None	Standard Cebeci-Smith	Numerical Unstart
1b	Uniform Core Inflow @$\bar{M}$=2.5	Standard UTRC	60% NSR	None	Adverse Pressure Gradient Modified Cebeci-Smith	Numerical Unstart
2a	Uniform Core Inflow @$\bar{M}$=2.5	Standard UTRC	60% NSR	Uniform Bank Blower @$\dot{M}_{bb}$=4.0 W_{bb}=.2	Standard Cebeci-Smith	Numerical Unstart
2b	Uniform Core Inflow @$\bar{M}$=2.5	Standard UTRC	60% NSR	Uniform Bank Blower @$\dot{M}_{bb}$=4.0 W_{bb}=.2	Adverse Pressure Gradient Modified Cebeci-Smith	Stable, Steady Solution SPOS=.239; (R/R_{de}) Normal Shock = 1.73
2c	Uniform Core Inflow @$\bar{M}$=2.5	Standard UTRC	47% NSR	Uniform Bank Blower @$\dot{M}_{bb}$=4.0	Adverse Pressure Gradient Modified Cebeci-Smith	Stable, Steady Solution SPOS=.407; (R/R_{de}) Normal Shock = 2.25
3a	Uniform Inflow @$\bar{M}$=2.5	12 x Length of UTRC	60% NSR	None	Adverse Pressure Gradient Modified Cebeci-Smith	Stable, Steady Solution SPOS=.156; (R/R_{de}) Normal Shock = 1.48
3b	Uniform Inflow @$\bar{M}$=2.5	12 x Length of UTRC	47% NSR	None	Adverse Pressure Gradient Modified Cebeci-Smith	Stable, Steady Solution SPOS=.322; (R/R_{de}) Normal Shock = 1.99
4a	Actual Inflow Profile @$\bar{M}$=2.55	Standard UTRC	60% NSR	$\dot{W}_{bb}$=.195	Adverse Pressure Gradient Modified Cebeci-Smith	Stable, Steady Solution SPOS=.182; (R/R_{de}) Normal Shock = 1.56
4b	Actual Inflow Profile @$\bar{M}$=2.55	Standard UTRC	47% NSR	$\dot{W}_{bb}$=.195	Adverse Pressure Gradient Modified Cebeci-Smith	Stable, Steady Solution SPOS=.343; (R/R_{de}) Normal Shock = 2.05
4c	Actual Inflow Profile @$\bar{M}$=2.55	Standard UTRC	47% NSR	$\dot{W}_{bb}$=.195	Standard Cebeci-Smith	Numerical Unstart
4d	Actual Inflow Profile @$\bar{M}$=2.55	Standard UTRC	47% NSR	$\dot{W}_{bb}$=.195	Adverse Pressure Gradient Modified Cebeci-Smith With Inner Region Mod. Altered	Unsteady Solution; Shock Oscillates
4e	Actual Inflow Profile @$\bar{M}$=2.55	Standard UTRC	47% NSR	$\dot{W}_{bb}$=.195	Adverse Pressure Gradient Modified Cebeci-Smith With Outer Region Mod. Altered	Unsteady solution; shock oscillates

64

normal shock recovery pressure. The experimental diffuser entrance, r_{de}, was at 6.095cm (0.2ft) from the center of the cylindrical test apparatus. From Figure 19, for the case where the back pressure was set at 60 percent of the normal shock recovery pressure, the normal shock occurred in the diffuser in the range $1.51 \leq r/r_{de} \leq 1.60$. Shock position could also be stated in terms of the percentage of the distance through the diffuser as

$$SPOS = \frac{r_{shock} - r_{diffuser\ entrance}}{l_{diffuser}} \qquad (6\text{-}1)$$

where $l_{diffuser}$ is the total length of the diffuser. Thus, for the 60 percent normal shock recovery backpressure case, normal shock position was in the range $0.166 \leq SPOS \leq 0.195$. This case was chosen as the baseline computational case, to be supplemented later with comparison to the 47 percent normal shock recovery backpressure case. For this second baseline case, the normal shock position is in the range $1.95 \leq r/r_{de} \leq 2.05$, or $0.309 \leq SPOS \leq 0.342$.

6.2 COMPUTATIONAL DETAILS

Solutions were attempted for the axisymmetric diffuser for the cases shown in Table II. The approach taken was incremental, beginning with the simplest cases and proceeding to the actual baseline computational case, where a solution was obtained for the actual inflow parameters of the UTRC experimental case. These solutions were all performed on a CRAY 1 digital computer located at Kirtland Air Force Base, New Mexico. The average rate of data processing was 2.41×10^{-5} second per grid point per iterative time

increment. In this section the results of these computations will be discussed. Full details of the computational case are contained in the appendices.

Case 1a

The first computational attempt was exercised against the condition of a uniform core inflow at $\bar{M}$ = 2.5. The exit pressure was set at 60 percent of normal shock recovery. The diffuser configuration was the baseline experimental vaneless diffuser. No wall flow energization was employed. The basic Cebeci-Smith two-layer algebraic eddy viscosity turbulence model was used to approximate the physics of the boundary layer. Computations were started from an initial condition that imposed the one-dimensional inviscid normal shock solution to the flow through the diffuser. As the computational algorithm progressed in time, the wall boundary layer developed an overly large unstable separation, choking the flow and forcing the core flow normal shock to travel upstream until it encountered the upstream boundary, at which time the computation was terminated. This result represented a numerical unstart of the diffuser. Figure 20 presents the time history of the normalized line of symmetry normal shock location (SPOS - percentage of distance through the diffuser). Numerically, it took the flow 2.8 milliseconds to unstart. The detailed results of these computations are presented as Mach number contour plots, wall and line of symmetry pressure plots, and line of symmetry temperature plots in Appendix C.

BASIC CEBECI–SMITH TIME HISTORY 60%NSR WBB=0
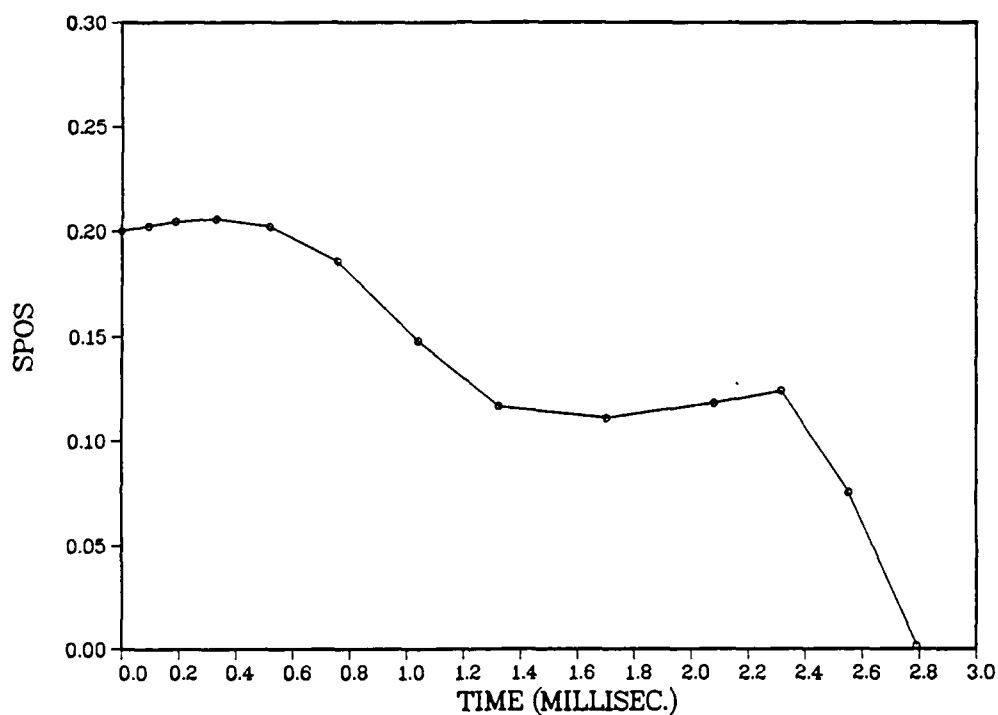
Figure 20. Time History of Normalized Core Flow Normal Shock
Position (SPOS); Navier-Stokes Code with Basic
Cebeci-Smith Turbulence Model; 60% NSR; Zero Wall
Bank Blower (Case 1a).

Case 1b

The second computational experiment was identical to the first with only one exception: the basic Cebeci-Smith eddy viscosity turbulence model was modified to account for adverse pressure gradient as discussed in Chapter V. Again, a uniform core inflow was assumed without wall flow energization employed. Computations were started from the inviscid one-dimensional normal shock condition matching this exit pressure. As the algorithm marched forward in time, the wall boundary layer again formed an overly large unstable separation region that again resulted in a numerical unstart of the diffuser as the core flow normal shock moved upstream until it encountered the upstream boundary. At this point, approximately 3.4 milliseconds after flow "start", computations were again terminated. Figure 21 presents the time history of normalized shock position in the diffuser. Detailed results for these computations are presented similarly to those of Case 1a in Appendix D.
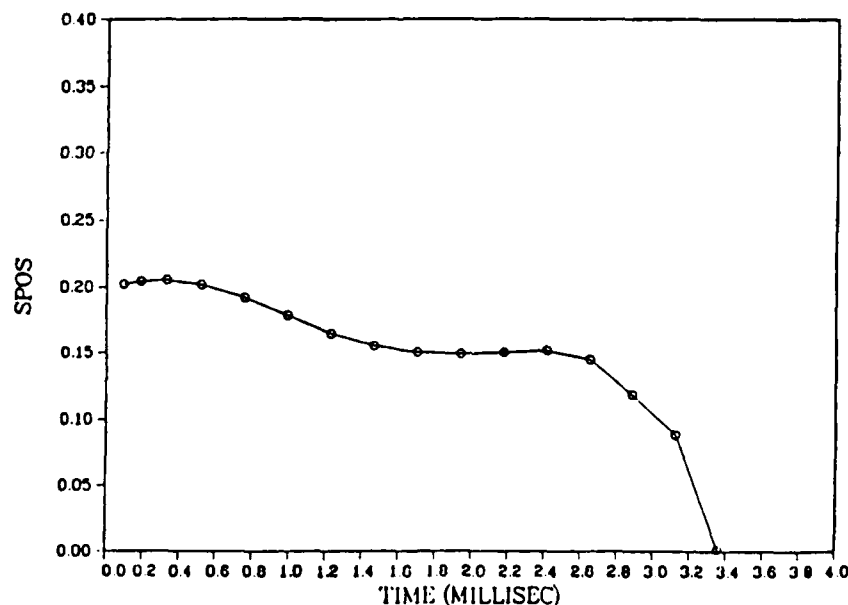
Figure 21. Core Flow Normal Shock Position Time History, Case 1b (Uniform Inflow, 60% NSR, wbb – 0, modified Cebeci-Smith Turbulence Model).

68

Case 2a

The basic Cebeci-Smith eddy-viscosity turbulence model was employed against the baseline diffuser configuration with a uniform core inflow and a uniform wall bank blower to energize the wall boundary layer. The core inflow was again at $\bar{M} = 2.5$, and the bank blower was run at a mass flow ratio of 0.20 of the core flow at $M_{bb} = 4.0$. These inflow conditions, also utilized in Case 2b, are shown in Figures 23, 24, 25, and 26. The starting condition was again the inviscid one-dimensional normal shock solution for the diffuser exit pressure of 60 percent of normal shock recovery pressure. Again, a numerical unstart occurred as the solution marched forward in time. Figure 22 presents the time history of this computation, showing that the unstart occurred 7.6 milliseconds after flow "initiation" from the initial condition. Details of these computations are provided in Appendix E.
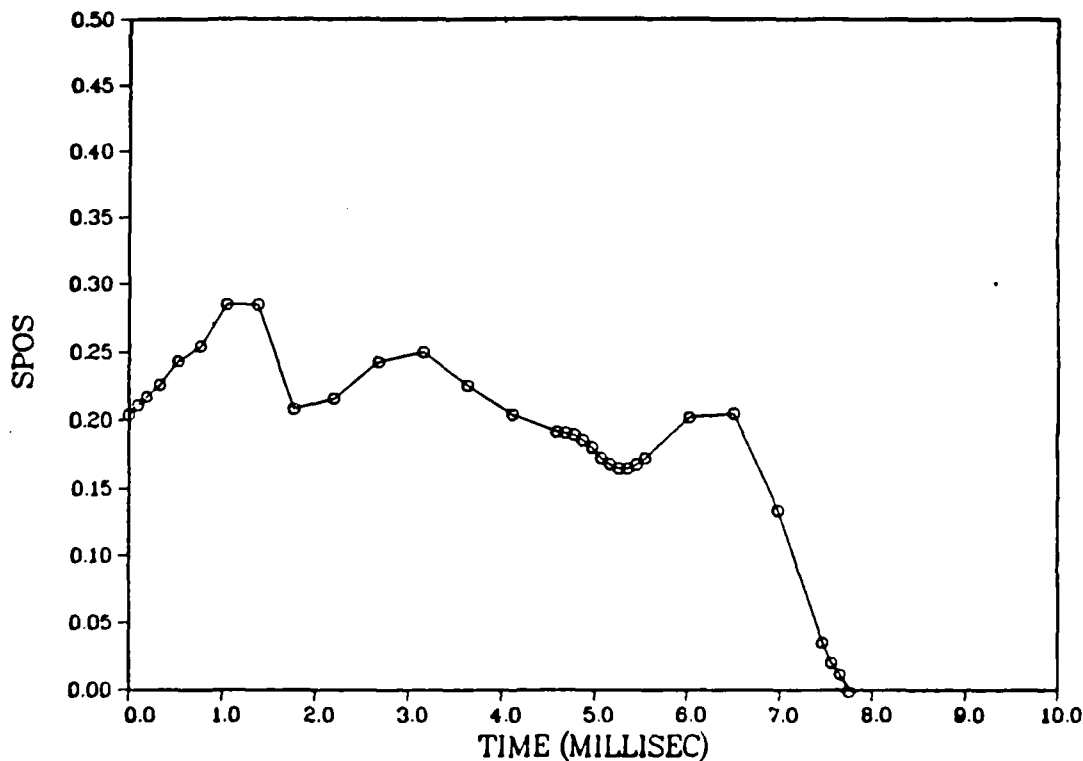
Figure 22. Core Flow Normal Shock Position Time History, Case 2a
(Ideal Inflow, 60% NSR, wbb = .2, basic Cebeci-Smith
Turbulence Model).

69

IDEAL INFLOW VELOCITY PROFILE
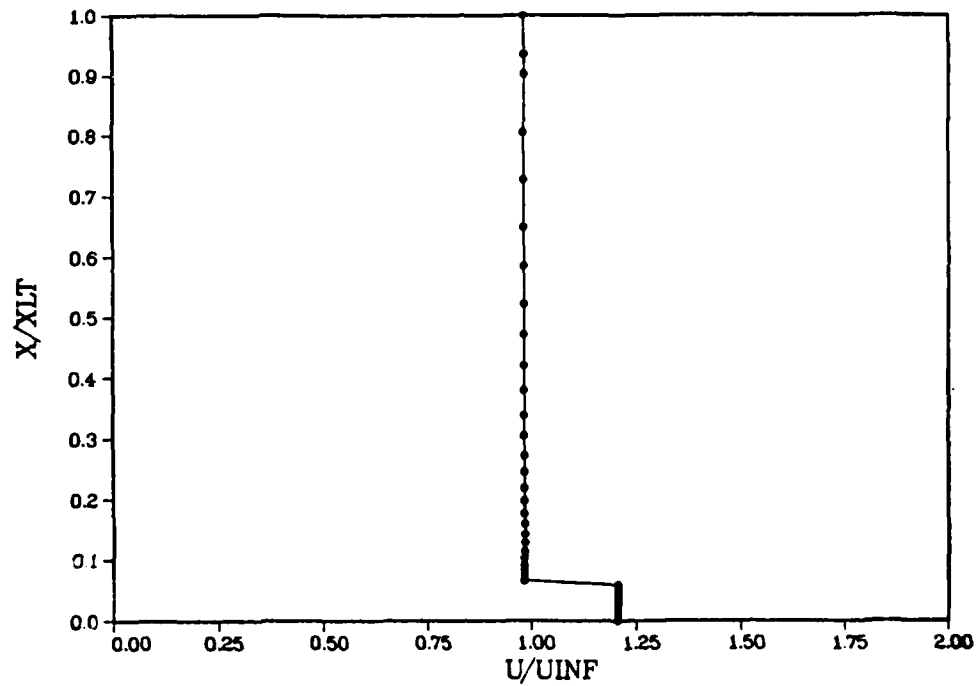
Figure 23. Ideal Inflow Velocity Profile.

VELOCITY VECTOR PLOT IDEAL INFLOW
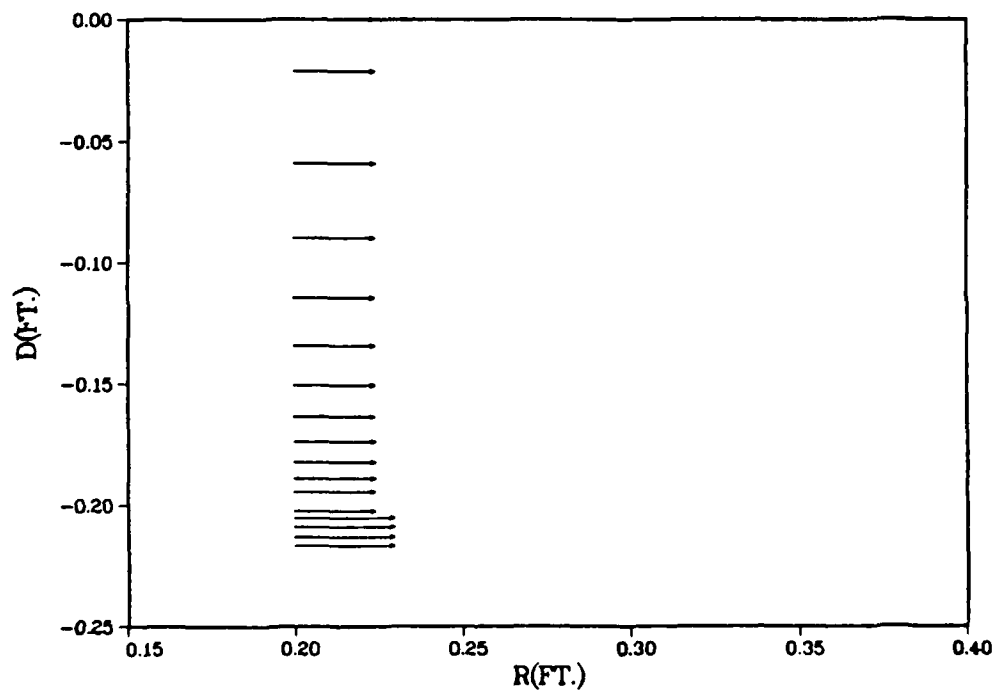
Figure 24. Ideal Inflow Velocity Vector Plot.

70

IDEAL INFLOW MACH NUMBER PROFILE
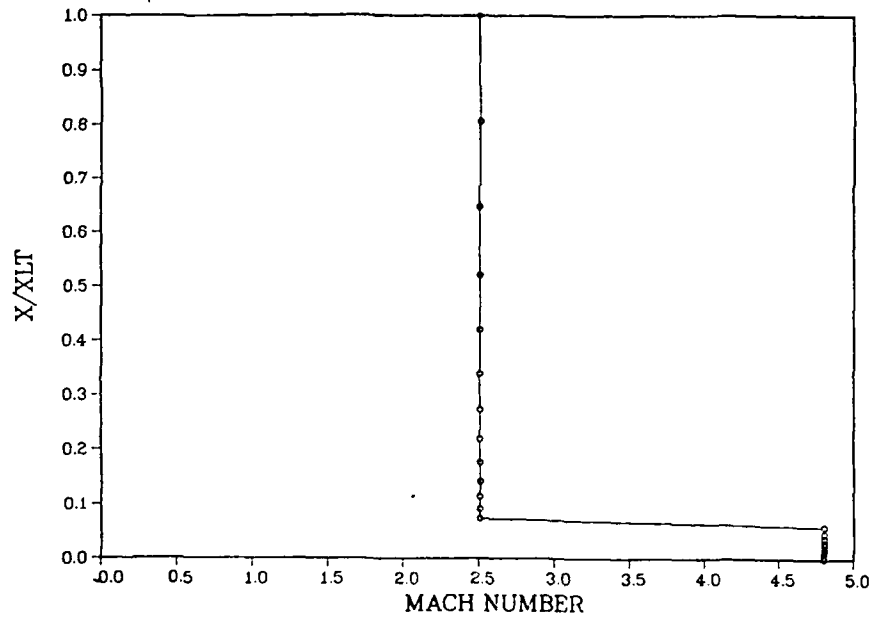
Figure 25. Ideal Inflow Mach Number Profile.

IDEAL INFLOW MOMENTUM PROFILE
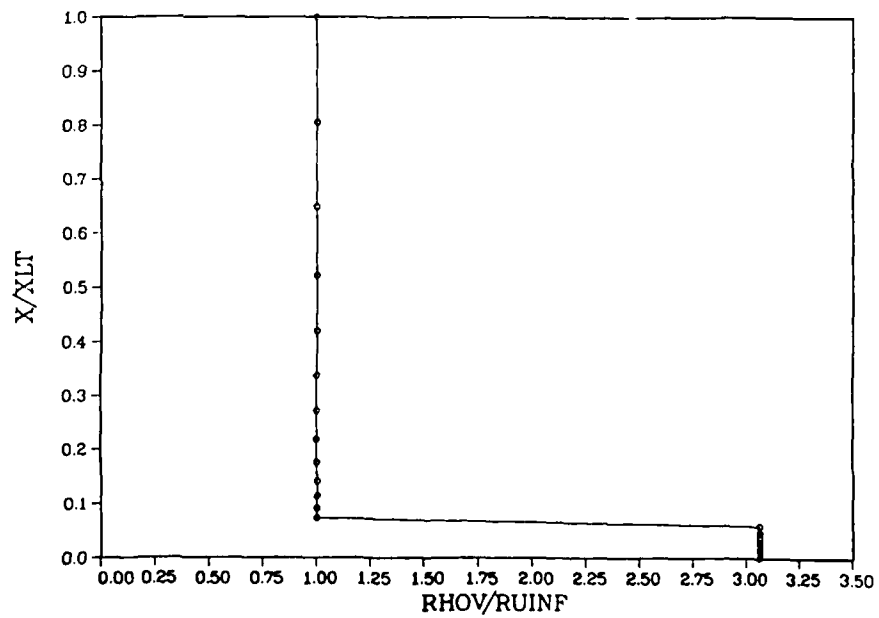
Figure 26. Ideal Inflow Momentum Profile.

71

Case 2b

The stiffened eddy-viscosity approach to turbulence modelling in the presence of an adverse pressure gradient was employed against the baseline diffuser configuration with a uniform core inflow and a uniform wall bank blower at the same flow conditions as in case 2a (Figures 23, 24, 25 and 26).The numerical code was written to incorporate the measurement of pressure gradient along the diffuser wall. When the onset of an adverse pressure gradient was computed during time step t, the algebraic eddy viscosity model's constants k_1, A^+, and k_2 were recalculated to reflect this effect and these new values were used to calculate the eddy viscosity applied at the next time step (for numerical efficiency new values of eddy viscosity were actually computed only every tenth time step). The starting condition was again the inviscid one-dimensional normal shock solution for 60 percent normal shock recovery diffuser exit pressure. After approximately five characteristic times a steady numerical solution was achieved, representing a started diffuser flowfield with the core flow normal shock located 23.9 percent down the duct (SPOS = .239; r/r_{de} = 1.734). Figure 27 presents the time history of these computations, and Figure 28 shows the Mach number contours of the converged solution. Figure 29 presents selected individual Mach number contours of the converged solution. Figure 30 displays the developed velocity profiles for the steady solution. These are presented as ratios of U/UINF. U represents the value of the local streamwise velocity component. UINF is a constant referenced to the flow at the diffuser entry, an is an average defined by

$$UINF = \dot{m}/\rho A \qquad\qquad (6-2)$$

72

Note that the wall flow energizing bank blower retains its high energy flow characteristic throughout the entire length of the diffuser. Figures 31 and 32 present the velocity vector plots for the converged solution. From this information the effect of the strong bank blower is evident; only a very small wall separation region occurs. This solution represents what is effectively an ideal case, since the ideal inflow conditions contain none of the crossflow effects (including turnback oblique shocks) or viscous losses that would result from supersonic mixing from multiple source nozzles.

The author concludes that both wall flow energization and the adverse pressure gradient modification to the basic Cebeci-Smith turbulence model are required to attain a "started" flow in the computational representation of a short diffuser. Wall pressure, and line of symmetry pressure and temperature ratios throughout the converged solution flowfield are presented in Figure 33, where the x axis is the percentage of distance along the diffuser length. The overshoot in the wall pressure in the lambda shock impingement region is particularly worthy of note because it was unanticipated and it appears in the experimental data of Zumpano, et al.

(30). Figure 34 presents the kinematic displacement thickness δ^* (as a percentage of the diffuser diameter) computed along the length of the diffuser. At its' maximum value immediately behind the shock separation point, δ^* is less than one percent of the diffuser diameter. Appendix F provides the details of these computations.
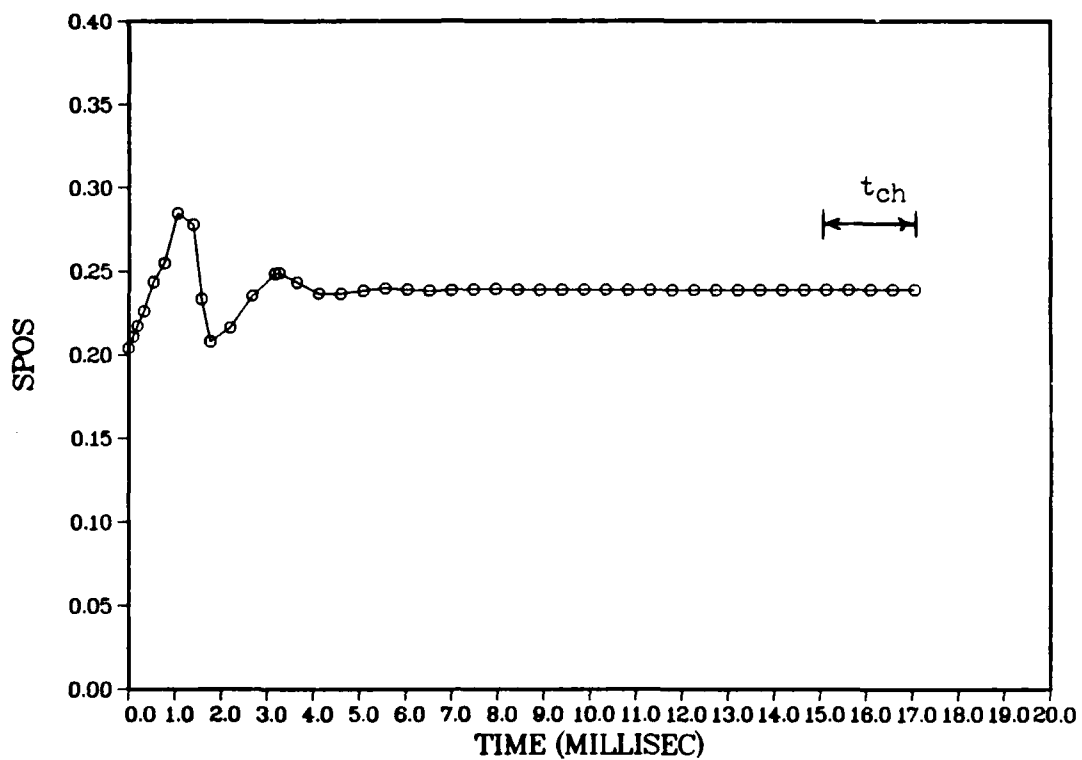
Figure 27. Core Flow Normal Shock Position Time History, Case 2b
(Ideal Inflow, 60% NSR, wbb - .2, modified Cebeci-
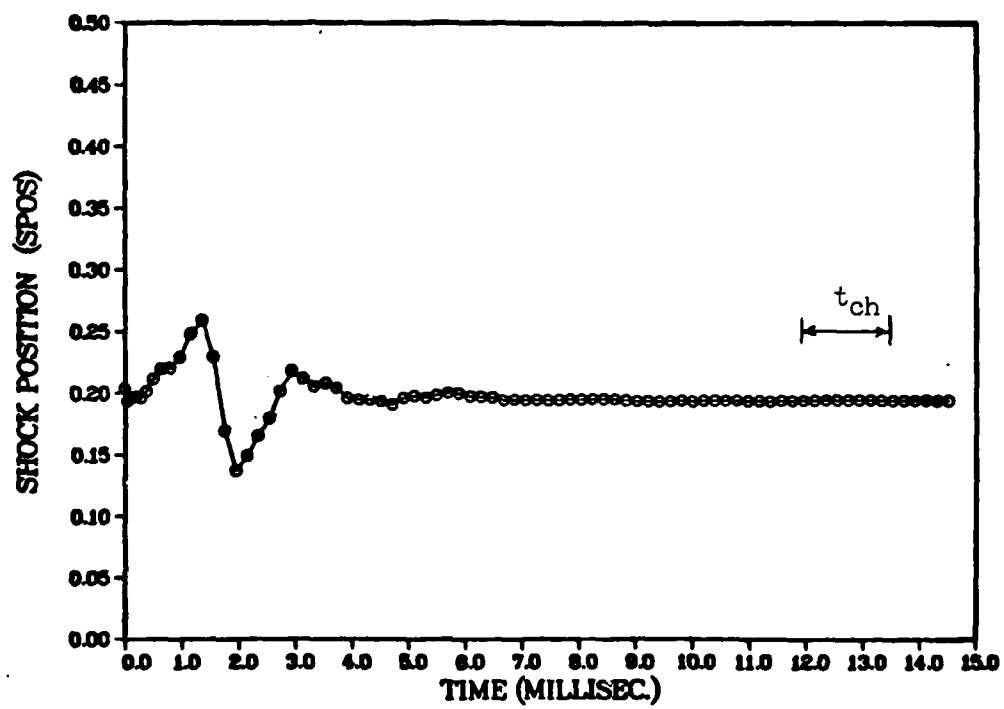Smith Turbulence Model).
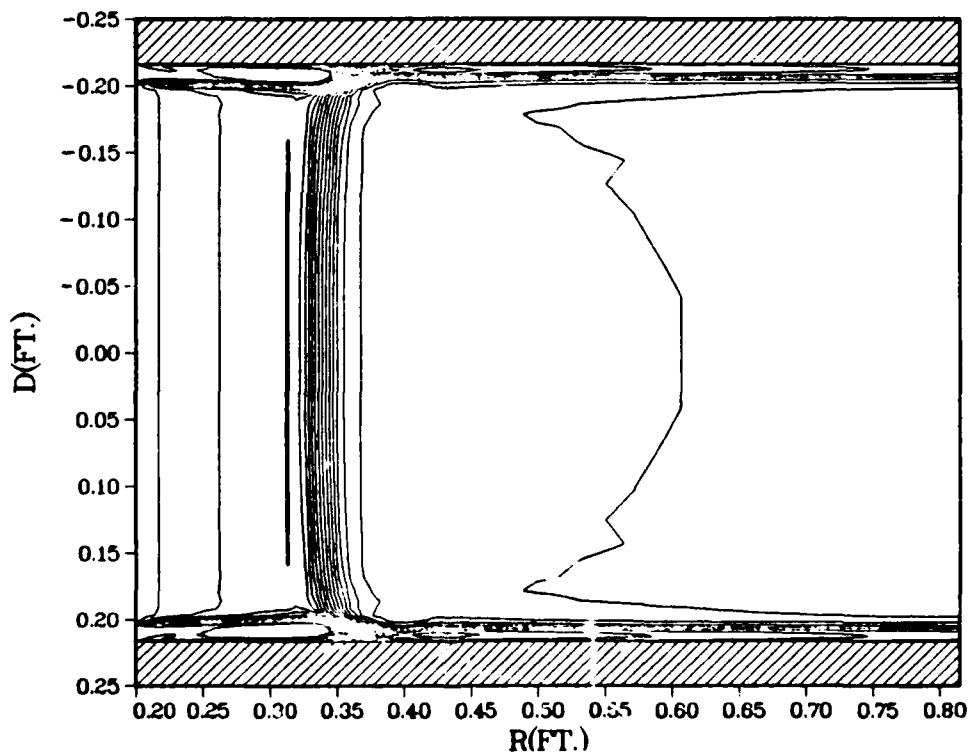
Figure 28. Converged Solution Mach Contours, Case 2b.

M=.25 CONTOUR 60%NSR Ideal Inflow Solution
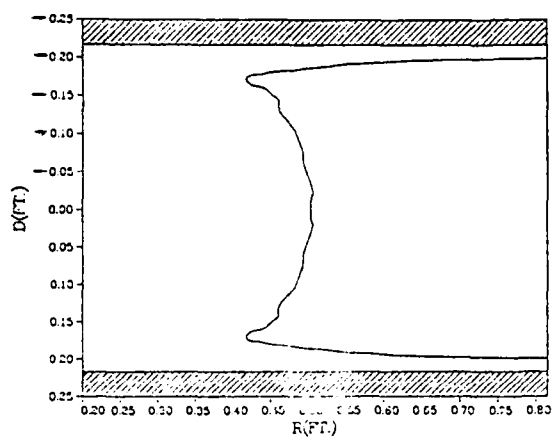
M=1.0 CONTOUR 60%NSR Ideal Inflow Solution
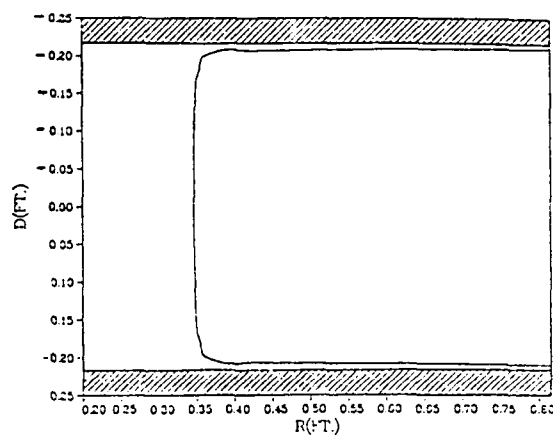
M=1.5 CONTOUR 60%NSR Ideal Inflow Solution
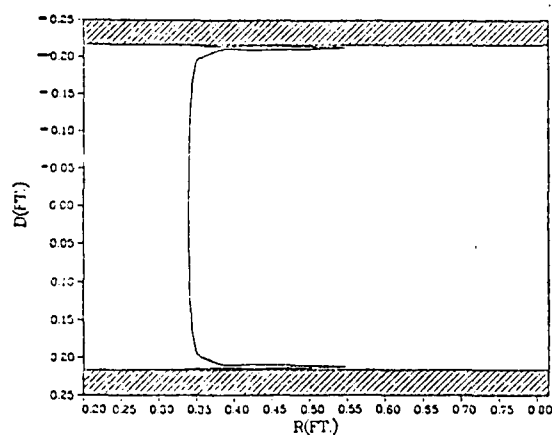
M=2.0 CONTOUR 60%NSR Ideal Inflow Solution
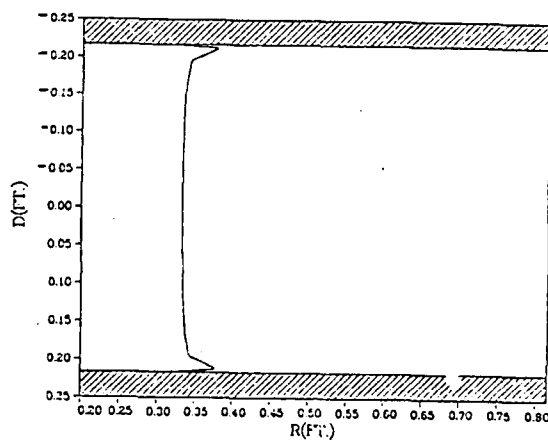
M=3.0 CONTOUR 60%NSR Ideal Inflow Solution
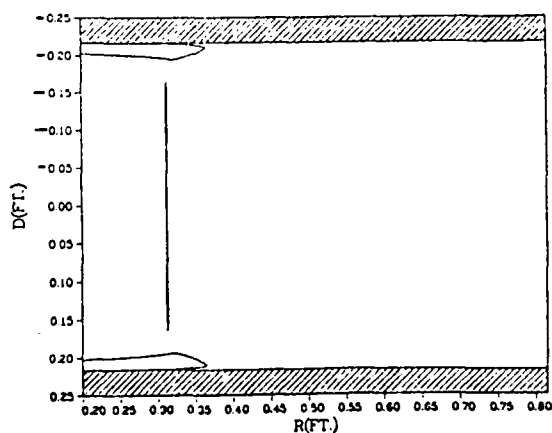
M=4.0 CONTOUR 60%NSR Ideal Inflow Solution
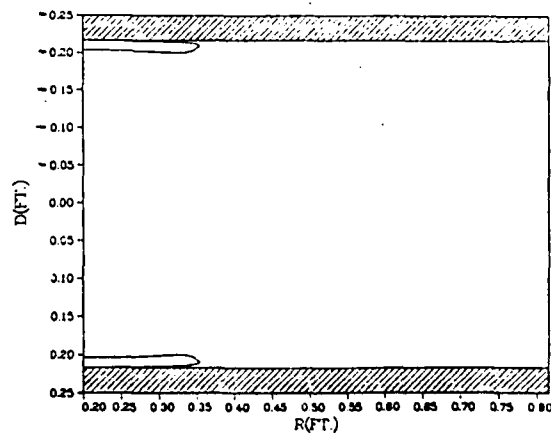
Figure 29. Selected Individual Mach Contours, Case 2b Solution.

75

MACH CONTOURS 60%NSR 60X80 GRID SOLUTION
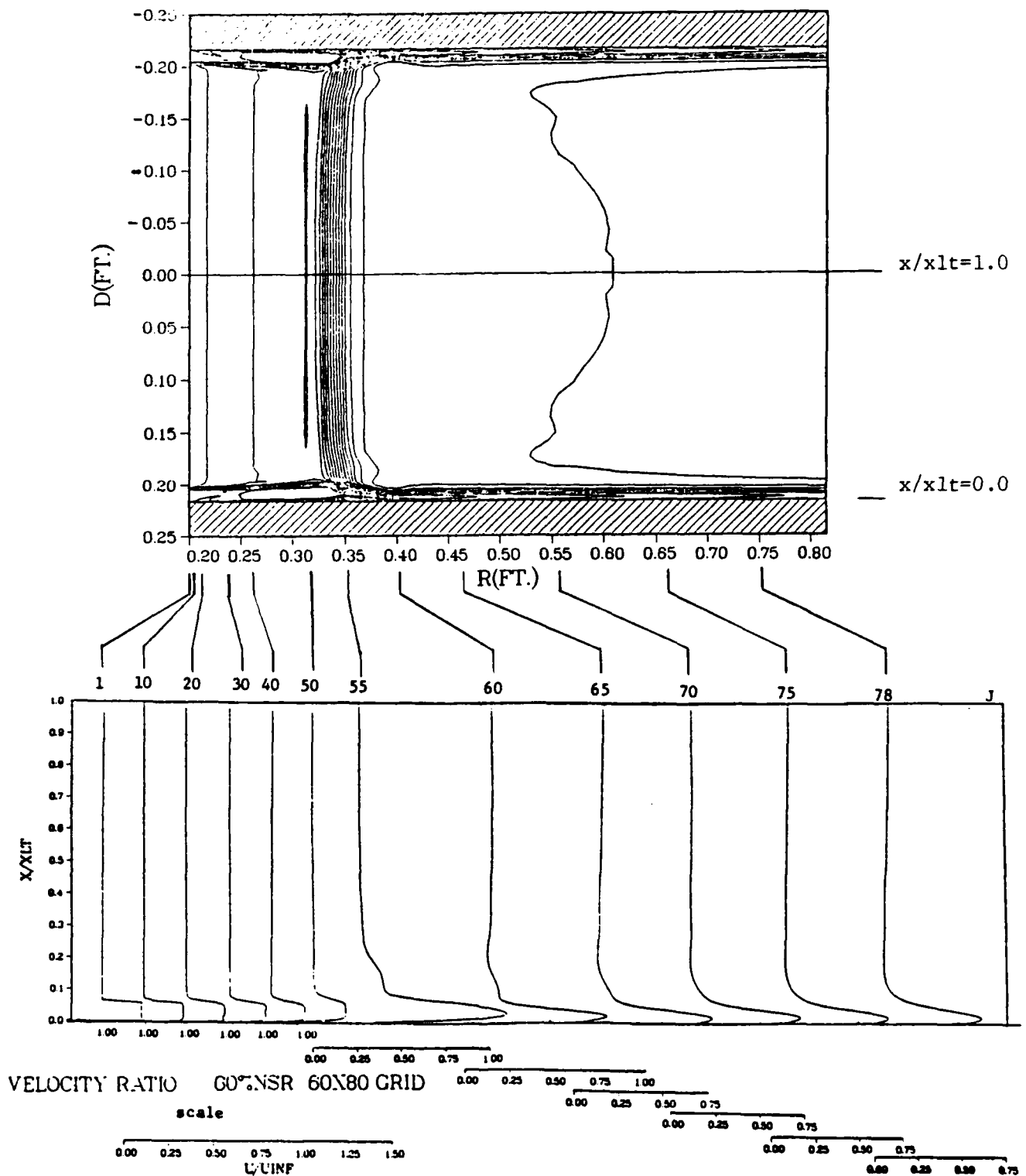
Figure 30. Velocity Profiles, Case 2b Converged Solution.

70

VELOCITY VECTOR PLOT 60%NSR Ideal Inflow Solution
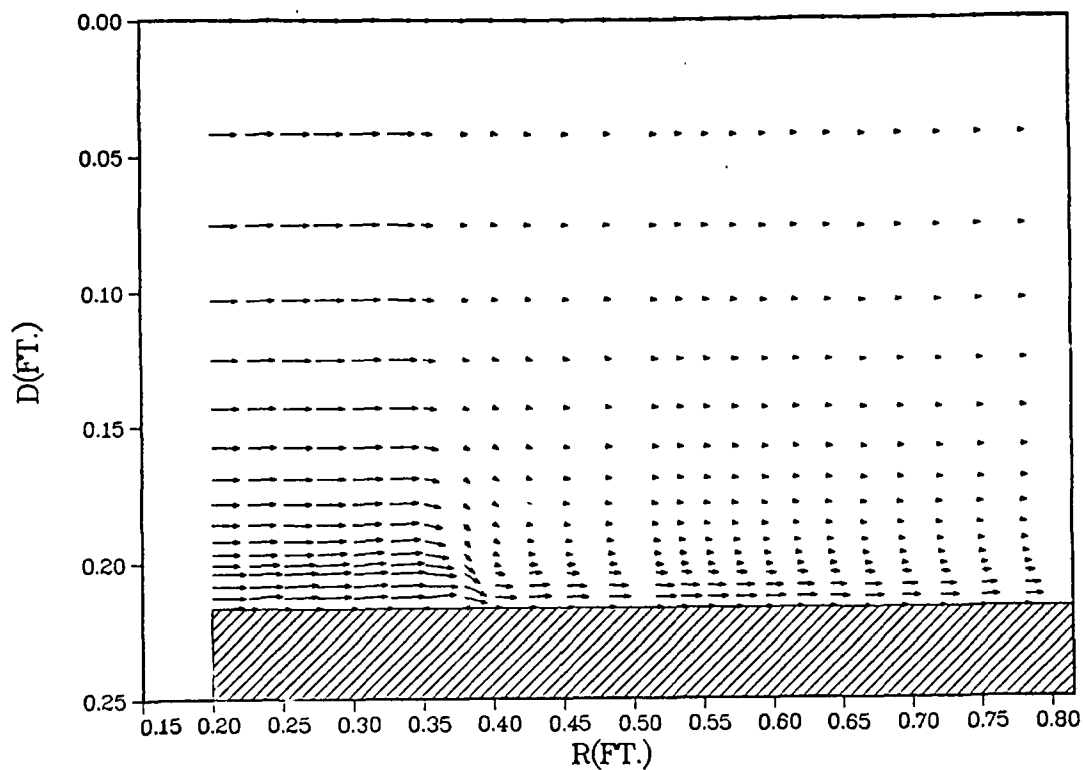
Figure 31. Velocity Vector Plot, Case 2b Converged Solution.
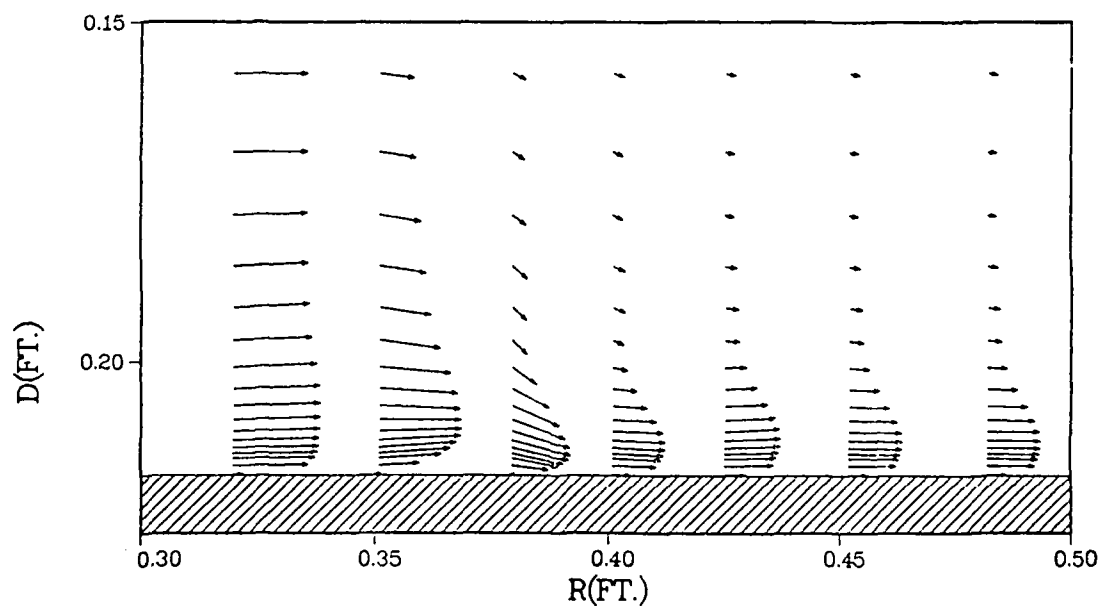
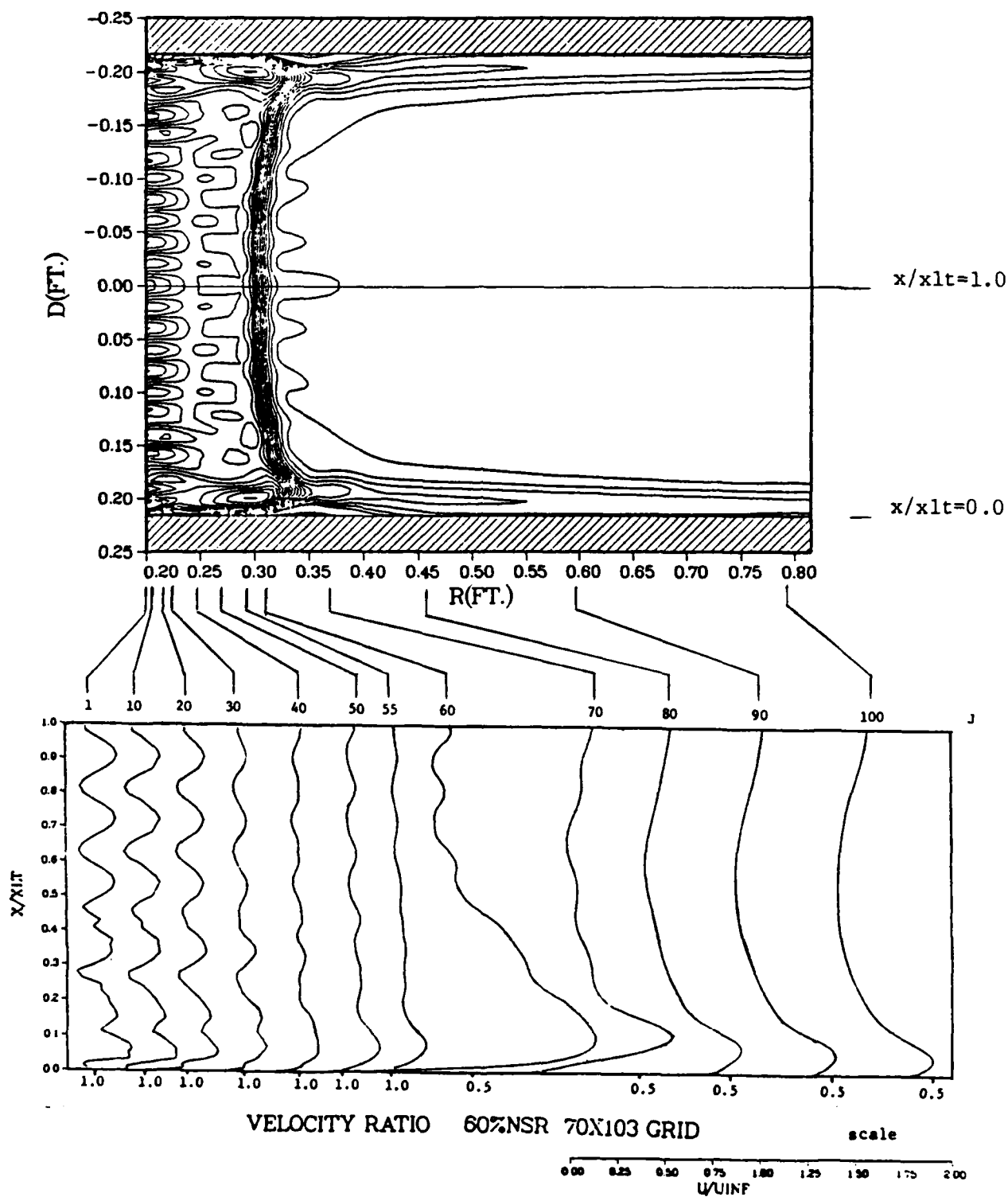Figure 32. Velocity Vector Plot, Case 2b Converged Solution, Expanded View Showing Separation Region Detail.
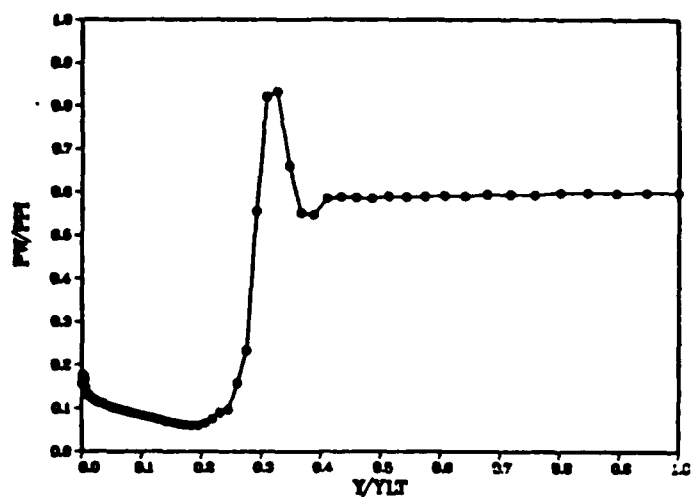
a. Wall Pressure Ratio
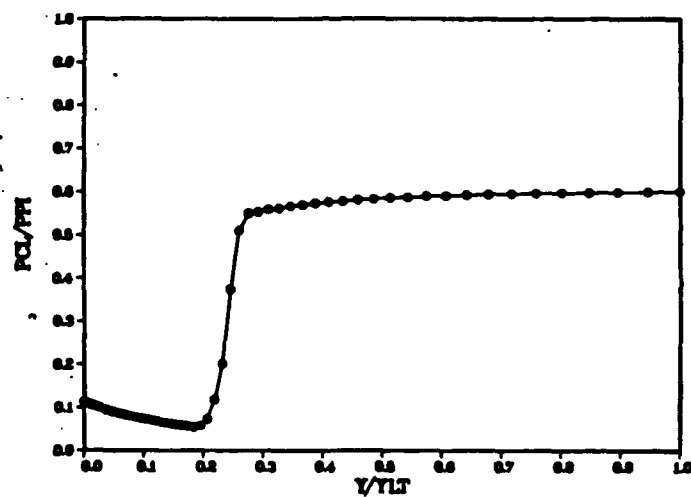
b. Line of Symmetry Pressure Ratio
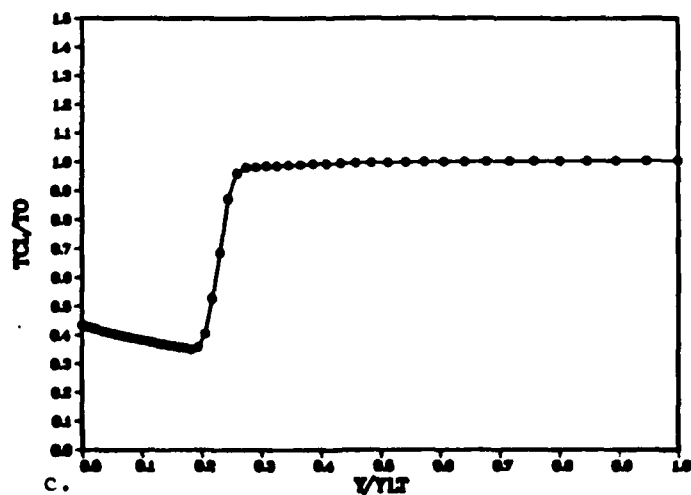
c.

Figure 33. Case 2b Converged Solution Flowfield Conditions;
a) Wall Pressure Ratio; b) Line of Symmetry Pressure
Ratio; c) Line of Symmetry Temperature Ratio.

Dstar Ratio 60%NSR Ideal Inflow Solution
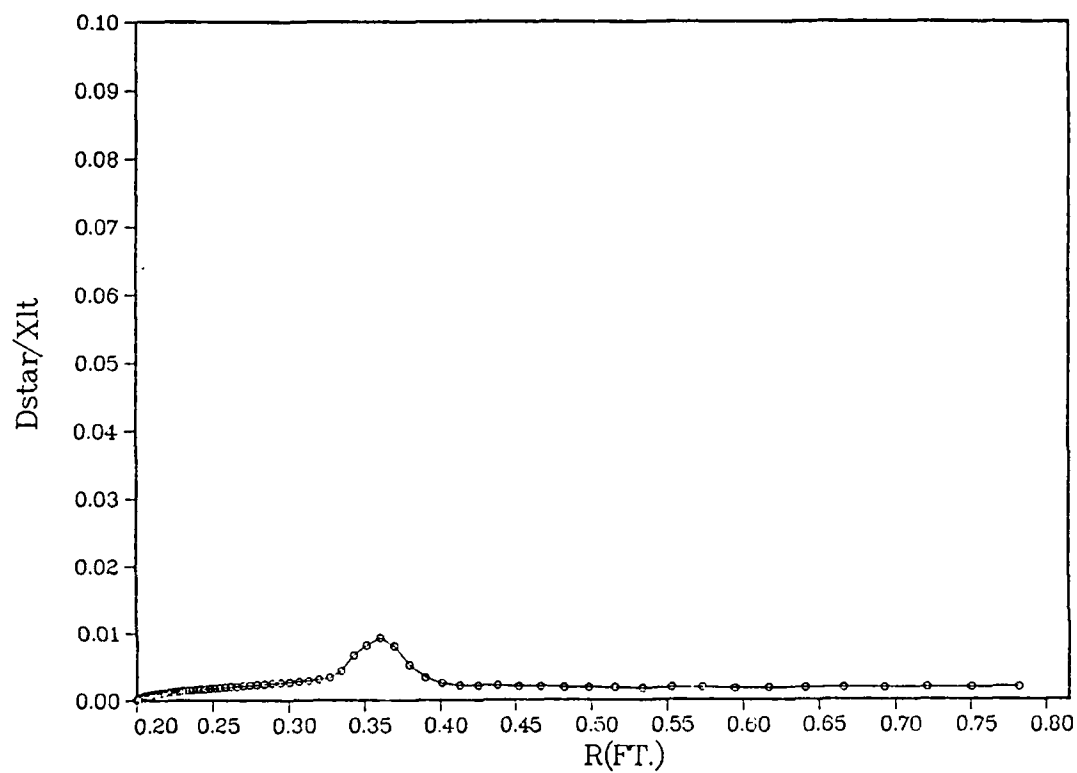
Figure 34. Plot of Case 2b Converged Solution Kinematic
Displacement Thickness.

Case 2c

From the converged solution of Case 2b, the exit pressure was lowered
to 47 percent of normal shock recovery and the algorithm was allowed to
march forward in time, achieving a new, steady, converged solution after ten
additional characteristic times. This solution contains a core flow normal
shock location at approximately 41 percent of the baseline diffuser length
(SPOS = 0.407; r/r_{de} = 2.253). The time history of this converged solution
is presented in Figure 35. Figure 36 presents a Mach contours plot of the
converged solution. Figure 37 presents selected individual Mach contours of
the converged solution. The developed velocity profiles for this steady
solution are presented in Figure 38, again showing similar characteristics
to the flowfield of Case 2b. Figure 39 presents the velocity vector plots,
which again show only a very small wall separation region. The converged
flowfield wall pressure, line of symmetry pressure and temperature ratios
are presented in Figure 40. The overshoot of the wall pressure in the
region of lambda shock impingement is still present, but it is not as severe
as for the 60 percent normal shock recovery backpressure case. The
variation in kinematic displacement thickness δ^* along the diffuser wall is
shown in Figure 41. Again, it is in the one percent range. Figure 42
displays a visual comparison of both the 60 percent and 47 percent normal
shock recovery backpressure steady solution Mach contours.
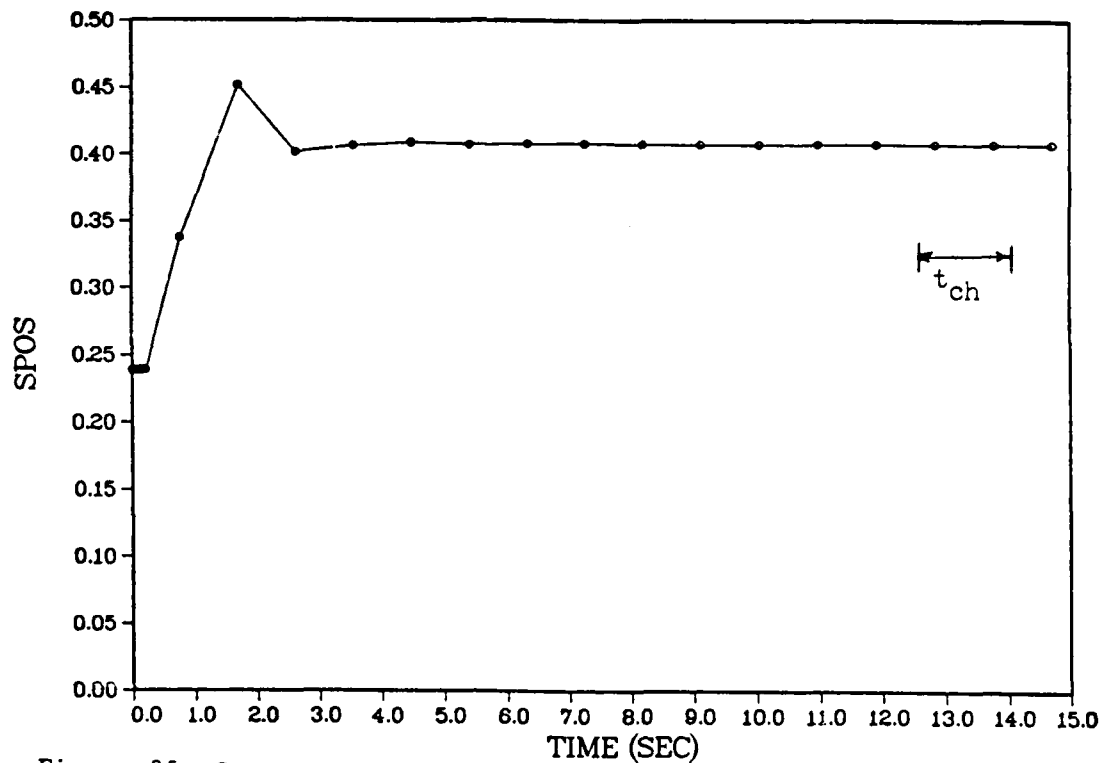
Figure 35. Core Flow Normal Shock Position Time History, Case 2c
(Ideal Inflow, 47% NSR, wbb = .2, modified Cebeci-
Smith Turbulence Model).
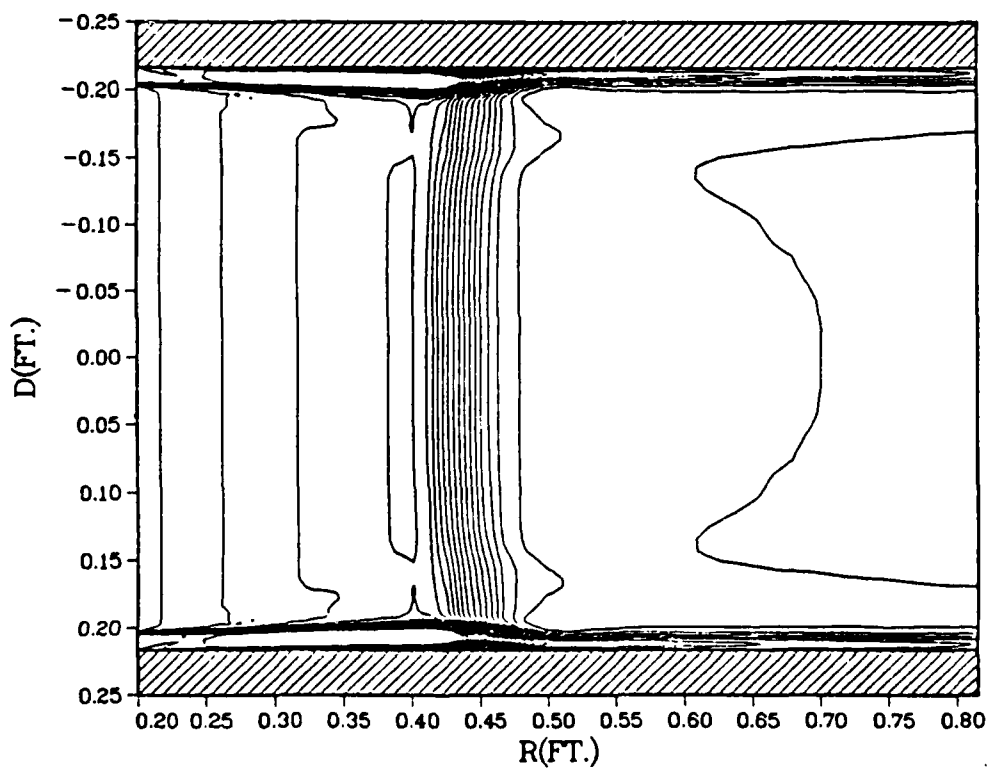
Figure 36. Converged Solution Mach Contours, Case 2c.

M=.50 CONTOUR 47%NSR Ideal Inflow Solution

M=1.0 CONTOUR 47%NSR Ideal Inflow Solution

M=1.50 CONTOUR 47%NSR Ideal Inflow Solution

M=2.0 CONTOUR 47%NSR Ideal Inflow Solution

M=3.0 CONTOUR 47%NSR Ideal Inflow Solution

M=4.0 CONTOUR 47%NSR Ideal Inflow Solution
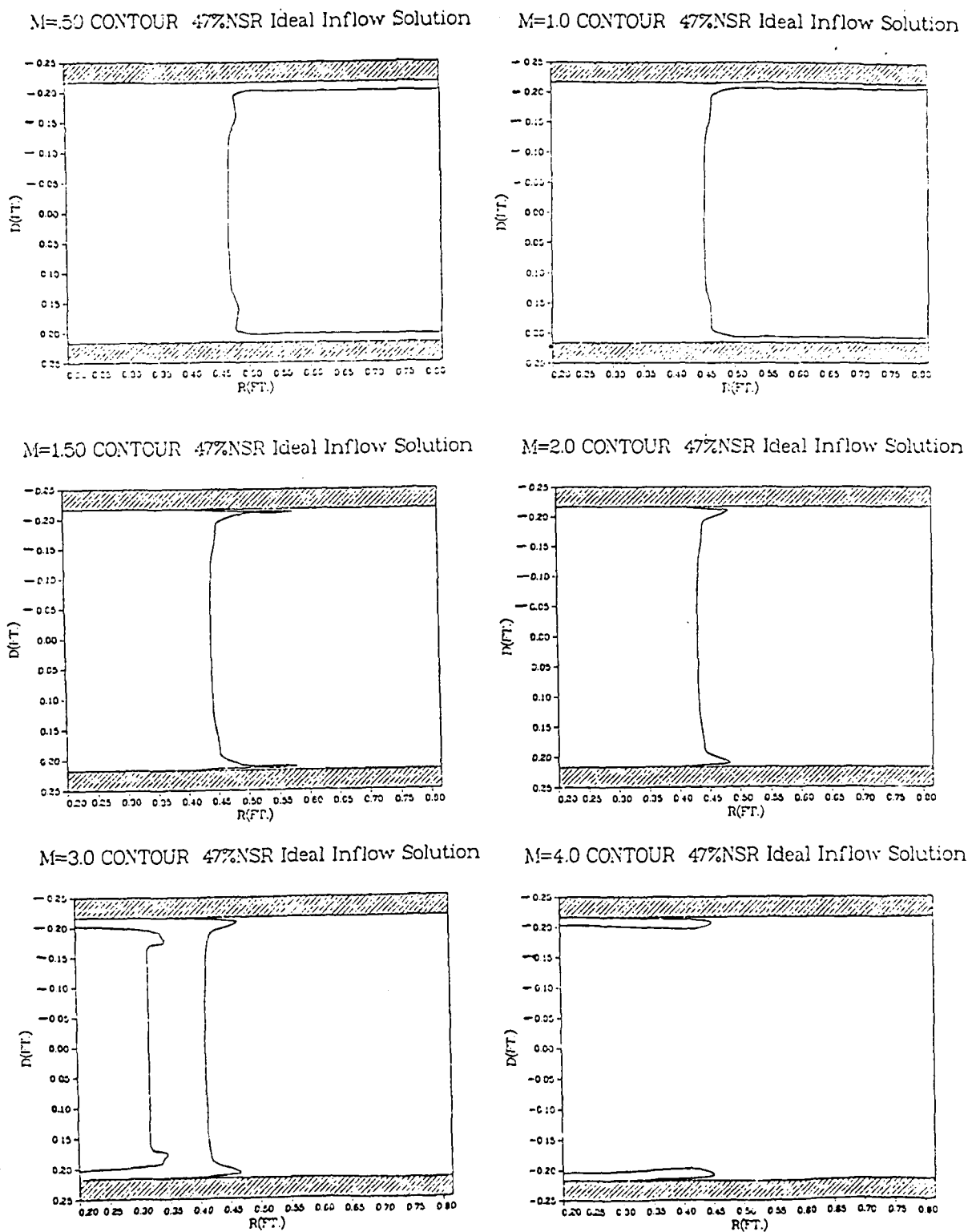
Figure 37. Selected Individual Mach Contours, Case 2c Solution.

MACH CONTOURS 47%NSR 60X80 GRID SOLUTION
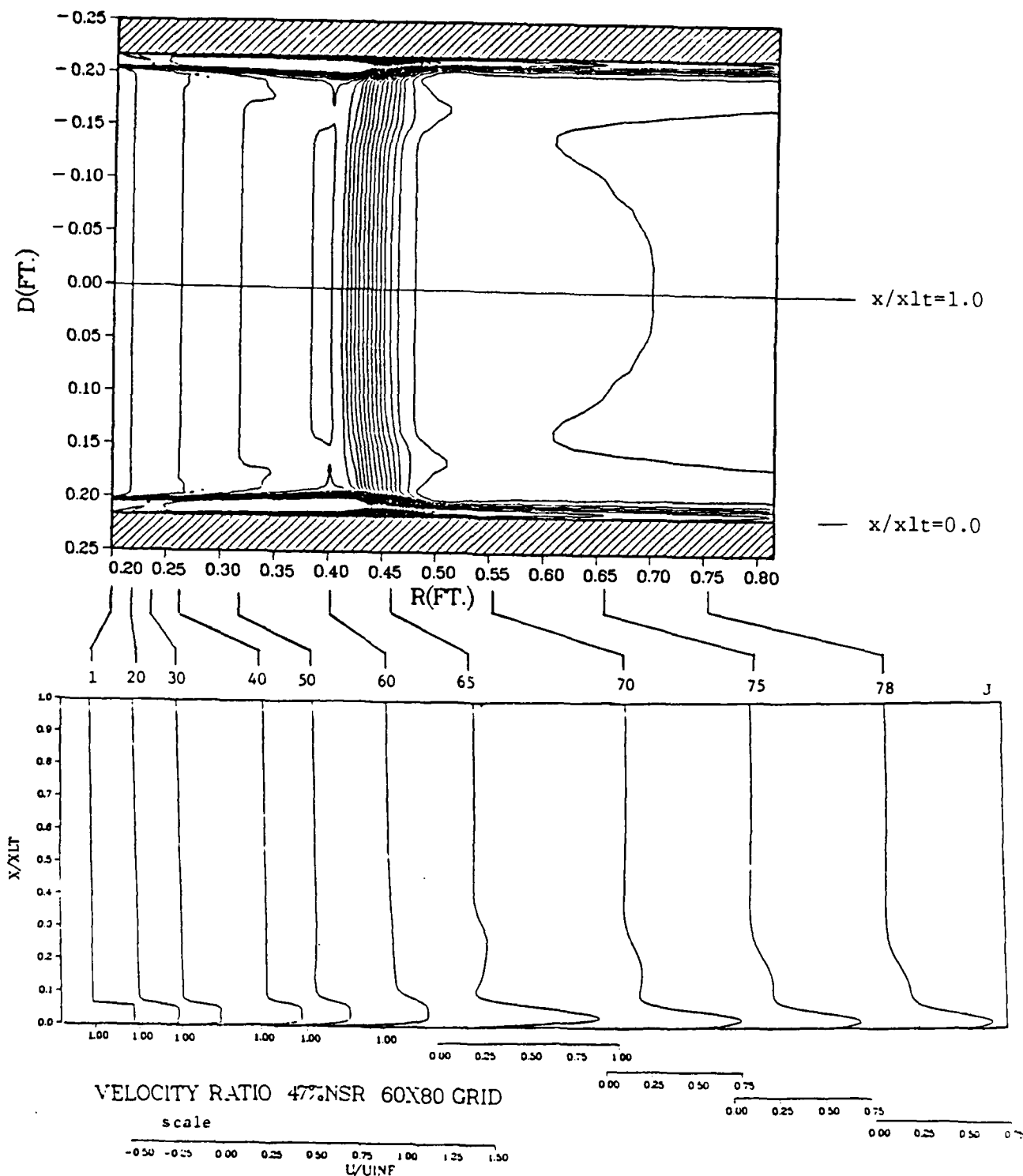
Figure 38. Velocity Profiles, Case 2c Converged Solution.

83

VELOCITY VECTOR PLOT 47%NSR Ideal Inflow Solution
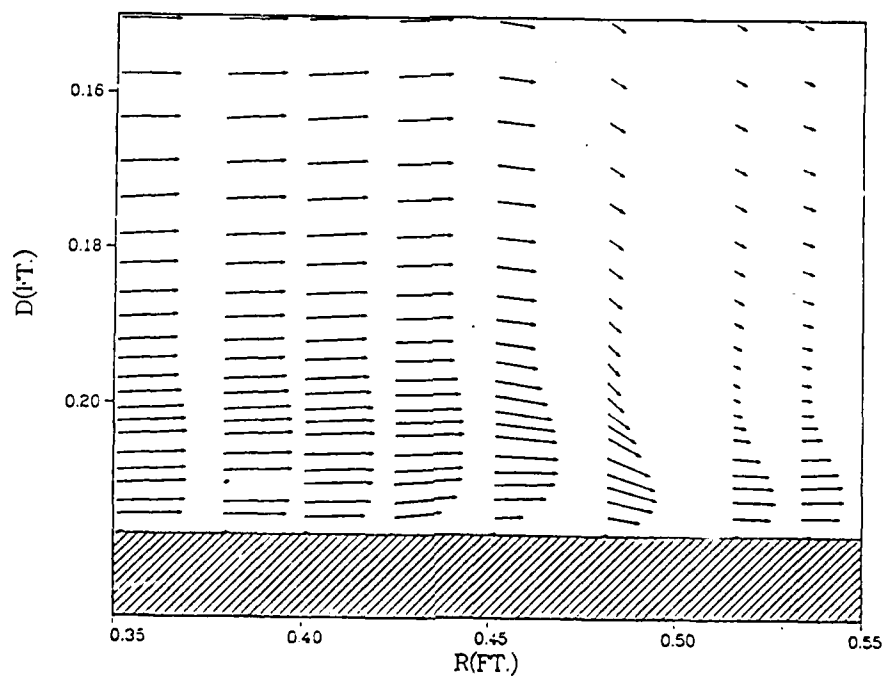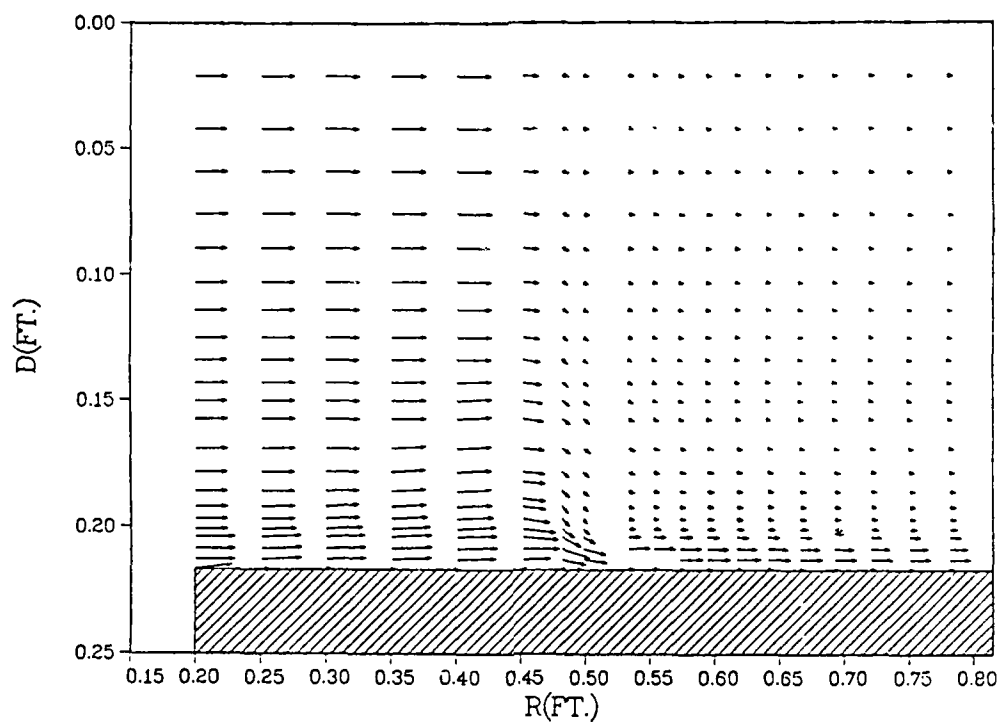
Figure 39. Velocity Vector Plot, Case 2c Converged Solution
a) Full Computational Domain; b) Expanded View Showing
Separation Region Detail.

84
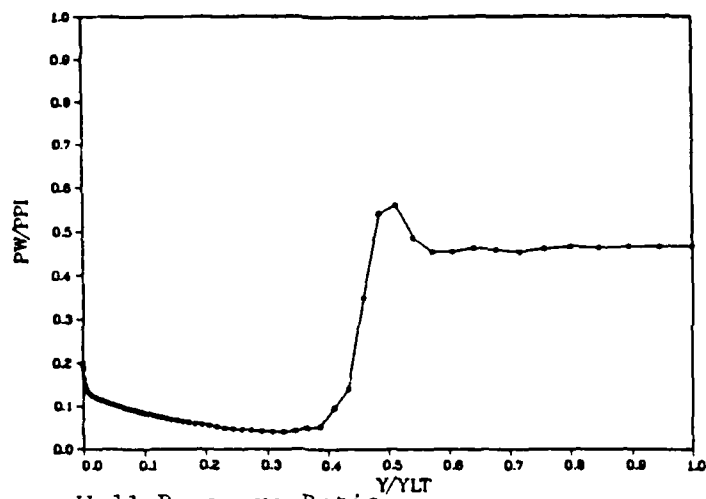
a. Wall Pressure Ratio
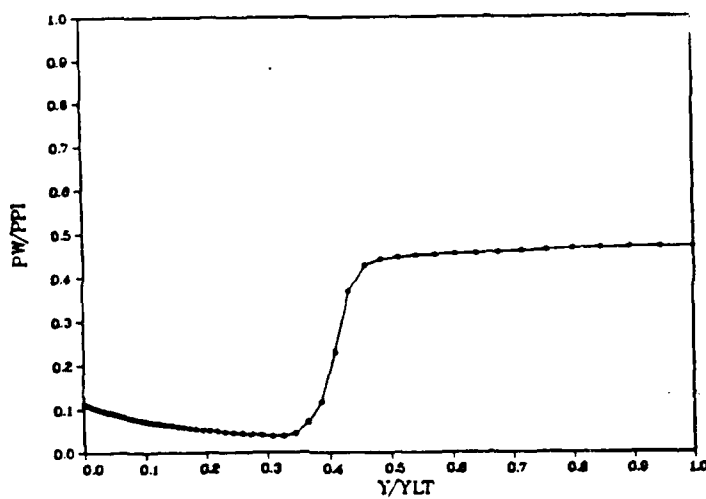
b. Line of Symmetry Pressure Ratio
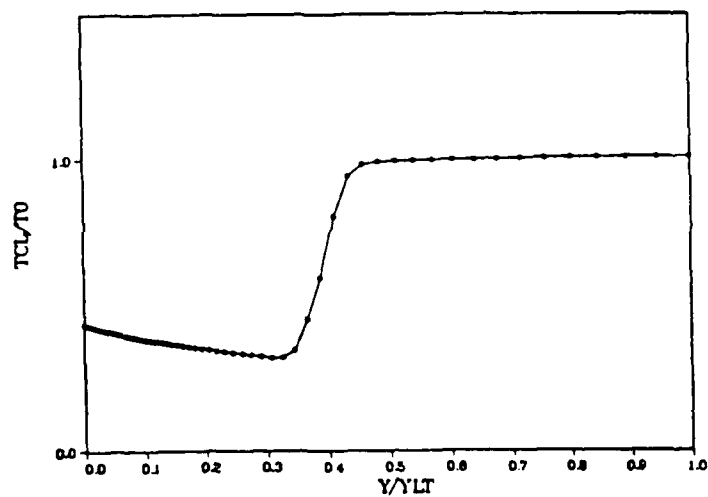
Figure 40. Case 2c Converged Solution Flowfield Conditions;
a) Wall Pressure Ratio; b) Line of Symmetry Pressure
Ratio; c) Line of Symmetry Temperature Ratio.

85

Dstar Ratio 47%NSR Ideal Inflow Solution
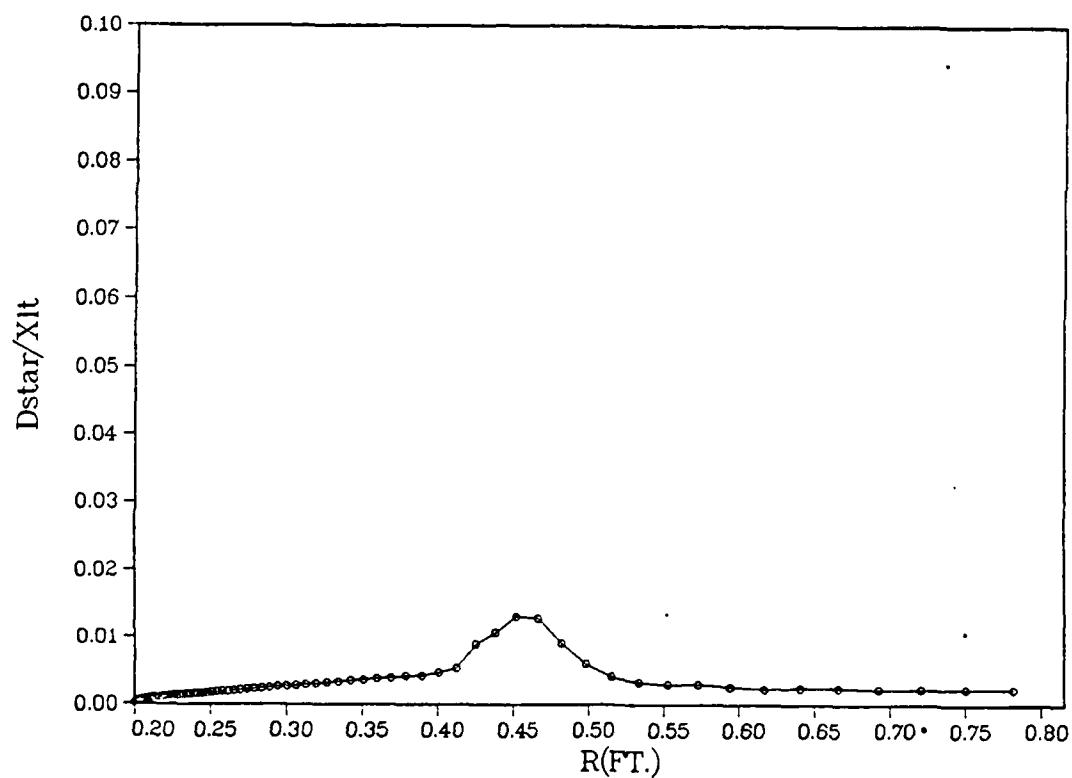
Figure 41. Plot of Case 2c Converged Solution Kinematic
Displacement Thickness.

86

MACH CONTOURS 60%NSR 60X80 GRID SOLUTION
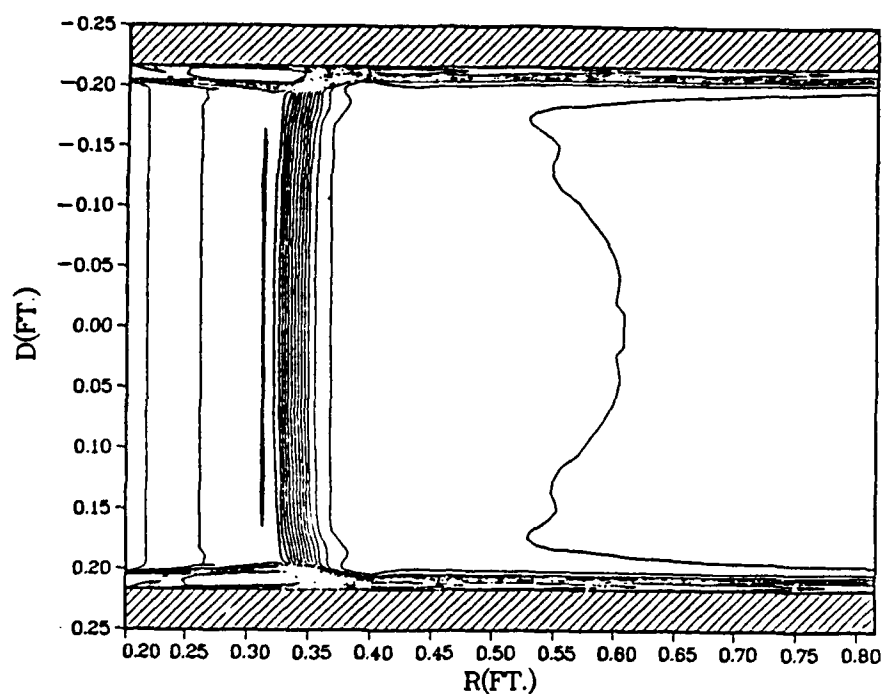
MACH CONTOURS 47%NSR 60X80 GRID SOLUTION
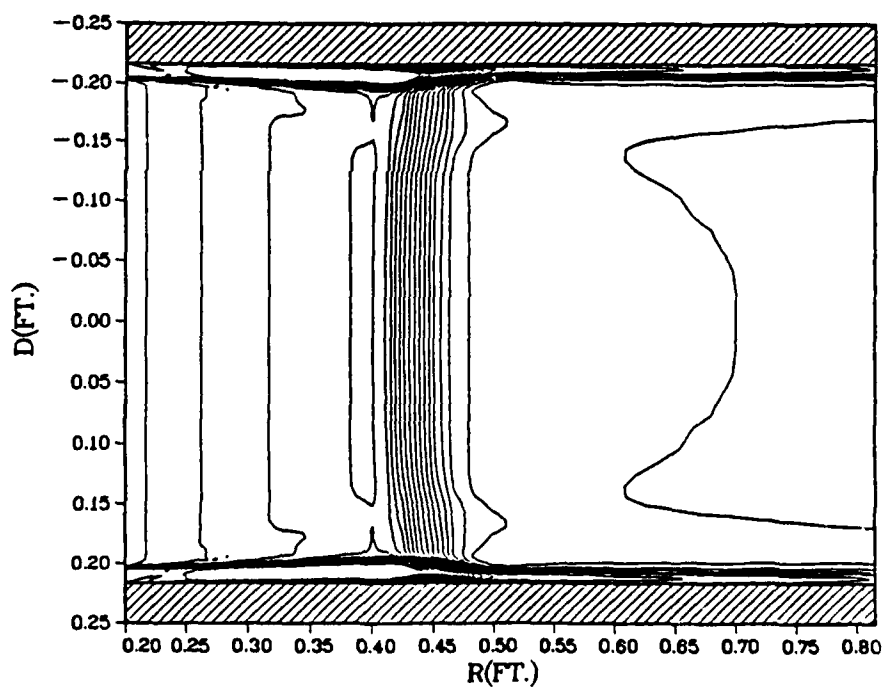
Figure 42. Comparison of Case 2b and 2c Converged Solution
Mach Contours.

Case 2d

For the next subset of this case, Cebeci's (outer layer only)
modification to the standard Cebeci-Smith eddy viscosity turbulence model
was substituted for the modification described in Chapter V and employed in
Case 2b. The numerical algorithm was allowed to evolve time from the Case
2b steady solution, and again the separation "bubble" along the diffuser
wall enlarged rapidly and the core flow normal shock moved upstream until it
reached the inflow boundary, representing a numerically unstarted diffuser.

Case 3a

In Neumann and Lustwerk's landmark supersonic wind tunnel diffuser
design effort (11), they reported that in order to obtain a started flow
condition in the wind tunnel test section (i.e., the test section was
entirely supersonic with a stable normal shock at a downstream location), a
very long diffuser was required if no wall boundary layer control was
employed. The long diffuser was required to accommodate the large
separation region caused by the terminal shock/boundary-layer interaction
and allow sufficient distance for flow reattachment. They presented a graph
in which the required diffuser length was given in multiples of the test
section diameter as a function of the test section Mach number. Based on
the mean inflow conditions for the experimental diffuser, Neumann and
Lustwerk's results indicated that a diffuser of length 12 times the diameter
of the baseline experimental configuration would be required to guarantee a
started condition. To determine if a numerical representation of a started
diffuser could be obtained for this configuration, a new grid was generated
to correspond to the required diffuser length and a numerical experiment was
run. Uniform inflow at $\bar{M} = 2.5$ was assumed with the exit pressure at 60

percent of normal shock recovery pressure, and no wall flow energization was employed. For this experiment, the adverse pressure gradient model developed in Chapter V was incorporated. This stiffened eddy-viscosity approach resulted in a started diffuser with the core flow normal shock fixed at r/r_{de} - 1.48, or in terms of percentage of distance through the diffuser of SPOS = 0.156 (15.6 percent of the baseline diffuser length). For the given inflow and backpressure conditions, the one-dimensional inviscid normal shock solution for shock position is SPOS = 0.25 (25 percent of the baseline diffuser length). The shock position is given here as a fraction of baseline diffuser length, rather than "long duct" diffuser length, for comparison purposes against the other computational cases run with the baseline diffuser length. Figure 43 presents the time history of these computations, showing that a stable, converged solution was achieved 250 milliseconds after flow "initiation" from the one-dimensional inviscid intial condition. Figure 44 presents the Mach contours for the converged solution, showing the full duct length. Figures 45a and b compare a closeup of a length corresponding to the baseline diffuser to the long diffuser length. Selected individual Mach contours are presented in Figure 46. Velocity profiles for the converged solution are shown in Figure 47, and the vector plots are presented in Figures 48 and 49, showing the persistence of the separated flow region through nearly 80 percent of the long diffuser length. This is consistent with Neumann and Lustwerk's (11) experimental conclusion. The converged solution flowfield wall pressure, line of symmetry pressure and temperature ratios are presented in Figure 50. Without the flow energizing wall bank blowers, no overpressure (or "overshoot") response is observed in the behavior of the wall pressure, as

it responds smoothly in recovering to the exit pressure. Plots of the computed values of the kinematic displacement thickness, δ^*, are presented in Figures 51a and b. The maximum value achieved is nearly 50 percent of the diffuser diameter, and is physically unreal. This is a direct result of the difficulty of computing δ^* when there is a large separation region present. Without wall energizing bank blowers (which are operated at a higher Mach number than the core flow) it is apparent that the long diffuser length is necessary to provide sufficient recovery distance for the large wall boundary layer separation region. Details are provided in Appendix G.
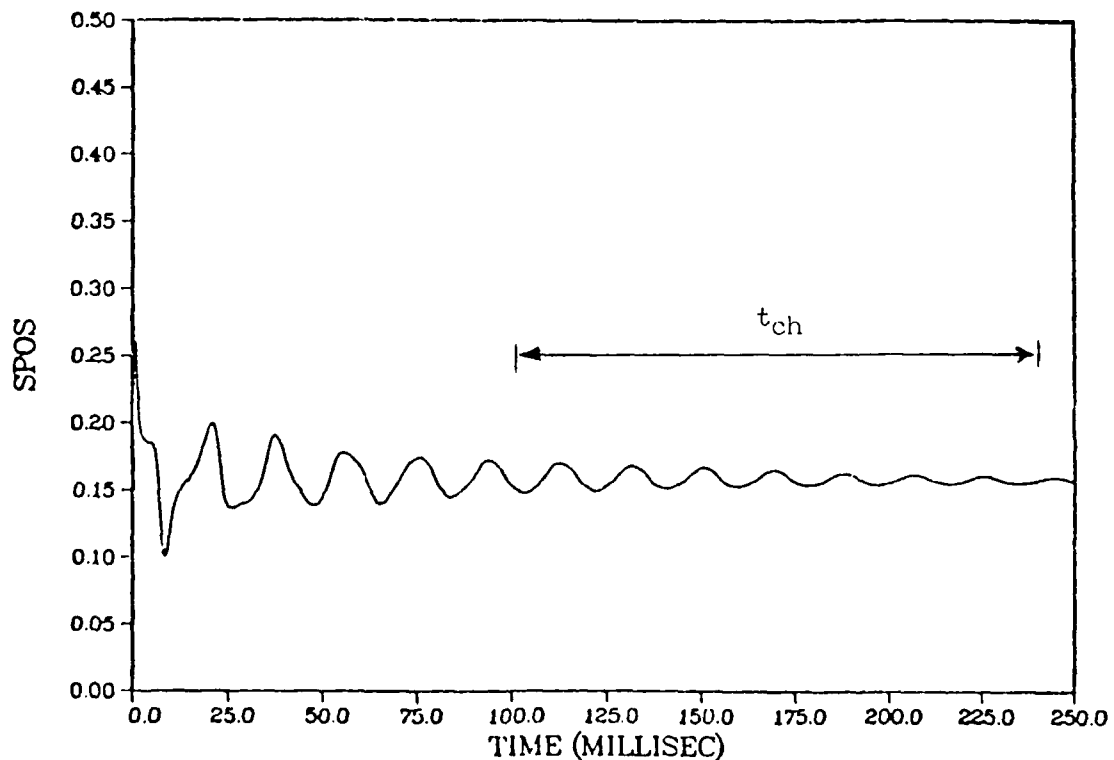
Figure 43. Core Flow Normal Shock Position Time History, Case 3a
(Long Duct Diffuser, Uniform Inflow, 60% NSR, wbb = 0,
modified Cebeci-Smith Turbulence Model).

MACH CONTOURS 60%NSR Long Duct Solution
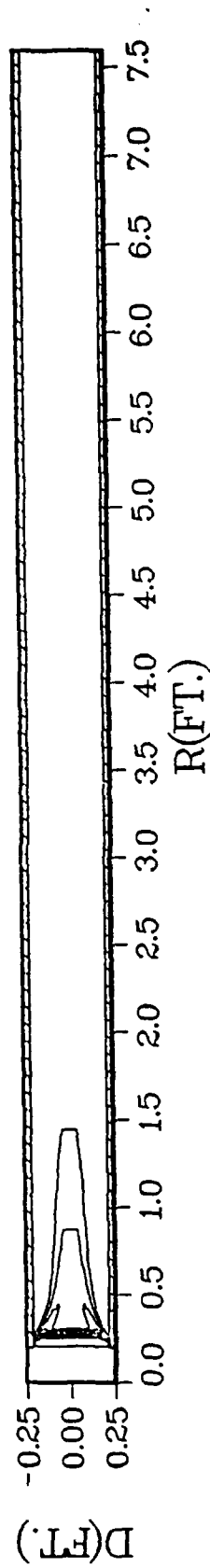
Figure 44. Converged Solution Mach Contours, Case 3a.

MACH CONTOURS 60%NSR Long Duct Solution

CONVERGED MACH CONTOURS LD 60%NSR WBB=0
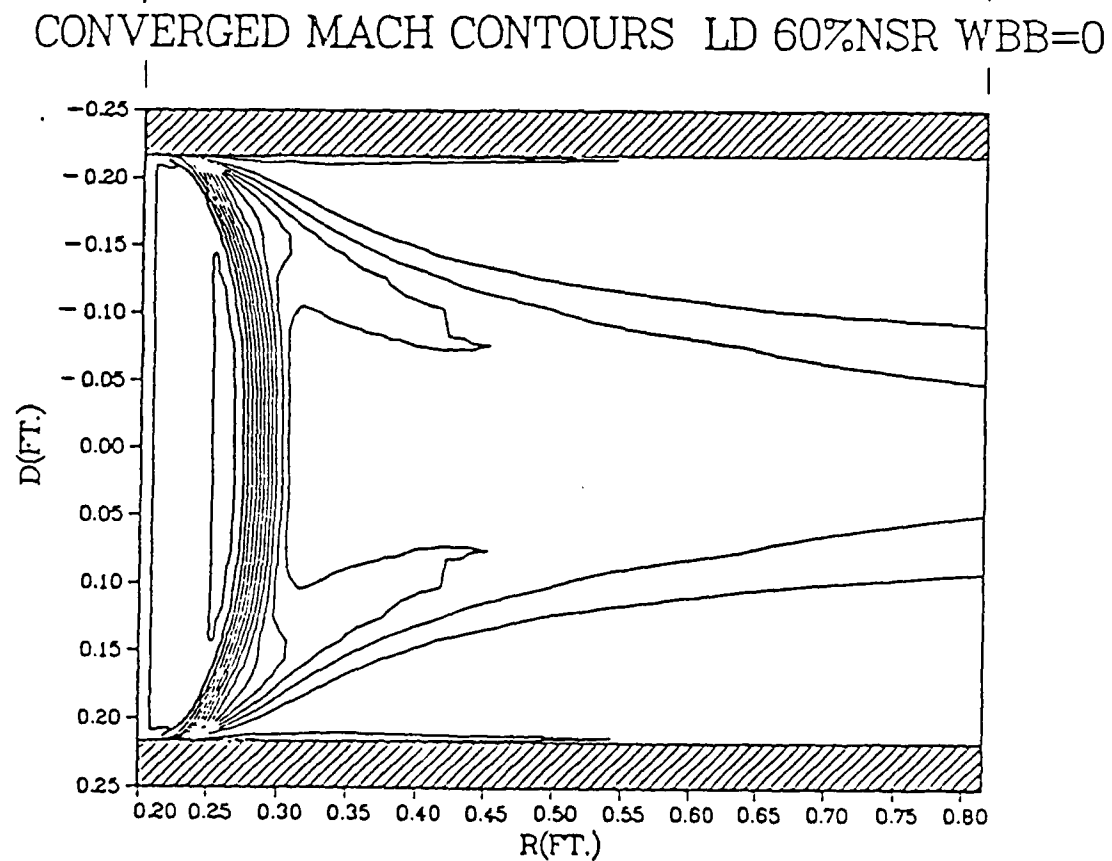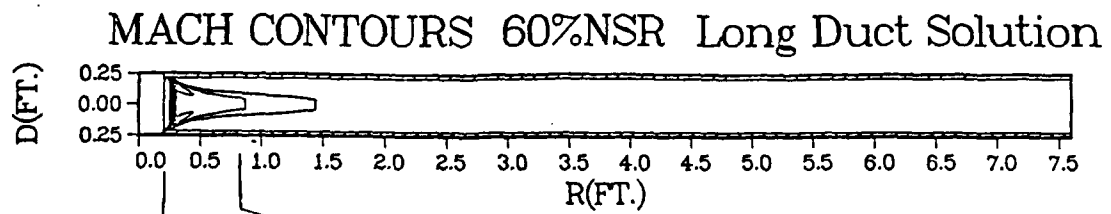
Figure 45. Case 3a Converged Solution Mach Contours; Close-up
of Long Diffuser Length Corresponding to Baseline
Diffuser.

M=.25 CONTOUR 60%NSR Long Duct Solution

M=.25 Contour 60%NSR Long Duct Solution

M=.50 CONTOUR 60%NSR Long Duct Solution

M=.50 Contour 60%NSR Long Duct Solution

M=1.0 CONTOUR 60%NSR Long Duct Solution

M=1.0 Contour 60%NSR Long Duct Solution
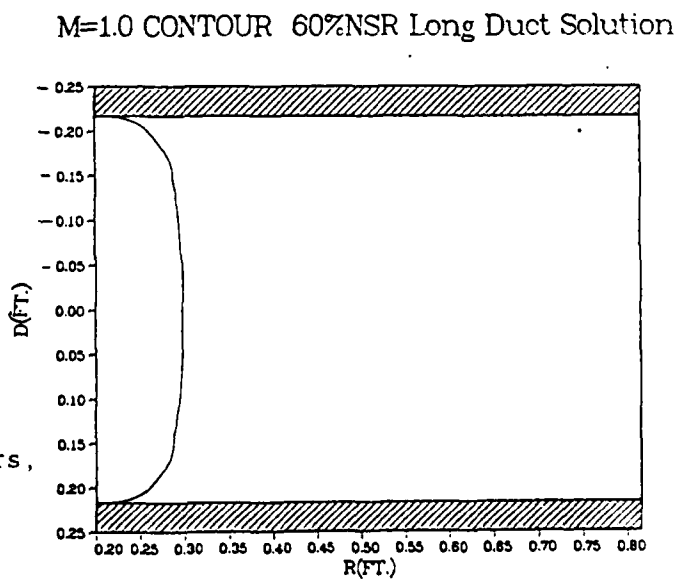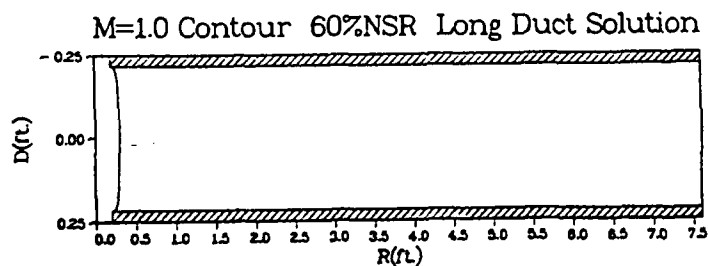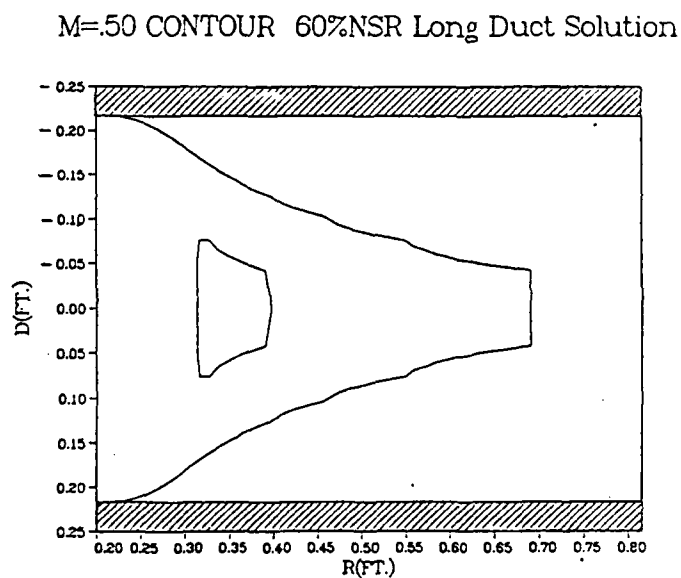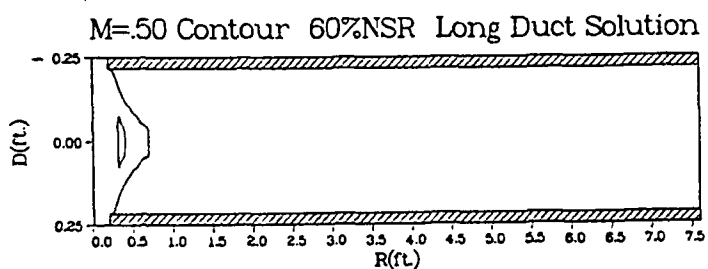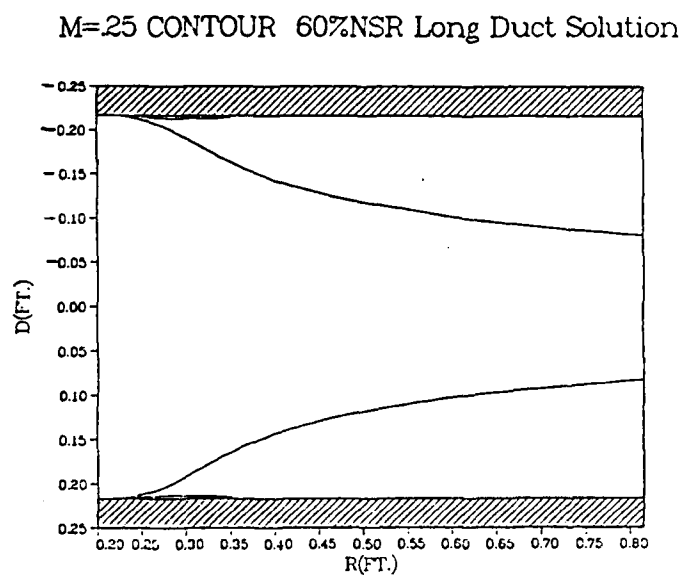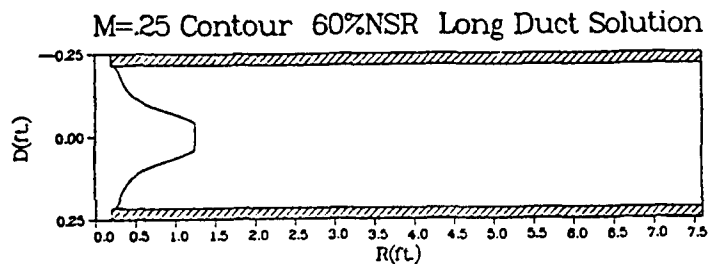
Figure 46. Selected Individual Mach Contours, Case 3a Solution.

93

M=1.5 CONTOUR 60%NSR Long Duct Solution

M=1.5 Contour 60%NSR Long Duct Solution

M=2.5 CONTOUR 60%NSR Long Duct Solution

M=2.5 Contour 60%NSR Long Duct Solution

M=2.75 CONTOUR 60%NSR Long Duct Solution

M=2.75 Contour 60%NSR Long Duct Solution
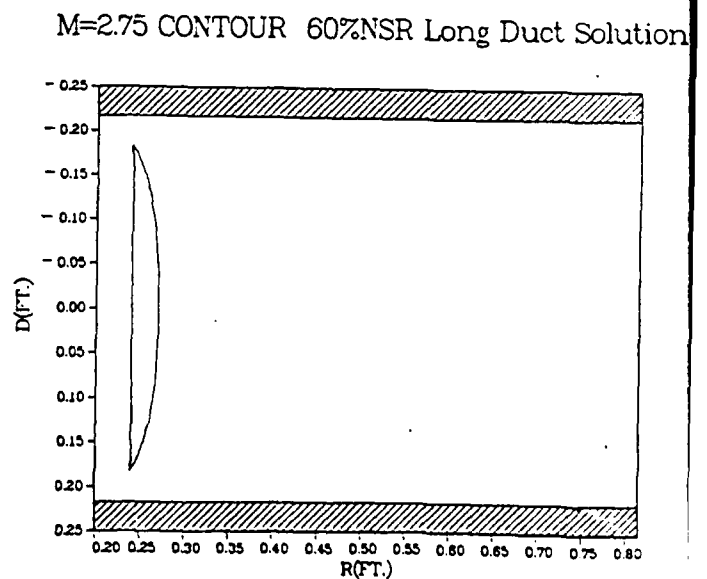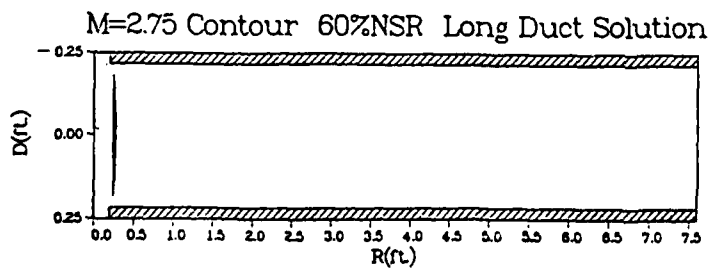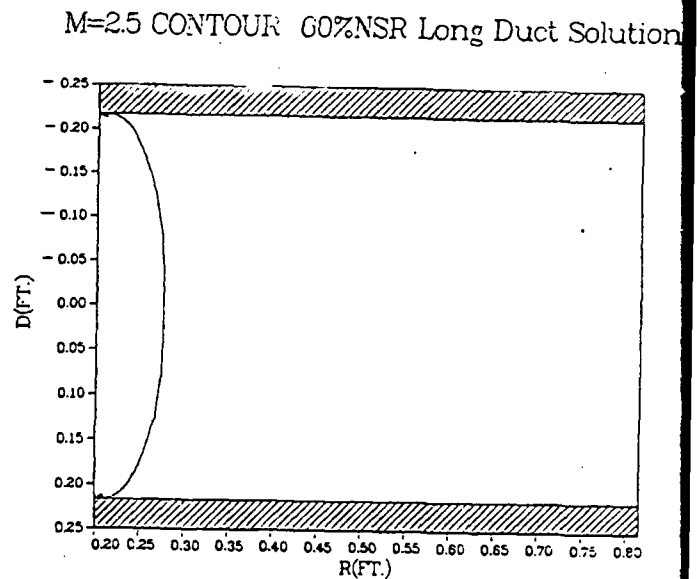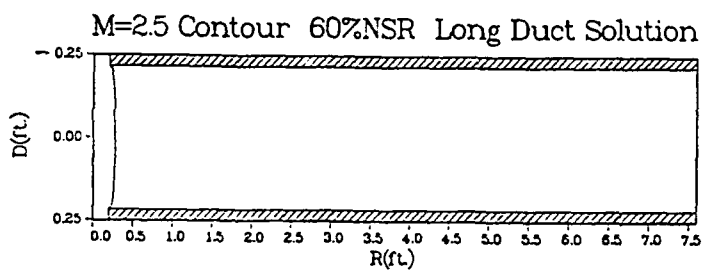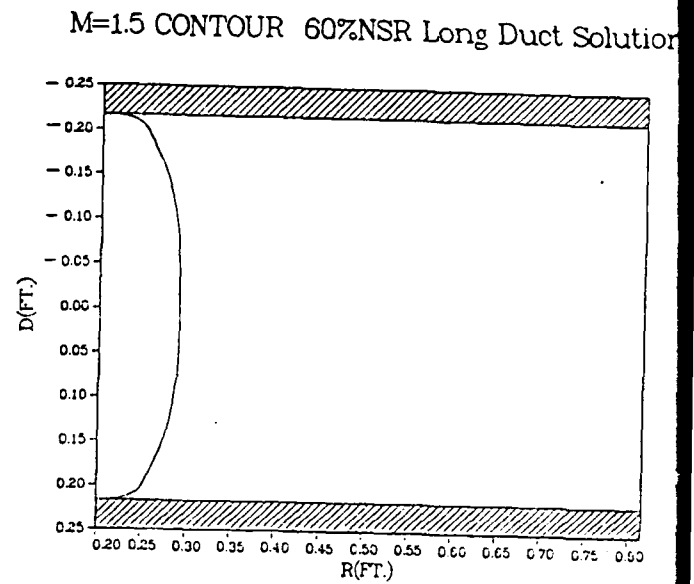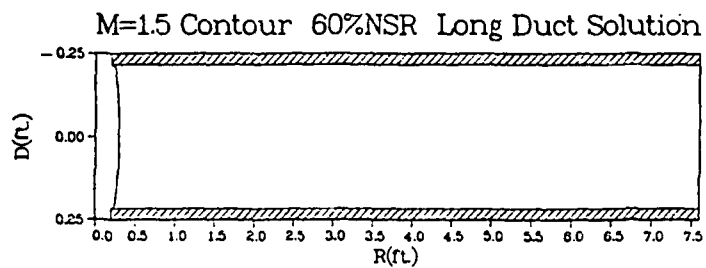
Mach Contours 60%NSR Long Duct Solution
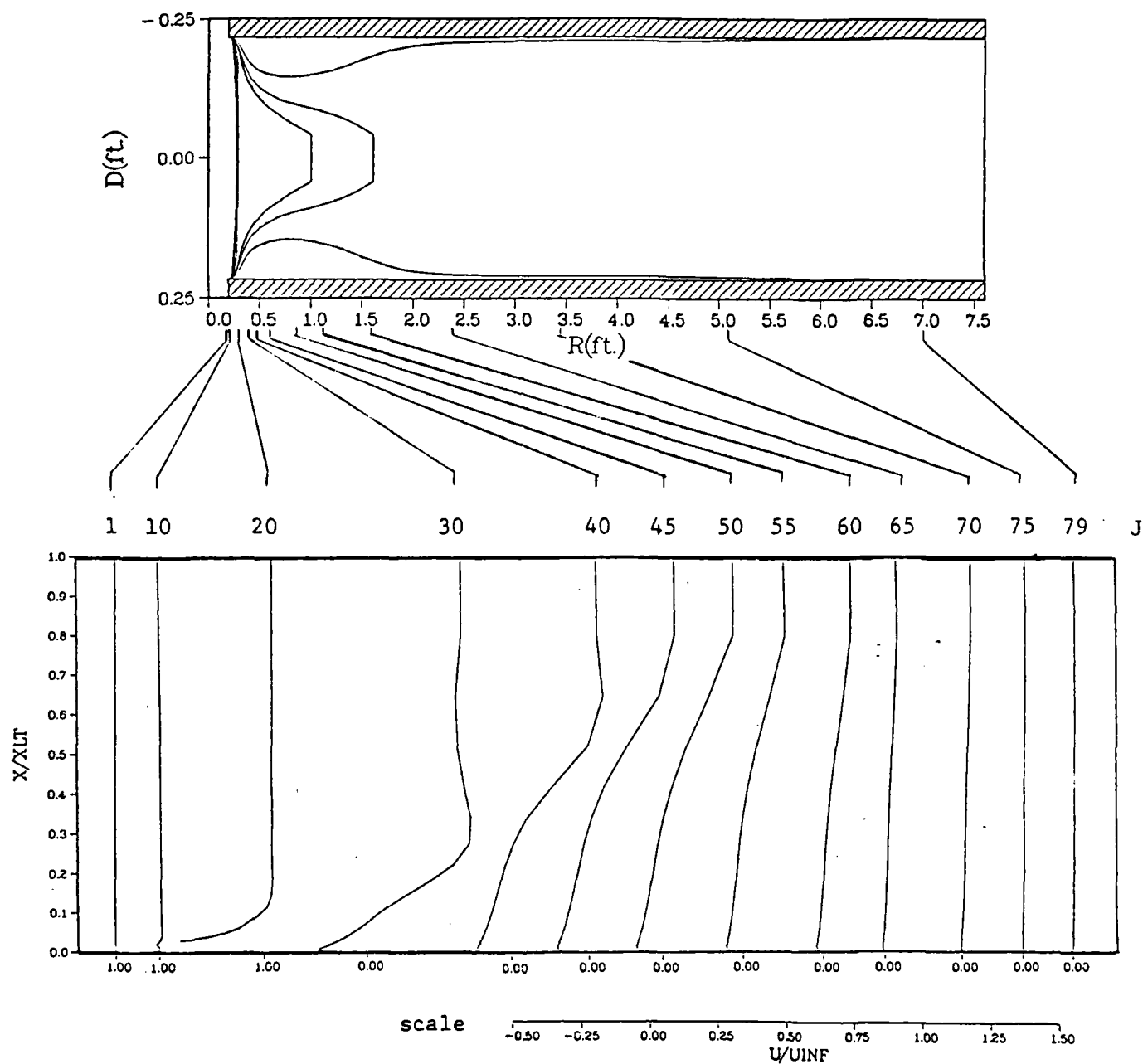
Figure 47. Velocity Profiles, Case 3a Converged Solution.

95

VELOCITY VECTOR PLOT 60%NSR Long Duct Solution
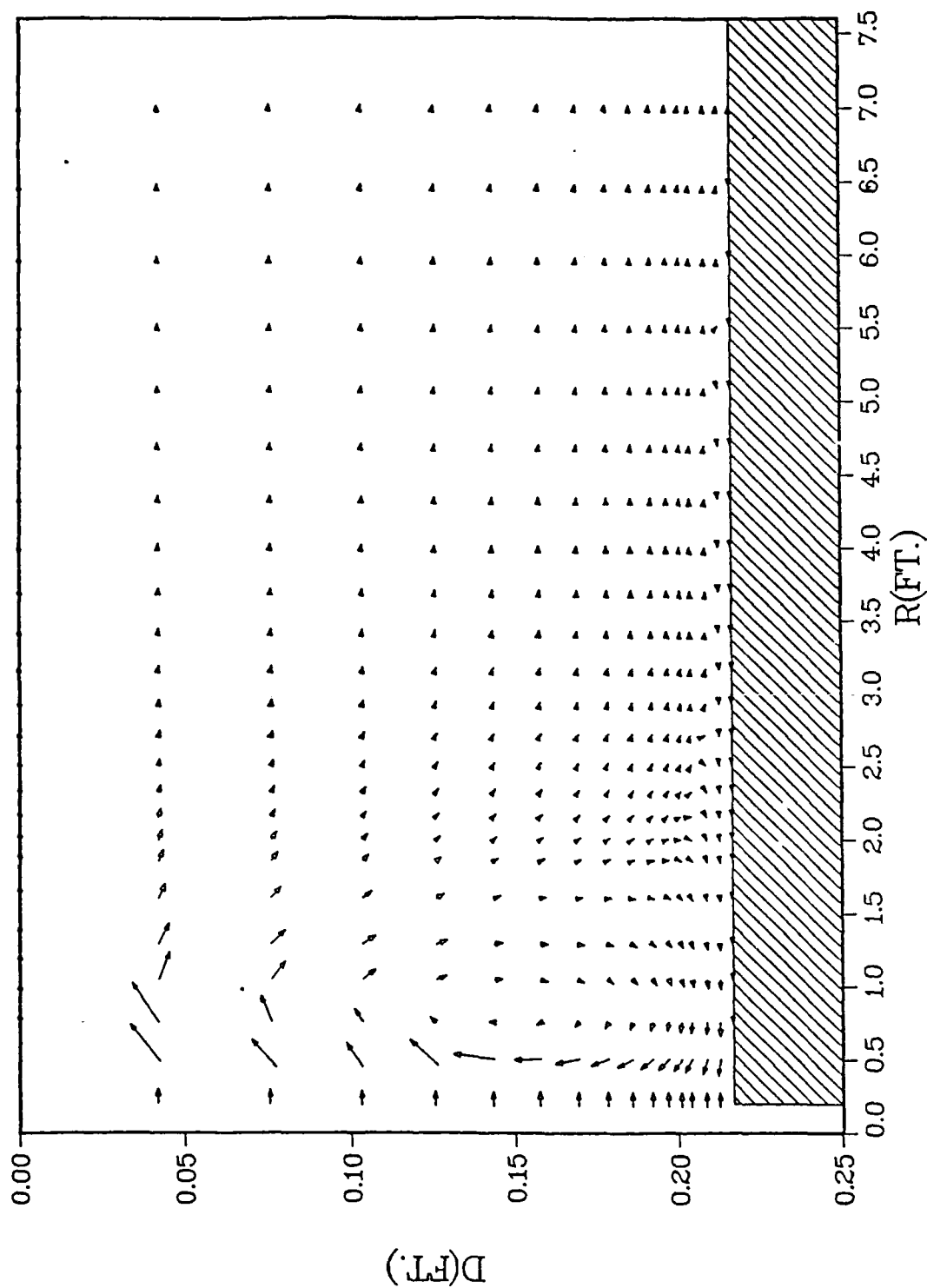
Figure 48. Velocity Vector Plot, Case 3a Converged Solution.
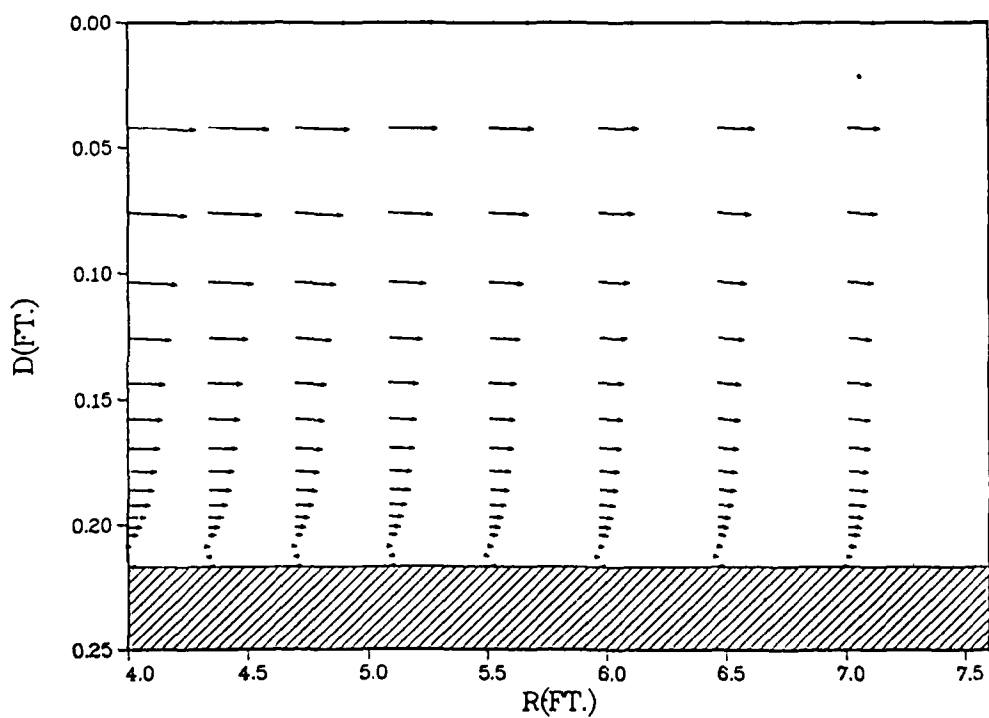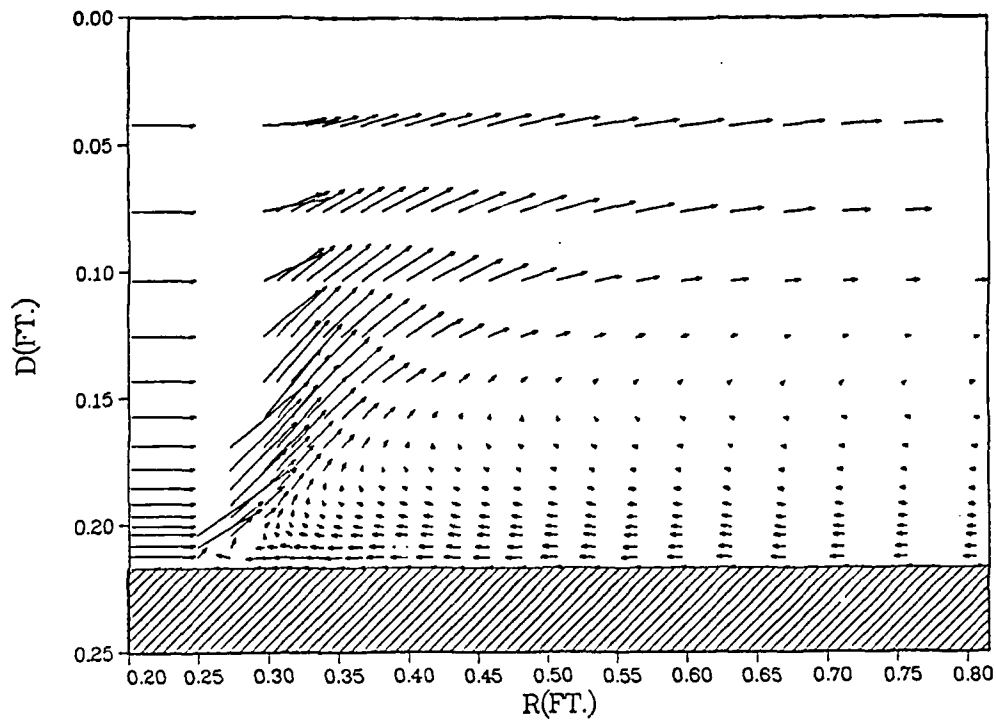
Figure 49. Case 3a Converged Solution Velocity Vector Plot;
a) Expanded View Corresponding to Baseline Diffuser
Length; b) Expanded View Showing Separation Region
Detail.

97
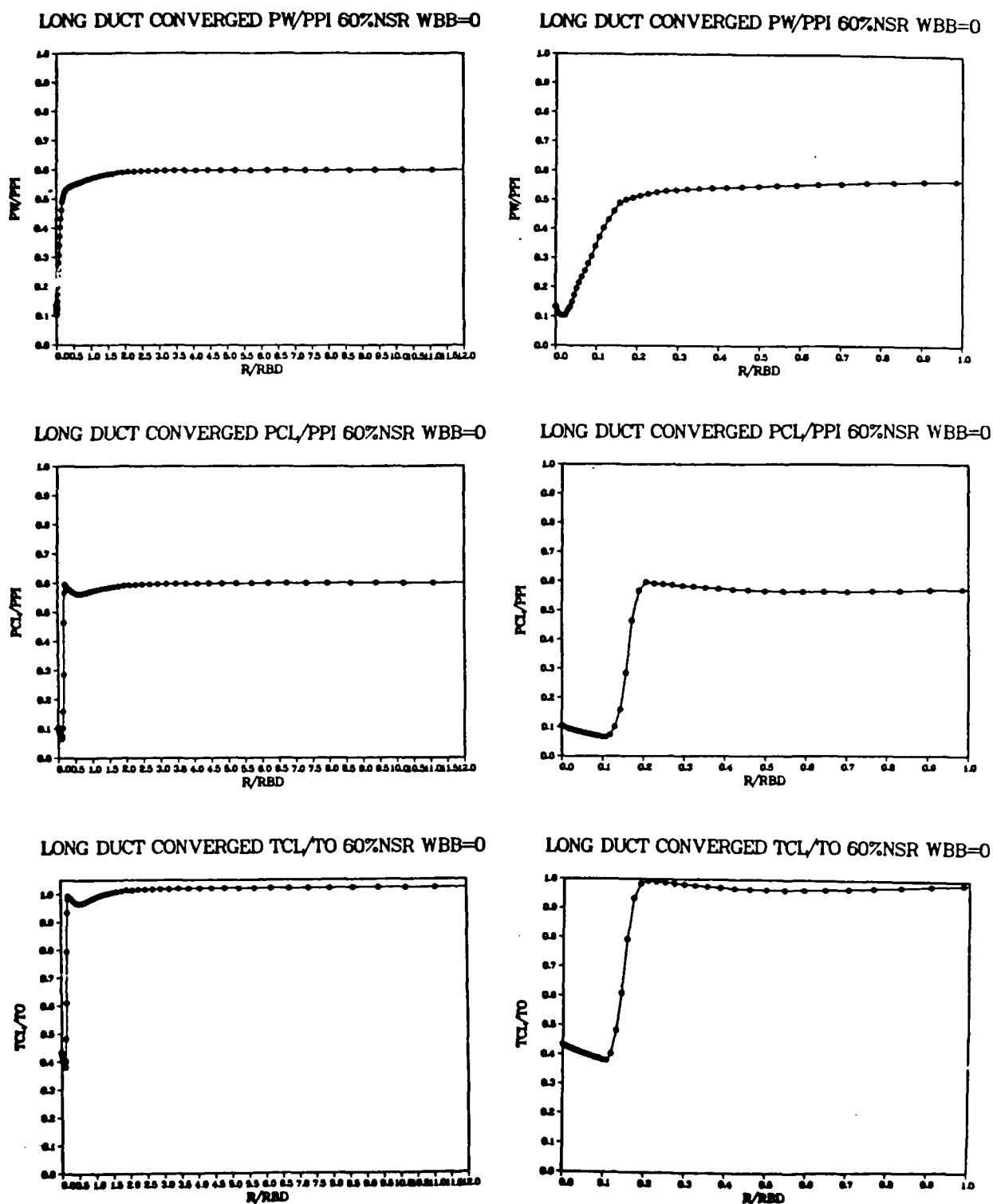
Figure 50. Case 3a Converged Solution Flowfield Conditions;
a) Wall Pressure Ratio; b) Line of Symmetry Pressure
Ratio; c) Line of Symmetry Temperature Ratio.

Dstar Ratio 60%NSR Long Duct Solution
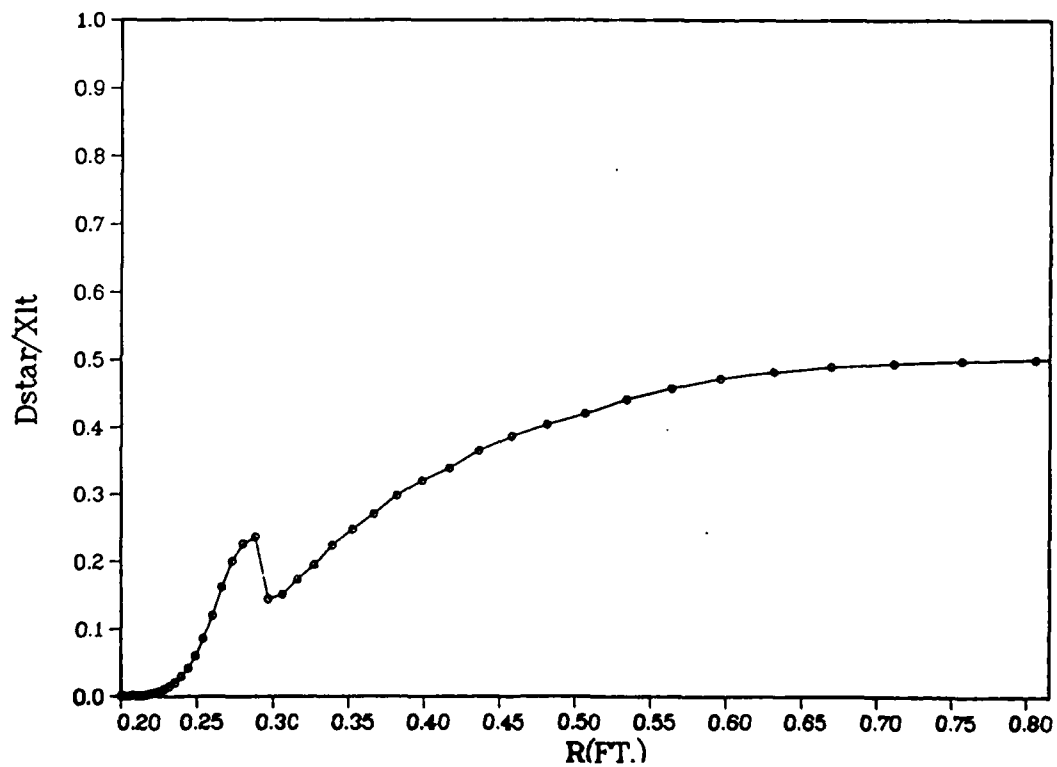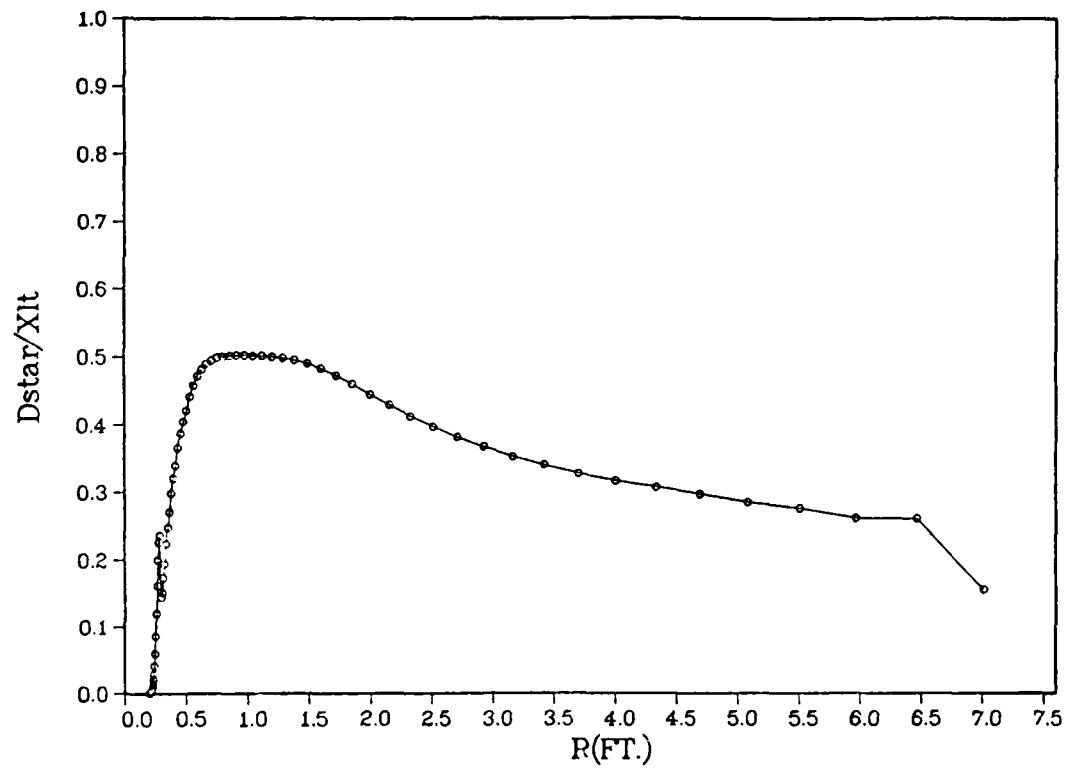
Figure 51. Plot of Case 3a Converged Solution Kinematic
Displacement Thickness; a)Full Diffuser Length;
b) Length Corresponding to Baseline Diffuser.

Case 3b

From the converged solution of case 3a, the exit backpressure was lowered to 47 percent of normal shock recovery pressure and the solution was marched forward in time. A new, steady state, converged solution was achieved after four characteristic times. This solution contains a core flow normal shock fixed at r/r_{de} - 1.99, or in terms of distance through the (baseline) diffuser of SPOS - 0.322 (32.2 percent of the baseline diffuser length). For the given inflow and exit backpressure conditions, the one-dimensional inviscid normal shock solution for line of symmetry shock position is SPOS = 0.455 (45.5 percent of the baseline diffuser length). Again, the shock position is presented as a fraction of baseline diffuser length, rather than "long duct" length, for comparison purposes with the other computational cases. Figure 52 presents the time history of this steady, stable solution. Figure 53 presents the Mach contours for the converged solution showing the full diffuser length. Figures 54a and b compare Mach contours for the full duct length with a close-up of a length corresponding to the baseline diffuser length. Selected individual Mach contours are presented in Figure 55. Velocity profiles for the converged solution are presented in Figure 56, and the corresponding velocity vector plots are shown in Figures 57 and 58. The persistence of the separated flow region well beyond the baseline diffuser length is again quite apparent. The converged solutions for wall pressure, line of symmetry pressure and temperature ratios are presented in Figure 59. Again, no "overshoot" response is observed for the wall pressure as it responds smoothly in recovering to exit pressure. Plots of the computed values of kinematic

displacement thickness δ^* are presented in Figures 60a and b, again showing unrealistically large values developed from the large separation region.
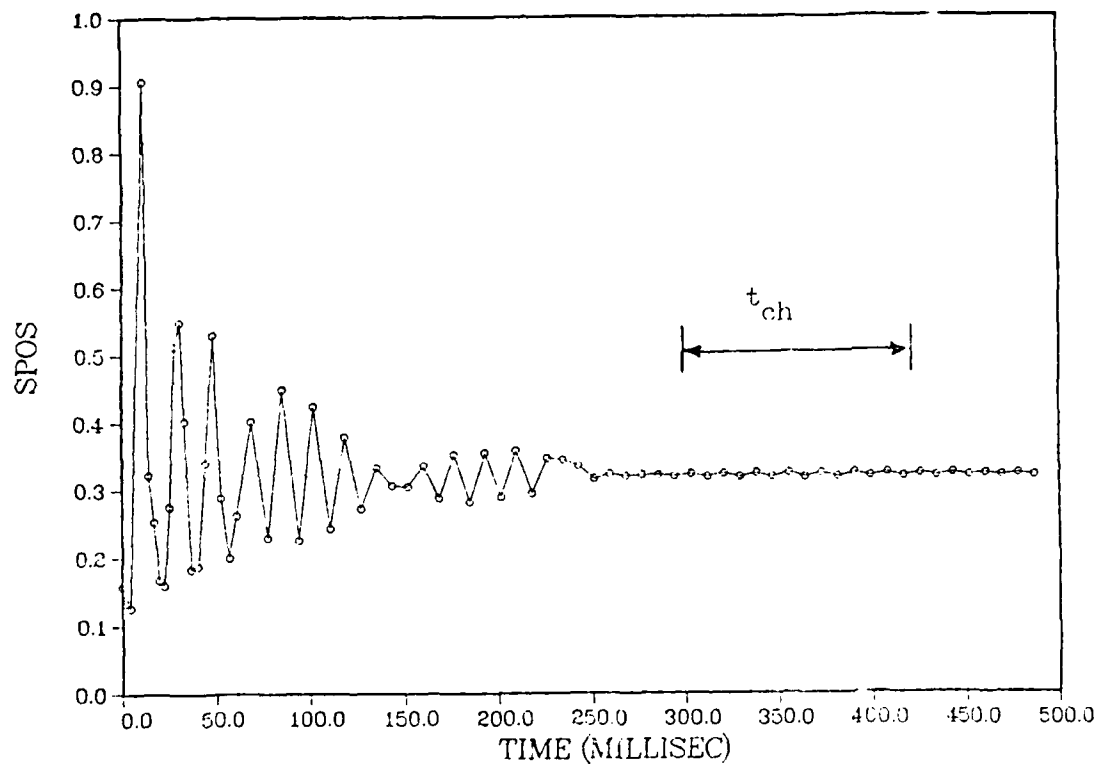
Figure 52. Core Flow Normal Shock Position Time History, Case 3b (Long Duct Diffuser, Uniform Inflow, 47% NSR, wbb = 0, modified Cebeci-Smith Turbulence Model).
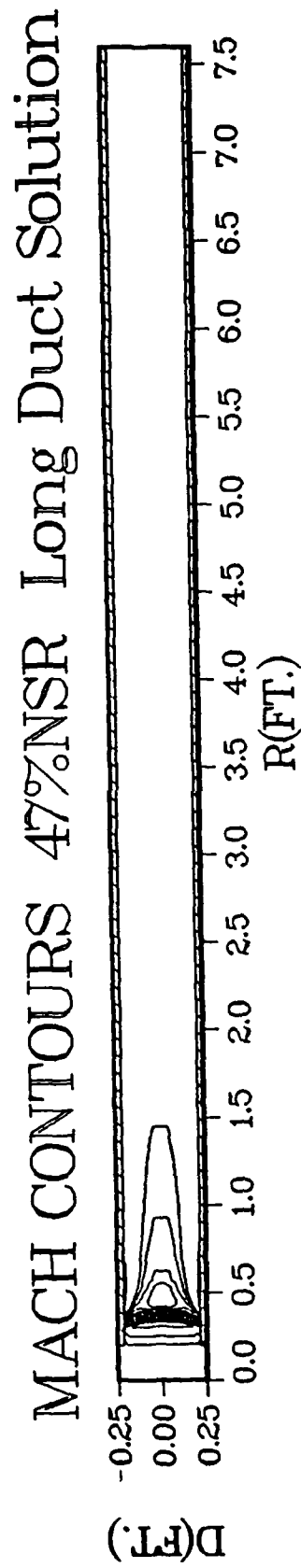
Figure 53. Converged Solution Mach Contours, Case 3b.

MACH CONTOURS 47%NSR Long Duct Solution

MACH CONTOURS 47%NSR Long Duct Solution
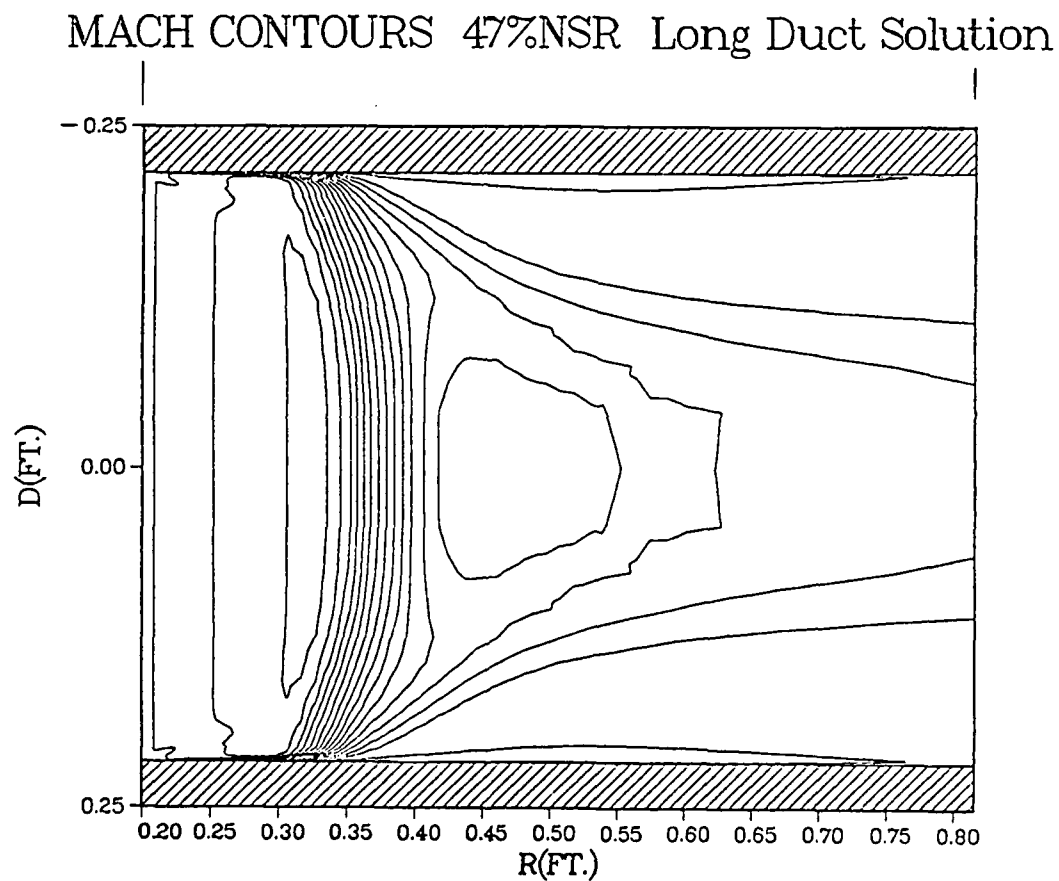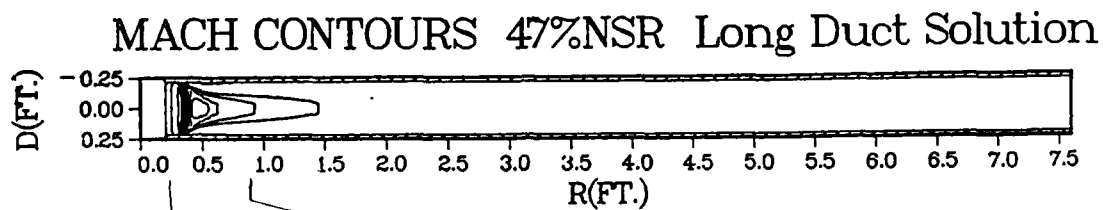
Figure 54. Case 3b Converged Solution Mach Contours; Close-up of Long Diffuser Length Corresponding to Baseline Diffuser.

103

M=.25 CONTOUR 47%NSR Long Duct Solution

M=0.25 Contour 47%NSR Long Duct Solution

M=.5 CONTOUR 47%NSR Long Duct Solution

M=0.50 Contour 47%NSR Long Duct Solution

M=1.0 CONTOUR 47%NSR Long Duct Solution

M=1.0 Contour 47%NSR Long Duct Solution
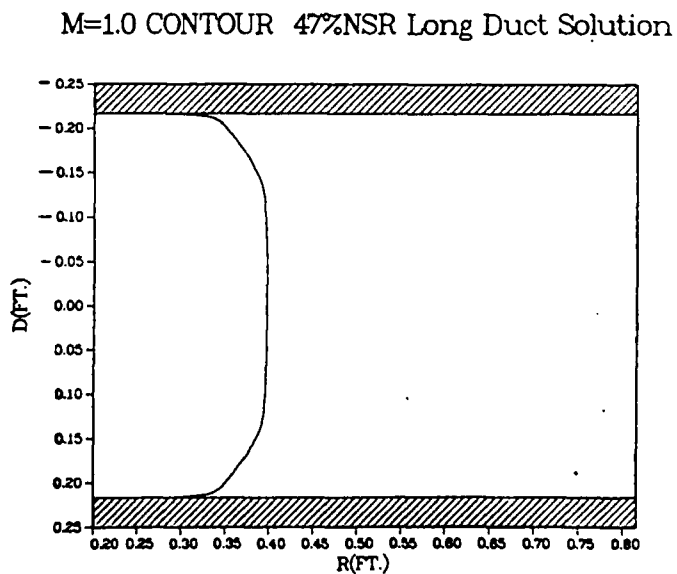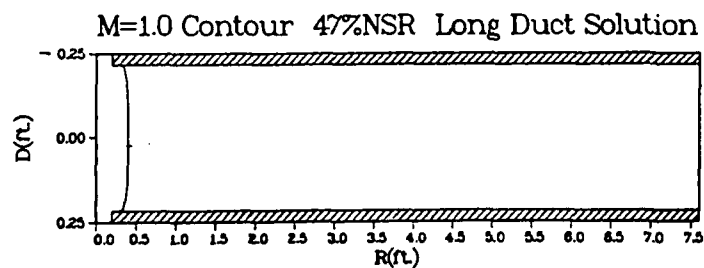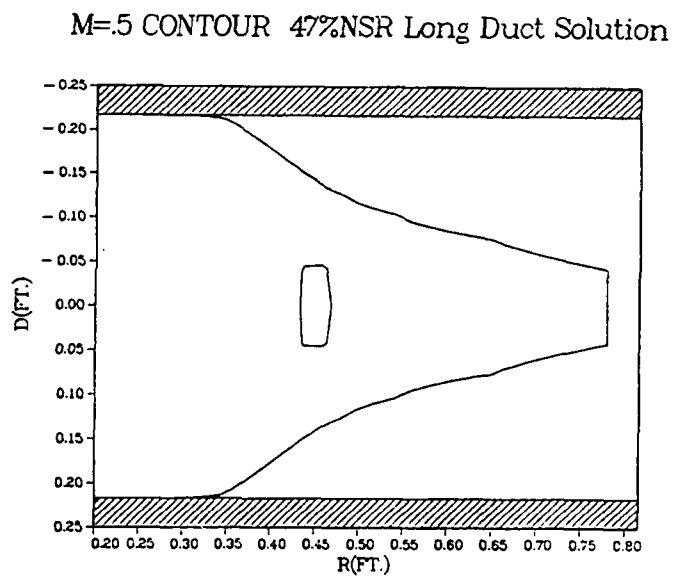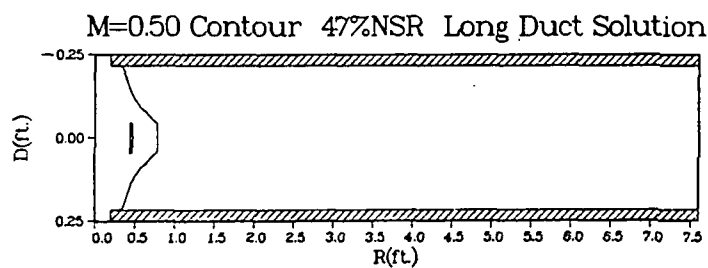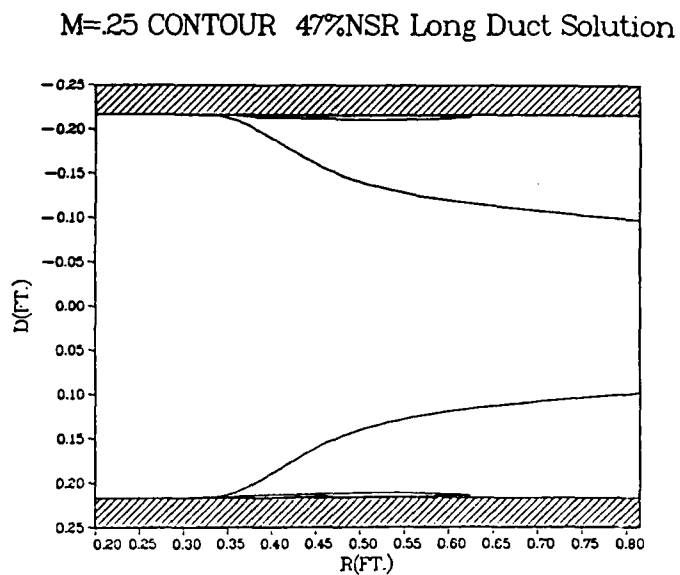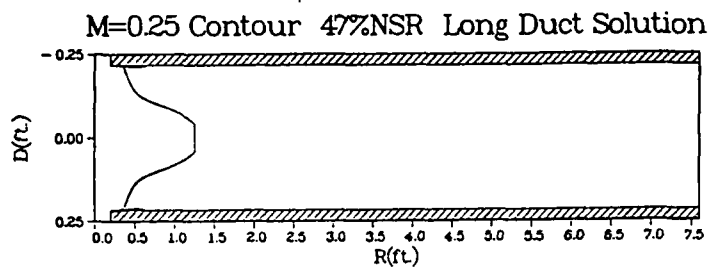
Figure 55. Selected Individual Mach Contours,

Case 3a Solution.

M=1.5 CONTOUR 47%NSR Long Duct Solution
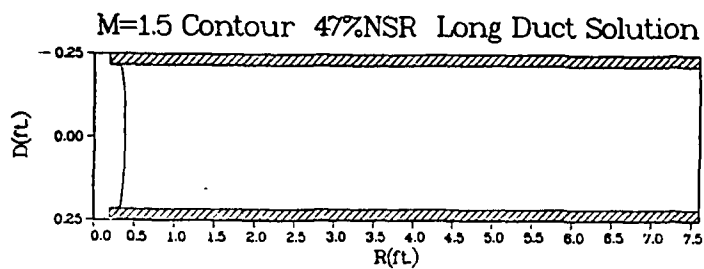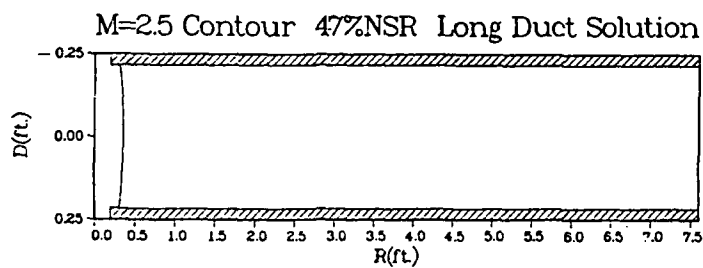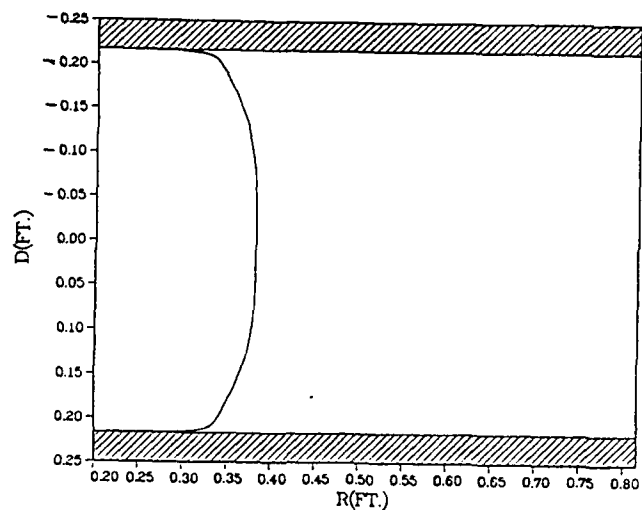
M=1.5 Contour 47%NSR Long Duct Solution

M=2.50 CONTOUR 47%NSR Long Duct Solution

M=2.5 Contour 47%NSR Long Duct Solution

M=2.75 CONTOUR 47%NSR Long Duct Solution

M=2.75 Contour 47%NSR Long Duct Solution

105
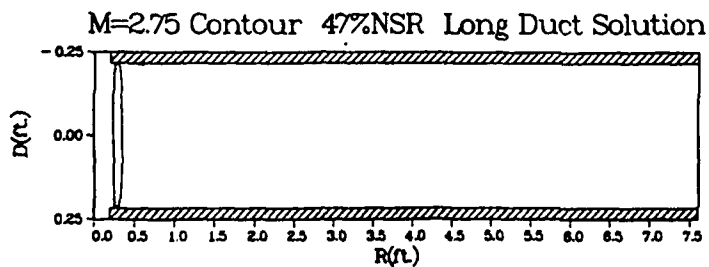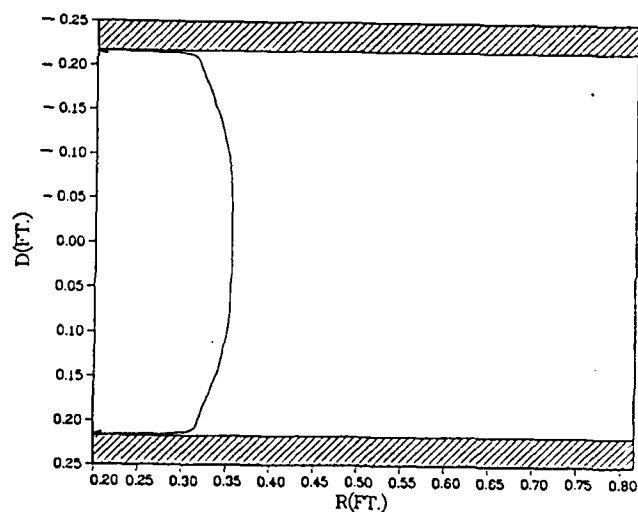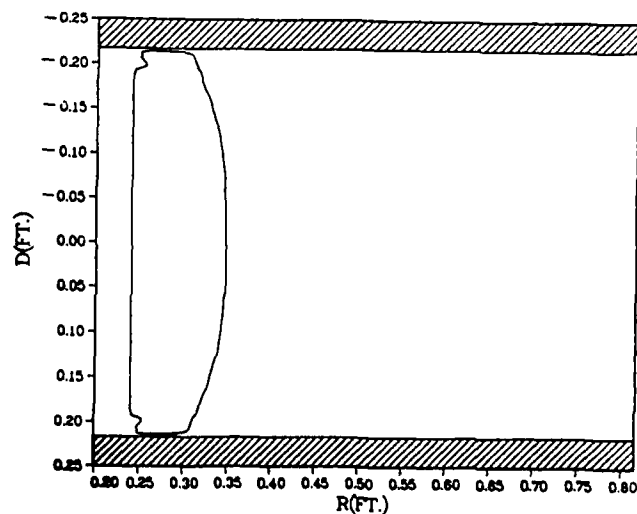
Mach Contours 47%NSR Long Duct Solution
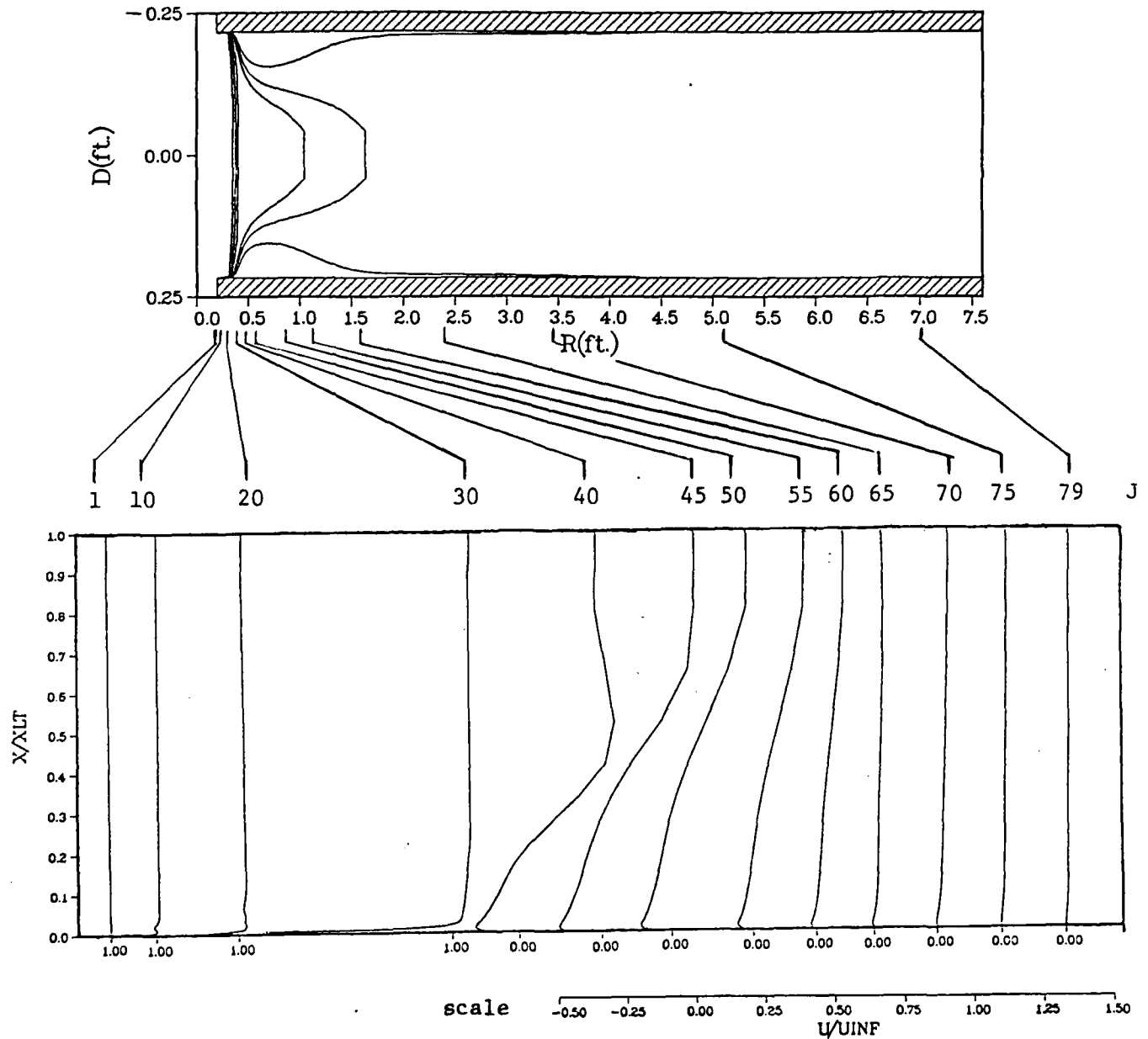
Figure 56. Velocity Profiles, Case 3b Converged Solution.

106

VELOCITY VECTOR PLOT 47%NSR Long Duct Solution
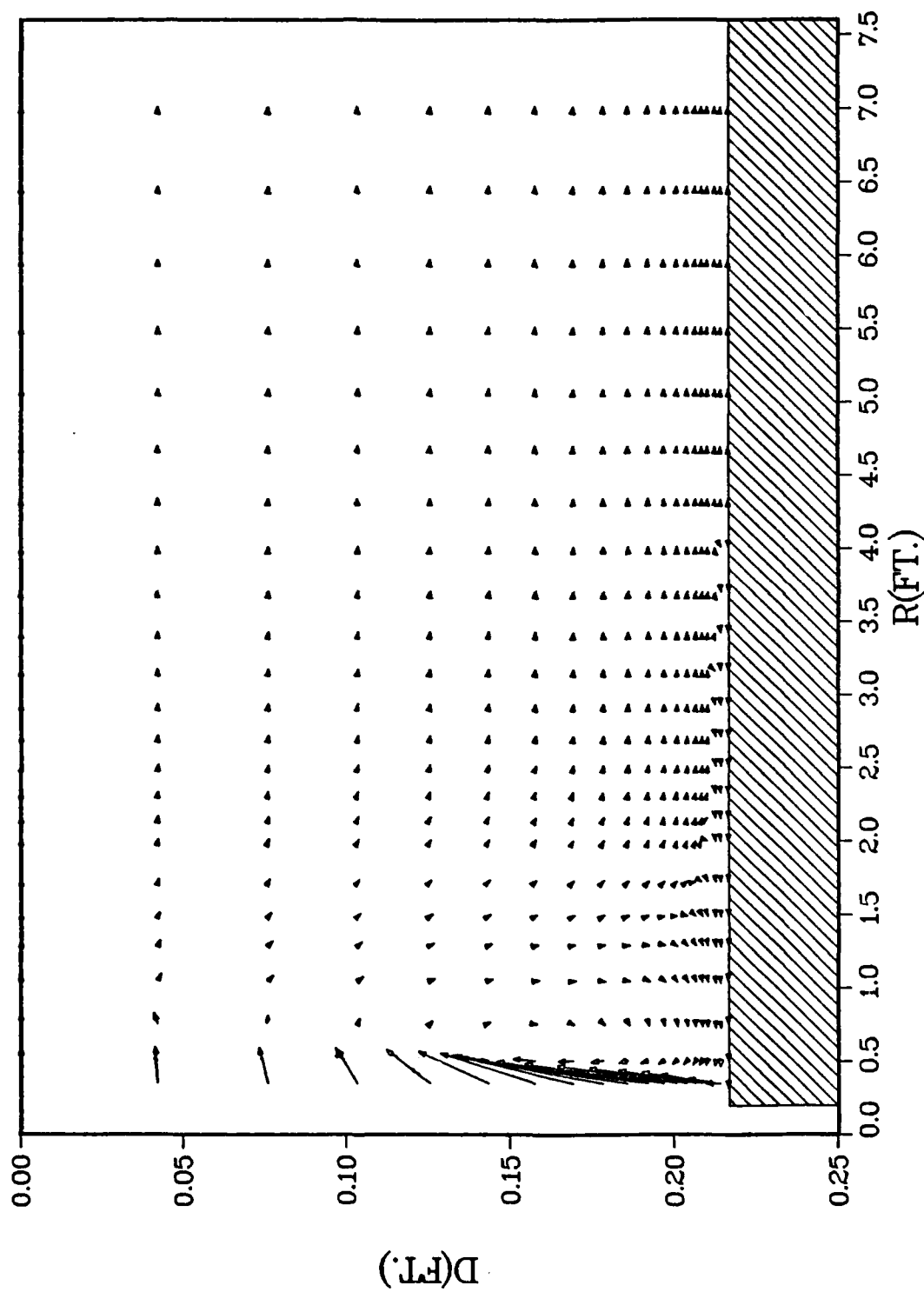
Figure 57. Velocity Vector Plot, Case 3b Converged Solution.
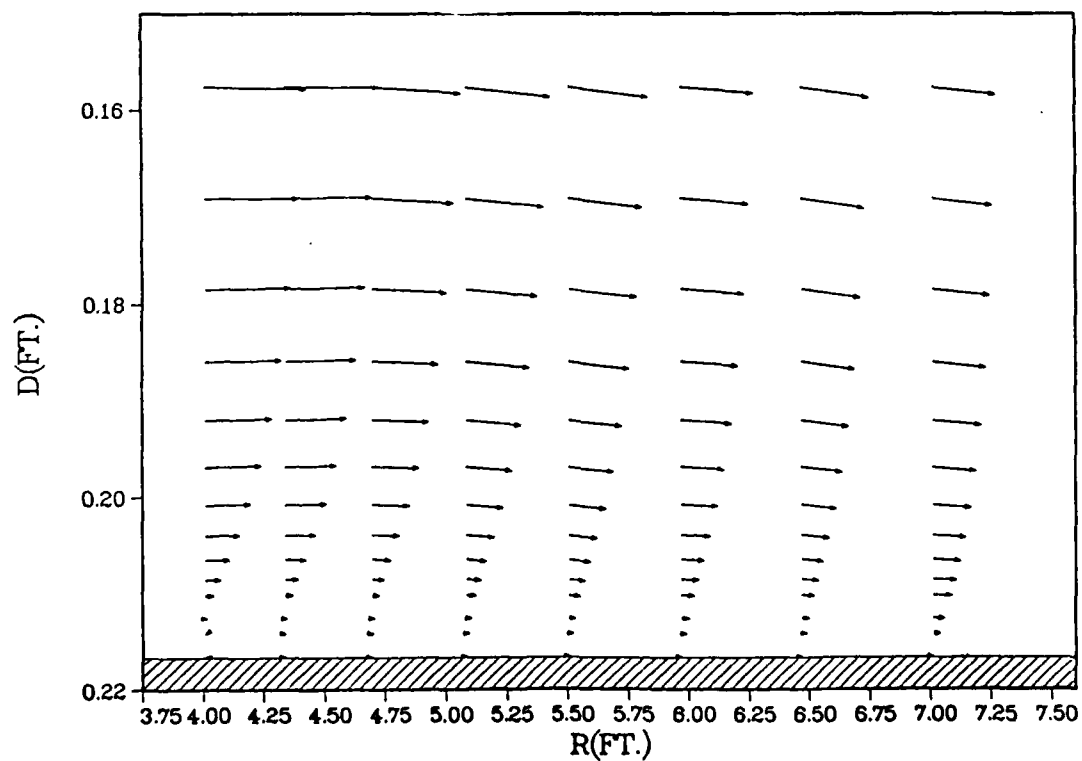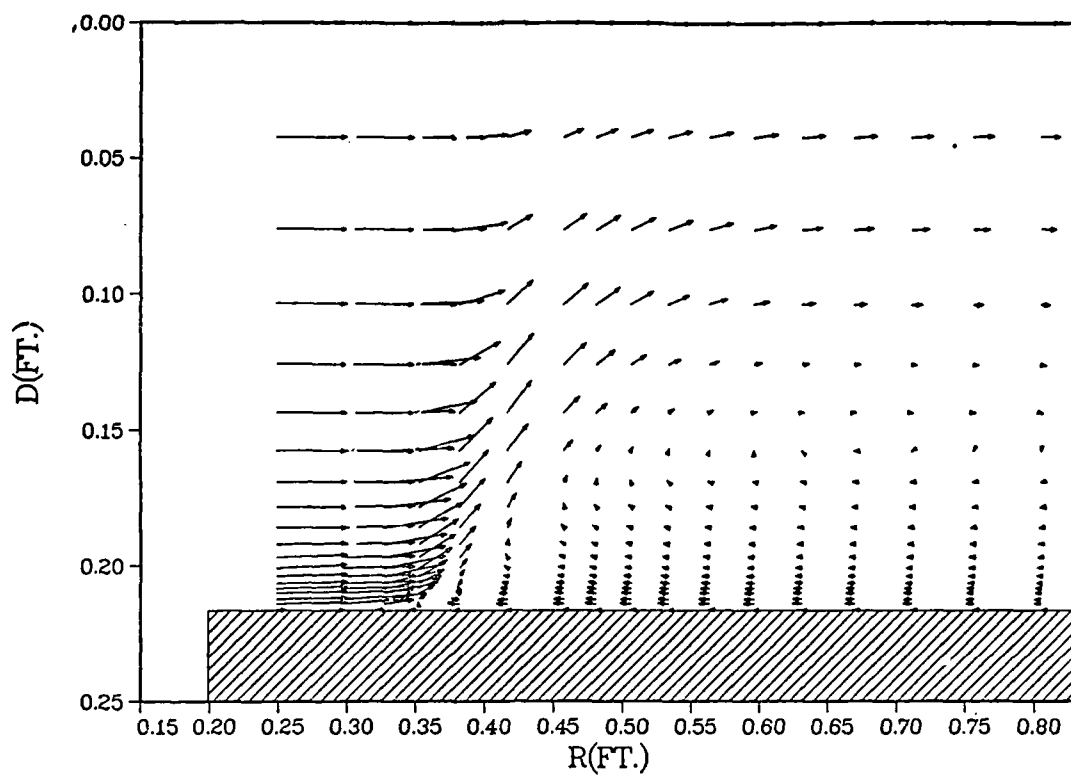
Figure 58. Case 3b Converged Solution Velocity Vector Plot;
a) Expanded View Corresponding to Baseline Diffuser
Length; b) Expanded View Showing Separation Region
Detail.

PW/PPI LONG DUCT SOLUTION 47%NSR

PW/PPI LONG DUCT SOLUTION 47%NSR

PCL/PPI LONG DUCT SOLUTION 47%NSR

PCL/PPI LONG DUCT SOLUTION 47%NSR

TCL/TO LONG DUCT SOLUTION 47%NSR

TCL/TO LONG DUCT SOLUTION 47%NSR
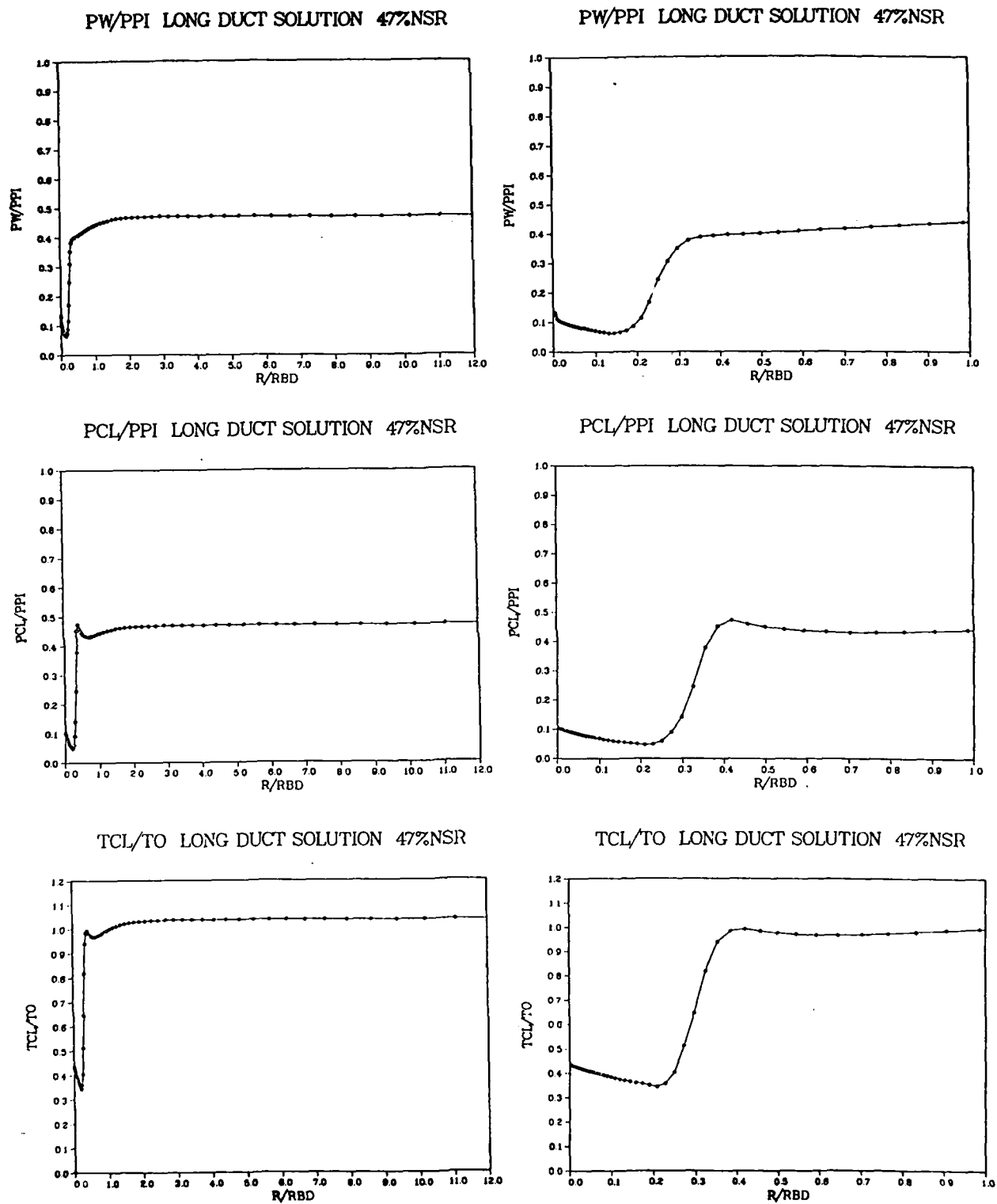
Figure 59. Case 3b Converged Solution Flowfield Conditions;
a) Wall Pressure Ratio; b) Line of Symmetry Pressure
Ratio; c) Line of Symmetry Temperature Ratio.

109

Dstar Ratio 47%NSR Long Duct Solution
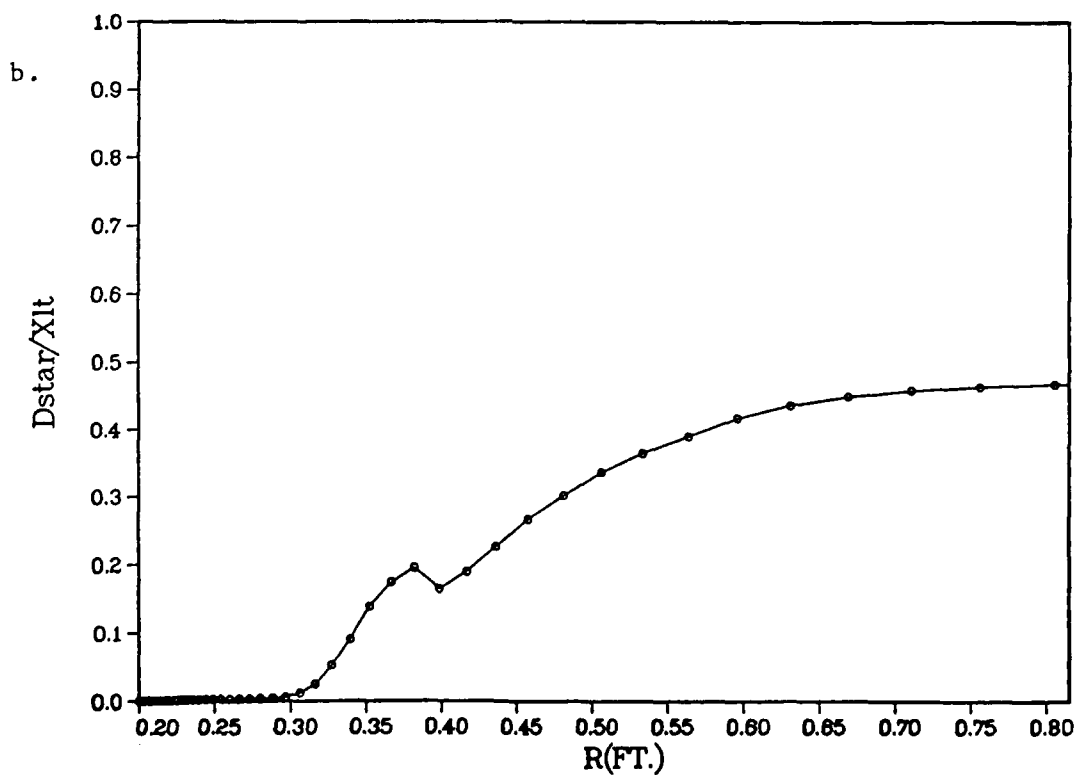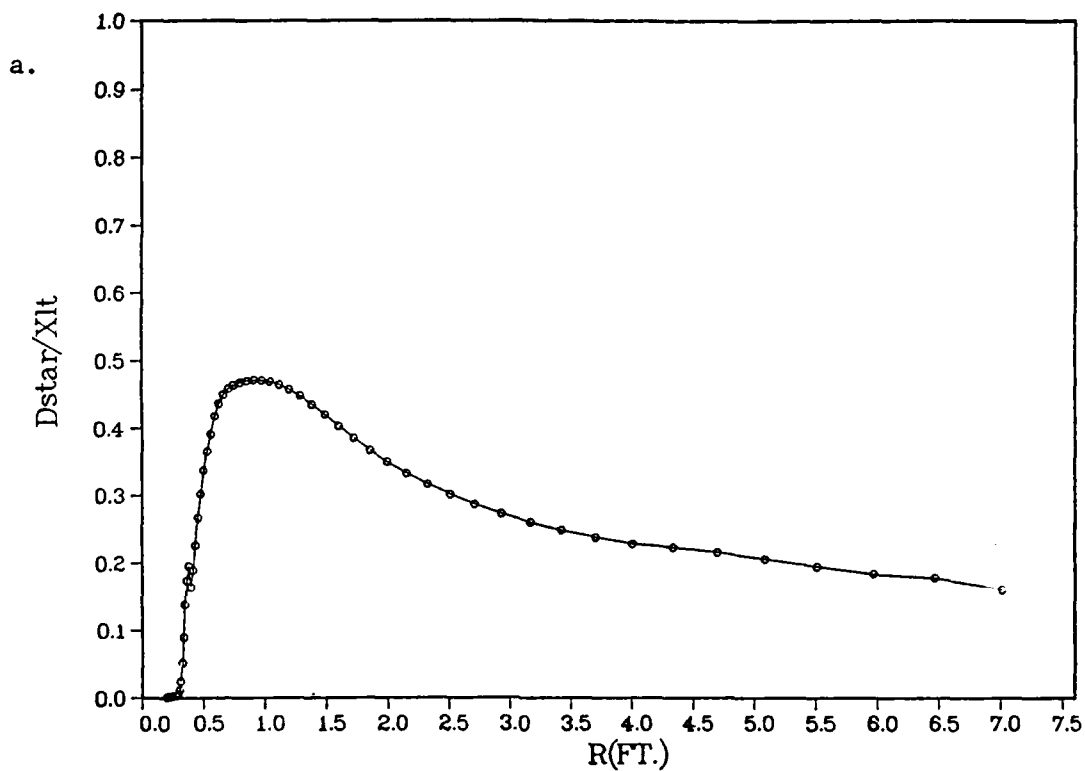
Figure 60. Plot of Case 3b Converged Solution Kinematic
Displacement Thickness; a)Full Diffuser Length;
b) Length Corresponding to Baseline Diffuser.

Case 4a

Employing a stiffened eddy viscosity turbulence model, steady, converged solutions for cases 2b and 2c were achieved. The same model was now employed to simulate the actual experimental flow conditions for the baseline UTRC experiment with the exit pressure set at 60 percent of normal shock recovery pressure. Figure 61 presents the actual inflow velocity conditions, obtained from the experimental data of Zumpano, et al. (13). Figures 62 and 63 present the actual inflow Mach number and momentum profiles, respectively. Computations were begun from the same inviscid one-dimensional case employed previously. After ten characteristic times, the numerical solution converged to a steady asymptote with the core flow normal shock located at 19 percent of the diffuser duct length (SPOS = 0.194; r/r_{de} = 1.59). The time history for this converged solution, presenting core flow normal shock position as a percentage of baseline diffuser length versus time, is presented in Figure 64.

Figure 65 presents the Mach number contours for this converged solution, followed by simulated Schlieren photographs in Figures 66 and 67. These presentations were developed from the Mach number and density data files. The strength of the wall energizing bank blowers and the reflection shocks in the nozzle mixing zone are readily apparent. Figure 68 displays developed velocity profiles in steady state. Examination of this information reveals that the inflow velocity profiles from the 10 source nozzles are thoroughly mixed just upstream of the core flow normal shock. The additional momentum of the wall energizing bank blower is also seen to persist all the way through the diffuser to the exit. Figure 69a presents a velocity vector plot for this solution, with an expanded view of the shock

region presented in Figure 69b. The flow separation along the wall is clearly shown to be less than 10 percent of the diffuser width. The flow separates from the diffuser wall at approximately 15 percent of the diffuser length, with reattachment occurring at approximately 33 percent of the diffuser length. Figure 70 shows sonic contour, again providing visual evidence of the shock impingement structure. Selected individual Mach contours for the converged solution are presented in Figure 71. The computed flowfield wall pressure, line of symmetry pressure and temperatue ratios are presented in Figure 72. Consistent with the ideal flow results, the behavior of the wall pressure also exhibits a large overshoot. This is attributable to the fact that the energizing bank blower flow remains essentially unmixed with the core flow. The higher energy, higher Mach number bank blower flow generates a stronger shock before mixing with the lower Mach number core flow and finally adjusting to diffuser exit pressure.

Figure 73 displays the computed kinematic displacement thickness δ^* (as a percentage of diffuser diameter) computed along the length of the diffuser At its' maximum value, δ^* is five percent of the diffuser diameter. Details of the solution evolution are presented in Appendix H.

Eddy viscosity coefficients for both the inner and outer regions of the modified Cebeci-Smith algebraic turbulence model are examined in Figures 74 through 77. In each figure these coefficients are presented first for the entire computational flowfield and then in an expanded view showing only the behavior near the wall. The kinematic displacement thickness δ^* for each corresponding streamwise flow location is also noted on each plot. The results of this numerical experiment are consistent with the theory presented in Chapter V, Figure 15. Application of the present modification

112

to accommodate severe adverse pressure gradients produces computational results consistent with expected theoretical behavior. The cross over from the laminar sublayer viscosity coefficient ϵ_i to the Clauser-type outer region eddy viscosity coefficient ϵ_o is seen to always occur at less than 10 percent of the distance from the diffuser wall. The outer region eddy viscosity length scale, based on the kinematic displacement thickness, also appears appropriate, especially upstream of the normal shock where the flow vorticity is observed to vary significantly across the flow field. The core flow normal shock occurs near grid line j = 60, and the effect on the outer region eddy viscosity coefficient is notable as seen in Figure 75e. At this station in the flow the eddy viscosity is an order of magnitude greater than its' value upstream of the normal shock. This is attributable to both the density jump across the shock as well as the recirculation zone in the separated flow region along the wall, which causes a large computed value for δ^*. Typically, this recirculation zone behavior is a weak point in zero order eddy viscosity models (59). It is observed that ϵ decreases once the flow is reattached.

113

ACTUAL INFLOW VELOCITY PROFILE
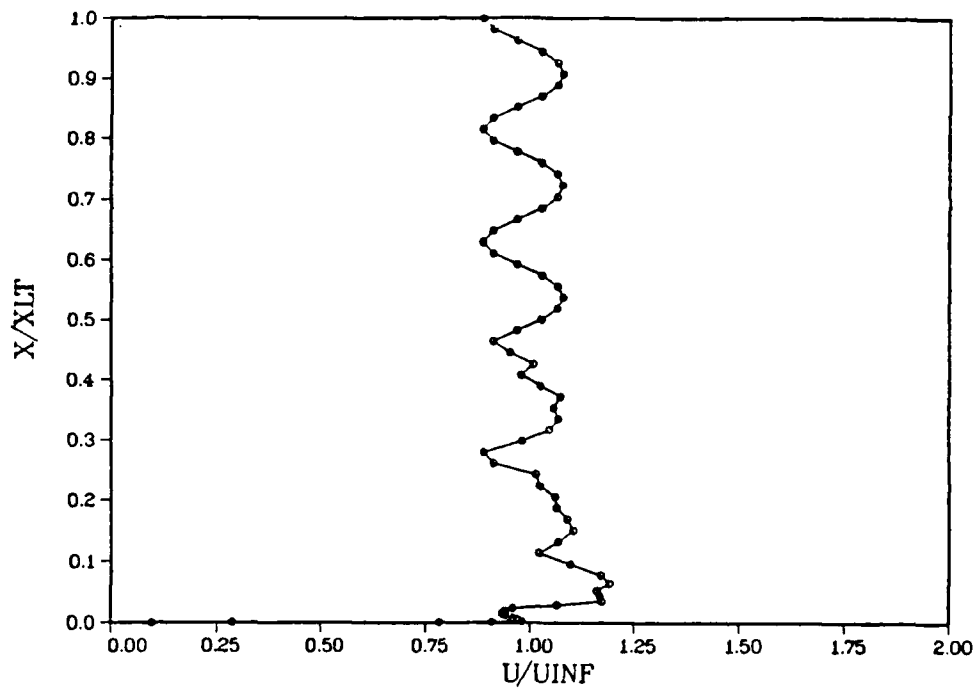
VELOCITY VECTOR PLOT INFLOW PROFILE
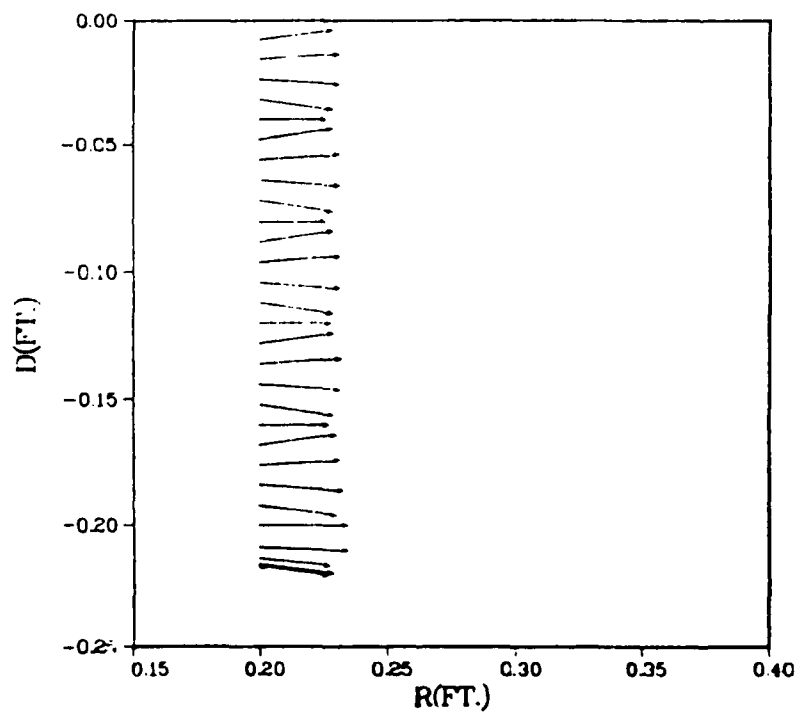
Figure 61. Actual Inflow Velocity Conditions (Ref. 13);
a) Velocity Profile; b) Velocity Vector Plot.

114

ACTUAL INFLOW MACH NUMBER PROFILE
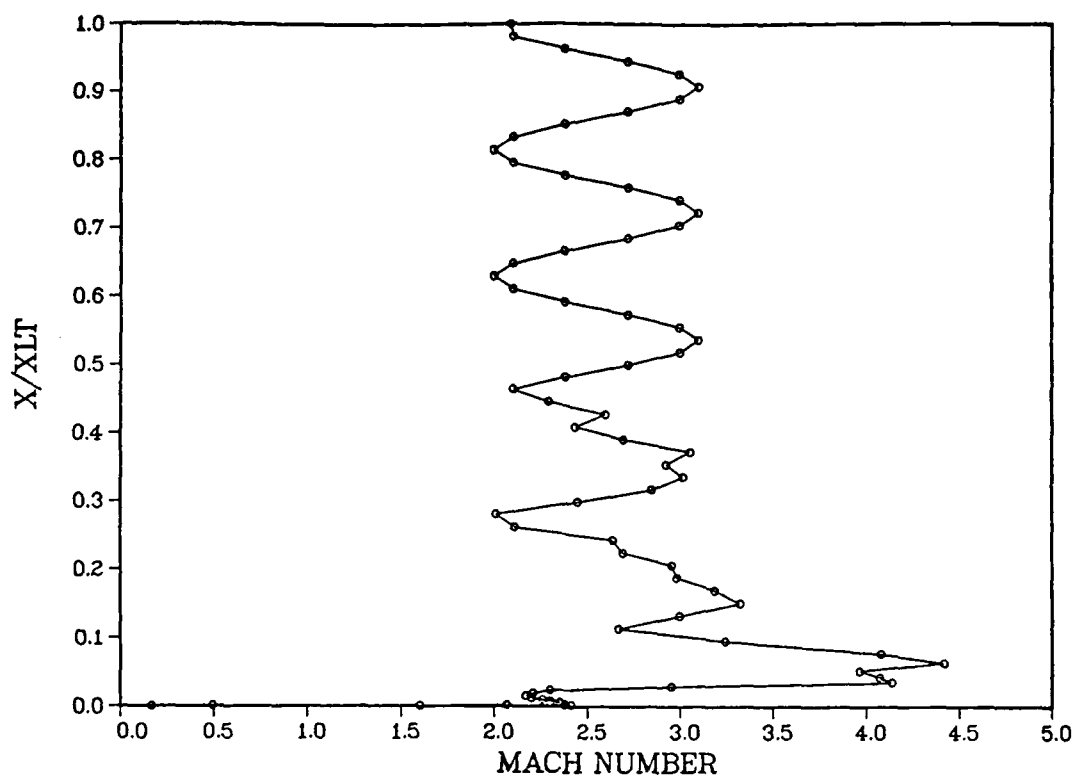
Figure 62. Actual Inflow Mach Number Profile (Ref. 13).

ACTUAL INFLOW MOMENTUM PROFILE
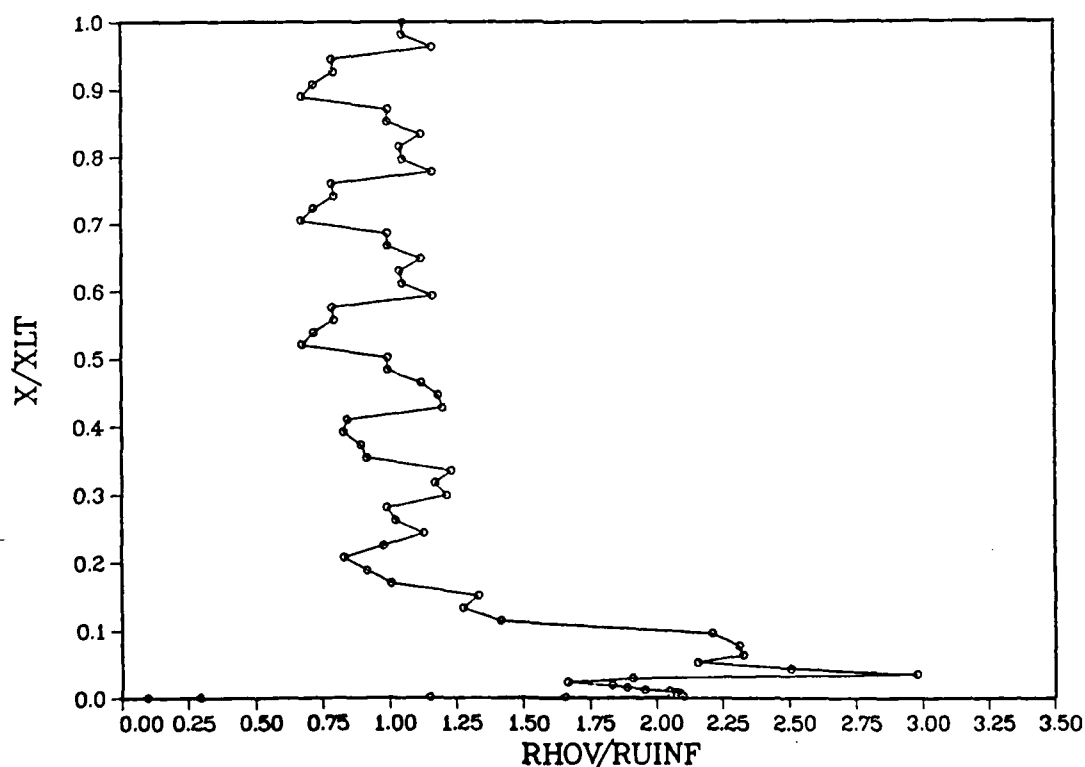
Figure 63. Actual Inflow Momentum Profile (Ref. 13.).

Figure 64. Core Flow Normal Shock Position Time History, Case 4a
(Actual Inflow, 60% NSR, wbb = .195,
modified Cebeci-Smith Turbulence Model).

116

MACH CONTOURS 60%NSR 70X103 GRID SOLUTION
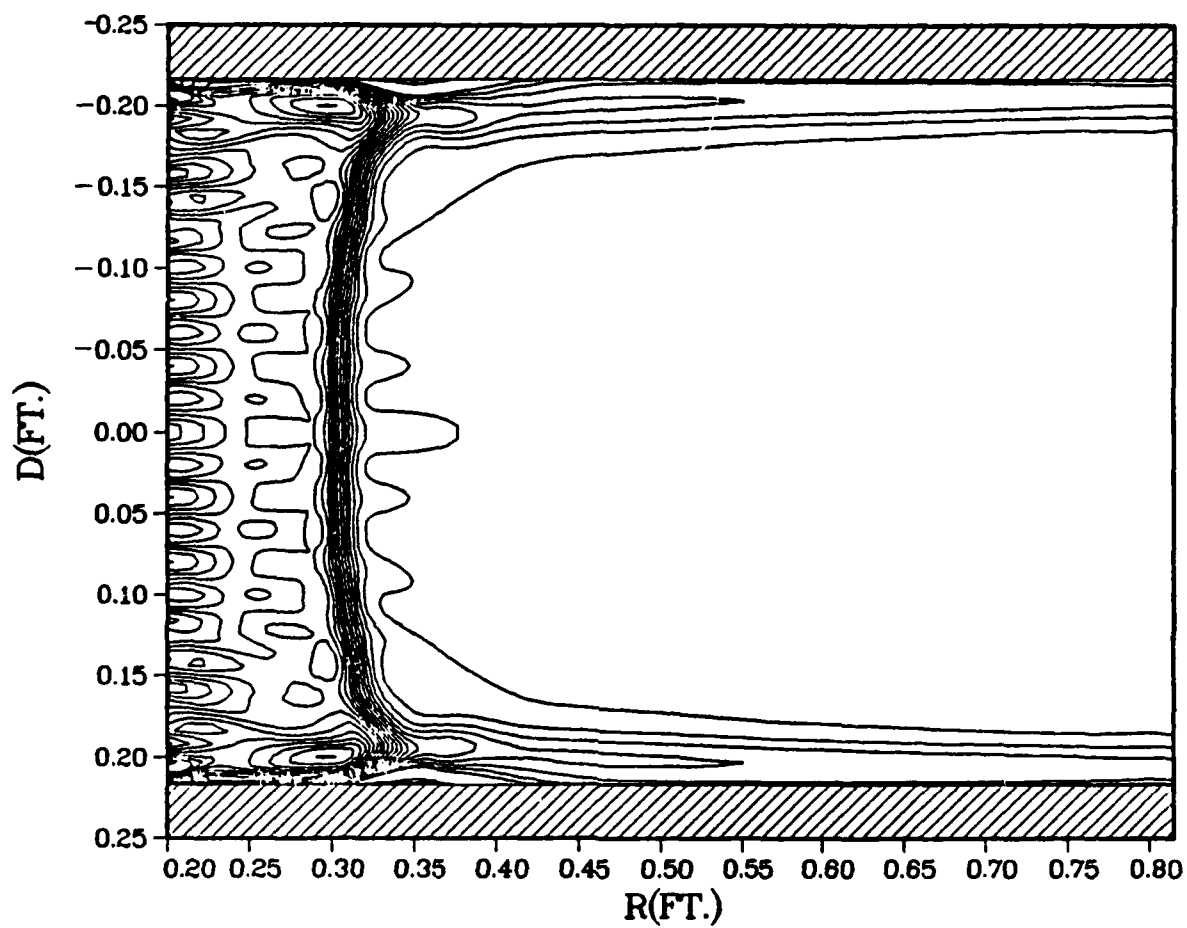
Figure 65. Converged Solution Mach Contours, Case 4a.
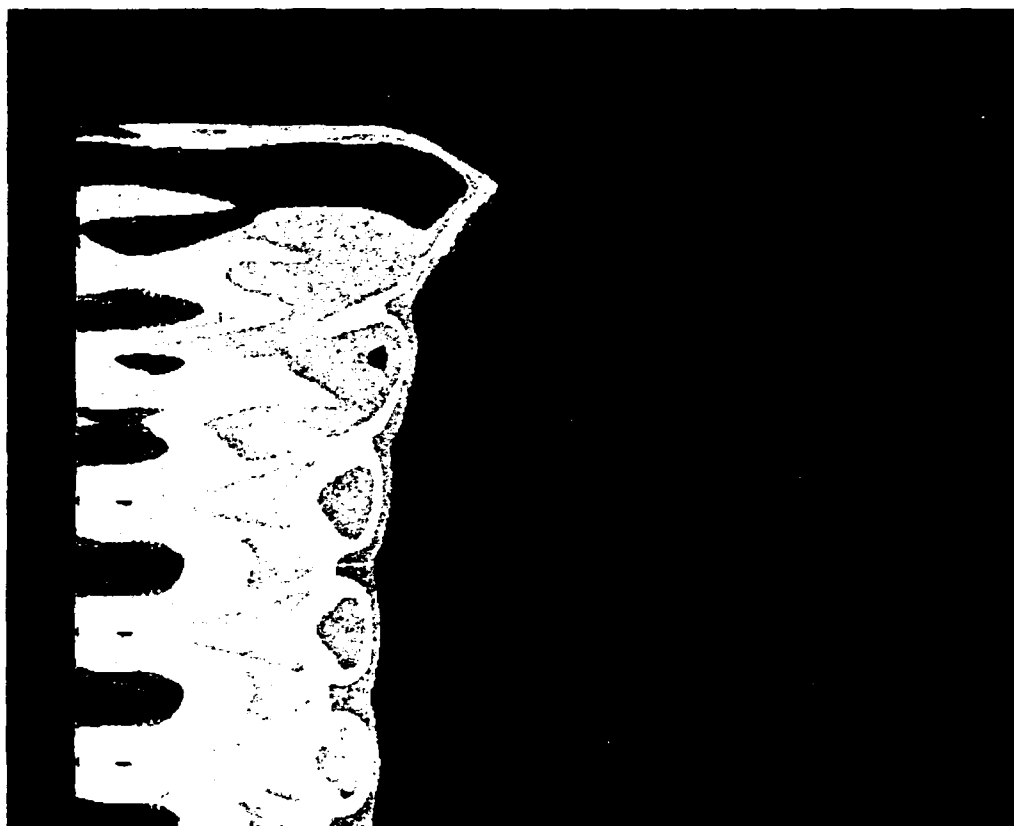
Figure 67. Computer Generated (Simulated) Schlieren Photograph,
Case 4a Converged Solution;   Detail of Wall Bank
Blower.

MACH CONTOURS 60%NSR 70X103 GRID SOLUTION

Figure 68. Velocity Profiles, Case 4a Converged Solution.

VELOCITY VECTOR PLOT 60%NSR STABLE SOLUTION
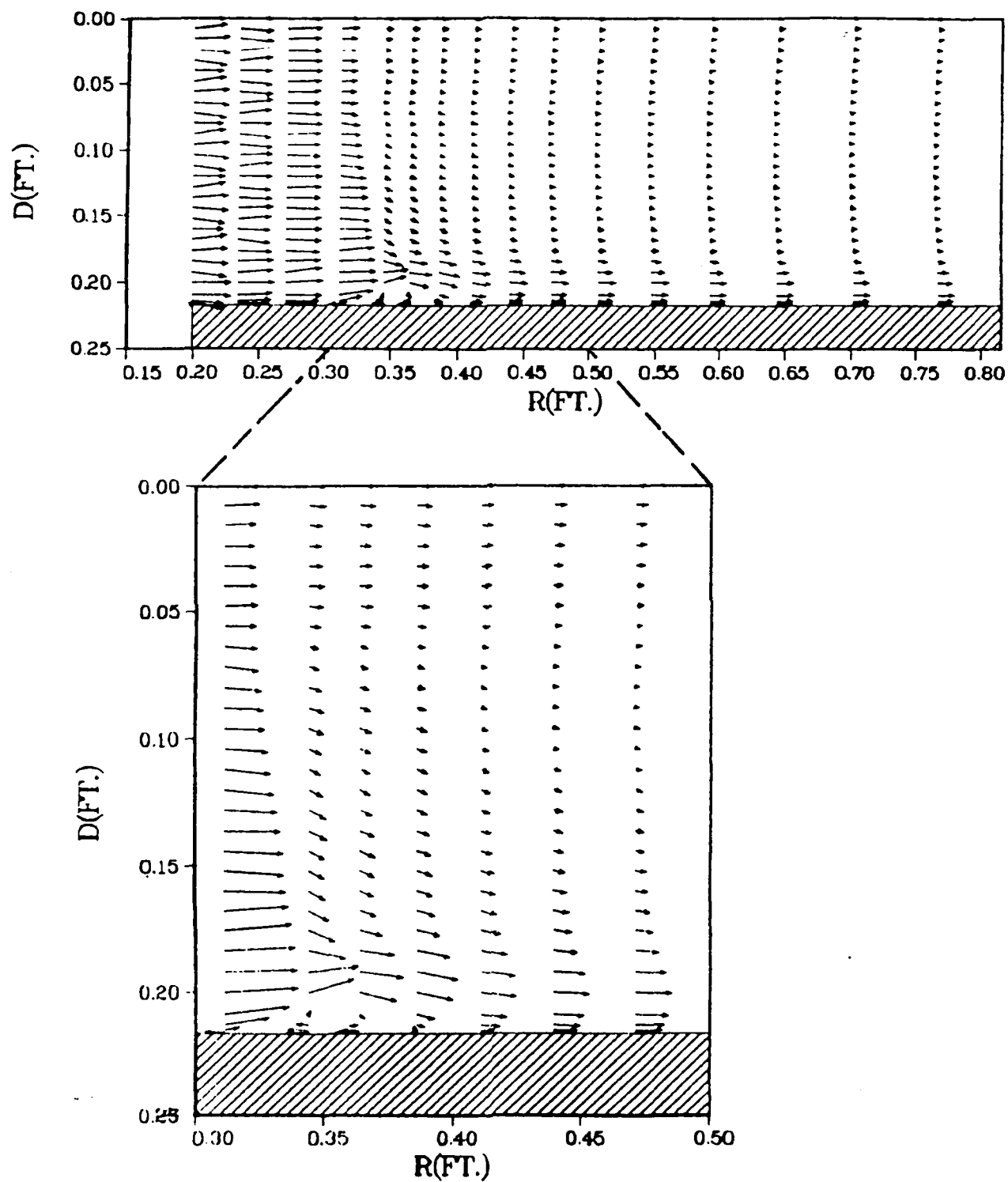
Figure 69. Velocity Vector Plot, Case 4a Converged Solution.

MACH=1 CONTOUR 60%NSR 70X103 GRID SOLUTION
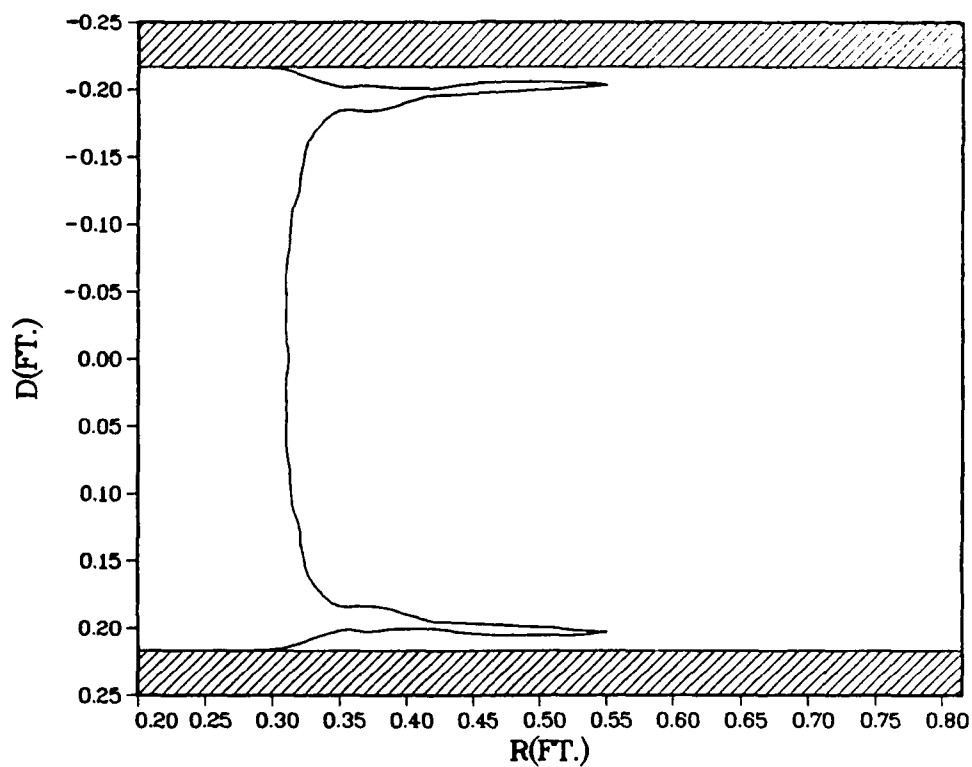
Figure 70. Sonic Contour, Case 4a Converged Solution.

M=0.50 CONTOUR 60%NSR Actual Inflow Solution
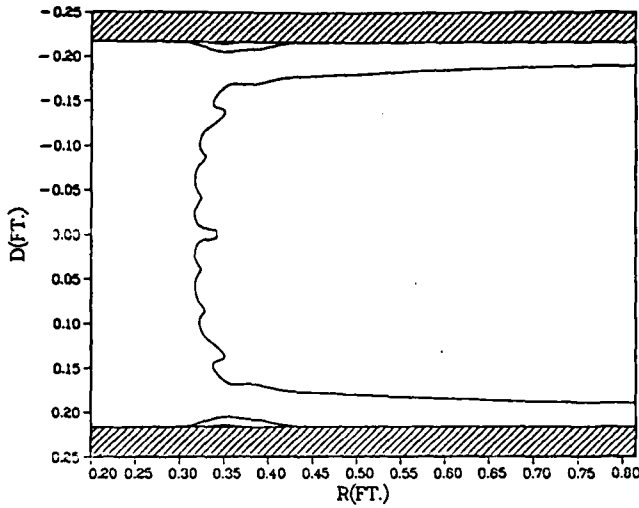
M=1.0 CONTOUR 60%NSR Actual Inflow Soluti
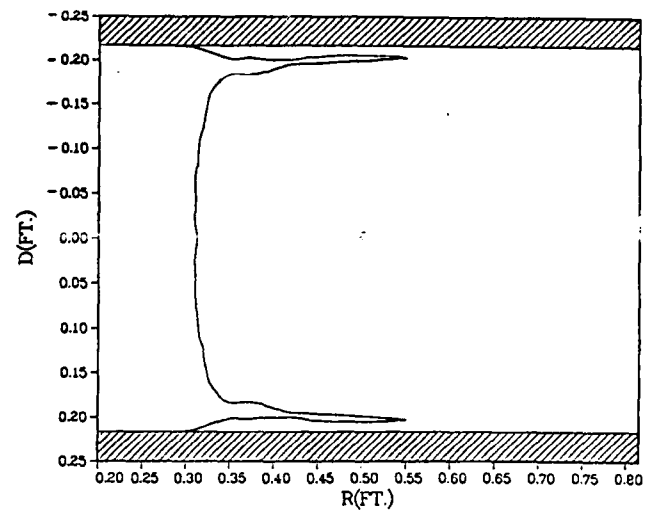
M=1.50 CONTOUR 60%NSR Actual Inflow Solution
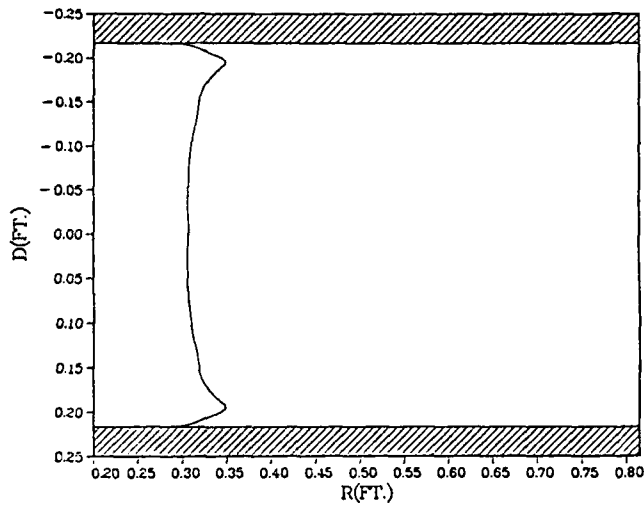
M=2.5 CONTOUR 60%NSR Actual Inflow Soluti
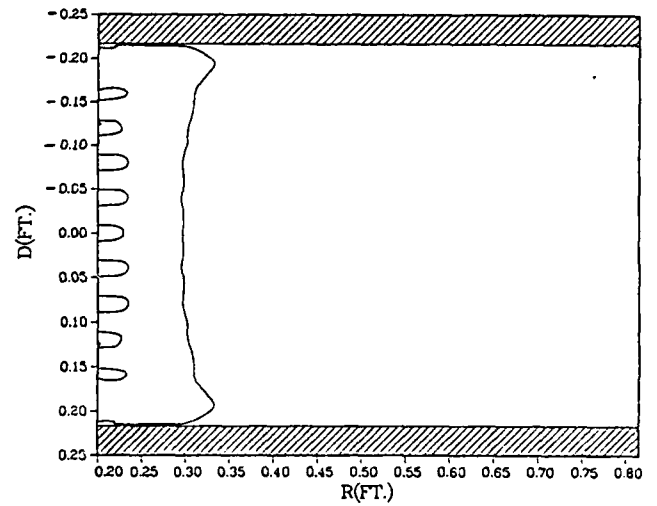
M=3.0 CONTOUR 60%NSR Actual Inflow Solution
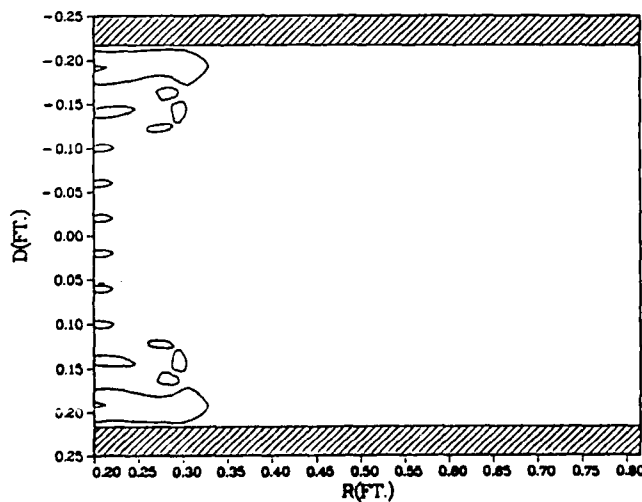
M=3.5 CONTOUR 60%NSR Actual Inflow Solution
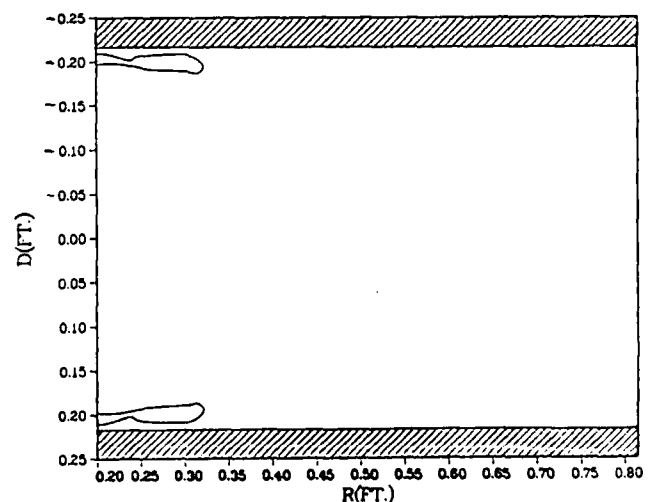
Figure 71. Selected Individual Mach Contours, Case 4a Solution.

123
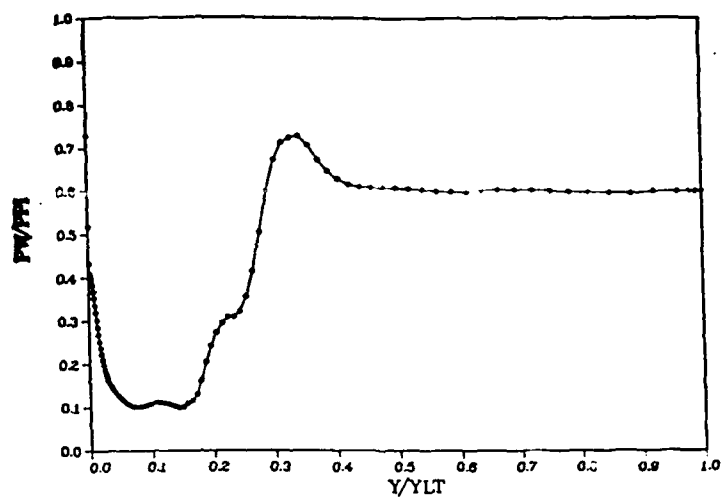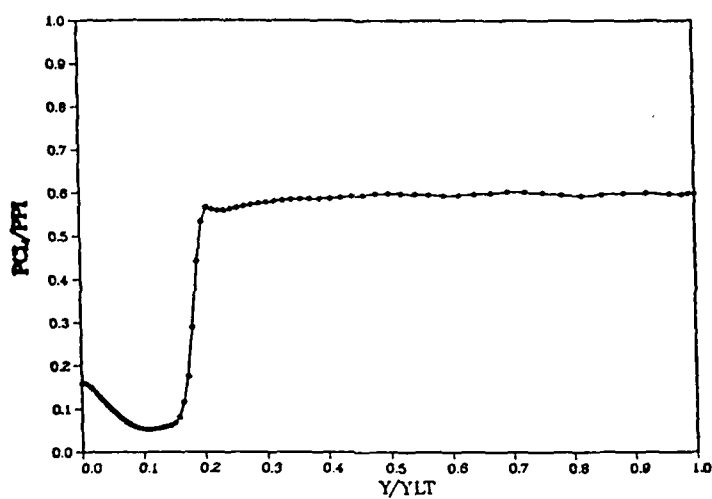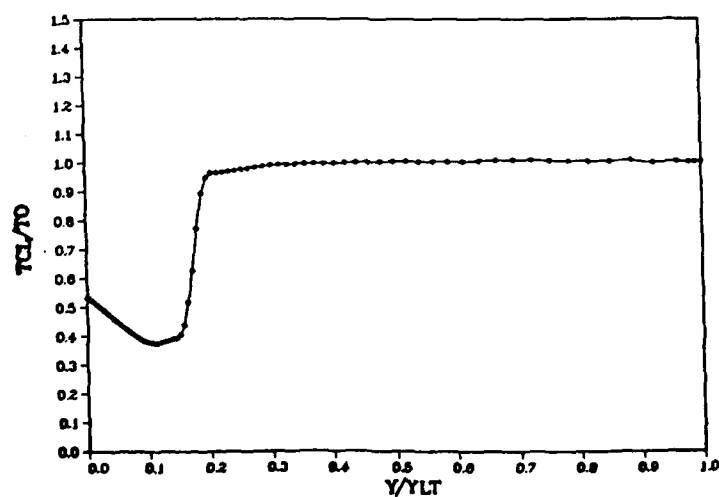
Figure 72. Case 4a Converged Solution Flowfield Conditions;
a) Wall Pressure Ratio; b) Line of Symmetry Pressure
Ratio; c) Line of Symmetry Temperature Ratio.

124

Dstar Ratio 60%NSR Actual Inflow Solution
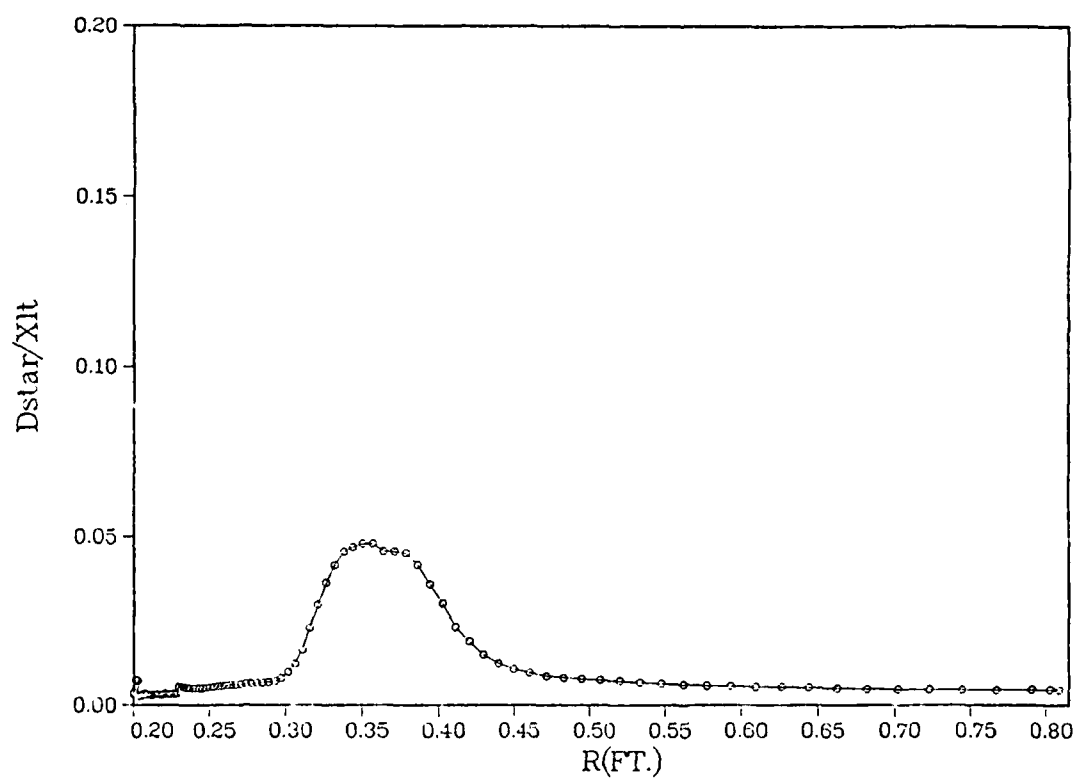
Figure 73. Plot of Case 4a Converged Solution Kinematic
Displacement Thickness.

PLOT OF EMI AND EMO 60%NSR SOLUTION (J=10)   PLOT OF EMI AND EMO 60% NSR SOLUTION (J=10)

PLOT OF EMI AND EMO 60%NSR SOLUTION (J=20)   PLOT OF EMI AND EMO 60% NSR SOLUTION (J=20)

PLOT OF EMI AND EMO 60%NSR SOLUTION (J=30)   PLOT OF EMI AND EMO 60% NSR SOLUTION (J=30)

Figure 74. Eddy Viscosity Coefficient Detail, Case 4a Converged
Solution (j=10, 20, 30).

126
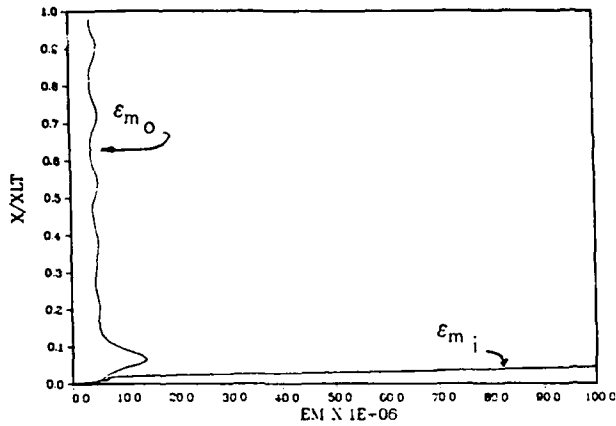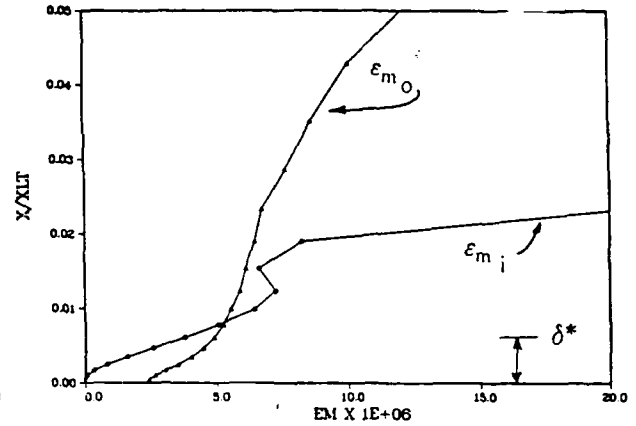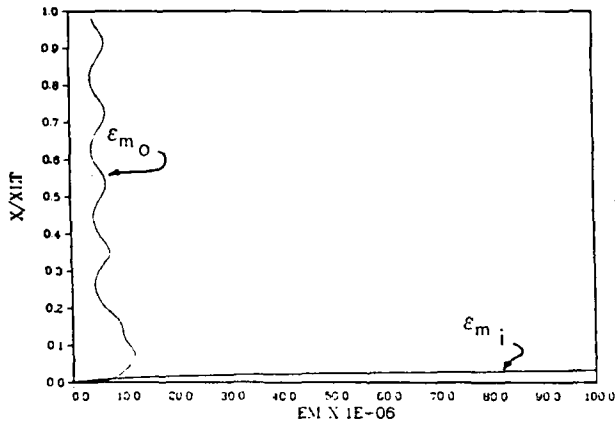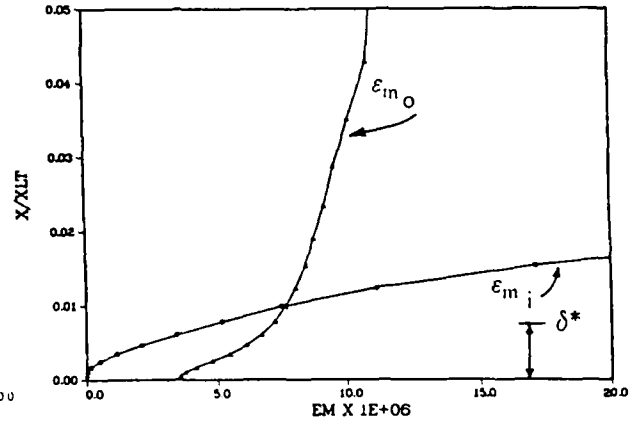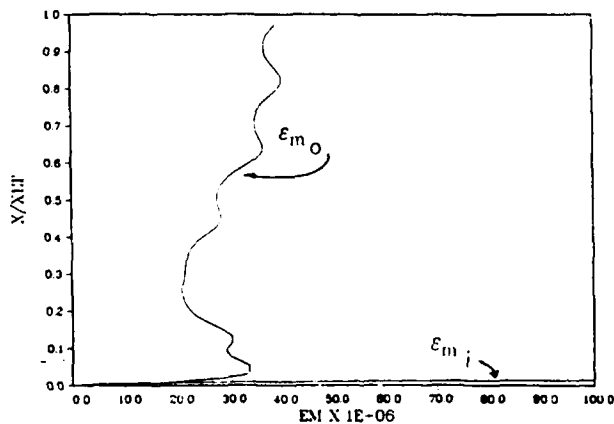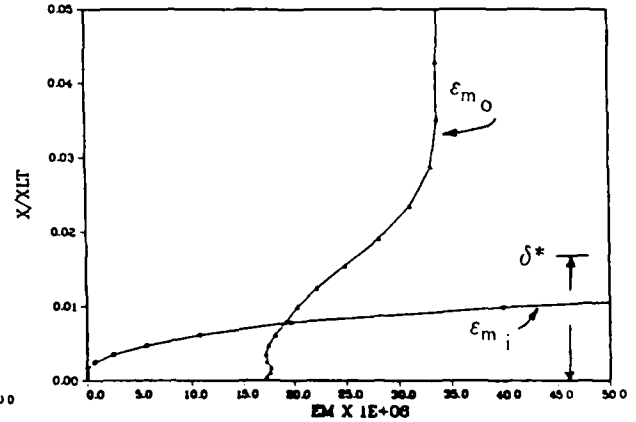
Figure 75. Eddy Viscosity Coefficient Detail, Case 4a Converged
Solution (j=40, 50, 60).

127

PLOT OF EMI AND EMO 60%NSR SOLUTION (J=70)   PLOT OF EMI AND EMO 60% NSR SOLUTION (J=70)
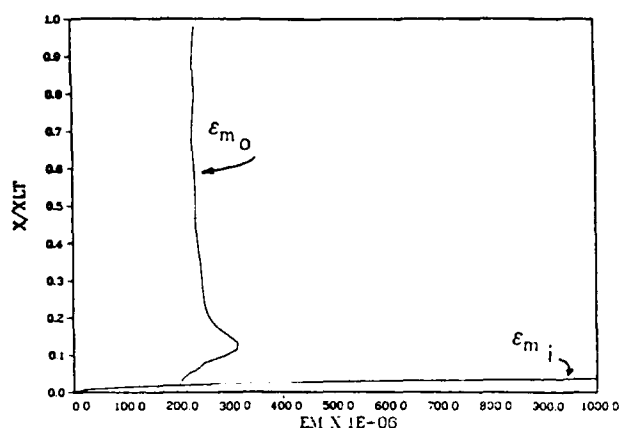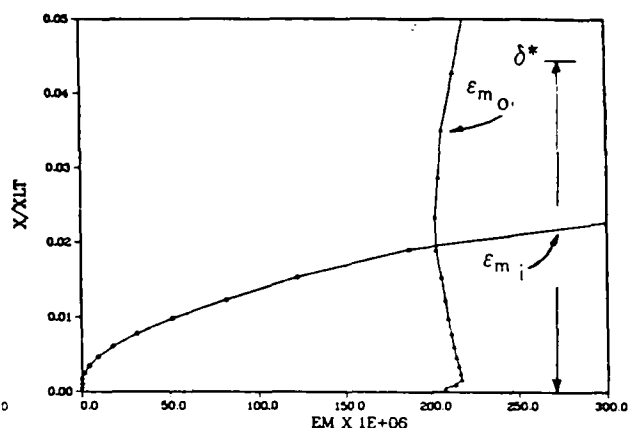
PLOT OF EMI AND EMO 60%NSR SOLUTION (J=80)   PLOT OF EMI AND EMO 60% NSR SOLUTION (J=80)
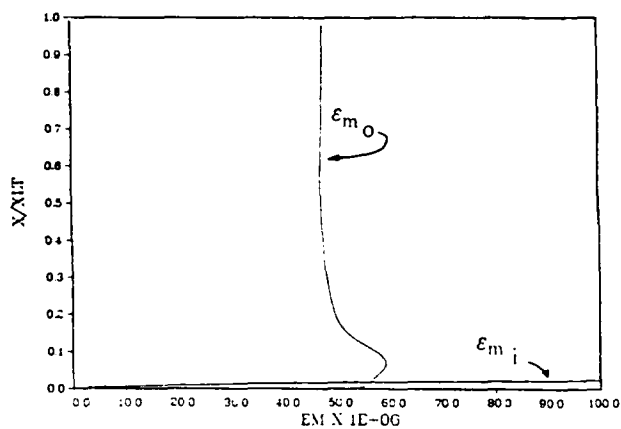
PLOT OF EMI AND EMO 60%NSR SOLUTION (J=90)   PLOT OF EMI AND EMO 60% NSR SOLUTION (J=90)

Figure 76. Eddy Viscosity Coefficient Detail, Case 4a Converged
Solution (j=70, 80, 90).

128
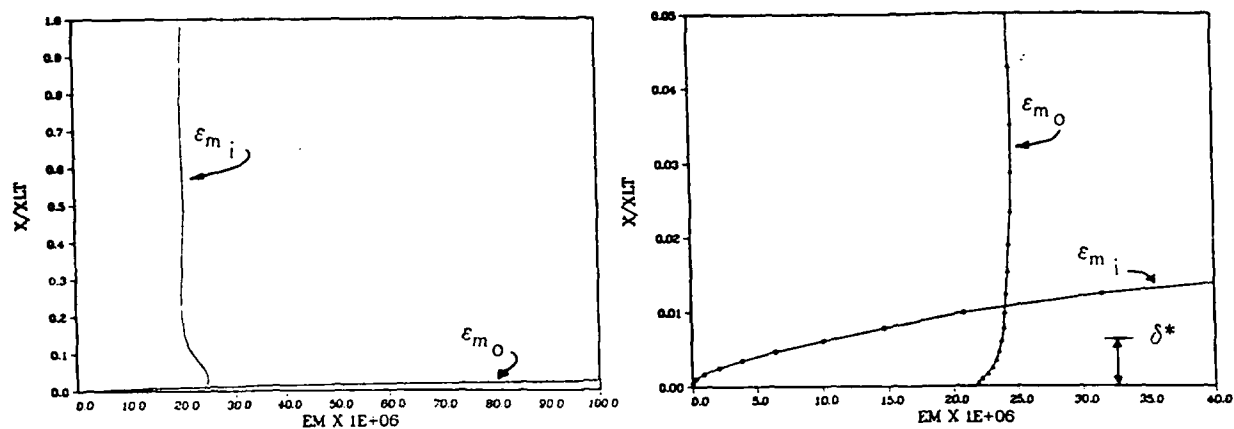
Figure 77. Eddy Viscosity Coefficient Detail, Case 4a Converged
Solution (j=100).

129

Case 4b

From the 60 percent normal shock recovery backpressure converged
solution for the actual inflow conditions (Figure 17), the exit backpressure
was lowered to 47 percent of normal shock recovery pressure and the
algorithm was allowed to march forward in time. A steady, converged
solution after five additional characteristic times was achieved with the
core flow normal shock position at approximately 35 percent of the baseline
diffuser length (SPOS = 0.343; r/r_{de} = 2.05). The time history of this
converged solution is presented in Figure 78; the Mach number contours are
presented in Figure 79.

Figure 80 displays the developed velocity profiles for the steady
solution, and Figure 81 presents the velocity vector plots. The size of the
large wall separation region, nearly 20 percent of the diffuser diameter,
with significant regions of reverse flow along the diffuser wall, is quite
apparent. Reattachment of this flowfield occurs only slightly upstream of
the diffuser exit. The size of this separation region is attributable to
the much stronger shock structure, as both the core flow and the wall flow
energizing bank blowers accelerate farther into the radially increasing duct
area before generating terminal shocks at higher Mach numbers than for the
60 percent normal shock recovery backpressure case. The sonic contour
is presented in Figure 82. Selected individual Mach contours are
presented in Figure 83. The computed wall pressure, line of symmetry
pressure and temperature ratios are presented in Figure 84. The overshoot
behavior of the wall pressure, observed in both ideal flow solutions and in
the 60 percent normal shock recovery backpressure case, is not evident here,

130

and the wall pressure is observed to recover smoothly to the diffuser exit pressure.   Details of the solution evolution are provided in Appendix I.

Figure 85 presents a plot of the computed kinematic displacement thickness δ^* along the length of the diffuser. It is seen to achieve a maximum value of approximately 25 percent of the diffuser diameter, a very large value attributable to the large separation/recirculation region present downstream of the shock impingement on the boundary-layer. Eddy viscosity coefficients for both the inner and outer regions of the modified Cebeci-Smith algebraic turbulence model are examined in Figures 86 through 89, in the same manner that they were presented for the 60 percent normal shock recovery converged solution, with similar conclusions.
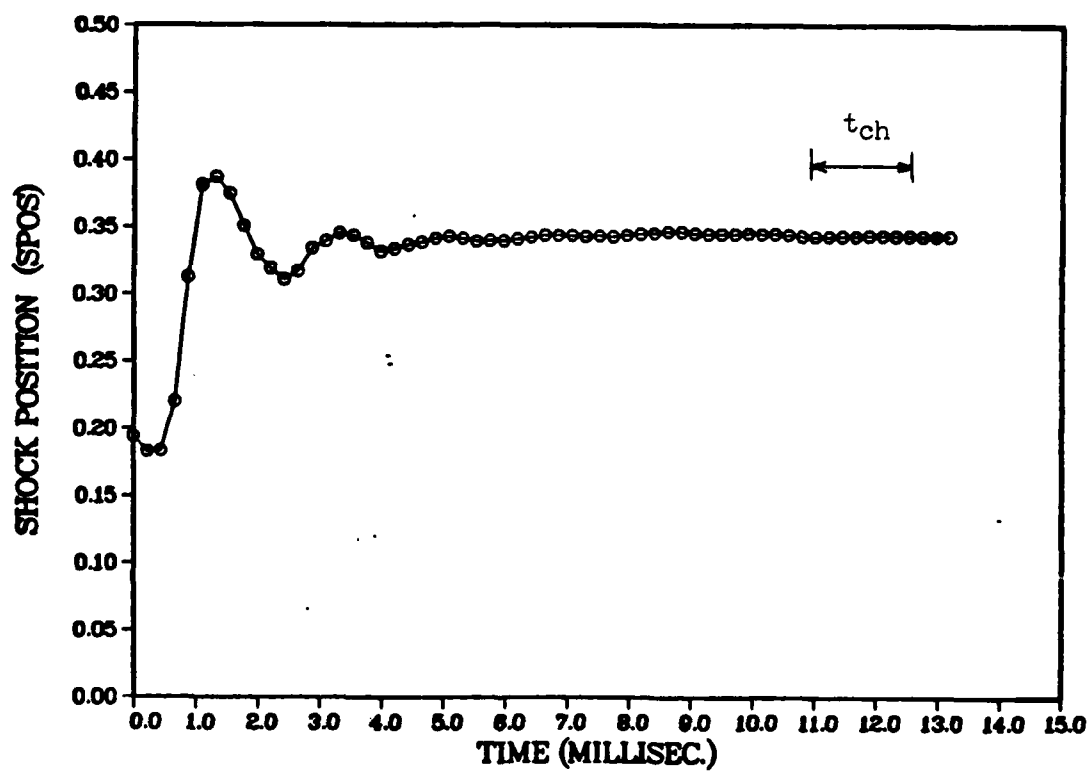
Figure 78. Core Flow Normal Shock Position Time History, Case 4b
(Actual Inflow, 47% NSR, wbb = .195,
modified Cebeci-Smith Turbulence Model).

MACH CONTOURS 47%NSR 70X103 GRID SOLUTION
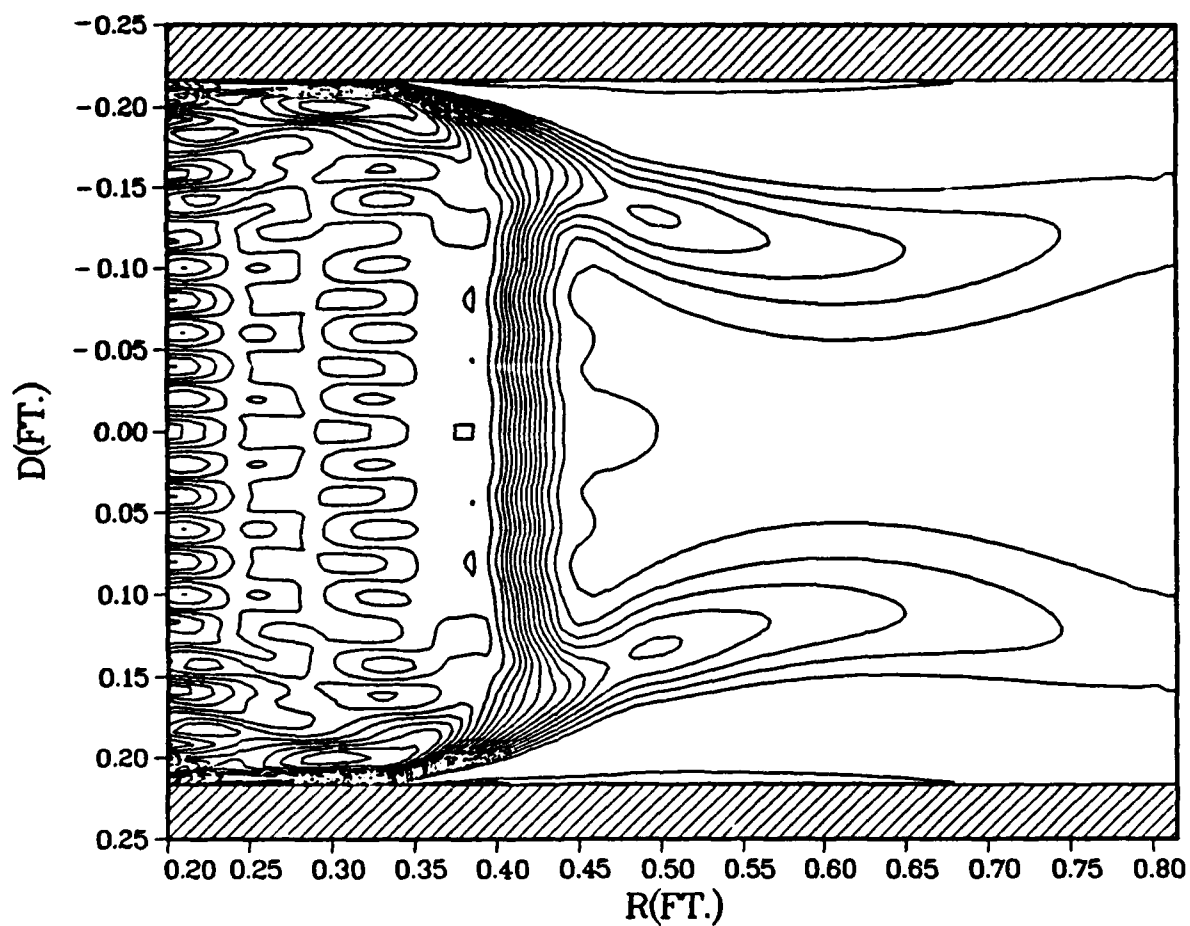
Figure 79. Converged Solution Mach Contours, Case 4b.

MACH CONTOURS 47%NSR 70X103 GRID SOLUTION
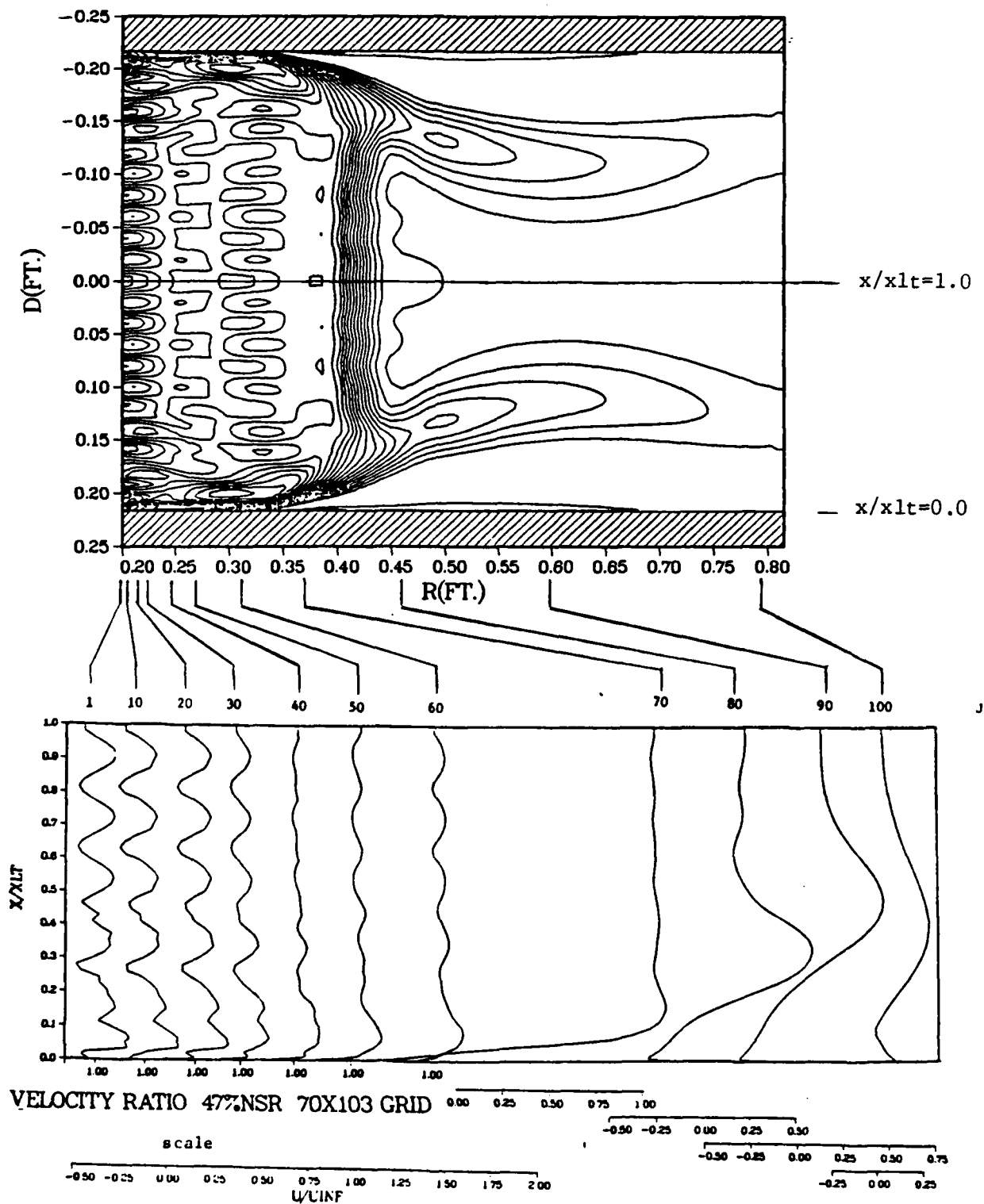
Figure 80. Velocity Profiles, Case 4b Converged Solution.

VELOCITY VECTOR PLOT   47%NSR SOLUTION
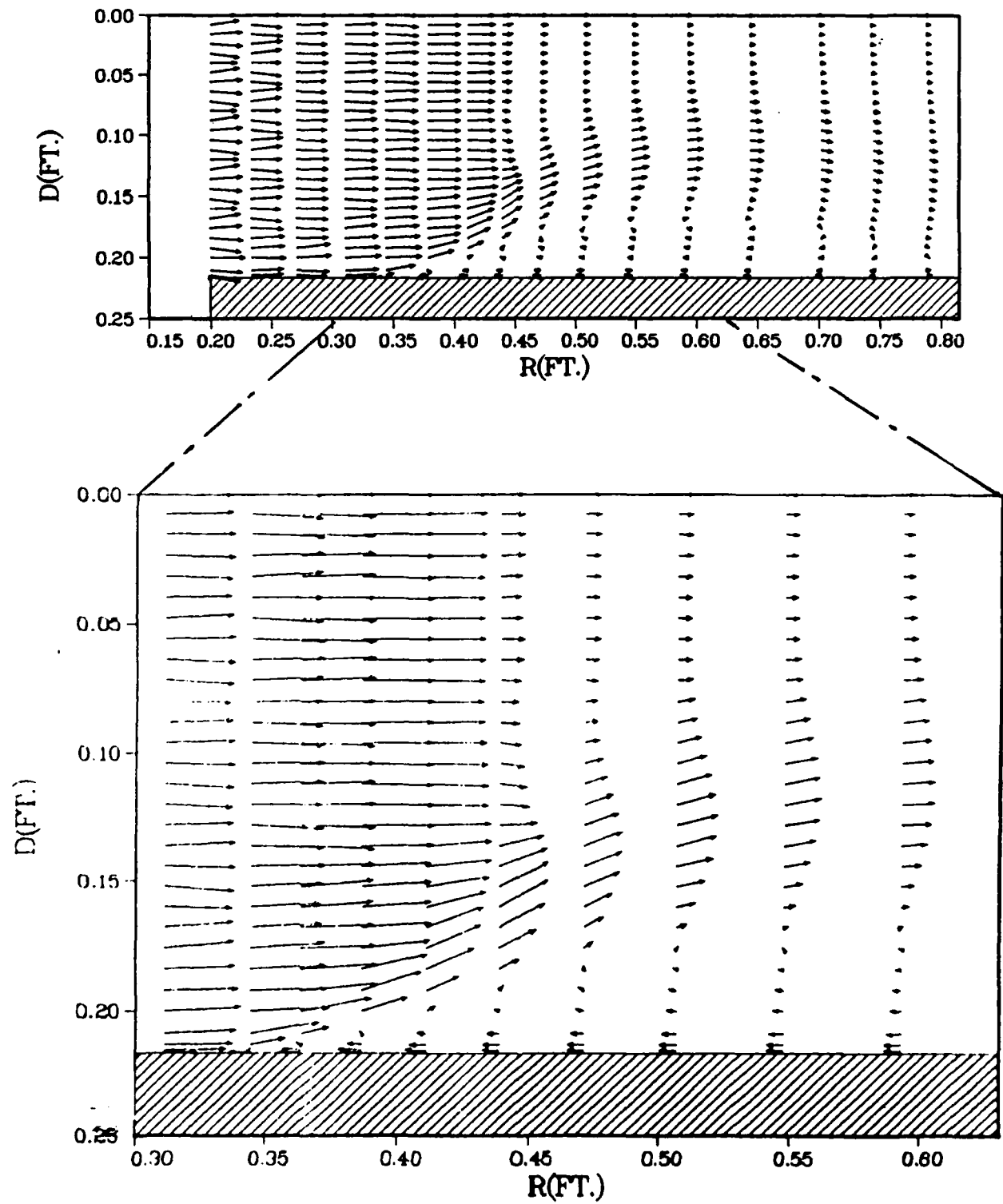
Figure 81. Velocity Vector Plot, Case 4b Converged Solution.

MACH=1 CONTOUR 47%NSR 70X103 GRID SOLUTION
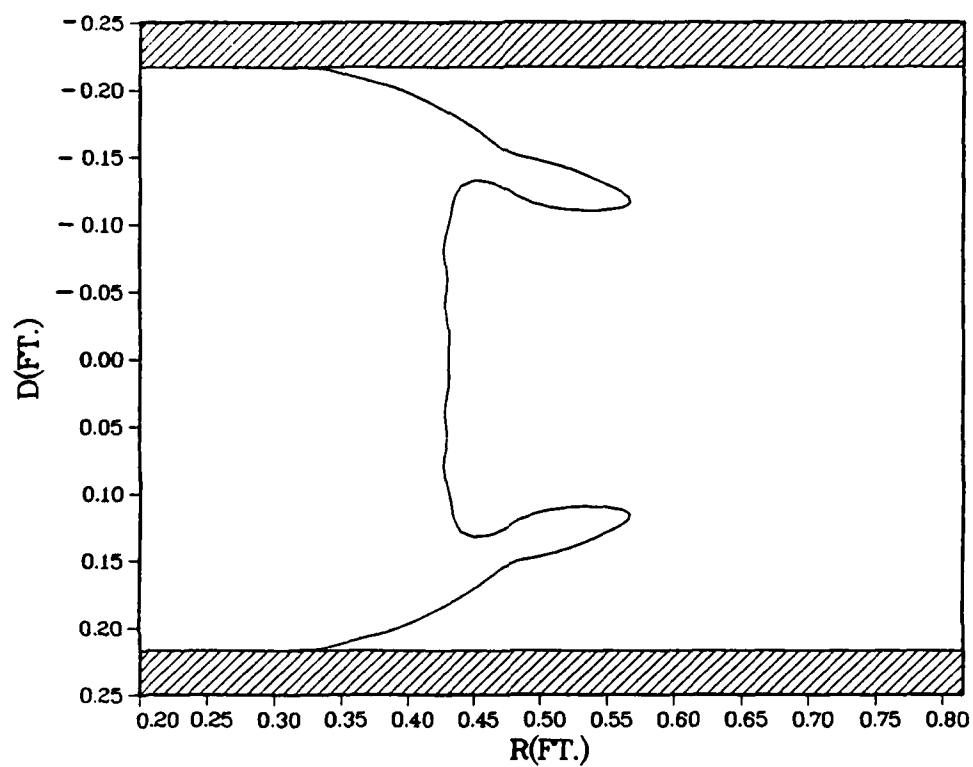
Figure 82. Sonic Contour, Case 4b Converged Solution.

M=.50 CONTOUR 47%NSR Actual Inflow Solution
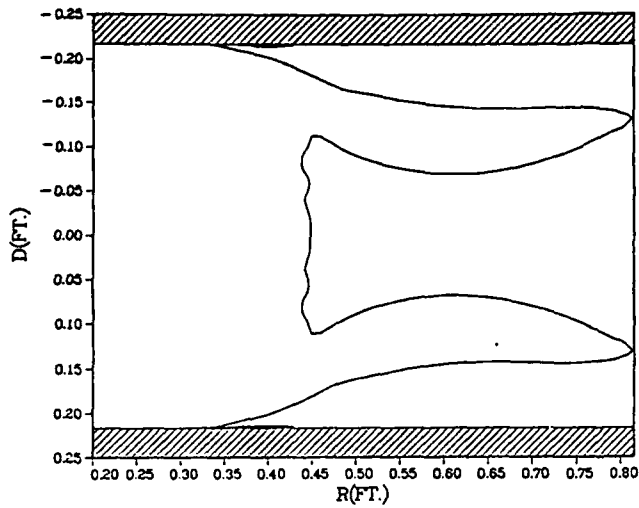
M=1.0 CONTOUR 47%NSR Actual Inflow Solution
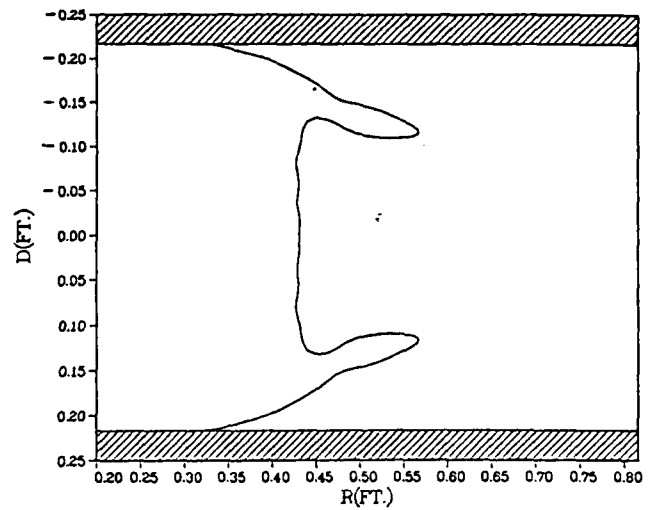
M=1.50 CONTOUR 47%NSR Actual Inflow Solution
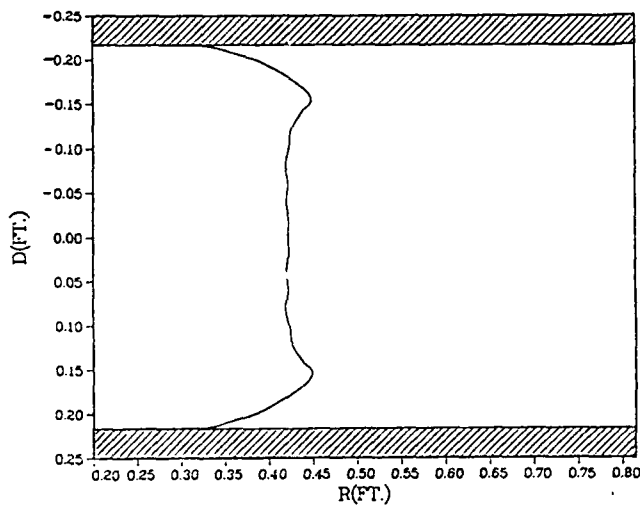
M=2.5 CONTOUR 47%NSR Actual Inflow Solution
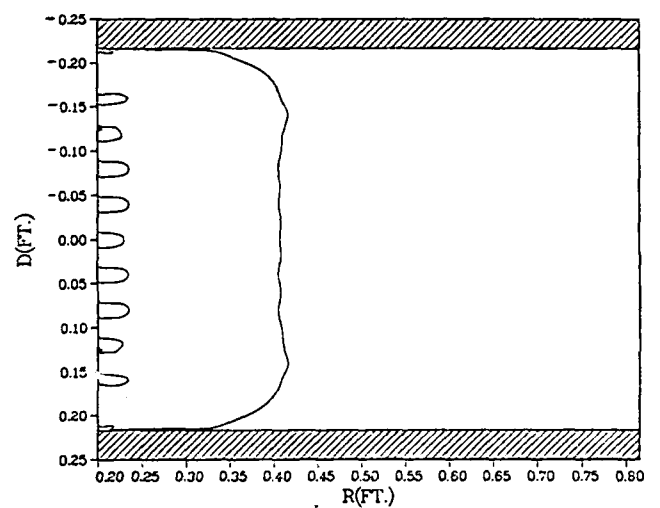
M=3.0 CONTOUR 47%NSR Actual Inflow Solution
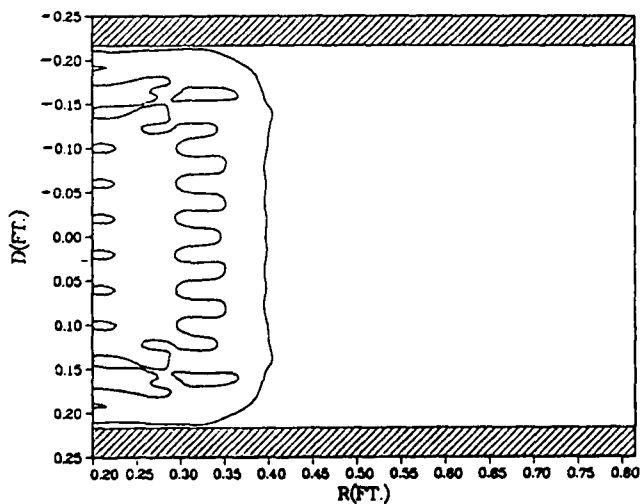
M=3.5 CONTOUR 47%NSR Actual Inflow Solution
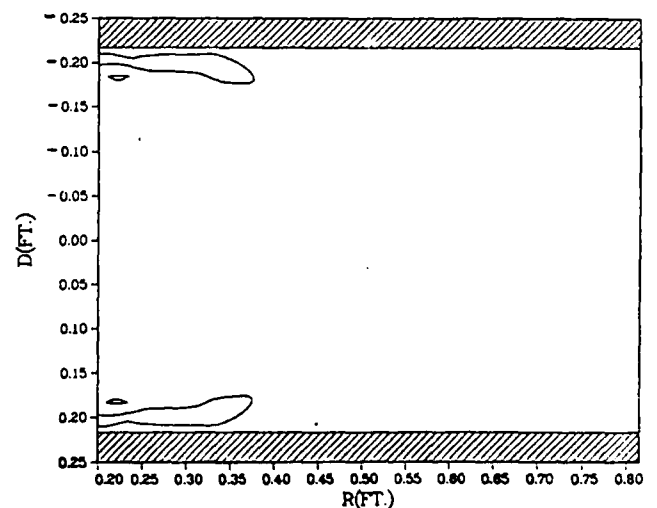
Figure 83. Selected Individual Mach Contours, Case 4b Solution.

137
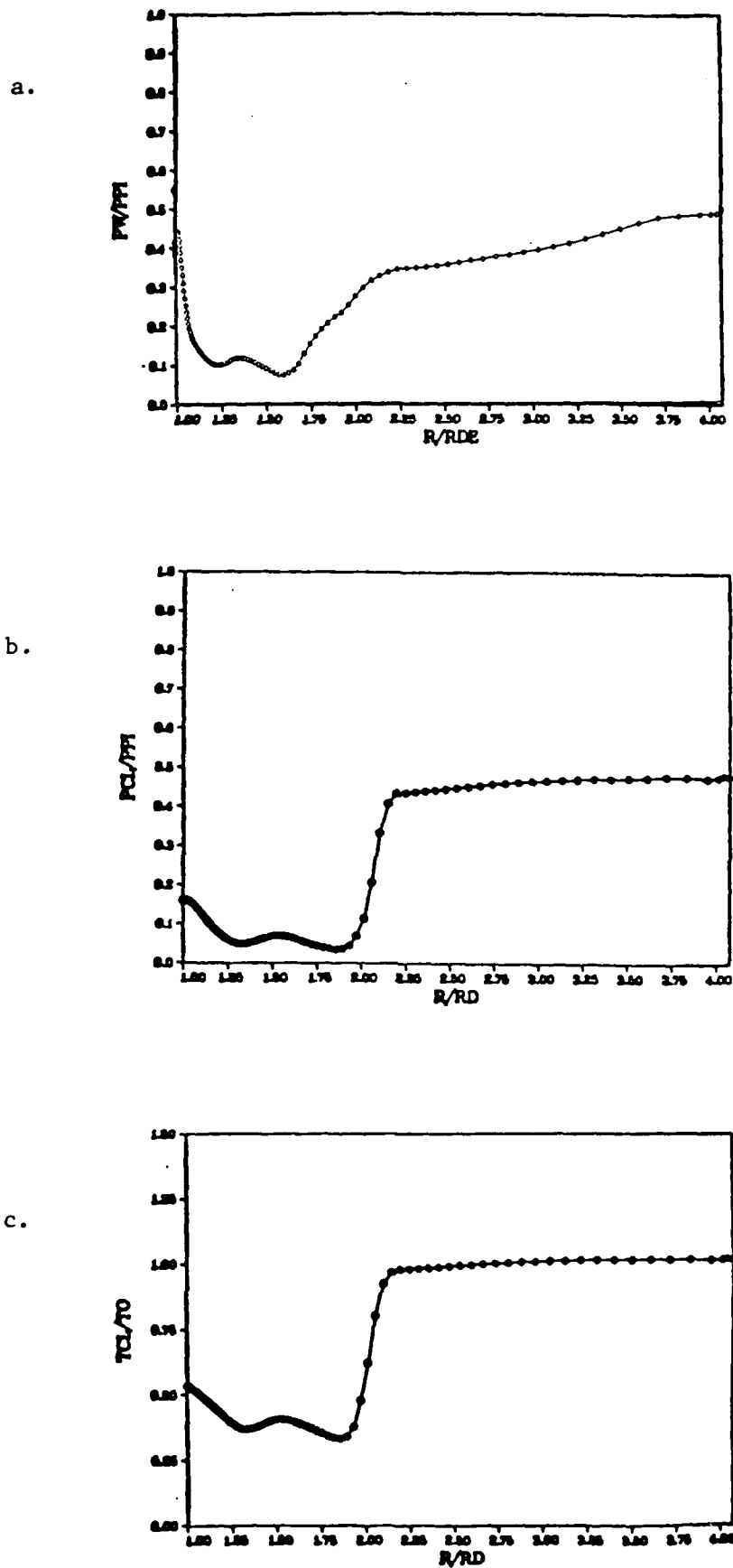
Figure 84. Case 4b Converged Solution Flowfield Conditions;
a) Wall Pressure Ratio; b) Line of Symmetry Pressure
Ratio; c) Line of Symmetry Temperature Ratio.

138

Dstar Ratio 47%NSR Actual Inflow Solution
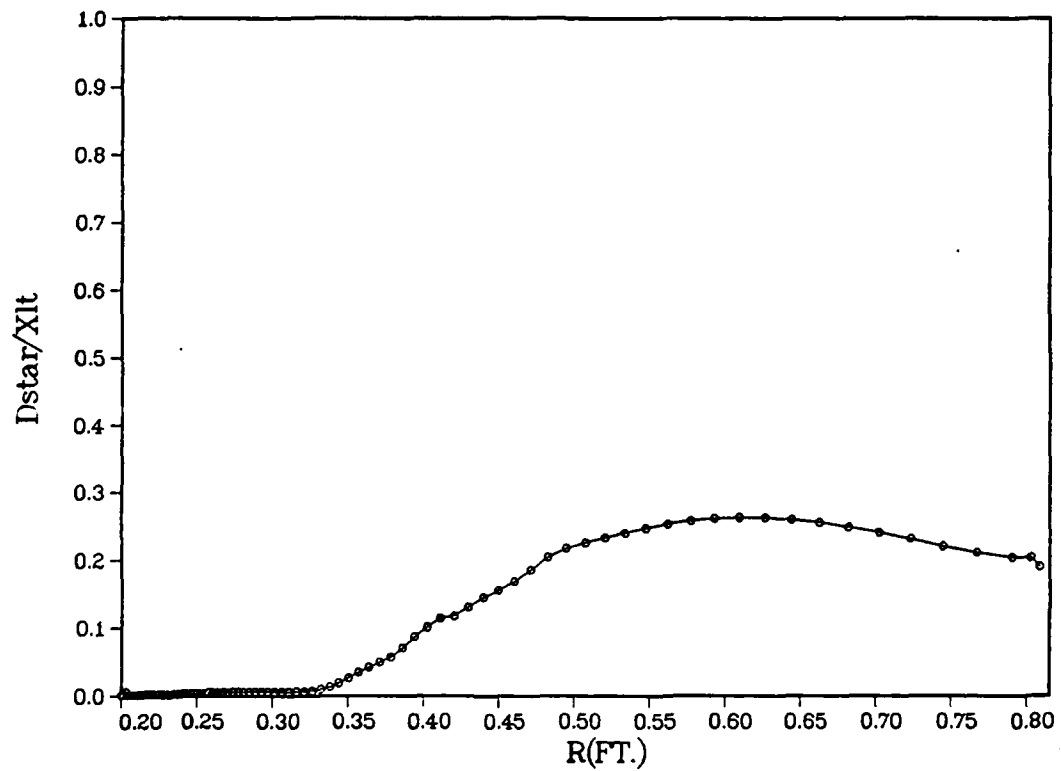
Figure 85. Plot of Case 4b Converged Solution Kinematic
Displacement Thickness.

PLOT OF EMI AND EMO 47%NSR SOLUTION (J=10)   PLOT OF EMI AND EMO 47%NSR SOLUTION (J=10)
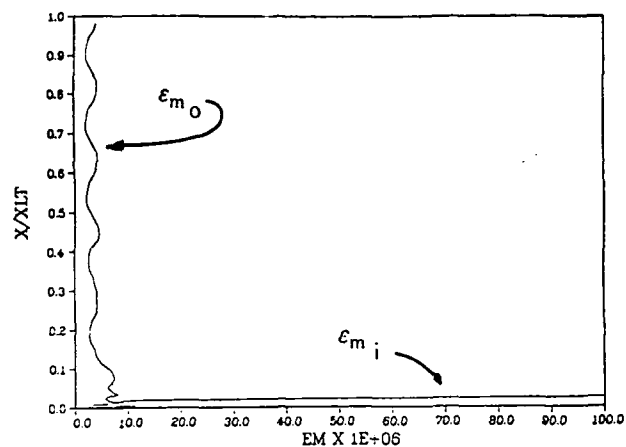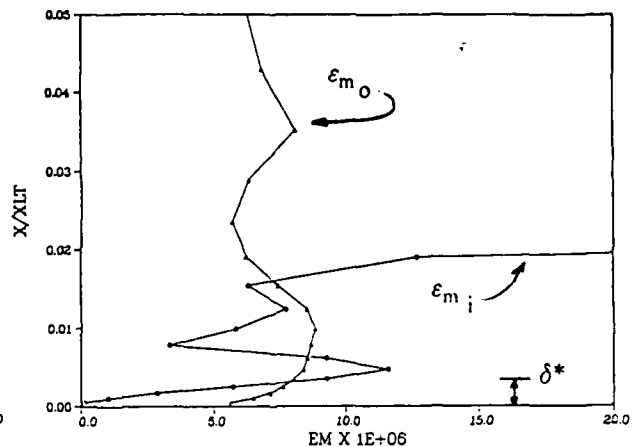
PLOT OF EMI AND EMO 47%NSR SOLUTION (J=20)   PLOT OF EMI AND EMO 47%NSR SOLUTION (J=20)
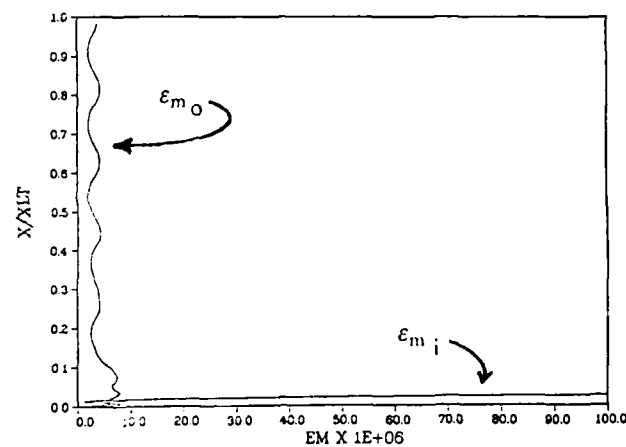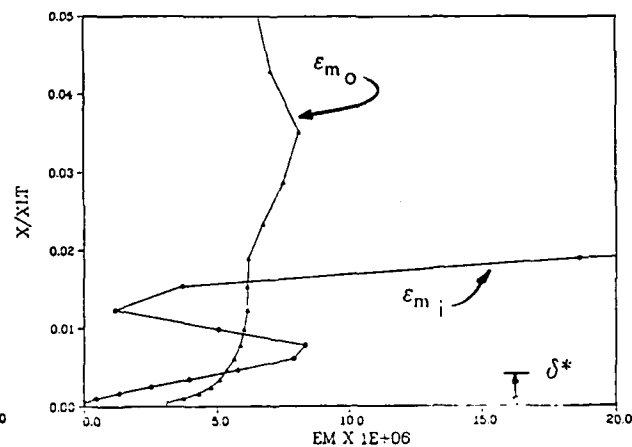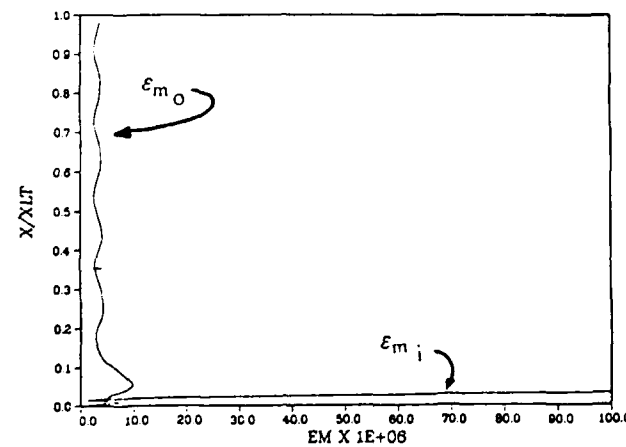
PLOT OF EMI AND EMO 47%NSR SOLUTION (J=30)   PLOT OF EMI AND EMO 47%NSR SOLUTION (J=30)
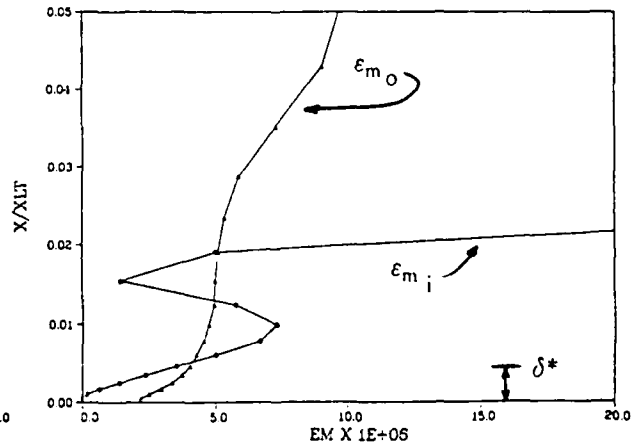
Figure 86 Eddy Viscosity Coefficient Detail, Case 4b Converged
Solution (j=10, 20, 30).

140

PLOT OF EMI AND EMO 47%NSR SOLUTION (J=40)   PLOT OF EMI AND EMO 47%NSR SOLUTION (J=40)
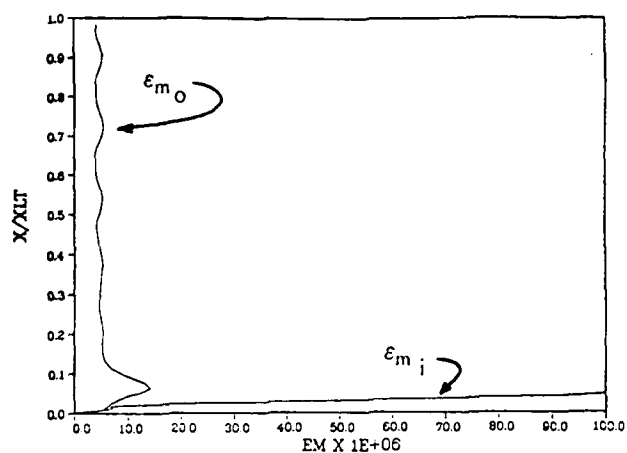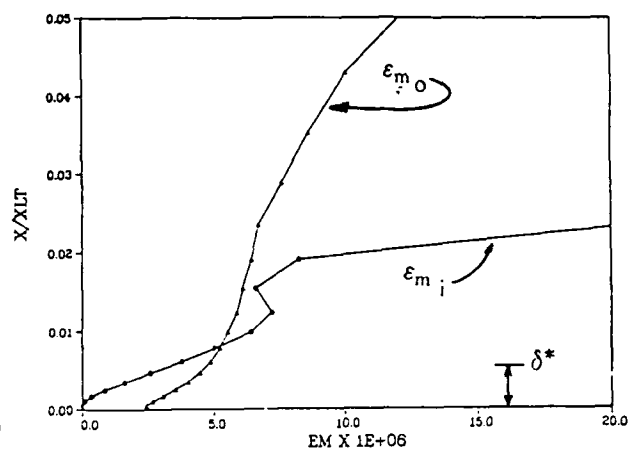
PLOT OF EMI AND EMO 47%NSR SOLUTION (J=50)   PLOT OF EMI AND EMO 47%NSR SOLUTION (J=50)
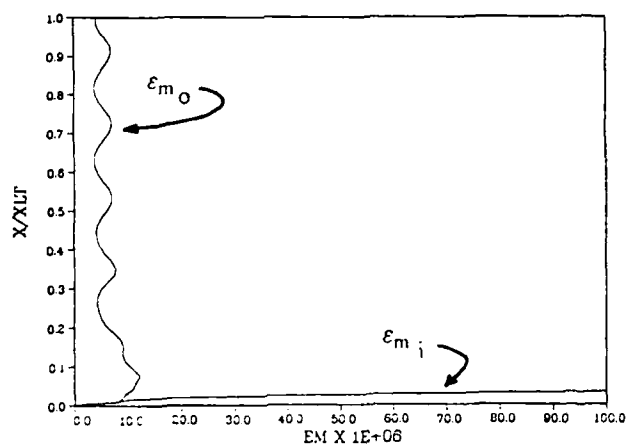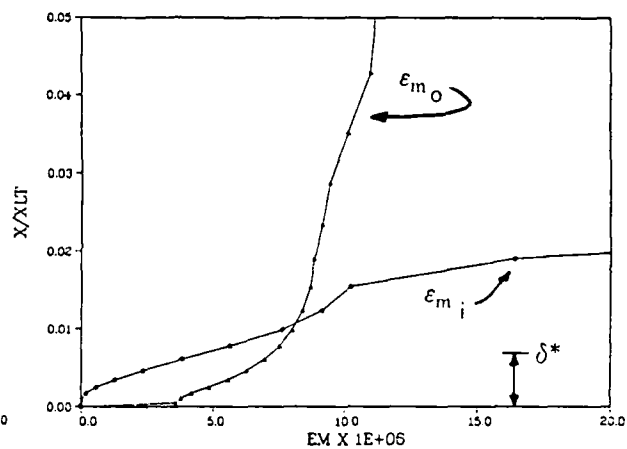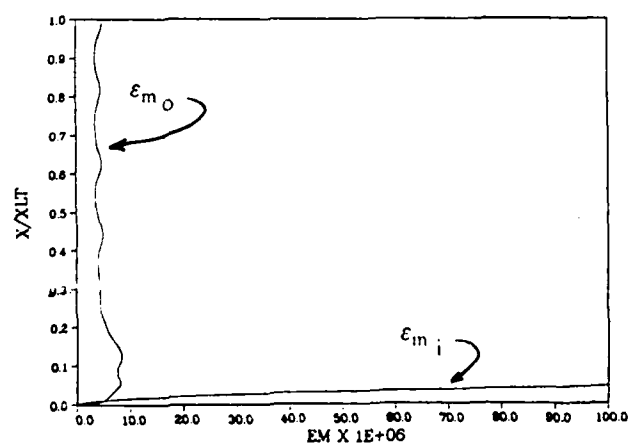
PLOT OF EMI AND EMO 47%NSR SOLUTION (J=60)   PLOT OF EMI AND EMO 47%NSR SOLUTION (J=60)
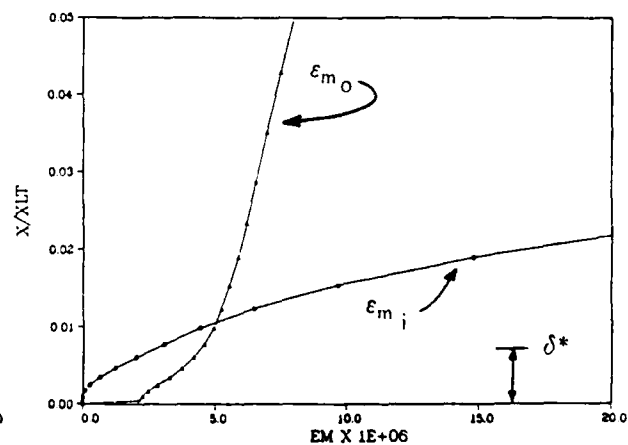
Figure 87. Eddy Viscosity Coefficient Detail, Case 4b Converged
Solution (j=40, 50, 60).

141

PLOT OF EMI AND EMO 47%NSR SOLUTION (J=70)   PLOT OF EMI AND EMO 47%NSR SOLUTION (J=70)
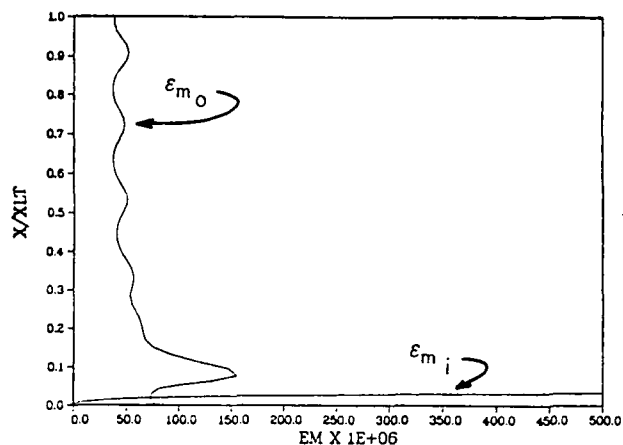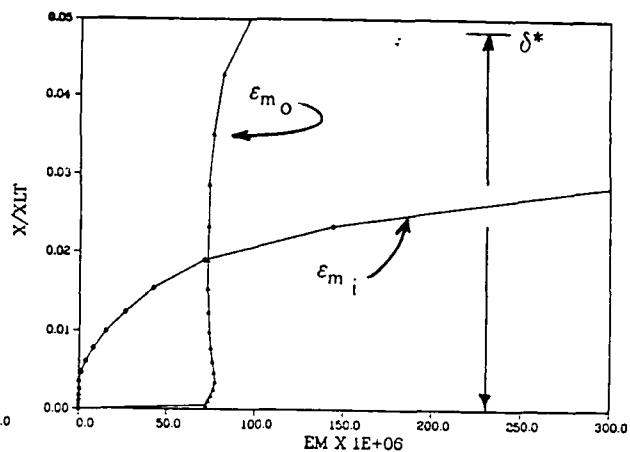
PLOT OF EMI AND EMO 47%NSR SOLUTION (J=75)   PLOT OF EMI AND EMO 47%NSR SOLUTION (J=75)
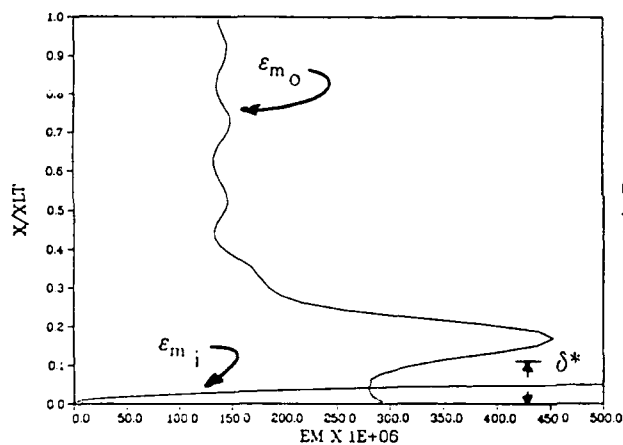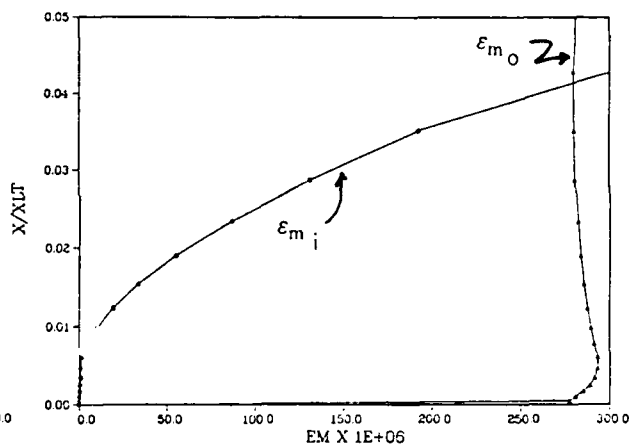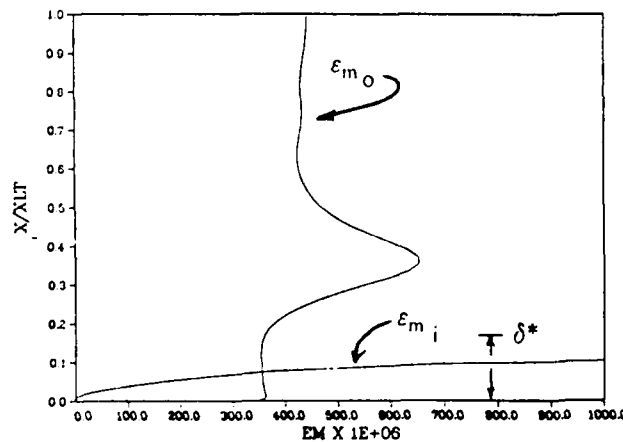
PLOT OF EMI AND EMO 47%NSR SOLUTION (J=80)   PLOT OF EMI AND EMO 47%NSR SOLUTION (J=80)
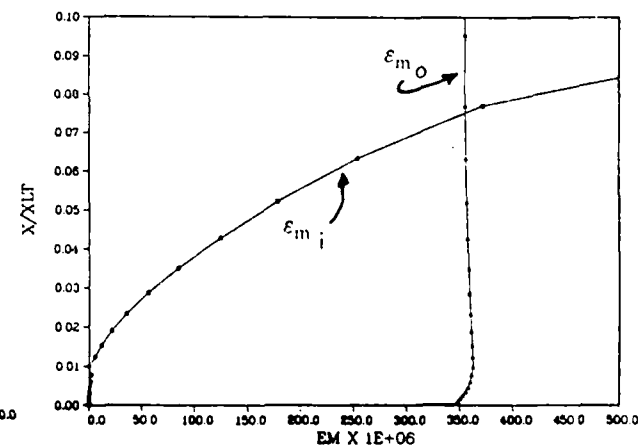
Figure 88. Eddy Viscosity Coefficient Detail, Case 4b Converged
Solution (j=70, 75, 80).

142

PLOT OF EMI AND EMO 47%NSR SOLUTION (J=90)   PLOT CF EMI AND EMO 47%NSR SOLUTION (J=90)
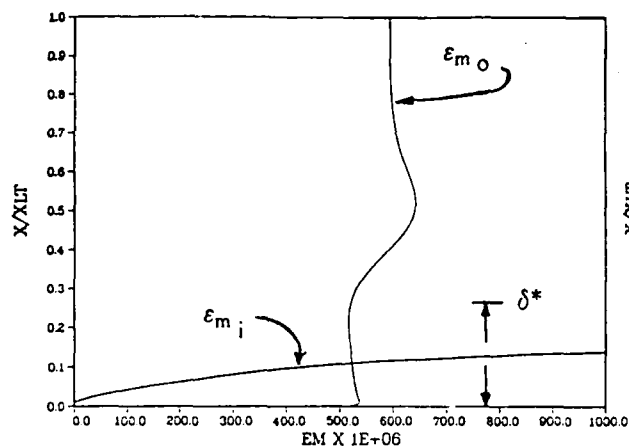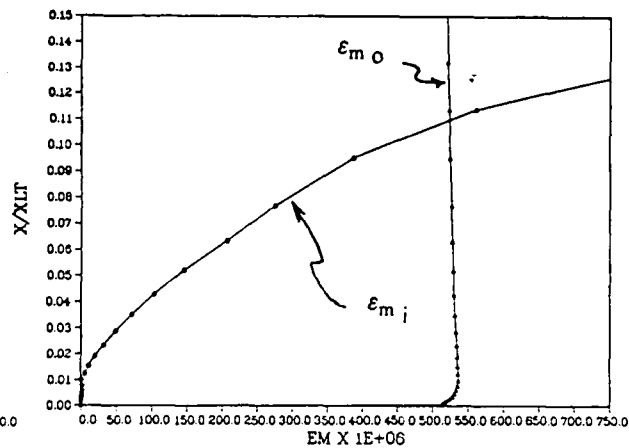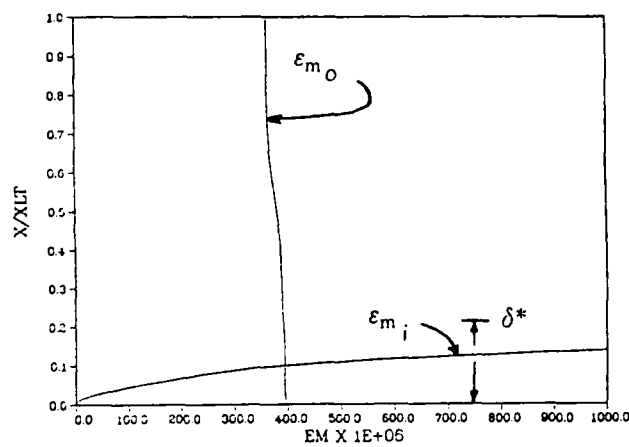
PLOT OF EMI AND EMO 47%NSR SOLUTION (J=100)   PLOT OF EMI AND EMO 47%NSR SOLUTION (J=100)
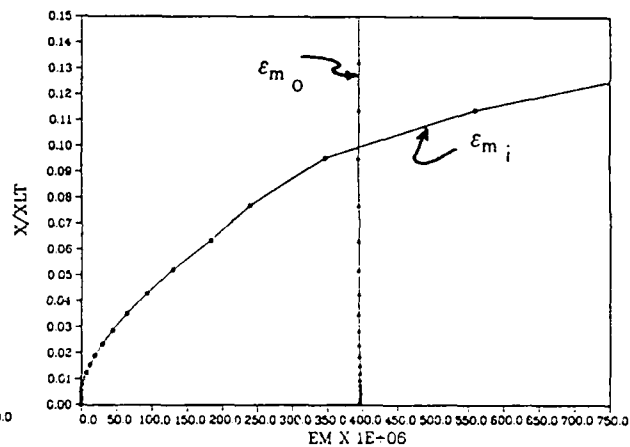
Figure 89. Eddy Viscosity Coefficient Detail, Case 4b Converged
Solution (j=90, 100).

Case 4c

From the 47 percent normal shock recovery (NSR) converged solution as an initial condition, the adverse pressure gradient modification to the conventional Cebeci-Smith eddy viscosity turbulence model was turned off. The numerical solution was then marched forward in time employing the basic Cebeci-Smith model. The diffuser unstarted in slightly more than 2.0 milliseconds. This behavior is shown in Figure 90, and the details of the unstart from the stable, converged solution are provided in Appendix J. This demonstrates conclusively that the adverse pressure gradient modification to the basic Cebeci-Smith eddy viscosity turbulence model is critical to achieve a numerical solution compatible with experimental results.
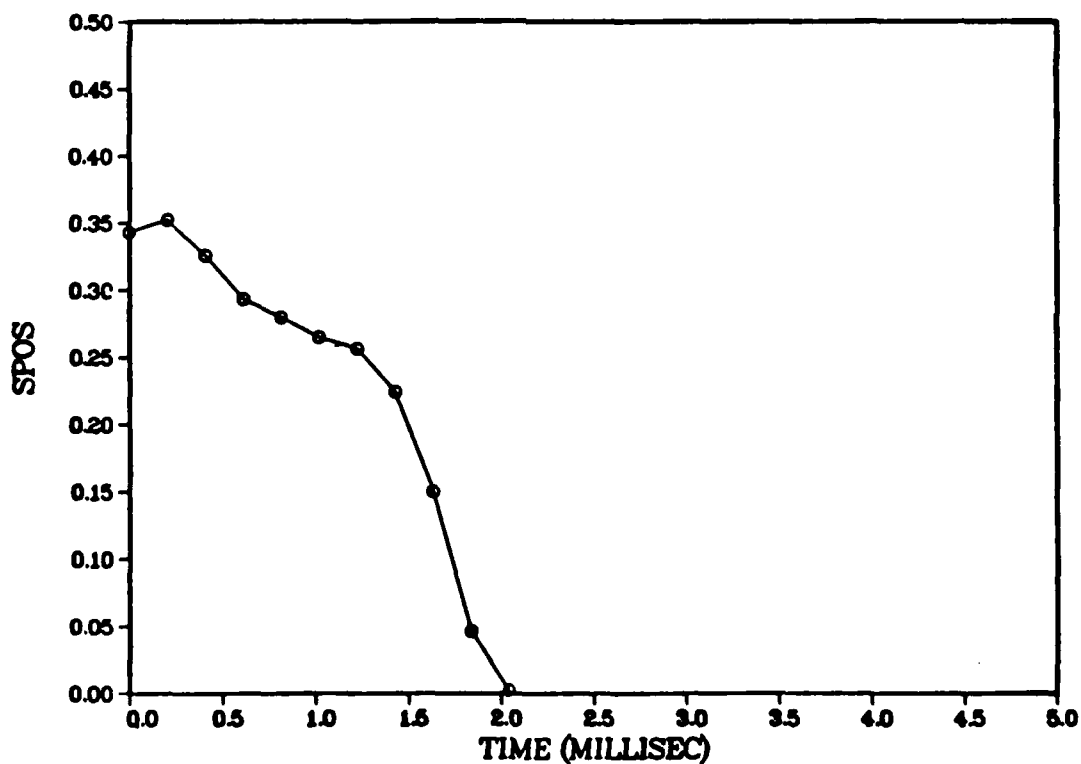
Figure 90. Core Flow Normal Shock Position Time History, Case 4c,

Case 4d

The 47 percent normal shock recovery backpressure case was used as the initial condition for two additional sensitivity analyses of the adverse pressure gradient modification to the basic Cebeci-Smith eddy viscosity turbulence model. For the first of these sensitivity analyses, the value of the von Karman (or universal mixing length) constant k_1 was increased from its nominal (no adverse pressure gradient) value of 0.40 to 0.50 (rather than to 0.65, the value computed by Jobe and Hankey). The immediate response of the sublayer thickness parameter (A^+) from its nominal value of 26 to 65 was retained, as was the change rate of the Clauser constant k_2 that was employed in the adverse pressure gradient modification developed in Chapter V. The numerical solution was marched forward in time from the converged 47 percent NSR case with this modification to the turbulence model. The core flow normal shock is observed to ocillate periodicaly in the diffuser, with shock position varying regularly from 25 percent to 42 percent of the diffuser length, but the diffuser did not unstart. Figure 91 presents the time history of these computations, with details presented in Appendix K.

The von Karman constant, k_1, strongly influences the mixing length (eqn. 5-2) in the sublayer model. For the situation postulated, the mixing length is only 77 percent of its' value computed using the higher value for k_1. This results in an inner region eddy viscosity coefficient only 60 percent as large. With a smaller inner region eddy viscosity, the flow along the diffuser wall is more susceptable to early separation. The crossover point for transition to the outer region model is also lowered.

The net effect is initially an overall lower value for the eddy viscosity, which allows the separation region to grow overly large. This leads to the calculation of a much larger displacement thickness δ^*, which in turn drives the outer region eddy viscosity to a much higher value and then over - suppresses the recirculation region. This interaction between the inner and outer region eddy viscosities results in a complex temporal behavior of separation and overcorrection.
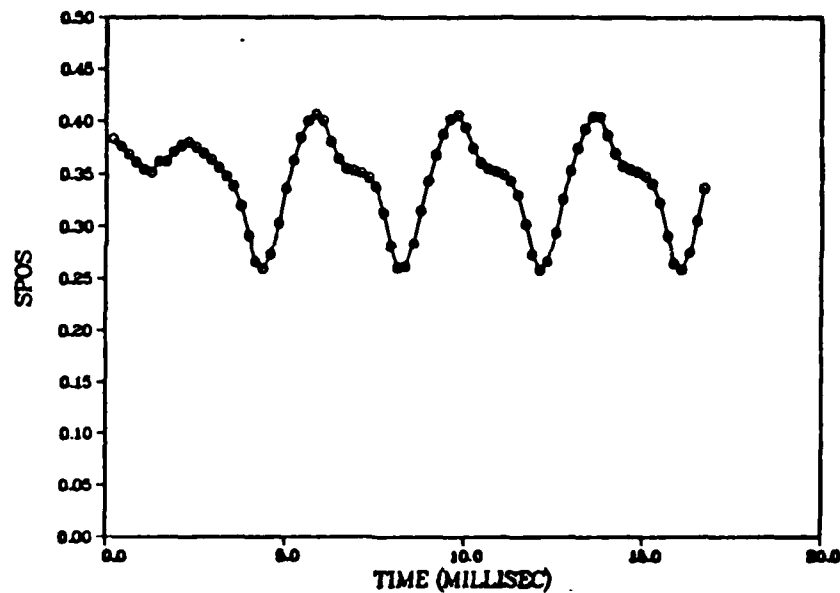
Figure 90. Core Flow Normal Shock Position Time History, Case 4c, (Actual Inflow, 47% NSR, wbb = .195, Basic Cebeci-Smith Turbulence Model.

Case 4e

The second sensitivity analysis of the adverse pressure gradient modification to the basic Cebeci-Smith eddy viscosity turbulence model was accomplished by employing the full inner region modifications, but relaxing the change rate of the outer region (Clauser) constant k_2 from 0.015 to 0.010. The solution was again marched forward in time from the 47 percent NSR converged solution, and again the core flow normal shock is observed to oscillate periodically from 21 percent to 41 percent of the diffuser duct length without the diffuser unstarting. Figure 92 presents the time history of these computations, and Appendix L provides the details.

In this situation, the inner region model is the same as that described for the overall "stiffened" eddy viscosity model presented in Chapter V. Only the outer region model is mathematically affected through the lower value of the Clauser constant, k_2, in equation 5-3. Although the calculated inner region eddy viscosity remains the same, the crossover point for transition to the outer region is again lowered and the net effect is a boundary layer more susceptable to separation. As discussed in the last section, separation region growth results in the calculation of a much larger displacement thickness which in turn drives the outer region eddy viscosity to a higher value. Again, this interaction between the inner and outer region eddy viscosities results in a complex temporal behavior of separation and overcorrection.
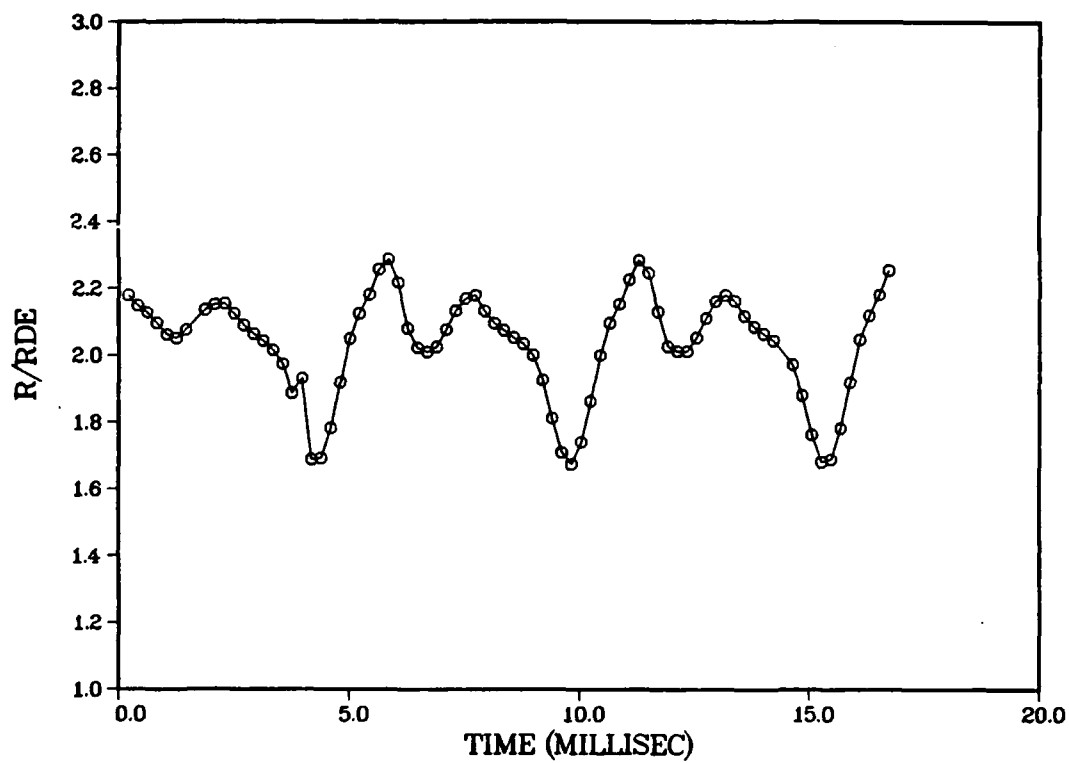
Figure 91. Core Flow Normal Shock Position Time History, Case 4d, (Actual Inflow, 47% NSR, wbb — .195, Inner Region Turbulence Model Variation.

6.3 COMPARISON WITH EXPERIMENTAL DATA

Comparisons between the numerical solutions and the experimental data can be made both qualitatively and quantitatively. Figure 93 summarizes the numerical results for both the 47 percent and 60 percent normal shock recovery cases. The location of the normal shock at the diffuser line of symmetry obtained from the numerical solution falls within the error bands of the shock positions determined from the UTRC experimental Schlieren photographs (13). The Mach contour plots (Figures 94 and 96 generated from the numerical solutions also compare well qualitatively with the respective Schlieren photographs (Figures 95 and 97). Qualitative flow feature comparisons worthy of note include location and size of the wall separation regions, which are reasonably well reproduced in the numerical solution. Persistence of the source nozzle flow interactions through several streamwise turnback shocks is also apparent in both the experimental Schlieren photographs and the Mach contour plots of the numerical solution. Table III summarizes the comparison between the computed normal shock positions and the UTRC experimental results.

The asymmetric behavior of the barrel shock in the UTRC experimental data is also to be noted, suggesting nonuniformities in the source nozzles and bank blowers. Figure 17, presenting the diffuser entrance flowfield conditions from the data of Zumpano, et al. (13), does imply asymmetric performance of the source nozzle and wall bank blower apparatus, especially in the total pressure profile (p_p). The Schlieren photographs also present barrel shocks that are convex with respect to the source flow. The numerical solution Mach contours, especially that for the 60 percent NSR case, present barrel shocks that are concave with respect to the source

flow. This may be attributable to the application of the turbulence model in the core flow region, where the approximation employed a mixing length based on δ^* to compute the eddy viscosity. Immediately downstream of the barrel shock this mixing length is artificially large due to the size of the separation region along the diffuser wall.

There are several physical aspects of the experimental apparatus that are not reproduced in the numerical simulation. The computational domain begins one grid point upstream of the diffuser entrance, so the effect of the simulated optical ducts is neglected. Other small physical hardware aspects, such as non-smooth wall junctions, can have a significant effect on the behavior of the wall boundary layer flow, and these are not reproduced in the numerical solution.
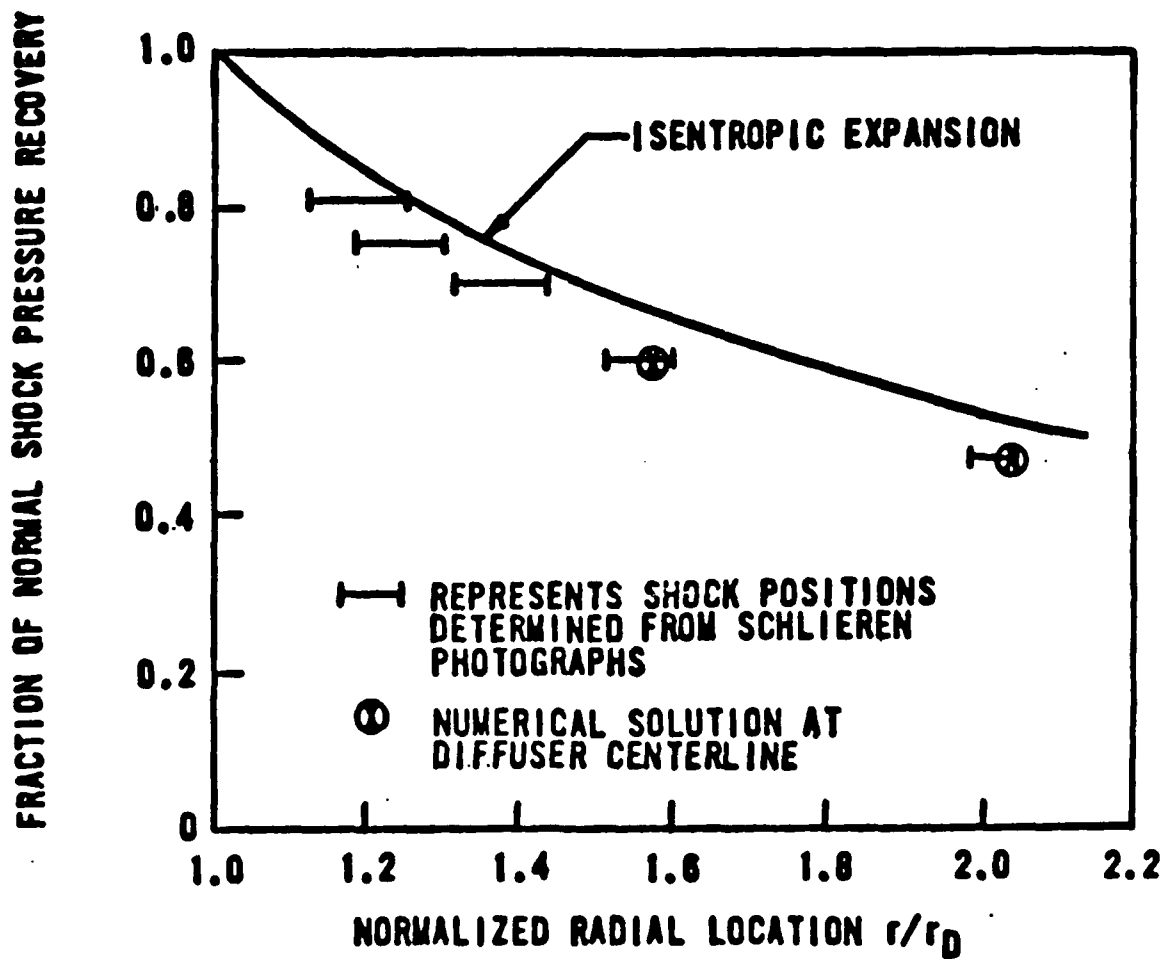
Figure 92. Core Flow Normal Shock Position Time History, Case 4e,
(Actual Inflow, 47% NSR, wbb = .195, Outer Region
Turbulence Model Variation.

TABLE III

COMPARISON OF COMPUTED SHOCK POSITIONS

Exit Pressure	Isentropic Expansion to Normal Shock	Uniform Inflow @ M = 2.5 Uniform Wall B.B. @ M = 4.0	Long Duct No B.B. M_i = 2.5	Actual Inflow Case M_i = 2.50
60% NSR	SPOS = .254	SPOS = .239	SPOS = .156	SPOS = .194
	R/Rde = 1.78	R/Rde = 1.73	R/Rde = 1.48	R/Rde = 1.59
47% NSR	SPOS = .455	SPOS = .407	SPOS = .322	SPOS = .343
	R/Rde = 2.40	R/Rde = 2.25	R/Rde = 1.99	R/Rde = 2.05

Figure 94. Converged Numerical
Solution Mach Contours,
Actual Inflow, 60%NSR.

$P_e/\bar{P}_{P_D} = 0.60$
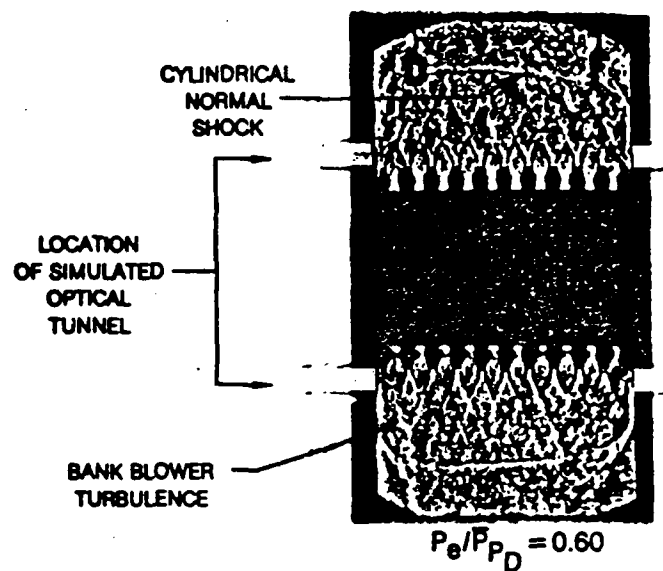
Figure 95. Schlieren Photograph,
60%NSR.
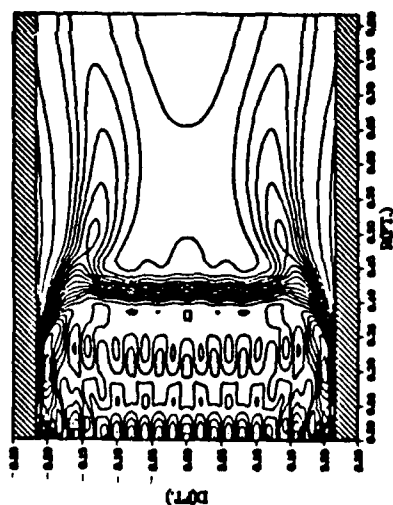
Figure 96. Converged Numerical
Solution Mach Contours,
Actual Inflow, 47%NSR.

$P_e/\bar{P}_{P_D} \approx 0.47$
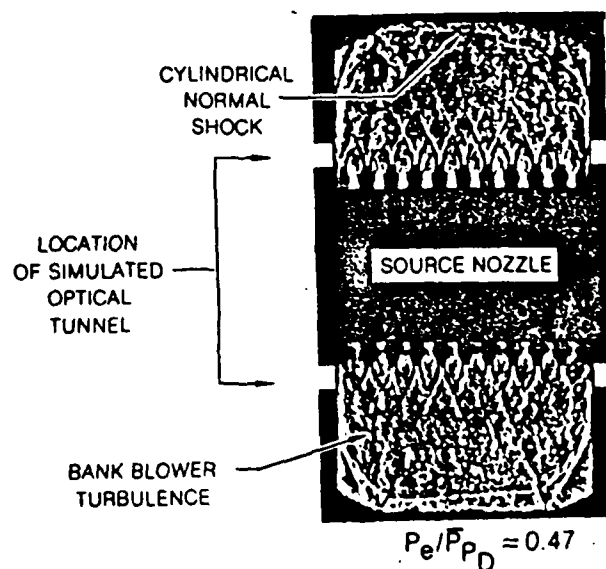
Figure 97. Schlieren Photograph,
47%NSR.

153

When the numerical result based on the actual inflow conditions is compared with that obtained from the ideal inflow conditions, the effects of viscous losses due to the mixing of the source nozzle inflows are apparent for both numerical cases (60 percent NSR and 47 percent NSR). For the 60 percent normal shock recovery exit pressure case the actual inflow numerical solution obtains the core flow normal shock at 0.194 of the diffuser length, while the ideal inflow numerical solution obtains the core flow normal shock at 0.239 of the diffuser length. The additional viscous losses due to viscous dissipation and shear layer mixing result in the core flow normal shock 19 percent farther upstream than in the "ideal" inflow case. For the 47 percent normal shock recovery exit pressure cases, the actual inflow numerical solution obtains the core flow normal shock at 0.343 of the diffuser length, while that for the ideal inflow case occurs at 0.407 of the diffuser length. For this numerical case the additional viscous losses due to mixing cause the core flow normal shock to occur 16 percent farther upstream than for the "ideal" case. Both numerical solutions are also shown to be significantly upstream of the inviscid normal shock predictions for the same inflow Mach number (Table III).

Comparison of the numerical results with experimentally obtained wall pressure data is accomplished in Figures 98 through 100. Figure 98 presents the UTRC experimentally obtained wall pressure data (13). Both diffuser walls were instrumented with static pressure taps. Because of the construction of the test apparatus, one of the diffuser wall was designated as the fixed side and the other was designated as the operator side. Examination of these plots of experimental wall pressure data yields two interesting observations; first, that the overshoot behavior of wall pressure obtained computationally does occur in many, but not all, of the
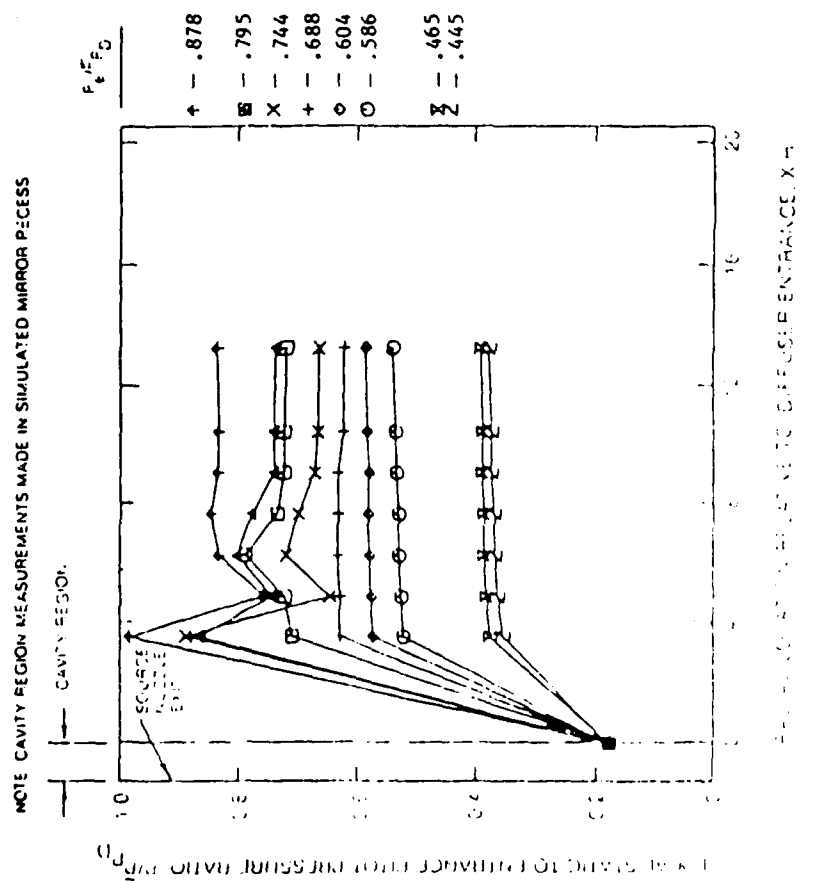
154

Figure 98. Experimental Wall Pressure Data (Ref. 13).

experimental cases; and second, that the wall pressure data obtained experimentally is inconsistent across the two diffuser walls. For this reason, both sets of experimental wall pressure data are plotted in Figures 99 and 100 for comparison with the information obtained in the numerical experiments. In Figure 99, the wall pressure data obtained in case 4a, 60 percent normal shock recovery exit pressure, is compared with the appropriate wall pressure data from experiment (from Figure 98). Serious divergence of the numerically obtained values is evident only in the region of the wall separation caused by the shock impingement on the boundary layer, where the numerical model is known to poorly reproduce the physics of the flowfield locally. The numerical prediction shows good agreement with the operator end wall experimental data and both sets of experimental data bound the numerical prediction downstream of the shock. No static pressure taps were located in the 5 to 15 percent range of the diffuser wall length, so comparison in this region cannot be accurately made.

The numerically predicted wall pressure behavior for the 47 percent normal shock recovery exit pressure case (case 4b) is compared to the experimental data in Figure 100. Again, the only significant divergence is apparent in the shock/boundary layer interaction region. The experimental data again bounds the numerical prediction. The numerically obtained wall pressure distribution is therefore observed to (1) overpredict the distance for shock recovery (i. e., a longer mixing region), but (2) reasonably predicts the recovery pressure from just downstream of the barrel shock to the end of the diffuser. Generalized diffuser performance, in terms of barrel shock location and final recovery pressure, is reasonably reproduced.
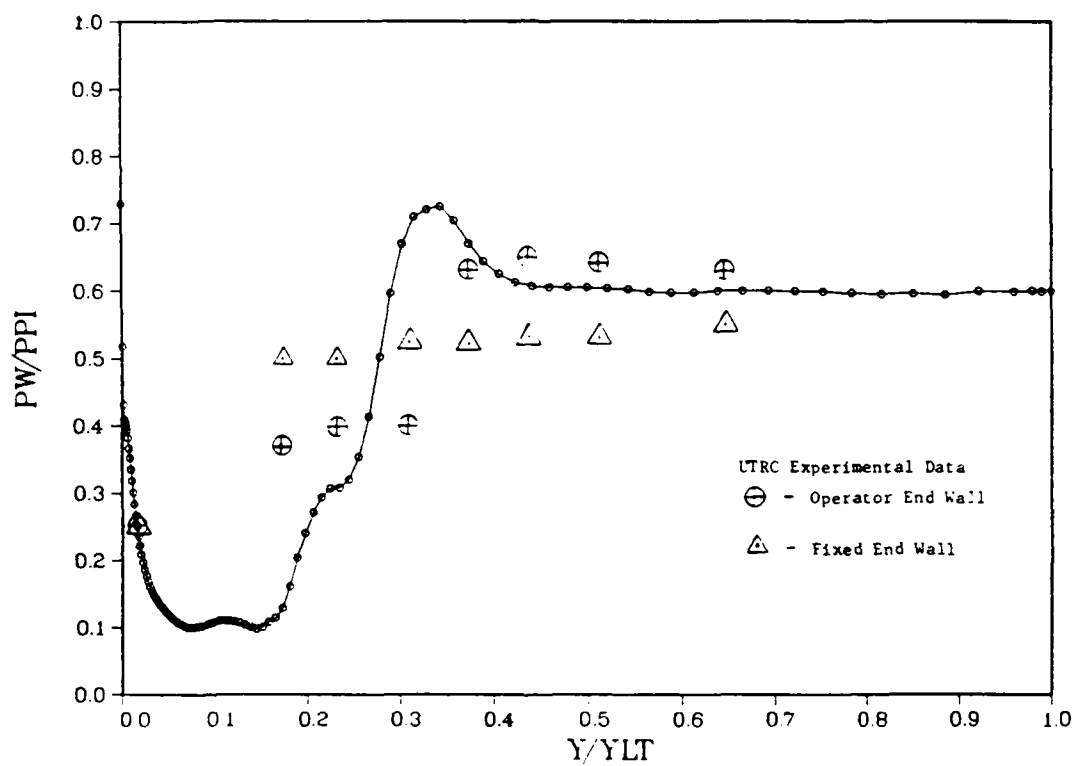
Figure 99. Comparison of Numerical With Experimental Wall
Pressure Data, Case 4a (60% NSR, Actual Inflow).
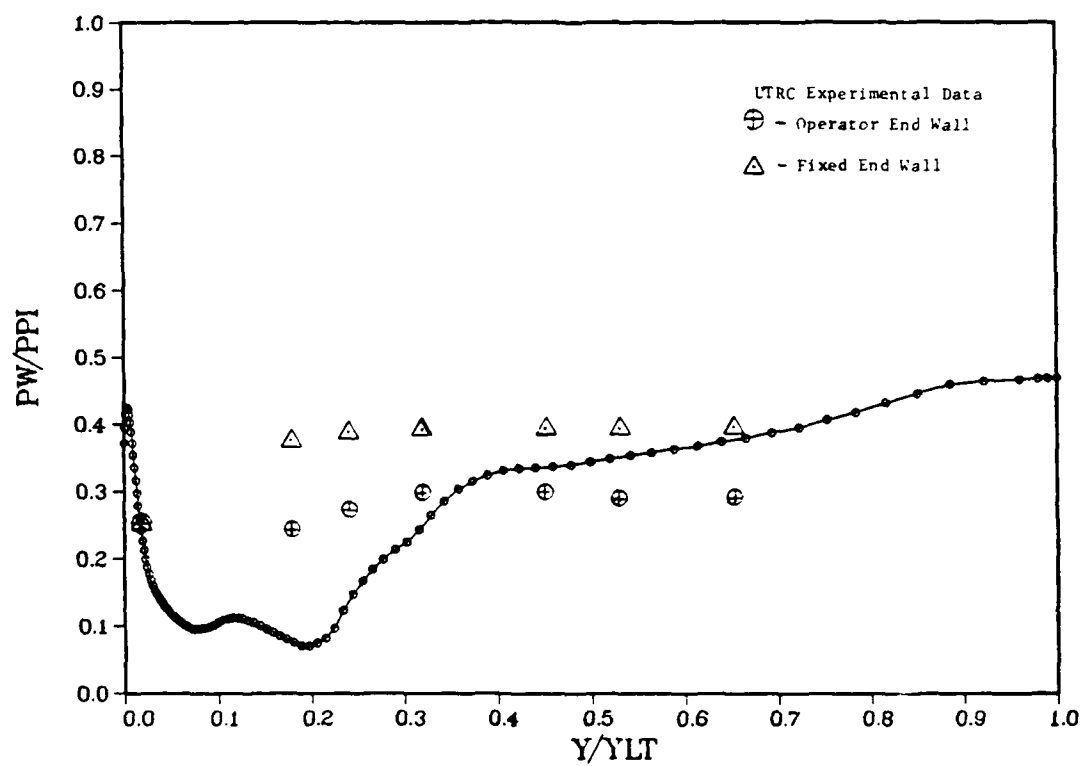
Figure 100. Comparison of Numerical With Experimental Wall
Pressure Data, Case 4b (47% NSR, Actual Inflow).

Higher diffuser performance (recoveries above 60 percent NSR) cases were not attempted. Considerations included cost of computer time, as each of the actual flow cases attempted took over twenty hours of Cray I processing time to resolve to a steady state solution. The 60 percent normal shock recovery backpressure case was initially selected as the baseline validating case because it exhibited the critical issues requiring examination: core flow dissipation due to source nozzle mixing, shock/wall boundary-layer interactions, and the behavior of a separation recirculation region immediately downstream of the barrel shock. The 47 percent normal shock recovery backpressure case, while less stressing on physical diffuser performance, is more stressing on the computational approach, because it provides a much larger separation/recirculation region and the attendant issues which therefore affect the calculation of the displacement thickness and the outer region eddy viscosity.

The approach demonstrated in this effort, based on modification of the eddy viscosity turbulence model, has achieved a reasonable prediction of diffuser performance, especially barrel shock location. This is a significant improvement over the results obtained by previous investigators, such as Johnson, Horstman, and Bachalo (74), who reported "the relatively poor predictions of shock locations obtained were due to the inadequacies in the immediate vicinity of the shock of the turbulence closure models used."

6.4 EDDY VISCOSITY TURBULENCE MODEL BEHAVIOR

Comparison was made of the relative behavior of the adverse pressure gradient modified Cebeci-Smith turbulence model to the basic, unmodified Cebeci-Smith model for the four primary computational cases; 60 percent normal shock recovery exit pressure and 47 percent normal shock recovery exit pressure for both the actual and ideal inflow conditions. These comparisons are presented in Figures 101 through 104 as plots of the ratio of the "modified" eddy viscosity coefficients to the "basic" eddy viscosity coefficients at various streamwise positions through the length of the diffuser. In all cases upstream of the lambda shock impingement point the ratio is unity as expected, for the modification employed only "turns on" after sensing the onset of an adverse pressure gradient along the diffuser wall. Along the i = 10 streamwise location (within the laminar sublayer region) the modified eddy viscosity coefficient is observed to first decrease before increasing above the basic eddy viscosity coefficient. This is attributable to the implications of the immediate response of the von Karman constant (k_1) and the Van Driest sublayer thickness parameter (A^+), which together comprise major determinants of the inner region mixing length (equation 5-2). At the same distance normal to the wall, for the same flow physical coefficient of viscosity μ, and the same shear stress at the wall τ_w, the imposition of the immediate changes to k_1 and A^+ result in a decrease in the calculated mixing length. This, coupled with a probable deerease in the tangential velocity parallel to the wall surface due to the adverse pressure gradient, results initially in a decrease in the inner eddy viscosity coefficient.

Once above the laminar sublayer and into the region where the outer region eddy viscosity based on the Clauser model is applied, all four numerical cases (Figures 101 through 104) show the effect of the lagging response (as discussed in Jobe and Hankey's research (67)) to the imposition of the adverse pressure gradient. Here the effect of the overshoot in the computed wall pressure is also notable, the behavior of ϵ_o naturally follows this higher wall pressure prediction before relaxing to its' downstream value. This behavior is not observed for the 47 percent NSR actual inflow case where the overshoot in wall pressure is not numerically obtained.

No correlation of the values of k_1, A^+, and k_2 with the intrinsic physical properties of the flow has been achieved. The experimental research necessary to obtain such a correlation is beyond the scope of this effort.

Figure 101.

MODIFIED/BASIC EDDY VISCOSITY RATIO 60%NSR A.F.
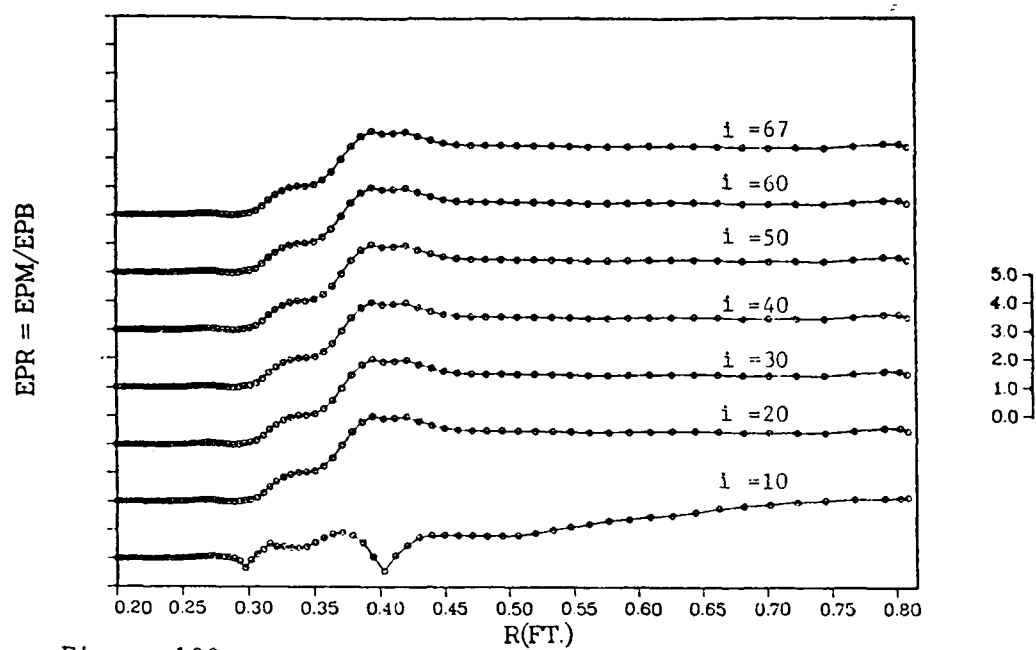
Figure 102.

MODIFIED/BASIC EDDY VISCOSITY RATIO 60%NSR I.F.
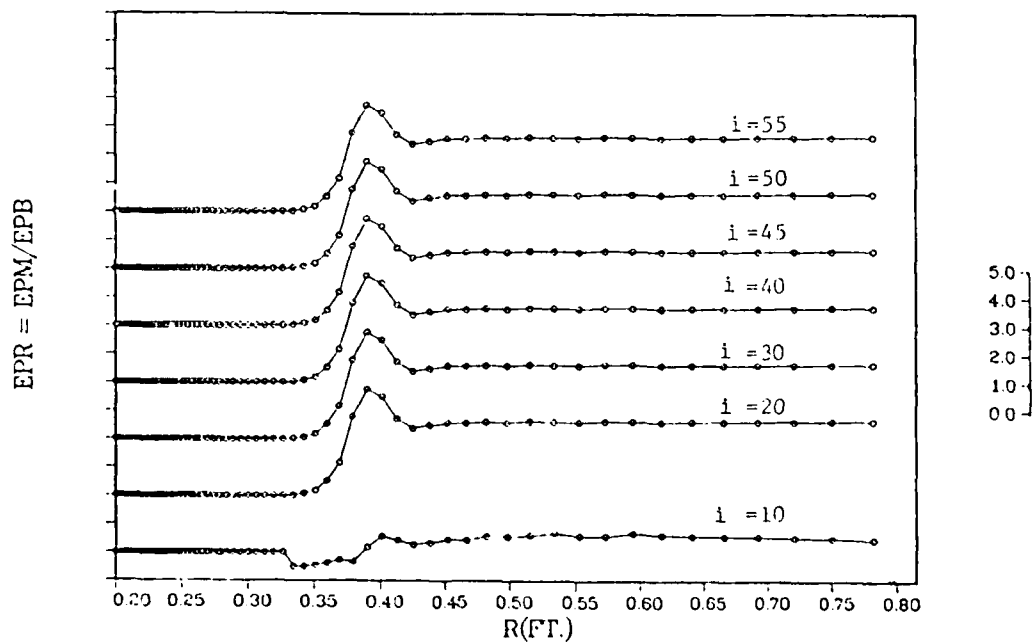
Figure 103.

MODIFIED/BASIC EDDY VISCOSITY RATIO 47%NSR A.F.
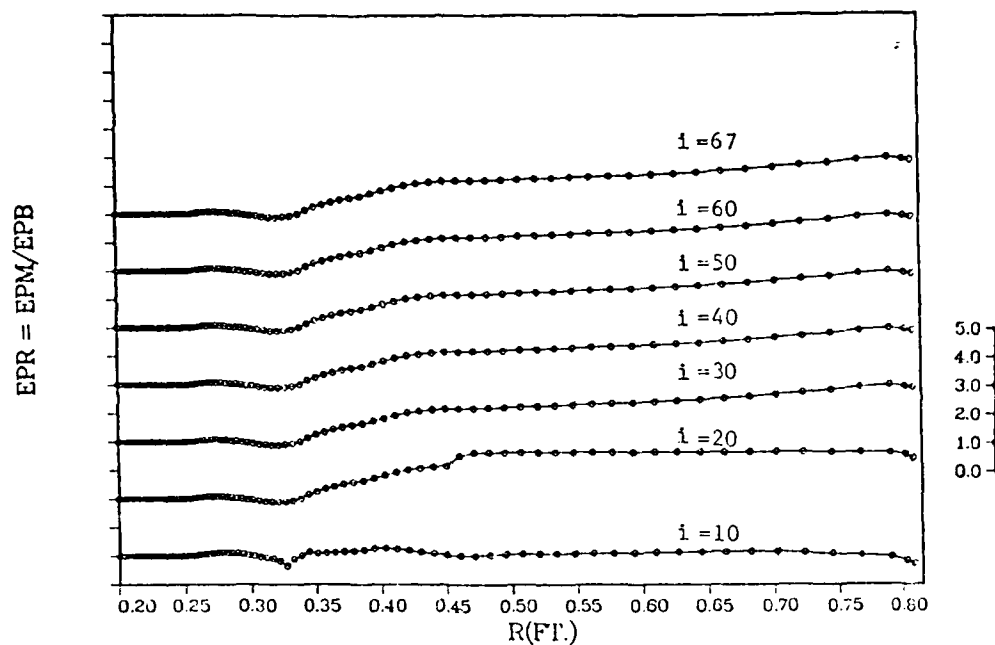
Figure 104.

MODIFIED/BASIC EDDY VISCOSITY RATIO 47%NSR I.F.
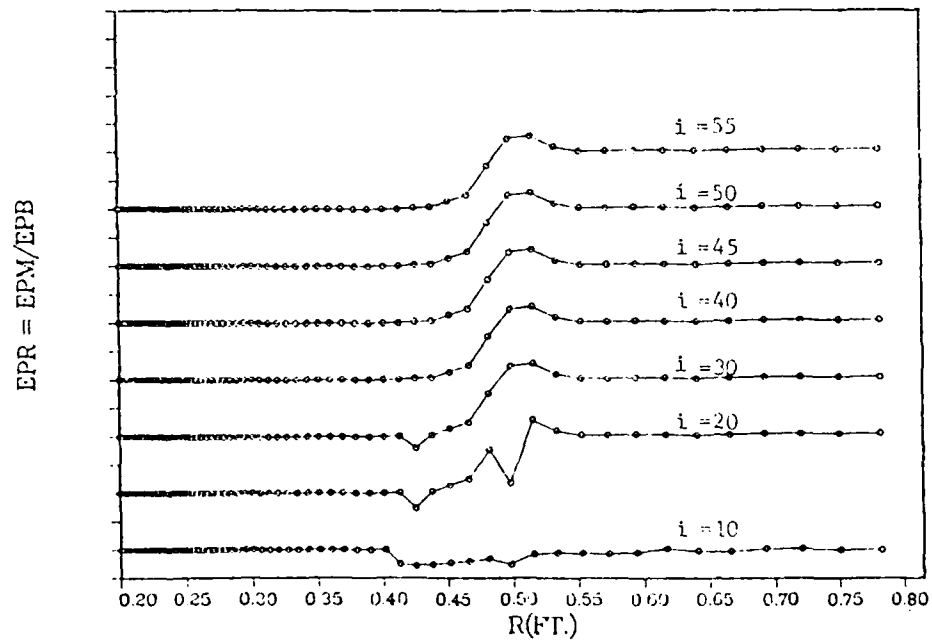
6.5 INVESTIGATION OF NUMERICAL ERROR

Two approaches were employed to evaluate the numerical error present in the computational solutions for the supersonic diffuser. The first consisted of a classic Richardson's extrapolation technique (40), where the solution is acquired by using more clustered (or stretched) grid elements, especially near the wall. The second was a study of the effect of numerical damping, performed by comparing the artificial viscosity (introduced by the smoothing terms in MacCormack's algorithm) with the modelled eddy viscosity $\mu+\epsilon$. This approach was first presented by Visbal (54) and provides useful additional insight into the nature of the numerical solutions.

Richardson's extrapolation technique

This technique was first applied to the 60 percent normal shock recovery exit pressure ideal inflow solution (case 2b). The original exponentially stretched 30X80 numerical grid was replaced with a 60X80 grid grid, where the spacing between the grid points in the direction normal to the wall was half that of the original grid. A third test grid, 90X80 points, was later employed, where the spacing between the grid points normal to the wall was one-third that of the original grid. Details of these grids are presented in Appendix M. The steady converged solution obtained for the 30X80 grid was mapped onto the two new grids and the numerical solution was marched forward in time by five additional characteristic times. The results for the ideal inflow cases are presented in Figures 105 and 106. No change in the steady solution core flow normal shock position occurred. The variation in wall pressures obtained from the solutions on these three different test grids is negligible, as seen in Figure 106.

The Richardson technique was then applied to the 60 percent normal shock recovery exit pressure actual inflow solution (case 4a). The original

164

70X103 grid was replaced with a 140X103 grid where the spacing between the grid points normal to the wall was half that of the basic grid. For the 70X103 grid, Δx_{min} = 0.0001 ft. (the spacing for the first grid point away from the wall; i = 1). For the 140X103 grid, Δx_{min} = 0.00005 ft. Details of both these grids are provided in Appendix M. The steady converged solution obtained for the 70X103 grid was mapped onto the new 140X103 grid and the numerical algorithm was marched forward in time by an additional five characteristic times until virtually no variation in flowfield conditions was observed. The results of this approach are presented in Figures 107 and 108. Again, as for the ideal inflow case, no change in the core flow normal shock position is obtained. The denser grid shows a slightly higher overshoot in the wall pressure response in the shock impingement region, shown in Figure 108a. Figure 108b presents the wall pressure ratio obtained through the Richardson's extrapolation. Appendix N presents the details of the extrapolation technique for selected streamwise locations in the physical domain. The Richardson's extrapolation technique thus shows very little change in the numerically obtained solutions for these cases and grid refinements. Therefore, the truncation error is demonstrated not to be attributable to grid refinement. The problem is then contained only in the physical description of turbulence and in the numerical smoothing required to maintain numerical stability.

MACH CONTOURS 60%NSR 30X80 GRID SOLUTION
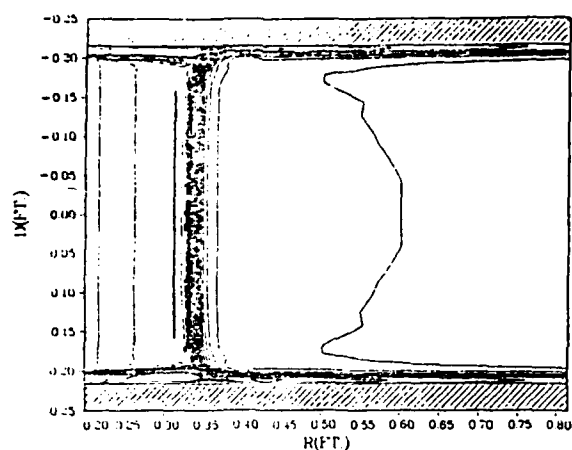
WALL PR RATIO 60%NSR 30X80 GRID SOLUTION
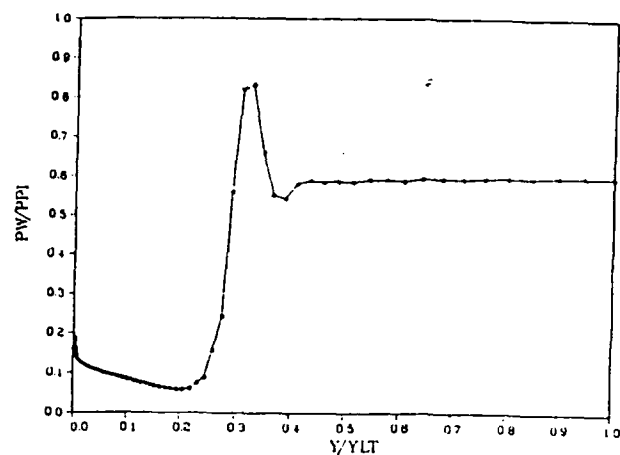
MACH CONTOURS 60%NSR 60X80 GRID SOLUTION
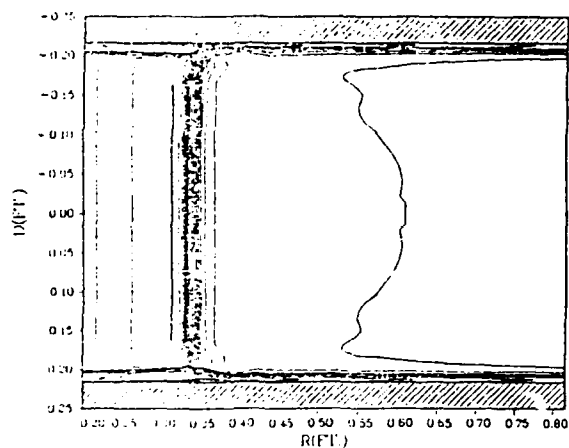
WALL PR RATIO 60%NSR 60X80 GRID SOLUTION
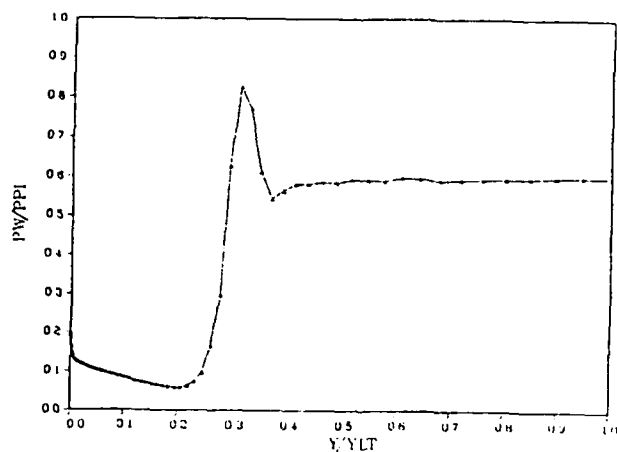
MACH CONTOURS 60%NSR 90X80 GRID SOLUTION
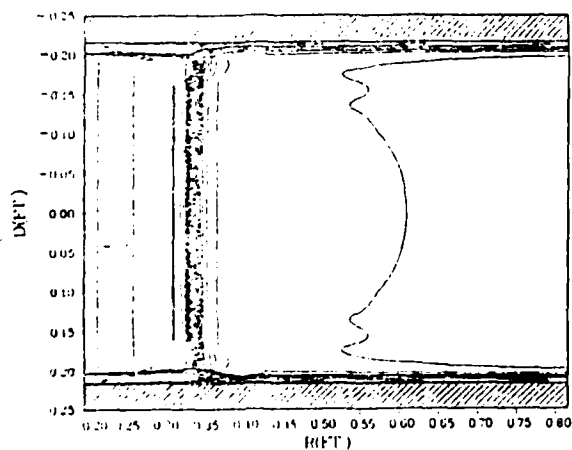
WALL PR RATIO 60%NSR 90X80 GRID SOLUTION
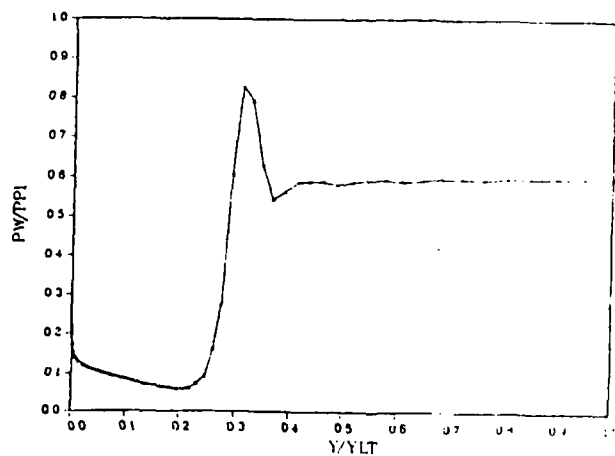
Figure 105. Comparison of Numerical Mach Contour and Wall
Pressure Solutions, 60% NSR Ideal Inflow Solution.

166

WALL PR RATIOS 60%NSR 3 TEST GRIDS
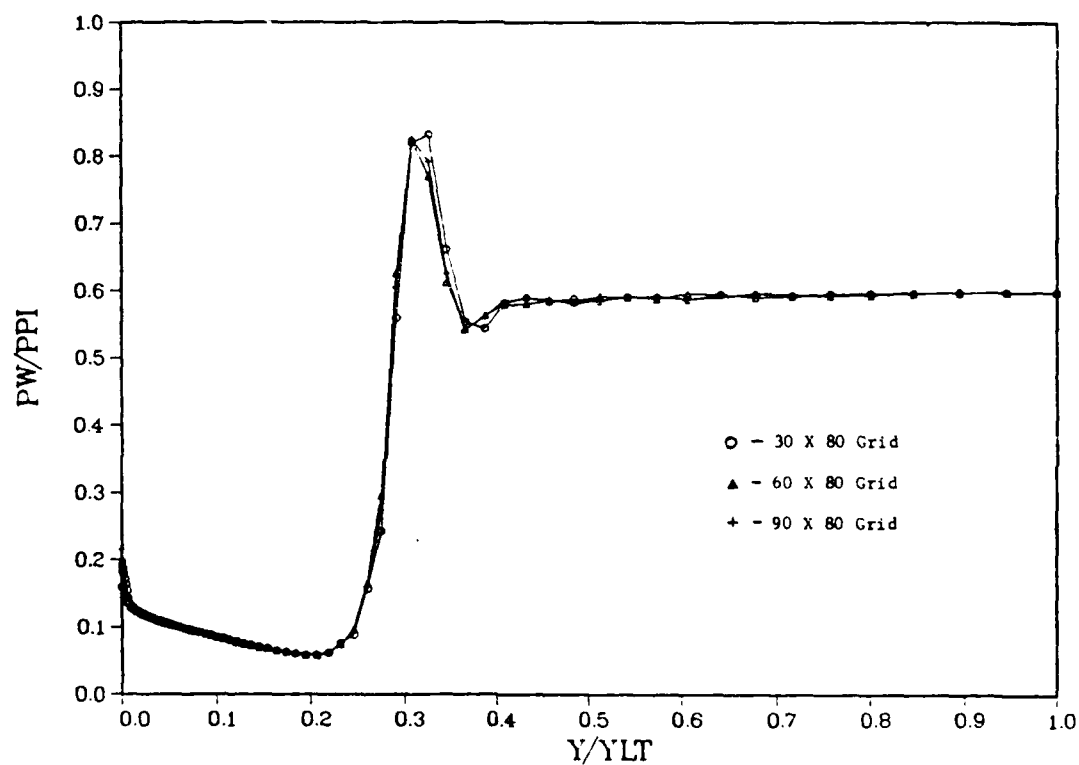
Figure 106. Comparison of Computed Wall Pressure Ratio; 3 Test
Grids, 60% NSR Ideal Inflow Solution.

167

MACH CONTOURS 60%NSR 70X103 GRID SOLUTION
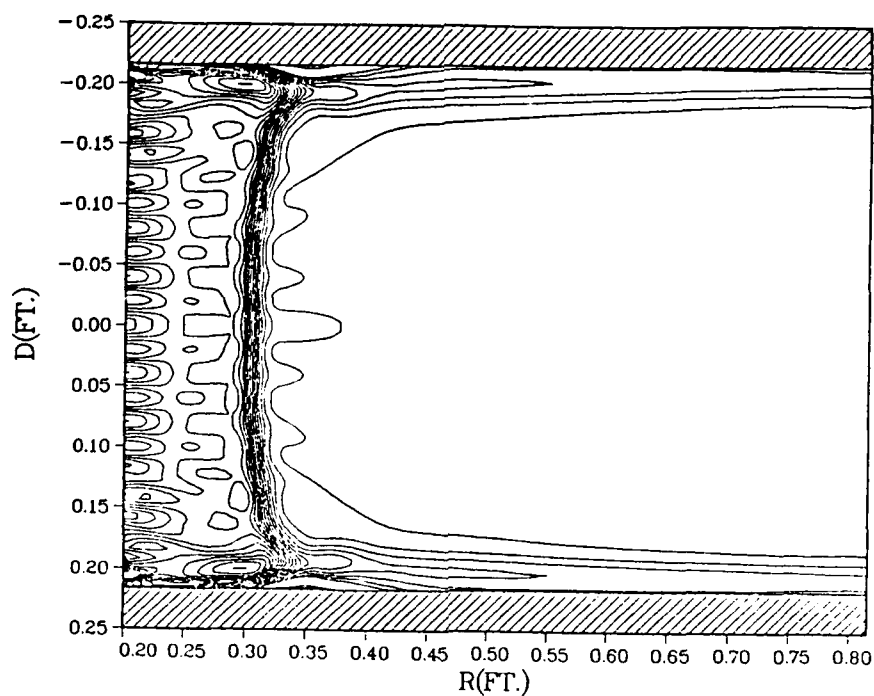
MACH CONTOURS 140X103 GRID 60%NSR A.f. SOLUTION
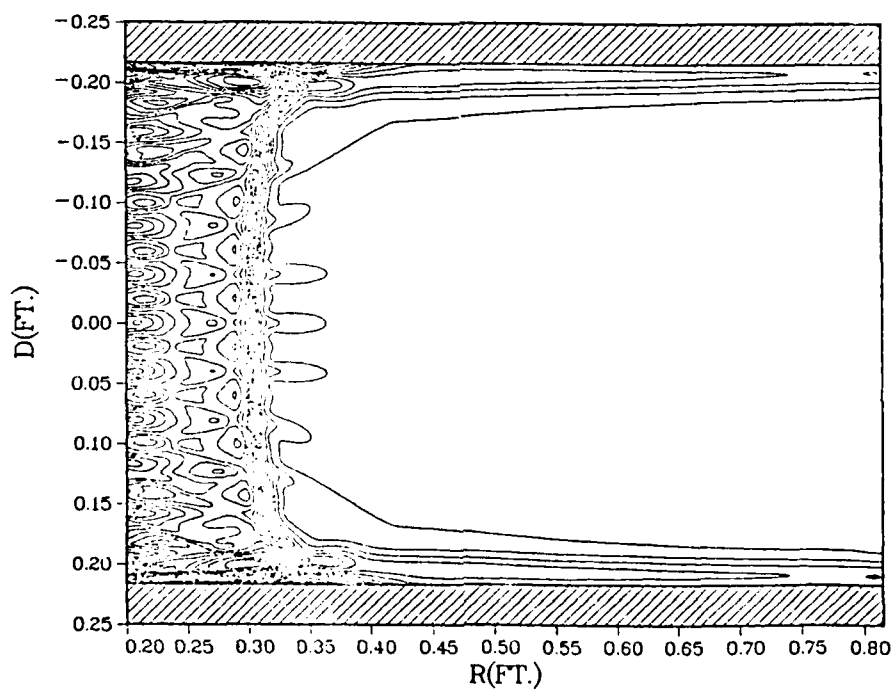
Figure 107. Comparison of Mach Contours, 60% NSR Actual Inflow
Case; Numerical Solutions for 70X103 and 140X103
Grids.

WALL PR RATIO COMPARISON 60%NSR ACTUAL FLOW
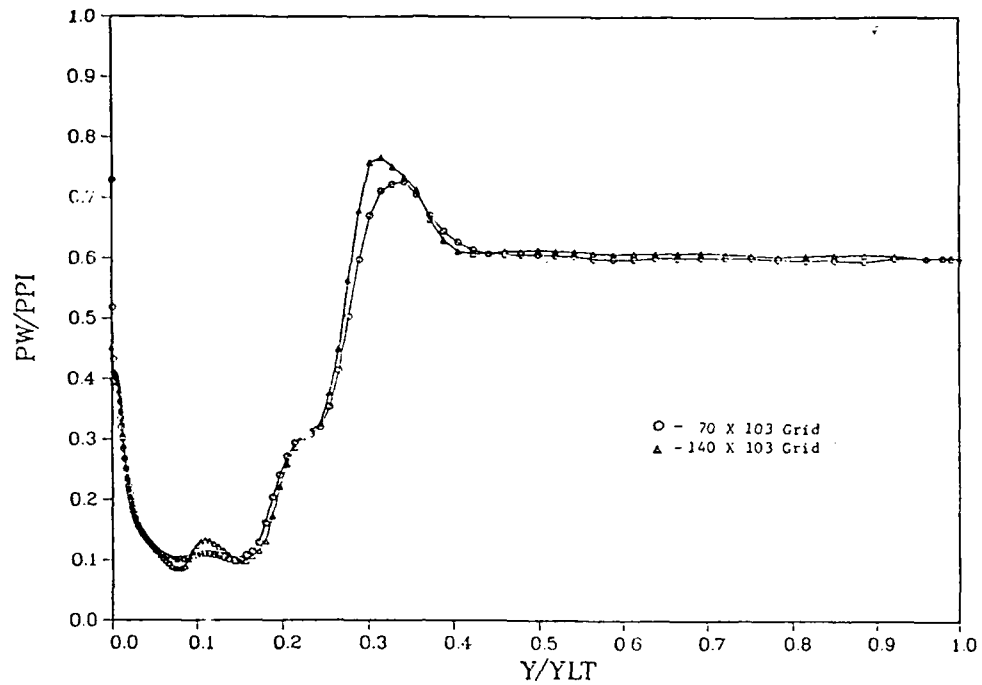
Figure 108a. Computed Wall Pressure Ratio Comparison, 60% NSR
Actual Inflow Solution, 70X103 and 140X103 Grids.

WP Ratio 60%NSR Richardson's Extrapolation
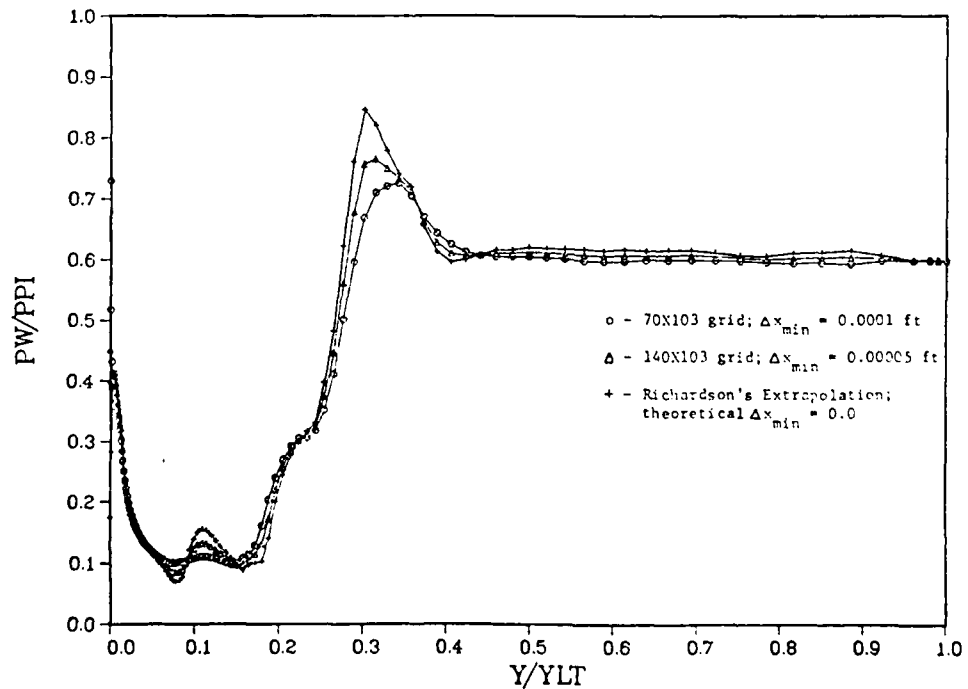
Figure 108b. Richardson's Extrapolation for Wall Pressure Ratio,
60% NSR Actual Inflow Solution, derived from 70X103
and 140X103 Grid Solutions.

Numerical Error Due To Damping

A second assessment of numerical error was performed by comparing the artificial viscosity (introduced by the smoothing terms in the MacCormack algorithm damping scheme) with the modelled eddy viscosity $\mu + \epsilon$. One is able to make this approach because of the particular form of the damping terms (equation 3-34) in the explicit algorithm. Comparison of the damping terms with the normal diffusive terms in the streamwise momentum equation (equations 2-27 through 2-34) yields the following approximate expression for the artificial-to-physical viscosity ratio (54):

$$\frac{\mu_{artificial}}{\mu + \epsilon} = \frac{\beta(|\vec{V}| + a |\vec{\nabla}\eta|)\frac{1}{4P}|\frac{\partial^2 \beta}{\partial \eta^2}| \rho \Delta \eta^3}{|\vec{\nabla}\eta|^2 (\mu + \epsilon)} \tag{6-1}$$

Contours of the above ratio are shown in Figures 109a through 112a for the actual and ideal inflow solutions for both the 60 percent and 47 percent normal shock recovery exit pressure numerical cases. In figures 109b through 112b the corresponding viscosity coefficient ratios are plotted for several constant streamwise locations through the length of the diffuser.

As seen in Figure 109a, there is considerable artificial damping contained within the steady solution flowfield for the 60 percent NSR actual inflow case (case 4a), especially in the nozzle mixing region and across the normal shock. Some additional damping induced by the smoothing procedure is also evident at the exit plane, in the region where exit pressure is not imposed to avoid overspecification of the problem. These artificial damping contours are, however, only 25 percent of the physical viscosity. Damping ratios representing artificial viscosities as much as an order of magnitude greater than the physical viscosity are present in the nozzle mixing region upstream of the core flow normal shock. Comparison of the damping ratio

170

contours for the actual inflow case (Figure 109a) and the ideal inflow case (Figure 110a) provides evidence to support the conclusion that the majority of the artificial damping present in the actual inflow solution is due to the algorithm's handling of the vigorous action of shock wave formation. For the ideal inflow cases (Figures 110a and 112a), the only evident damping ratio contours are in the region of the core flow normal shocks and the interaction region between the wall energizing bank blower flow and the core flow. A similar assessment results from the comparison of the viscosity error ratio contours for the actual and ideal inflow solutions for the 47 percent normal shock recovery exit pressure cases. Although the grid spacing in the mixing region for the actual inflow cases was relatively close in the flow direction, it was somewhat coarser in the direction normal to the flow. The flowfield contravariant velocities are large in this mixing region, as is the second derivative of the pressure (effect of the turnback shocks). These effects result in relatively high numerical damping ratios; however, without this large imposed artificial damping, the numerical algorithm may not be able to successfully handle the gross variations of the highly complex flowfield present in the actual inflow cases.

DAMPING RATIO CONTOURS 60%NSR A.F.
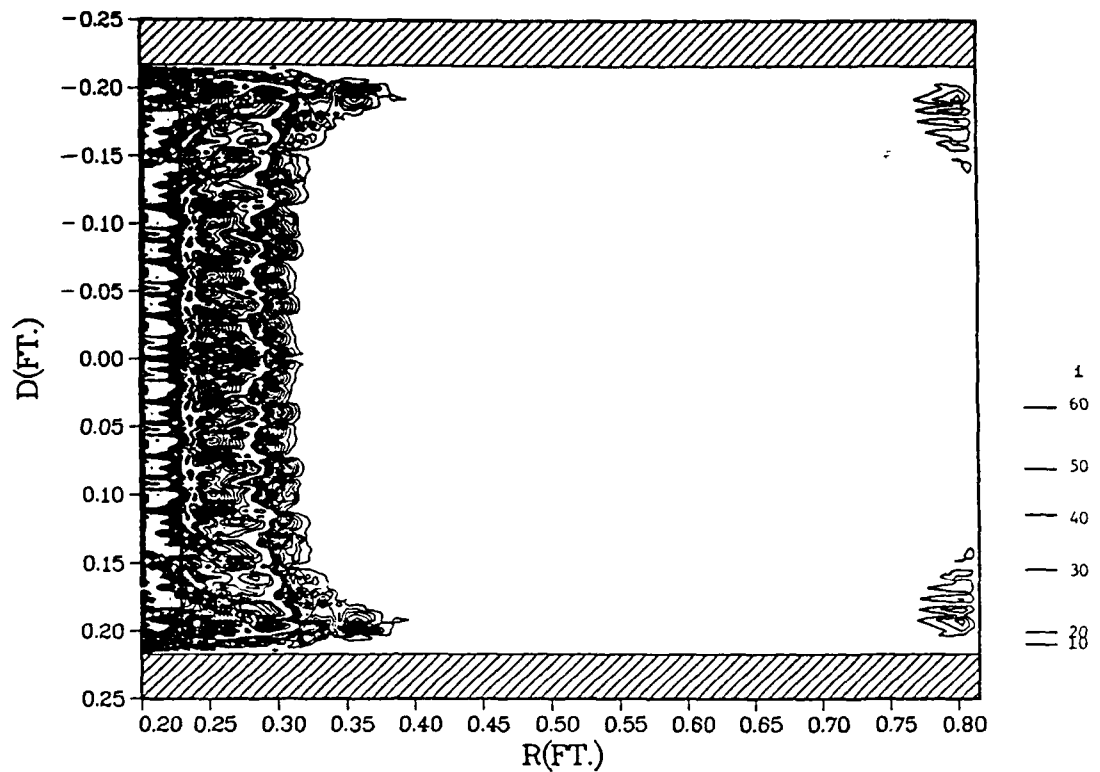
Figure 109a. Damping Ratio Contours, 60% NSR Actual Inflow
Numerical Solution.
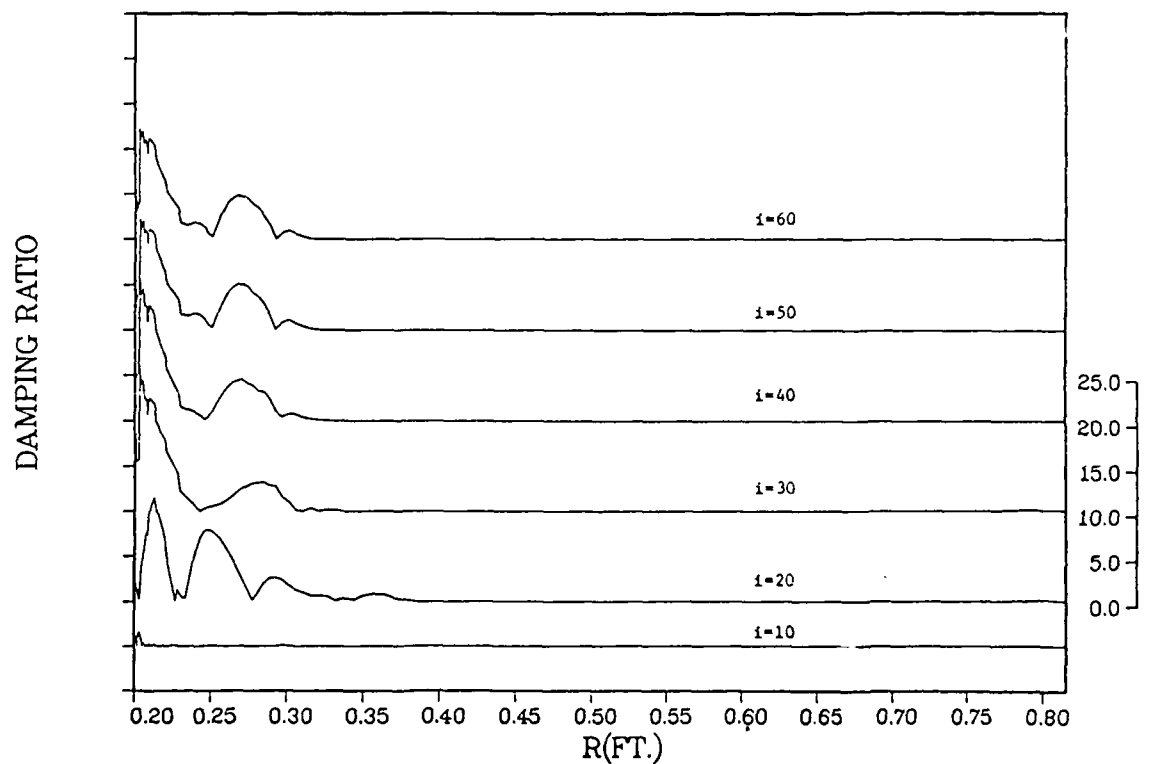
Figure 109b. Damping Ratios, 60% NSR Actual Inflow Numerical
Solution.

Figure 110a. Damping Ratio Contours, 60% NSR Ideal Inflow Numerical Solution.
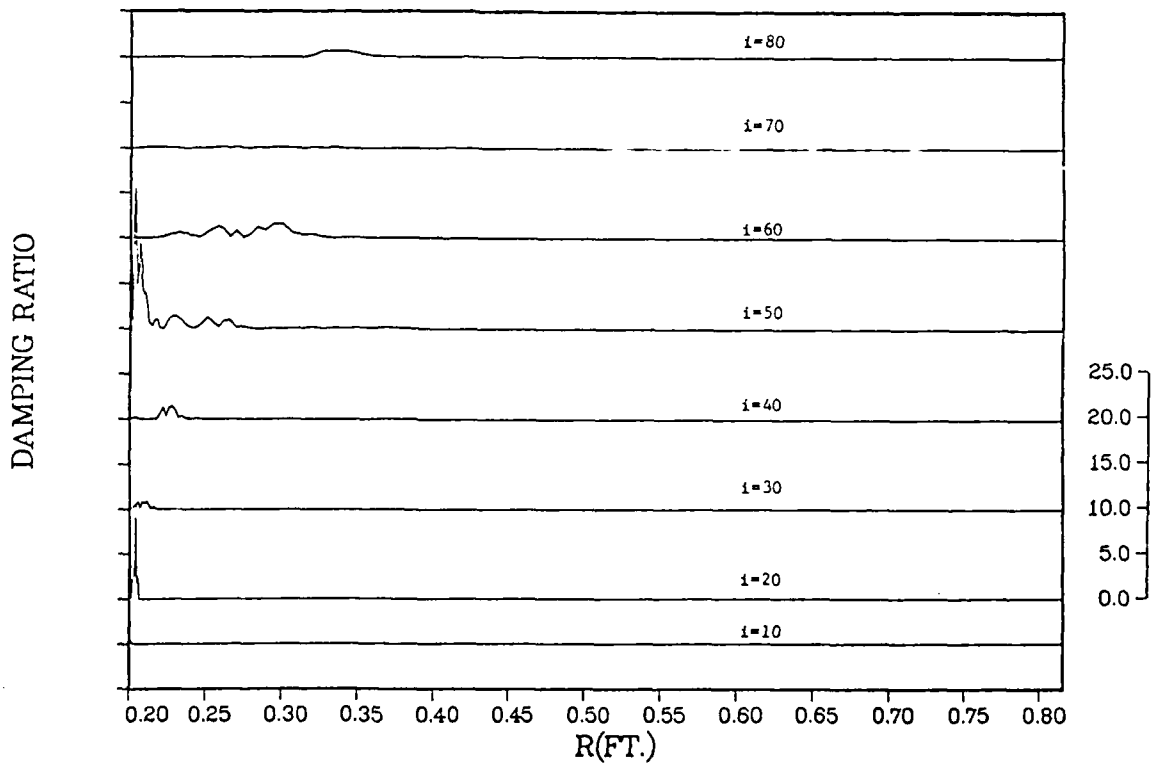
Figure 110b. Damping Ratios, 60% NSR Ideal Inflow Numerical Solution.

DAMPING RATIO CONTOURS 47%NSR A.F.
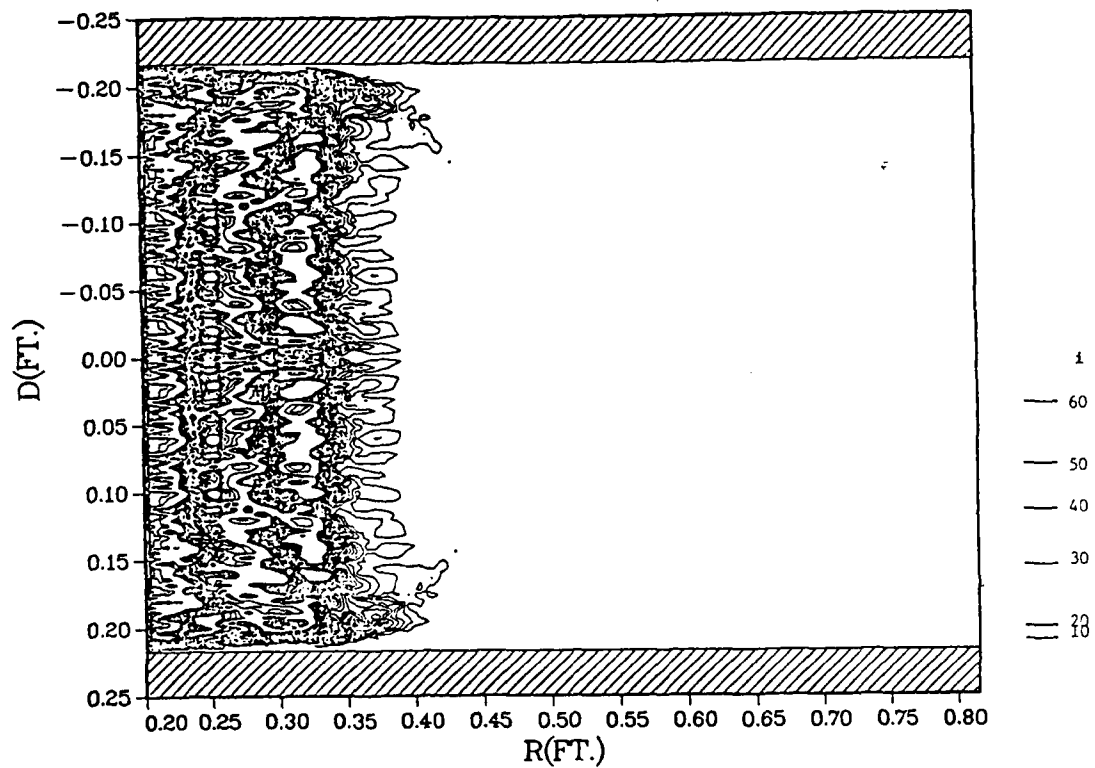
Figure 111a. Damping Ratio Contours, 47% NSR Actual Inflow
Numerical Solution.
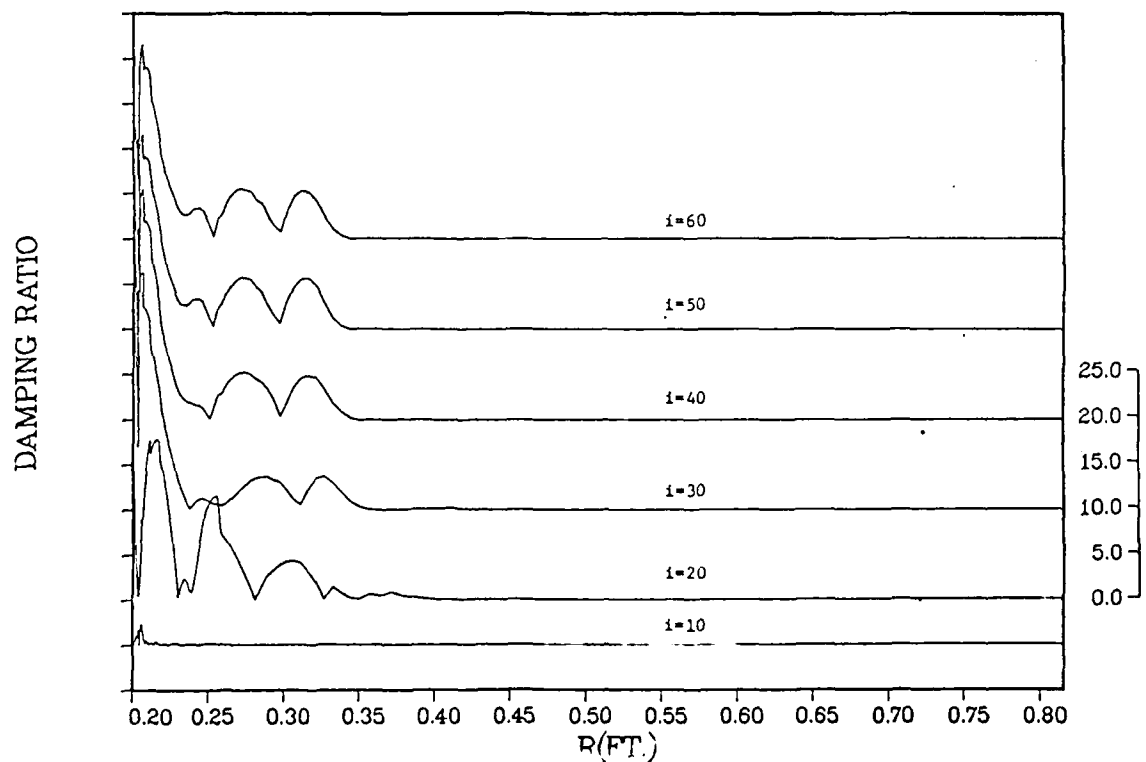
Figure 111b. Damping Ratios, 47% NSR Actual Inflow Numerical
Solution.

Figure 112a. Damping Ratio Contours, 47% NSR Ideal Inflow
Numerical Solution.
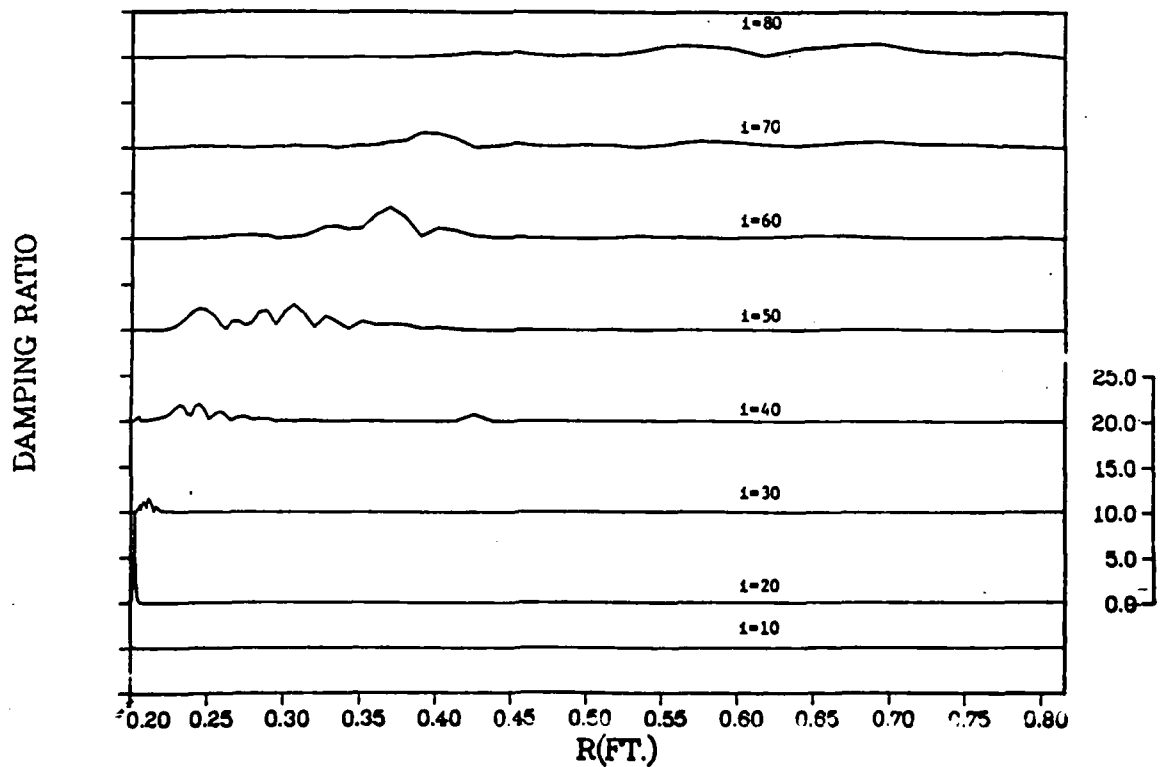
Figure 112b. Damping Ratios, 47% NSR Ideal Inflow Numerical
Solution.

CHAPTER VII

CONCLUSIONS AND RECOMMENDATIONS

CONCLUSIONS

A numerical method of obtaining solutions to the Navier-Stokes equations for supersonic axisymmetric diffusers has been developed from a selection of appropriate techniques. Based on the numerical analysis and computational results obtained through this study, the following conclusions are drawn:

1. The present effort is the first full Navier-Stokes solution that has accurately simulated the viscous-inviscid interactions present in a supersonic axisymmetric diffuser. Numerous previous attempts required artificial and arbitrary numerical control of the wall boundary layers to achieve convergence.

2. The numerical solution of the Navier-Stokes equations applied to supersonic vaneless axisymmetric diffusers requires modification to the basic Cebeci-Smith two-layer algebraic eddy viscosity turbulence model to properly accommodate the physics of flows with strong adverse pressure gradients. When properly modified to stiffen the turbulence model, the numerical solution successfully reproduced all of the essential flow features including boundary layers, location and size of wall separation regions, location of the core flow normal shock, and the persistence of source nozzle flow interactions through several streamwise turnback shocks. Comparison with experimentally obtained wall pressure data is acceptable; the only notable discrepancy occurs in the lambda shock impingement region where the numerical solution fails to accurately reproduce the intrinsic physics of the flowfield.

Although the numerical compatibility of zero-equation algebraic eddy viscosity models is high (59), their deficiency in length scale determination in the presence of large separation/recirculation zones leads to a great reduction in their general applicability and simplicity. This weakness is the underlying cause of discrepancies in predicted wall pressures and recovery distances in the shock impingement/recirculation region.

3. The required modifications to the basic Cebeci-Smith two-layer algebraic eddy viscosity turbulence model are extremely sensitive to the von Karman universal mixing length constant (k_1), the sublayer thickness parameter (A^+), the Clauser outer region constant (k_2), and the downstream location in the diffuser duct at which these modifications are implemented. The sudden short wall pressure rise experienced as the flow first encounters the diffuser walls must be accommodated carefully to allow proper representation of the ensuing flow acceleration into the diffuser before the true macroscopic effects of the adverse pressure gradient are imposed, otherwise the numerical procedure will proceed towards a physically unrealistic condition.

4 Diffuser performance is constrained by the requirement for wall boundary layer energization if the design requires a relatively short duct. The numerical computations confirmed Neumann and Lustwerk's experimental conclusions regarding minimum diffuser duct length required if no wall boundary layer energization is employed. In practical applications the weight penalty for extremely long diffuser ducts outweighs the inefficiency of having to add wall bank blowers at a significant mass fraction of the core flow in order to control the wall boundary layer separation region.

177

5. A significant percentage of the viscous losses experienced in supersonic diffuser performance are caused by the source flow nozzles. Comparison of the uniform inflow, 20 percent bank blower, 60 percent normal shock recovery numerical solution to that for the actual inflow case at the same exit backpressure reveals a 19 percent loss in shock recovery distance due to wall interactions and shear layer mixing. For the uniform inflow case, the core flow normal shock stabilized at a position 24 percent of the duct length from the diffuser entrance. For the actual inflow case, the core flow normal shock stabilized at a position 19 percent of the duct length from the diffuser entrance. The closer the shock gets to the diffuser entrance for a given backpressure, the less stable the diffuser operation, and the closer the flow is to an unstart situation. A loss of 6 percent of absolute diffuser duct length in normal shock position, against an "ideal inflow" condition for normal shock location of 24 percent of diffuser duct length, represents a loss of approximately 19 percent in shock recovery distance due to source nozzle mixing losses.

6. Boundary conditions must be carefully formulated and implemented in order to prevent physically unrealistic results or numerical divergence of the solution. The downstream boundary is extremely sensitive to proper application of the zero gradient condition across the core flow region. It was found that the exit conservative flow variables must first be set using a first-order, zero gradient condition. The exit pressure is then imposed for all points across the outflow boundary outside the boundary layer. This was done by deriving u, v, and T from the conservative variables, and then using the imposed exit pressure to calculate new values of the conservative variables for the next

178

iteiation of the numerical solution. Implementation of the exit
pressure in this manner across too few points at the downstream boundary
caused the algorithm to march towards physically unrealistic results as
did application of the exit pressure within the boundary layer, which
resulted in an overspecified problem.

7. The final steady state solutions were found to be insensitive to the
initial conditions applied over the computational domain. However, the
time to converge to the final solution was highly dependent on the
application of specific initial conditions.

Recommendations

Based on the numerical analysis and results obtained through
this study, the following recommendations are made:

1. The present numerical solver should be modified to include the effects
of a calorically imperfect gas with variable specific heat and thermal
conductivity. This modification would allow accurate simulation of
temperature dependent effects for hot source flow nozzles and the
attendant heat release in the laser cavity and diffuser expected in true
laser operation.

2. After implementation of the previous recommendation for a single
species, it would be desirable to incorporate the effects of species
mixing into the numerical solver. Many practical cases of interest in
the evaluation of laser diffuser performance involve gas flow with
different species due to incomplete combustion in the gain generator
between the fuel and oxidizer, the injection of diluents to decrease the
rate of collisional deactivation of the excited lasing media and thus
stretch the lasing region, and the use of inert gases such as helium for

the wall bank blower energizers. This modification would require a significant code revision, since the equation of mass diffusion would be required, as would the correct modeling of appropriate mass diffusion coefficients.

3. Correlation of the values of the eddy viscosity model constants k_1, A^+, and k_2 with the intrinsic physical properties of turbulent flow should be studied in detail through experimental research.

BIBLIOGRAPHY

1. Christiansen, W. H., Russell, D. A., and Hertzberg, A., "Flow Lasers," in Annual Review of Fluid Mechanics, 7, 1975, pp. 115-139.

2. Warren, W. R., Jr., "Chemical Lasers," Aeronautics and Astronautics, Vol. 13, No. 4, Apr. 1975, pp. 36-53.

3. Kompa, K. L., Chemical Lasers, Topics in Current Chemistry, 37, Springer-Verlag, New York, N.Y. 1973.

4. Knight, Doyle D., and Hankey, W. L., Jr., "Numerical Simulation Of Nonchemically Reacting Radial Supersonic Diffusion Laser," AIAA Paper 76-60, Jan. 1976.

5. Cylindrical Gas Dynamic Laser, AFWL-TR-74-5, June 1974.

6. Kothari, A. P., Anderson, J. D., Jr., and Jones, E., "Navier-Stokes Solutions for Chemical Laser Flows," AIAA Journal, Vol. 15, No. 1., Jan. 1977, pp. 42-100.

7. Ortwerth, P. J., Watkins, W. B., and Finke, J. R. "Diffusers for Cylindrical Source Flow Lasers," Laser Digest, Fall 1974, AFWL-TR-74-344.

8. Howard, James H. and Hasinger, Siegfried H., "Diffusion Characteristics of Large L/D Radial Outflow Nozzle Systems," Laser Digest, Summer 1975, AFWL-TR-75-229.

9. Zumpano, F. R., Guile, R. N., and Eckerle, W. A., High Aspect Ratio Supersonic Diffuser Performance Characteristics, TR R-80-914767-3, AD #B047863, UTRC Technical Report for AFWL, June 1980.

10. Zumpano, F. R., Guile, R. N., and Eckerle, W. A., Supersonic Radial-Flow Diffuser Investigations, UTRC TR R-80-914767-2, AD #B047862, UTRC Technical Report for AFWL, June 1980.

11. Neumann, E. P. and Lustwerk, F., "Supersonic Diffusers for Wind Tunnels," Journal of Applied Mechanics, Vol. 16, No. 2, ASME, New York, June 1949.

12. Zumpano, F. R., Guile, R. N., and Eckerle, W. A., Proposal for a Radial Flow Diffuser Technology Program, UTRC P-82-130, UTRC, East Hartford, Ct., April 1982.

13. Zumpano, F. R., Guile, R. N., Haas, M., and Sobel, D. R., Radial Flow Diffuser Technology Program, UTRC R-84-958412-1, UTRC, East Hartford, Ct., June 1984.

14. Zumpano, F. R., Analysis of Cylindrical Laser Diffuser Data With Comparisons to the Performance of a Subscale, Cold-Flow Model, UTRC R-81-112199-1, UTRC, East Hartford, Ct., Dec. 1981.

181

15. Johnson, Joseph A. and Wu, Benjamin J. C., Pressure Recovery and Related Properties in Supersonic Diffusers: A Review, Yale University, New Haven, Ct., Report prepared for AFOSR Research Grant F44620-73-C-0032, April 1974.

16. Guderly, K. G., The Theory of Transonic Flow, Addison-Wesley, Reading, Mass., 1962.

17. Ferrari, C. and Tricomi, F. G., Transonic Aerodynamics, Academic Press, New York, 1968.

18. Sichel, M., "Two-Dimensional Shock Structure in Transonic and Hypersonic Flow," Advances in Applied Mechanics, Vol. 11, Academic Press, New York, 1971.

19. Szaniawski, A., "Transonic Approximations to the Flow Through a Nozzle," Archiwum Mechaniki Stosowanej, Vol. 17, No. 1, 1965.

20. Messiter, A. F. and Adamson, T. C., Jr., "On the Flow Near a Weak Shock Wave Downstream of a Nozzle Throat," Journal of Fluid Mechanics, Vol. 69, May 1975.

21. Adamson, T. C., Jr., Messiter, A. F., and Liou, M. -S., "Large Amplitude Shock Motion in Two-Dimensional Transonic Channel Flow," AIAA Journal, Vol. 16, Dec. 1978.

22. Liou, M. -S., and Sabjen, M., "Analysis of Unsteady Viscous Transonic Flow with a Shock Wave in a Two-Dimensional Channel," AIAA Paper 80-0195, Jan. 1980.

23. Liou, M. -S., "Analysis of Viscous-Inviscid Interaction in Transonic Internal Flows," AIAA Paper 81-0004, Jan. 1981.

24. Buggeln, R. C., McDonald, H., Kreskovsky, J. P., and Levy, R., "Computation of Three-Dimensional Viscous Supersonic Flow In Inlets," AIAA Paper 80-0194, Jan. 1980.

25. Liu, N. -S., Shamroth, S. J., and McDonald, H., "Numerical Solution of the Navier-Stokes Equations for Compressible Turbulent Two/Three Dimensional Flow in the Terminal Shock Region of an Inlet/Diffuser," AIAA Paper 83-1892, June 1983.

26. Liu, N. -S., Shamroth, S. J., and McDonald, H., Dynamic Response of Shock Waves in Transonic Diffuser and Supersonic Inlet: An Analysis with the Navier-Stokes Equations and Adaptive Grid," AIAA Paper 84-1609, June 1984.

27. Talcott, Noel A., Jr., and Kumar, Ajay, "Numerical Simulation of Flow Through Inlets/Diffusers with Terminal Shocks," AIAA Paper 84-1362, June 1984.

28. MacCormack, R. W., "The Effect of Viscosity in Hypervelocity Impact Cratering," AIAA Paper 69-354, May 1969.

29. MacCormack, R. W., "A Numerical Method for Solving the Equations of Compressible Viscous Flow," AIAA Paper 81-0110, Jan. 1981.

30. Knight, Doyle D., "Numerical Simulation of Realistic High-Speed Inlets Using the Navier-Stokes Equations," AIAA Paper 77-146, Jan. 1977.

31. Cebeci, T., Smith, A. M. O., and Mosinskis, G., "Calculations of Compressible Adiabatic Turbulent Boundary Layers," AIAA Journal, Vol. 8, Nov. 1970, pp. 1974-1982.

32. Cebeci, T., "Calculations of Compressible Turbulent Boundary Layers with Heat and Mass Transfer," AIAA Journal, Vol. 9, June 1971, pp. 1091-1097.

33. Hsieh, T., Wardlow, A. W., Jr., and Coakley, T., "Numerical Simulation of a Ramjet Inlet Flowfield in Response to Large Amplitude Combustor Pressure Oscillation," AIAA Paper 84-1363, June 1984.

34. Rose, W. C., and Perkins, E. W., Innovative Boundary Layer Control Methods in High Speed Inlet System, Final Report, Phase I, SBIR Contract No. NAS 3-25408, NASA Lewis Research Center, September 1988.

35. Reddy, D. R., Benson, T. J., and Weir, L. J., "Comparison of 3-D Viscous Flow Computations of Mach 5 Inlet With Experimental Data," AIAA Paper 90-0600, January 1990.

36. Baldwin, B. S., and Lomax, H., "Thin Layer Approximation and Algebraic Model for Separated Turbulent Flows," AIAA Paper 78-527, January 1978.

37. Rapagnani, N. L., and Lankford, D. W., "Time-Dependent Nozzle and Base Flow/Cavity Model of CW Laser Flow Fields," AIAA Paper 81-1135, June 1981.

38. Rapagnani, N. L., "The Effect of Heat Release in a Chemical Laser Cavity," AIAA Paper 84-1619, June 19{ ·

39. Hasen, G. A., Navier Stokes Solutions For Flow Through A Two-Dimensional Supersonic Diffuser, AFWAL-TM-84-184, December 1983.

40. Roache, P. J., Computational Fluid Mechanics, Hermosa Publishers, Albuquerque, New Mexico, 1972.

41. Ames Research Staff, Equations, Tables and Charts for Compressible Flow, NACA Report 1135, 1953.

42. Rubesin, M. W., and Rose, W. C., The Turbulent Mean-Flow, Reynolds-Stress, and Heat Flux Equations in Mass Averaged Dependent Variables, NASA TMX-62, 248, March 1973.

43. Chapman, D. R., "Computational Aerodynamics Development and Outlook," AIAA Journal, Vol. 17, No. 12, December 1979, pp. 1293-1313.

44. Schlichting, H., Boundary Layer Theory, McGraw-Hill Book Company, New York, N.Y., 1968.

183

45. Tennekes, H., and Lumley, J. L., _A First Course in Turbulence_, The MIT Press, Cambridge, Ma., 1972.

46. Johnson, L. W., and Riess, R. D., _Numerical Analysis_, Addison-Wesley Publishing Company, Reading, Ma., 1982.

47. Anderson, J. D., Jr., _Gasdynamic Lasers: An Introduction_, Academic Press, New York, N. Y., 1976.

48. Anderson, J. D., Jr., "A Time-Dependent Analysis for Vibrational and Chemical Nonequilibrium Nozzle Flows," _AIAA Journal_, Vol. 18, No. 3, March 1970, pp 545-550.

49. MacCormack, R. W., "Numerical Solution of the Interaction of a Shock Wave with a Laminar Boundary Layer," _Proceedings of the Second International Conference on Numerical Methods in Fluid Dynamics_, University of California, Berkeley, September 15-19, 1970.

50. MacCormack, R. W., _An Efficient Numerical Method for Solving the Time Dependent Compressible Navier-Stokes Equations at High Reynolds Numbers_, NASA TMX-73,129, July 1976.

51. MacCormack, R. W., and Lomax, H., "Numerical Solution of Compressible Viscous Flows," _Annual Review of Fluid Mechanics, 1979_, Vol. 11; pp 289-316.

52. MacCormack, R. W., and Paullay, A. J., "Computational Efficiency Achieved by Time Splitting of Finite-Difference Operators," AIAA Paper 72-154, January 1972.

53. MacCormack, R. W. and Baldwin, B. S., "A Numerical Method for Solving the Navier-Stokes Equations with Application to Shock-Boundary Layer Interactions," AIAA Paper 75-1, January 1975.

54. Visbal, M. R. _Calculation Of Viscous Transonic Flows About A Supercritical Airfoil_, AFWAL-TR-86-3013.

55. Mahajan, A. J., Dowell, E. H., and Bliss, D. B., "On the Role of Artificial Viscosity in Navier-Stokes Solvers," AIAA Paper 89-1947, June 1989.

56. Griffin, M. D., Jones, E., and Anderson, J. D., Jr., "A Computational Fluid Dynamic Technique Valid at the line of symmetry for Non-Axisymmetric Problems in Cylindrical Coordinates," _Journal of Computational Physics_, Vol. 30, No. 3, March 1979.

57. Marvin, J. G., "Turbulence Modeling for Computational Aerodynamics," _AIAA Journal_, Vol. 27, No. 7, July 1983.

58. Coakley, T. J., and Bergman, M. Y., "Effects of Turbulence Model Selection on the Prediction of Complex Aerodynamic Flows," AIAA Paper 79-0070, January 1979.

59. Coakley, T. J., "Turbulence Modeling Methods for the Compressible Navier-Stokes Equations," AIAA Paper 83-1693, July 1983.

60. Arad, E., and Wolfshtein, M., "Efficient Numerical Simulation of Turbulent Flows," ICAS-88-4.2.3.

61. Harsha, P. T., Free Turbulent Mixing: A Critical Evaluation of Theory and Experiment, AEDC-TR-71-36, February, 1971.

62. Baldwin, B. S., and Lomax, H., "Thin Layer Approximation and Algebraic Model for Separated Turbulent Flows," AIAA Papar 78-257, January 1978.

63. Visbal, M., and Knight, D., "Evaluation of the Baldwin-Lomax Turbulence Model for Two-Dimensional Shock Wave - Boundary Layer Interactions," AIAA Paper 83-1697, July 1983.

64. Stock, H. W., and Haase, W., "Determination of Length Scales in Algebraic Turbulence Models for Navier-Stokes Methods," AIAA Journal, Vol. 29, No. 1, January 1989.

65. Van Driest, E., "On Turbulent Flow Near a Wall," Journal of Aerospace Science, Vol. 23, 1956, p. 1007.

66. Klebanoff, P. S., "Characteristics of Turbulence in a Boundary Layer with Zero Pressure Gradient," NACA Technical Note 3178, 1954.

67. Jobe, C. E., and Hankey, W. L., Jr., "Turbulent Boundary Layer Calculations in Adverse Pressure Gradient Flows," AIAA Paper 80-0136, January 1980.

68. Cebeci, T., Private Communication, 11 June 1984.

69. Laderman, A. J., Pressure Gradient Effects on Supersonic Boundary Layer Turbulence, Report No. U-6467, Ford Aeroneutronic Division, Newport Beach, CA., October 1978. Also AIAA Paper 79-1563, July 1979.

70. Sturek, W. B., "An Experimental Investigation of the Supersonic Turbulent Boundary Layer in a Moderate Adverse Pressure Gradient, Part 1. A Detailed Description of the Experiment and Data Tabulation," BRL Report 1506, October 1970. Also AIAA Journal, Vol. 10, No. 4, April 1972.

71. Waltrup, P. J., and Schetz, J. A., "An Experimental Investigation of a Compressible Turbulent Boundary Layer Subjected to a Systematic Variation of Adverse Pressure Gradients," VPI-E-71-18, August 1971. Also AIAA Journal, Vol. 11, No. 1, January 1973.

72. Shang, J. S., Hankey, W. L., Jr., et al., "Numerical Analysis of Eddy Viscosity Models in Supersonic Turbulent Boundary Layers," AIAA Paper 73-164, January 1973.

73. Galbraith, R. A. McD., and Head, M. R., "Eddy Viscosity and Mixing Length from Measured Boundary Layer Developments," Aero. Quarterly, Vol. 26, Part 2, May 1975.

74. Glowacki, W. J. and Chi, S. W., "A Study of the Effect of Pressure Gradient on the Eddy Viscosity and Mixing Length for Incompressible Equilibrium Boundary Layers," NOLTR-74-105, May 1974, Naval Ordnance Laboratory, Silver Spring, MD.

75. Horstman, C. C., "A Turbulence Model for Nonequilibrium Adverse Pressure Gradient Flows," AIAA Paper 76-412, June 1976. Also AIAA Journal, Vol. 15, No. 2, February 1977.

76. Johnson, D. A., Horstman, C. C., and Bachalo, W. D., "Comparison Between Experiment and Prediction for a Transonic Turbulent Separated Flow," AIAA Journal, Vol. 20, No. 6, June 1982.

77. Launder, B. E., and Spaulding, D. B., "The Numerical Computation of Turbulent Flows," Computer Methods in Applied Mechanics and Engineering, Vol. 3, pp. 269-289, 1974.

78. Shang, J. S., Buning, P. G., Hankey, W. L., Jr., and Wirth, M. C., "Performance of a Vectorized Three-Dimensional Navier-Stokes Code on the CRAY-1 Computer," AIAA Journal, Vol. 18, No. 9, September 1980, pp. 1073-1079.

79. Kays, W. M., Convective Heat and Mass Transfer, McGraw-Hill, Inc., 1966.

80. Hasen, G. A., Navier-Stokes solutions For A Supersonic Coflowing Axisymmetric Nozzle With A Thick Base Annulus, PhD Dissertation. School of Engineering, Air Force Institute of Technology (AU), Wright-Patterson AFB OH, April 1981.

81. Horkovich, J. A., Hodge, J. K., and Shang, J. S., "Numerical Solution for a Cylindrical Laser Diffuser Flowfield," AIAA Paper 87-1393, June 1987.

82. Hankey, W. L., Introduction to Computational Aerodynamics, AFWAL TR-82-3031, April 1983.

83. Lin, C. C., Turbulent Flows and Heat Transfer, Princeton University Press, Princeton, N. J., 1959.

84. Chow, C-Y., An Introduction to Computational Fluid Mechanics, John Wiley & Sons, New York, N. Y., 1979.

85. Peyret, R., and Taylor, T. D., Computational Methods for Fluid Flow, Springer-Verlag, New York, N. y., 1983.

86. Anderson, D. A., Tannehill, J. C., and Pletcher, R. H., Computational Fluid Mechanics and Heat Transfer, Hemisphere Publishing Corporation, New York, N. Y., 1984.

APPENDIX A

VECTORIZED NAVIER-STOKES COMPUTER CODE

WITH ADVERSE PRESSURE GRADIENT MODIFIED EDDY VISCOSITY TURBULENCE MODEL

187

VECTORIZED NAVIER-STOKES COMPUTER CODE
WITH ADVERSE PRESSURE GRADIENT MODIFIED EDDY VISCOSITY TURBULENCE MODEL

```
  1     1.         PROGRAM MAIN (INPUT,OUTPUT,TAPE5=INPUT,TAPE6=OUTPUT,
  2               1 TAPE1,TAPE2,TAPE3,TAPE4,TAPE7)
  3     2.         COMMON / / PW,DETA,DZETA,CV,RC,PR,PRT,GAMMA,EP(70,103,1),
  4               1 GAMM1,CFL,BETA,UINF,RHOINF,CINF,TINF,TW,DT,CX,CY,CZ,L,
  5               2 IL,JL,KL,ILM,JLM,KLM,ILE,LS,ISMTHX,ISMTHY,ISMTHZ,
  6               3 FLOWF,WN,WFBB,WT,OMEGA(70,103)
  7     3.         COMMON /DEPP/ RHOP(70,103,1),RHOUP(70,103,1),RHOVP(70,103,1),
  8               1 RHOWP(1,1,1),RHOEP(70,103,1)
  9     4.         COMMON /DEP/ RHO(70,103,1),RHOU(70,103,1),RHOV(70,103,1),
 10               1 RHOW(1,1,1),RHOE(70,103,1)
 11     5.         COMMON /DOF/ X(70,103,1),Y(70,103,1),Z(1,1,1)
 12     6.         COMMON /TV/ ETX(70,103,1),ETY(70,103,1),ETZ(1,1,1),
 13               1 ZTX(70,103,1),ZTY(70,103,1),ZTZ(1,1,1)
 14           C
 15           C   CONSTANTS AND PARAMETER FOR AIR
 16           C
 17     7.         CV=4290.
 18     8.         RC=1718.
 19     9.         GAMMA=1.4
 20    10.         GAMM1=GAMMA-1.0
 21    11.         PR=0.73
 22    12.         PRT=0.90
 23    13.         RCV=1.0/CV
 24           C
 25    14.  100    FORMAT(7F10.4)
 26    15.  110    FORMAT(10I5)
 27    16.  495    FORMAT(*      TCH=*,E15.7/)
 28    17.  500    FORMAT(* FREESTREAM MACH NO.=*,F10.4,* REYNOLDS NO.=*,E15.7,
 29               1 * SURFACE TEMP.(RANKIN)=*,F10.4,* REFERENCE LENGTH=*,F10.4/)
 30    18.  505    FORMAT(*    MASS FLOW RATE (WN) = *,F6.3,* (KG/SEC)  WBB/WN = *,
 31               1 F7.4,*    PPI(PSF)= *,F10.4/)
 32    19.  510    FORMAT(*RHOINF=*,E15.7,* UINF=*,F10.4,* CINF=*,F10.4,* TINF=*,
 33               1 F8.3,* PINF=*,F8.3,* RMUINF=*,E15.7/)
 34    20.  520    FORMAT(* PEXIT(PSF)=*,F10.4,* DETA=*,F10.4,* DZETA=*,F10.4,
 35               1 * XL=*,F10.4,* YL=*,F10.4/)
 36    21.  530    FORMAT(* CFL=*,F8.4,* CX=*,F8.4,* CY=*,F8.4,* CZ=*,F8.4,
 37               1 *BETA=*,F10.4/)
 38    22.  540    FORMAT(* LS=*,I5,* JFM=*,I5,* KFM=*,I5,* ISHK=*,I5,* JSHK=*,
 39               1 I5,* KSHK=*,I5/)
 40    23.  550    FORMAT(*    NEND=*,I5,* IL=*,I5,* JL=*,I5,* KL=*,I5/)
 41    24.  580    FORMAT(* N=*,I5,* DTCFL=*,E15.7,* TMS2=*,E15.7,* TMS1=*,E15.7,
 42               1 * TMS2/TCH=*,E15.7,*   TCH=*,E15.7)
 43    25.  590    FORMAT(/,*   J  K      Y          X          M         P          RHO
 44               1 U          V         OMEGA              T          P          EP*/)
 45    26.  600    FORMAT(1X,2I3,11E11.4)
 46    27.  610    FORMAT(6E11.4)
 47    28.  630    FORMAT(I3,4F10.4)
 48    29.  650    FORMAT(5E11.4)
 49           C   ************************
 50           C   READ IN THE INPUT DATA
 51           C   ************************
 52    30.         READ(5,100) XM,PINF,TW,RL,PW,PPI
 53    31.         READ(5,100) WN,WFBB,WFJ
 54    32.         READ(5,100) CX,CY,CZ,CFL,BETA
 55    33.         READ(5,110) ISTART,ILE,IG
 56    34.         READ(5,110) LS,JFM,KFM,ISHK,JSHK,KSHK
 57    35.         READ(5,110) NEND,IL,JL,KL,ISMTHX,ISMTHY,ISMTHZ
 58           C
 59           C   GENERATING THE MEAN FREESTREAM INFORMATION
 60           C
 61    36.         XL=0.21669996
 62    37.         YL=0.61479659
 63    38.         YDE=0.20
 64    39.         TINF=TW*(1./(1.+GAMM1*XM**2/2.))
 65    40.         CINF=SQRT(GAMMA*RC*TINF)
 66    41.         UINF=CINF*XM
 67    42.         PI=4.*ATAN(1.)
 68    43.         AI=0.8*PI*(XL-.013)
 69    44.         RMUINF=2.27E-08*SQRT(TINF**3)/(TINF+198.6)
 70    45.         WF=6.8521E-02*WN
```

```
71    46.        WBB=WFBB*WF
72    47.        WT=WBB+WF
73    48.        RUINF=WF/AI
74    49.        RHOINF=RUINF/UINF
75    50.        REY=RUINF*RL/RMUINF
76    51.        BETA=0.0
77        C
78    52.        ILM=IL-1
79    53.        JLM=JL-1
80    54.        KLM=KL-1
81    55.        DETA=1./JLM
82    56.        DZETA=1./KLM
83        C
84        C      WRITE OUT THE INPUT AND FLOW FIELD INFORMATION
85        C
86    57.        WRITE(6,500) XM,REY,TW,RL
87    58.        WRITE(6,505)WN,WFBB,PPI
88    59.        WRITE(6,510) RHOINF,UINF,CINF,TINF,PINF,RMUINF
89    60.        WRITE(6,520) PW,DETA,DZETA,XL,YL
90    61.        WRITE(6,530) CFL,CX,CY,CZ
91    62.        WRITE(6,540) LS,JFM,KFM,ISHK,JSHK,KSHK
92    63.        WRITE(6,550) NEND,IL,JL,KL
93    64.        RLS=FLOAT(LS)
94        C
95    65.        NI=1
96    66.        TMS1=0.0
97    67.        TMS2=0.0
98        C
99        C      READ IN THE GRID POINTS IN CARTESIAN FRAME
100       C      *******************************************
101   68.        Z(1,1,1)=0.0
102       C      INITIALIZATION OF ALL DEPENDENT VARIABLES
103       C      *******************************************
104       C
105       C      READ IN THE RESTART DATA FROM PREVIOUS RUNS
106       C      *******************************************
107   69.        IF(ISTART.NE.0) READ(1) NI,TMS1,TMS2,RHO,RHOU,RHOV,RHOW,RHOE,
108              1 X,Y,Z,EP
109       C
110   70.        RHO(70,1,1)=1.841E-04
111   71.        RHOV(70,1,1)=0.319045
112       C      SET FLOW FIELD PREDICTOR STEP VALUES
113       C
114   72.        DO 25 J=1,JL
115   73.        DO 25 K=1,KL
116   74.        RHOP(K,J,1)=RHO(K,J,1)
117   75.        RHOUP(K,J,1)=RHOU(K,J,1)
118   76.        RHOVP(K,J,1)=RHOV(K,J,1)
119   77.        RHOEP(K,J,1)=RHOE(K,J,1)
120   78.     25 CONTINUE
121   79.        RHOWP(1,1,1)=0.0
122       C
123       C      COMPUTE CHARACTERISTIC TIME AT CENTERLINE
124       C
125   80.        TCH=0.0
126   81.        DO 800 J=2,JL
127   82.        RHJ=1.0/RHO(KL,J,1)
128   83.        RHJM=1.0/RHO(KL,J-1,1)
129   84.        VJ=RHOV(KL,J,1)*RHJ
130   85.        VJM=RHOV(KL,J-1,1)*RHJM
131   86.        TCH=TCH+2.0*(Y(KL,J,1)-Y(KL,J-1,1))/(VJ+VJM)
132   87.    800 CONTINUE
133       C
134   88.     30 CALL TRANS
135   89.        CALL TMSTEP
136       C
137   90.        DO 1 N=NI,NEND
138       C
139   91.        IF((N/10)*10.NE.N) GO TO 5
140       C      DETERMINE THE ALLOWABLE TIME STEP SIZE (DT CFL)
141       C      *******************************************
142   92.        CALL TMSTEP
143   93.        CALL EDDY
144       C
145       C      CONTROL THE DATA FLOW AND DIFFERENCE OPERATORS
146       C      *******************************************
147   94.   5    CALL PAGE
148       C
149   95.        TMS2=TMS1+DT
150       C      COMPUTE CHARACTERISTIC TIME AT CENTERLINE
```

189

```
151     C
152     C       RECOMPUTE TCH ONLY EVERY 100 ITERATIONS
153     C
154   96.        IF((N/100)*100.NE.N) GO TO 950
155   97.        TCH=0.0
156   98.        DO 900 J=2,JL
157   99.        RHJ=1.0/RHO(KL,J,1)
158  100.        RHJM=1.0/RHO(KL,J-1,1)
159  101.        VJ=RHOV(KL,J,1)*RHJ
160  102.        VJM=RHOV(KL,J-1,1)*RHJM
161  103.        TCH=TCH+2.0*(Y(KL,J,1)-Y(KL,J-1,1))/(VJ+VJM)
162  104.   900 CONTINUE
163  105.        T=TMS2/TCH
164  106.        WRITE(6,580) N,DT,TMS2,TMS1,T,TCH
165  107.   950 CONTINUE
166  108.        TMS1=TMS2
167     C
168     C
169  109.  1    CONTINUE
170     C
171  110.        WRITE(6,495) TCH
172     C       WRITE THE RESTART DATA INTO RESTART TAPE
173     C       ***************************************
174  111.        NEND=NEND+1
175  112.        WRITE(2) NEND,TMS1,TMS2,RHO,RHOU,RHOV,RHOW,RHOE,X,Y,Z,EP
176     C
177     C       ********************************
178     C       WRITE OUT THE COMPUTED FLOW DATA
179     C       ******************************
180     C       GENERATING THE GRAPHICAL DATA FILE ON TAPE4
181     C
182  113.        XC=-0.250
183  114.        WRITE(4,610) Y(1,1,1),X(1,1,1)
184  115.        WRITE(4,610) Y(1,JL,1),X(1,JL,1)
185  116.        WRITE(4,610) Y(1,JL,1),XC
186  117.        WRITE(4,610) Y(1,1,1),XC
187  118.        I=1
188     C
189  119.        DO 20 J=1,JL
190  120.        WRITE(6,590)
191  121.        DO 20 K=1,KL
192     C
193  122.        RH=1.0/RHO(K,J,1)
194  123.        U=RHOU(K,J,1)*RH
195  124.        UP=U/UINF
196  125.        V=RHOV(K,J,1)*RH
197  126.        VP=V/UINF
198  127.        W=U*RUINF
199  128.        T=(RHOE(K,J,1)*RH-0.5*(U**2+V**2))*RCV
200  129.        P=RHO(K,J,1)*RC*T
201  130.        XM=SQRT((U**2+V**2)/(GAMMA*RC*T))
202     C
203  131.        WRITE(6,600) J,K,Y(K,J,1),X(K,J,1),XM,RHO(K,J,1),
204            1 U,V,OMEGA(K,J),T,P,EP(K,J,1)
205  132.        WRITE(4,610) Y(K,J,1),X(K,J,1),UP,VP,XM,P
206     C
207  133.  20   CONTINUE
208     C
209     C       COMPUTE RATIO OF LOCAL WALL STATIC PRESSURE
210     C            TO INLET PITOT PRESSURE
211     C
212  134.        WRITE(6,625)
213  135.  625 FORMAT(/,*  J        Y/YLT       PW/PPI      PCL/PPI     TCL/TO*/)
214  136.        DO 40 J=2,JL
215  137.        YR=(Y(1,J,1)-Y(1,2,1))/YL
216  138.        YRD=(Y(1,J,1))/YDE
217  139.        PE=RHOE(1,J,1)*RC*RCV/PPI
218  140.        RH=1.0/RHO(KL,J,1)
219  141.        V=RHOV(KL,J,1)*RH
220  142.        TCL=(RHOE(KL,J,1)*RH-0.5*V**2)*RCV
221  143.        TRT=TCL/TW
222  144.        PCL=RHO(KL,J,1)*RC*TCL/PPI
223  145.        WRITE(6,630)J,YR,PE,PCL,TRT
224  146.        WRITE(7,650)YR,YRD,PE,PCL,TRT
225  147.   40 CONTINUE
226  148.        STOP
227  149.        END
MAIN.                VECTOR LOOP BEGINS AT SEQ. NO.        73, P=    1005B
MAIN.                VECTOR LOOP BEGINS AT SEQ. NO.        81, P=    1040C
MAIN.                VECTOR LOOP BEGINS AT SEQ. NO.        98, P=    1133D
```

```
228    1.        SUBROUTINE TMSTEP
229    2.        COMMON / / PW,DETA,DZETA,CV,RC,PR,PRT,GAMMA,EP(70,103,1),
230             1 GAMM1,CFL,BETA,UINF,RHOINF,CINF,TINF,TW,DT,CX,CY,CZ,L,
231             2 IL,JL,KL,ILM,JLM,KLM,ILE,LS,ISMTHX,ISMTHY,ISMTHZ
232    3.        COMMON /TV/ ETX(70,103,1),ETY(70,103,1),ETZ(1,1,1),
233             1 ZTX(70,103,1),ZTY(70,103,1),ZTZ(1,1,1)
234    4.        COMMON /DEP/ RHO(70,103,1),RHOU(70,103,1),RHOV(70,103,1),
235             1 RHOW(1,1,1),RHOE(70,103,1)
236    5.        DIMENSION UET(70),UZT(70),DTC(70),U(70),V(70),C(70)
237    C
238    C         SET UP INITIAL CFL TIME STEP VALUE
239    C
240    6.        DTC(1)=1.0
241    7.        GAMM2=GAMMA*GAMM1
242    8.        DTCFL=1.0
243    9.        RDET=1.0/DETA
244    10.       RDZT=1.0/DZETA
245    C
246    11.       DO 1 J=2,JLM
247    12.       DO 2 K=2,KLM
248    C
249    13.       RH=1.0/RHO(K,J,1)
250    14.       U(K)=RHOU(K,J,1)*RH
251    15.       V(K)=RHOV(K,J,1)*RH
252    16.       C(K)=SQRT(GAMM2*(RHOE(K,J,1)*RH-0.5*(U(K)**2+V(K)**2)))
253    C
254    17.       UET(K)=ETX(K,J,1)*U(K)+ETY(K,J,1)*V(K)
255    18.       UZT(K)=ZTX(K,J,1)*U(K)+ZTY(K,J,1)*V(K)
256    C
257    19.       DTC(K)=1.0/(ABS(UET(K))*RDET+ABS(UZT(K))*RDZT+
258             1 C(K)*SQRT((ETX(K,J,1)*RDET+ZTX(K,J,1)*RDZT)**2+
259             2           (ETY(K,J,1)*RDET+ZTY(K,J,1)*RDZT)**2))
260    C
261    20.  2    CONTINUE
262    C
263    C         PERFORM THE COMPARISON AND MODIFIED THE CFL TIME STEP
264    C
265    21.       DTMIN=DTC(1)
266    22.       DO 3 K=2,KLM
267    23.       KM1=K-1
268    24.       DTMIN=AMIN1(DTC(K),DTMIN)
269    25.  3    CONTINUE
270    C
271    C         COMPARING DTMIN BETWEEN ADJACENT PLANES
272    26.       DTCFL=AMIN1(DTCFL,DTMIN)
273    C
274    27.  1    CONTINUE
275    C
276    C         ADJUST DTCFL FOR VISCOUS EFFECT (TRAIL AND ERROR)
277    28.       DT=CFL*DTCFL
278    C
279    29.       RETURN
280    30.       END
TMSTEP          VECTOR LOOP BEGINS AT SEQ. NO.        12, P=      676B
```

191

```
281    1.          SUBROUTINE BC
282    2.          COMMON / / PW,DETA,DZETA,CV,RC,PR,PRT,GAMMA,EP(70,103,1),
283              1 GAMM1,CFL,BETA,UINF,RHOINF,CINF,TINF,TW,DT,CX,CY,CZ,L,
284              2 IL,JL,KL,ILM,JLM,KLM,ILE,LS,ISMTHX,ISMTHY,ISMTHZ
285    3.          COMMON /DOF/ X(70,103,1),Y(70,103,1),Z(1,1,1)
286    4.          COMMON /TV/ ETX(70,103,1),ETY(70,103,1),ETZ(1,1,1),
287              1 ZTX(70,103,1),ZTY(70,103,1),ZTZ(1,1,1)
288    5.          COMMON /DEP/ RHO(70,103,1),RHOU(70,103,1),RHOV(70,103,1),
289              1 RHOW(1,1,1),RHOE(70,103,1)
290    6.          COMMON /DEPP/ RHOP(70,103,1),RHOUP(70,103,1),RHOVP(70,103,1),
291              1 RHOWP(1,1,1),RHOEP(70,103,1)
292       C
293    7.          RUINF=RHOINF*UINF
294    8.          REINF=RHOINF*(CV*TINF+0.5*UINF**2)
295    9.          KLM4=KL-4
296   10.          KLM2=KL-2
297   11.          KLM3=KL-3
298       C
299   12.          IF(L.EQ.2) GO TO 10
300       C
301       C                    ****************
302       C                    PREDICTOR SWEEP
303       C                    ****************
304       C
305       C          ON THE SOLID CONTOUR, NO-SLIP FOR U,V,W,CONSTANT SURFACE TEMP.
306       C          AND DP/DN=0. APPROXIMATION
307       C
308   13.          DO 1 J=2,JLM
309   14.          RH=1.0/RHOP(2,J,1)
310   15.          RHOUP(1,J,1)=0.0
311   16.          RHOVP(1,J,1)=0.0
312   17.          RHOP(1,J,1)=RHOP(2,J,1)*(RHOEP(2,J,1)*RH-0.5*
313              1 ((RHOUP(2,J,1)*RH)**2+(RHOVP(2,J,1)*RH)**2))/(CV*TW)
314   18.          RHOEP(1,J,1)=RHOP(1,J,1)*CV*TW
315   19.  1       CONTINUE
316       C
317       C          DOWNSTREAM BOUNDARY CONDITION
318       C
319   20.          DO 2 K=1,KL
320   21.          RHOP(K,JL,1)=RHOP(K,JLM,1)
321   22.          RHOUP(K,JL,1)=RHOUP(K,JLM,1)
322   23.          RHOVP(K,JL,1)=RHOVP(K,JLM,1)*Y(K,JLM,1)/Y(K,JL,1)
323   24.          RHOEP(K,JL,1)=RHOEP(K,JLM,1)
324   25.  2       CONTINUE
325       C
326       C          SET OUTFLOW PRESSURE
327       C
328   26.          DO 20 K=35,KLM
329   27.          RH=1.0/RHOP(K,JL,1)
330   28.          U=RHOUP(K,JL,1)*RH
331   29.          V=RHOVP(K,JL,1)*RH
332   30.          T=(RHOEP(K,JL,1)*RH-0.5*(U**2+V**2))/CV
333   31.          RHOP(K,JL,1)=PW/(RC*T)
334   32.          RHOUP(K,JL,1)=RHOP(K,JL,1)*U
335   33.          RHOVP(K,JL,1)=RHOP(K,JL,1)*V
336   34.          RHOEP(K,JL,1)=RHOP(K,JL,1)*(CV*T+0.5*(U**2+V**2))
337   35.  20      CONTINUE
338       C
339       C          THE SYMMETRY BOUNDARY CONDITIONS
340       C
341   36.          DO 3 J=2,JL
342   37.          RHOP (KL,J,1)=RHOP (KLM,J,1)
343   38.          RHOUP(KL,J,1)=0.0
344   39.          RHOVP(KL,J,1)=RHOVP(KLM,J,1)
345   40.          RHOEP(KL,J,1)=RHOEP(KLM,J,1)
346   41.  3       CONTINUE
347       C
348       C
349   42.          GO TO 100
350       C
351       C                    ****************
352       C                    CORRECTOR SWEEP
353       C                    ****************
354       C
355       C          ON THE SOLID CONTOUR, NO-SLIP FOR U,V,W, CONSTANT SURFACE TEMP.
356       C          AND DP/DN=0. APPROXIMATION
357       C
358   43.  10      DO 11 J=2,JLM
359   44.          RH=1.0/RHO(2,J,1)
360   45.          RHOU(1,J,1)=0.0
```

192

```
361   46.        RHOV(1,J,1)=0.0
362   47.        RHO(1,J,1)=RHO(2,J,1)*(RHOE(2,J,1)*RH-0.5*
363            1 ((RHOU(2,J,1)*RH)**2+(RHOV(2,J,1)*RH)**2))/(CV*TW)
364   48.        RHOE(1,J,1)=RHO(1,J,1)*CV*TW
365   49.     11 CONTINUE
366         C
367         C     DOWNSTREAM BOUNDARY CONDITIONS
368         C
369   50.        DO 13 K=1,KL
370   51.        RHO(K,JL,1)=RHO(K,JLM,1)
371   52.        RHOU(K,JL,1)=RHOU(K,JLM,1)
372   53.        RHOV(K,JL,1)=RHOV(K,JLM,1)*Y(K,JLM,1)/Y(K,JL,1)
373   54.        RHOE(K,JL,1)=RHOE(K,JLM,1)
374   55.     13 CONTINUE
375         C
376         C     SET OUTFLOW PRESSURE
377         C
378   56.        DO 21 K=35,KLM
379   57.        RH=1.0/RHO(K,JL,1)
380   58.        U=RHOU(K,JL,1)*RH
381   59.        V=RHOV(K,JL,1)*RH
382   60.        T=(RHOE(K,JL,1)*RH-0.5*(U**2+V**2))/CV
383   61.        RHO(K,JL,1)=PW/(RC*T)
384   62.        RHOU(K,JL,1)=RHO(K,JL,1)*U
385   63.        RHOV(K,JL,1)=RHO(K,JL,1)*V
386   64.        RHOE(K,JL,1)=RHO(K,JL,1)*(CV*T+0.5*(U**2+V**2))
387   65.     21 CONTINUE
388         C
389         C     SET SYMMETRY BOUNDARY CONDITIONS
390   66.        DO 14 J=2,JL
391   67.        RHO (KL,J,1)=RHO (KLM,J,1)
392   68.        RHOU(KL,J,1)=0.0
393   69.        RHOV(KL,J,1)=RHOV(KLM,J,1)
394   70.        RHOE(KL,J,1)=RHOE(KLM,J,1)
395   71.     14 CONTINUE
396         C
397         C
398   72.   100 RETURN
399   73.        END
BC            VECTOR LOOP BEGINS AT SEQ. NO.           13, P=      22B
BC            VECTOR LOOP BEGINS AT SEQ. NO.           20, P=      72C
BC            VECTOR LOOP BEGINS AT SEQ. NO.           26, P=     130C
BC            VECTOR LOOP BEGINS AT SEQ. NO.           36, P=     173B
BC            VECTOR LOOP BEGINS AT SEQ. NO.           43, P=     224C
BC            VECTOR LOOP BEGINS AT SEQ. NO.           50, P=     262D
BC            VECTOR LOOP BEGINS AT SEQ. NO.           56, P=     320D
BC            VECTOR LOOP BEGINS AT SEQ. NO.           66, P=     363C
```

```
400     1.          SUBROUTINE TRANS
401     2.          COMMON / / PW,DETA,DZETA,CV,RC,PR,PRT,GAMMA,EP(70,103,1),
402               1 GAMM1,CFL,BETA,!!INF,RHOINF,CINF,TINF,TW,DT,CX,CY,CZ,L,
403               2 IL,JL,KL,ILM,JLM,KLM,ILE,LS,ISMTHX,ISMTHY,ISMTHZ
404     3. .      COMMON /TV/ ETX(70,103,1),ETY(70,103,1),ETZ(1,1,1),
405               1 ZTX(70,103,1),ZTY(70,103,1),ZTZ(1,1,1)
406     4.          COMMON /DOF/ X(70,103,1),Y(70,103,1),Z(1,1,1)
407     5.          DIMENSION XET(70,103),YET(70,103),DJ(70,103),
408               1 XZT(70,103),YZT(70,103),RDJ(70,103)
409          C
410     6.          RDET=1.0/(2.0*DETA)
411     7.          RDZT=1.0/(2.0*DZETA)
412     8.          JLM2=JLM-1
413     9.          KLM2=KLM-1
414          C
415          C      SET THE DUMMY THREE DIMENSIONAL METRICS
416          C
417    10.          ETZ(1,1,1)=0.0
418    11.          ZTZ(1,1,1)=0.0
419          C
420          C
421          C      GENERATING DX/DTEA AND DY/DTEA
422          C
423          C
424          C      ONE-SIDE DIFFERENCING FOR J=1
425          C
426    12.          DO 101 KV=1,KL
427    13.          XET(KV,1)=(4.0*X(KV,2,1)-X(KV,3,1)-3.0*X(KV,1,1))*RDET
428    14.          YET(KV,1)=(4.0*Y(KV,2,1)-Y(KV,3,1)-3.0*Y(KV,1,1))*RDET
429    15.  101     CONTINUE
430          C
431          C      ONE-SIDE DIFFERENCING FOR J=JL
432          C
433    16.          DO 102 KV=1,KL
434    17.          XET(KV,JL)=-(4.0*X(KV,JLM,1)-X(KV,JLM2,1)-3.0*X(KV,JL,1))*RDET
435    18.          YET(KV,JL)=-(4.0*Y(KV,JLM,1)-Y(KV,JLM2,1)-3.0*Y(KV,JL,1))*RDET
436    19.  102     CONTINUE
437          C
438          C      CENTRAL DIFFERENCING FOR FIELD POINTS
439          C
440    20.          DO 103 JV=2,JLM
441    21.          JP=JV+1
442    22.          JM=JV-1
443    23.          DO 104 KV=1,KL
444    24.          XET(KV,JV)=(X(KV,JP,1)-X(KV,JM,1))*RDET
445    25.          YET(KV,JV)=(Y(KV,JP,1)-Y(KV,JM,1))*RDET
446    26.  104     CONTINUE
447    27.  103     CONTINUE
448          C
449          C      GENERATING DX/DZETA AND DY/DZETA
450          C
451          C
452          C      ONE-SIDE DIFFERENCING FOR K=1
453          C
454    28.          DO 201 JV=1,JL
455    29.          XZT(1,JV)=(4.0*X(2,JV,1)-X(3,JV,1)-3.0*X(1,JV,1))*RDZT
456    30.          YZT(1,JV)=(4.0*Y(2,JV,1)-Y(3,JV,1)-3.0*Y(1,JV,1))*RDZT
457    31.  201     CONTINUE
458          C
459          C      ONE-SIDE DIFFERENCING FOR K=KL
460          C
461    32.          DO 202 JV=1,JL
462    33.          XZT(KL,JV)=-(4.0*X(KLM,JV,1)-X(KLM2,JV,1)-3.0*X(KL,JV,1))*RDZT
463    34.          YZT(KL,JV)=-(4.0*Y(KLM,JV,1)-Y(KLM2,JV,1)-3.0*Y(KL,JV,1))*RDZT
464    35.  202     CONTINUE
465          C
466          C      CENTRAL DIFFERENCING FOR FIELD POINTS
467          C
468    36.          DO 203 JV=1,JL
469    37.          DO 204 KV=2,KLM
470    38.          KP=KV+1
471    39.          KM=KV-1
472    40.          XZT(KV,JV)=(X(KP,JV,1)-X(KM,JV,1))*RDZT
473    41.          YZT(KV,JV)=(Y(KP,JV,1)-Y(KM,JV,1))*RDZT
474    42.  204     CONTINUE
475    43.  203     CONTINUE
476          C
477          C      GENERATING THE INVERSE JACOBIAN OF TRANSFORMATION
478          C
```

```
479   44.          DO 300 JV=1,JL
480   45.          DO 301 KV=1,KL
481   46.          DJ(KV,JV)=XET(KV,JV)*YZT(KV,JV)-XZT(KV,JV)*YET(KV,JV)
482   47.   301    CONTINUE
483   48.   300    CONTINUE
484        C
485        C
486   49.          DO 303 JV=1,JL
487   50.          DO 304 KV=1,KL
488   51.          RDJ(KV,JV)=1.0/DJ(KV,JV)
489   52.   304    CONTINUE
490   53.   303    CONTINUE
491        C
492        C      GENERATING THE METRICS OF COORDINATES TRANSFORMATION
493        C
494   54.          DO 305 JV=1,JL
495   55.          DO 306 KV=1,KL
496        C
497   56.          ETX(KV,JV,1)= YZT(KV,JV)*RDJ(KV,JV)
498        C
499   57.          ZTX(KV,JV,1)=-YET(KV,JV)*RDJ(KV,JV)
500        C
501   58.          ETY(KV,JV,1)=-XZT(KV,JV)*RDJ(KV,JV)
502        C
503   59.          ZTY(KV,JV,1)= XET(KV,JV)*RDJ(KV,JV)
504        C
505        C
506   60.   306    CONTINUE
507   61.   305    CONTINUE
508        C
509   62.          RETURN
510   63.          END
TRANS            VECTOR LOOP BEGINS AT SEQ. NO.         12, P=  124415B
TRANS            VECTOR LOOP BEGINS AT SEQ. NO.         16, P=  124460D
TRANS            VECTOR LOOP BEGINS AT SEQ. NO.         23, P=  124525C
TRANS            VECTOR LOOP BEGINS AT SEQ. NO.         28, P=  124563B
TRANS            VECTOR LOOP BEGINS AT SEQ. NO.         32, P=  124617D
TRANS            VECTOR LOOP BEGINS AT SEQ. NO.         37, P=  124663C
TRANS            VECTOR LOOP BEGINS AT SEQ. NO.         45, P=  124725B
TRANS            VECTOR LOOP BEGINS AT SEQ. NO.         50, P=  124757C
TRANS            VECTOR LOOP BEGINS AT SEQ. NO.         55, P=  125005D
```

```
511     1.        SUBROUTINE PAGE
512     2.        COMMON / / PW,DETA,DZETA,CV,RC,PR,PRT,GAMMA,EP(70,103,1),
513              1 GAMM1,CFL,BETA,UINF,RHOINF,CINF,TINF,TW,DT,CX,CY,CZ,L,
514              2 IL,JL,KL,ILM,JLM,KLM,ILE,LS,ISMTHX,ISMTHY,ISMTHZ
515     3.        COMMON /DV/ R(70,103,1),U(70,103,1),V(70,103,1),W(1,1,1),
516              1 P(70,103,1),T(70,103,1)
517     4.        COMMON /TV/ ETX(70,103,1),ETY(70,103,1),ETZ(1,1,1),
518              1 ZTX(70,103,1),ZTY(70,103,1),ZTZ(1,1,1)
519     5.        COMMON /DEP/ RHO(70,103,1),RHOU(70,103,1),RHOV(70,103,1),
520              1 RHOW(1,1,1),RHOE(70,103, )
521     6.        COMMON /DEPP/ RHOP(70,103,1),RHOUP(70,103,1),RHOVP(70,103,1),
522              1 RHOWP(1,1,1),RHOEP(70,103,1)
523     C
524     7.        W(1,1,1)=0.0
525     C
526     C              *****************
527     C              PREDICTOR SWEEP
528     C              *****************
529     C
530     8.                    L=1
531     C
532     C        GENERATING THREE PAGES TEMPORAL VECTOR ARRAYS
533     C
534     9.        DO 1 JV=1,JL
535    10.        DO 1 KV=1,KL
536     C
537    11.        R(KV,JV,1)=RHO (KV,JV,1)
538    12.        U(KV,JV,1)=RHOU(KV,JV,1)/R(KV,JV,1)
539    13.        V(KV,JV,1)=RHOV(KV,JV,1)/R(KV,JV,1)
540    14.        T(KV,JV,1)=(RHOE(KV,JV,1)/R(KV,JV,1)-0.5*(U(KV,JV,1)**2
541              1 +V(KV,JV,1)**2))/CV
542    15.        P(KV,JV,1)=R(KV,JV,1)*RC*T(KV,JV,1)
543     C
544    16.  1     CONTINUE
545     C
546     C
547     C
548    17.        DO 2 J=2,JLM
549    18.        CALL LETA(J)
550    19.        CALL LZETA(J)
551    20.        CALL SUM(J)
552    21.  2     CONTINUE
553     C
554    22.        CALL BC
555     C
556     C
557     C              *****************
558     C              CORRECTOR SWEEPS
559     C              *****************
560     C
561    23.                    L=2
562     C
563     C
564     C        GENERATING THREE PAGES TEMPORAL VECTOR ARRAYS
565     C
566    24.        DO 10 JV=1,JL
567    25.        DO 10 KV=1,KL
568     C
569    26.        R(KV,JV,1)=RHOP (KV,JV,1)
570    27.        U(KV,JV,1)=RHOUP(KV,JV,1)/R(KV,JV,1)
571    28.        V(KV,JV,1)=RHOVP(KV,JV,1)/R(KV,JV,1)
572    29.        T(KV,JV,1)=(RHOEP(KV,JV,1)/R(KV,JV,1)-0.5*(U(KV,JV,1)**2
573              1 +V(KV,JV,1)**2))/CV
574    30.        P(KV,JV,1)=R(KV,JV,1)*RC*T(KV,JV,1)
575     C
576    31.  10    CONTINUE
577     C
578     C
579     C
580    32.        DO 11 J=2,JLM
581    33.        CALL LETA(J)
582    34.        CALL LZETA(J)
583    35.        CALL SUM(J)
584    36.  11    CONTINUE
585     C
586    37.        CALL BC
587     C
588    38.        RETURN
589    39.        END
PAGE          VECTOR LOOP BEGINS AT SEQ. NO.         10, P=      16C
PAGE          VECTOR LOOP BEGINS AT SEQ. NO.         25, P=      104A
```

```
590     1.          SUBROUTINE LETA(J)
591     2.          COMMON / / PH,DETA,DZETA,CV,RC,PR,PRT,GAMMA,EP(70,103,1),
592                 1 GAMM1,CFL,BETA,UINF,RHOINF,CINF,TINF,TW,DT,CX,CY,CZ,L,
593                 2 IL,JL,KL,ILM,JLM,KLM,ILE,LS,ISMTHX,ISMTHY,ISMTHZ
594     3.          COMMON /FLUET/ F21(70,2),F22(70,2),F23(70,2),F25(70,2),
595                 1 G21(70,2),G22(70,2),G23(70,2),G25(70,2),H(70)
596     4.          COMMON /DV/ R(70,103,1),U(70,103,1),V(70,103,1),W(1,1,1),
597                 1 P(70,103,1),T(70,103,1)
598     5.          COMMON /TV/ ETX(70,103,1),ETY(70,103,1),ETZ(1,1,1),
599                 1 ZTX(70,103,1),ZTY(70,103,1),ZTZ(1,1,1)
600     6.          COMMON /DOF/ X(70,103,1),Y(70,103,1),Z(1,1,1)
601     7.          DIMENSION UET(70),UZT(70),VET(70),VZT(70),RMU(70),
602                 1 RLMBD(70),SMU(70),RK(70),TAUXX(70),TAUXR(70),
603                 2 TAURR(70),TX(70),TY(70),TET(70),TZT(70),DUDX(70),
604                 3 DVDR(70)
605         C
606     8.          RDET=1.0/DETA
607     9.          RDZT=1.0/(2.0*DZETA)
608         C
609     10.         DO 1 M=1,2
610         C
611         C
612         C       FORWARD & BACKWARD DIFFERENCING FOR PREDICTOR & CORRECTOR
613         C
614         C
615         C       **********
616     11.         JV=L+M+J-3
617     12.         JM=J+M-2
618     13.         JP=JM+1
619         C       **********
620         C
621         C
622     14.         DO 2 KV=2,KLM
623         C
624     15.         KP=KV+1
625     16.         KM=KV-1
626         C       GENERATING THE SHEAR STRESS & HEAT FLUX TERMS
627         C
628     17.         UET(KV)=(U(KV,JP,1)-U(KV,JM,1))*RDET
629     18.         VET(KV)=(V(KV,JP,1)-V(KV,JM,1))*RDET
630     19.         TET(KV)=(T(KV,JP,1)-T(KV,JM,1))*RDET
631         C
632     20.         UZT(KV)=(U(KP,JV,1)-U(KM,JV,1))*RDZT
633     21.         VZT(KV)=(V(KP,JV,1)-V(KM,JV,1))*RDZT
634     22.         TZT(KV)=(T(KP,JV,1)-T(KM,JV,1))*RDZT
635         C
636         C       GENERATING THE VISCOSITY COEFFS & HEAT CONDUCTIVITY
637         C
638     23.         RMU(KV)=2.27E-08*SQRT(T(KV,JV,1)**3)/(T(KV,JV,1)+198.6)
639     24.         RK(KV)=GAMMA*CV*(RMU(KV)/PR+EP(KV,JV,1)/PRT)
640     25.         RMU(KV)=RMU(KV)+EP(KV,JV,1)
641     26.         RLMBD(KV)=-(2.0/3.0)*RMU(KV)
642     27.         SMU(KV)=2.0*RMU(KV)+RLMBD(KV)
643         C
644     28.  2      CONTINUE
645         C
646     29.         DO 3 KV=2,KLM
647         C
648     30.         RY=1.0/Y(KV,JV,1)
649         C
650     31.         DUDX(KV)=ETX(KV,JV,1)*UET(KV)+ZTX(KV,JV,1)*UZT(KV)
651         C
652     32.         DVDR(KV)=ETY(KV,JV,1)*VET(KV)+ZTY(KV,JV,1)*VZT(KV)
653         C
654     33.         TAUXX(KV)=SMU(KV)*DUDX(KV)+RLMBD(KV)*(V(KV,JV,1)*RY
655                 1 +DVDR(KV))-P(KV,JV,1)
656         C
657     34.         TAURR(KV)=SMU(KV)*DVDR(KV)+RLMBD(KV)*(V(KV,JV,1)*RY
658                 1 +DUDX(KV))-P(KV,JV,1)
659         C
660     35.         TAUXR(KV)=RMU(KV)*(ETY(KV,JV,1)*UET(KV)+ZTY(KV,JV,1)*
661                 1 UZT(KV)+ETX(KV,JV,1)*VET(KV)+ZTX(KV,JV,1)*VZT(KV))
662         C
663     36.  3      CONTINUE
664         C
665     37.         IF(JV.NE.J) GO TO 20
666         C
667     38.         DO 10 KV=2,KLM
668         C
669     39.         RY=1.0/Y(KV,J,1)
```

```
670          C
671    40.     DUDX(KV)=ETX(KV,J,1)*(U(KV,J+1,1)-U(KV,J-1,1))*(0.5*RDET)
672           1 +ZTX(KV,J,1)*(U(KV+1,J,1)-U(KV-1,J,1))*RDZT
673          C
674    41.     DVDR(KV)=ETY(KV,J,1)*(V(KV,J+1,1)-V(KV,J-1,1))*(0.5*RDET)
675           1 +ZTY(KV,J,1)*(V(KV+1,J,1)-V(KV-1,J,1))*RDZT
676          C
677    42.     H(KV)=(SMU(KV)*V(KV,J,1)*RY+RLMBD(KV)*(DUDX(KV)
678           1 +DVDR(KV))-P(KV,J,1))*RY
679          C
680    43.  10  CONTINUE
681          C
682          C
683          C     GENERATING THE HEAT FLUX TERMS
684          C
685    44.  20  DO 4 KV=2,KLM
686          C
687    45.     TX(KV)=ETX(KV,JV,1)*TET(KV)+ZTX(KV,JV,1)*TZT(KV)
688    46.     TY(KV)=ETY(KV,JV,1)*TET(KV)+ZTY(KV,JV,1)*TZT(KV)
689          C
690    47.  4   CONTINUE
691          C
692          C     GENERATING THE FLUX TERMS
693          C
694    48.     DO 5 KV=2,KLM
695          C
696    49.     F21(KV,M)=R(KV,JV,1)*U(KV,JV,1)
697    50.     F22(KV,M)=F21(KV,M)*U(KV,JV,1)-TAUXX(KV)
698    51.     F23(KV,M)=F21(KV,M)*V(KV,JV,1)-TAUXR(KV)
699    52.     F25(KV,M)=F21(KV,M)*(CV*T(KV,JV,1)+0.5*(U(KV,JV,1)**2+
700           1 V(KV,JV,1)**2))-RK(KV)*TX(KV)
701           2 -(U(KV,JV,1)*TAUXX(KV)+V(KV,JV,1)*TAUXR(KV))
702          C
703    53.     G21(KV,M)=R(KV,JV,1)*V(KV,JV,1)*Y(KV,JV,1)
704    54.     G22(KV,M)=G21(KV,M)*U(KV,JV,1)-TAUXR(KV)*Y(KV,JV,1)
705    55.     G23(KV,M)=G21(KV,M)*V(KV,JV,1)-TAURR(KV)*Y(KV,JV,1)
706    56.     G25(KV,M)=G21(KV,M)*(CV*T(KV,JV,1)+0.5*(U(KV,JV,1)**2+
707           1 V(KV,JV,1)**2))-(RK(KV)*TY(KV)
708           2 +(U(KV,JV,1)*TAUXR(KV)+V(KV,JV,1)*TAURR(KV)))*Y(KV,JV,1)
709          C
710    57.  5   CONTINUE
711          C
712    58.  1   CONTINUE
713    59.     RETURN
714    60.     END
LETA         VECTOR LOOP BEGINS AT SEQ. NO.          14, P=     2300A
LETA         VECTOR LOOP BEGINS AT SEQ. NO.          29, P=     2424A
LETA         VECTOR LOOP BEGINS AT SEQ. NO.          38, P=     2520A
LETA         VECTOR LOOP BEGINS AT SEQ. NO.          44, P=     2613D
LETA         VECTOR LOOP BEGINS AT SEQ. NO.          48, P=     2647A
```

```
715    1.        SUBROUTINE LZETA(J)
716    2.        COMMON / / PW,DETA,DZETA,CV,RC,PR,PRT,GAMMA,EP(70,103,1),
717           1 GAMM1,CFL,BETA,UINF,RHOINF,CINF,TINF,TW,DT,CX,CY,CZ,L,
718           2 IL,JL,KL,ILM,JLM,KLM,ILE,LS,ISMTHX,ISMTHY,ISMTHZ
719    3.        COMMON /FLUZT/ F31(70),F32(70),F33(70),F35(70),
720           1 G31(70),G32(70),G33(70),G35(70)
721    4.        COMMON /DV/ R(70,103,1),U(70,103,1),V(70,103,1),W(1,1,1),
722           1 P(70,103,1),T(70,103,1)
723    5.        COMMON /TV/ ETX(70,103,1),ETY(70,103,1),ETZ(1,1,1),
724           1 ZTX(70,103,1),ZTY(70,103,1),ZTZ(1,1,1)
725    6.        COMMON /DOF/ X(70,103,1),Y(70,103,1),Z(1,1,1)
726    7.        DIMENSION UET(70),UZT(70),VET(70),VZT(70),RMU(70),
727           1 RLMBD(70),SMU(70),RK(70),TAUXX(70),TAUXR(70),
728           2 TAURR(70),TX(70),TY(70),TET(70),TZT(70),DUDX(70),
729           3 DVDR(70)
730    C
731    8.        RDET=1.0/(2.0*DETA)
732    9.        RDZT=1.0/DZETA
733   10.        JP=J+1
734   11.        JM=J-1
735    C
736   12.        DO 1 KK=1,KLM
737    C
738    C
739    C         FORWARD & BACKWARD DIFFERENCING FOR PREDICTOR & CORRECTOR
740    C
741    C         *********
742   13.        KV=KK+L-1
743   14.        KM=KK
744   15.        KP=KM+1
745    C         *********
746    C
747    C         GENERATING THE SHEAR STRESS & HEAT FLUX TERMS
748    C
749   16.        UET(KK)=(U(KV,JP,1)-U(KV,JM,1))*RDET
750   17.        VET(KK)=(V(KV,JP,1)-V(KV,JM,1))*RDET
751   18.        TET(KK)=(T(KV,JP,1)-T(KV,JM,1))*RDET
752    C
753   19.        UZT(KK)=(U(KP,J,1)-U(KM,J,1))*RDZT
754   20.        VZT(KK)=(V(KP,J,1)-V(KM,J,1))*RDZT
755   21.        TZT(KK)=(T(KP,J,1)-T(KM,J,1))*RDZT
756    C
757    C         GENERATING THE VISCOSITY COEFFS & HEAT CONDUCTIVITY
758    C
759   22.        RMU(KK)=2.27E-08*SQRT(T(KV,J,1)**3)/(T(KV,J,1)+198.6)
760   23.        RK(KK)=GAMMA*CV*(RMU(KK)/PR+EP(KV,J,1)/PRT)
761   24.        RMU(KK)=RMU(KK)+EP(KV,J,1)
762   25.        RLMBD(KK)=-(2.0/3.0)*RMU(KK)
763   26.        SMU(KK)=2.0*RMU(KK)+RLMBD(KK)
764    C
765   27.  1     CONTINUE
766    C
767   28.        DO 2 KK=1,KLM
768    C
769   29.        KV=KK+L-1
770    C
771   30.        RY=1.0/Y(KV,J,1)
772    C
773   31.        DUDX(KK)=ETX(KV,J,1)*UET(KK)+ZTX(KV,J,1)*UZT(KK)
774    C
775   32.        DVDR(KK)=ETY(KV,J,1)*VET(KK)+ZTY(KV,J,1)*VZT(KK)
776    C
777   33.        TAUXX(KK)=SMU(KK)*DUDX(KK)+RLMBD(KK)*(V(KV,J,1)*RY
778           1 +DVDR(KK))-P(KV,J,1)
779    C
780   34.        TAURR(KK)=SMU(KK)*DVDR(KK)+RLMBD(KK)*(V(KV,J,1)*RY
781           1 +DUDX(KK))-P(KV,J,1)
782    C
783   35.        TAUXR(KK)=RMU(KK)*(ETY(KV,J,1)*UET(KK)+ZTY(KV,J,1)*
784           1 UZT(KK)+ETX(KV,J,1)*VET(KK)+ZTX(KV,J,1)*VZT(KK))
785    C
786    C         GENERATING THE HEAT FLUX TERMS
787    C
788   36.        TX(KK)=ETX(KV,J,1)*TET(KK)+ZTX(KV,J,1)*TZT(KK)
789   37.        TY(KK)=ETY(KV,J,1)*TET(KK)+ZTY(KV,J,1)*TZT(KK)
790    C
791   38.  2     CONTINUE
792    C
793    C
794    C         GENERATING THE FLUX TERMS
795    C
```

```
796    39.         DO 3 KK=1,KLM
797        C
798    40.         KV=KK+L-1
799        C
800    41.         F31(KK)=R(KV,J,1)*U(KV,J,1)
801    42.         F32(KK)=F31(KK)*U(KV,J,1)-TAUXX(KK)
802    43.         F33(KK)=F31(KK)*V(KV,J,1)-TAUXR(KK)
803    44.         F35(KK)=F31(KK)*(CV*T(KV,J,1)+0.5*(U(KV,J,1)**2+
804            1 V(KV,J,1)**2))-RK(KK)*TX(KK)
805            2 -(U(KV,J,1)*TAUXX(KK)+V(KV,J,1)*TAUXR(KK))
806        C
807    45.         G31(KK)=R(KV,J,1)*V(KV,J,1)*Y(KV,J,1)
808    46.         G32(KK)=G31(KK)*U(KV,J,1)-TAUXR(KK)*Y(KV,J,1)
809    47.         G33(KK)=G31(KK)*V(KV,J,1)-TAURR(KK)*Y(KV,J,1)
810    48.         G35(KK)=G31(KK)*(CV*T(KV,J,1)+0.5*(U(KV,J,1)**2+
811            1 V(KV,J,1)**2))-(RK(KK)*TY(KK))
812            2 +(U(KV,J,1)*TAUXR(KK)+V(KV,J,1)*TAURR(KK)))*Y(KV,J,1)
813        C
814    49.  3      CONTINUE
815    50.         RETURN
816    51.         END
LZETA             VECTOR LOOP BEGINS AT SEQ. NO.          12, P=    2271B
LZETA             VECTOR LOOP BEGINS AT SEQ. NO.          28, P=    2420D
LZETA             VECTOR LOOP BEGINS AT SEQ. NO.          39, P=    2534D
```

```
817    1.        SUBROUTINE SUM(J)
818    2.        COMMON / / PW,DETA,DZETA,CV,RC,PR,PRT,GAMMA,EP(70,103,1),
819           1 GAMM1,CFL,BETA,UINF,RHOINF,CINF,TINF,TW,DT,CX,CY,CZ,L,
820           2 IL,JL,KL,ILM,JLM,KLM,ILE,LS,ISMTHX,ISMTHY,ISMTHZ
821    3.        COMMON /FLUET/ F21(70,2),F22(70,2),F23(70,2),F25(70,2),
822           1 G21(70,2),G22(70,2),G23(70,2),G25(70,2),H(70)
823    4.        COMMON /FLUZT/ F31(70),F32(70),F33(70),F35(70),
824           1 G31(70),G32(70),G33(70),G35(70)
825    5.        COMMON /TV/ ETX(70,103,1),ETY(70,103,1),ETZ(1,1,1),
826           1 ZTX(70,103,1),ZTY(70,103,1),ZTZ(1,1,1)
827    6.        COMMON /DEP/ RHO(70,103,1),RHOU(70,103,1),RHOV(70,103,1),
828           1 RHOW(1,1,1),RHOE(70,103,1)
829    7.        COMMON /DEPP/ RHOP(70,103,1),RHOUP(70,103,1),RHOVP(70,103,1),
830           1 RHOWP(1,1,1),RHOEP(70,103,1)
831    8.        COMMON /DAMP/ ADD1(70),ADD2(70),ADD3(70),ADD5(70)
832    9.        COMMON /DOF/ X(70,103,1),Y(70,103,1),Z(1,1,1)
833       C
834   10.        RDET=1.0/DETA
835   11.        RDZT=1.0/DZETA
836   12.        RHOWP(1,1,1)=0.0
837   13.        RHOW (1,1,1)=0.0
838       C
839   14.        IF(L.EQ.2) GO TO 100
840       C
841       C                        ****************
842       C                        PREDICTOR SWEEPS
843       C                        ****************
844       C
845   15.        DO 1 KV=2,KLM
846       C
847   16.        KM=KV-1
848   17.        RY=1.0/Y(KV,J,1)
849       C
850   18.        RHOP(KV,J,1)=RHO(KV,J,1)-DT*((ETX(KV,J,1)*(F21(KV,2)-F21(KV,1))
851           1 +ETY(KV,J,1)*RY*(G21(KV,2)-G21(KV,1)))*RDET+(ZTX(KV,J,1)*
852           2 (F31(KV)-F31(KM))+ZTY(KV,J,1)*RY*(G31(KV)-G31(KM)))*RDZT)
853       C
854   19.        RHOUP(KV,J,1)=RHOU(KV,J,1)-DT*((ETX(KV,J,1)*(F22(KV,2)-F22(KV,1))
855           1 +ETY(KV,J,1)*RY*(G22(KV,2)-G22(KV,1)))*RDET+(ZTX(KV,J,1)*
856           2 (F32(KV)-F32(KM))+ZTY(KV,J,1)*RY*(G32(KV)-G32(KM)))*RDZT)
857       C
858   20.  1     CONTINUE
859       C
860   21.        DO 2 KV=2,KLM
861       C
862   22.        KM=KV-1
863   23.        RY=1.0/Y(KV,J,1)
864       C
865   24.        RHOVP(KV,J,1)=RHOV(KV,J,1)-DT*((ETX(KV,J,1)*(F23(KV,2)-F23(KV,1))
866           1 +ETY(KV,J,1)*RY*(G23(KV,2)-G23(KV,1)))*RDET+(ZTX(KV,J,1)*
867           2 (F33(KV)-F33(KM))+ZTY(KV,J,1)*RY*(G33(KV)-G33(KM)))*RDZT+H(KV))
868       C
869   25.        RHOEP(KV,J,1)=RHOE(KV,J,1)-DT*((ETX(KV,J,1)*(F25(KV,2)-F25(KV,1))
870           1 +ETY(KV,J,1)*RY*(G25(KV,2)-G25(KV,1)))*RDET+(ZTX(KV,J,1)*
871           2 (F35(KV)-F35(KM))+ZTY(KV,J,1)*RY*(G35(KV)-G35(KM)))*RDZT)
872       C
873   26.  2     CONTINUE
874       C
875   27.        IF((ISMTHX.EQ.0).AND.(ISMTHY.EQ.0)) GO TO 200
876       C
877   28.        CALL DAMPING(J)
878       C
879   29.        DO 10 KV=2,KLM
880       C
881   30.        RHOP (KV,J,1)=RHOP (KV,J,1)+ADD1(KV)
882   31.        RHOUP(KV,J,1)=RHOUP(KV,J,1)+ADD2(KV)
883   32.        RHOVP(KV,J,1)=RHOVP(KV,J,1)+ADD3(KV)
884   33.        RHOEP(KV,J,1)=RHOEP(KV,J,1)+ADD5(KV)
885   34.  10    CONTINUE
886       C
887   35.        GO TO 200
888       C
889       C                        ****************
890       C                        CORRECTOR SWEEPS
891       C                        ****************
892   36.  100   DO 3 KV=2,KLM
893       C
894   37.        KM=KV-1
895   38.        RY=1.0/Y(KV,J,1)
```

```
 896          C
 897    39.      RHO(KV,J,1)=0.5*(RHO(KV,J,1)+RHOP(KV,J,1)-DT*((ETX(KV,J,1)*
 898           1 (F21(KV,2)-F21(KV,1))+ETY(KV,J,1)*RY*(G21(KV,2)-G21(KV,1)))*RDET
 899           2 +(ZTX(KV,J,1)*(F31(KV)-F31(KM))+ZTY(KV,J,1)*RY*(G31(KV)-G31(KM)))
 900           3 *RDZT))
 901          C
 902    40.      RHOU(KV,J,1)=0.5*(RHOU(KV,J,1)+RHOUP(KV,J,1)-DT*((ETX(KV,J,1)*
 903           1 (F22(KV,2)-F22(KV,1))+ETY(KV,J,1)*RY*(G22(KV,2)-G22(KV,1)))*RDET
 904           2 +(ZTX(KV,J,1)*(F32(KV)-F32(KM))+ZTY(KV,J,1)*RY*(G32(KV)-G32(KM)))
 905           3 *RDZT))
 906          C
 907    41.  3   CONTINUE
 908          C
 909    42.      DO 4 KV=2,KLM
 910          C
 911    43.      KM=KV-1
 912    44.      RY=1.0/Y(KV,J,1)
 913          C
 914    45.      RHOV(KV,J,1)=0.5*(RHOV(KV,J,1)+RHOVP(KV,J,1)-DT*((ETX(KV,J,1)*
 915           1 (F23(KV,2)-F23(KV,1))+ETY(KV,J,1)*RY*(G23(KV,2)-G23(KV,1)))*RDET
 916           2 +(ZTX(KV,J,1)*(F33(KV)-F33(KM))+ZTY(KV,J,1)*RY*(G33(KV)-G33(KM)))
 917           3 *RDZT+H(KV)))
 918          C
 919    46.      RHOE(KV,J,1)=0.5*(RHOE(KV,J,1)+RHOEP(KV,J,1)-DT*((ETX(KV,J,1)*
 920           1 (F25(KV,2)-F25(KV,1))+ETY(KV,J,1)*RY*(G25(KV,2)-G25(KV,1)))*RDET
 921           2 +(ZTX(KV,J,1)*(F35(KV)-F35(KM))+ZTY(KV,J,1)*RY*(G35(KV)-G35(KM)))
 922           3 *RDZT))
 923          C
 924    47.  4   CONTINUE
 925          C
 926    48.      IF((ISMTHX.EQ.0).AND.(ISMTHY.EQ.0)) GO TO 200
 927          C
 928    49.      CALL DAMPING(J)
 929          C
 930    50.      DO 20 KV=2,KLM
 931          C
 932    51.      RHO (KV,J,1)=RHO (KV,J,1)+ADD1(KV)
 933    52.      RHOU(KV,J,1)=RHOU(KV,J,1)+ADD2(KV)
 934    53.      RHOV(KV,J,1)=RHOV(KV,J,1)+ADD3(KV)
 935    54.      RHOE(KV,J,1)=RHOE(KV,J,1)+ADD5(KV)
 936          C
 937    55. 20   CONTINUE
 938          C
 939    56. 200  RETURN
 940    57.      END
SUM           VECTOR LOOP BEGINS AT SEQ. NO.        15, P=        15B
SUM           VECTOR LOOP BEGINS AT SEQ. NO.        21, P=       126B
SUM           VECTOR LOOP BEGINS AT SEQ. NO.        29, P=       234A
SUM           VECTOR LOOP BEGINS AT SEQ. NO.        36, P=       276C
SUM           VECTOR LOOP BEGINS AT SEQ. NO.        42, P=       404B
SUM           VECTOR LOOP BEGINS AT SEQ. NO.        50, P=       514B
```

```
941    1.       SUBROUTINE DAMPING(J)
942    2.       COMMON / / PW,DETA,DZETA,CV,RC,PR,PRT,GAMMA,EP(70,103,1),
943           1 GAMM1,CFL,BETA,UINF,RHOINF,CINF,TINF,TW,DT,CX,CY,CZ,L,
944           2 IL,JL,KL,ILM,JLM,KLM,ILE,LS,ISMTHX,ISMTHY,ISMTHZ
945    3.       COMMON /DEP/ RHO(70,103,1),RHOU(70,103,1),RHOV(70,103,1),
946           1 RHOW(1,1,1),RHOE(70,103,1)
947    4.       COMMON /DEPP/ RHOP(70,103,1),RHOUP(70,103,1),RHOVP(70,103,1),
948           1 RHOWP(1,1,1),RHOEP(70,103,1)
949    5.       COMMON /DAMP/ ADD1(70),ADD2(70),ADD3(70),ADD5(70)
950    6.       COMMON /DV/ R(70,103,1),U(70,103,1),V(70,103,1),W(1,1,1),
951           1 P(70,103,1),T(70,103,1)
952    7.       COMMON /TV/ ETX(70,103,1),ETY(70,103,1),ETZ(1,1,1),
953           1 ZTX(70,103,1),ZTY(70,103,1),ZTZ(1,1,1)
954    8.       DIMENSION ADDG1(70),ADDG2(70),ADDG3(70),
955           2 ADDG5(70),ADDH1(70),ADDH2(70),ADDH3(70),
956           3 ADDH5(70),PD(70,2)
957        C
958    9.       KLM2=KLM-1
959    10.      GAMMR=GAMMA*RC
960    11.      RDET=1.0/DETA
961    12.      RDZT=1.0/DZETA
962        C
963        C    SET DAMPING TERMS TO ZERO FOR END POINTS
964        C
965    13.      DO 1 KV=1,KL
966        C
967    14.      ADDG1(KV)=0.0
968    15.      ADDG2(KV)=0.0
969    16.      ADDG3(KV)=0.0
970    17.      ADDG5(KV)=0.0
971        C
972    18.      ADDH1(KV)=0.0
973    19.      ADDH2(KV)=0.0
974    20.      ADDH3(KV)=0.0
975    21.      ADDH5(KV)=0.0
976        C
977    22.  1   CONTINUE
978        C
979        C        *** GENERATING ADDG ***
980        C
981    23.      IF((J.LE.2).OR.(J.GE.JLM)) GO TO 200
982        C
983    24.      DO 110 M=1,2
984        C
985    25.      JV=J+M+L-3
986    26.      JP=JV+1
987    27.      JM=JV-1
988        C
989    28.      DO 120 KV=1,KL
990    29.      PD(KV,M)=CY*(ABS(P(KV,JP,1)-2.0*P(KV,JV,1)+
991           1 P(KV,JM,1))/(P(KV,JP,1)+2.0*P(KV,JV,1)+P(KV,JM,1)))*
992           2 (ABS(ETX(KV,JV,1)*U(KV,JV,1)+ETY(KV,JV,1)*V(KV,JV,1))+
993           3 SQRT(GAMMR*T(KV,JV,1)*(ETX(KV,JV,1)**2+ETY(KV,JV,1)**2)))
994    30. 120  CONTINUE
995    31. 110  CONTINUE
996        C
997    32.      IF(L.EQ.2) GO TO 140
998        C
999        C            PREDICTOR
1000       C
1001   33.      JP=J+1
1002   34.      JM=J-1
1003       C
1004   35.      DO 130 KV=1,KL
1005       C
1006   36.      ADDG1(KV)=DT*(PD(KV,2)*(RHO (KV,JP,1)-RHO (KV,J,1))-
1007          1 PD(KV,1)*(RHO (KV,J,1)-RHO (KV,JM,1)))*RDET
1008   37.      ADDG2(KV)=DT*(PD(KV,2)*(RHOU(KV,JP,1)-RHOU(KV,J,1))-
1009          1 PD(KV,1)*(RHOU(KV,J,1)-RHOU(KV,JM,1)))*RDET
1010   38.      ADDG3(KV)=DT*(PD(KV,2)*(RHOV(KV,JP,1)-RHOV(KV,J,1))-
1011          1 PD(KV,1)*(RHOV(KV,J,1)-RHOV(KV,JM,1)))*RDET
1012   39.      ADDG5(KV)=DT*(PD(KV,2)*(RHOE(KV,JP,1)-RHOE(KV,J,1))-
1013          1 PD(KV,1)*(RHOE(KV,J,1)-RHOE(KV,JM,1)))*RDET
1014       C
1015   40. 130  CONTINUE
1016   41.      GO TO 200
1017       C
1018       C            CORRECTOR
1019   42. 140  JP=J+1
1020   43.      JM=J-1
```

```
1021        C
1022   44.        DO 150 KV=1,KL
1023        C
1024   45.        ADDG1(KV)=DT*(PD(KV,2)*(RHOP (KV,JP,1)-RHOP (KV,J,1))-
1025          1 PD(KV,1)*(RHOP (KV,J,1)-RHOP (KV,JM,1)))*RDET
1026   46.        ADDG2(KV)=DT*(PD(KV,2)*(RHOUP(KV,JP,1)-RHOUP(KV,J,1))-
1027          1 PD(KV,1)*(RHOUP(KV,J,1)-RHOUP(KV,JM,1)))*RDET
1028   47.        ADDG3(KV)=DT*(PD(KV,2)*(RHOVP(KV,JP,1)-RHOVP(KV,J,1))-
1029          1 PD(KV,1)*(RHOVP(KV,J,1)-RHOVP(KV,JM,1)))*RDET
1030   48.        ADDG5(KV)=DT*(PD(KV,2)*(RHOEP(KV,JP,1)-RHOEP(KV,J,1))-
1031          1 PD(KV,1)*(RHOEP(KV,J,1)-RHOEP(KV,JM,1)))*RDET
1032        C
1033   49.   150 CONTINUE
1034        C
1035        C
1036        C              *** GENERATING ADDH ***
1037        C
1038   50.   200  DO 210 M=1,2
1039   51.        DO 220 K=3,KLM2
1040        C
1041   52.        KV=K+M+L-3
1042   53.        KP=KV+1
1043   54.        KM=KV-1
1044        C
1045   55.        PD(K,M)=CZ*(ABS(P(KP,J,1)-2.0*P(KV,J,1)+
1046          1 P(KM,J,1))/(P(KP,J,1)+2.0*P(KV,J,1)+P(KM,J,1)))*
1047          2 (ABS(ZTX(KV,J,1)*U(KV,J,1)+ZTY(KV,J,1)*V(KV,J,1))+
1048          3 SQRT(GAMMR*T(KV,J,1)*(ZTX(KV,J,1)**2+ZTY(KV,J,1)**2)))
1049        C
1050   56.   220  CONTINUE
1051        C
1052        C    EXTEND THE DAMPING RANGE FROM 3<K<KLM2 TO 3<K<KLM
1053        C    USE THE SYMMETRIC PROPERTY OF THE FLOW FIELD
1054        C
1055   57.        KV=KLM+M+L-3
1056   58.        KP=KV+1
1057   59.        KM=KV-1
1058   60.        PP=P(KLM2,J,1)
1059   61.        IF(KP.LE.KL) PP=P(KP,J,1)
1060   62.        PD(KLM,M)=CZ*(ABS(PP-2.0*P(KV,J,1)+P(KM,J,1))/
1061          1 (PP+2.0*P(KV,J,1)+P(KM,J,1)))*
1062          2 (ABS(ZTX(KV,J,1)*U(KV,J,1)+ZTY(KV,J,1)*V(KV,J,1))
1063          3 +SQRT(GAMMR*T(KV,J,1)*(ZTX(KV,J,1)**2+ZTY(KV,J,1)**2)))
1064        C
1065   63.   210 CONTINUE
1066        C
1067   64.        IF(L.EQ.2) GO TO 240
1068        C
1069        C              PREDICTOR
1070        C
1071   65.        DO 230 KV=3,KLM
1072        C
1073   66.        KP=KV+1
1074   67.        KM=KV-1
1075        C
1076   68.        ADDH1(KV)=DT*(PD(KV,2)*(RHO (KP,J,1)-RHO (KV,J,1))-
1077          1 PD(KV,1)*(RHO (KV,J,1)-RHO (KM,J,1)))*RDZT
1078   69.        ADDH2(KV)=DT*(PD(KV,2)*(RHOU(KP,J,1)-RHOU(KV,J,1))-
1079          1 PD(KV,1)*(RHOU(KV,J,1)-RHOU(KM,J,1)))*RDZT
1080   70.        ADDH3(KV)=DT*(PD(KV,2)*(RHOV(KP,J,1)-RHOV(KV,J,1))-
1081          1 PD(KV,1)*(RHOV(KV,J,1)-RHOV(KM,J,1)))*RDZT
1082   71.        ADDH5(KV)=DT*(PD(KV,2)*(RHOE(KP,J,1)-RHOE(KV,J,1))-
1083          1 PD(KV,1)*(RHOE(KV,J,1)-RHOE(KM,J,1)))*RDZT
1084        C
1085   72.   230 CONTINUE
1086        C
1087   73.        GO TO 300
1088        C
1089        C              CORRECTOR
1090        C
1091   74.   240  DO 250 KV=3,KLM
1092        C
1093   75.        KP=KV+1
1094   76.        KM=KV-1
1095        C
```

```
1096    77.        ADDH1(KV)=DT*(PD(KV,2)*(RHOP (KP,J,1)-RHOP (KV,J,1))-
1097                1 PD(KV,1)*(RHOP (KV,J,1)-RHOP (KM,J,1)))*RDZT
1098    78.        ADDH2(KV)=DT*(PD(KV,2)*(RHOUP(KP,J,1)-RHOUP(KV,J,1))-
1099                1 PD(KV,1)*(RHOUP(KV,J,1)-RHOUP(KM,J,1)))*RDZT
1100    79.        ADDH3(KV)=DT*(PD(KV,2)*(RHOVP(KP,J,1)-RHOVP(KV,J,1))-
1101                1 PD(KV,1)*(RHOVP(KV,J,1)-RHOVP(KM,J,1)))*RDZT
1102    80.        ADDH5(KV)=DT*(PD(KV,2)*(RHOEP(KP,J,1)-RHOEP(KV,J,1))-
1103                1 PD(KV,1)*(RHOEP(KV,J,1)-RHOEP(KM,J,1)))*RDZT
1104           C
1105    81. 250   CONTINUE
1106           C
1107           C   SUMMING THE ARTIFICIAL VISCOSITY-LIKE TERMS
1108           C
1109    82. 300   DO 310 KV=1,KL
1110           C
1111    83.        ADD1(KV)=ISMTHX*ADDG1(KV)+ISMTHY*ADDH1(KV)
1112    84.        ADD2(KV)=ISMTHX*ADDG2(KV)+ISMTHY*ADDH2(KV)
1113    85.        ADD3(KV)=ISMTHX*ADDG3(KV)+ISMTHY*ADDH3(KV)
1114    86.        ADD5(KV)=ISMTHX*ADDG5(KV)+ISMTHY*ADDH5(KV)
1115           C
1116    87. 310   CONTINUE
1117           C
1118    88.        RETURN
1119    89.        END
DAMPING            VECTOR LOOP BEGINS AT SEQ. NO.          13, P=     1321B
DAMPING            VECTOR LOOP BEGINS AT SEQ. NO.          28, P=     1364C
DAMPING            VECTOR LOOP BEGINS AT SEQ. NO.          35, P=     1444C
DAMPING            VECTOR LOOP BEGINS AT SEQ. NO.          44, P=     1534D
DAMPING            VECTOR LOOP BEGINS AT SEQ. NO.          51, P=     1620D
DAMPING            VECTOR LOOP BEGINS AT SEQ. NO.          65, P=     1702A
DAMPING            VECTOR LOOP BEGINS AT SEQ. NO.          74, P=     2026C
DAMPING            VECTOR LOOP BEGINS AT SEQ. NO.          82, P=     2111C
```

```
1120    1.          SUBROUTINE EDDY
1121    2.          COMMON / / PW,DETA,DZETA,CV,RC,PR,PRT,GAMMA,EP(70,103,1),
1122               1 GAMM1,CFL,BETA,UINF,RHOINF,CINF,TINF,TW,DT,CX,CY,CZ,L,
1123               2 IL,JL,KL,ILM,JLM,KLM,ILE,LS,ISMTHX,ISMTHY,ISMTHZ,
1124               3 FLOWF,WN,WFBB,WT,OMEGA(70,103)
1125    3.          COMMON /DEP/ RHO(70,103,1),RHOU(70,103,1),RHOV(70,103,1),
1126               1 RHOW(1,1,1),RHOE(70,103,1)
1127    4.          COMMON /DOF/ X(70,103,1),Y(70,103,1),Z(1,1,1)
1128    5.          COMMON /TV/ ETX(70,103,1),ETY(70,103,1),ETZ(1,1,1),
1129               1 ZTX(70,103,1),ZTY(70,103,1),ZTZ(1,1,1)
1130    6.          COMMON /DV/ R(70,103,1),U(70,103,1),V(70,103,1),W(1,1,1),
1131               1 P(70,103,1),T(70,103,1)
1132    7.          DIMENSION F(70,103),JMAX(70),SL(70,103),XM(70,103,1),
1133               1 EPMAX(103),UET(70,103),VET(70,103),UZT(70,103),VZT(70,103),
1134               2 QE(103),DSTAR(103),Q(70),DEL(70),DX(70),EMO(70),YPB(70,103)
1135               3 ,XK1(103),XK2(103),APLUS(103),ISW(103),ISOM(103),DELT(103),
1136               4 ISXM(103)
1137        C
1138    8.          RMU=2.270E-08*SQRT(TW**3)/(TW+198.6)
1139    9.          RMUINF=2.27E-08*SQRT(TINF**3)/(TINF+198.6)
1140   10.          RCV=1.0/CV
1141   11.          PINF=RHOINF*RC*TINF
1142   12.          XKE=0.0168
1143   13.          YL=0.614797
1144        C
1145   14.          DO 1 J=1,JL
1146   15.          XK1(J)=0.40
1147   16.          XK2(J)=XKE
1148   17.          APLUS(J)=26.0
1149   18.       1 CONTINUE
1150   19.          DO 3 J=1,JL
1151   20.          DO 3 K=1,KL
1152   21.          RR=1.0/RHO(K,J,1)
1153   22.          U(K,J,1)=RHOU(K,J,1)*RR
1154   23.          V(K,J,1)=RHOV(K,J,1)*RR
1155   24.          T(K,J,1)=(RHOE(K,J,1)*RR-0.5*(U(K,J,1)**2+V(K,J,1)**2))*RCV
1156   25.          P(K,J,1)=RHO(K,J,1)*RC*T(K,J,1)
1157   26.          XM(K,J,1)=SQRT((U(K,J,1)**2+V(K,J,1)**2)/(GAMMA*RC*T(K,J,1)))
1158   27.    3     CONTINUE
1159        C
1160        C     GENERATING THE DERIVATIVES OF VELOCITY
1161        C
1162   28.          RDET=1.0/(2.0*DETA)
1163   29.          RDZT=1.0/(2.0*DZETA)
1164        C
1165   30.          DO 4 J=2,JLM
1166   31.          DO 4 K=2,KLM
1167   32.          UET(K,J)=(U(K,J+1,1)-U(K,J-1,1))*RDET
1168   33.          VET(K,J)=(V(K,J+1,1)-V(K,J-1,1))*RDET
1169   34.          UZT(K,J)=(U(K+1,J,1)-U(K-1,J,1))*RDZT
1170   35.          VZT(K,J)=(V(K+1,J,1)-V(K-1,J,1))*RDZT
1171   36.    4     CONTINUE
1172        C
1173        C     GENERATING THE VORTICITY DISTRIBUTION
1174        C
1175   37.          DO 5 J=2,JLM
1176   38.          DO 5 K=2,KLM
1177   39.          OMEGA(K,J)=SQRT(
1178               1 (ETX(K,J,1)*VET(K,J)+ZTX(K,J,1)*VZT(K,J)
1179               2 -ETY(K,J,1)*UET(K,J)-ZTY(K,J,1)*UZT(K,J))**2)
1180   40.    5     CONTINUE
1181        C
1182        C     GENERATING THE SCALING LENGTH
1183        C
1184   41.          DO 6 J=1,JL
1185   42.          DO 6 K=1,KL
1186   43.          SL(K,J)=SQRT((Y(K,J,1)-Y(1,J,1))**2+(X(K,J,1)-X(1,J,1))**2)
1187   44.    6     CONTINUE
1188        C
1189        C     GENERATING THE SURFACE VORTICITY
1190        C     ONE-SIDED DIFFERENCING IN K-DIRECTION FOR K=1
1191L       C
1192   45.          RDZT=1.0/DZETA
1193        C
```

206

```
1194   46.        DO 7 J=2,JLM
1195   47.        UET(1,J)=(U(1,J+1,1)-U(1,J-1,1))*RDET
1196   48.        VET(1,J)=(V(1,J+1,1)-V(1,J-1,1))*RDET
1197   49.        UZT(1,J)=(U(2,J,1)-U(1,J,1))*RDZT
1198   50.        VZT(1,J)=(V(2,J,1)-V(1,J,1))*RDZT
1199   51.        OMEGA(1,J)=SQRT((ETX(1,J,1)*VET(1,J)
1200              1+ZTX(1,J,1)*VZT(1,J)-ETY(1,J,1)*UET(1,J)
1201              2-ZTY(1,J,1)*UZT(1,J))**2)
1202   52.   7    CONTINUE
1203        C
1204        C      GENERATING THE INNER VISCOSITY COEFFICIENT
1205        C
1206   53.        IPSW=0
1207   54.        DO 8 J=2,JLM
1208        C      CHECK FOR ADVERSE PRESSURE GRADIENT ON WALL
1209        C
1210   55.        IF(J.LE.25)GO TO 60
1211   56.        DELP=P(1,J,1)-P(1,J-1,1)
1212   57.        IF(DELP.GT.0.0) IPSW=1
1213   58.        IF(IPSW.EQ.1) GO TO 55
1214   59.        GO TO 60
1215   60.   55   XK1(J)=0.65
1216   61.        APLUS(J)=65.0
1217   62.        PGRAD=(P(1,J,1)-P(1,J-1,1))*YL/((Y(1,J,1)-Y(1,J-1,1))*PINF)
1218   63.        XKS=0.015*PGRAD
1219   64.        XK2(J)=XK2(J-1)+XKS*(Y(1,J,1)-Y(1,J-1,1))
1220   65.   60   CONTINUE
1221        C
1222   66.        DO 8 K=2,KLM
1223        C
1224        C      SUPRESS THE UNDERFLOW MESSAGE FROM EXPONENTIAL CALCULATIONS
1225        C
1226   67.        YPB(K,J)=SQRT(RHO(1,J,1)*OMEGA(1,J)/RMU)*SL(K,J)/APLUS(J)
1227   68.        YPB(K,J)=AMIN1(YPB(K,J),50.0)
1228   69.        EP(K,J,1)=RHO(K,J,1)*(XK1(J)*SL(K,J)*(1.0-EXP(-YPB(K,J))))**2*
1229              1 OMEGA(K,J)
1230        C
1231   70.   8    CONTINUE
1232        C
1233        C      CEBICI SMITH MODEL
1234        C
1235        C      SEARCH FOR QMAX AT EACH J LOCATION
1236        C
1237   71.        DO 100 J=2,JLM
1238   72.        QABS=0.0
1239   73.        QMAX=0.0
1240   74.        DO 90 K=2,KL
1241   75.        QABS=SQRT(U(K,J,1)**2+V(K,J,1)**2)
1242   76.        QMAX=AMAX1(QABS,QMAX)
1243   77.        QE(J)=QMAX
1244   78.   90   CONTINUE
1245   79.  100   CONTINUE
1246        C
1247        C      FIND INFLECTION POINT IN VELOCITY GRADIENTS
1248        C       IF ONE EXISTS
1249        C
1250   80.        DO 830 J=2,JLM
1251   81.        DO 801 K=4,KLM
1252   82.        ISW(J)=K-1
1253   83.        IF(V(K,J,1).LT.0.) GO TO 801
1254   84.        DELV=V(K,J,1)-V(K-1,J,1)
1255   85.        IF(DELV.LE.0) GO TO 830
1256   86.  801   CONTINUE
1257   87.  830   CONTINUE
1258        C
1259        C      COMPUTE DEL STAR AT EACH LOCATION
1260        C
1261   88.        DO 105 J=2,JLM
1262   89.        N=ISW(J)
1263   90.        DSTAR(J)=0.0
1264   91.        DX(2)=X(2,J,1)-X(1,J,1)
1265   92.        Q(1)=0.0
1266   93.        Q(2)=SQRT(U(2,J,1)**2+V(2,J,1)**2)
1267   94.        DEL(2)=((1.0-Q(2)/QE(J))+(1.0-Q(1)/QE(J)))*DX(2)/2.0
1268   95.        DO 106 K=3,N
1269   96.        DX(K)=X(K,J,1)-X(K-1,J,1)
1270   97.        Q(K)=SQRT(U(K,J,1)**2+V(K,J,1)**2)
1271   98.        DEL(K)=DEL(K-1)+((1.-Q(K)/QE(J))+(1.-Q(K-1)/QE(J)))*DX(K)/2.0
1272   99.        DSTAR(J)=DEL(K)
1273  100.  106   CONTINUE
1274  101.  105   CONTINUE
```

```
1275        C
1276        C        COMPUTE EDDY VISCOSITY FOR OUTER REGION
1277        C
1278        C        AT EACH LOCATION COMPUTE EMO(K)
1279        C
1280  102.           DO 150 J=2,JLM
1281  103.           DO 130 K=2,KLM
1282  104.           EMO(K)=XK2(J)*RHO(K,J,1)*QE(J)*DSTAR(J)
1283  105.    130 CONTINUE
1284        C
1285        C        SELECT APPROPRIATE EDDY VISCOSITY VALUE FOR OUTER REGION
1286        C
1287  106.           ISWTH=0
1288  107.           DO 140 K=2,KLM
1289  108.           IF(EMO(K).LE.EP(K,J,1)) ISWTH=1
1290  109.           IF(ISWTH.EQ.1) EP(K,J,1)=EMO(K)
1291  110.           IF(EP(K,J,1).EQ.0.0) EP(K,J,1)=EP(K,J-1,1)
1292  111.    140 CONTINUE
1293  112.    150 CONTINUE
1294        C
1295        C
1296        C        COMPLETE THE EDDY VISCOSITY MATRIX
1297        C
1298  113.           EP(KLM,JL,1)=EP(KLM,JLM,1)
1299  114.           EP(KLM,JL,1)=EP(KLM,JLM,1)
1300  115.           DO 20 J=1,JL
1301  116.           EP(1,J,1)=0.0
1302  117.           EP(KL,J,1)=EP(KLM,J,1)
1303  118.     20 CONTINUE
1304  119.           DO 30 K=1,KL
1305  120.           EP(K,1,1)=0.0
1306  121.           EP(K,JL,1)=EP(K,JLM,1)
1307  122.     30 CONTINUE
1308  123.           RETURN
1309  124.           END
EDDY                 VECTOR LOOP BEGINS AT SEQ. NO.          14, P=  163326B
EDDY                 VECTOR LOOP BEGINS AT SEQ. NO.          20, P=  163373D
EDDY                 VECTOR LOOP BEGINS AT SEQ. NO.          31, P=  163452D
EDDY                 VECTOR LOOP BEGINS AT SEQ. NO.          38, P=  163526C
EDDY                 VECTOR LOOP BEGINS AT SEQ. NO.          42, P=  163572B
EDDY                 VECTOR LOOP BEGINS AT SEQ. NO.          46, P=  163622B
EDDY                 VECTOR LOOP BEGINS AT SEQ. NO.          66, P=  163706B
0   AT SEQUENCE NUMBER -      98.
PRNAME EDDY      COMMENT -     DEPENDENCY INVOLVING ARRAY "DEL" xxxxxxxxxxxxxxxxx
EXPLANATION:  PREVIOUS MINUS WITH AN INCREMENTING SUBSCRIPT
EDDY                 VECTOR LOOP BEGINS AT SEQ. NO.         103, P=  164134A
EDDY                 VECTOR LOOP BEGINS AT SEQ. NO.         115, P=  164204A
EDDY                 VECTOR LOOP BEGINS AT SEQ. NO.         119, P=  164231D
```

```
1.          SUBROUTINE PREAMB
2.          COMMON / / PW,DETA,DZETA,CV,RC,PR,PRT,GAMMA,EP(70,103,1),
           1 GAMM1,CFL,BETA,UINF,RHOINF,CINF,TINF,TW,DT,CX,CY,CZ,L,
           2 IL,JL,KL,ILM,JLM,KLM,ILE,LS,ISMTHX,ISMTHY,ISMTHZ,
           3 FLOWF,WN,WFBB,WT,OMEGA(70,103)
3.          COMMON /FLUET/ F21(70,2),F22(70,2),F23(70,2),F25(70,2),
           1 G21(70,2),G22(70,2),G23(70,2),G25(70,2),H(70)
4.          COMMON /FLUZT/ F31(70),F32(70),F33(70),F35(70),
           1 G31(70),G32(70),G33(70),G35(70)
5.          COMMON /TV/ ETX(70,103,1),ETY(70,103,1),ETZ(1,1,1),
           1 ZTX(70,103,1),ZTY(70,103,1),ZTZ(1,1,1)
6.          COMMON /DEP/ RHO(70,103,1),RHOU(70,103,1),RHOV(70,103,1),
           1 RHOW(1,1,1),RHOE(70,103,1)
7.          COMMON /DEPP/ RHOP(70,103,1),RHOUP(70,103,1),RHOVP(70,103,1),
           1 RHOWP(1,1,1),RHOEP(70,103,1)
8.          COMMON /DOF/ X(70,103,1),Y(70,103,1),Z(1,1,1)
9.          COMMON /NEWT/ AR,XM
C
10.         WRITE(8,6666) WT
11.  6666 FORMAT(* WT = *,E15.9/)
12.         WRITE(8,6000)
13.  6000 FORMAT(*  J         Y         RHO        RHOU       RHOV
           1        RHOE*/)
14.         XL=0.21669996
15.         YL=0.61479659
16.         RCV=1.0/CV
17.         CP=CV+RC
18.         RUINF=RHOINF*UINF
19.         PI=4.*ATAN(1.)
20.         ASTAR1=0.1971133
21.         ASTAR2=0.576395
22.         PINF=RHOINF*RC*TINF
23.         RHOW(1,1,1)=0.0
24.         EP(1,1,1)=0.0
C
C        SET FLOWFIELD WITH ACTUAL INFLOW CONDITIONS
C
25.         XM=UINF/CINF
26.         READ(1) NI,TMS1,TMS2,RHO,RHOU,RHOV,RHOW,RHOE,
           1 X,Y,Z,EP
27.         NI=1
28.         TMS1=0.0
29.         TMS2=0.0
30.         ENTHO=CP*TW
C
C        SPECIFY INITIAL CONDITIONS
C
C        EXIT PLANE CONDITIONS
C
31.         RHO(KL,JL,1)=4.280731E-04
32.         TE=PW/(RC*RHO(KL,JL,1))
33.         RHOU(KL,JL,1)=0.0
34.         V=SQRT(2.0*(ENTHO-CP*TE))
35.         RHOV(KL,JL,1)=RHO(KL,JL,1)*V
36.         RHOE(KL,JL,1)=RHO(KL,JL,1)*(CV*TE+0.5*V**2)
37.         XM=V/SQRT(GAMMA*RC*TE)
C
C        SET UP 1.D. NORMAL SHOCK SOLUTION FOR I.C.
C
38.  4000 FORMAT(I3,2X,6E13.6)
39.         XM=2.55
40.         DO 100 J=2,55
41.         A=4.*PI*XL*Y(KL,J,1)
42.         RHOV(KL,J,1)=WT/A
43.         AR=ASTAR1/A
44.         CALL NEWTON
45.         T=TW/(1.0+0.2*XM**2)
46.         V=SQRT(2.0*(ENTHO-CP*T))
47.         RHO(KL,J,1)=RHOV(KL,J,1)/V
48.         RHOU(KL,J,1)=0.0
49.         RHOE(KL,J,1)=RHO(KL,J,1)*(CV*T+0.5*V**2)
50.         WRITE(8,4000) J,Y(KL,J,1),RHO(KL,J,1),RHOU(KL,J,1),RHOV(KL,J,1),
           1 RHOE(KL,J,1)
51.   100 CONTINUE
```

```
C
C          NORMAL SHOCK OCCURS BETWEEN J=56 AND J=57
C
52.          J=56
53.          XM=0.478052
54.          A=4.*PI*XL*Y(KL,J,1)
55.          RHOV(KL,J,1)=WT/A
56.          T=TW/(1.0+0.2*XM**2)
57.          C=SQRT(GAMMA*RC*T)
58.          V=XM*C
59.          RHO(KL,J,1)=RHOV(KL,J,1)/V
-60.         RHOU(KL,J,1)=0.0
61.          RHOE(KL,J,1)=RHO(KL,J,1)*(CV*T+0.5*V**2)
62.          WRITE(8,4000) J,Y(KL,J,1),RHO(KL,J,1),RHOU(KL,J,1),RHOV(KL,J,1),
            1 RHOE(KL,J,1)
C
C          SET UP DOWNSTREAM FLOWFIELD
C
63.          DO 105 J=57,JLM
64.          A=4.*PI*XL*Y(KL,J,1)
65.          AR=ASTAR2/A
66.          RHOV(KL,J,1)=WT/A
67.          CALL NEWTON
68.          V=SQRT(2.0*(ENTHO-CP*T))
69.          RHO(KL,J,1)=RHOV(KL,J,1)/V
70.          RHOU(KL,J,1)=0.0
71.          RHOE(KL,J,1)=RHO(KL,J,1)*(CV*T+0.5*V**2)
72.          WRITE(8,4000) J,Y(KL,J,1),RHO(KL,J,1),RHOU(KL,J,1),RHOV(KL,J,1),
            1 RHOE(KL,J,1)
73.     105 CONTINUE
C
74.          DO 120 J=2,JL
75.          DO 120 K=2,KL
76.          RHO(K,J,1)=RHO(KL,J,1)
77.          RHOU(K,J,1)=RHOU(KL,J,1)
78.          RHOV(K,J,1)=RHOV(KL,J,1)
79.          RHOE(K,J,1)=RHOE(KL,J,1)
80.          EP(K,J,1)=0.0
81.     120 CONTINUE
C
C          SPECIFY THE NO-SLIP SURFACE B.C.
C
82.          RHOWL=RHOINF*TINF/TW
83.          RHOEW=RHOWL*CV*TW
C
84.          DO 2 J=ILE,JL
85.          RHO(1,J,1)=RHOWL
86.          RHOU(1,J,1)=0.0
87.          RHOV(1,J,1)=0.0
88.          RHOE(1,J,1)=RHOEW
89.       2 CONTINUE
C
C          INITIALIZE PREDICTOR VARIABLES
C
90.          DO 6 J=1,JL
91.          DO 6 K=1,KL
92.          RHOP(K,J,1)=RHO(K,J,1)
93.          RHOUP(K,J,1)=RHOU(K,J,1)
94.          RHOVP(K,J,1)=RHOV(K,J,1)
95.          RHOEP(K,J,1)=RHOE(K,J,1)
96.       6 CONTINUE
97.          RHOWP(1,1,1)=0.0
C
C          INITIALIZE FLUX COMPONENTS
C
98.          DO 3 J=1,2
99.          DO 3 K=1,KL
100.         F21(K,J)=0.0
101.         F22(K,J)=0.0
102.         F23(K,J)=0.0
103.         F25(K,J)=0.0
104.         G21(K,J)=0.0
105.         G22(K,J)=0.0
106.         G23(K,J)=0.0
107.         G25(K,J)=0.0
108.       3 CONTINUE
```

```
109.          DO 4 K=1,KL
110.          F31(K)=0.0
111.          F32(K)=0.0
112.          F33(K)=0.0
113.          F35(K)=0.0
114.          G31(K)=0.0
115.          G32(K)=0.0
116.          G33(K)=0.0
117.          G35(K)=0.0
118.          H(K)=0.0
119.        4 CONTINUE
      C
120.   1000 FORMAT(/,*   J           Y           M           T*/)
121.   2000 FORMAT(I3,1X,3E12.5)
122.          WRITE(8,1000)
123.          DO 3000 J=1,JL
124.          RH=1.0/RHO(KL,J,1)
125.          V=RHOV(KL,J,1)*RH

126.          T=(RHOE(KL,J,1)*RH-0.5*V**2)*RCV
127.          XM=V/SQRT(GAMMA*RC*T)
128.          WRITE(8,2000) J,Y(KL,J,1),XM,T
129.   3000 CONTINUE
130.          RETURN
131.          END




1.            SUBROUTINE NEWTON
2.            COMMON /NEWT/ AR,XM
      C
3.            TOL=0.0001
4.            DO 10 I=1,100
5.            F=AR*XM**6+15.*AR*XM**4+75.*AR*XM**2-216.*XM+125.*AR
6.            FP=6.*AR*XM**5+60.*AR*XM**3+150.*AR*XM-216.
7.            DEL=F/FP
8.            XMN=XM-DEL
9.            TR=ABS((XMN-XM)/XMN)
10.           IF(TR.LE.TOL) GO TO 20
11.           XM=XMN
12.        10 CONTINUE
      C
13.        20 XM=XMN
14.           RETURN
15.           END
```

APPENDIX B

TABULATED INFLOW PROPERTIES FROM UTRC EXPERIMENTAL DATA

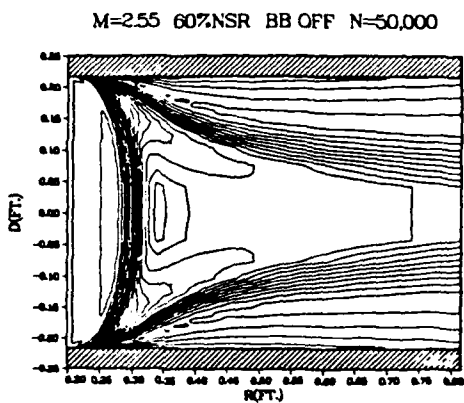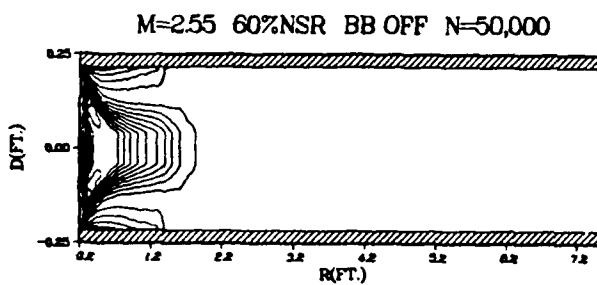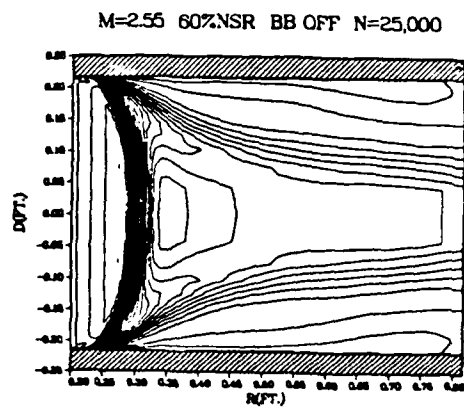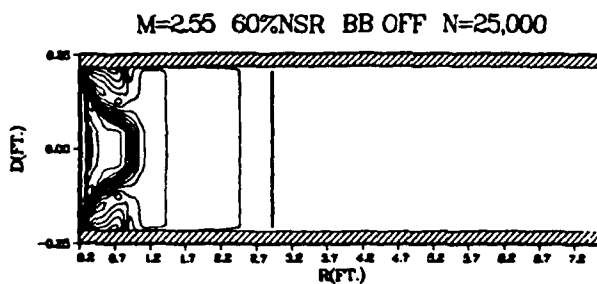APPENDIX C

NUMERICAL CASE 1A COMPUTATIONAL DETAILS

Details of the first numerical case show the progress of the core flow

barrel shock shock through the diffuser from the imposed one-dimensional,

inviscid normal shock initial condition through the "unstart" at 2.8

milliseconds. For this numerical experiment, a uniform core inflow was

assumed at M - 2.5, with no wall flow energization. Exit pressure was set

at 60% of normal shock recovery pressure. The Navier-Stokes computer code

employed the standard Cebeci-Smith two-layer algebraic eddy viscosity

turbulence model. No modification for adverse pressure gradient was

incorporated. The first figure repeats the time history of the core

flow normal shock position (from Figure 20). Presented next are a series of

Mach contour plots, beginning with the initial condition and proceeding in

increments of 5,000 numerical iterations through N - 60,000, when the

numerical "unstart" is observed. Each plot presents the Mach contours from

M - 0.0 through M - 5.0, in increments of 0.20. Following the Mach contour

plots are a series of corresponding nondimensionalized wall pressure, line

of symmetry pressure, and line of symmetry temperature plots. Pressure is

nondimensionalized in a ratio with calculated stagnation pitot pressure and

temperature is nondimensionalized in a ratio with stagnation temperature.

Development of the wall boundary layer separation is quite apparent by N -

10,000, and this is also readily seen in the corresponding wall pressure

plot. Line of symmetry pressure and temperature lag the wall pressure

significantly as indicators of diffuser flow behavior; by N - 25,000 the

wall pressure indicates that the wall boundary layer separation is out of

control by its sharp rise immediately after the entrance to the diffuser.

By N = 60,000, the nature of the "unstart" is clear as both wall and line of symmetry pressure achieve values corresponding to normal shock pitot pressure at the diffuser entrance. This numerical experiment required 57.9 minutes of CRAY 1 CPU time.

TABLE IV

NUMERICAL CASE 1A COMPUTED SHOCK POSITION VS TIME

N Number of Iterations	CFL	TIME (Milliseconds)	R/R_{de}	SPOS
0		0	1.614800	0.200000
5,000	.10	0.094638	1.621806	0.202280
10,000	.10	0.189240	1.628633	0.204501
15,000	.15	0.331140	1.632423	0.205734
20,000	.20	0.520342	1.621053	0.202035
25,000	.25	0.756839	1.570787	0.185683
30,000	.30	1.040636	1.454744	0.147933
35,000	.30	1.324432	1.358651	0.116673
40,000	.40	1.702826	1.341394	0.111059
45,000	.40	2.081220	1.363403	0.118219
50,000	.25	2.317719	1.381380	0.124067
55,000	.25	2.554216	1.231846	0.075422
60,000	.25	2.791833	1.004322	0.001406

BASIC CEBECI–SMITH TIME HISTORY 60%NSR WBB=0
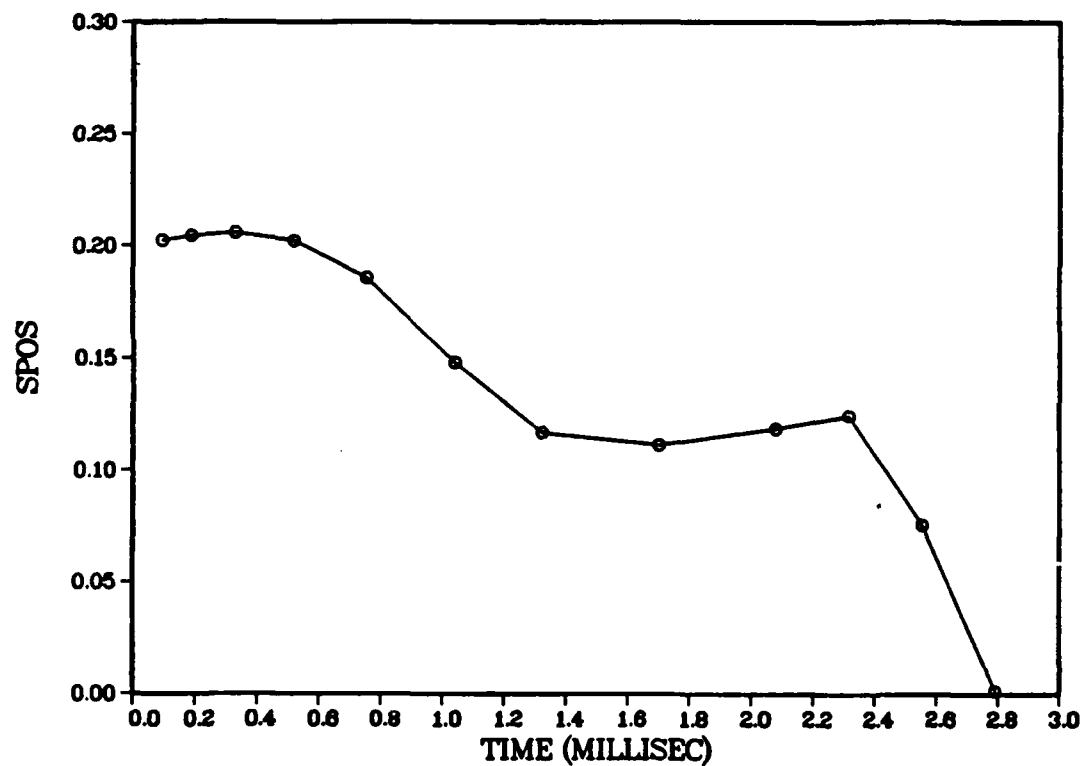
N=1 MACH CONTOURS CSB 60%NSR WBB=0
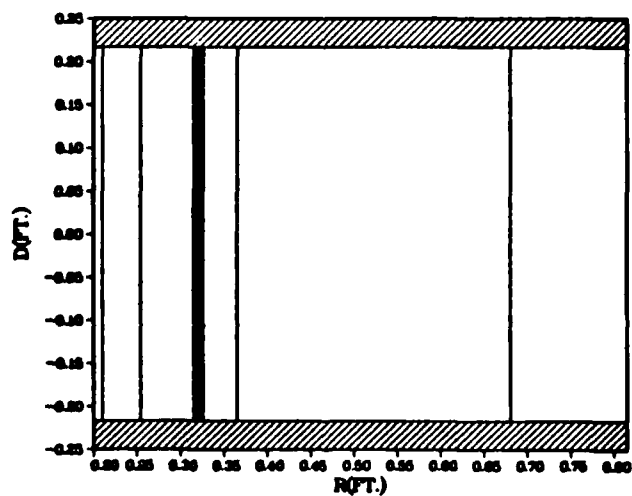
N=5K MACH CONTOURS CSB 60%NSR WBB=0
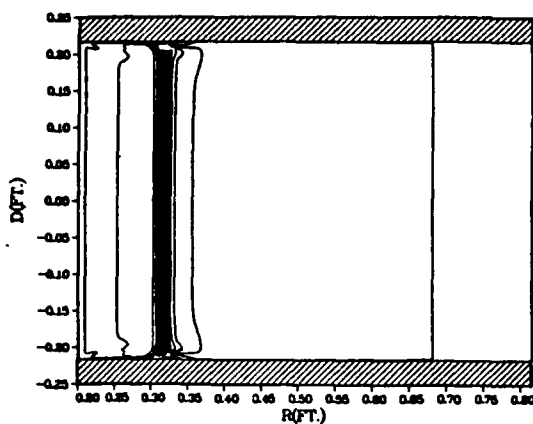
N=10K MACH CONTOURS CSB 60%NSR WBB=0
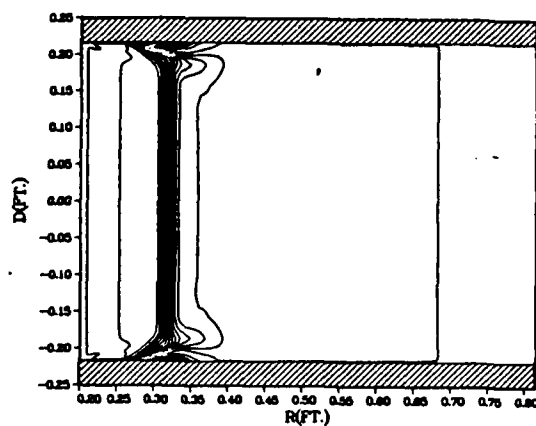
N=15K MACH CONTOURS CSB 60%NSR WBB=0
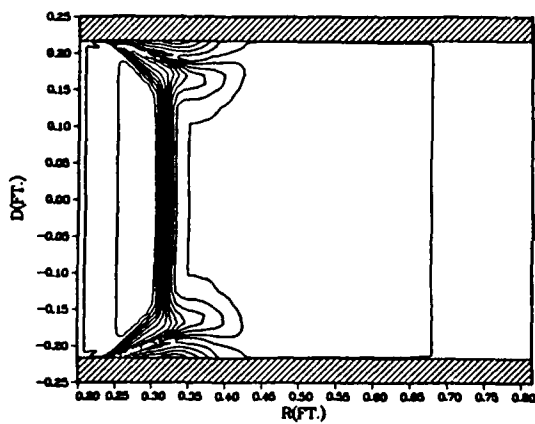
N=20K MACH CONTOURS CSB 60%NSR WBB=0
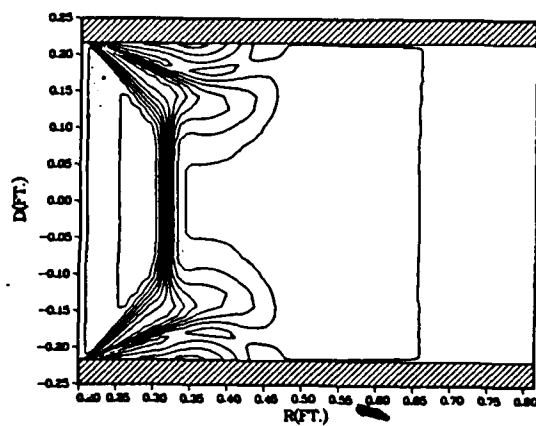
N=25K MACH CONTOURS CSB 60%NSR WBB=0

N=30K CSB MACH CONTOURS 60%NSR WBB=0

217
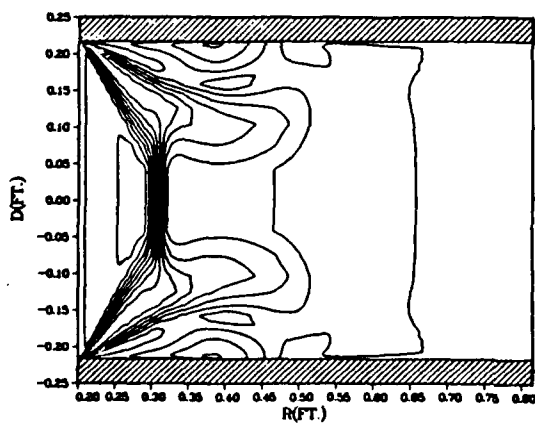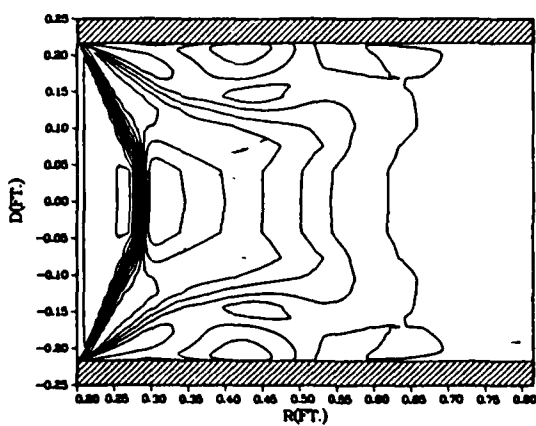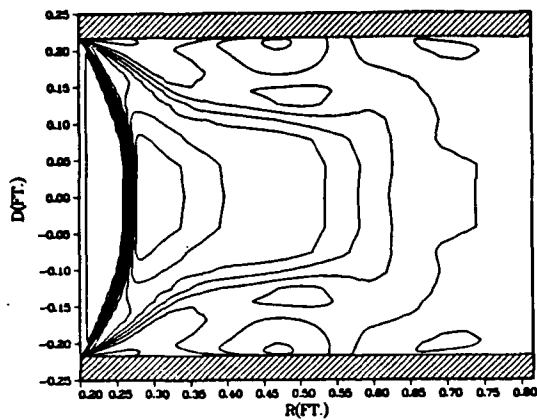
N=35K CSB MACH CONTOURS 60%NSR WBB=0   N=40K CSB MACH CONTOURS 60%NSR WBB=0
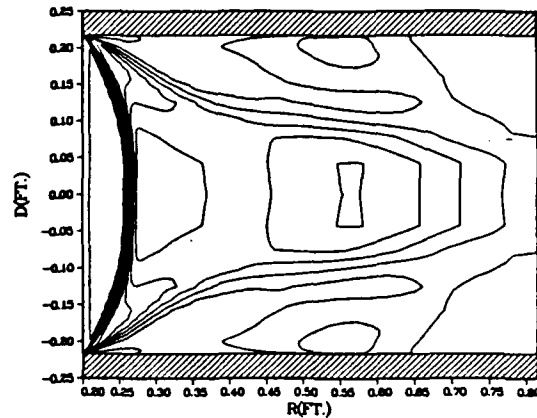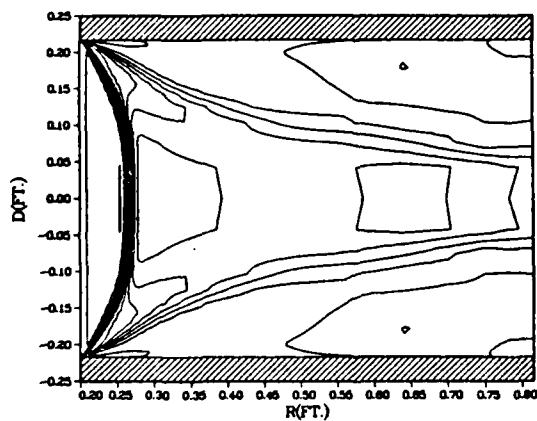
N=45K CSB MACH CONTOURS 60%NSR WBB=0   N=50K CSB MACH CONTOURS 60%NSR WBB=0
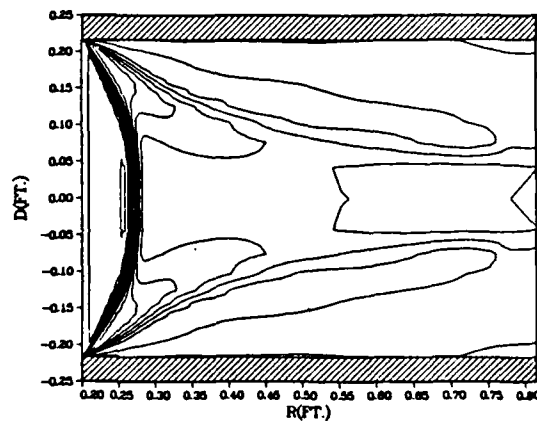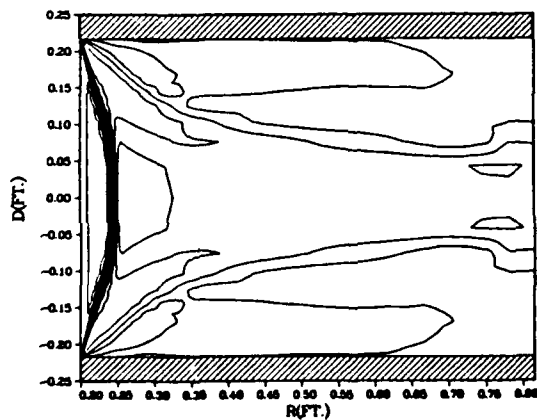
N=55K CSB MACH CONTOURS 60%NSR WBB=0   N=60K CSB MACH CONTOURS 60%NSR WBB=0
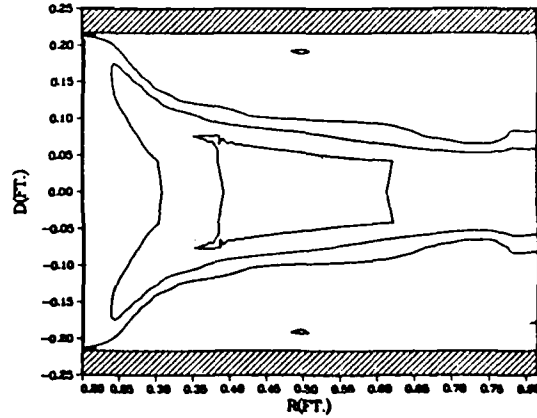
N=1 PW/PPI CSB 60%NSR WBB=0
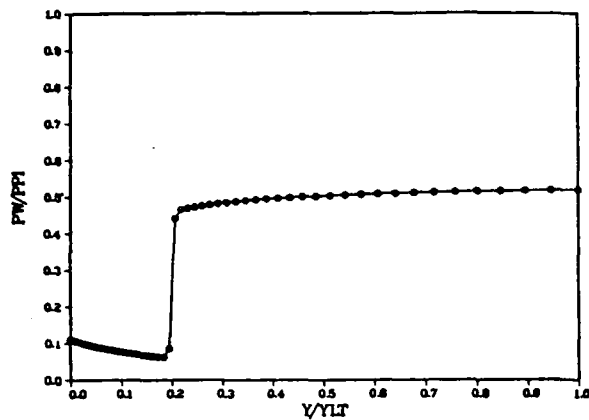
N=5K PW/PPI CSB 60%NSR WBB=0
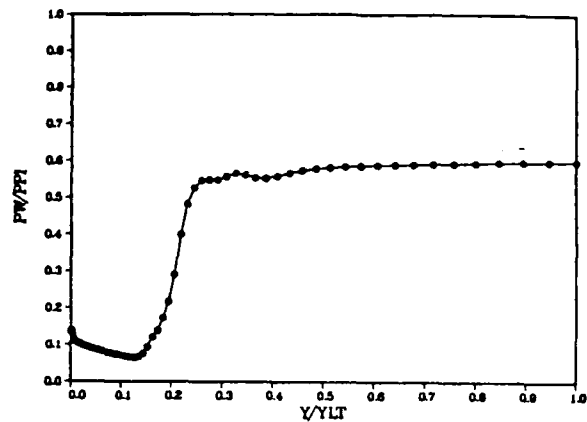
N=1 PCL/PPI CSB 60%NSR WBB=0
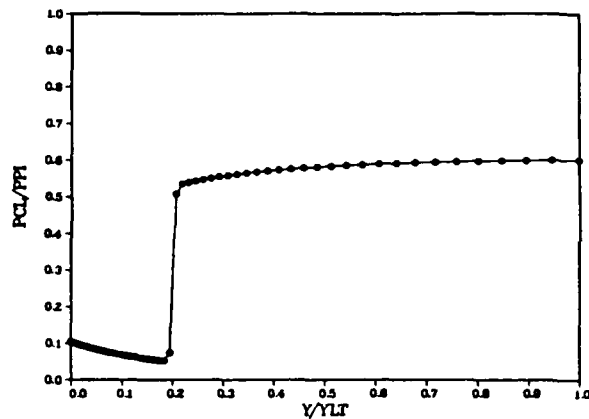
N=5K PCL/PPI CSB 60%NSR WBB=0
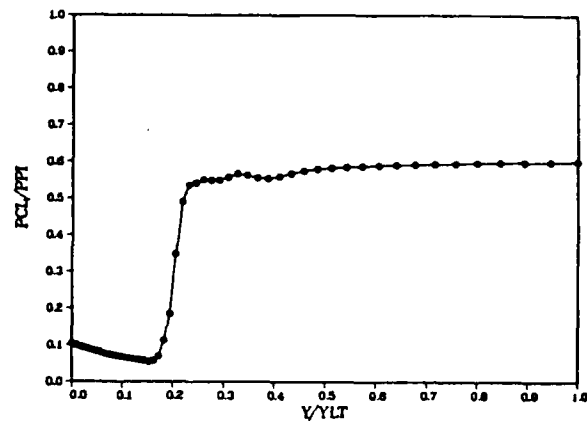
N=1 TCL/TO CSB 60%NSR WBB=0
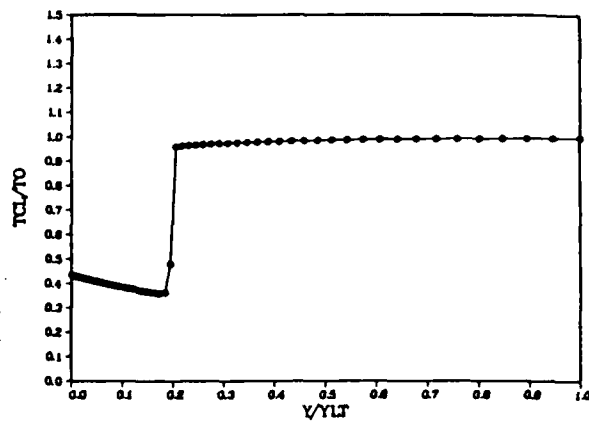
N=5K TCL/TO CSB 60%NSR WBB=0
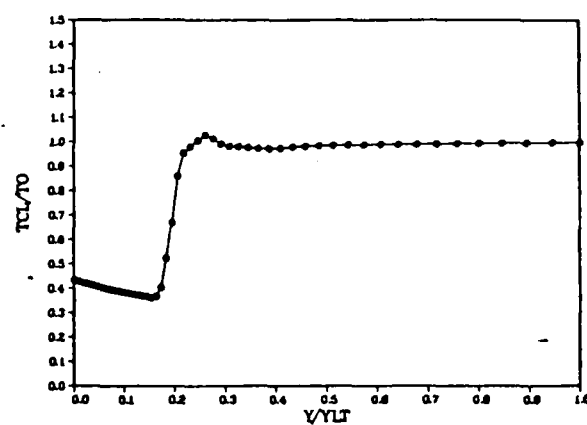
N=10K PW/PPI CSB 60%NSR WBB=0
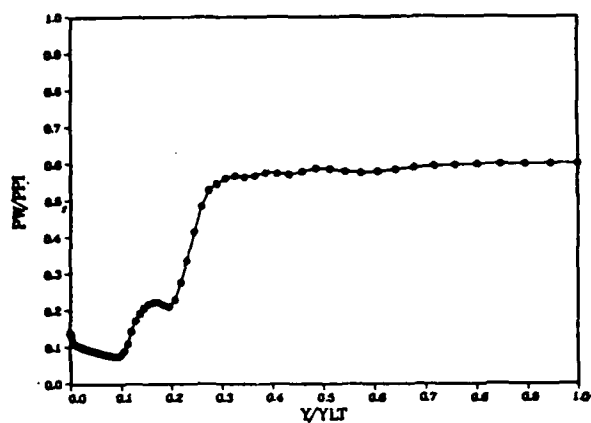
N=15K PW/PPI CSB 60%NSR WBB=0
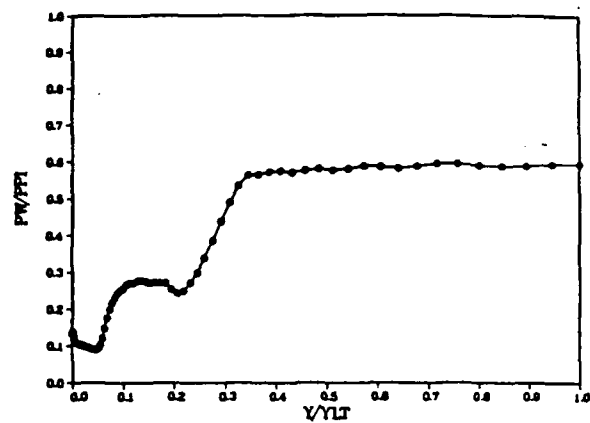
N=10K PCL/PPI CSB 60%NSR WBB=0
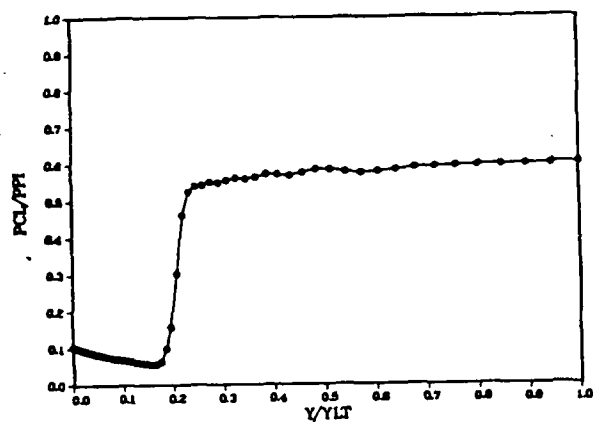
N=15K PCL/PPI CSB 60%NSR WBB=0
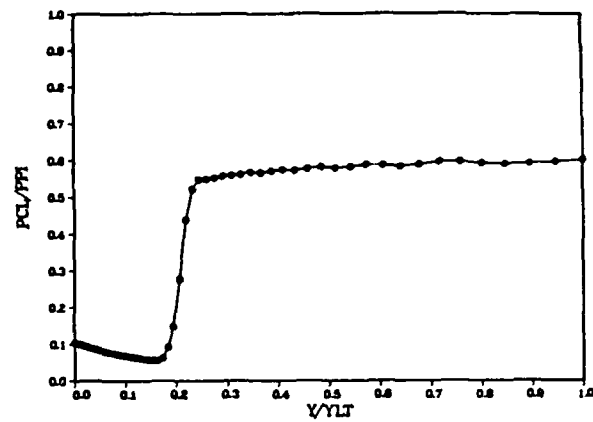
N=10K TCL/TO CSB 60%NSR WBB=0
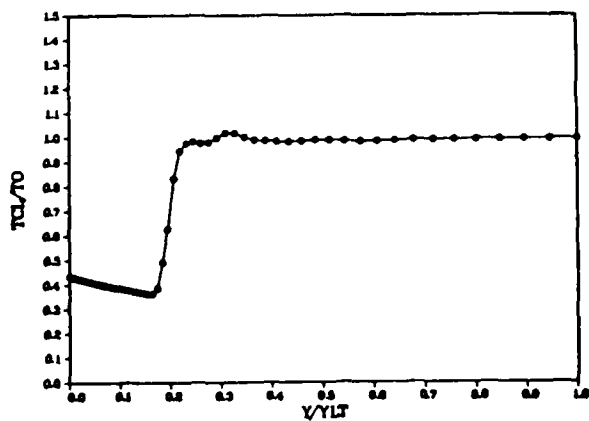
N=15K TCL/TO CSB 60%NSR WBB=0
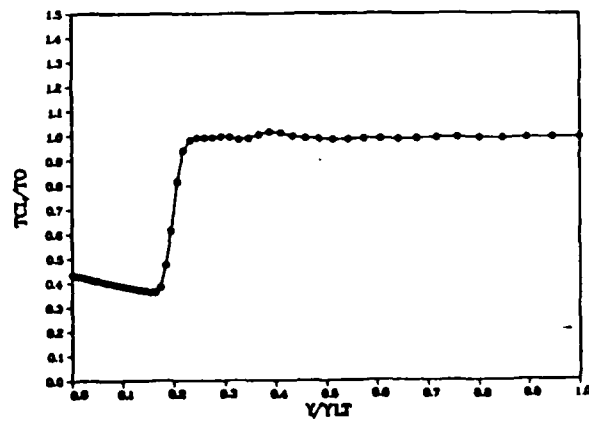
N=20K PW/PPI CSB 60%NSR WBB=0
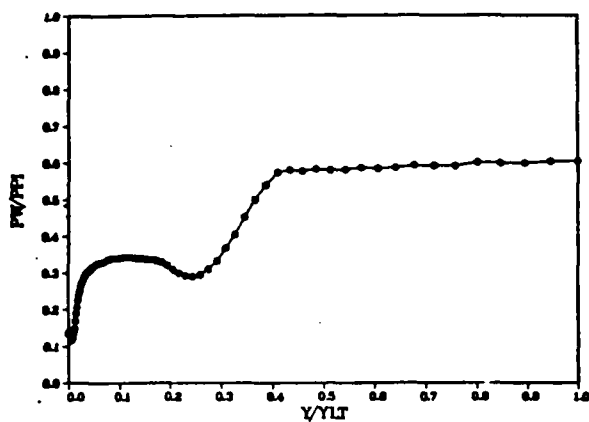
N=25K PW/PPI CSB 60%NSR WBB=0
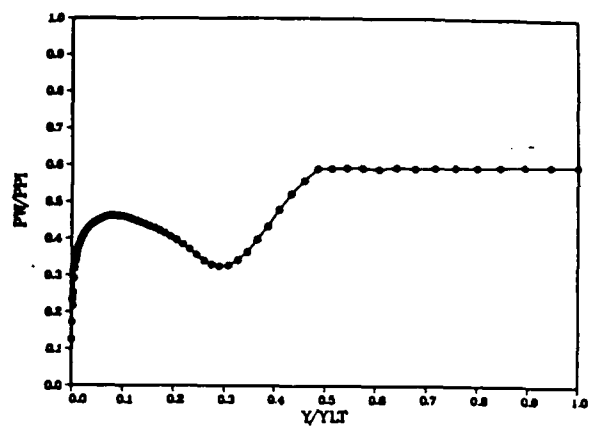
N=20K PCL/PPI CSB 60%NSR WBB=0
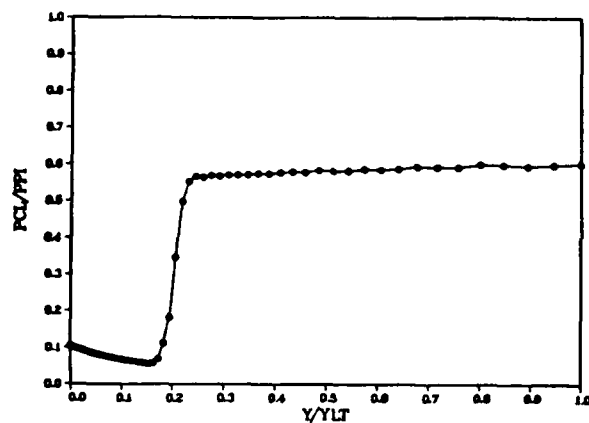
N=25K PCL/PPI CSB 60%NSR WBB=0
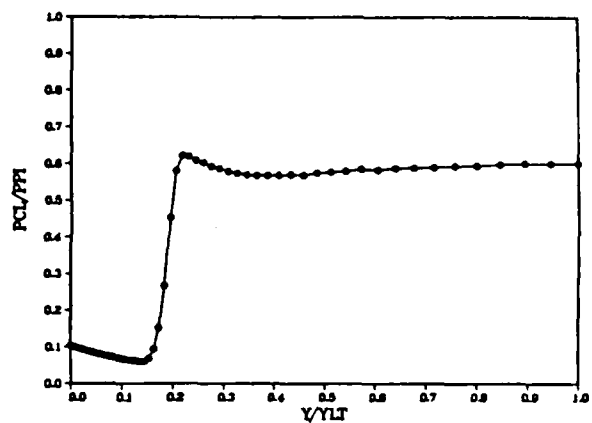
N=20K TCL/TO CSB 60%NSR WBB=0

N=25K TCL/TO CSB 60%NSR WBB=0

221
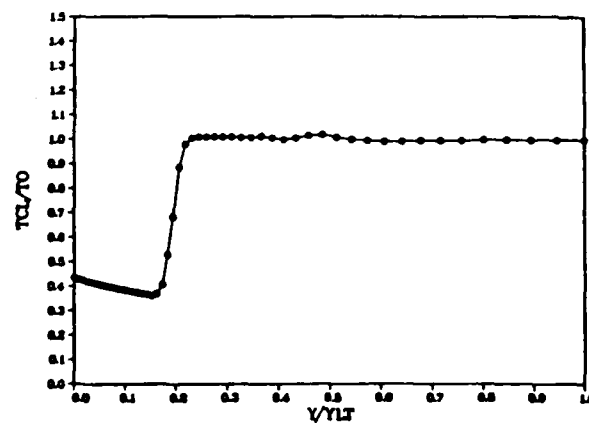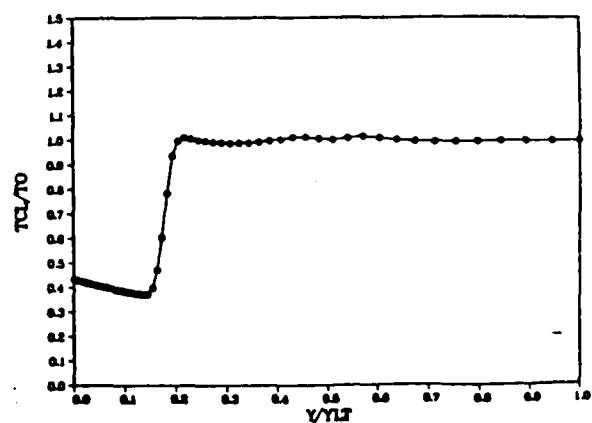
N=30K PW/PPI CSB 60%NSR WBB=0
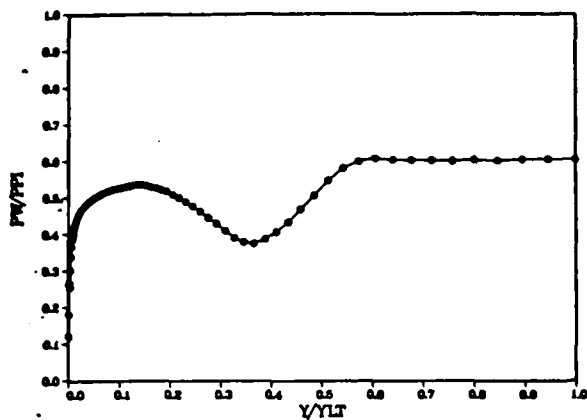
N=35K PW/PPI CSB 60%NSR WBB=0
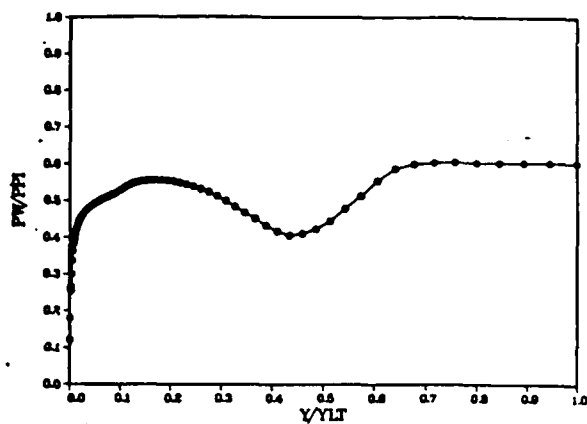
N=30K PCL/PPI CSB 60%NSR WBB=0
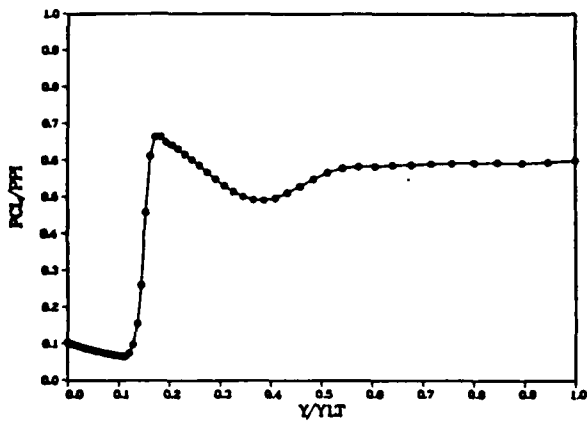
N=35K PCL/PPI CSB 60%NSR WBB=0
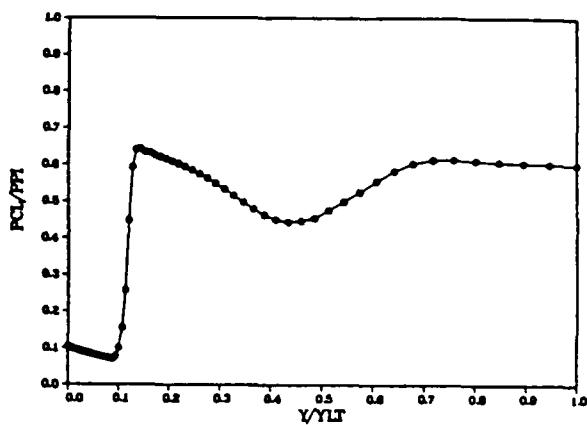
N=30K TCL/TO CSB 60%NSR WBB=0

N=35K TCL/TO CSB 60%NSR WBB=0

222
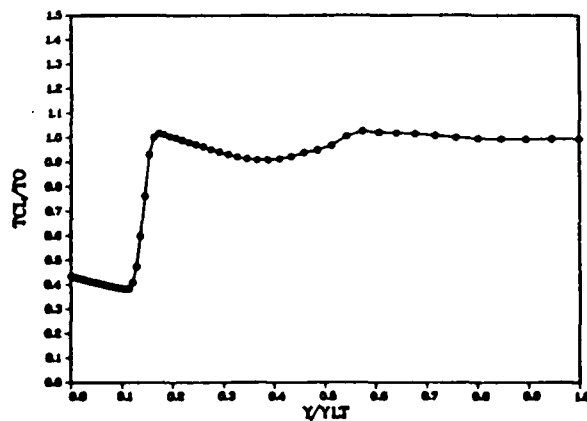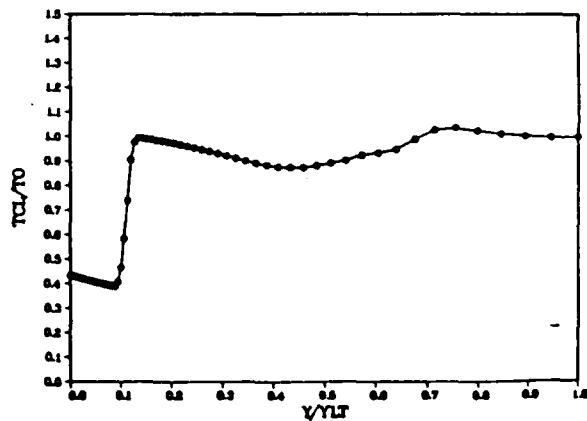
N=40K PW/PPI CSB 60%NSR WBB=0
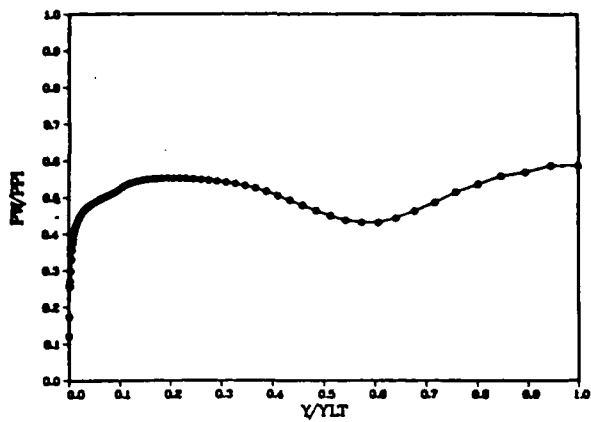
N=45K PW/PPI CSB 60%NSR WBB=0
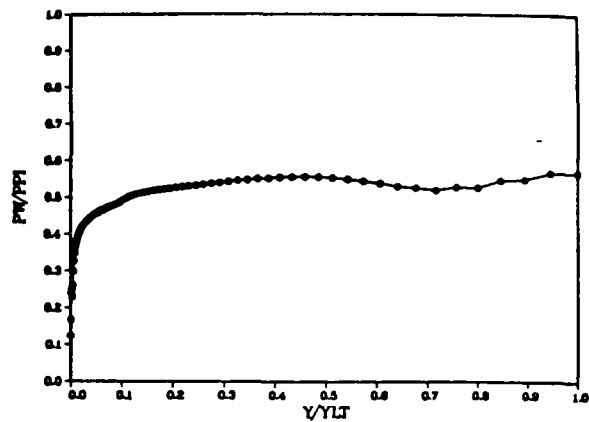
N=40K PCL/PPI CSB 60%NSR WBB=0
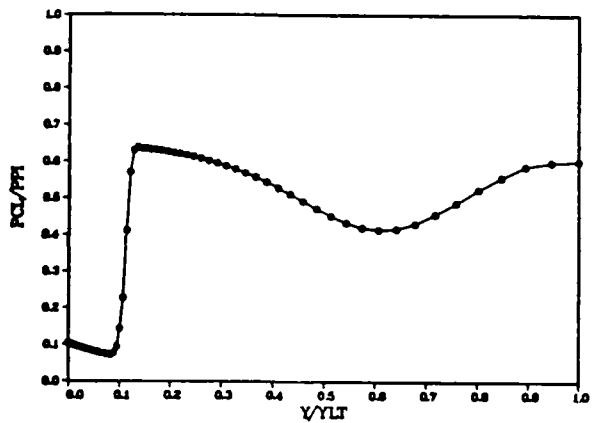
N=45K PCL/PPI CSB 60%NSR WBB=0
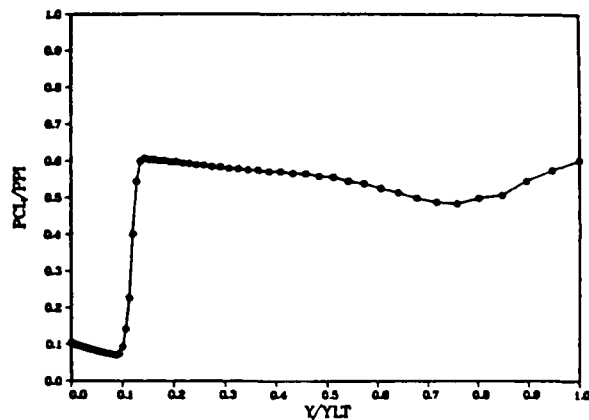
N=40K TCL/TO CSB 60%NSR WBB=0

N=45K TCL/TO CSB 60%NSR WBB=0

223
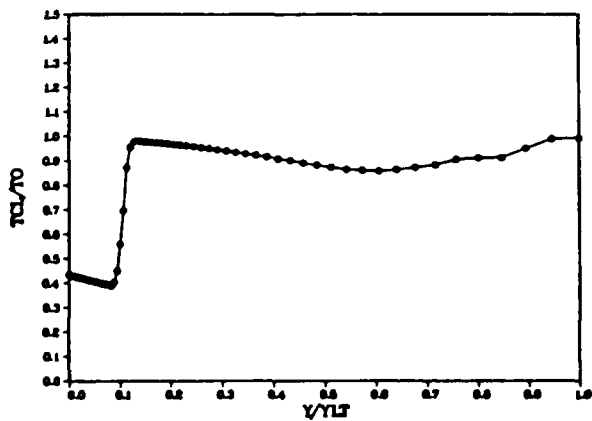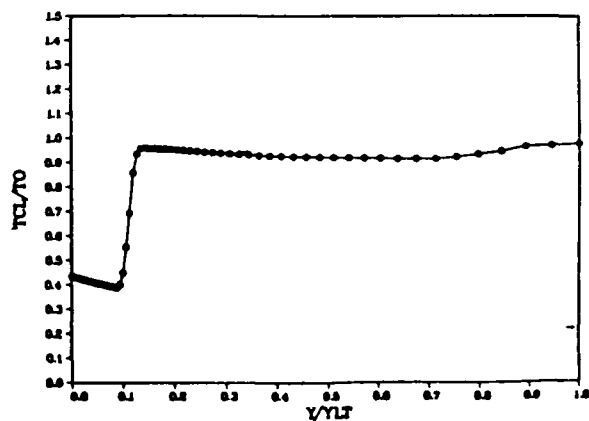
N=55K PW/PPI CSB 60%NSR WBB=0
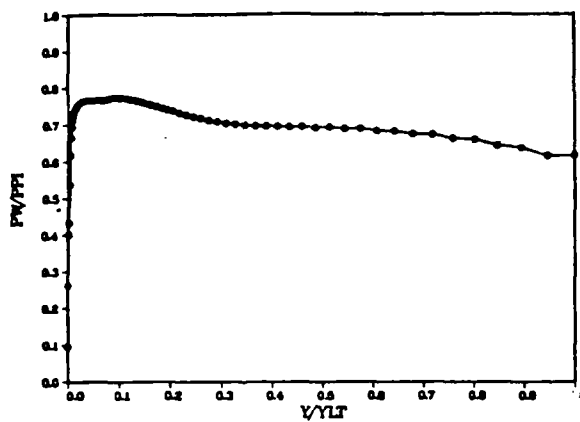
N=60K PW/PPI CSB 60%NSR WBB=0
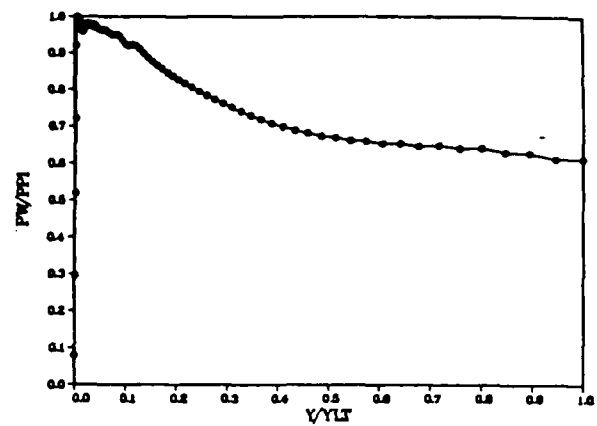
N=55K PCL/PPI CSB 60%NSR WBB=0
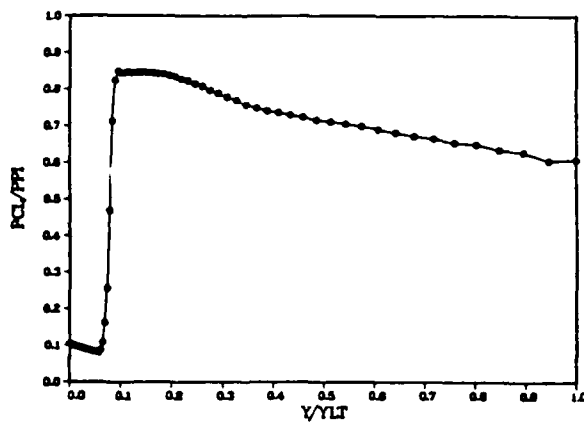
N=60K PCL/PPI CSB 60%NSR WBB=0
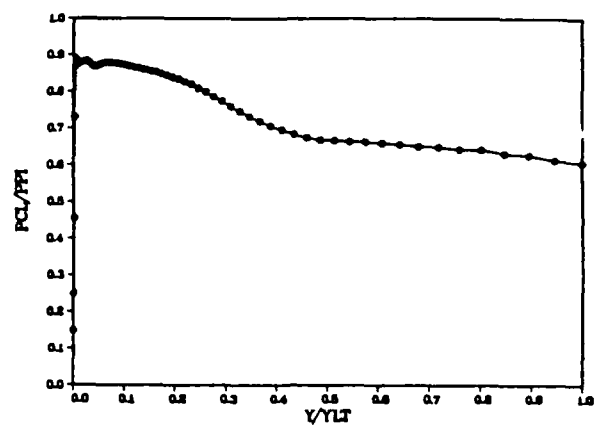
N=55K TCL/TO CSB 60%NSR WBB=0
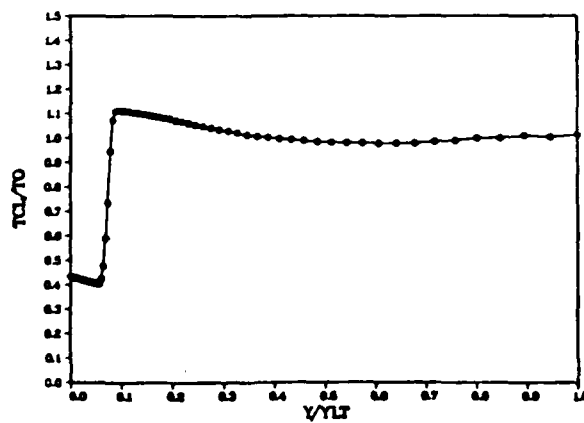
N=60K TCL/TO CSB 60%NSR WBB=0
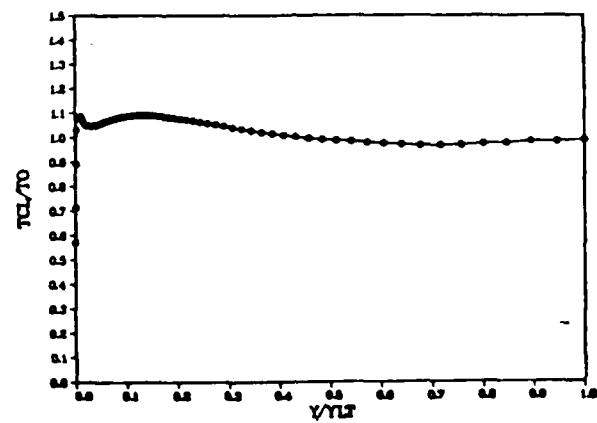
APPENDIX D

NUMERICAL CASE 1B COMPUTATIONAL DETAILS

For this numerical experiment a uniform core inflow was assumed at M = 2.5, with no wall flow energization. Exit pressure was set at 60% of normal shock recovery pressure. The Navier-Stokes computer code employed the Cebeci-Smith two-layer eddy viscosity turbulence model modified for the effect of an adverse pressure gradient as described in Chapter V, Section 5.3. Details of the progress of the core flow normal shock through the diffuser from the imposed one-dimensional, inviscid normal shock initial condition to an "unstart" at approximately 3.4 milliseconds are presented. The first figure repeats the time history plot of the core flow normal shock (the terminal normal shock computed on the line of symmetry) position (from Figure 21). Presented next are a series of Mach contour plots, beginning with the initial condition and proceeding in increments of 5,000 numerical iterations through N = 80,000, when the numerical "unstart" is observed. Each plot presents the Mach contours from M = 0.0 through M = 5.0, in increments of 0.20. Following the Mach contour plots are a series of corresponding nondimensionalized wall pressure, line of symmetry pressure, and line of symmetry temperature plots. Flow development is essentially identical to that from case 1a, with development of the wall boundary layer separation quite apparent by N = 10,000. Again, this is clearly seen in the corresponding wall pressure plot, with the sudden pressure rise along the diffuser wall immediately after the flow has entered the diffuser. line of symmetry pressure and temperature again lag wall pressure significantly as indicators of diffuser flow behavior. The "stiffer" eddy viscosity turbulence model delays the growth of this wall boundary layer separation,

225

but not to the extent sufficient to prevent core flow choking which ultimately leads to the "unstarted" condition depicted in the Mach contour plot for N = 80,000. The effect of incorporating the adverse pressure gradient modification to the turbulence model is to delay the "unstart" from 2.8 milliseconds to 3.4 milliseconds of computational flow "time." This numerical experiment required 77.2 minutes of CRAY 1 CPU time.

MODIFIED C-S TIME HISTORY 60%NSR WBB=0
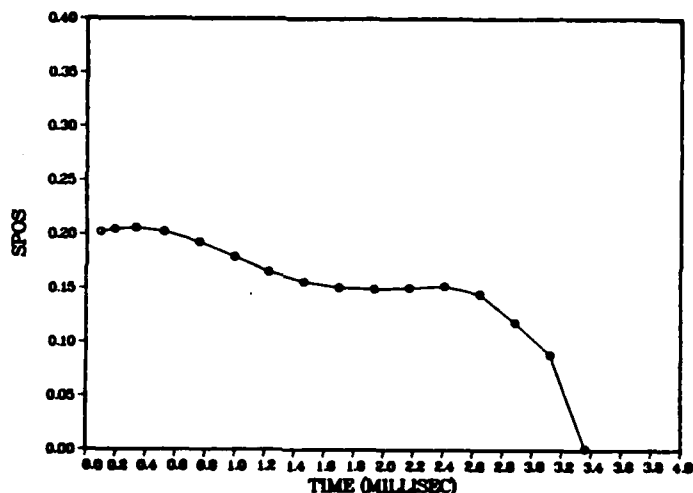
N=1 MACH CONTOURS 60%NSR WBB=0
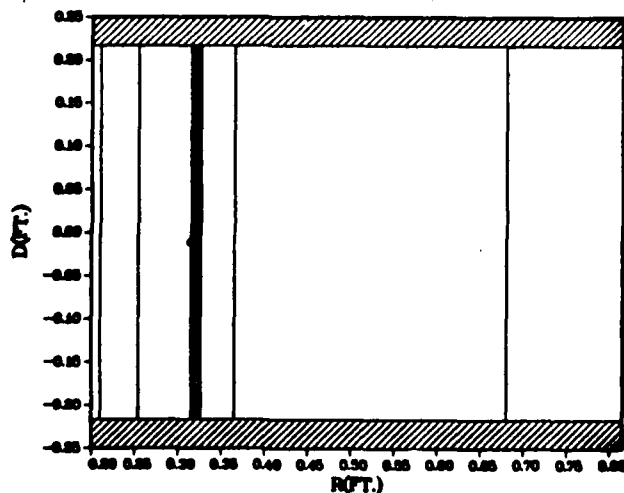
TABLE V

NUMERICAL CASE 1B COMPUTED SHOCK POSITION VS TIME

N Number of Iterations	CFL	TIME (Milliseconds)	R/R_{de}	SPOS
0		0	1.614800	0.200000
5,000	.10	0.0946375	1.621403	0.202149
10,000	.10	0.1892396	1.628000	0.204295
15,000	.10	0.3311419	1.631304	0.205370
20,000	.20	0.5203417	1.621268	0.202105
25,000	.25	0.7568380	1.590961	0.192246
30,000	.25	0.9933348	1.549825	0.178864
35,000		1.2298320	1.507312	0.165034
40,000		1.4663280	1.478441	0.155642
45,000		1.7028260	1.463093	0.150649
50,000		1.9393220	1.458888	0.149281
55,000		2.1758180	1.462349	0.150407
60,000		2.4123150	1.467083	0.151947
65,000		2.6488130	1.444796	0.144697
70,000		2.8853090	1.363560	0.118270
75,000		3.1218060	1.271319	0.088263
80,000		3.3583020	1.024958	0.008119

N=5K MACH CONTOURS 60%NSR WBB=0
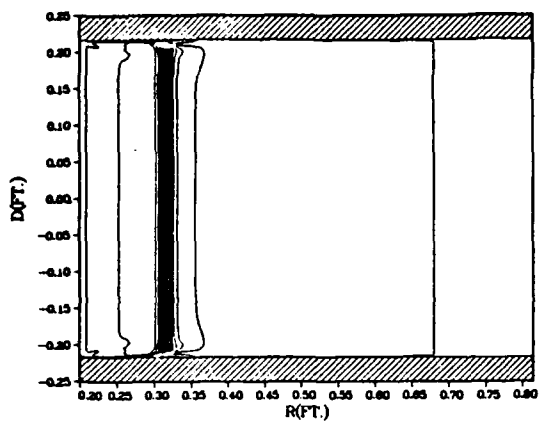
N=10K MACH CONTOURS 60%NSR WBB=0
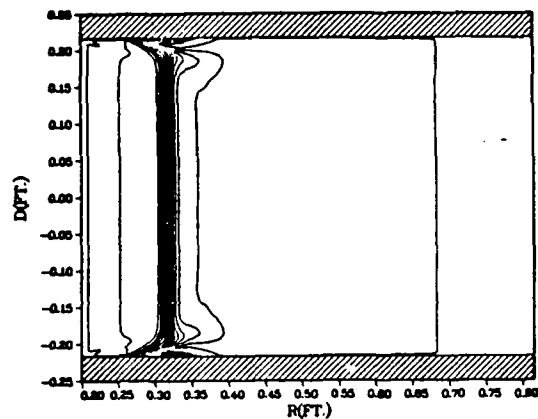
N=15K MACH CONTOURS 60%NSR WBB=0
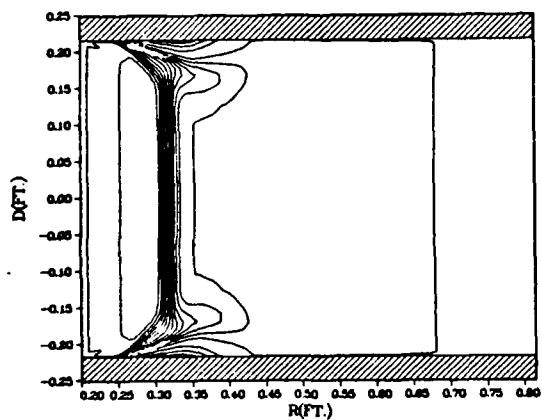
N=20K MACH CONTOURS 60%NSR WBB=0
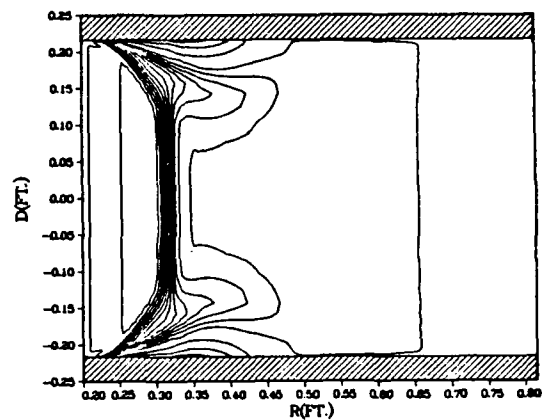
N=25K MACH CONTOURS 60%NSR WBB=0

N=30K MACH CONTOURS 60%NSR WBB=0

228
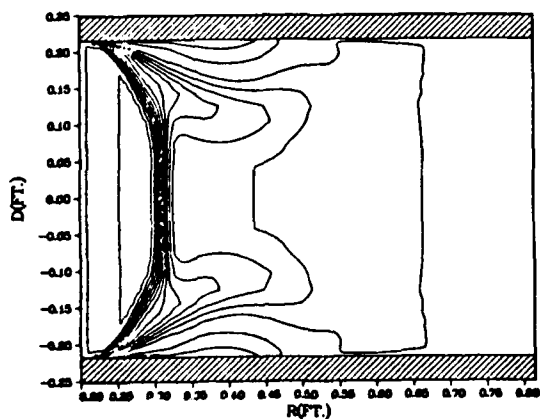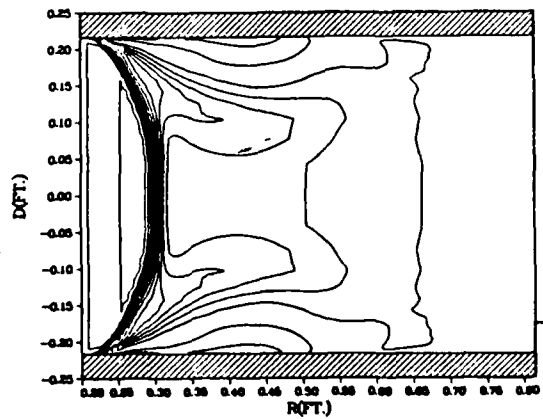
N=35K MACH CONTOURS 60%NSR WBB=0
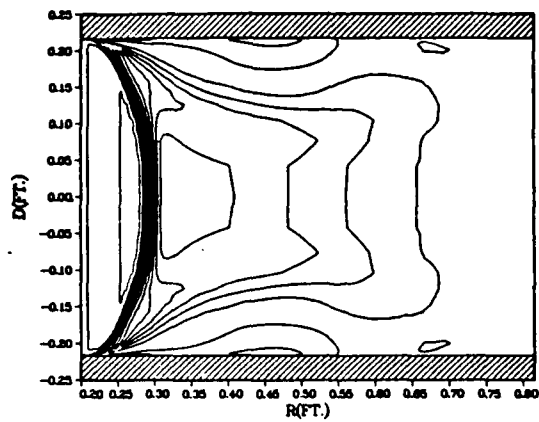
N=40K MACH CONTOURS 60%NSR WBB=0
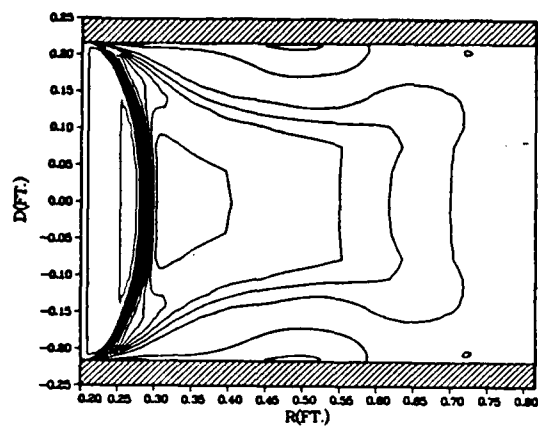
N=45K MACH CONTOURS 60%NSR WBB=0
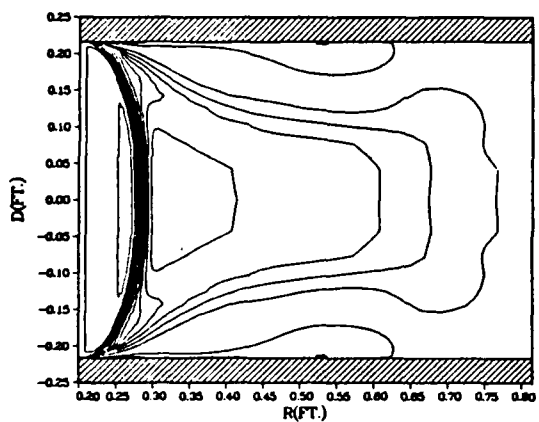
N=50K MACH CONTOURS 60%NSR WBB=0
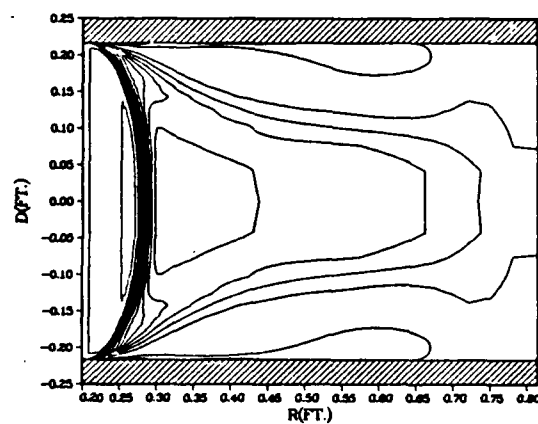
N=55K MACH CONTOURS 60%NSR WBB=0
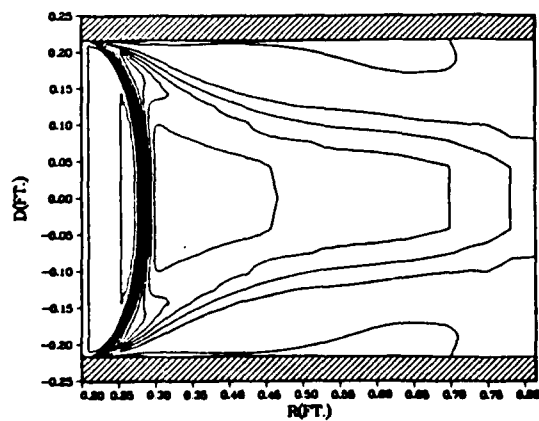
N=60K MACH CONTOURS 60%NSR WBB=0
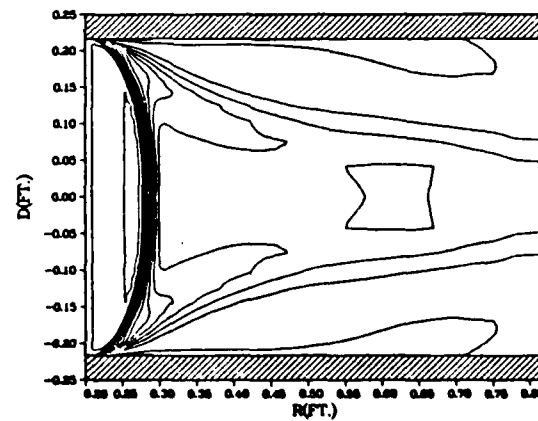
N=65K MACH CONTOURS 60%NSR WBB=0
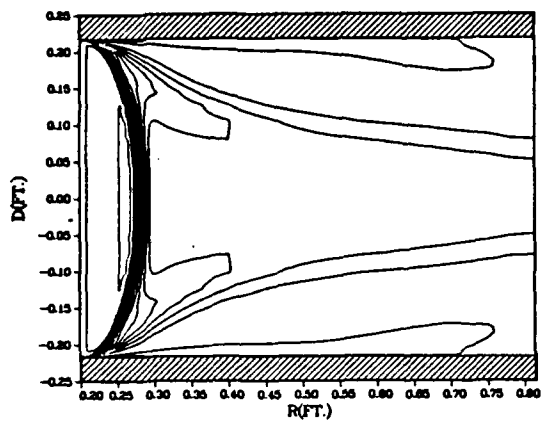
N=70K MACH CONTOURS 60%NSR WBB=0
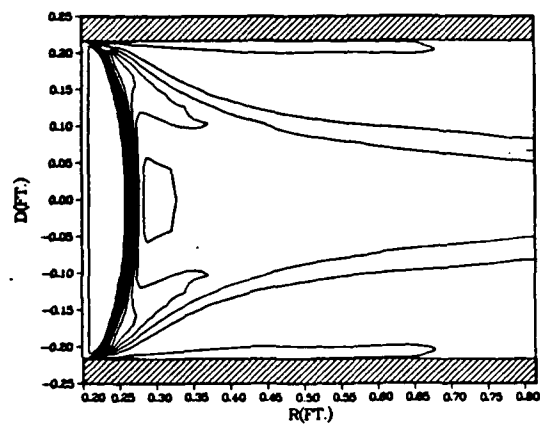
N=75K MACH CONTOURS 60%NSR WBB=0
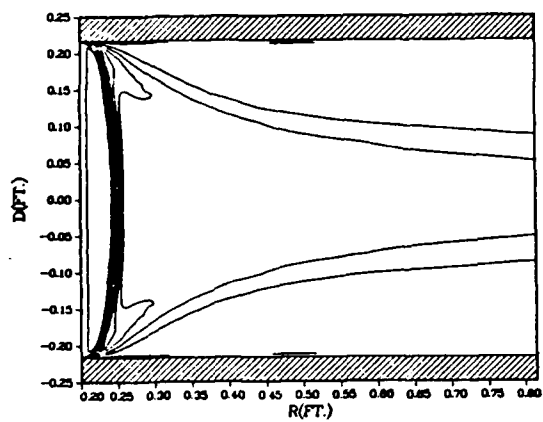
N=80K MACH CONTOURS 60%NSR WBB=0
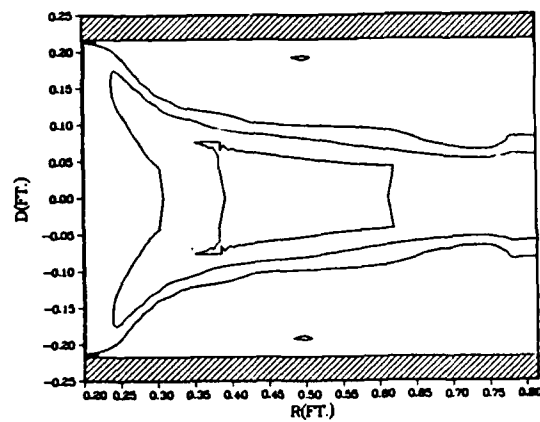
N=1 PW/PPI CSM 60%NSR WBB=0
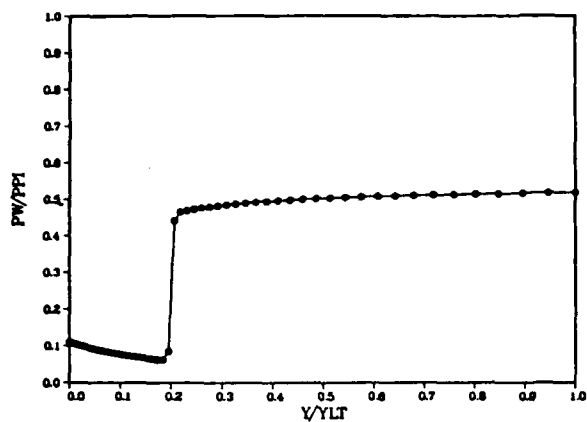
N=5K PW/PPI CSM 60%NSR WBB=0
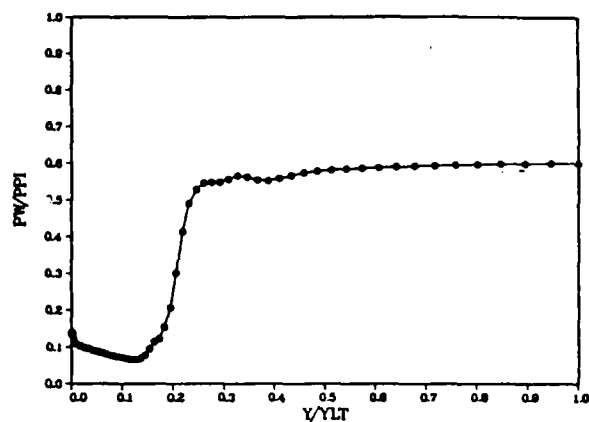
N=1 PCL/PPI CSM 60%NSR WBB=0
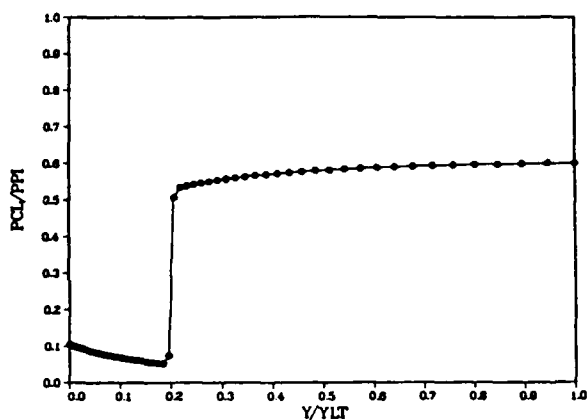
N=5K PCL/PPI CSM 60%NSR WBB=0
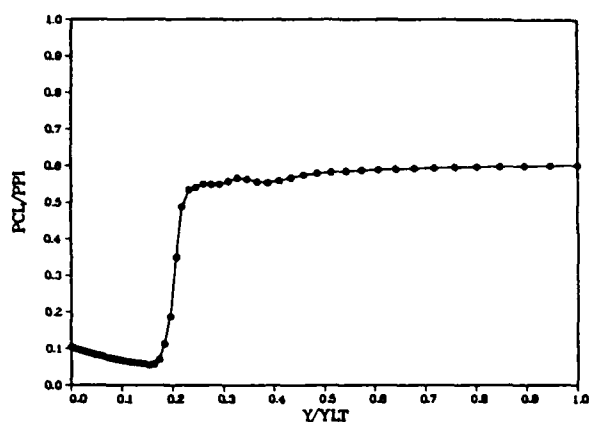
N=1 TCL/TO CSM 60%NSR WBB=0
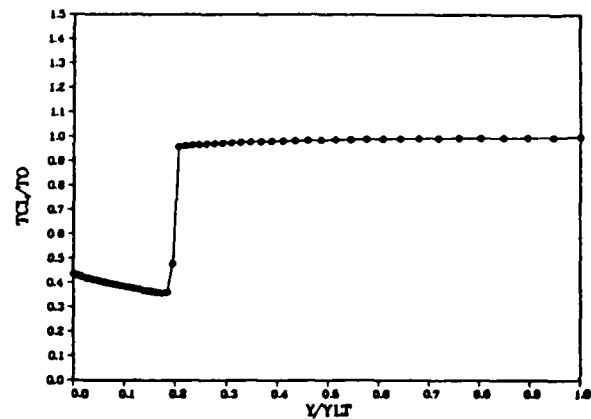
N=5K TCL/TO CSM 60%NSR WBB=0
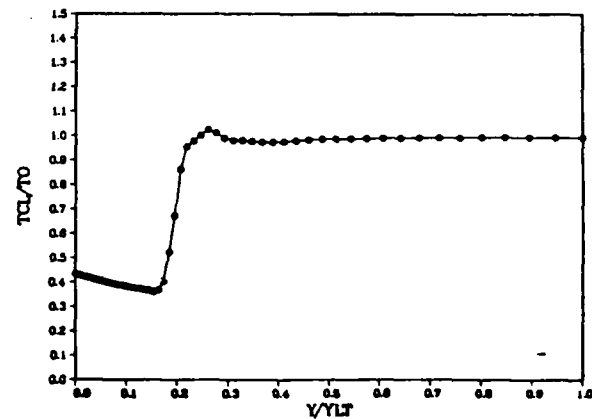
N=10K PW/PPI CSM 60%NSR WBB=0
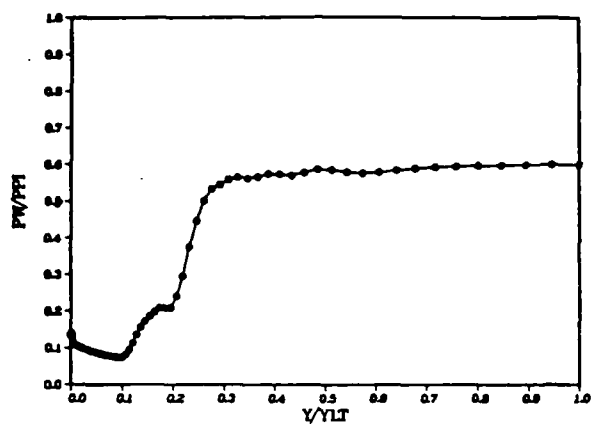
N=15K PW/PPI CSM 60%NSR WBB=0
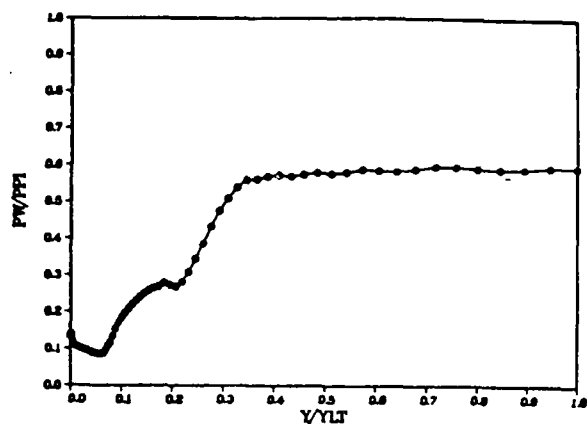
N=10K PCL/PPI CSM 60%NSR WBB=0
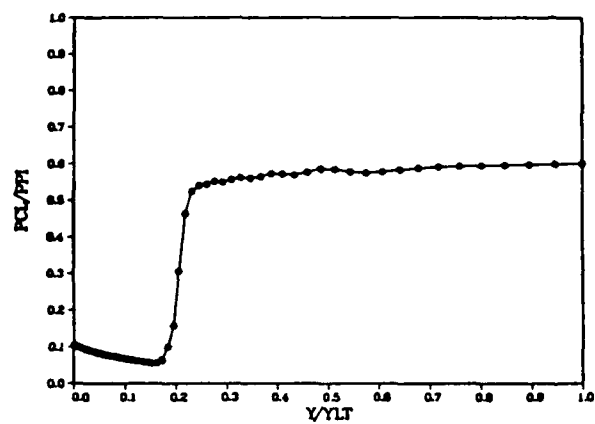
N=15K PCL/PPI CSM 60%NSR WBB=0
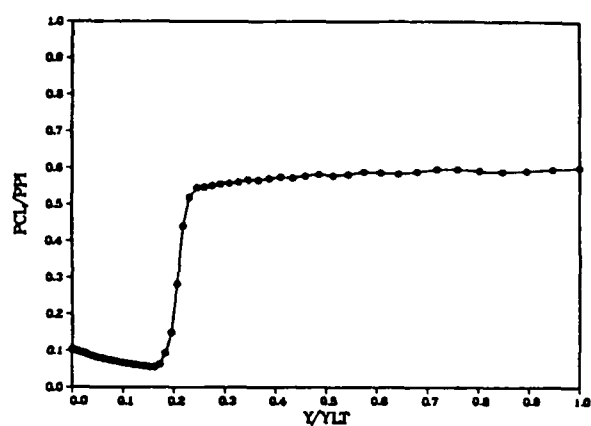
N=10K TCL/TO CSM 60%NSR WBB=0

N=15K TCL/TO CSM 60%NSR WBB=0

232
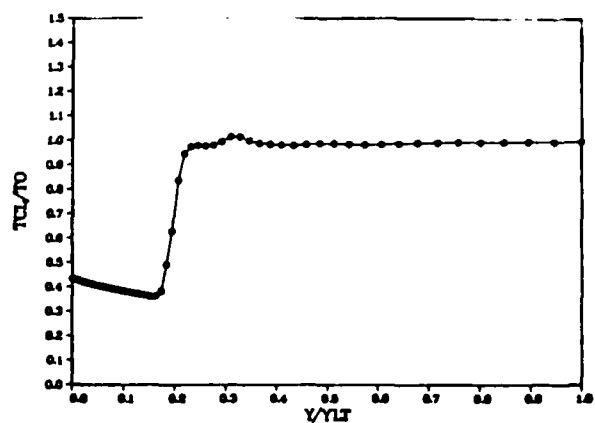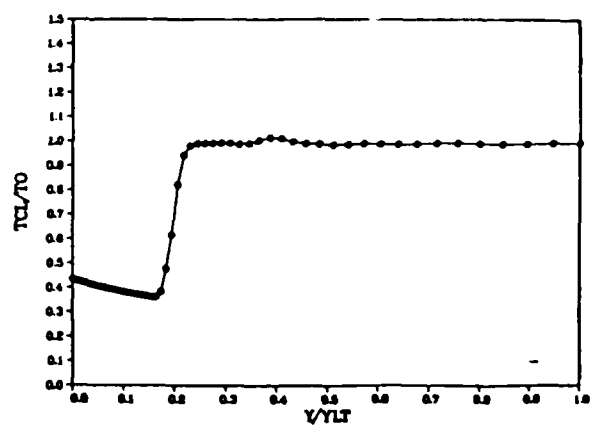
N=20K PW/PPI CSM 60%NSR WBB=0
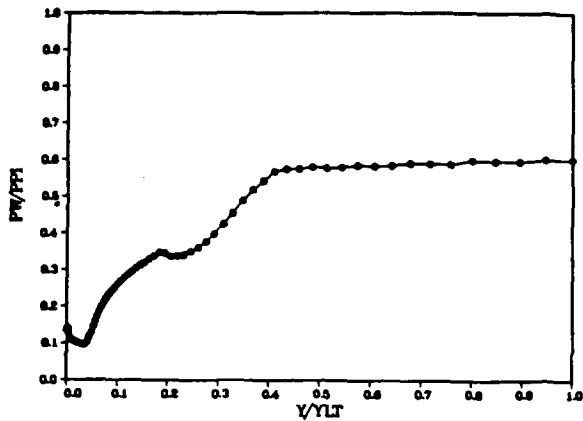
N=25K PW/PPI CSM 60%NSR WBB=0
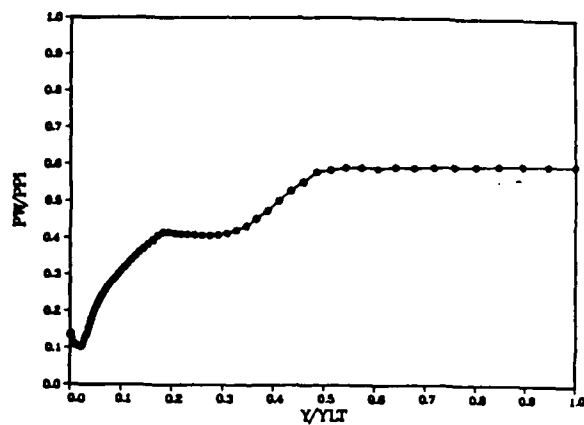
N=20K PCL/PPI CSM 60%NSR WBB=0
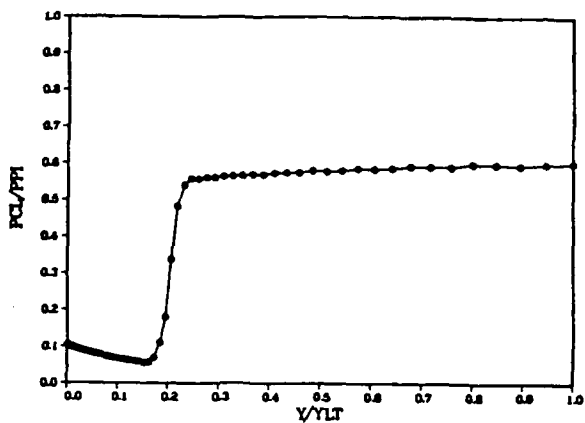
N=25K PCL/PPI CSM 60%NSR WBB=0
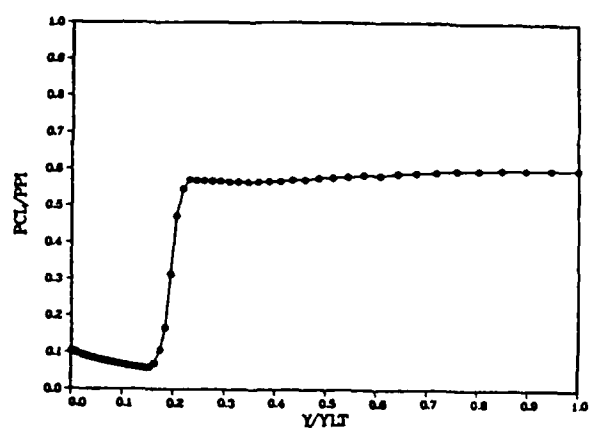
N=20K TCL/TO CSM 60%NSR WBB=0
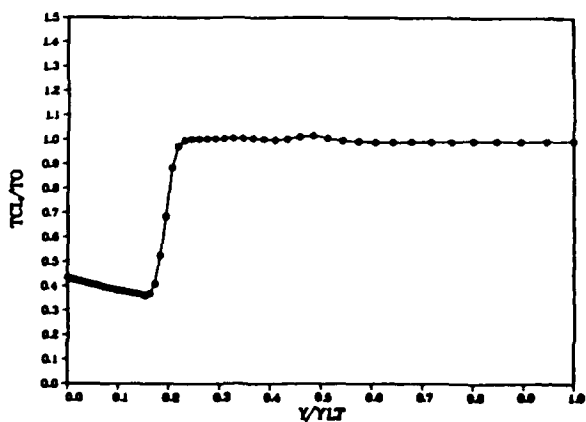
N=25K TCL/TO CSM 60%NSR WBB=0
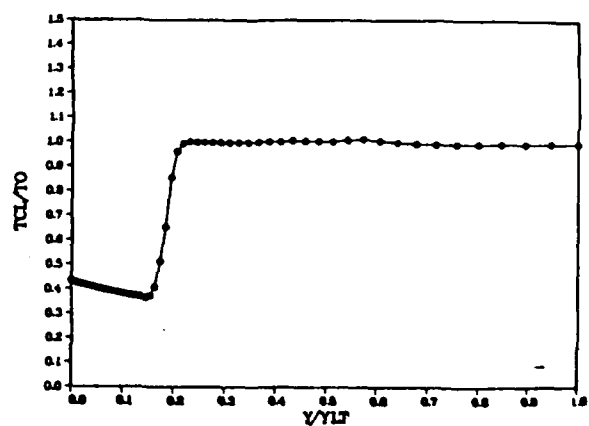
N=30K PW/PPI CSM 60%NSR WBB=0
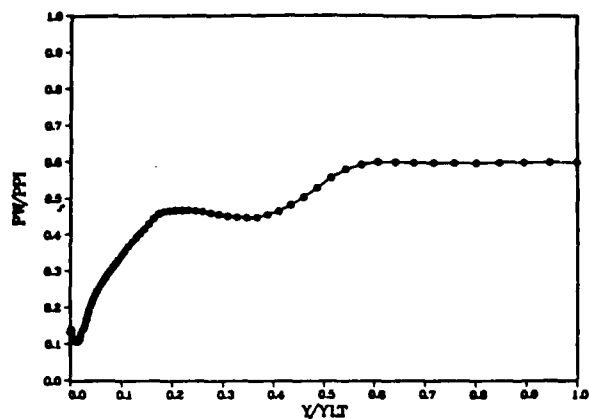
N=35K PW/PPI CSM 60%NSR WBB=0
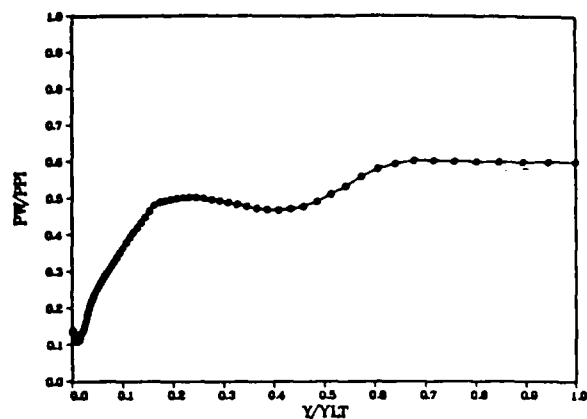
N=30K PCL/PPI CSM 60%NSR WBB=0
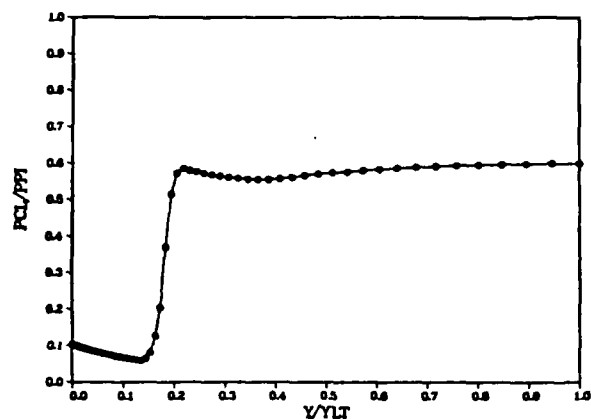
N=35K PCL/PPI CSM 60%NSR WBB=0
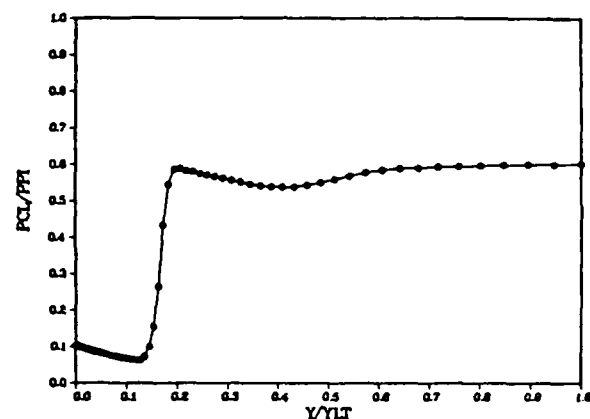
N=30K TCL/TO CSM 60%NSR WBB=0

N=35K TCL/TO CSM 60%NSR WBB=0

234
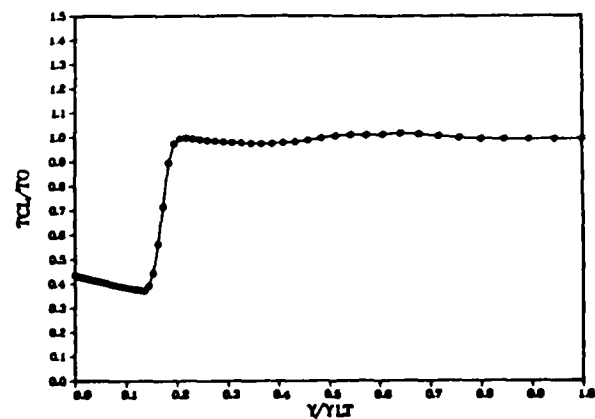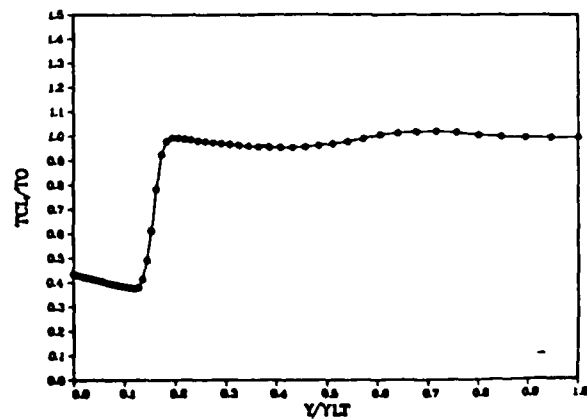
N=40K PW/PPI CSM 60%NSR WBB=0
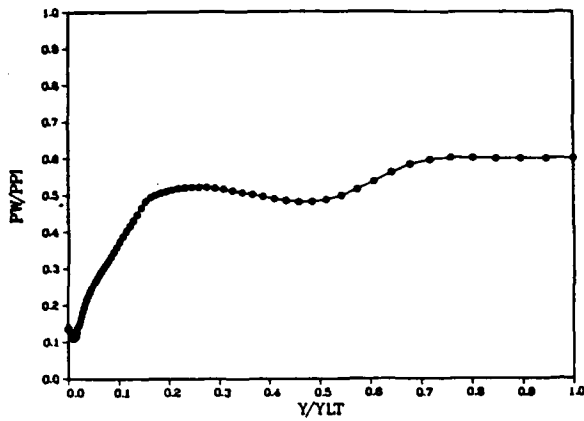
N=45K PW/PPI CSM 60%NSR WBB=0
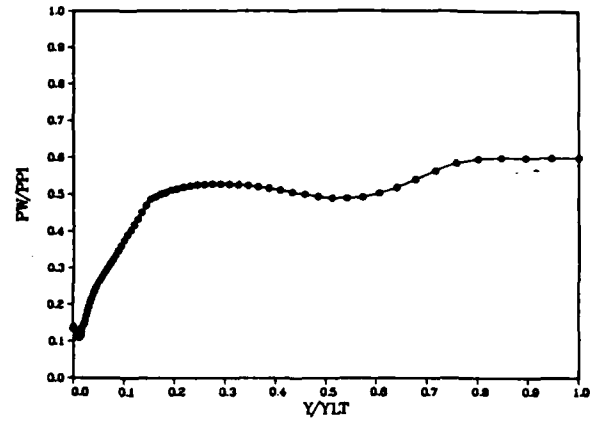
N=40K PCL/PPI CSM 60%NSR WBB=0
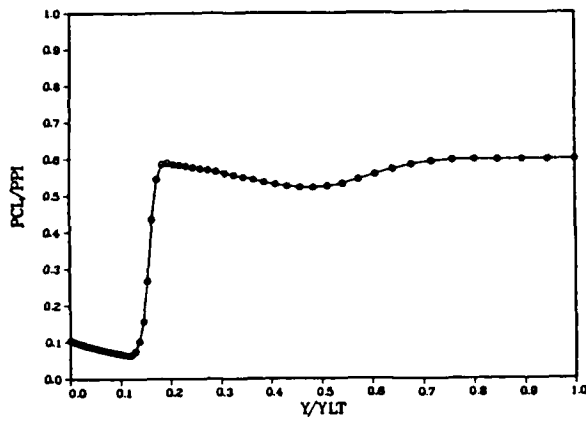
N=45K PCL/PPI CSM 60%NSR WBB=0
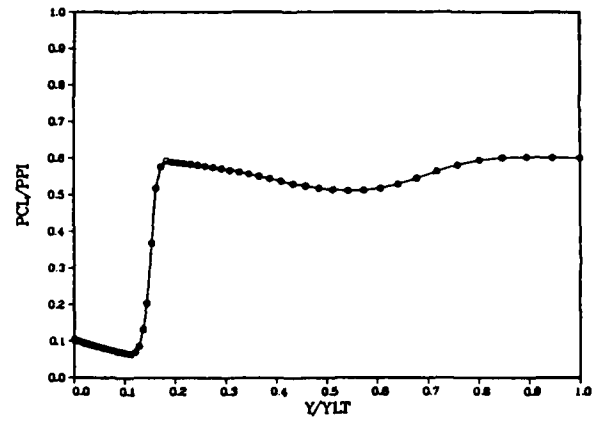
N=40K TCL/TO CSM 60%NSR WBB=0

N=45K TCL/TO CSM 60%NSR WBB=0

235
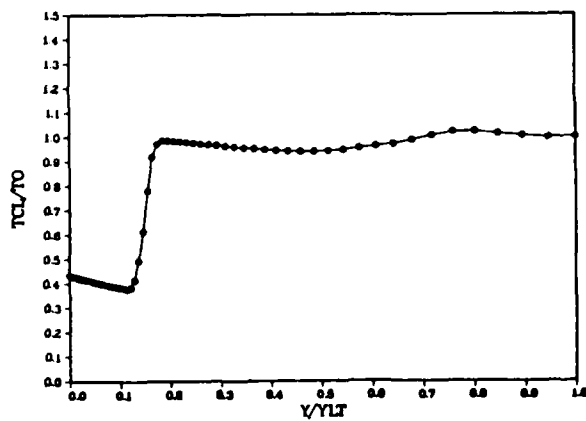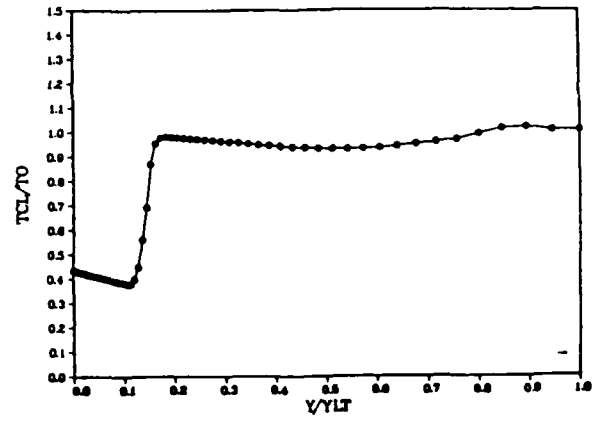
N=50K PW/PPI CSM 60%NSR WBB=0
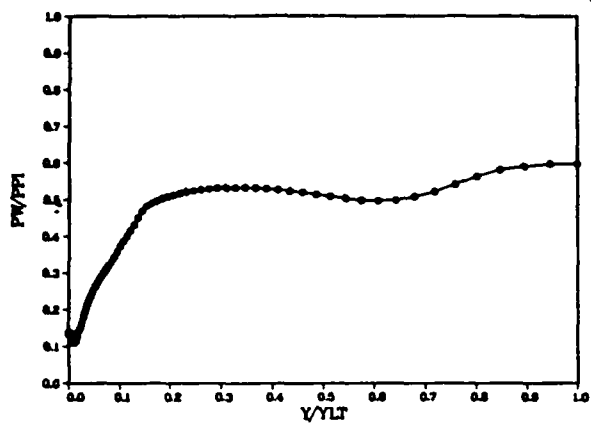
N=55K PW/PPI CSM 60%NSR WBB=0
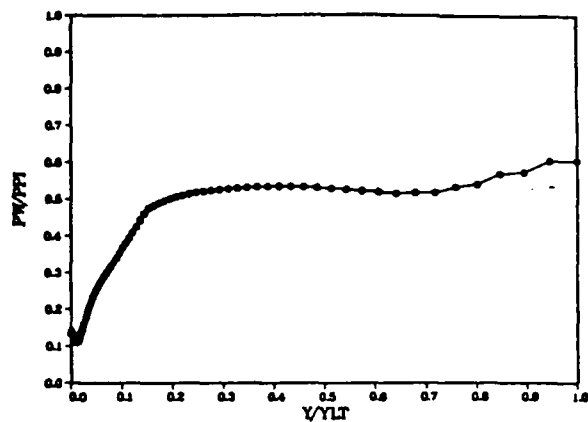
N=50K PCL/PPI CSM 60%NSR WBB=0
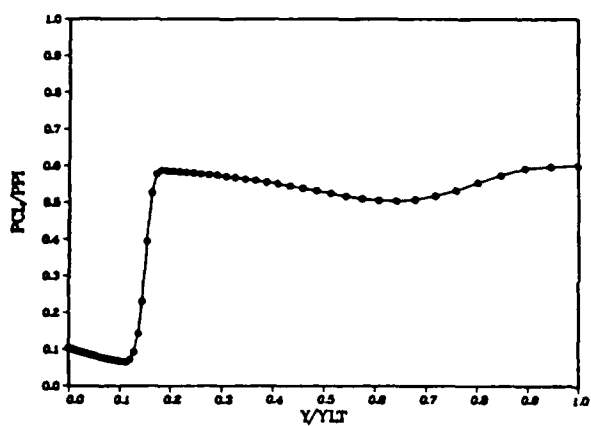
N=55K PCL/PPI CSM 60%NSR WBB=0
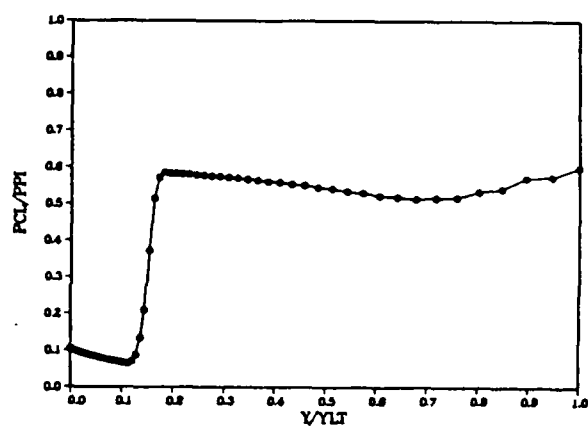
N=50K TCL/TO CSM 60%NSR WBB=0
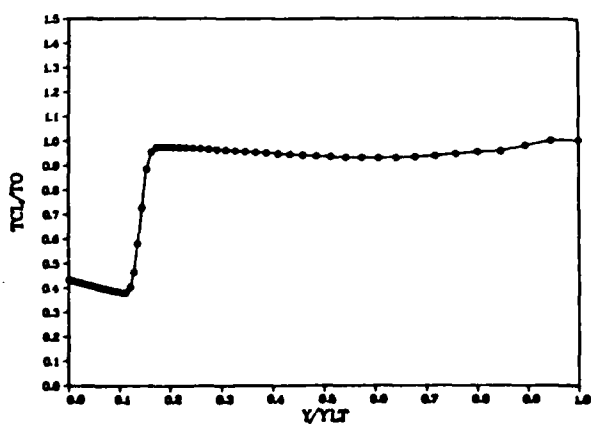
N=55K TCL/TO CSM 60%NSR WBB=0
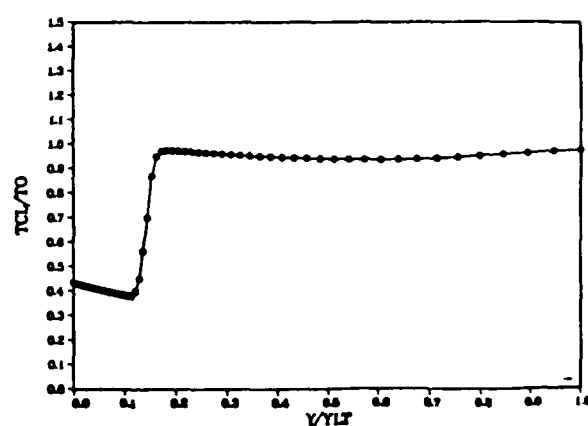
N=60K PW/PPI CSM 60%NSR WBB=0
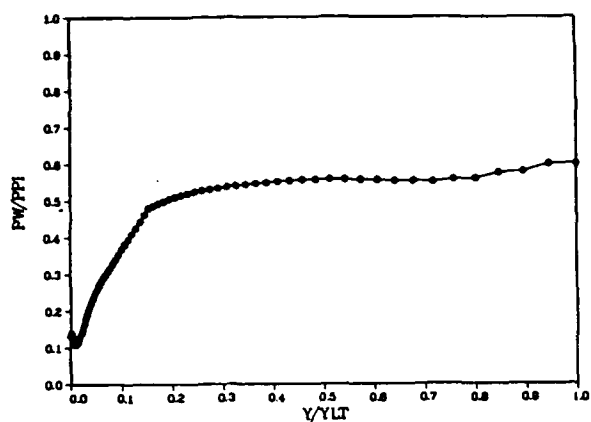
N=65K PW/PPI CSM 60%NSR WBB=0
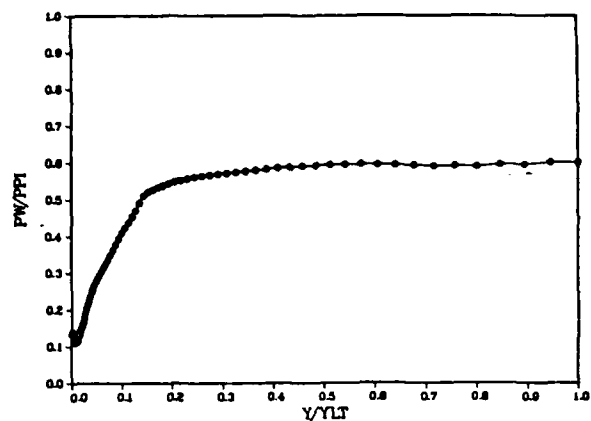
N=60K PCL/PPI CSM 60%NSR WBB=0
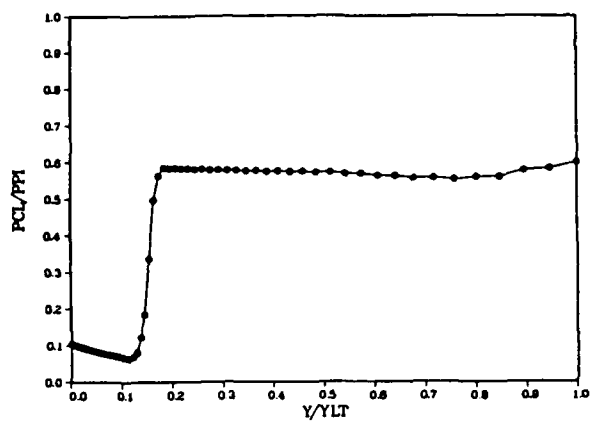
N=65K PCL/PPI CSM 60%NSR WBB=0
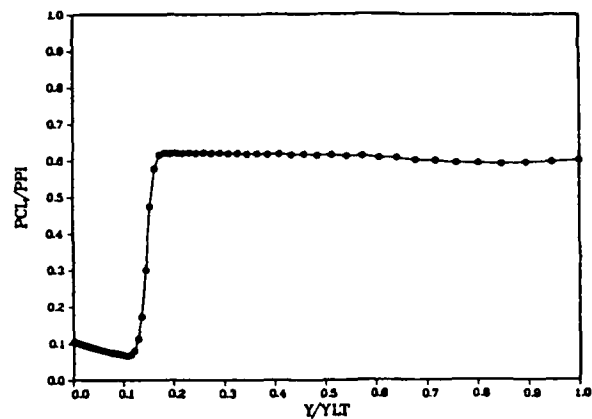
N=60K TCL/TO CSM 60%NSR WBB=0

N=65K TCL/TO CSM 60%NSR WBB=0

237
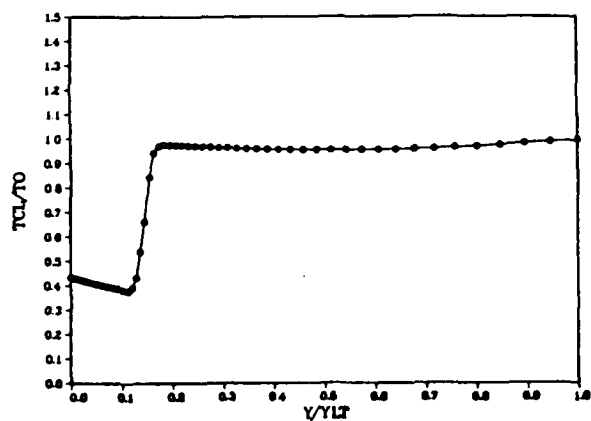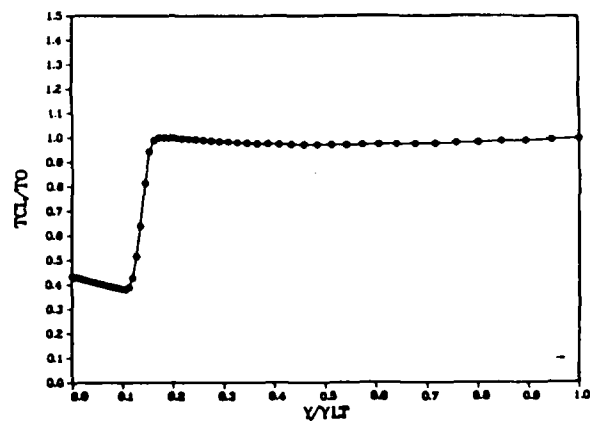
N=70K PW/PPI CSM 60%NSR WBB=0
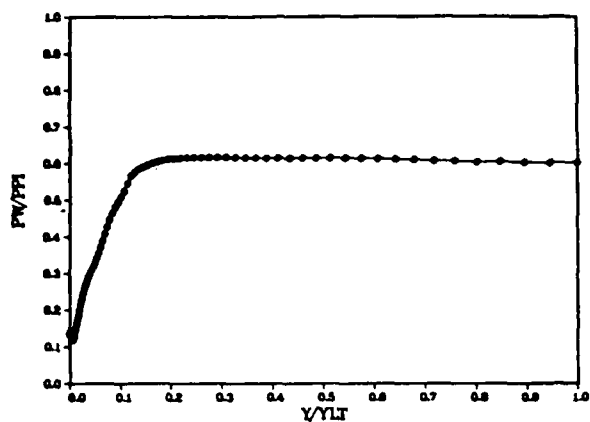
N=75K PW/PPI CSM 60%NSR WBB=0
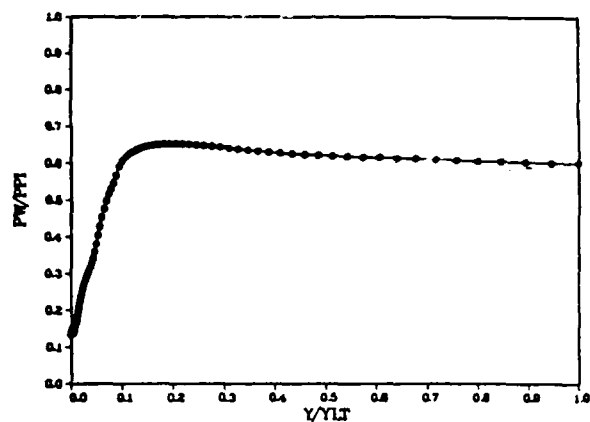
N=70K PCL/PPI CSM 60%NSR WBB=0
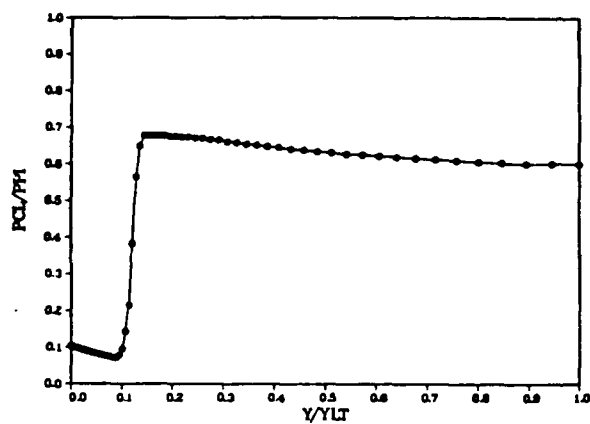
N=75K PCL/PPI CSM 60%NSR WBB=0
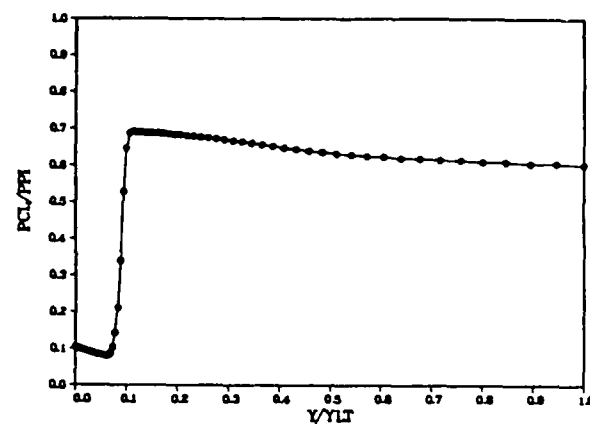
N=70K TCL/TO CSM 60%NSR WBB=0
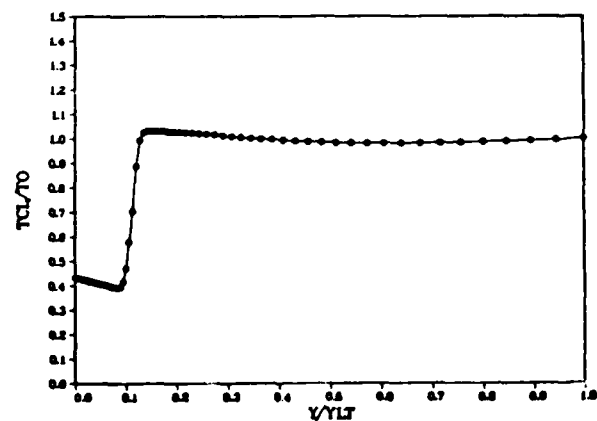
N=75K TCL/TO CSM 60%NSR WBB=0
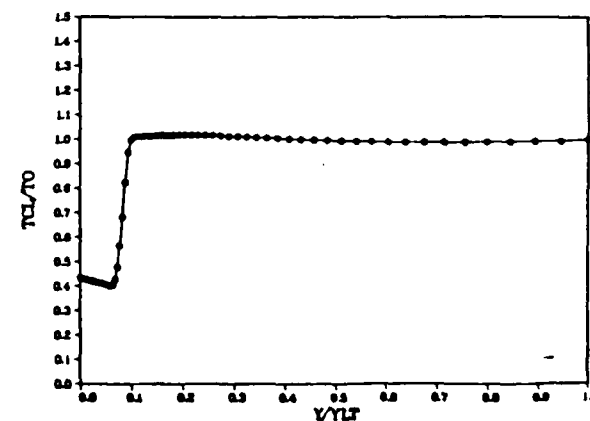
N=80K PW/PPI CSM 60%NSR WBB=0
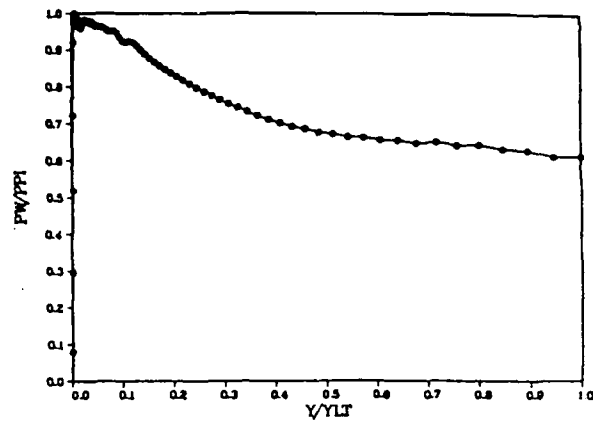
N=80K PCL/PPI CSM 60%NSR WBB=0
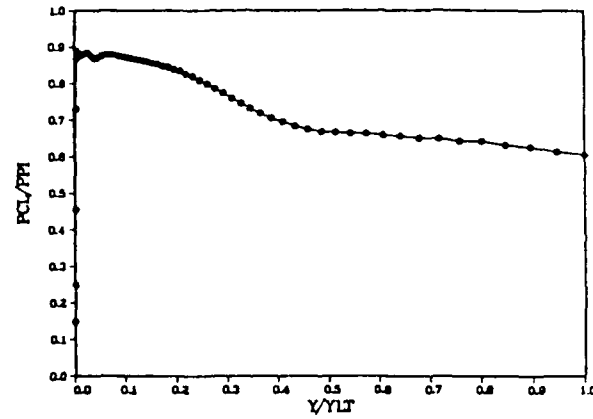
N=80K TCL/TO CSM 60%NSR WBB=0
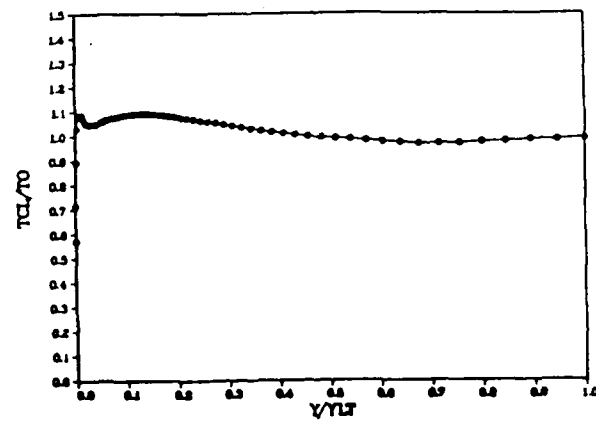
APPENDIX E

NUMERICAL CASE 2A COMPUTATIONAL DETAILS

In this numerical experiment wall flow energization was added to a
uniform core inflow.   The core flow was set at M = 2.5.   Wall bank blowers
were added at a mass fraction of 20 percent of the core flow, operating at
M = 4.0.   Fxit pressure was set at 60% of normal shock recovery pressure.
The Navier-Stokes computer code employed the standard Cebeci-Smith two-layer
algebraic eddy viscosity turbulence model unmodified for the effects of an
adverse pressure gradient.   Details of this numerical case show the progress
of the core flow normal shock through the diffuser from the imposed one-
dimensional, inviscid normal shock initial condition through the diffuser
"unstart" at 7.6 milliseconds after flow "initiation."   The time history is
presented first repeating Figure 22.   The application of wall flow
energization is clearly seen in the delay of the "unstart" by a factor of
nearly three in time;   this is reflected in the Mach contour plots presented
beginning with the initial condition and proceeding in increments of 5,000
numerical iterations through N = 101,000, when the numerical "unstart" is
observed.   Each plot presents the Mach contours from M = 0.0 through M =
5.0, in increments of 0.20.   Following the Mach contour plots are a series
of corresponding nondimensionalized wall pressure, line of symmetry
pressure, and line of symmetry temperature plots.   Flow development, as
observed from the Mach contour plots, is seen to be considerably different
from that in case 1, where no wall flow energization was employed.   Worthy
of special note is the persistence of the wall bank blower flow throughout
the diffuser and the resulting definition of an entirely different wall
boundary layer separation region.   Evaluation of the wall pressure plots

again shows a too severe pressure gradient along the wall, and the result is again core flow choking and diffuser "unstart." This numerical experiment required 97.5 minutes of CRAY 1 CPU time.

CSB TIME HISTORY 60%NSR WBB=.2
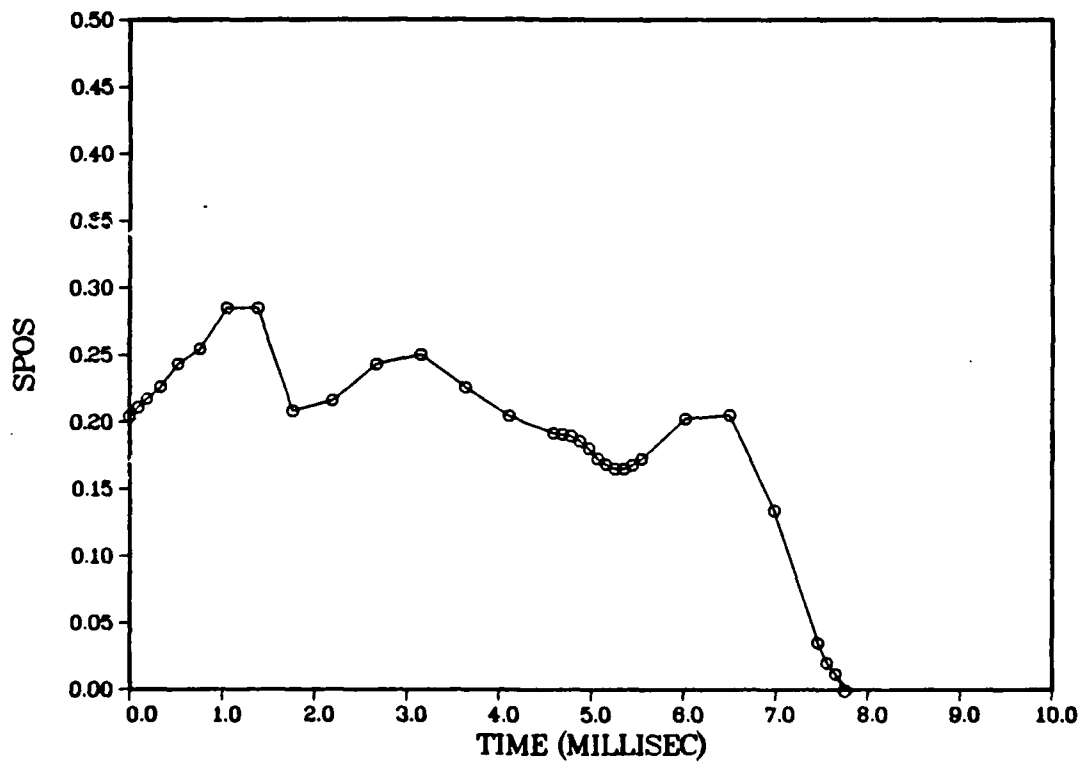
TABLE VI

NUMERICAL CASE 2A COMPUTED SHOCK POSITION VS TIME

N Number of Iterations	CFL	TIME (Milliseconds)	R/R_{de}	SPOS
0		0	1.614800	0.200000
5,000	.10	0.095720	1.648144	0.210848
10,000	.10	0.191400	1.667660	0.217197
15,000	.15	0.334900	1.694493	0.225926
20,000	.20	0.526300	1.747688	0.243231
25,000	.25	0.765500	1.781665	0.254284
30,000	.30	1.052500	1.875062	0.284667
35,000	.35	1.387400	1.874970	0.284637
40,000	.40	1.770100	1.640185	0.208259
45,000	.45	2.200700	1.664012	0.216010
50,000	.50	2.679100	1.746628	0.242886
55,000		3.157500	1.768914	0.250136
60,000		3.635900	1.693651	0.225652
65,000		4.114300	1.628362	0.204413
70,000		4.592700	1.588687	0.191506
75,000		5.071150	1.530465	0.172566
80,000		5.549600	1.529617	0.172290
85,000		6.027965	1.621766	0.202267
90,000		6.506400	1.630656	0.205159
95,000		6.984800	1.411284	0.133795
100,000		7.463186	1.107168	0.034863
101,000		7.558770	1.061157	0.019895

242

N=1 CSB MACH CONTOURS 60%NSR WBB=2
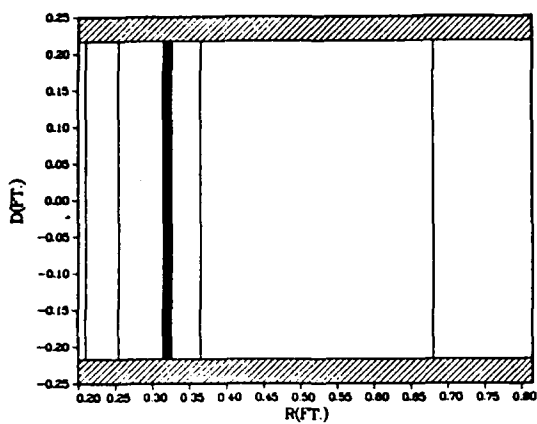
N=5K CSB MACH CONTOURS 60%NSR WBB=2
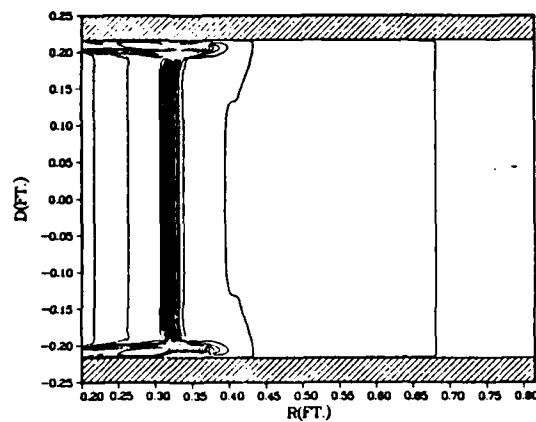
N=10K CSB MACH CONTOURS 60%NSR WBB=2
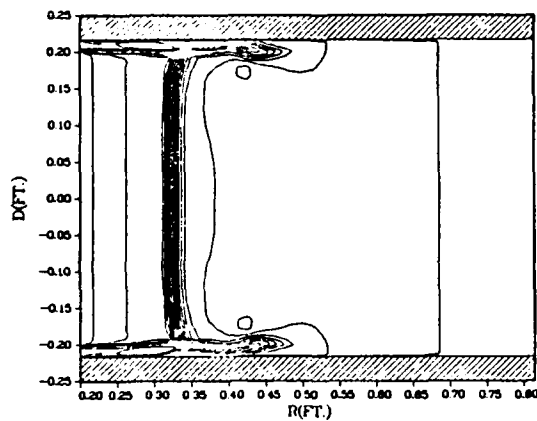
N=15K CSB MACH CONTOURS 60%NSR WBB=2
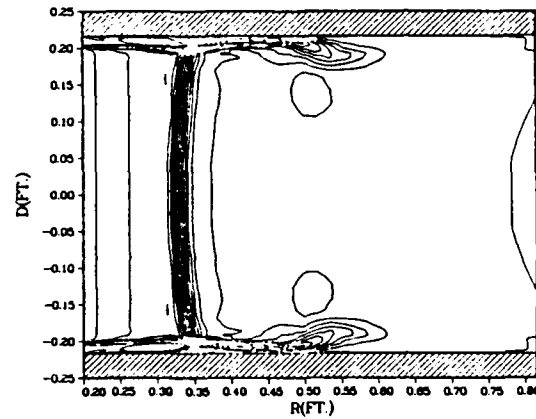
N=20K CSB MACH CONTOURS 60%NSR WBB=2
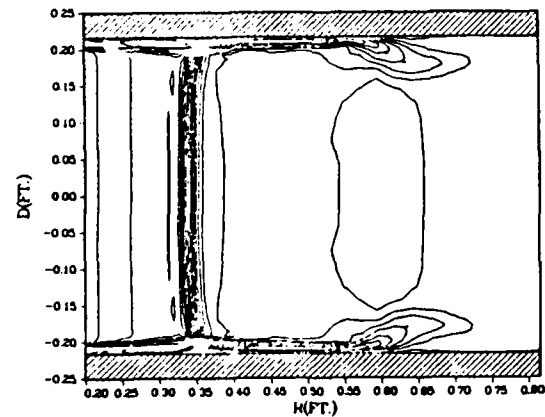
N=25K CSB MACH CONTOURS 60%NSR WBB=2
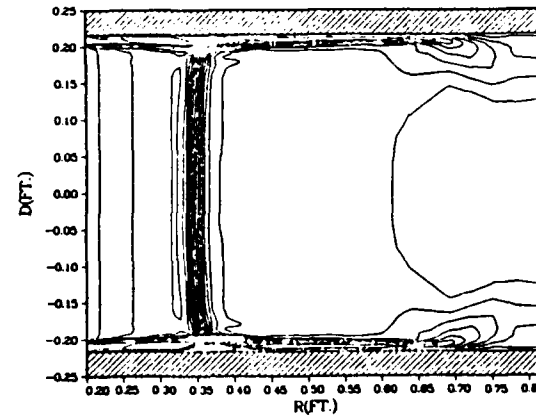
N=30K CSB MACH CONTOURS 60%NSR WBB=2
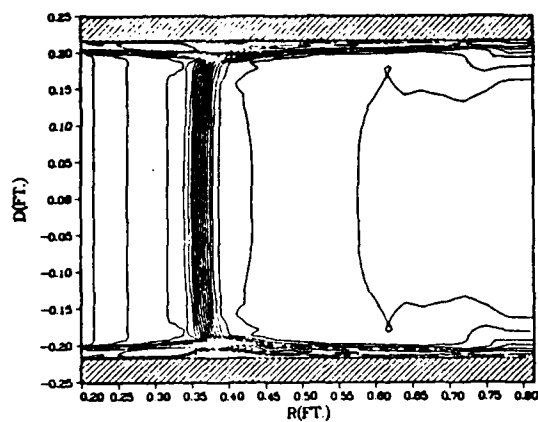
N=35K CSB MACH CONTOURS 60%NSR WBB=2
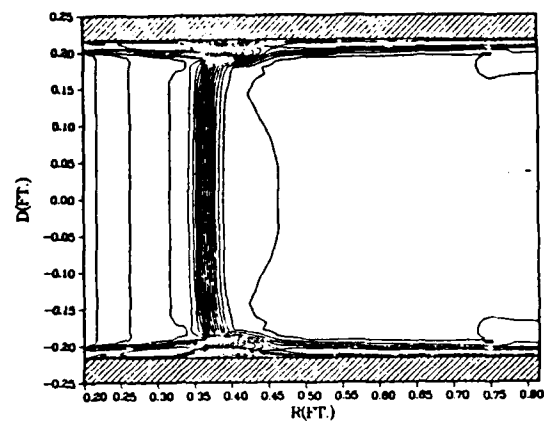
N=40K CSB MACH CONTOURS 60%NSR WBB=2
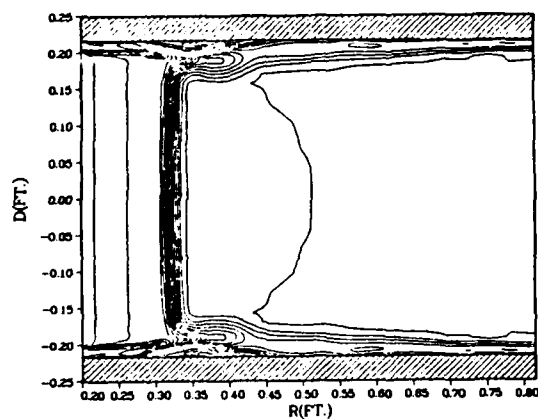
N=45K CSB MACH CONTOURS 60%NSR WBB=2
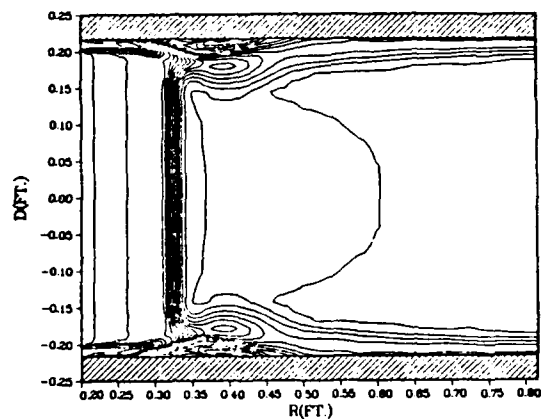
N=50K CSB MACH CONTOURS 60%NSR WBB=2
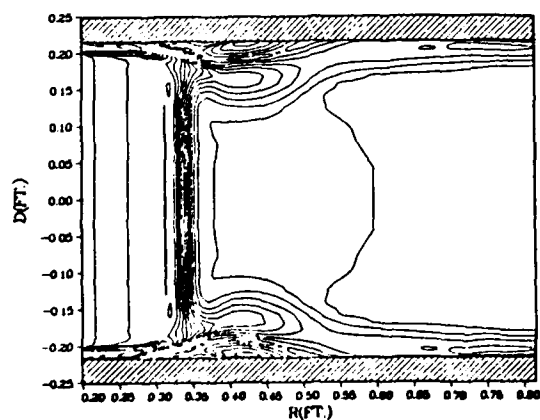
N=55K CSB MACH CONTOURS 60%NSR WBB=2
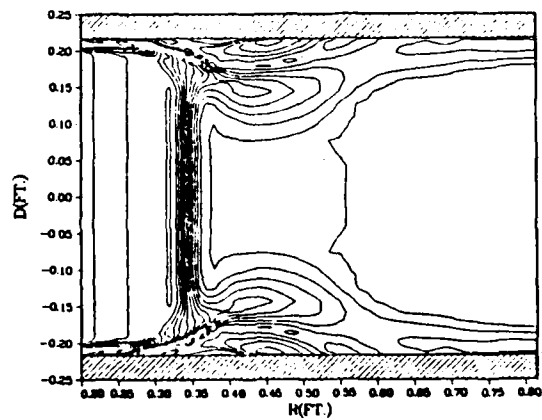
N=60K CSB MACH CONTOURS 60%NSR WBB=.2
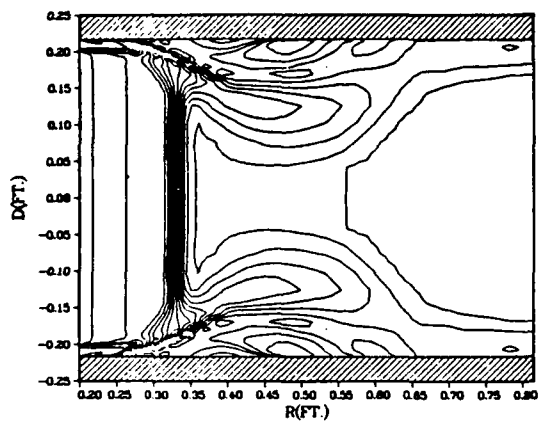
N=65K CSB MACH CONTOURS 60%NSR WBB=.2
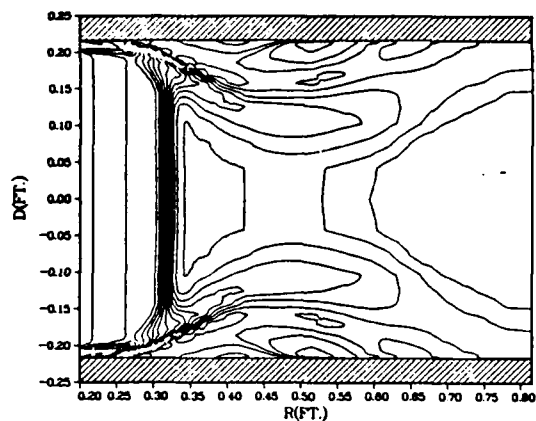
N=70K CSB MACH CONTOURS 60%NSR WBB=.2
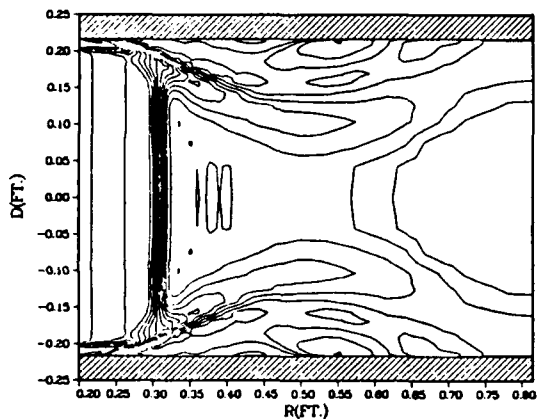
N=75K CSB MACH CONTOURS 60%NSR WBB=.2
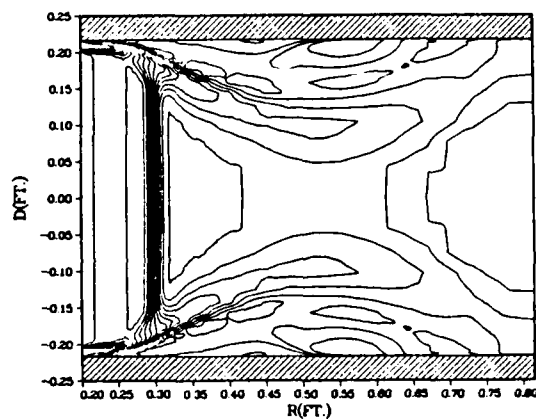
N=80K CSB MACH CONTOURS 60%NSR WBB=.2
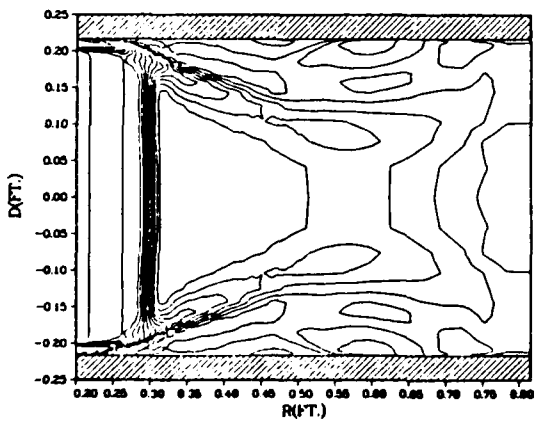
N=85K CSB MACH CONTOURS 60%NSR WBB=.2
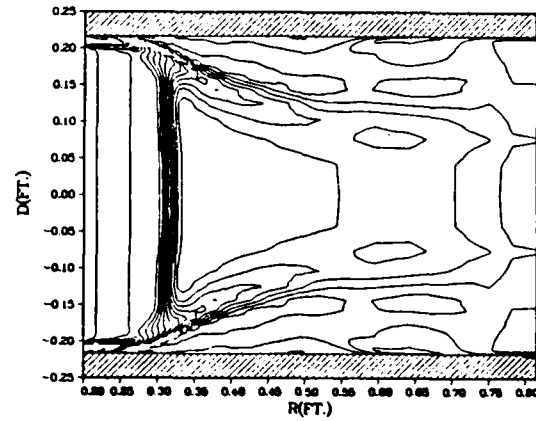
N=90K CSB MACH CONOUTRS 60%NSR WBB=.2   N=95K CSB MACH CONTOURS 60%NSR WBB=.2
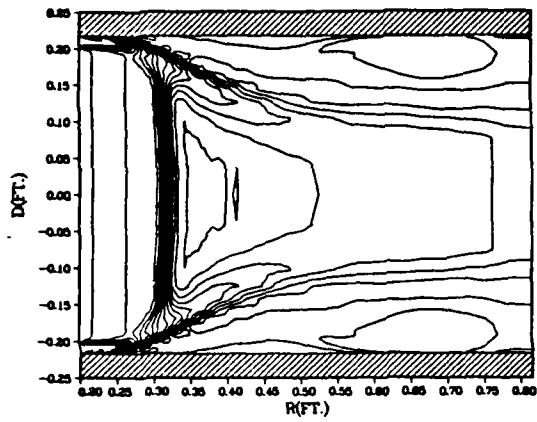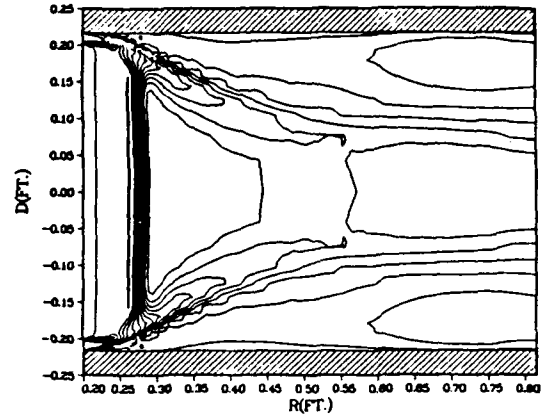
N=100K CSB MACH CONTOURS 60%NSR WBB=.2   N=101K CSB MACH CONTOURS 60%NSR WBB=.2
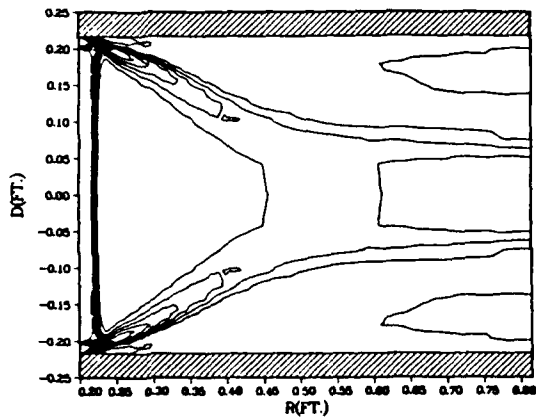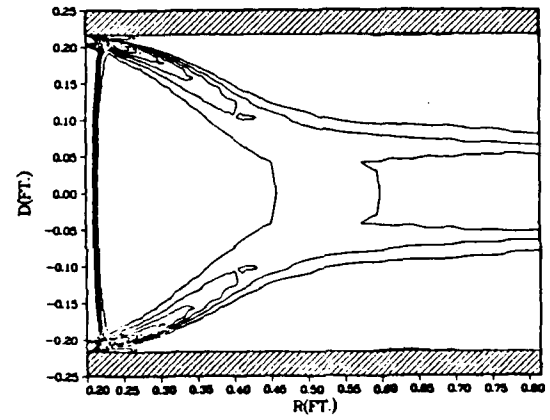
N=1 PW/PPI CSB 60%NSR WBB=2
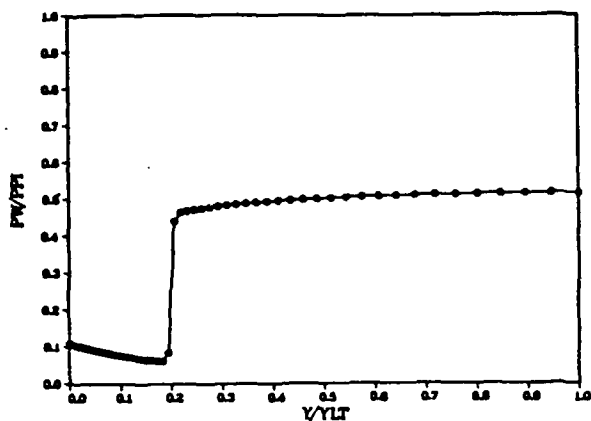
N=5K PW/PPI CSB 60%NSR WBB=2
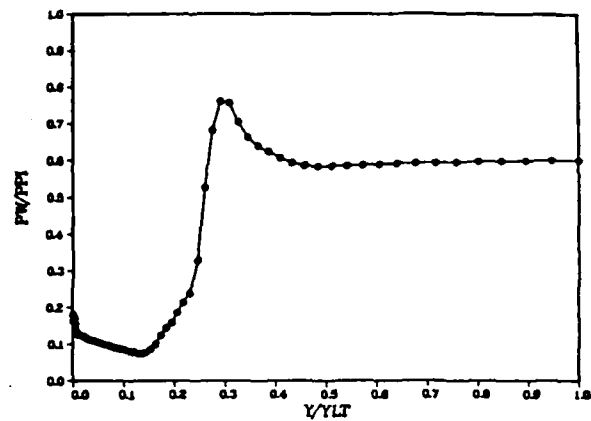
N=1 PCL/PPI CSB 60%NSR WBB=2
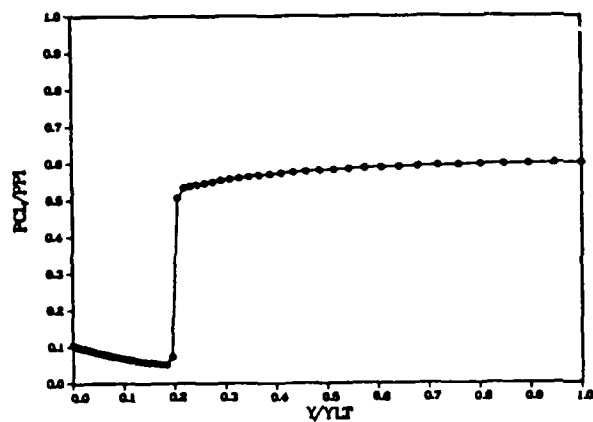
N=5K PCL/PPI CSB 60%NSR WBB=2
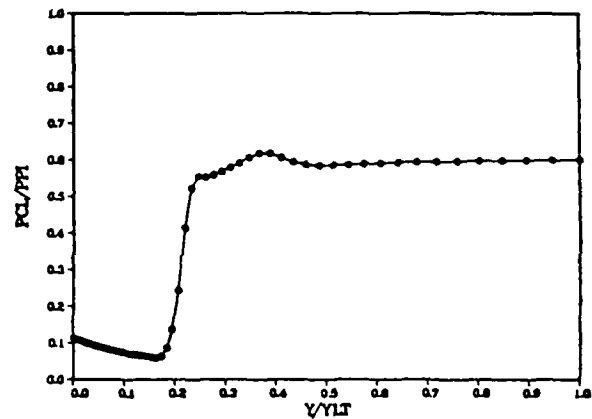
N=1 TCL/TO CSB 60%NSR WBB=2
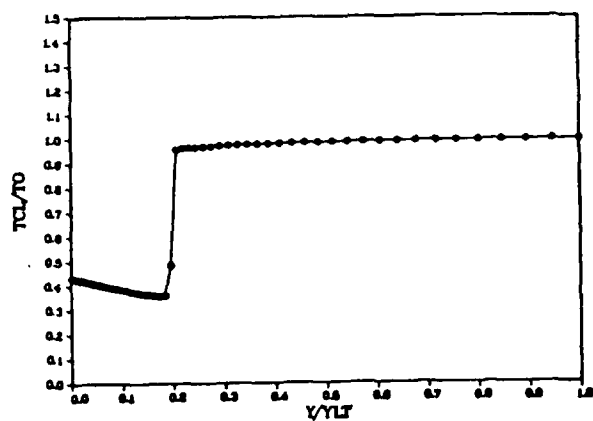
N=5K TCL/TO CSB 60%NSR WBB=2
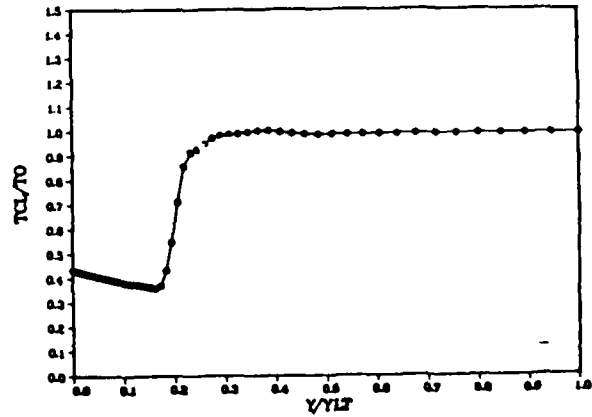
N=10K PW/PPI CSB 60%NSR WBB=.2
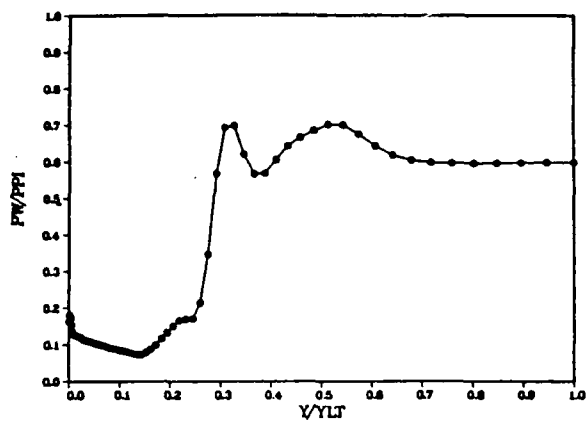
N=15K PW/PPI CSB 60%NSR WBB=.2
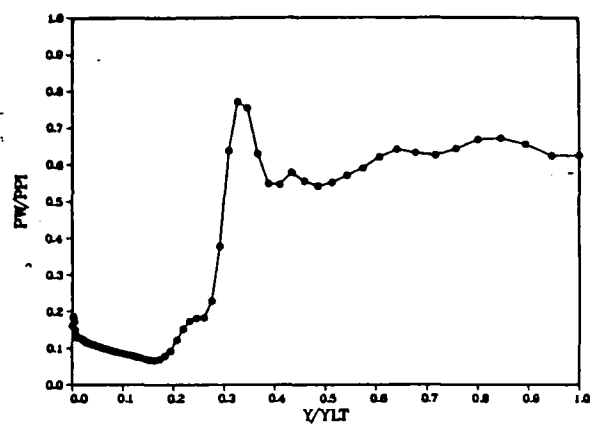
N=10K PCL/PPI CSB 60%NSR WBB=.2
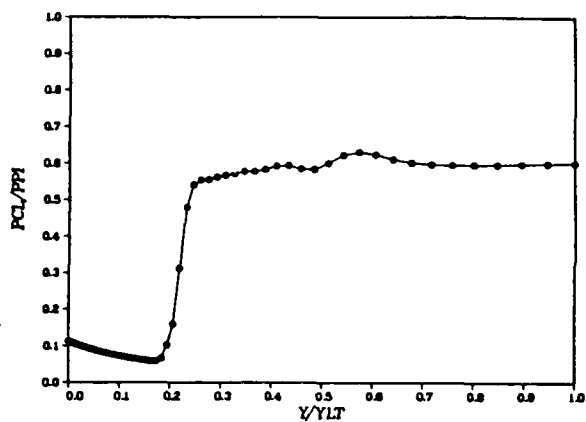
N=15K PCL/PPI CSB 60%NSR WBB=.2
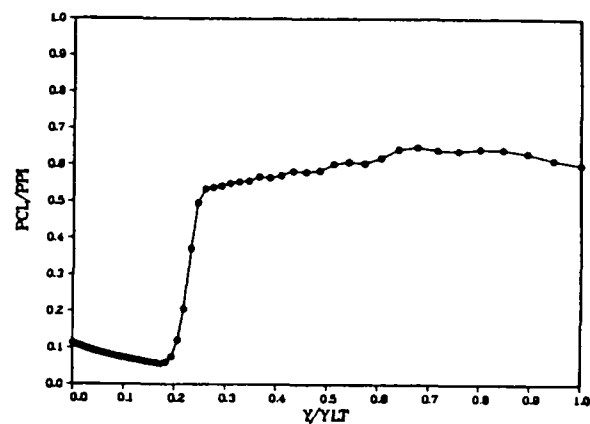
N=10K TCL/TO CSB 60%NSR WBB=.2
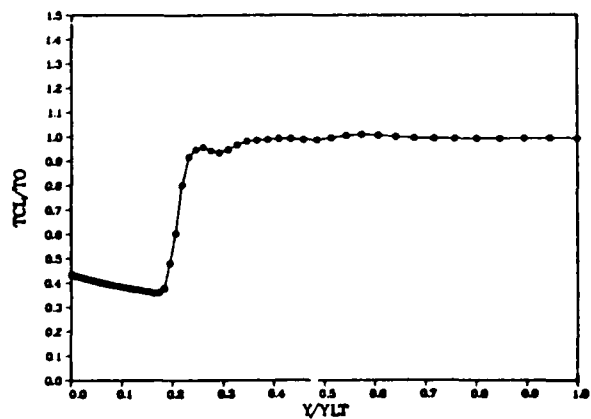
N=15K TCL/TO CSB 60%NSR WBB=.2
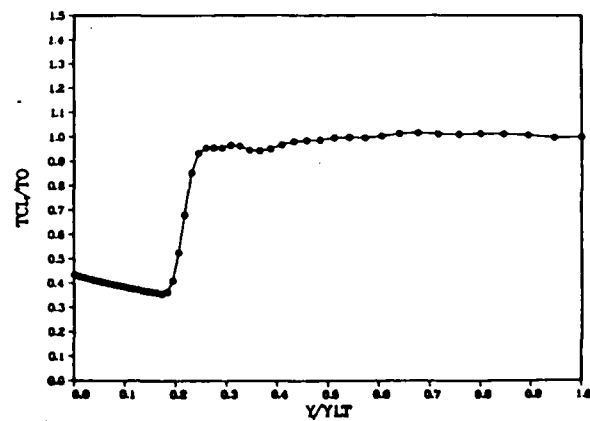
N=20K PW/PPI CSB 60%NSR WBB=2
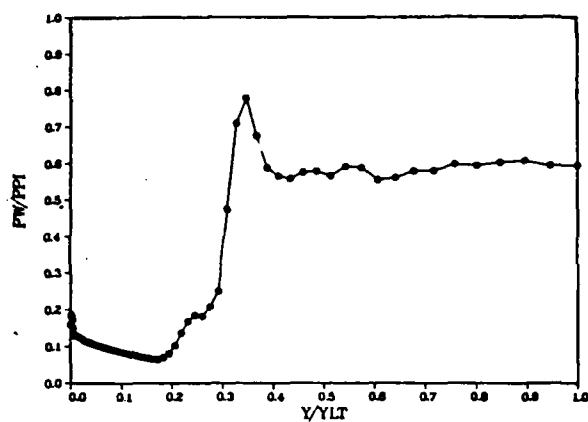
N=25K PW/PPI CSB 60%NSR WBB=2
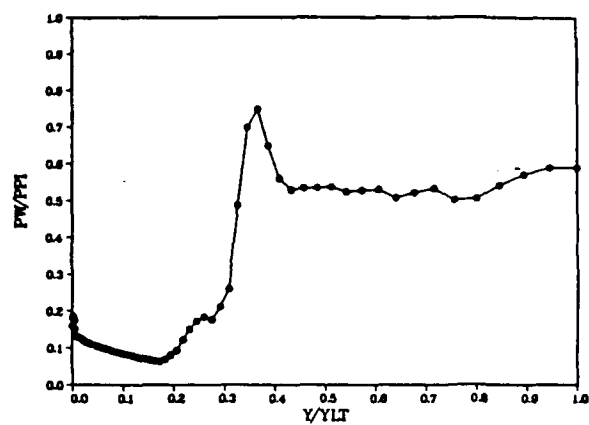
N=20K PCL/PPI CSB 60%NSR WBB=2
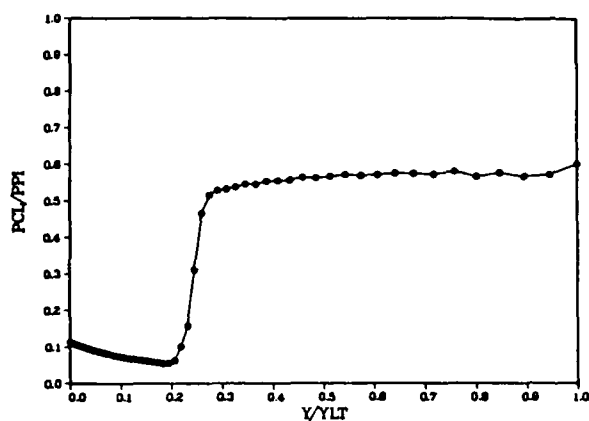
N=25K PCL/PPI CSB 60%NSR WBB=2
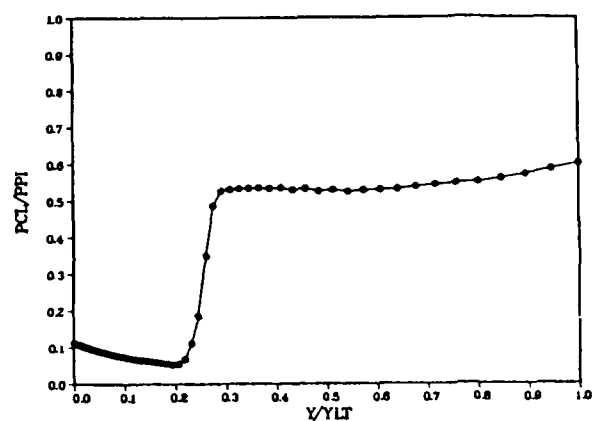
N=20K TCL/TO CSB 60%NSR WBB=2
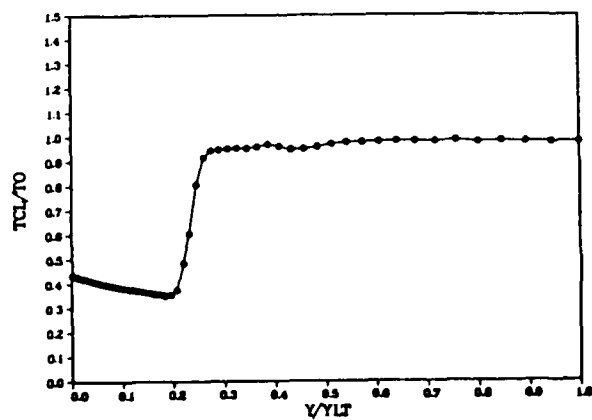
N=25K TCL/TO CSB 60%NSR WBB=2
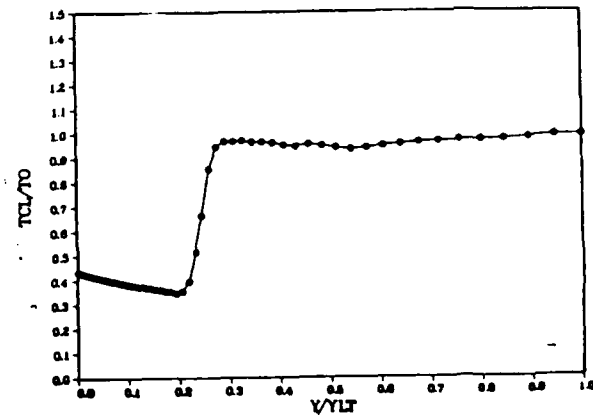
N=30K PW/PPI CSB 60%NSR WBB=2
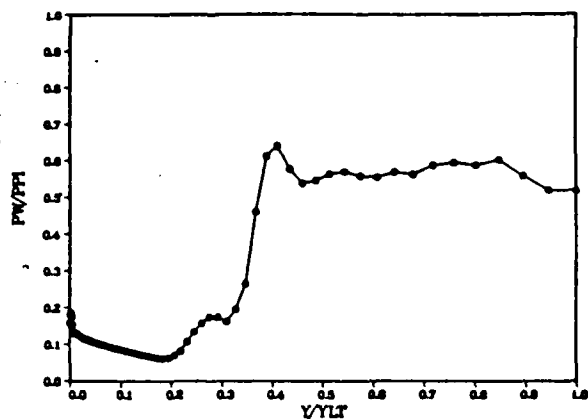
N=35K PW/PPI CSB 60%NSR WBB=2
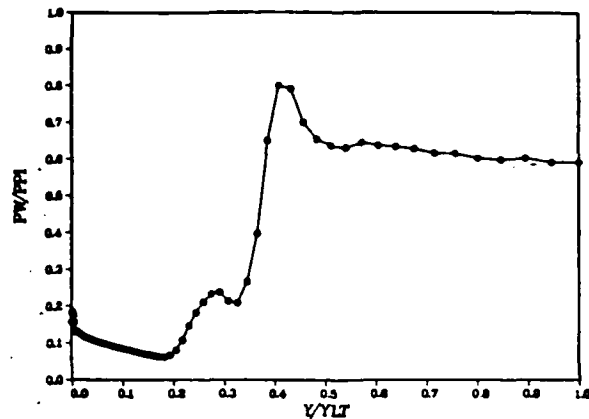
N=30K PCL/PPI CSB 60%NSR WBB=2
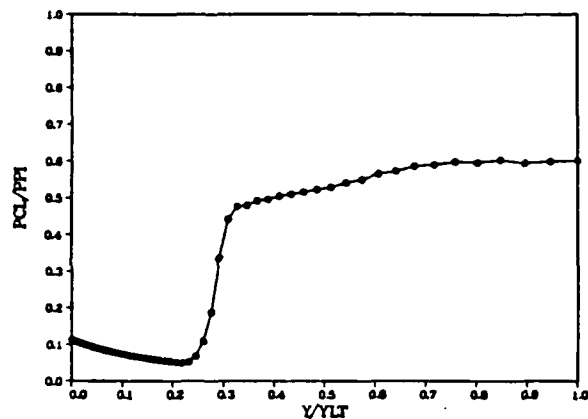
N=35K PCL/PPI CSB 60%NSR WBB=2
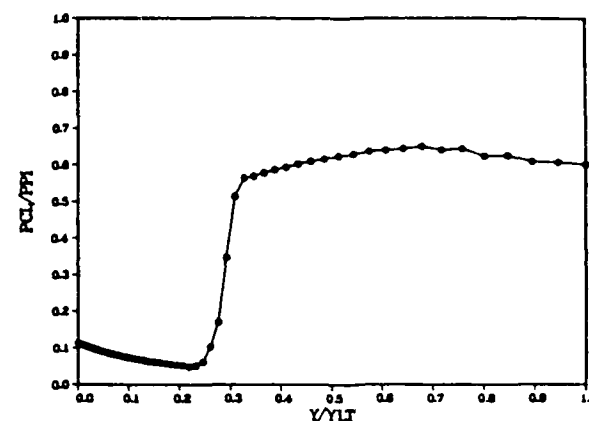
N=30K TCL/TO CSB 60%NSR WBB=2
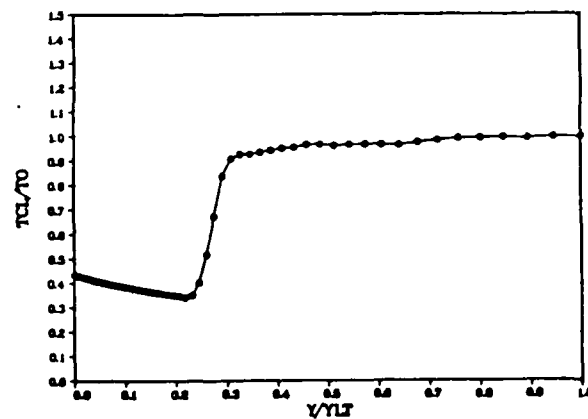
N=35K TCL/TO CSB 60%NSR WBB=2
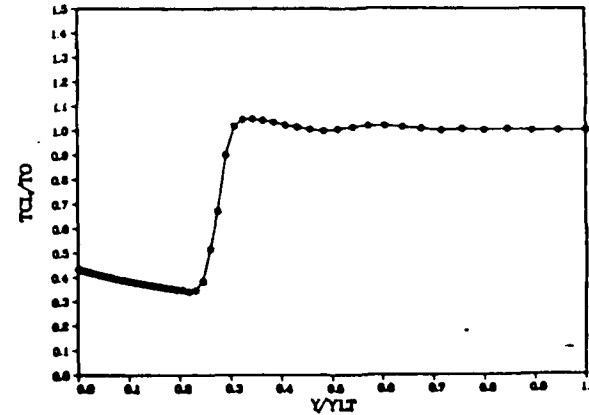
N=40K PW/PPI CSB 60%NSR WBB=.2
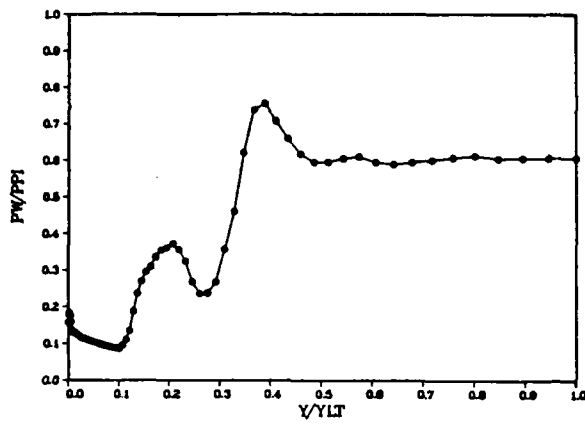
N=45K PW/PPI CSB 60%NSR WBB=.2
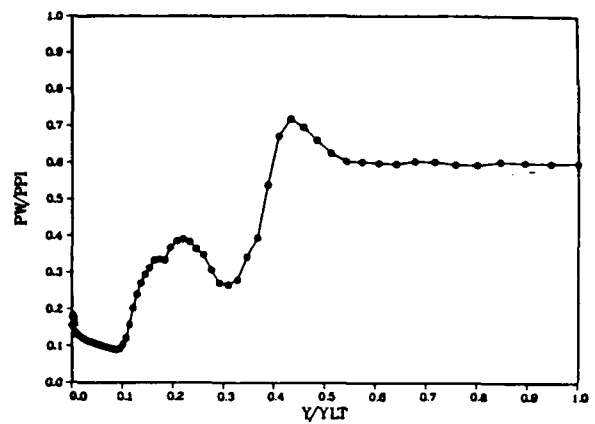
N=40K PCL/PPI CSB 60%NSR WBB=.2
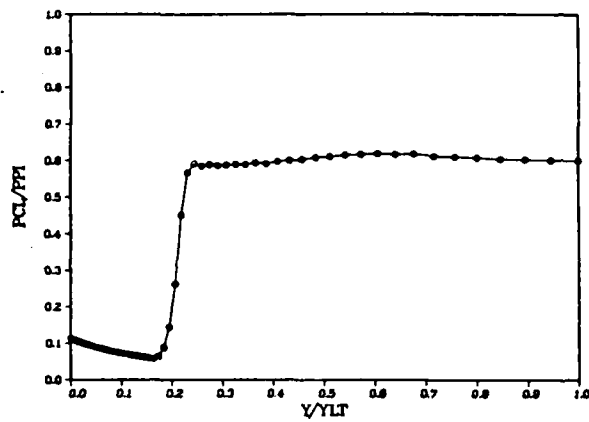
N=45K PCL/PPI CSB 60%NSR WBB=.2
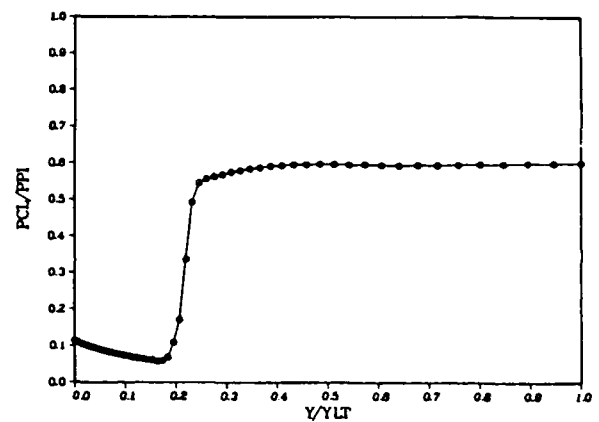
N=40K TCL/TO CSB 60%NSR WBB=.2
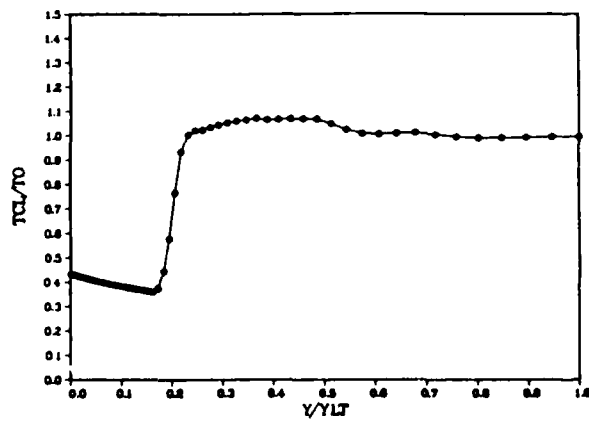
N=45K TCL/TO CSB 60%NSR WBB=.2
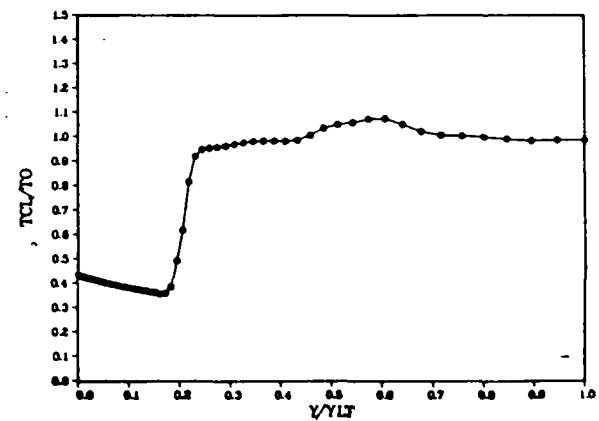
N=50K PW/PPI CSB 60%NSR WBB=2
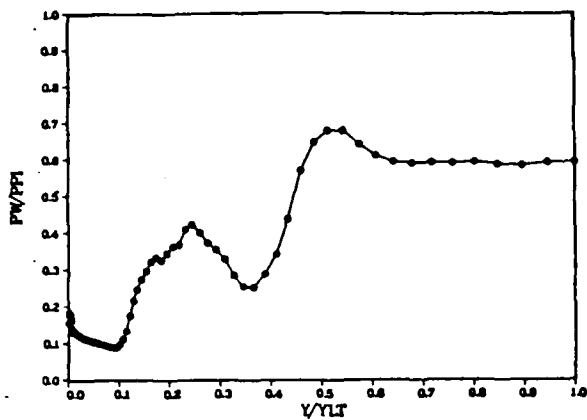
N=55K PW/PPI CSB 60%NSR WBB=2
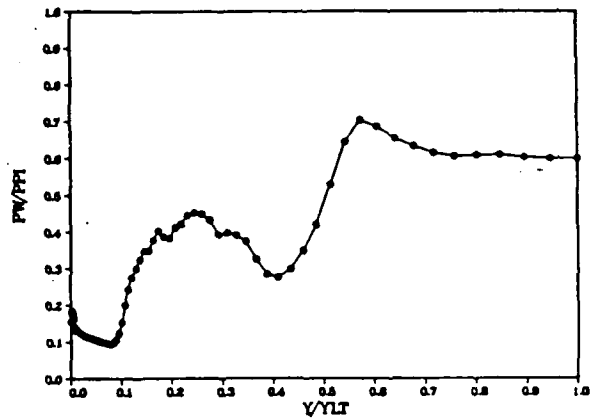
N=50K PCL/PPI CSB 60%NSR WBB=2
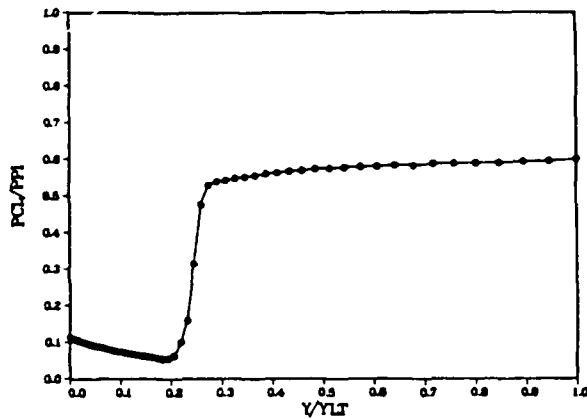
N=55K PCL/PPI CSB 60%NSR WBB=2
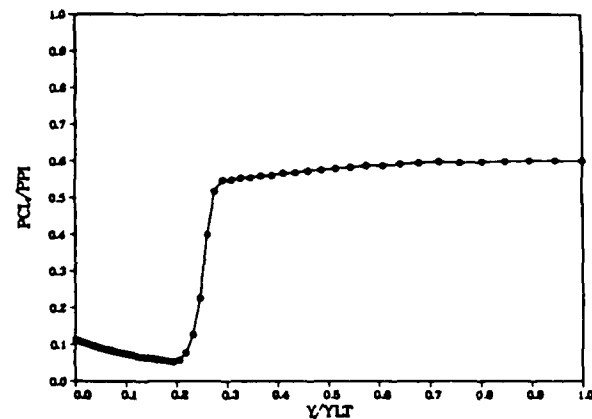
N=50K TCL/TO CSB 60%NSR WBB=2
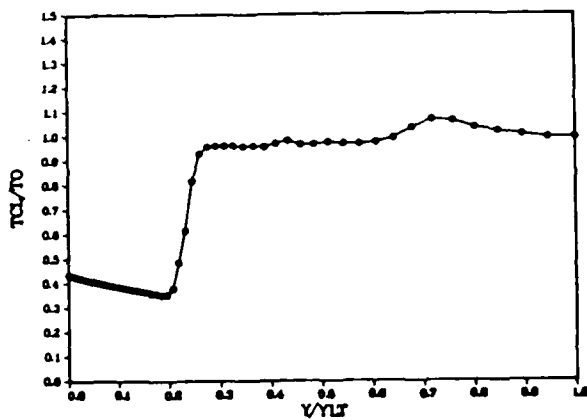
N=55K TCL/TO CSB 60%NSR WBB=2
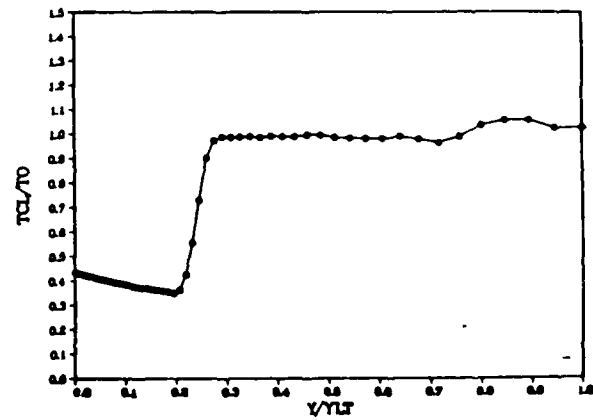
N=60K PW/PPI CSB 60%NSR WBB=2
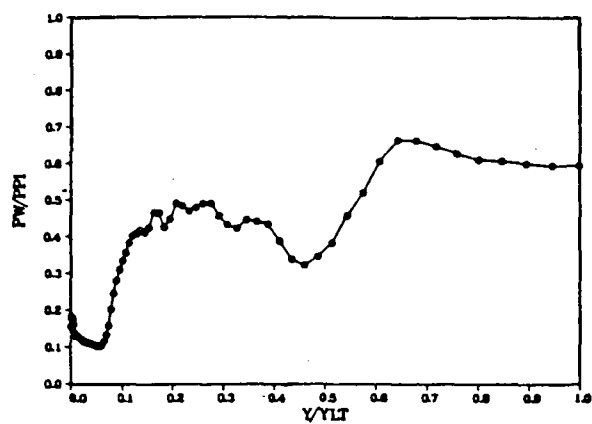
N=65K PW/PPI CSB 60%NSR WBB=2
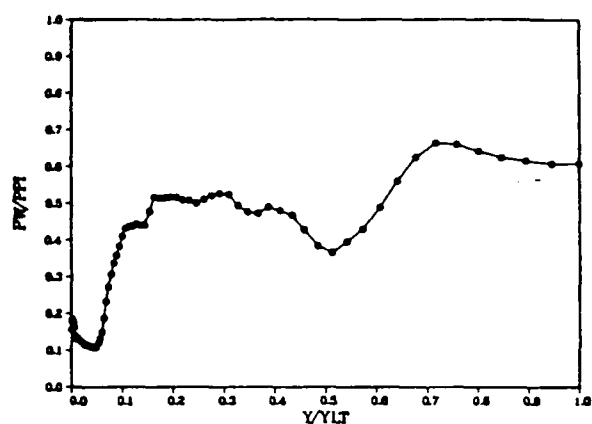
N=60K PCL/PPI CSB 60%NSR WBB=2
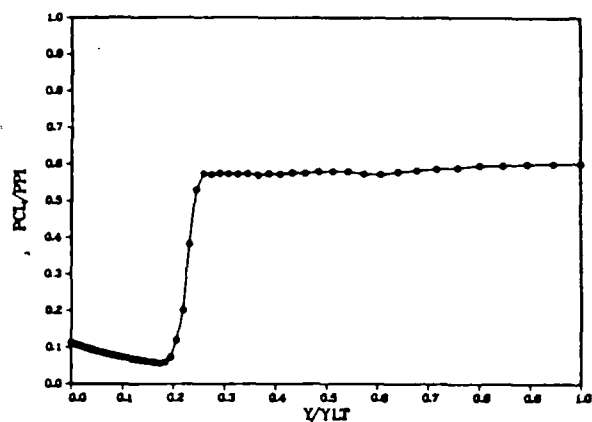
N=65K PCL/PPI CSB 60%NSR WBB=2
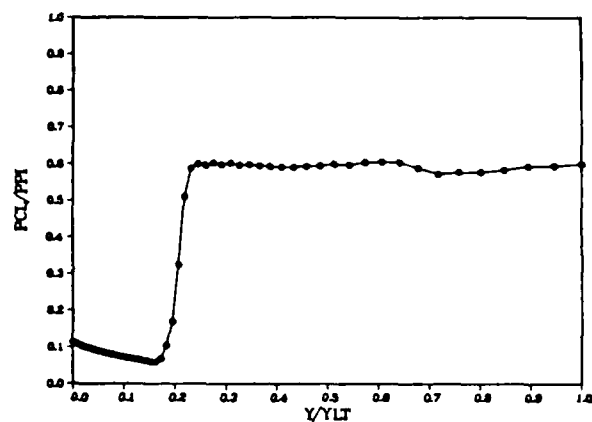
N=60K TCL/TO CSB 60%NSR WBB=2
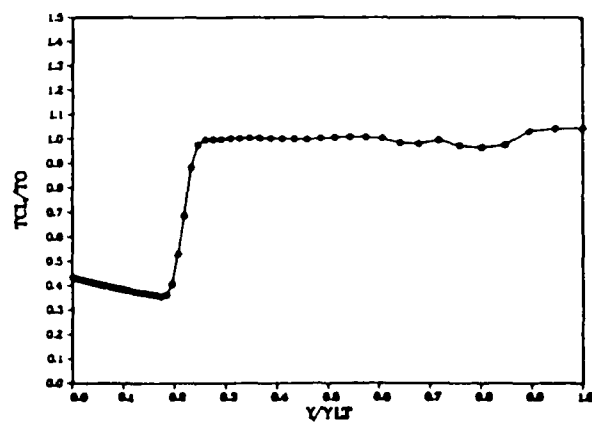
N=65K TCL/TO CSB 60%NSR WBB=2

253
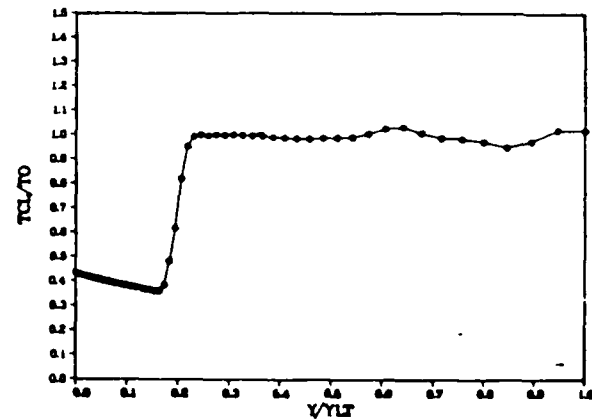
N=70K PW/PPI CSB 60%NSR WBB=2
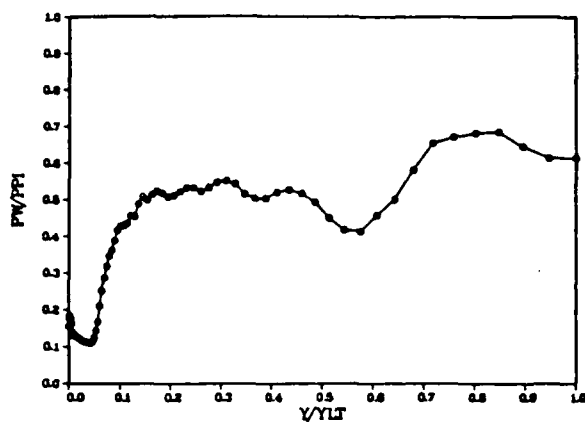
N=75K PW/PPI CSB 60%NSR WBB=2
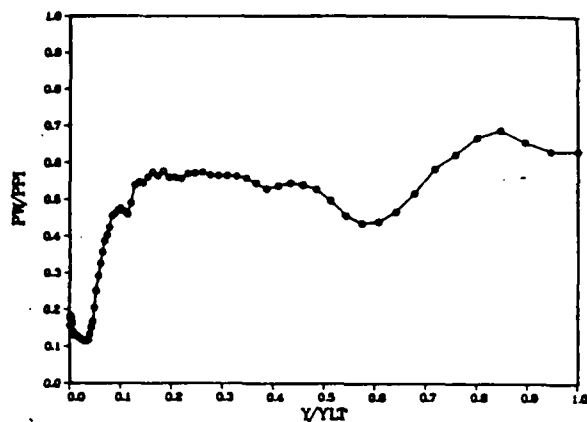
N=70K PCL/PPI CSB 60%NSR WBB=2
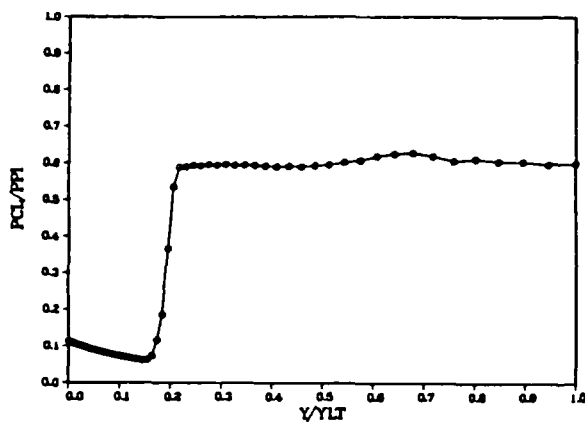
N=75K PCL/PPI CSB 60%NSR WBB=2
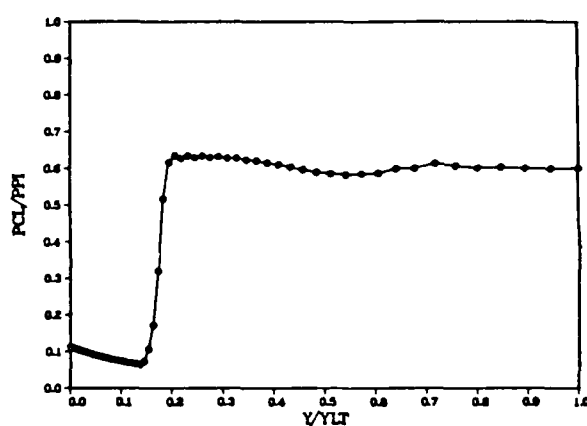
N=70K TCL/TO CSB 60%NSR WBB=2
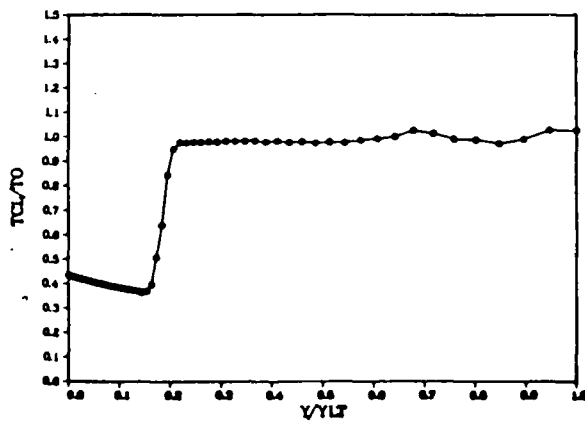
N=75K TCL/TO CSB 60%NSR WBB=2
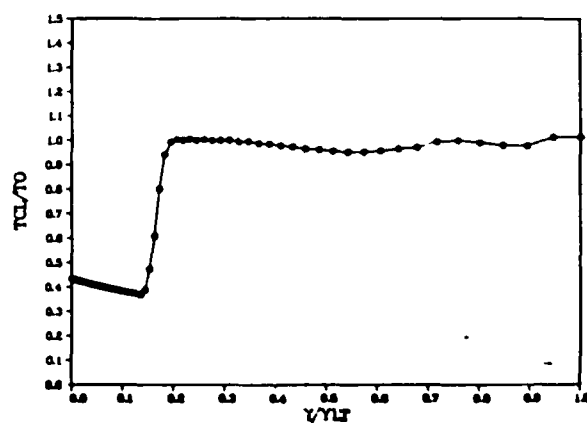
N=85K PW/PPI CSB 60%NSR WBB=2
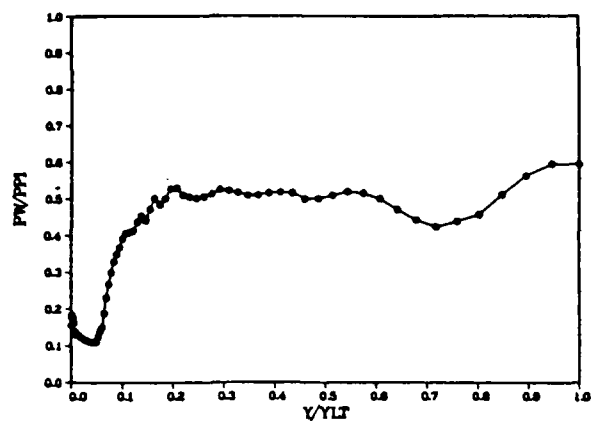
N=90K PW/PPI CSB 60%NSR WBB=2
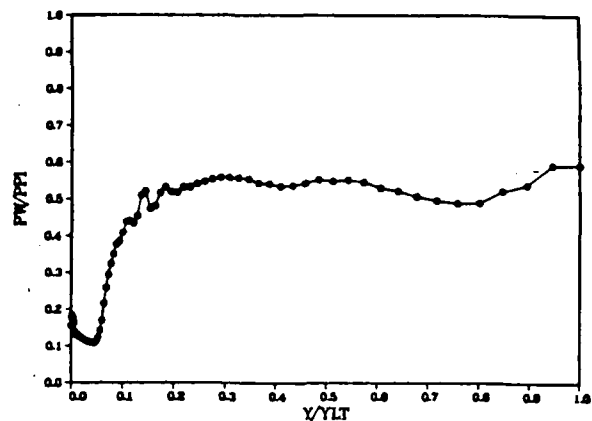
N=85K PCL/PPI CSB 60%NSR WBB=2
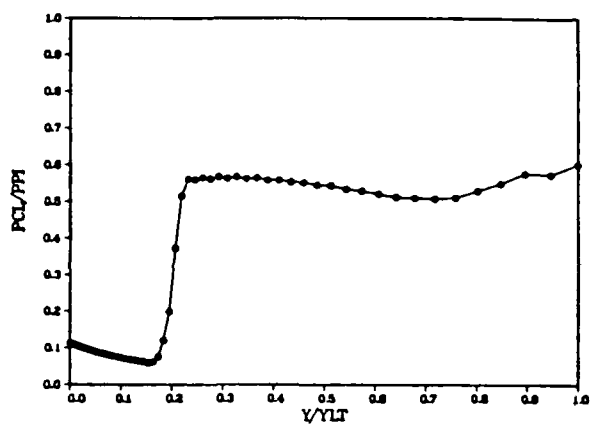
N=90K PCL/PPI CSB 60%NSR WBB=2
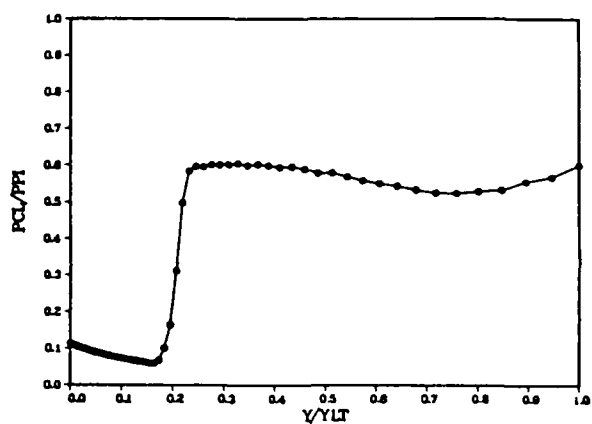
N=85K TCL/TO CSB 60%NSR WBB=2
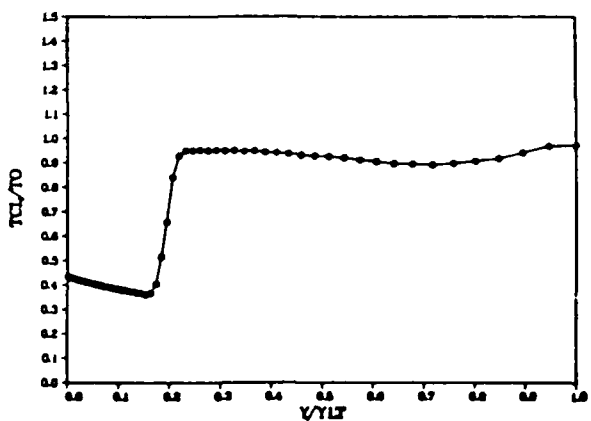
N=90K TCL/TO CSB 60%NSR WBB=2

255
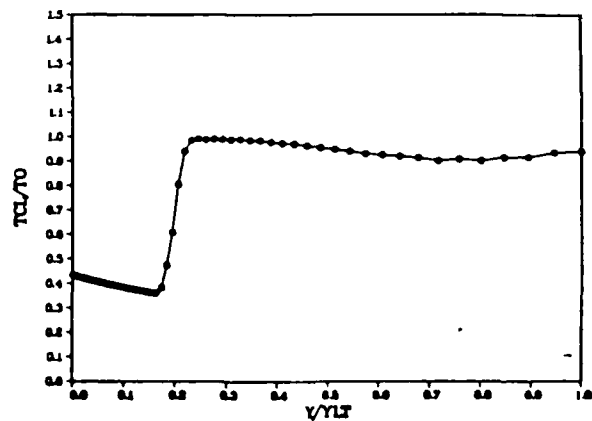
N=95K PW/PPI CSB 60%NSR WBB=2
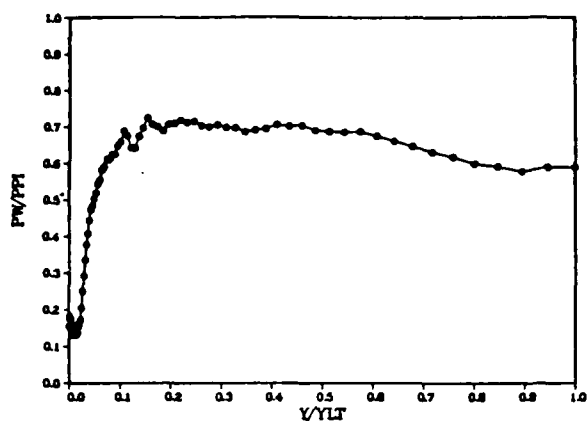
N=100K PW/PPI CSB 60%NSR WBB=2
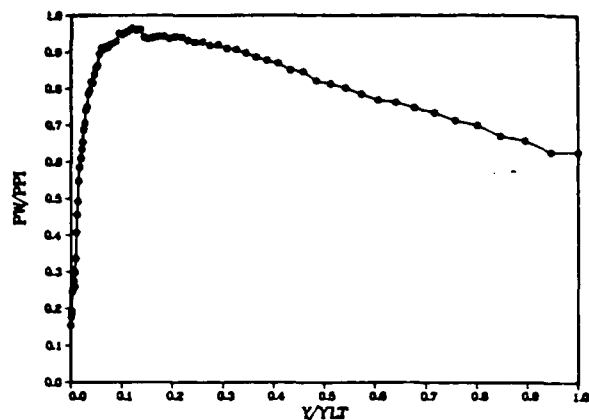
N=95K PCL/PPI CSB 60%NSR WBB=2
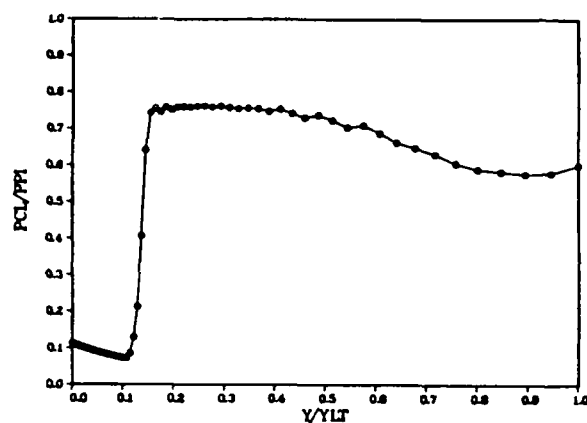
N=100K PCL/PPI CSB 60%NSR WBB=2
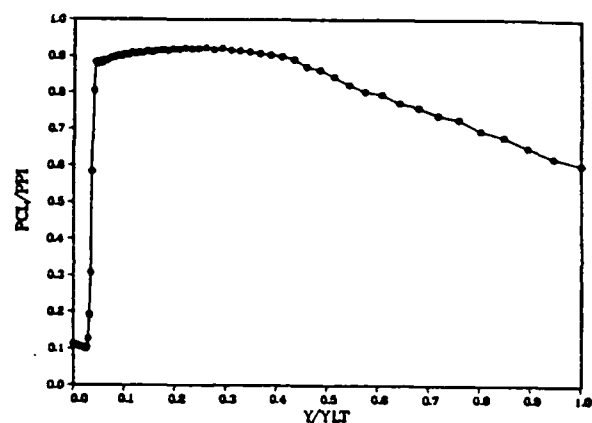
N=95K TCL/TO CSB 60%NSR WBB=2
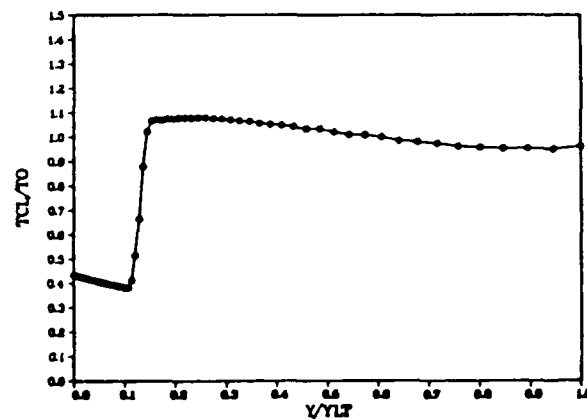
N=100K TCL/TO CSB 60%NSR WBB=2

256
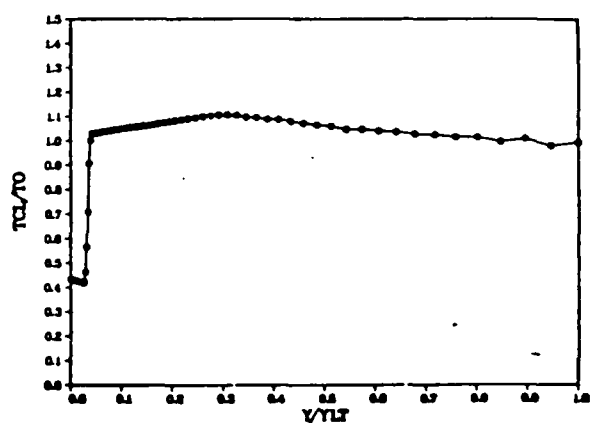
N=101K PW/PPI CSB 60%NSR WBB=2
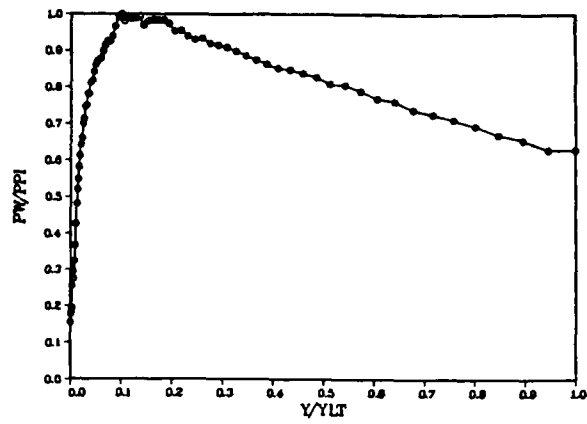
N=101K PCL/PPI CSB 60%NSR WBB=2
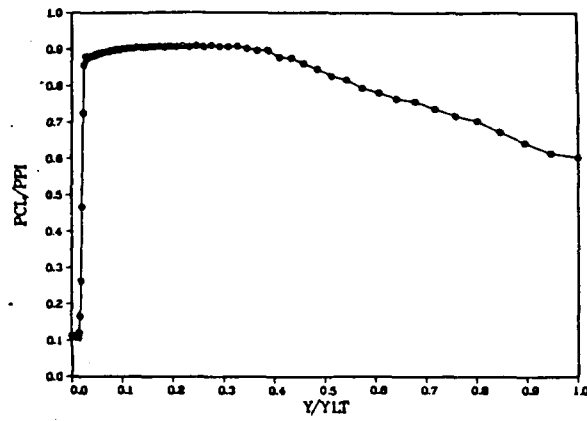
N=101K TCL/TO CSB 60%NSR WBB=2
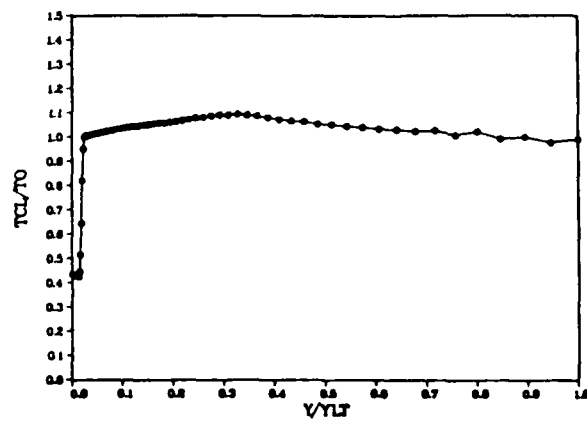
APPENDIX F

NUMERICAL CASE 2B COMPUTATIONAL DETAILS

Details of the fourth numerical case show the progress in achieving the first stable numerical solution. For this numerical experiment wall flow energization was added to a uniform core inflow. The core flow was set at M = 2.5. Wall bank blowers were added at a mass fraction of 20 percent of the core flow, operating at M = 4.0. Exit pressure was set at 60% of normal shock recovery pressure. The Navier-Stokes computer code employed the Cebeci-Smith two-layer eddy viscosity turbulence model modified for the effect of an adverse pressure gradient as described in Chapter V, Section 5.3. Details of the progress of the core flow normal shock through the diffuser from the imposed one-dimensional, inviscid normal shock initial condition to a converged, stable solution after approximately 5 characteristic times are presented. The first figure repeats the time history plot of the core flow normal shock position (from Figure 27). Presented next are a series of Mach contour plots, beginning with the initial condition and proceeding in increments of 5,000 numerical iterations through N = 100,000, and thereafter in increments of 25,000, until the converged solution is achieved at N = 200,000. Each plot presents the Mach contours from M = 0.0 through M = 5.0, in increments of 0.20. Following the Mach contour plots are a series of corresponding nondimensionalized wall pressure, line of symmetry pressure, and line of symmetry temperature plots. In the Mach contour plots, the persistence of the wall bank blower flow through the diffuser all the way to the exit is again quite evident, as is the significantly smaller wall boundary layer separation region. Also notable is the "smooth" behavior of the wall pressure from the diffuser

entrance to a large overpressure spike that occurs slightly downstream of the core flow normal shock; the higher energy, higher Mach number bank blower flow passes through a stronger shock before adjusting to diffuser exit pressure. From this numerical experiment, it was concluded that both wall flow energization and the adverse pressure gradient modification to the turbulence model are required to attain a "started" diffuser flow in a short diffuser.

This numerical experiment required 193 minutes of CRAY 1 CPU time.

CSM TIME HISTORY 60%NSR WBB=2
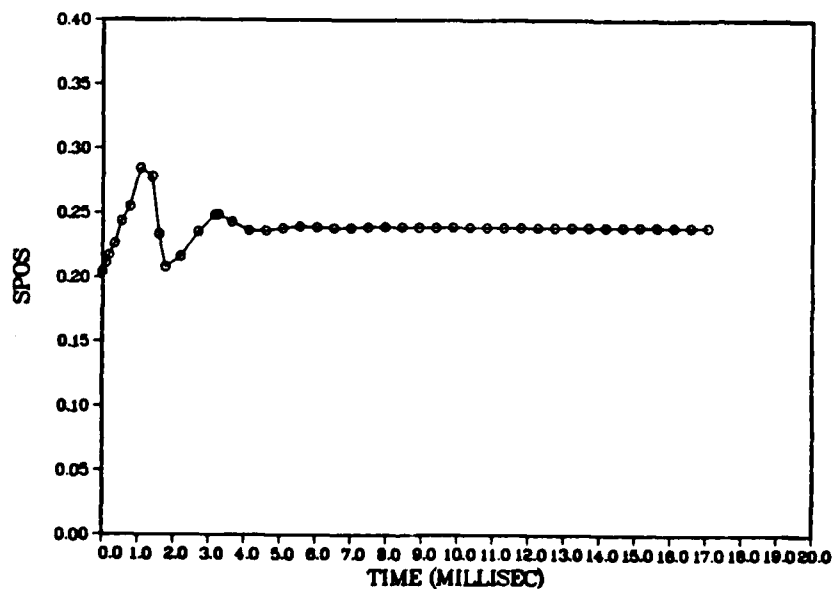
TABLE VII

NUMERICAL CASE 2B COMPUTED SHOCK POSITION VS TIME

N	CFL	TIME	R/R_{de}	SPOS
Number of Iterations		(Milliseconds)		
0		0	1.614800	0.200000
5,000	.10	0.095720	1.648144	0.210848
10,000	.10	0.191400	1.667660	0.217197
15,000	.15	0.334900	1.694493	0.225926
20,000	.20	0.526300	1.748190	0.243394
25,000	.25	0.765500	1.782913	0.254690
30,000	.30	1.052500	1.874352	0.284436
35,000	.35	1.387400	1.853772	0.277741
40,000	.40	1.770100	1.639180	0.207932
45,000	.45	2.200700	1.664639	0.216214
50,000	.50	2.679100	1.723284	0.235292
55,000		3.157500	1.763615	0.248412
60,000		3.635900	1.747175	0.243064
65,000		4.114300	1.727047	0.236516
70,000		4.592700	1.726616	0.236376
75,000		5.071200	1.732761	0.238375
80,000		5.549600	1.736607	0.239626
85,000		6.028000	1.734538	0.238953
90,000		6.506400	1.732564	0.238311
95,000		6.984800	1.732936	0.238452
100,000		7.463200	1.734790	0.239035
105,000		7.941500	1.735429	0.239243
110,000		8.419900	1.734652	0.238990
115,000		8.898300	1.733960	0.238765
120,000		9.376700	1.734080	0.238804
125,000		9.855100	1.734606	0.238975
130,000		10.333500	1.734609	0.238976
135,000		10.811900	1.734381	0.238902
140,000		11.290400	1.734071	0.238801
145,000		11.768800	1.734344	0.238890
150,000		12.247200	1.734510	0.238944
155,000		12.725600	1.734436	0.238920
160,000		13.204000	1.734188	0.238839
165,000		13.682400	1.734341	0.238889
170,000		14.160800	1.734390	0.238905
175,000		14.639200	1.734452	0.238925
180,000		15.117600	1.734335	0.238887
185,000		15.596000	1.734353	0.238893
190,000		16.074400	1.734329	0.238885
195,000		16.552800	1.734292	0.238873
200,000		17.031200	1.734381	0.238902

N=5K MACH CONTOURS 60%NSR WBB=2
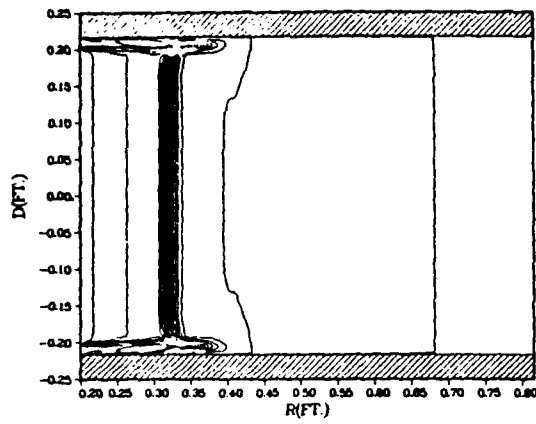
N=10K MACH CONTOURS 60%NSR WBB=2
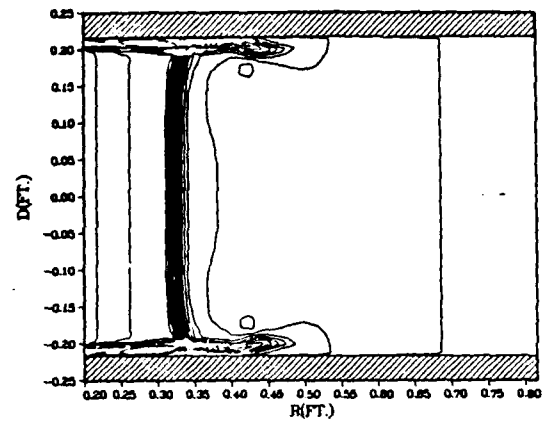
N=15K MACH CONTOURS 60%NSR WBB=2
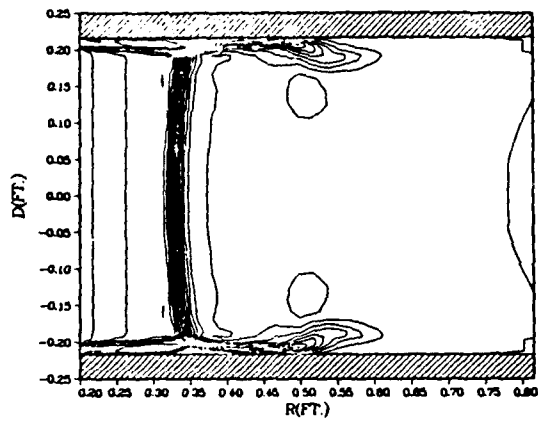
N=20K MACH CONTOURS 60%NSR WBB=2
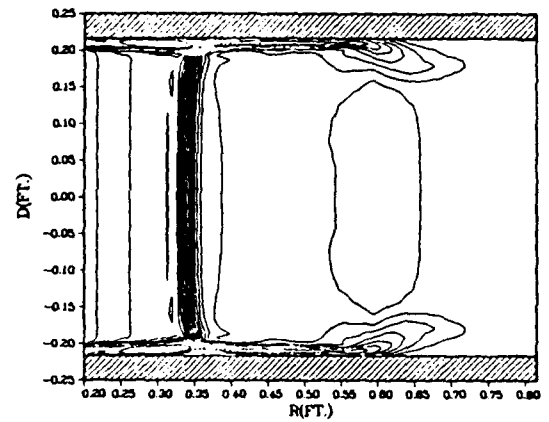
N=25K MACH CONTOURS 60%NSR WBB=2
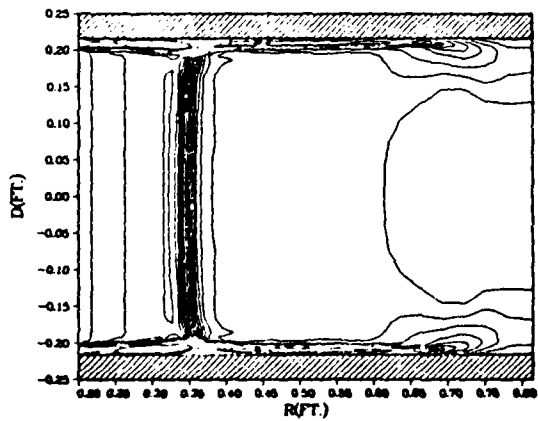
N=30K MACH CONTOURS 60%NSR WBB=2
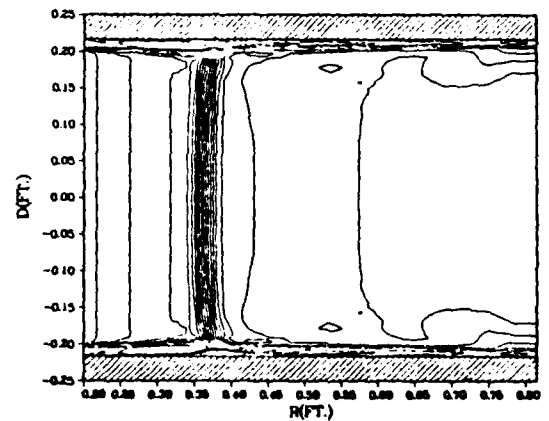
N=35K MACH CONTOURS 60%NSR WBB=.2
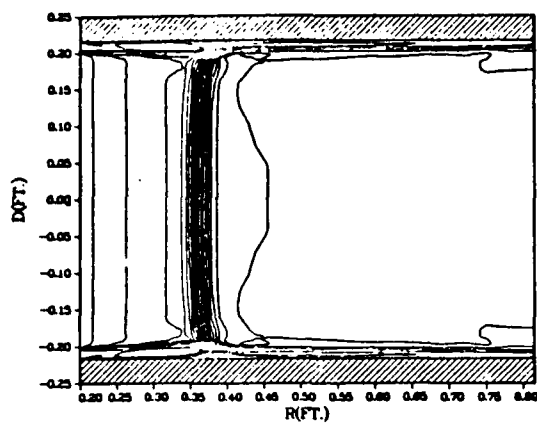
N=40K MACH CONTOURS 60%NSR WBB=.2
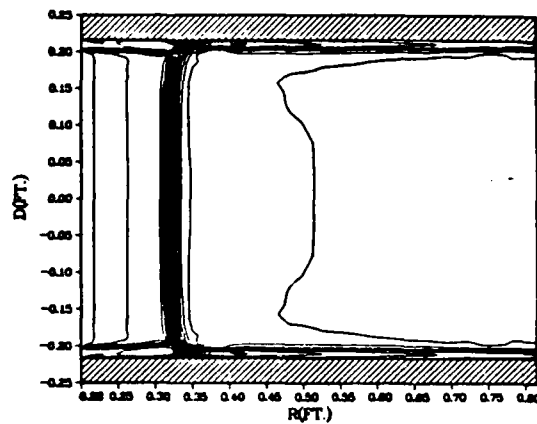
N=45K MACH CONTOURS 60%NSR WBB=.2
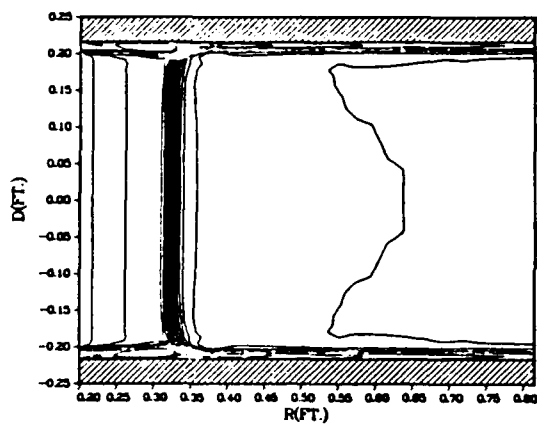
N=50K MACH CONTOUR 60%NSR WBB=.2
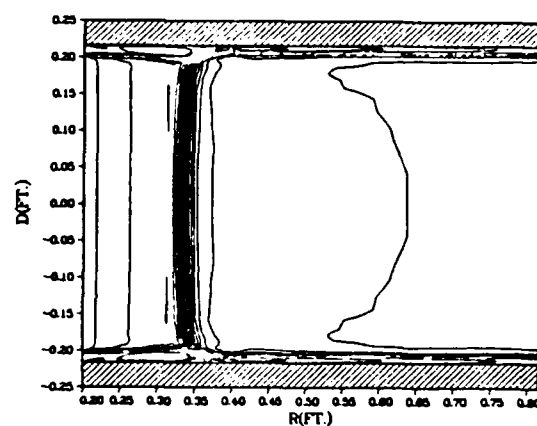
N=55K MACH CONTOURS 60%NSR WBB=.2
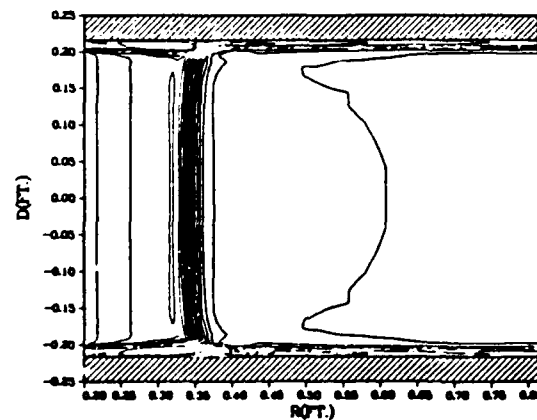
N=60K MACH CONTOURS 60%NSR WBB=.2
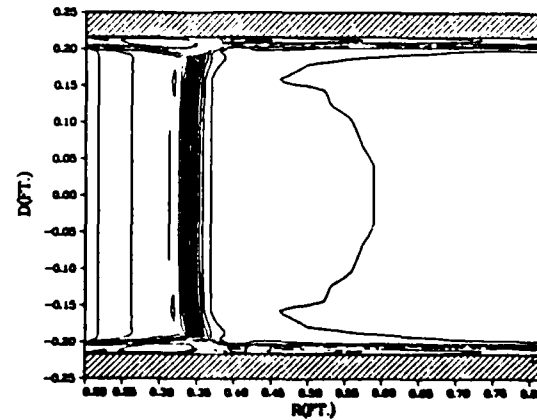
N=65K MACH CONTOURS 60%NSR WBB=2
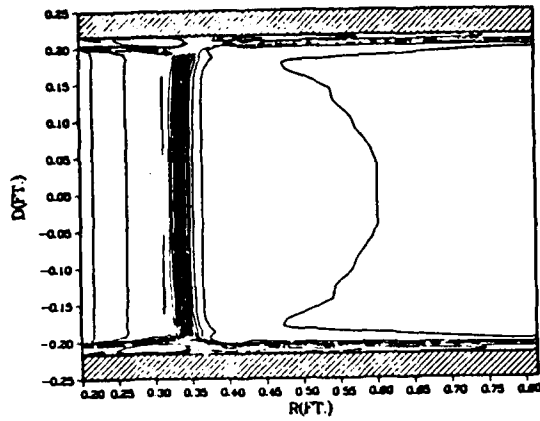
N=70K MACH CONTOURS 60%NSR WBB=2
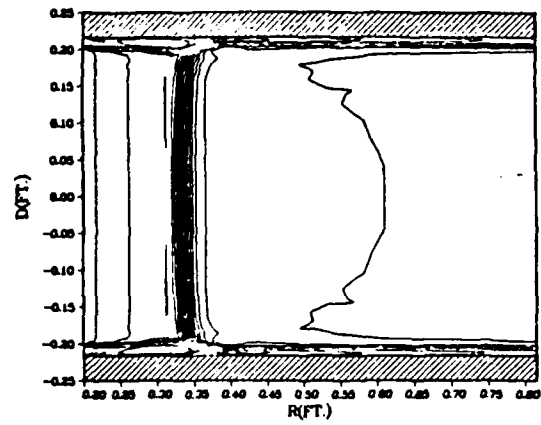
N=75K MACH CONTOURS 60%NSR WBB=2
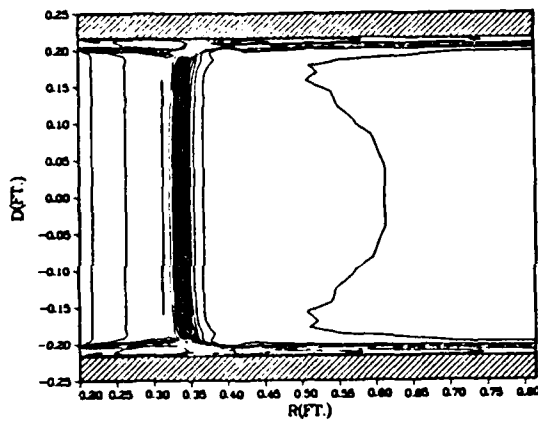
N=80K MACH CONTOURS 60%NSR WBB=2
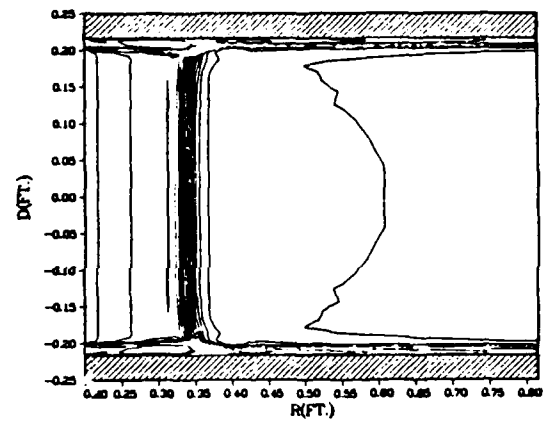
N=85K MACH CONTOURS 60%NSR WBB=2
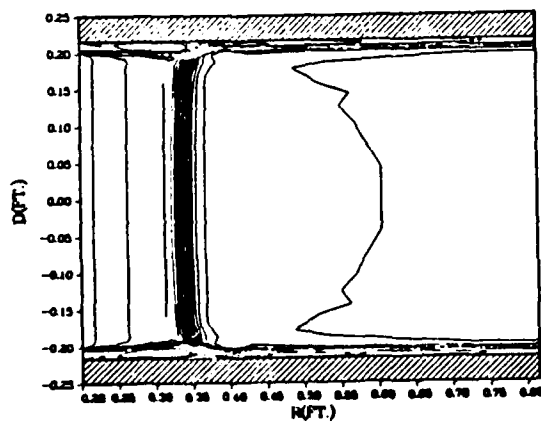
N=90K MACH CONTOURS 60%NSR WBB=2

263
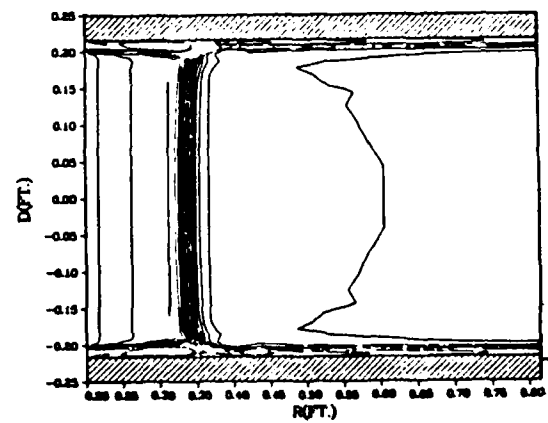
N=95K MACH CONTOURS 60%NSR WBB=2
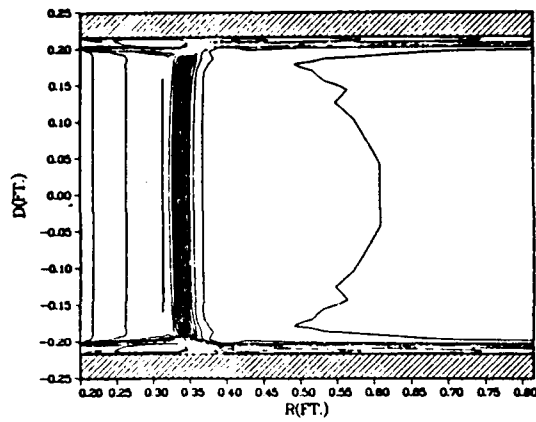
N=100K MACH CONTOURS 60%NSR WBB=2
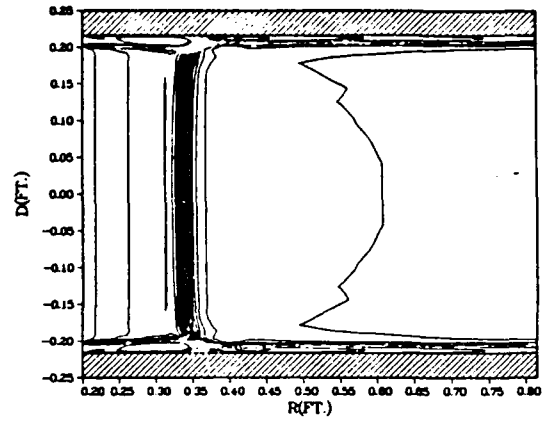
N=125K MACH CONTOURS 60%NSR WBB=2
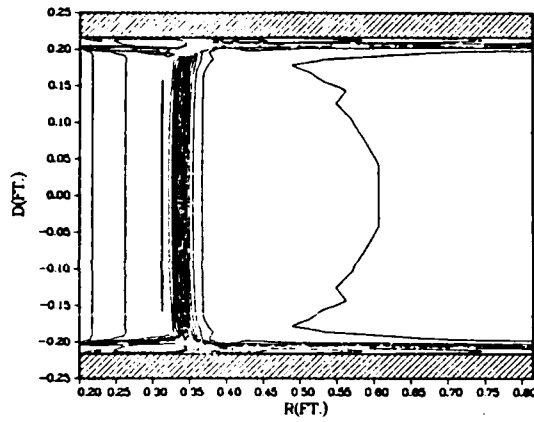
N=150K MACH CONTOURS 60%NSR WBB=2
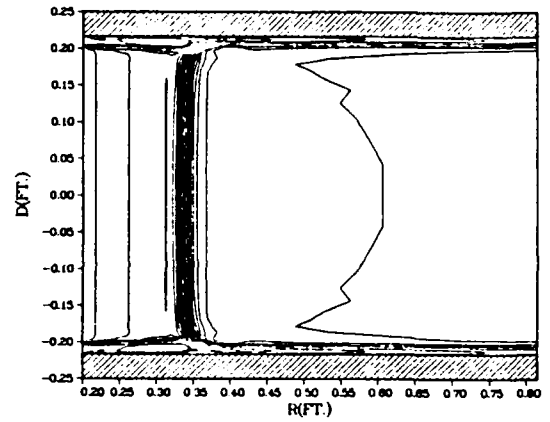
N=175K MACH CONTOURS 60%NSR WBB=2
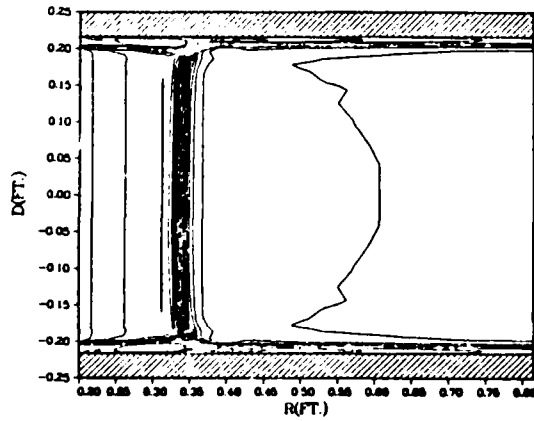
N=200K MACH CONTOURS 60%NSR WBB=2

264
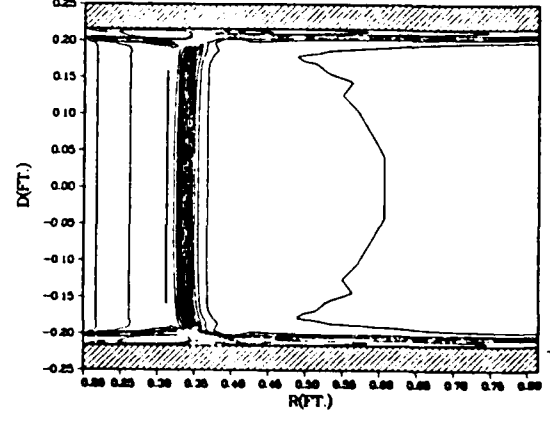
N=1 PW/PPI CSM 60%NSR WBB=2
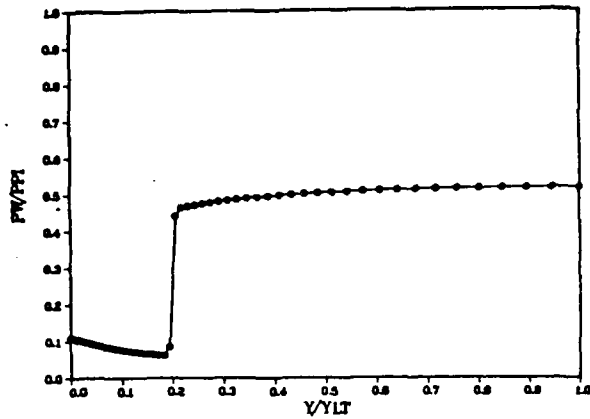
N=5K PW/PPI CSM 60%NSR WBB=2
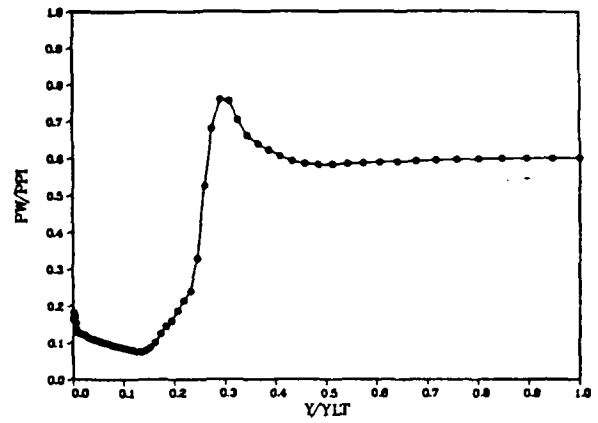
N=1 PCL/PPI CSM 60%NSR WBB=2
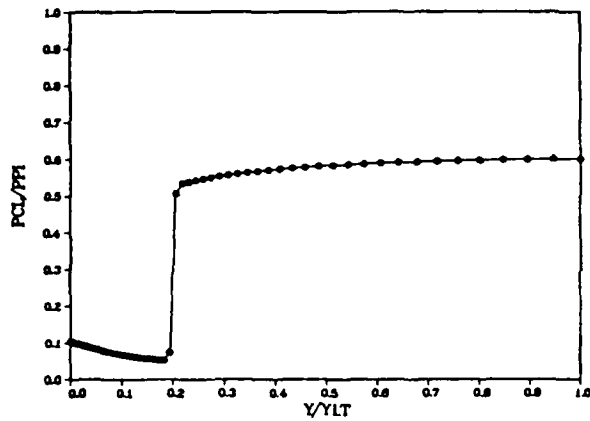
N=5K PCL/PPI CSM 60%NSR WBB=2
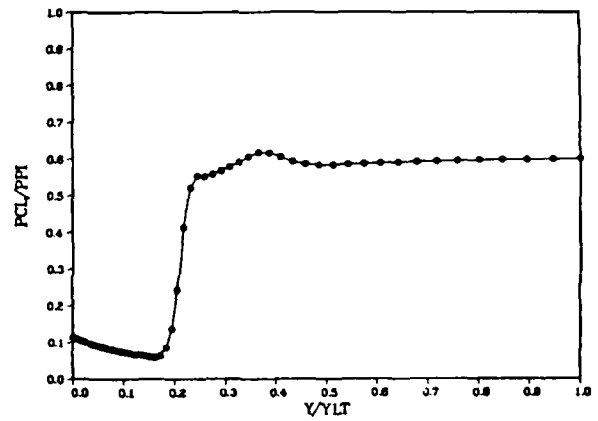
N=1 TCL/TO CSM 60%NSR WBB=2
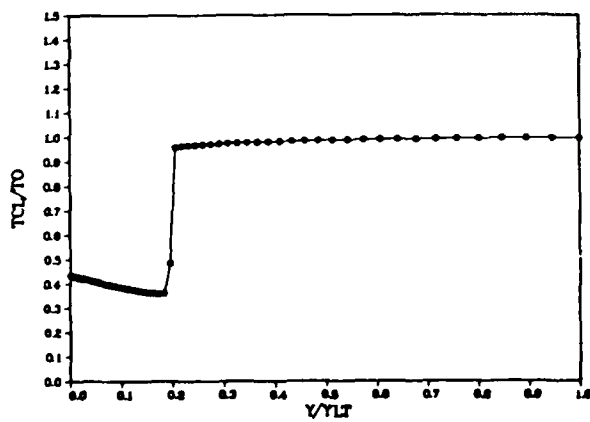
N=5K TCL/TO CSM 60%NSR WBB=2
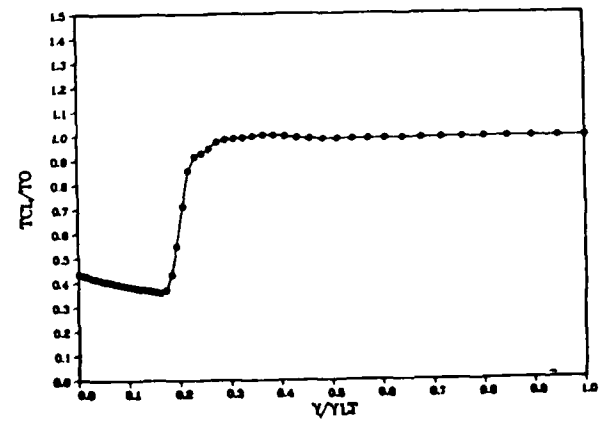
N=10K PW/PPI CSM 60%NSR WBB=2
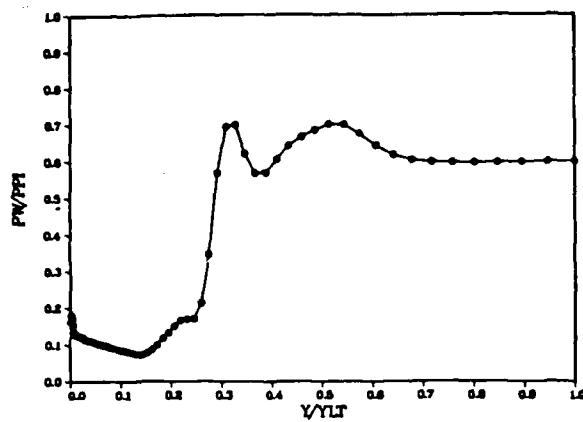
N=15K PW/PPI CSM 60%NSR WBB=2
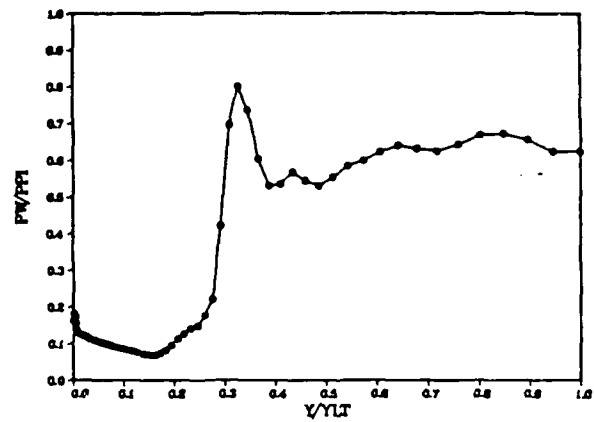
N=10K PCL/PPI CSM 60%NSR WBB=2
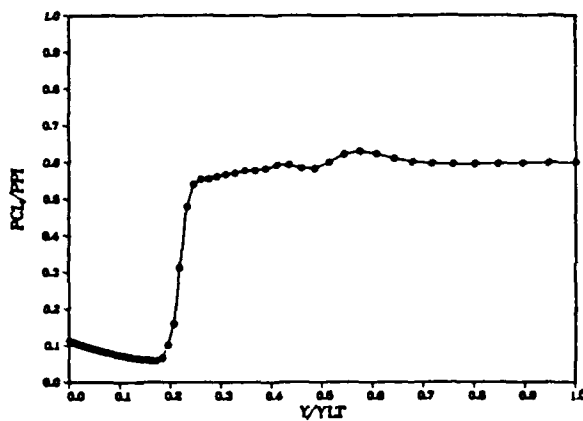
N=15K PCL/PPI CSM 60%NSR WBB=2
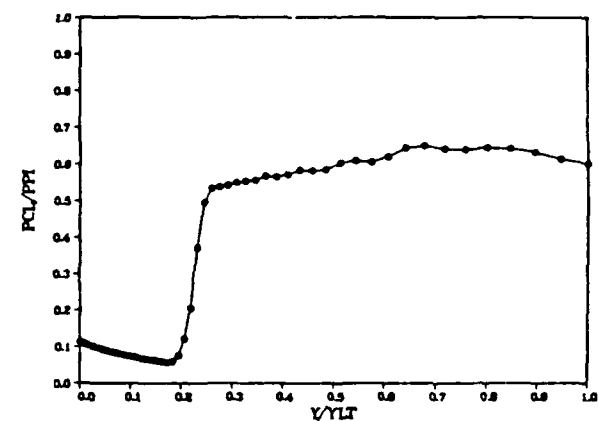
N=10K TCL/TO CSB 60%NSR WBB=2
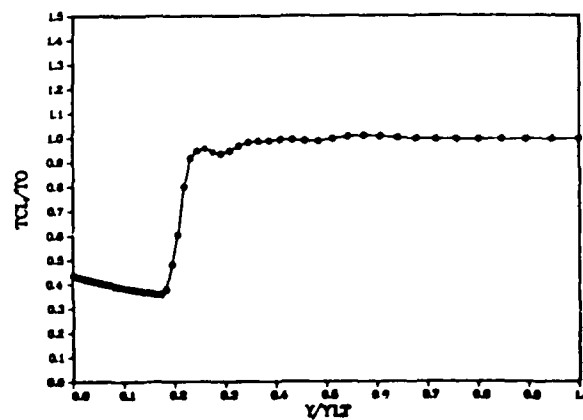
N=15K TCL/TO CSM 60%NSR WBB=2
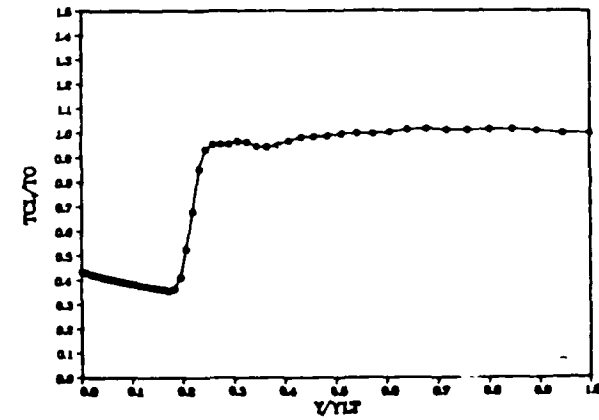
N=20K PW/PPI CSM 60%NSR WBB=2
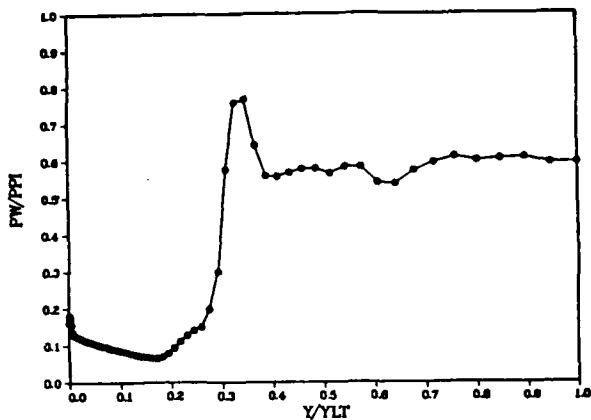
N=25K PW/PPI CSM 60%NSR WBB=2
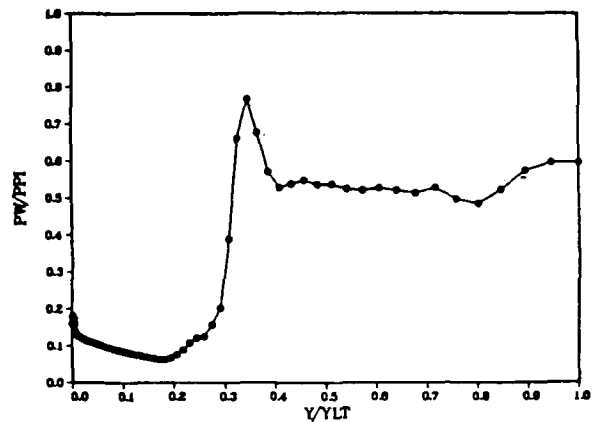
N=20K PCL/PPI CSM 60%NSR WBB=2
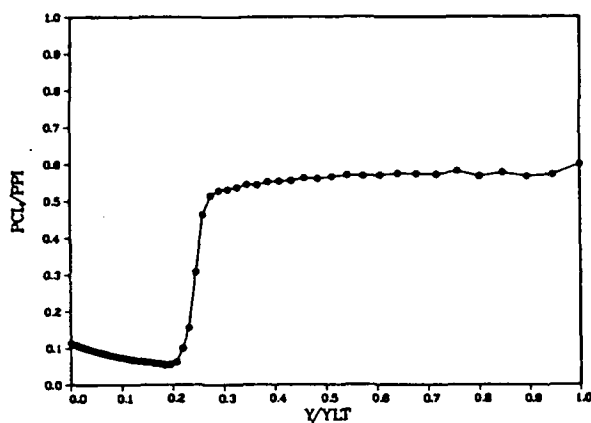
N=25K PCL/PPI CSM 60%NSR WBB=2
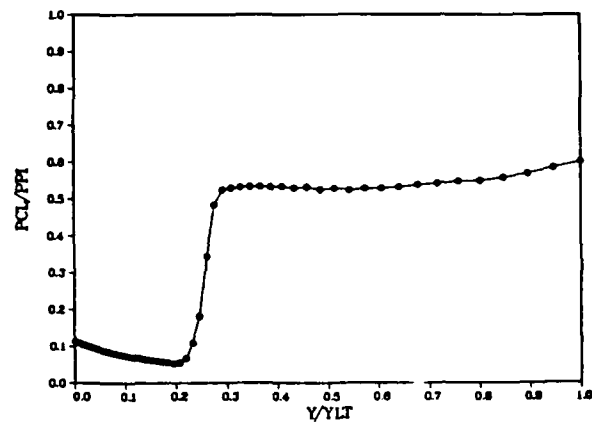
N=20K TCL/TO CSM 60%NSR WBB=2
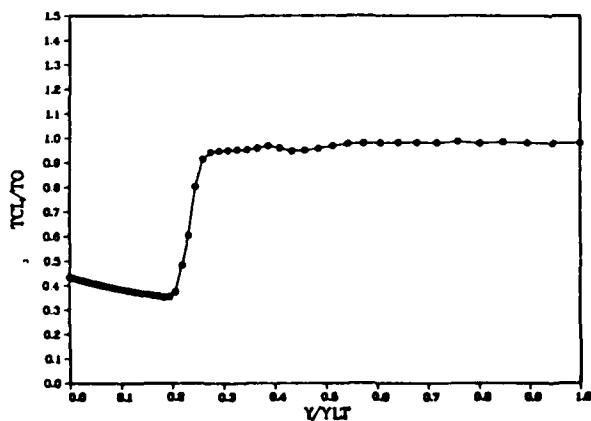
N=25K TCL/TO CSM 60%NSR WBB=2
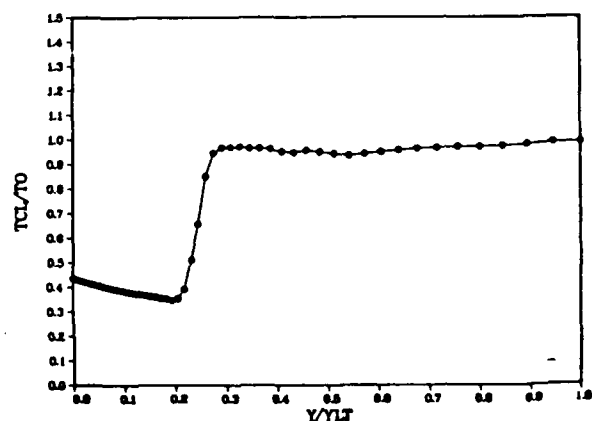
N=30K PW/PPI CSM 60%NSR WBB=.2
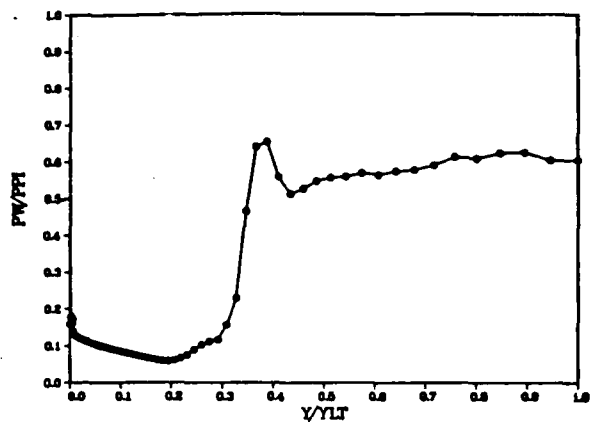
N=35K PW/PPI CSM 60%NSR WBB=.2
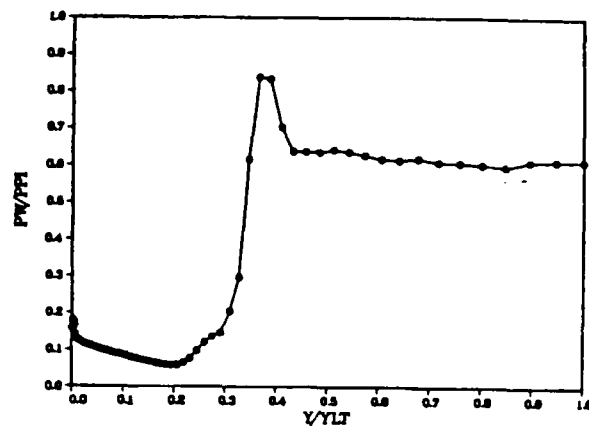
N=30K PCL/PPI CSM 60%NSR WBB=.2
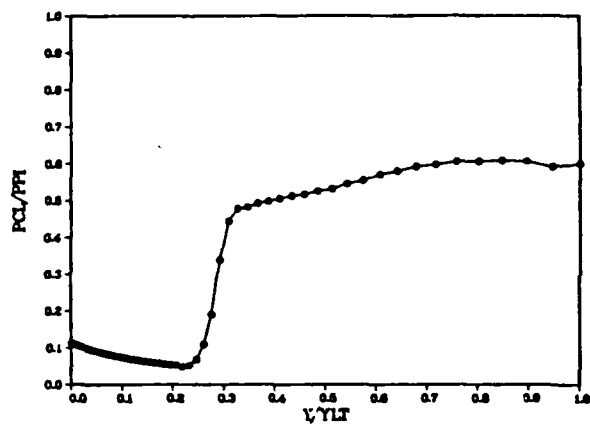
N=35K PCL/PPI CSM 60%NSR WBB=.2
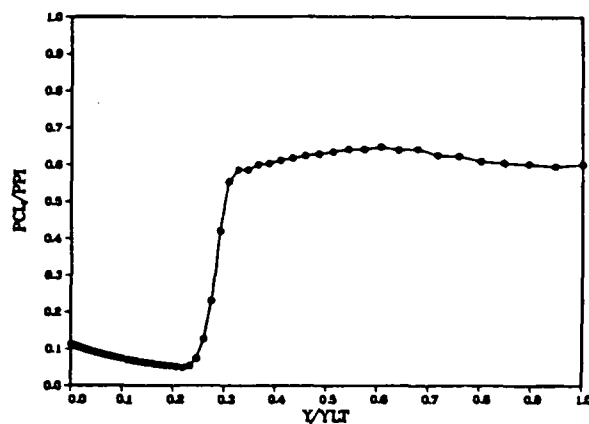
N=30K TCL/TO CSM 60%NSR WBB=.2

N=35K TCL/TO CSM 60%NSR WBB=.2

268
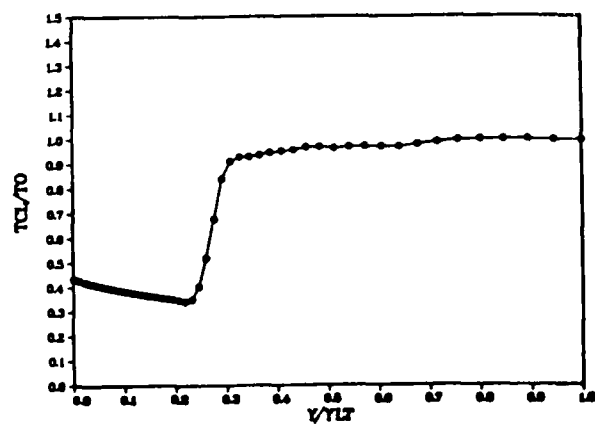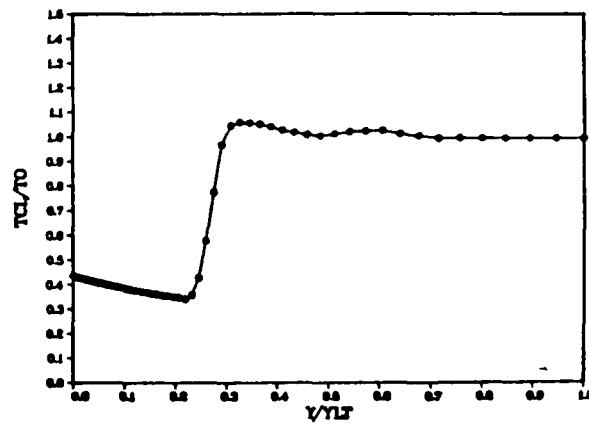
N=40K PW/PPI CSM 60%NSR WBB=2
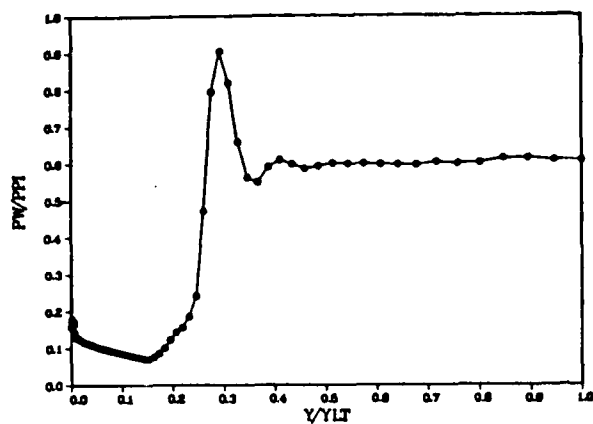
N=45K PW/PPI CSM 60%NSR WBB=2
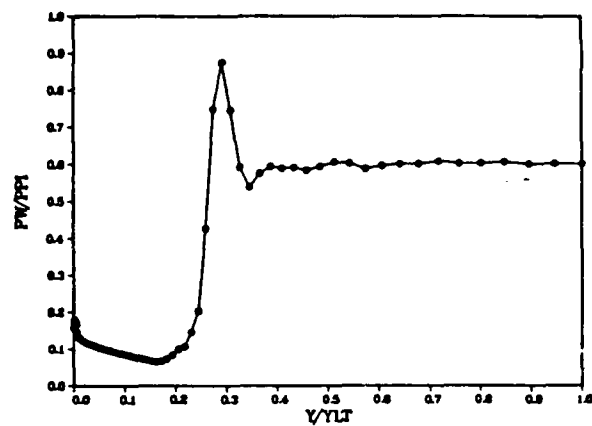
N=40K PCL/PPI CSM 60%NSR WBB=2
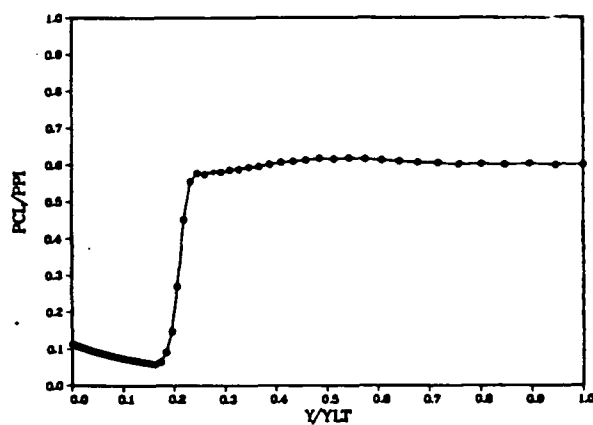
N=45K PCL/PPI CSM 60%NSR WBB=2
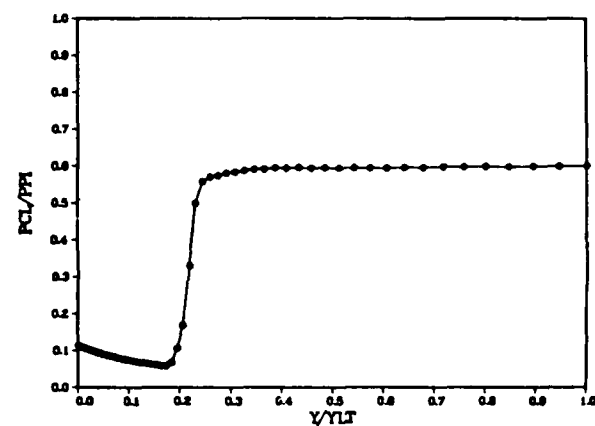
N=40K TCL/TO CSM 60%NSR WBB=2
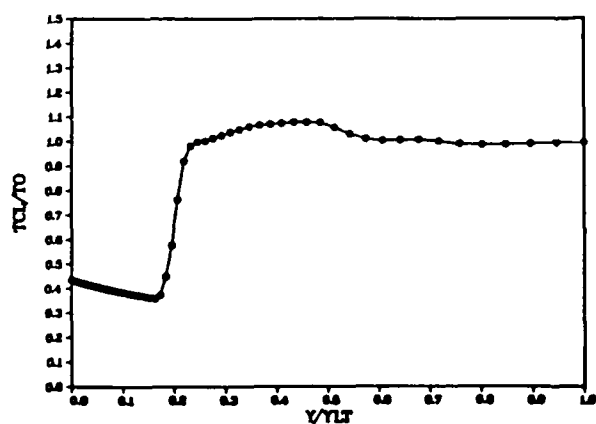
N=45K TCL/TO CSM 60%NSR WBB=2
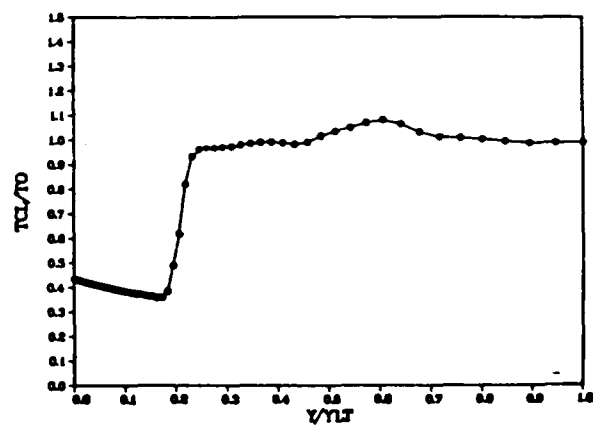
N=50K PW/PPI CSM 60%NSR WBB=.2
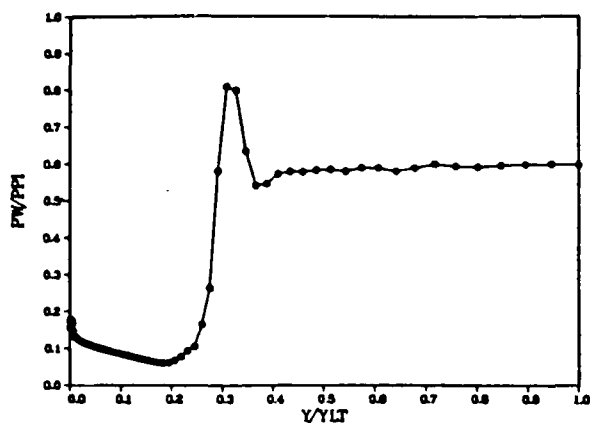
N=55K PW/PPI CSM 60%NSR WBB=.2
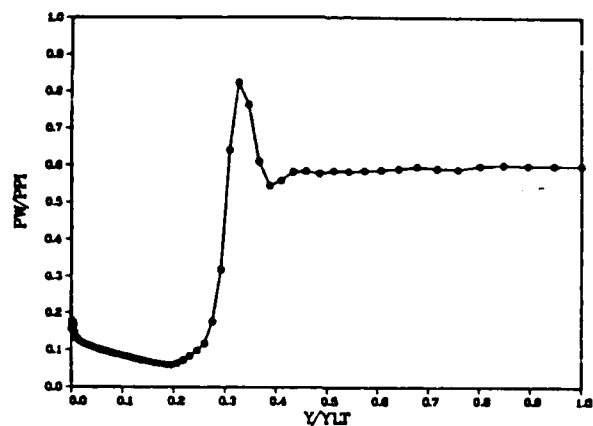
N=50K PCL/PPI CSM 60%NSR WBB=.2
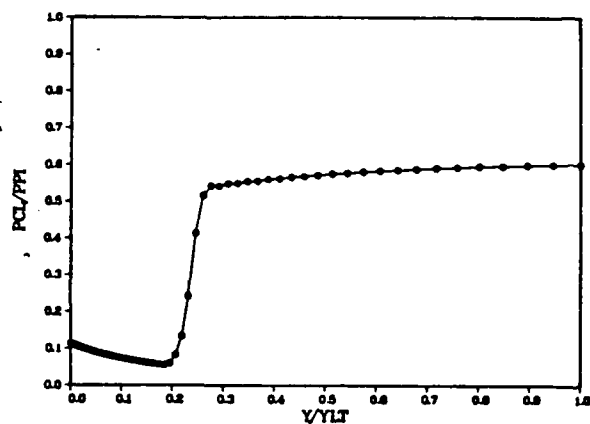
N=55K PCL/PPI CSM 60%NSR WBB=.2
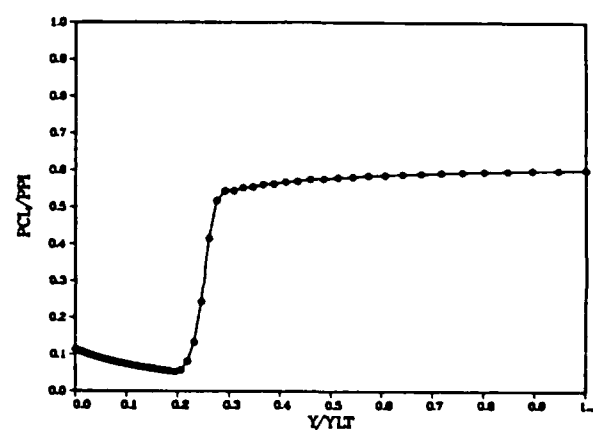
N=50K TCL/TO CSM 60%NSR WBB=.2

N=55K TCL/TO CSM 60%NSR WBB=.2

270
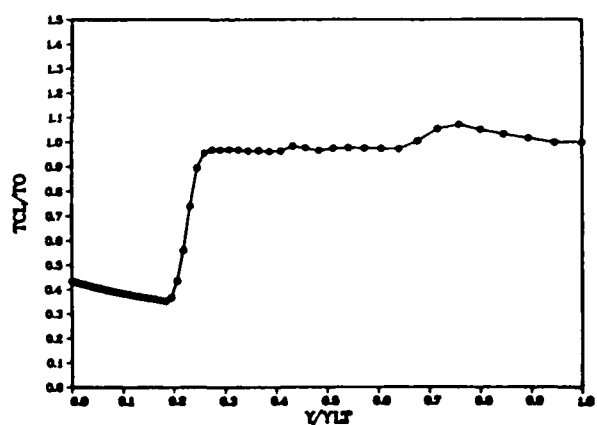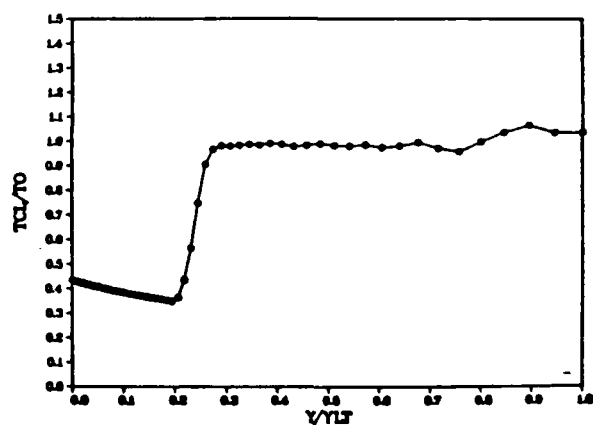
N=60K PW/PPI CSM 60%NSR WBB=.2
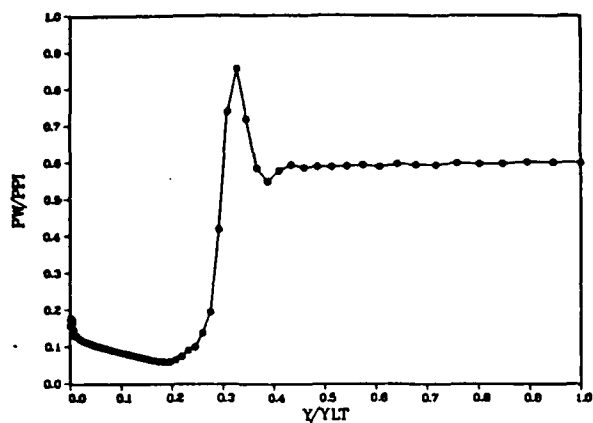
N=65K PW/PPI CSM 60%NSR WBB=.2
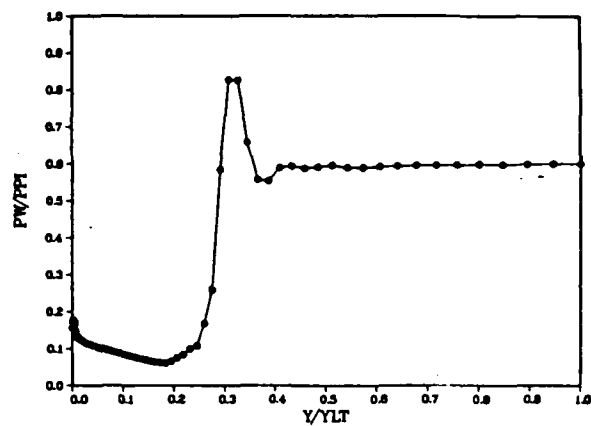
N=60K PCL/PPI CSM 60%NSR WBB=.2
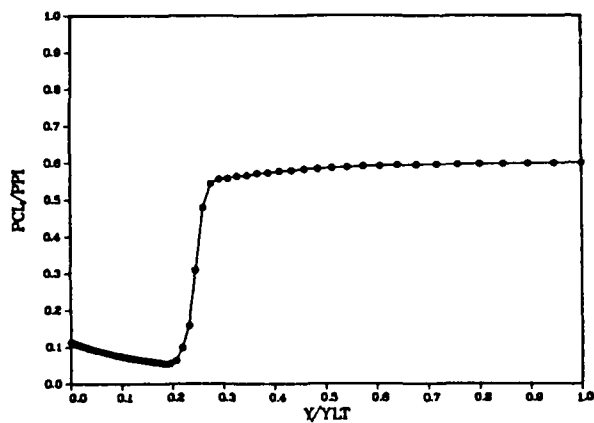
N=65K PCL/PPI CSM 60%NSR WBB=.2
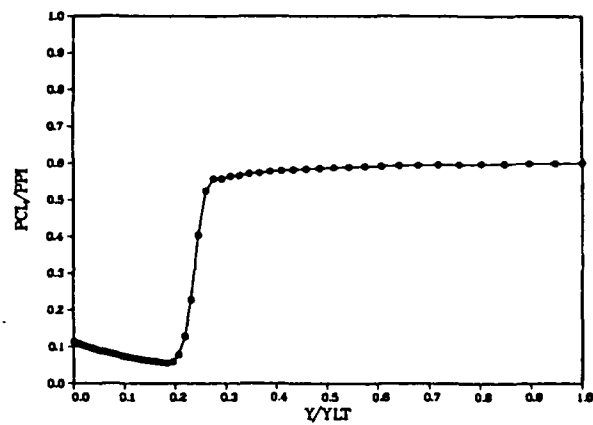
N=60K TCL/TO CSM 60%NSR WBB=.2
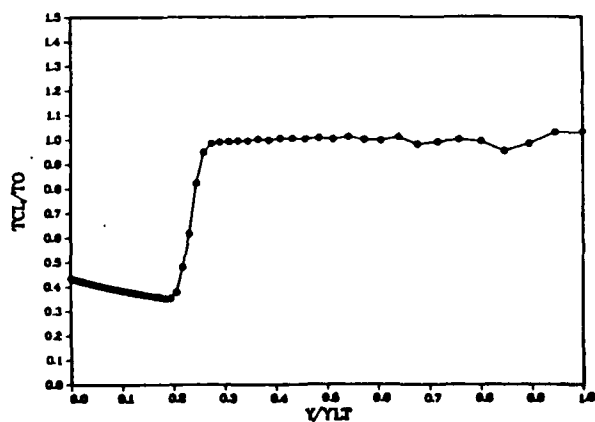
N=65K TCL/TO CSM 60%NSR WBB=.2
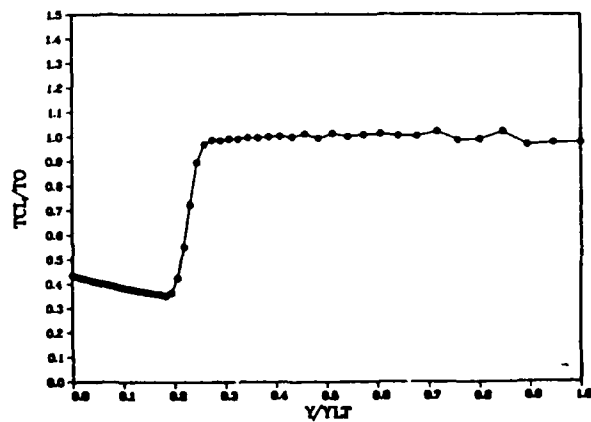
N=70K PW/PPI CSM 60%NSR WBB=2
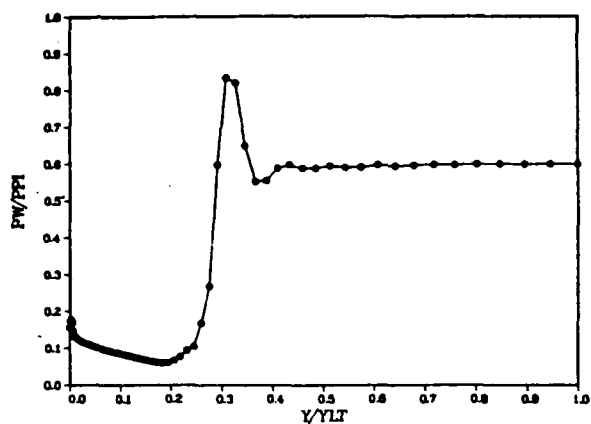
N=75K PW/PPI CSM 60%NSR WBB=2
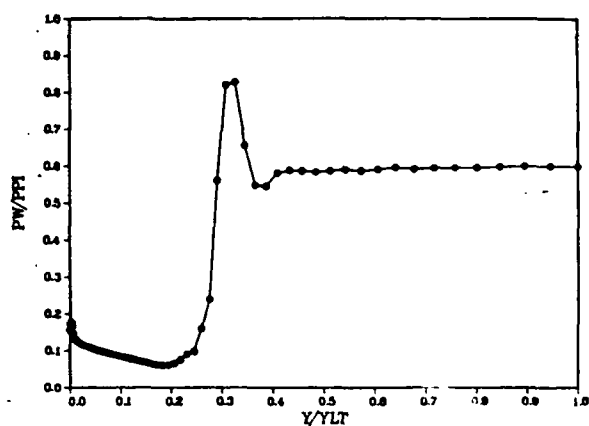
N=70K PCL/PPI CSM 60%NSR WBB=2
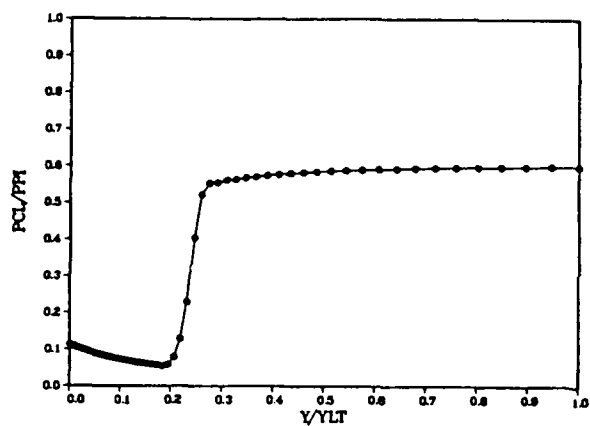
N=75K PCL/PPI CSM 60%NSR WBB=2
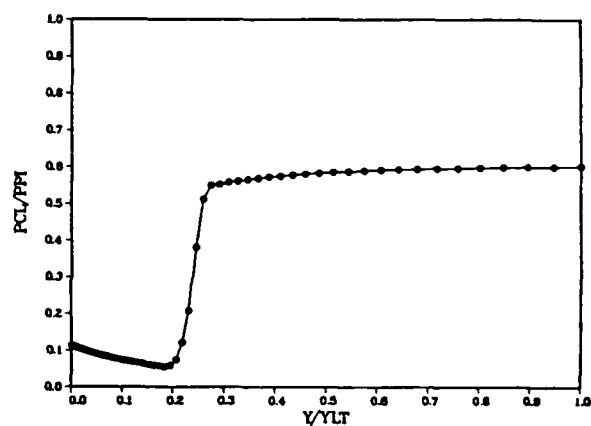
N=70K TCL/TO CSM 60%NSR WBB=2
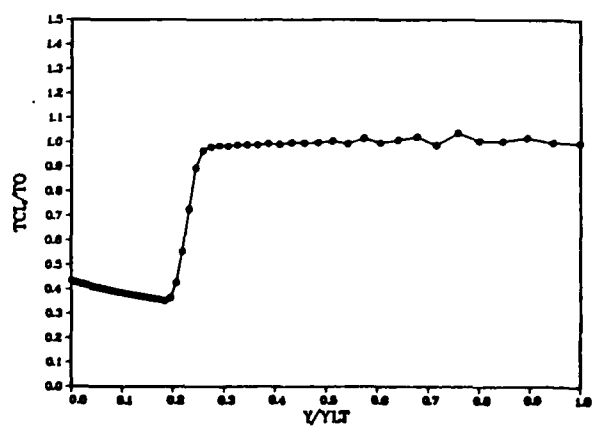
N=75K TCL/TO CSM 60%NSR WBB=2

272
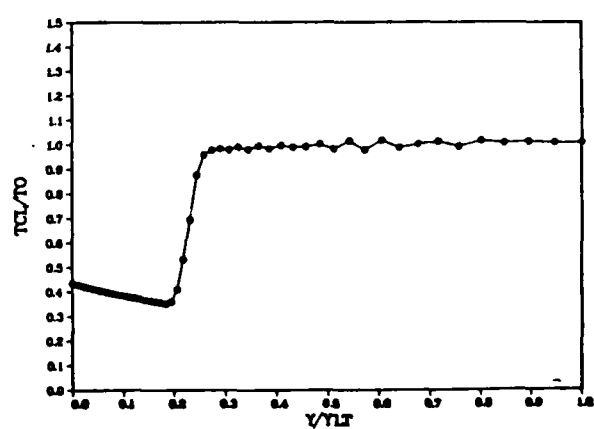
N=80K PW/PPI CSM 60%NSR WBB=2
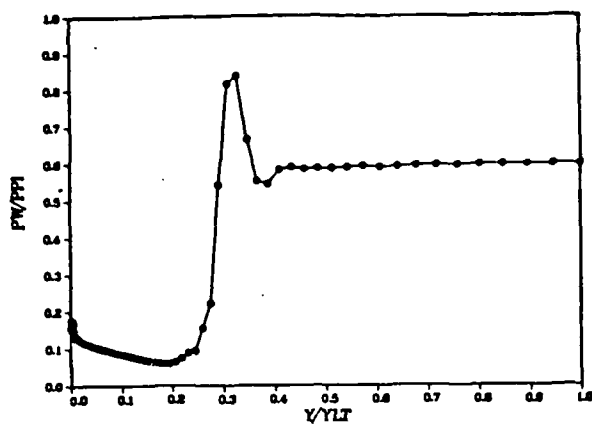
N=85K PW/PPI CSM 60%NSR WBB=2
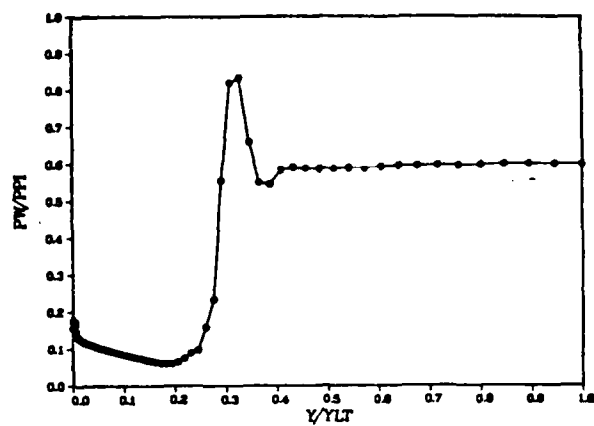
N=80K PCL/PPI CSM 60%NSR WBB=2
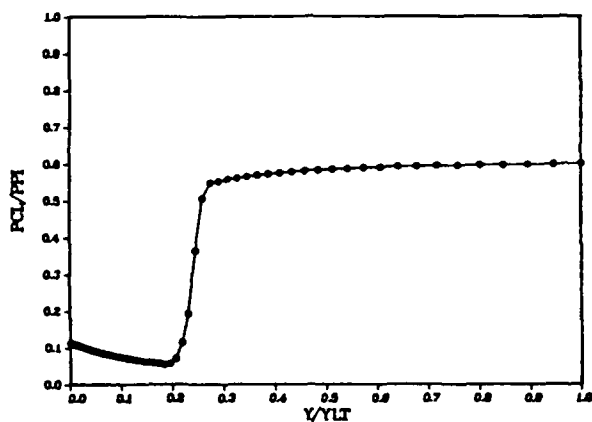
N=85K PCL/PPI CSM 60%NSR WBB=2
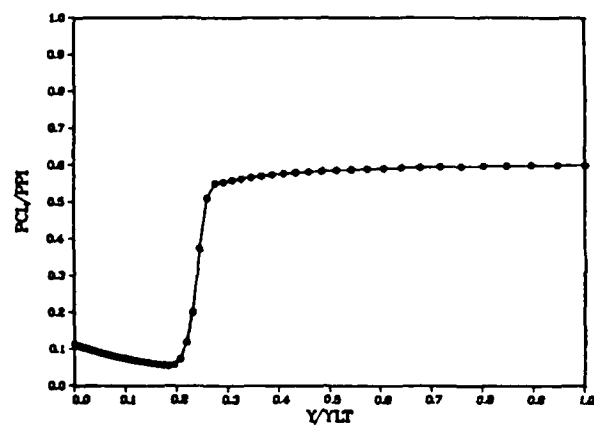
N=80K TCL/TO CSM 60%NSR WBB=2
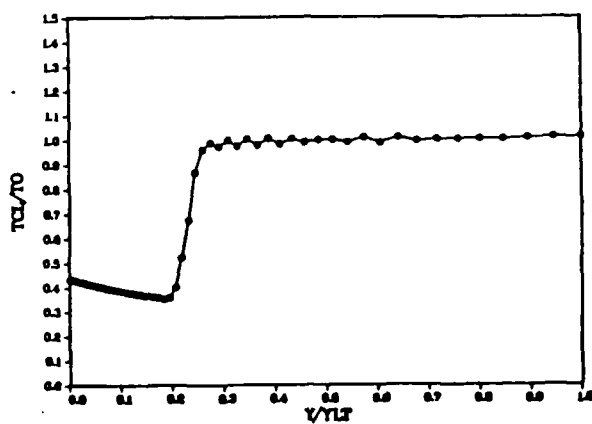
N=85K TCL/TO CSM 60%NSR WBB=2
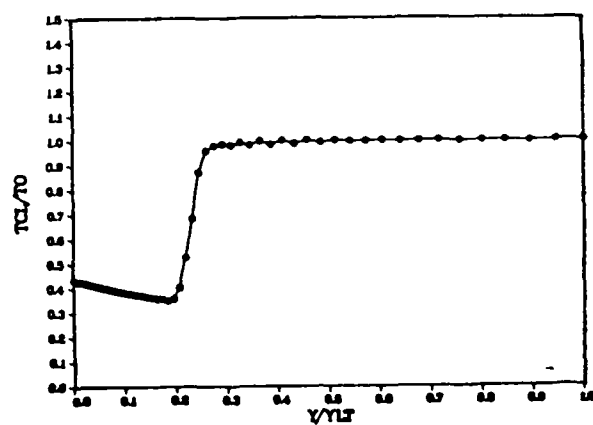
N=90K PW/PPI CSM 60%NSR WBB=2
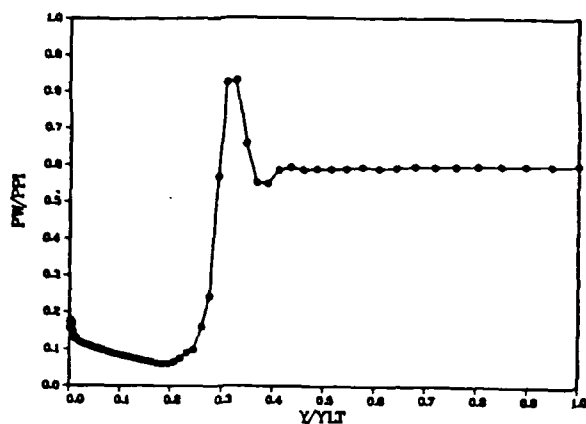
N=95K PW/PPI CSM 60%NSR WBB=2
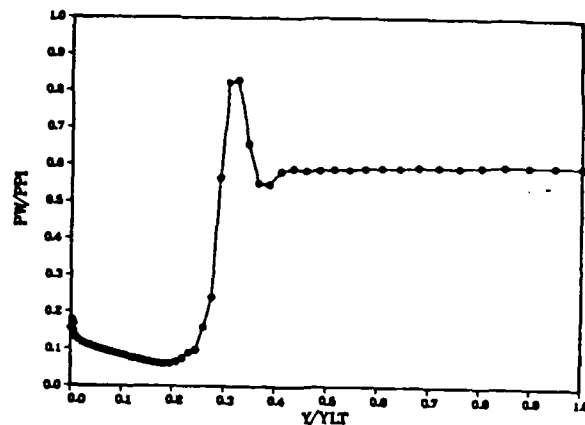
N=90K PCL/PPI CSM 60%NSR WBB=2
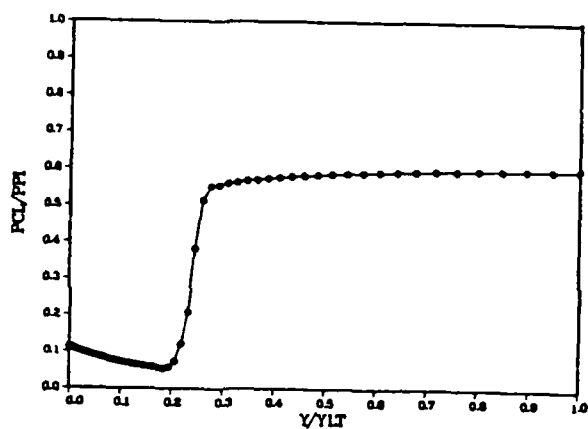
N=95K PCL/PPI CSM 60%NSR WBB=2
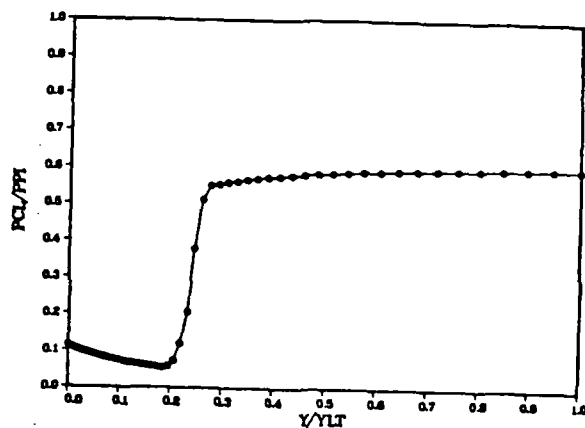
N=90K TCL/TO CSM 60%NSR WBB=2
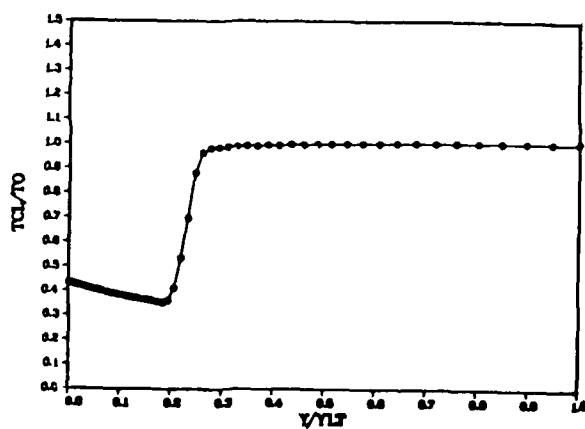
N=95K TCL/TO CSM 60%NSR WBB=2

274
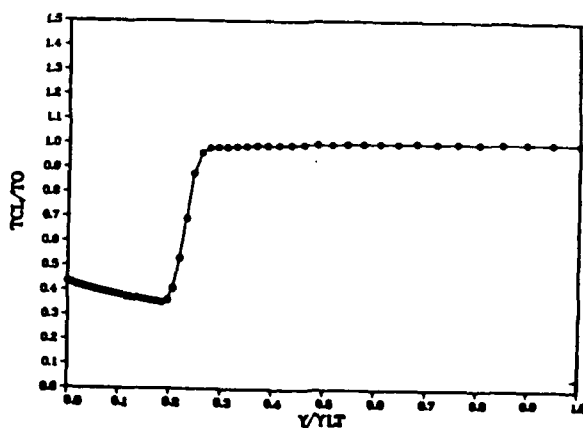
N=100K PW/PPI CSM 60%NSR WBB=2
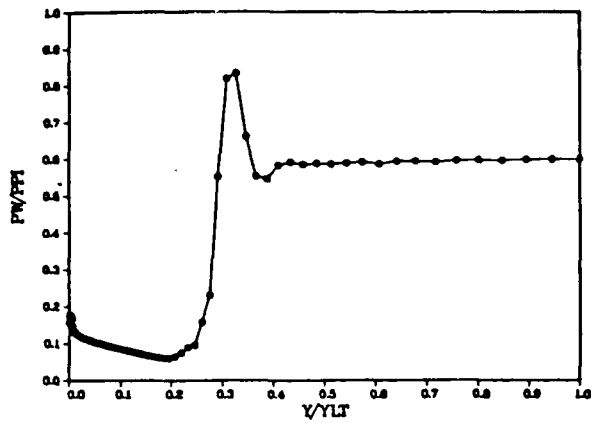
N=125K PW/PPI CSM 60%NSR WBB=2
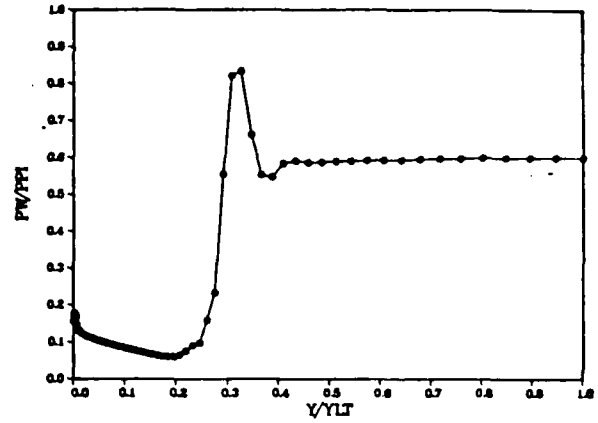
N=100K PCL/PPI CSM 60%NSR WBB=2
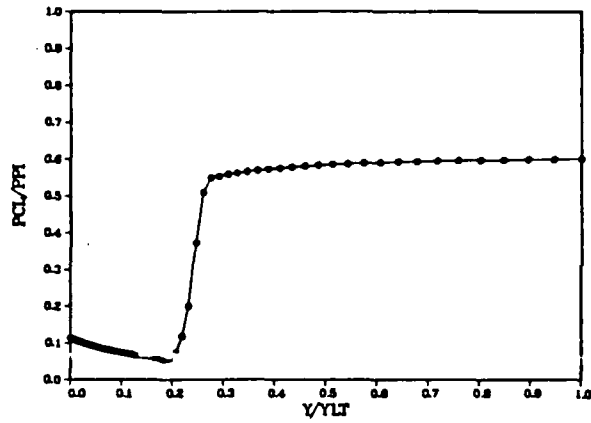
N=125K PCL/PPI CSM 60%NSR WBB=2
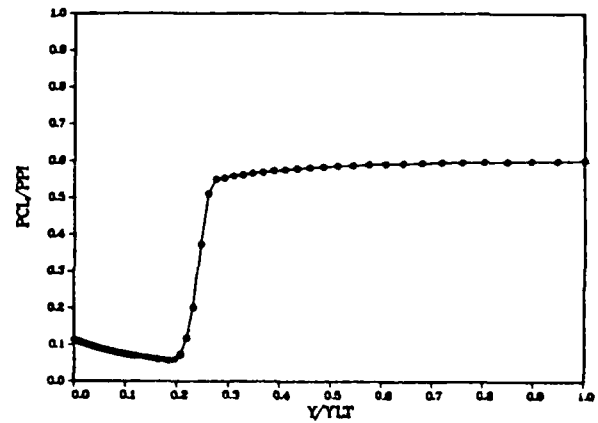
N=100K TCL/TO CSM 60%NSR WBB=2
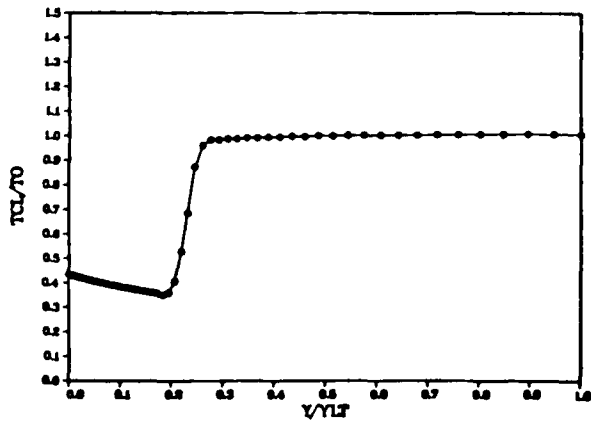
N=125K TCL/TO CSM 60%NSR WBB=2
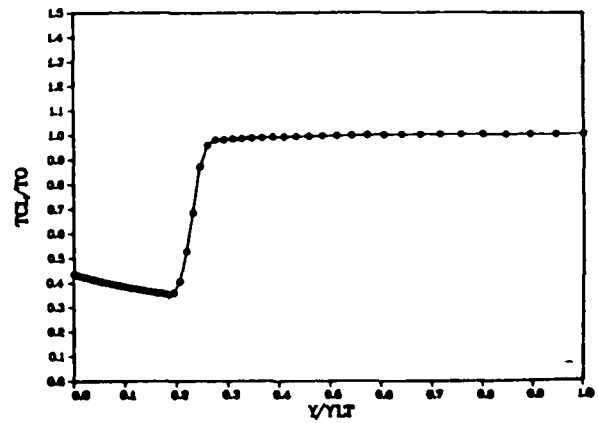
N=150K PW/PPI CSM 60%NSR WBB=.2
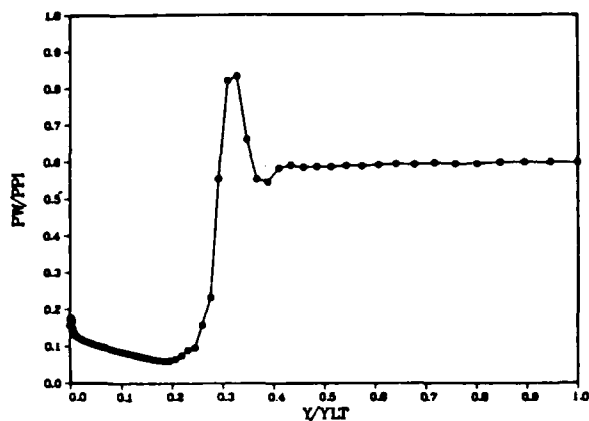
N=175K PW/PPI CSM 60%NSR WBB=.2
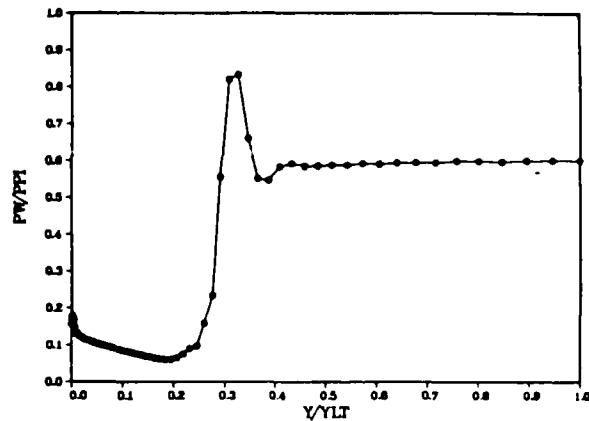
N=150K PCL/PPI CSM 60%NSR WBB=.2
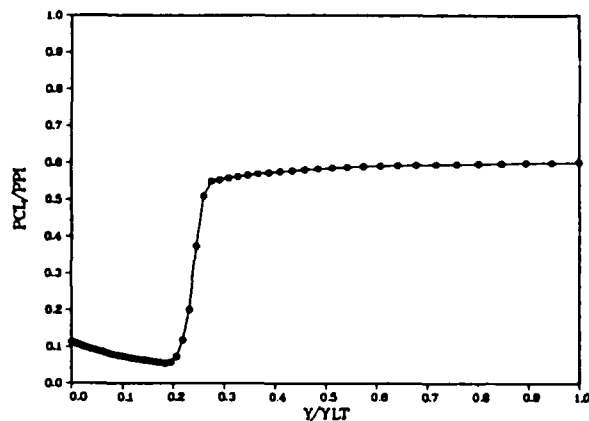
N=175K PCL/PPI CSM 60%NSR WBB=.2
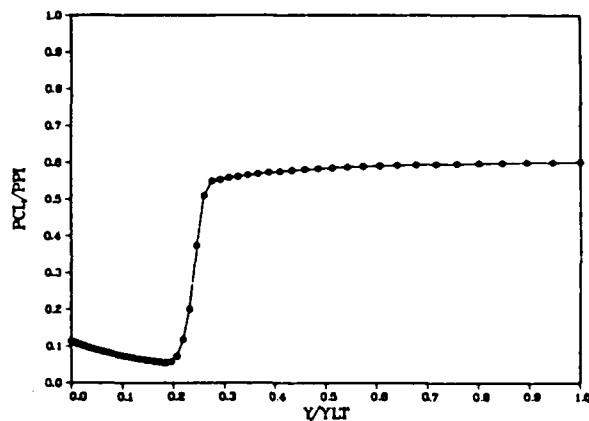
N=150K TCL/TO CSM 60%NSR WBB=.2
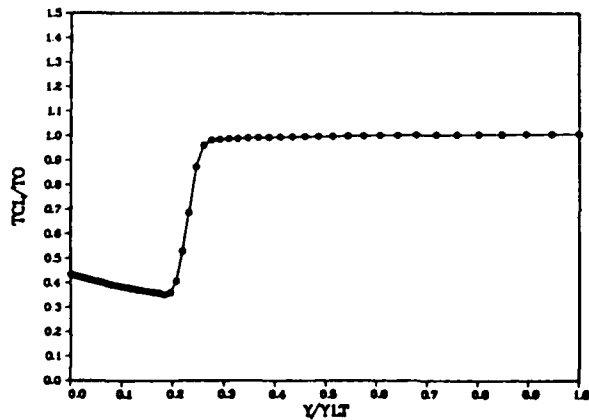
N=175K TCL/TO CSM 60%NSR WBB=.2
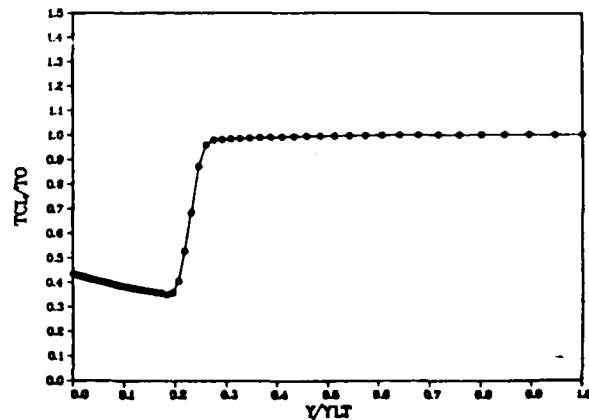
N=200K PW/PPI CSM 60%NSR WBB=2
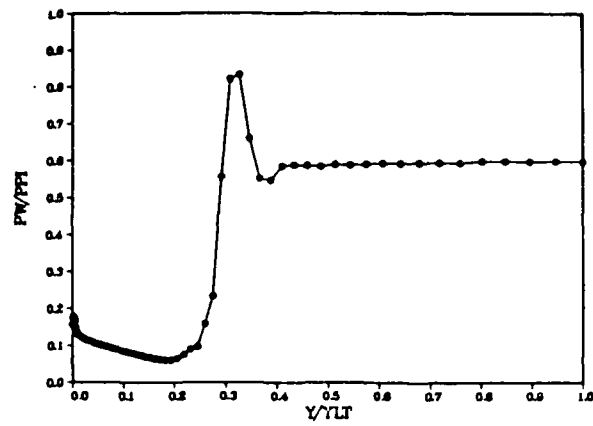
N=200K PCL/PPI CSM 60%NSR WBB=2
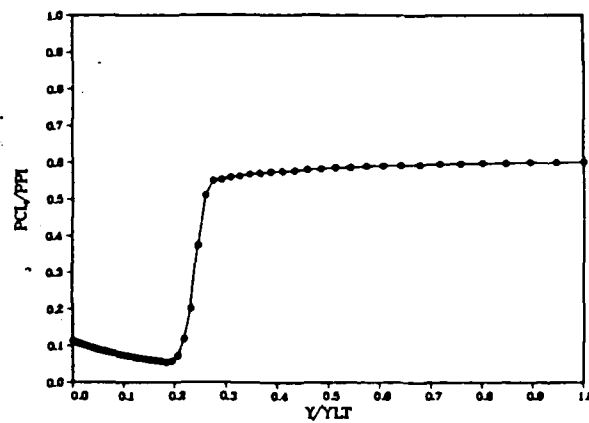
N=200K TCL/TO CSM 60%NSR WBB=2
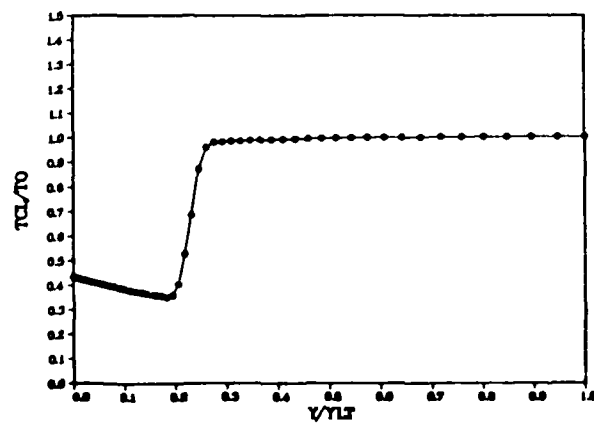
APPENDIX G

NUMERICAL CASE 3A COMPUTATIONAL DETAILS

Details of the first "long duct" numerical experiment are presented, showing the progress of the line of symmetry normal shock to a stable, "started" condition in the diffuser. For this numerical experiment a uniform core inflow was assumed at M = 2.5, with no wall flow energization. Exit pressure was set at 60% of normal shock recovery pressure. The Navier-Stokes computer code employed the Cebeci-Smith two-layer eddy viscosity turbulence model modified for the effect of an adverse pressure gradient as described in Chapter V, Section 5.3. Selected Mach contour, nondimensionalized wall pressure, line of symmetry pressure, and line of symmetry temperature plots portray flow behavior in a long diffuser with no wall boundary layer control. Figure 43 is repeated, presenting the time history of normal shock position in the diffuser for two characteristic times when convergence was assured (but not entirely achieved - at this point 2,500,000 computational iterations had been executed and further computation was deemed unnecessary and uneconomical). The Mach contour plots again present graphic flow images from M = 0.0 to M = 5.0, in increments of 0.20. Without wall flow energization, it is apparent that the long diffuser length is necessary to provide sufficient recovery distance for the large wall boundary layer separation region. Without wall bank blowers, no overpressure response is observed in the behavior of the wall pressure, and it is seen to respond smoothly in recovering to the exit pressure. Results of this numerical experiment are consistent with well established experimental results (11). This numerical experiment required 40.2 hours of CRAY 1 CPU time.

LONG DUCT TIME HISTORY   CSM 60%NSR WBB=0

M=2.55 60%NSR BB OFF N=25,000

M=2.55 60%NSR BB OFF N=25,000

M=2.55 60%NSR BB OFF N=50,000

M=2.55 60%NSR BB OFF N=50,000

M=2.55 60%NSR BB OFF N=75,000

M=2.55 60%NSR BB OFF N=75,000

M=2.55 60%NSR BB OFF N=100,000

M=2.55 60%NSR BB OFF N=100,000

M=2.55 60%NSR BB OFF N=150K

M=2.55 60%NSR BB OFF N=150K

M=2.55 60%NSR BB OFF N=180K

M=2.55 60%NSR BB OFF N=180K

281

60%NSR WBB=0 N=230,000

60%NSR WBB=0 N=230,000

60%NSR BB OFF N=250,000

60%NSR BB OFF N=250,000

CONVERGED MACH CONTOURS 60%NSR WBB=0

CONVERGED MACH CONTOURS LD 60%NSR WBB=0

282

M=2.55 60%NSR BB OFF WALL PR N=25,000

M=2.55 60%NSR BB OFF WALL PR N=25,000

M=2.55 60%NSR BB OFF C/L PR N=25,000

M=2.55 60%NSR BB OFF C/L PR N=25,000

M=2.55 60%NSR BB OFF C/L TR N=25,000

M=2.55 60%NSR BB OFF C/L TR N=25,000

283

M=2.55 60%NSR BB OFF WALL PR N=50,000

M=2.55 60%NSR BB OFF WALL PR N=50,000

M=2.55 60%NSR BB OFF C/L PR N=50,000

M=2.55 60%NSR BB OFF C/L PR N=50,000

M=2.55 60%NSR BB OFF C/L TR N=50,000

M=2.55 60%NSR BB OFF C/L TR N=50,000
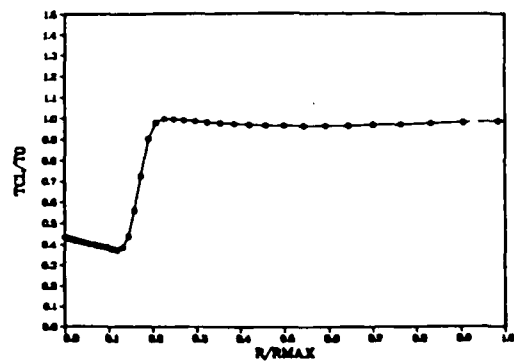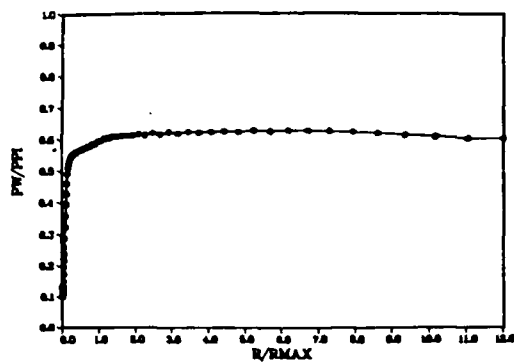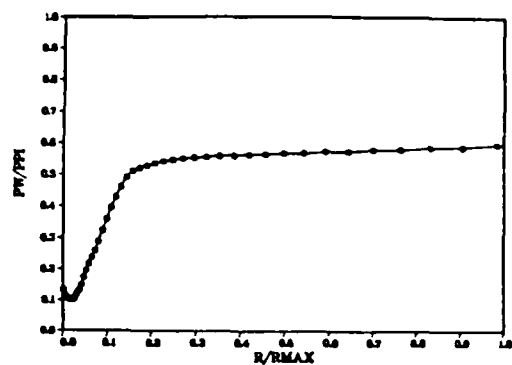
284

M=2.55 60%NSR BB OFF WALL PR N=100,000

PW/PPI

R/RMAX

M=2.55 60%NSR BB OFF WALL PR N=100,000

PW/PPI

R/RMAX

M=2.55 60%NSR BB OFF C/L PR N=100,000

PCL/PPI

R/RMAX

M=2.55 60%NSR BB OFF C/L PR N=100,000

PCL/PPI

R/RMAX

M=2.55 60%NSR BB OFF C/L TR N=100,000

TCL/T0

R/RMAX

M=2.55 60%NSR BB OFF C/L TR N=100,000

TCL/T0

R/RMAX
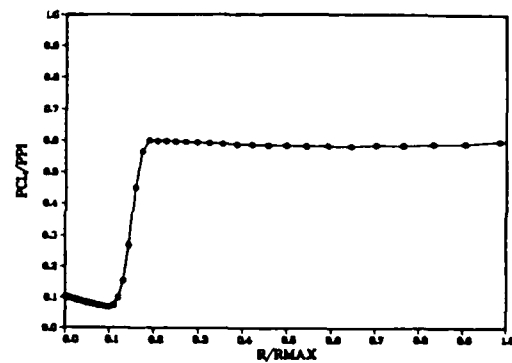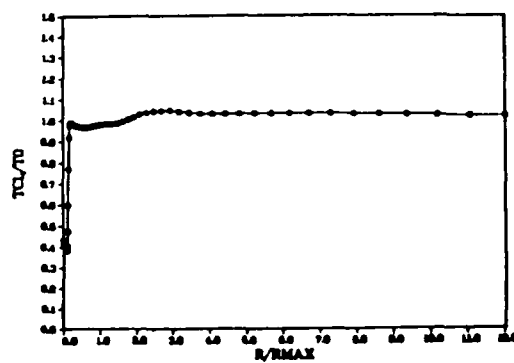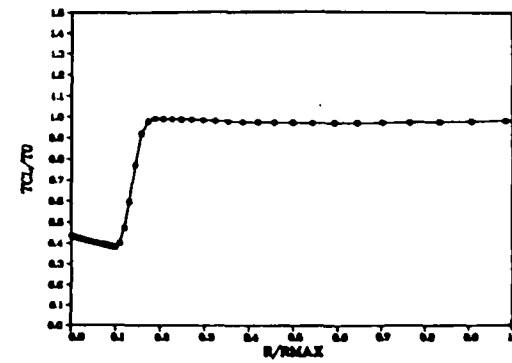
M=2.55 60%NSR BB OFF WALL PR N=150K
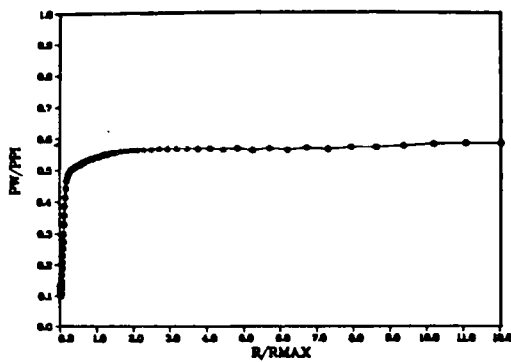
M=2.55 60%NSR BB OFF WALL PR N=150K
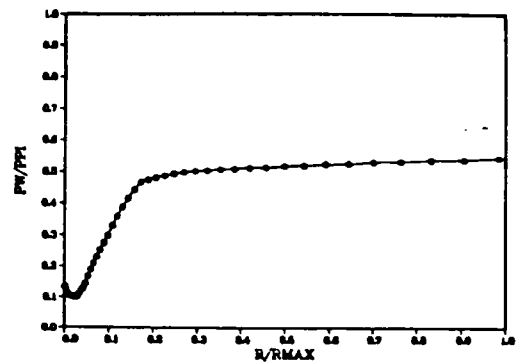
M=2.55 60%NSR BB OFF C/L PR N=150K
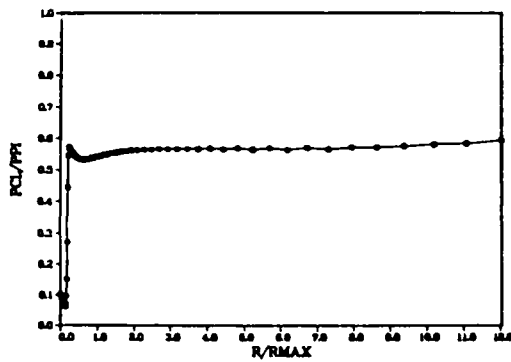
M=2.55 60%NSR BB OFF C/L PR N=150K
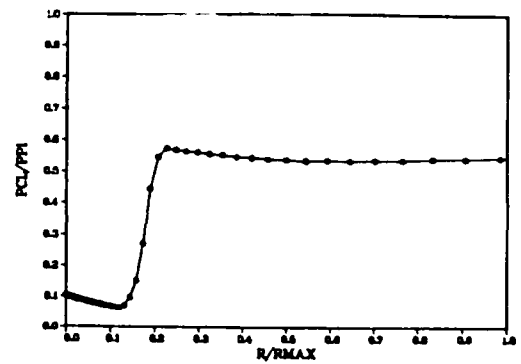
M=2.55 60%NSR BB OFF C/L TR N=150K
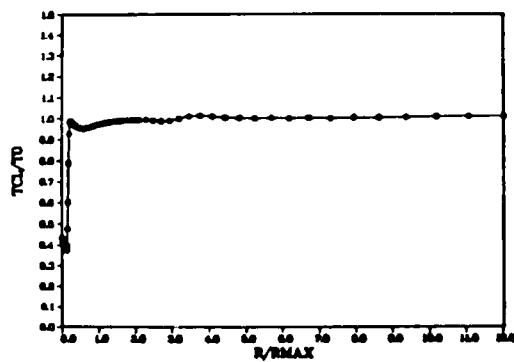
M=2.55 60%NSR BB OFF C/L TR N=150K
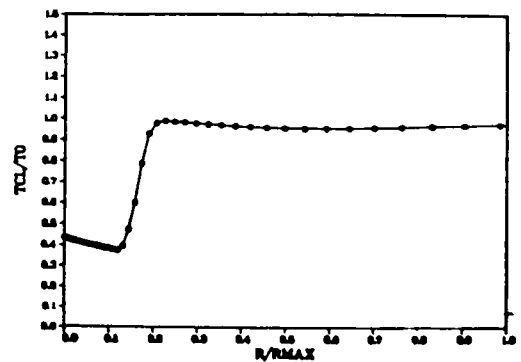
M=2.55 60%NSR BB OFF WALL PR N=180K

M=2.55 60%NSR BB OFF WALL PR N=180K
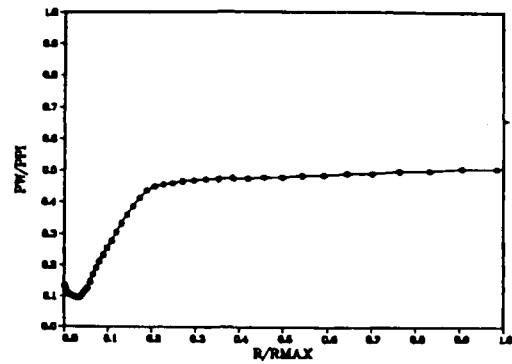
M=2.55 60%NSR BB OFF C/L PR N=180K
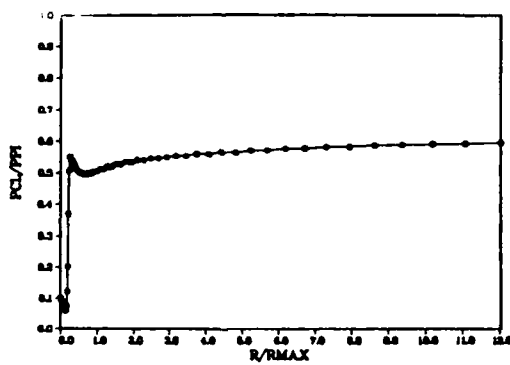
M=2.55 60%NSR BB OFF C/L PR N=180K
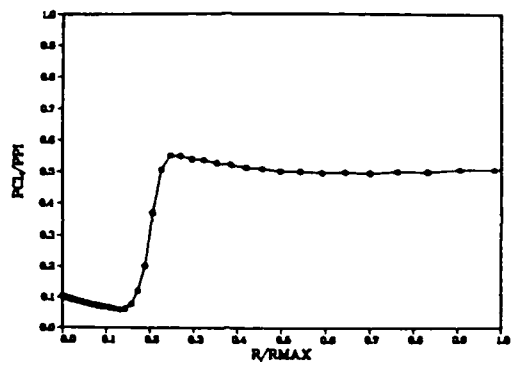
M=2.55 60%NSR BB OFF C/L TR N=180K

M=2.55 60%NSR BB OFF C/L TR N=180K

287
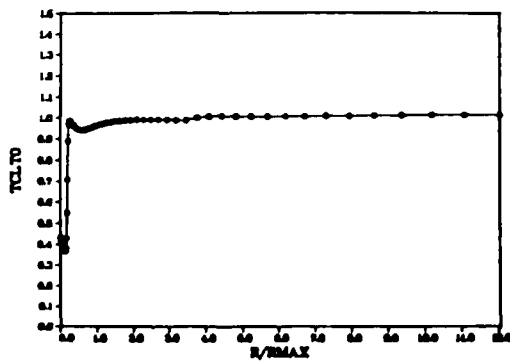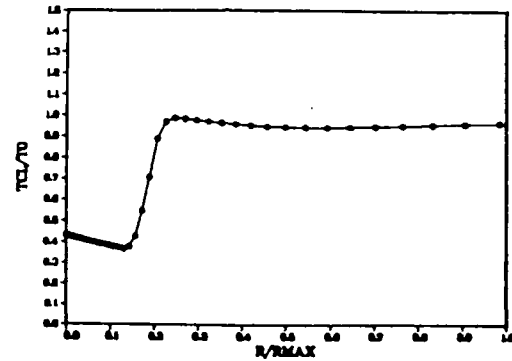
60%NSR BB OFF WALL PR N=200K

60%NSR BB OFF WALL PR N=200K
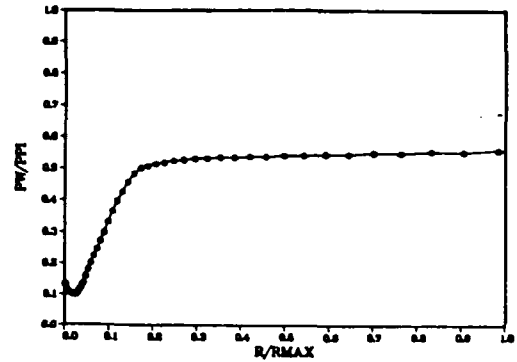
60%NSR BB OFF C/L PR N=200K
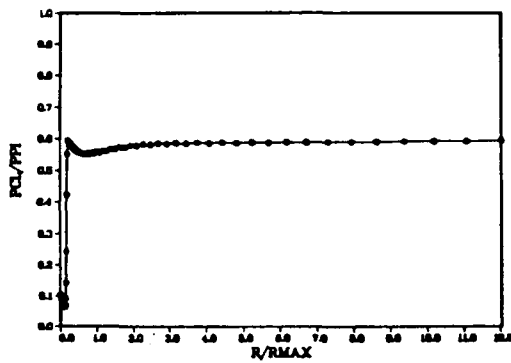
60%NSR BB OFF C/L PR N=200K
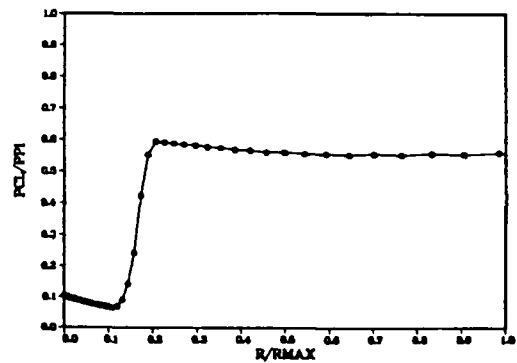
60%NSR BB OFF C/L TR N=200K
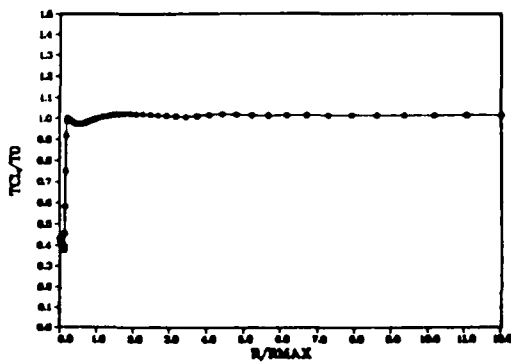
60%NSR BB OFF C/L TR N=200K
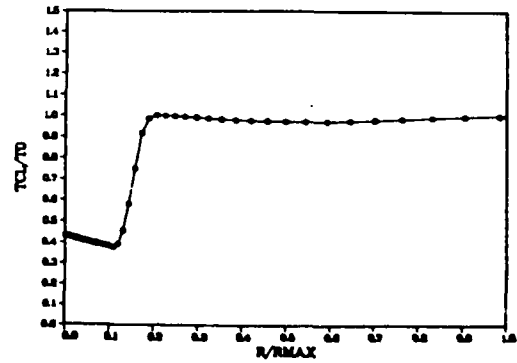
LONG DUCT CONVERGED PW/PPI 60%NSR WBB=0
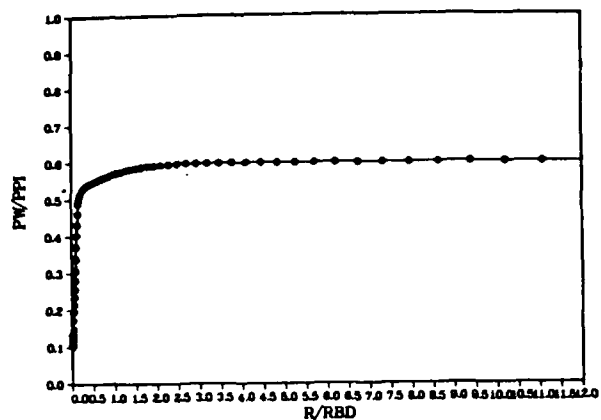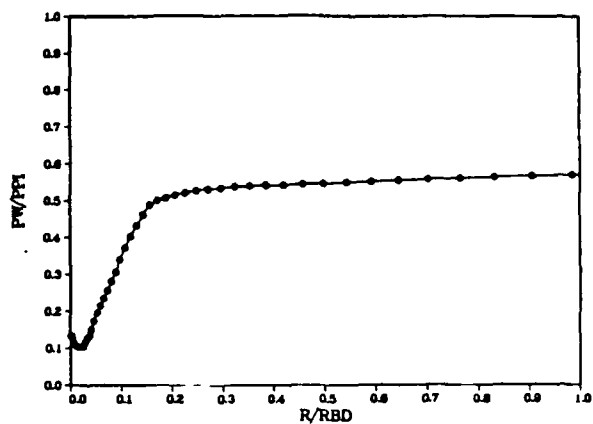
LONG DUCT CONVERGED PW/PPI 60%NSR WBB=0

LONG DUCT CONVERGED PCL/PPI 60%NSR WBB=0
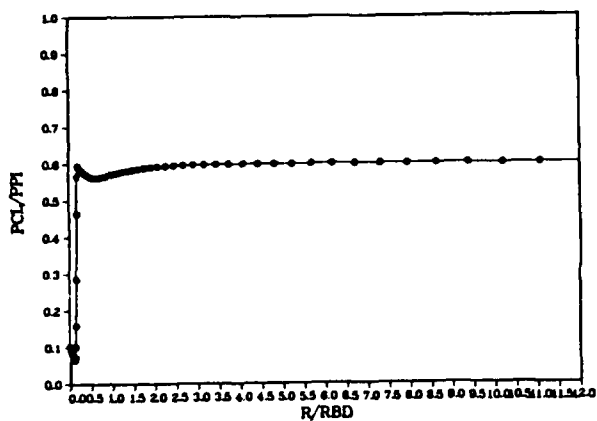
LONG DUCT CONVERGED PCL/PPI 60%NSR WBB=0
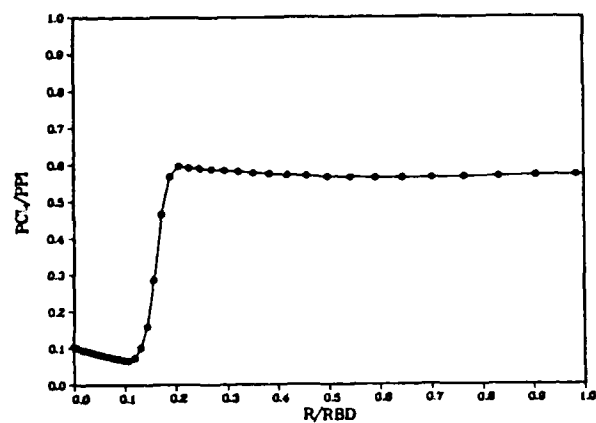
LONG DUCT CONVERGED TCL/TO 60%NSR WBB=0

LONG DUCT CONVERGED TCL/TO 60%NSR WBB=0

289
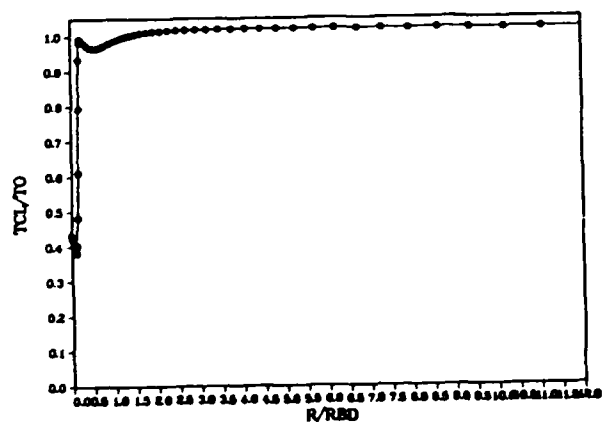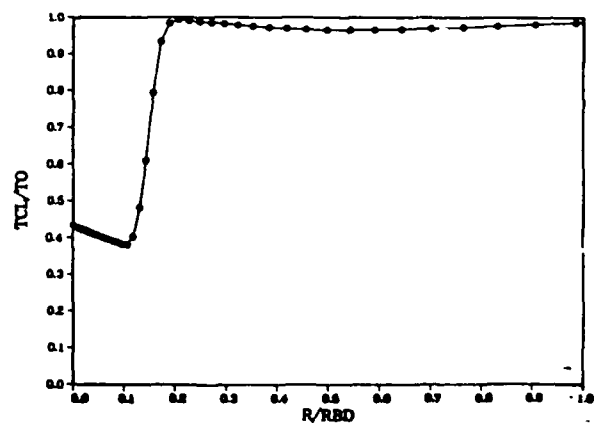
APPENDIX H

NUMERICAL CASE 4A COMPUTATIONAL DETAILS

For this numerical experiment the stiffened eddy viscosity model developed in Chapter V was employed for a flow field based on the actual. experimental inflow profiles for the baseline UTRC experiment, with the exit pressure set at 60% of normal shock recovery pressure. Figure 64 is repeated, presenting core flow normal shock position time history. Selected Mach contour, nondimensionalized wall pressure, line of symmetry pressure, and line of symmetry temperature plots portray the flow behavior. The Mach contour plots again present graphic flow images from M = 0.0 to M = 5.0, in increments of 0.20. Clearly visible are the nozzle profiles and the persistence of the wall bank blower flow energizers to the diffuser exit. Again notable is the "smooth" behavior of the wall pressure from the diffuser entrance to a large overpressure spike that occurs slightly downstream of the core flow normal shock; the higher energy, higher Mach number bank blower flow passes through a stronger shock before adjusting to diffuser exit pressure. This numerical experiment required 24.2 hours of CRAY 1 CPU time.

CONVERGENCE TIME HISTORY 60%NSR
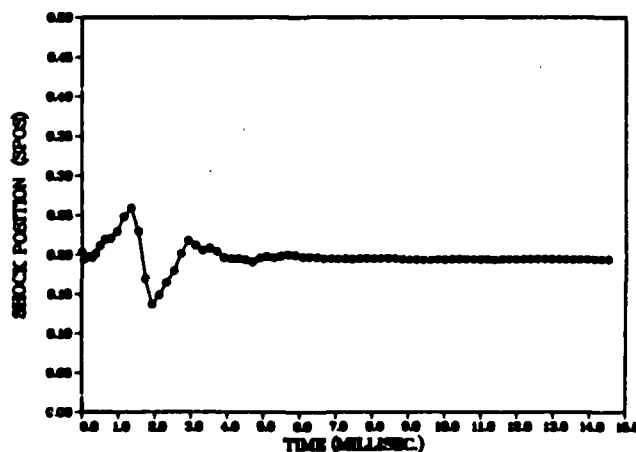
TABLE VIII

NUMERICAL CASE 4A COMPUTED SHOCK POSITION VS TIME

N Number of Iterations	CFL	TIME (Milliseconds)	R/R_{de}	SPOS
0		0	1.627127	0.204011
5,000	.10	0.039450	1.593350	0.193350
10,000	.10	0.079081	1.599307	0.194961
15,000	.10	0.118710	1.604072	0.196511
20,000	.10	0.158348	1.605842	0.197087
25,000	.10	0.197980	1.606872	0.197422
30,000	.20	0.276900	1.603386	0.196288
35,000	.25	0.375390	1.619977	0.201685
40,000	.30	0.493440	1.650566	0.211636
45,000	.35	0.631040	1.675210	0.219653
50,000	.40	0.788180	1.677635	0.220442
55,000	.45	0.964870	1.704932	0.229322
60,000	.50	1.161098	1.763719	0.248446
65,000		1.357392	1.796577	0.259135
70,000		1.553560	1.705504	0.229508
75,000		1.749790	1.522451	0.169959
80,000		1.946022	1.421609	0.137154
85,000		2.142250	1.458614	0.149192
90,000		2.338480	1.508409	0.165391
95,000		2.534720	1.553428	0.180036
100,000		2.730950	1.620622	0.201895
105,000		2.927433	1.671426	0.218422
110,000		3.123964	1.653151	0.212477
115,000		3.320495	1.632900	0.205889
120,000		3.517026	1.641338	0.208634
125,000		3.713557	1.628934	0.204599
130,000		3.910088	1.603632	0.196368
135,000		4.106619	1.599439	0.195004
140,000		4.303150	1.599713	0.195093
145,000		4.499682	1.595880	0.193846
150,000		4.696213	1.587180	0.191018
155,000		4.892744	1.602563	0.196020
160,000		5.089275	1.608311	0.197890
165,000		5.285806	1.603970	0.196478
170,000		5.482337	1.610761	0.198687
175,000		5.678868	1.616030	0.200401
180,000		5.875399	1.613650	0.199627
185,000		6.071931	1.606691	0.197363
190,000		6.268462	1.606995	0.197462
195,000		6.464993	1.605922	0.197113
200,000		6.661523	1.599369	0.194981

N Number of Iterations	CFL	TIME (Milliseconds)	R/R_{de}	SPOS
205,000	.50	6.858016	1.600389	0.195313
210,000		7.054547	1.599329	0.194968
215,000		7.251078	1.599839	0.195134
220,000		7.447609	1.598652	0.194748
225,000		7.644140	1.599682	0.195083
230,000		7.840671	1.601348	0.195625
235,000		8.037202	1.599728	0.195098
240,000		8.233734	1.600460	0.195336
245,000		8.430265	1.600983	0.195506
250,000		8.626796	1.600303	0.195285
255,000		8.823033	1.597669	0.194428
260,000		9.019264	1.595603	0.193756
265,000		9.215495	1.596473	0.194039
270,000		9.411726	1.594825	0.193503
275,000		9.607957	1.595874	0.193844
280,000		9.804188	1.596691	0.194110
285,000		10.000420	1.595351	0.193674
290,000		10.196650	1.597414	0.194345
295,000		10.392880	1.597577	0.194398
300,000		10.585190	1.597143	0.194257
305,000		10.785300	1.596857	0.194164
310,000		10.981540	1.596064	0.193906
315,000		11.177770	1.596633	0.194091
320,000		11.374000	1.595382	0.193684
325,000		11.570230	1.596670	0.194103
330,000		11.766460	1.596857	0.194164
335,000		11.962690	1.597171	0.194266
340,000		12.158920	1.597810	0.194474
345,000		12.355150	1.598176	0.194593
350,000		12.551380	1.598754	0.194781
355,000		12.747610	1.598739	0.194776
360,000		12.943850	1.598502	0.194699
365,000		13.140080	1.598419	0.194672
370,000		13.336310	1.597610	0.194409
375,000		13.532540	1.597389	0.194337
380,000		13.728770	1.597229	0.194285
385,000		13.925000	1.597518	0.194379
390,000		14.121230	1.597435	0.194352
395,000		14.317460	1.597675	0.194430
400,000		14.513690	1.597816	0.194476

N=1 ACTUAL INFLOW 60%NSR
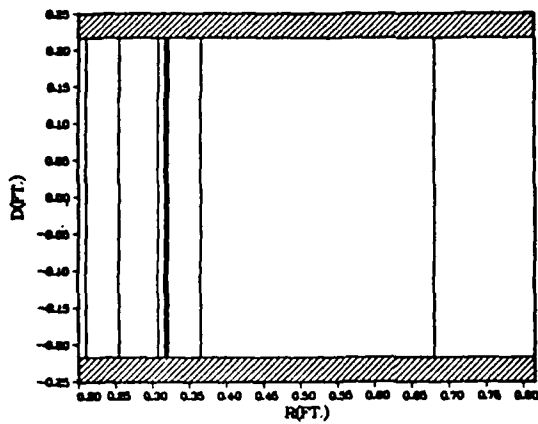
N=5K ACTUAL INFLOW 60%NSR WBB=.195
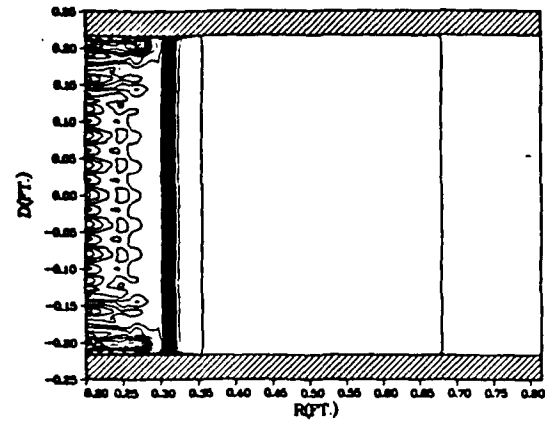
N=10K ACTUAL INFLOW 60%NSR
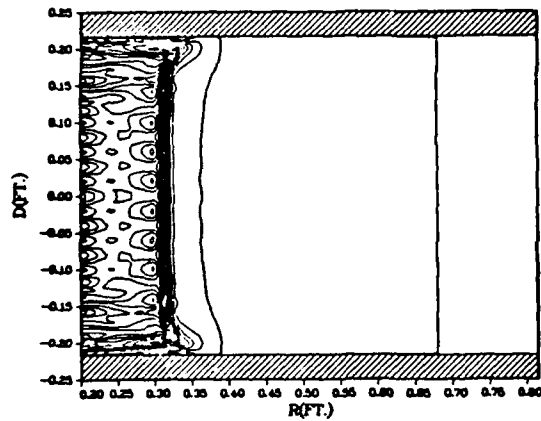
N=15K ACTUAL INFLOW 60%NSR
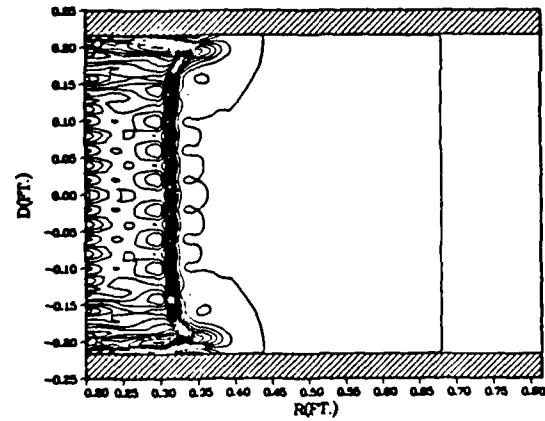
N=20K ACTUAL INFLOW 60%NSR WBB=.195
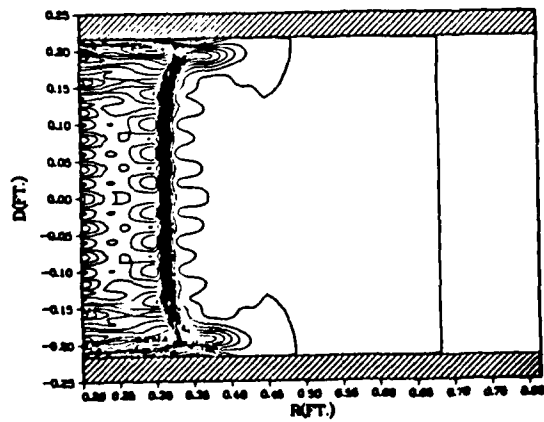
N=25K ACTUAL INFLOW 60%NSR WBB=.195
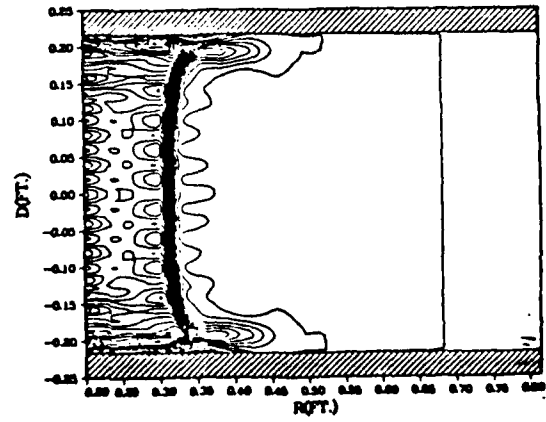
N=30K ACTUAL INFLOW 60%NSR WBB=.195
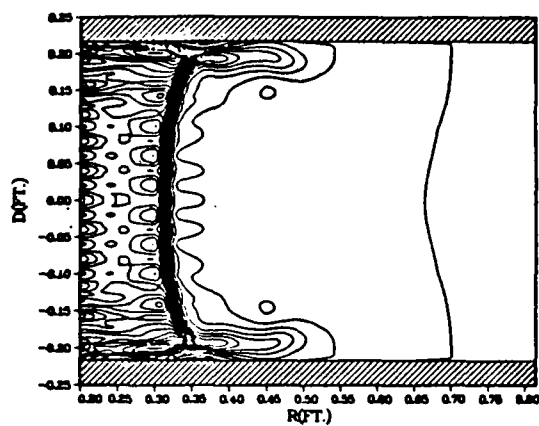
N=35K ACTUAL INFLOW 60%NSR WBB=.195
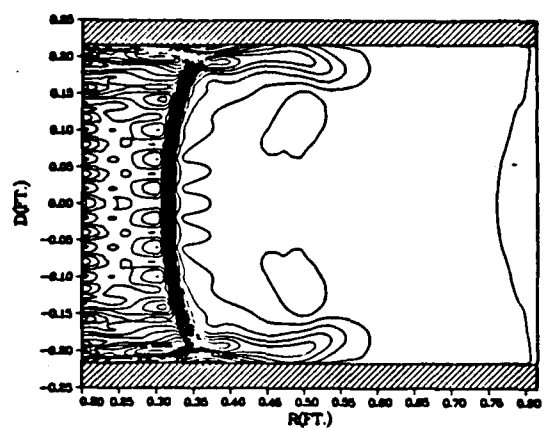
N=40K ACTUAL INFLOW 60%NSR WBB=.195
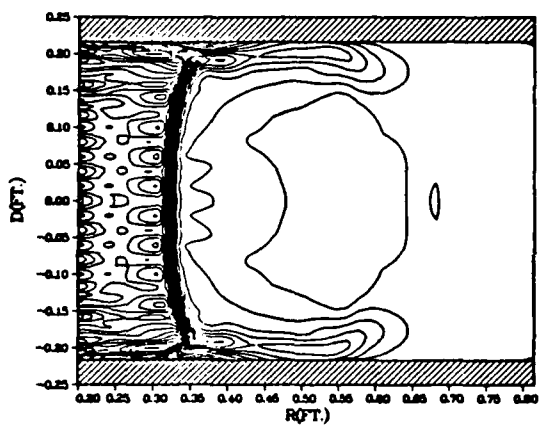
N=45K ACTUAL INFLOW 60%NSR WBB=.195
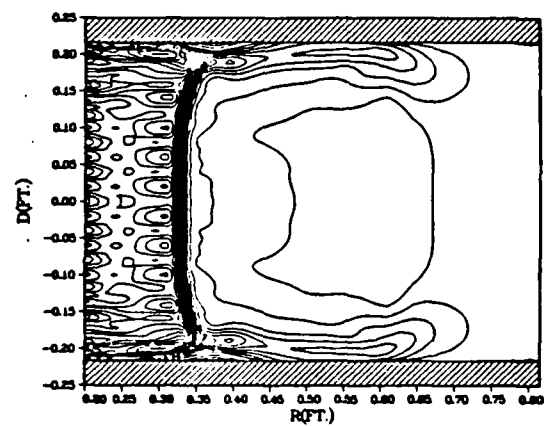
N=50K ACTUAL INFLOW 60%NSR WBB=.195
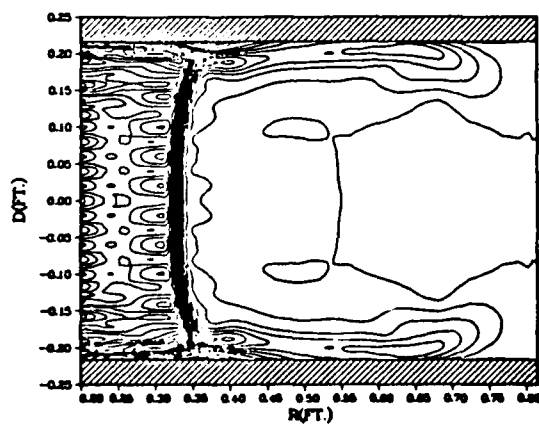
N=55K ACTUAL INFLOW 60%NSR WBB=.195
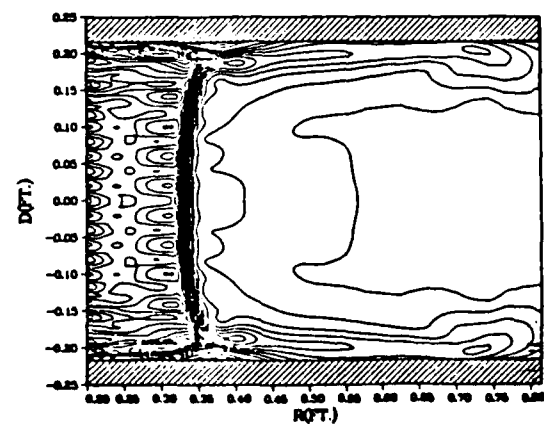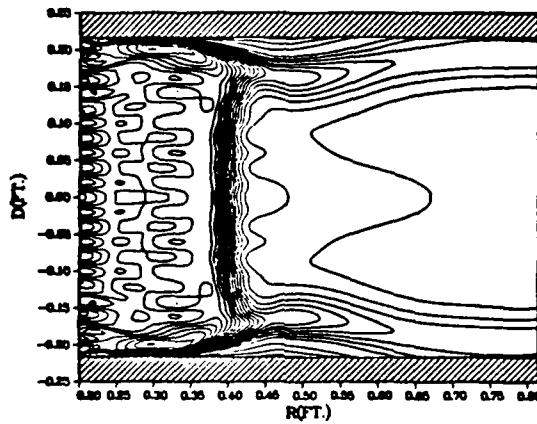
N=60K ACTUAL INFLOW 60%NSR WBB=.195
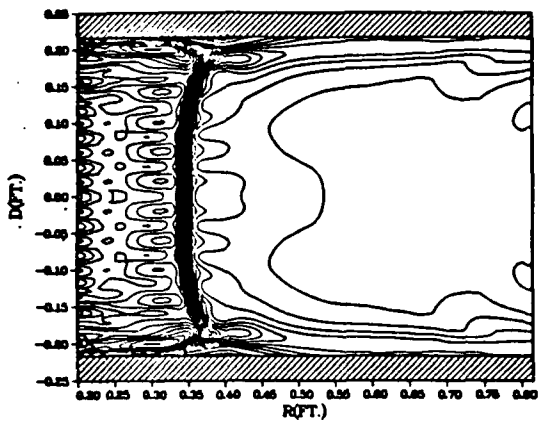
N=65K ACTUAL INFLOW 60%NSR WBB=.195
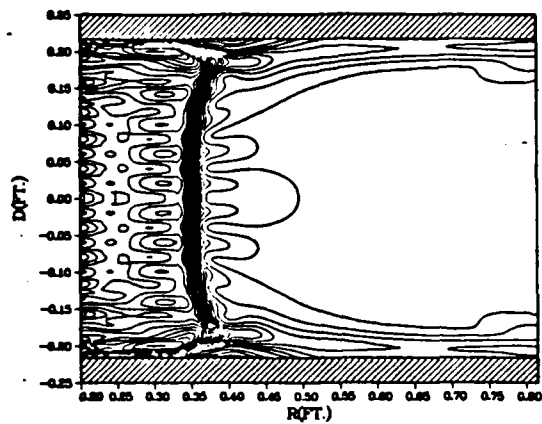
N=70K ACTUAL INFLOW 60%NSR WBB=.195
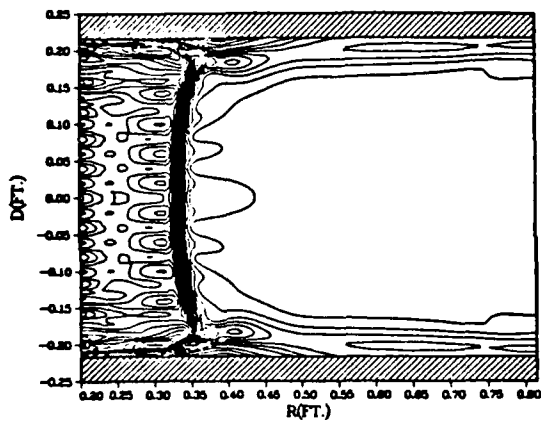
N=75K ACTUAL INFLOW 60%NSR WBB=.195
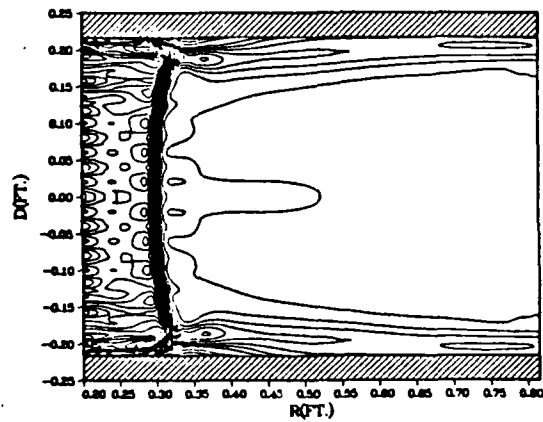
N=80K ACTUAL INFLOW 60%NSR WBB=.195
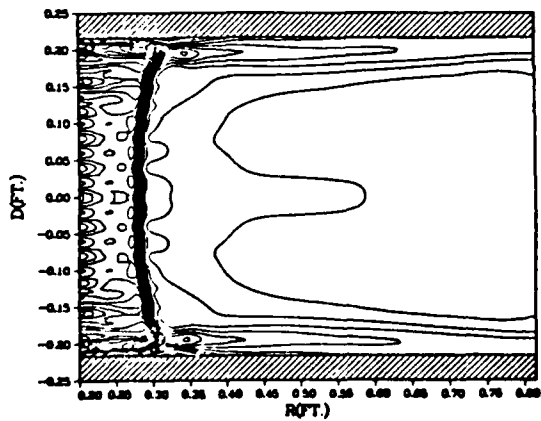
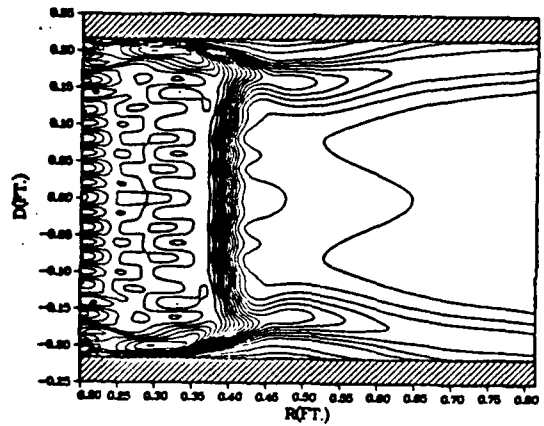N=85K ACTUAL INFLOW 60%NSR WBB=.195


295
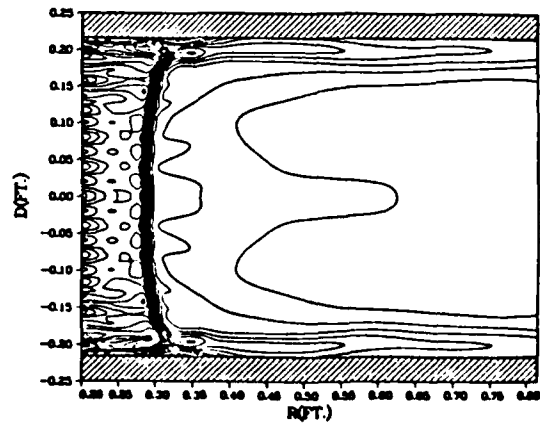
N=90K ACTUAL INFLOW 60%NSR WBB=.195
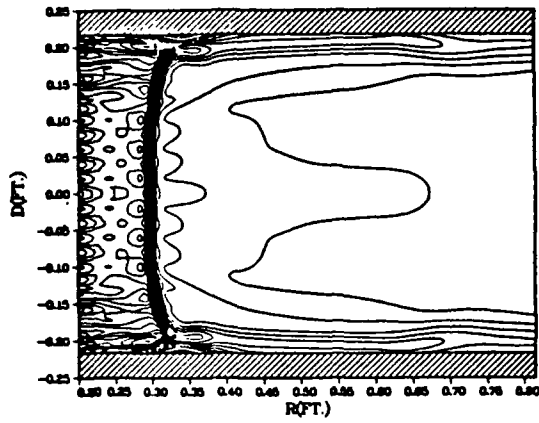
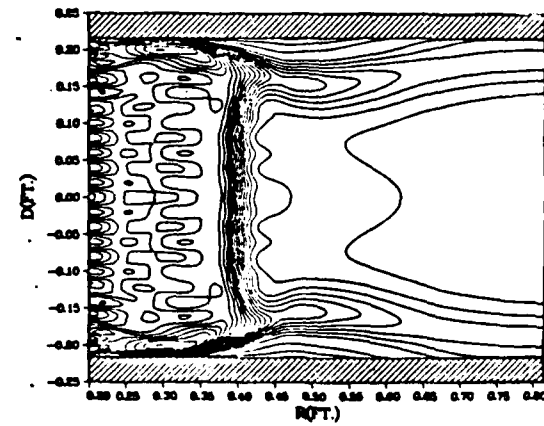N=95K ACTUAL INFLOW 60%NSR WBB=.195
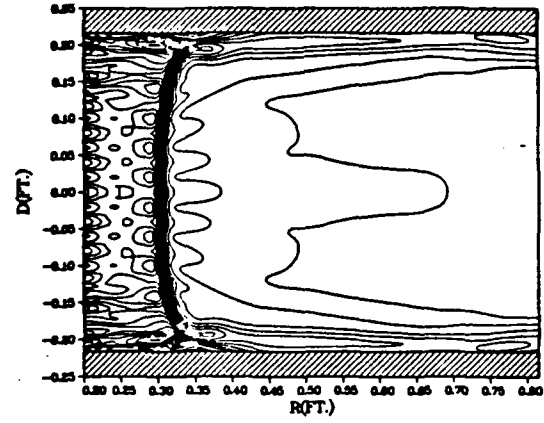
N=100K ACTUAL INFLOW 60%NSR WBB=.195
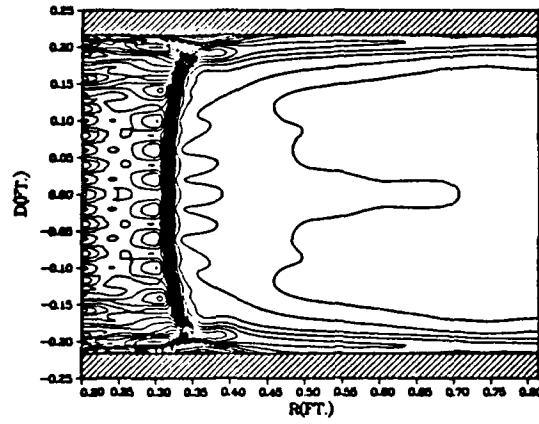
N=105K ACTUAL INFLOW 60%NSR WBB=.195
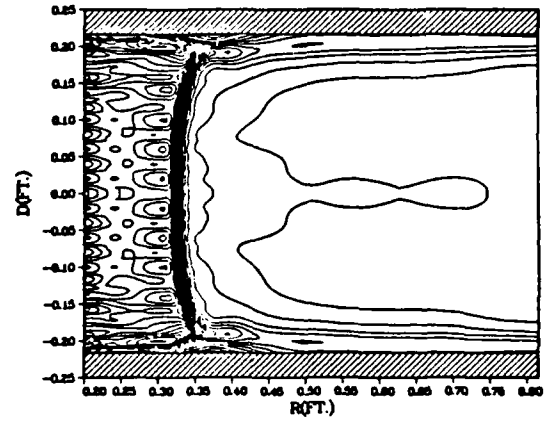
N=110K ACTUAL INFLOW 60%NSR WBB=.195
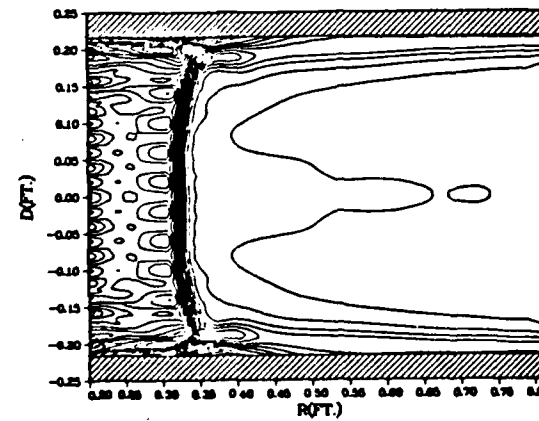
N=115K ACTUAL INFLOW 60%NSR WBB=.195
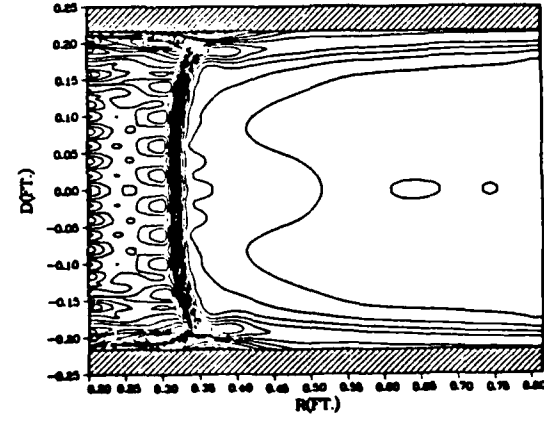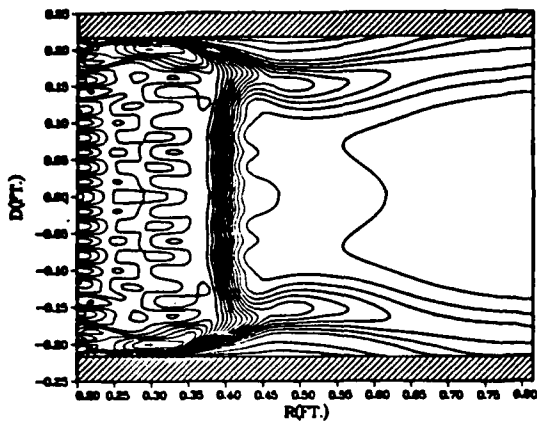
N=120K ACTUAL INFLOW 60%NSR WBB=.195
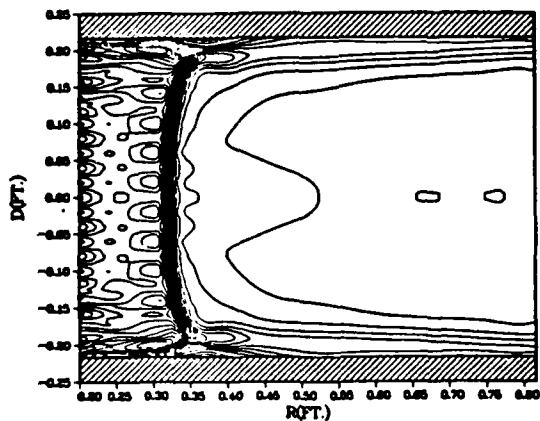
N=125K ACTUAL INFLOW 60%NSR WBB=.195
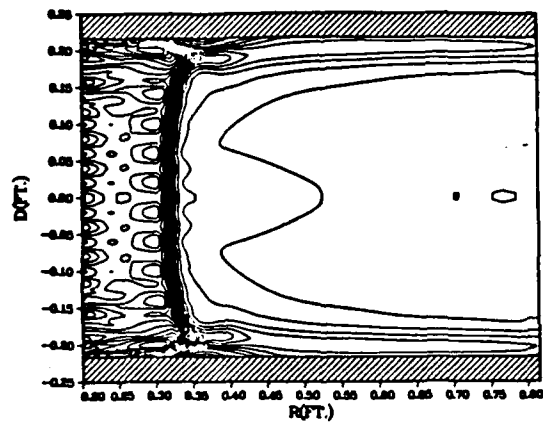
N=130K ACTUAL INFLOW 60%NSR WBB=.195
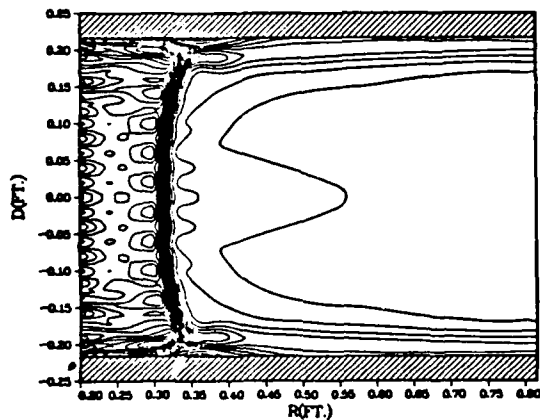
N=135K ACTUAL INFLOW 60%NSR WBB=.195
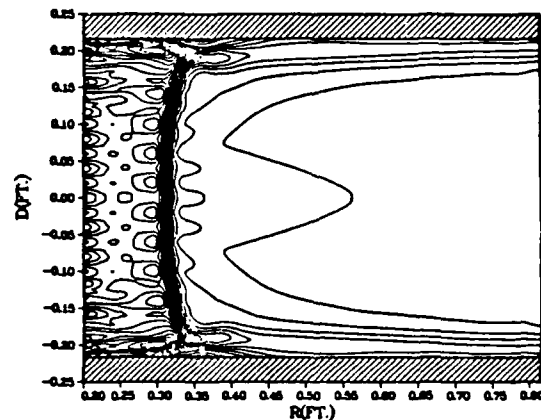
N=140K ACTUAL INFLOW 60%NSR WBB=.195
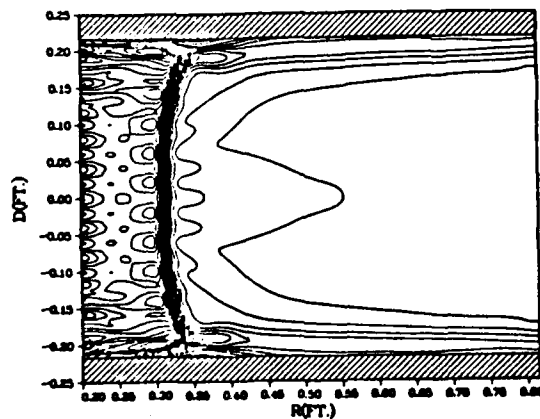
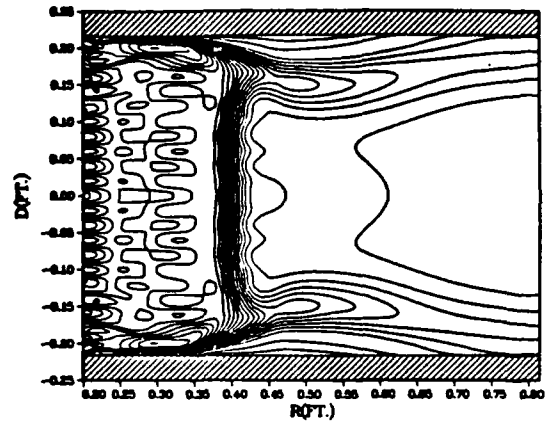N=145K ACTUAL INFLOW 60%NSR WBB=.195

297
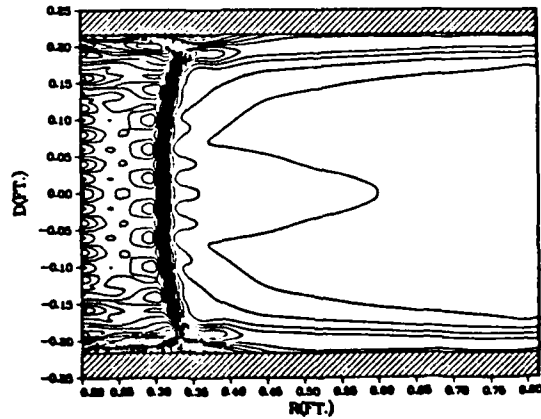
N=150K ACTUAL INFLOW 60%NSR WBB=.195
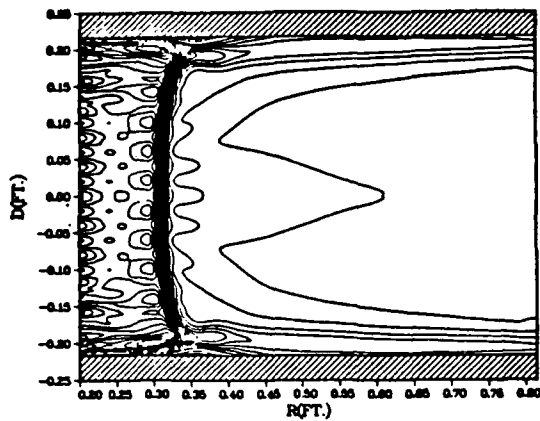
N=155K ACTUAL INFLOW 60%NSR WBB=.195
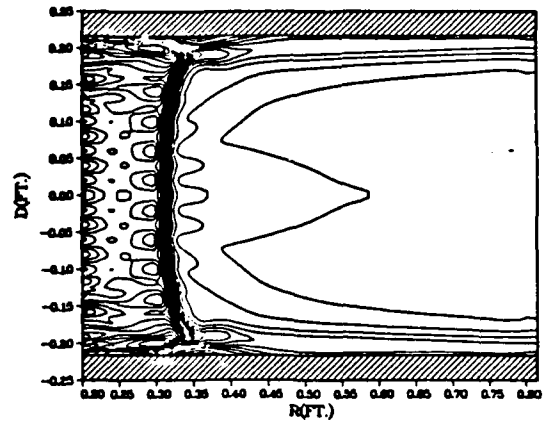
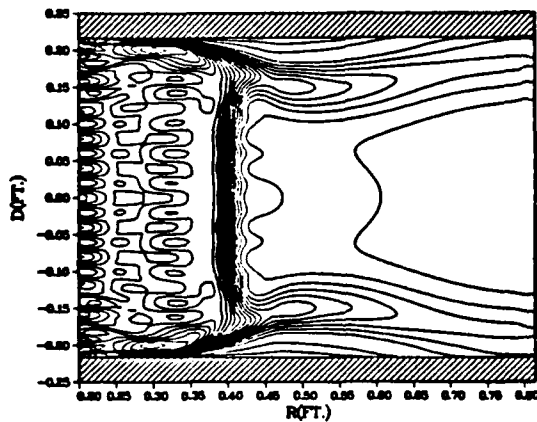N=160:: ACTUAL INFLOW 60%NSR WBB=.195
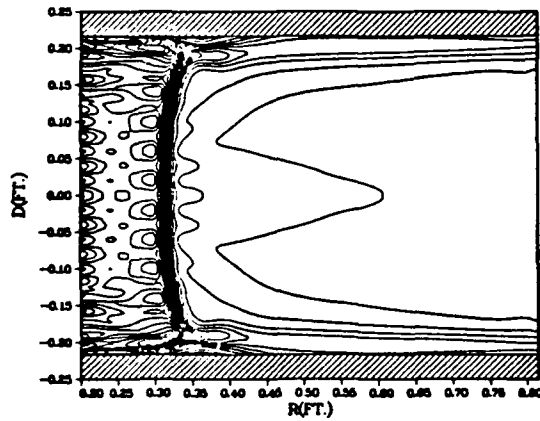
N=165K ACTUAL INFLOW 60%NSR WBB=.195
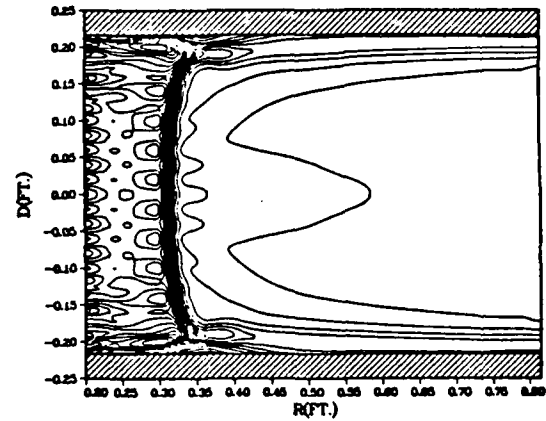
N=170K ACTUAL INFLOW 60%NSR WBB=.195

N=175K ACTUAL INFLOW 60%NSR WBB=.195

298
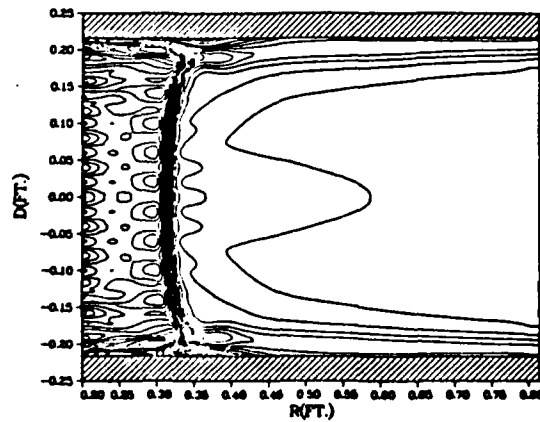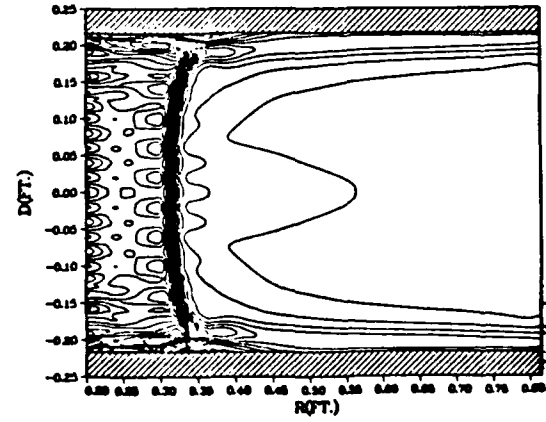
N=180K ACTUAL INFLOW 60%NSR WBB=.195
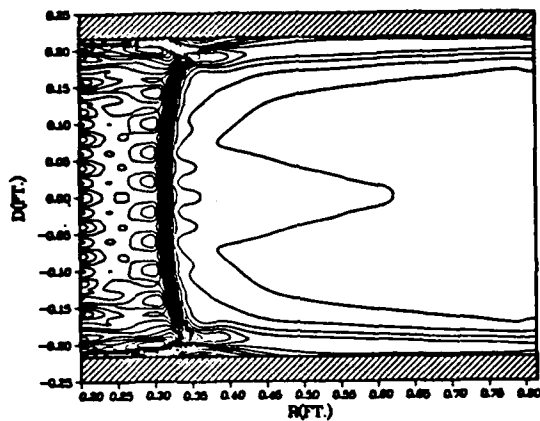
N=185K ACTUAL INFLOW 60%NSR WBB=.195
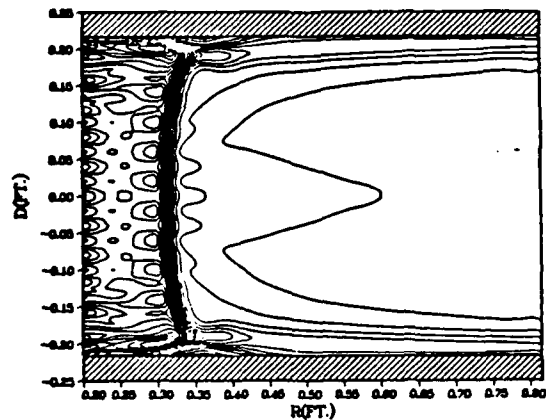
N=190K ACTUAL INFLOW 60%NSR WBB=.195
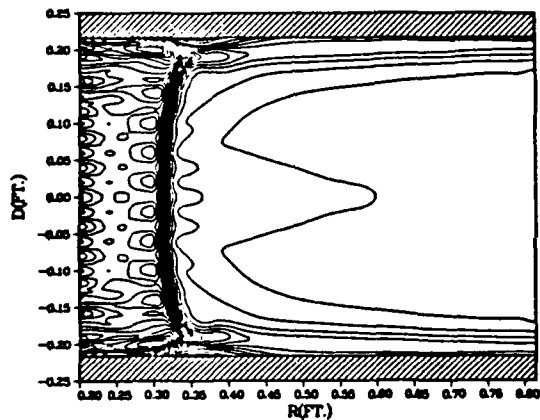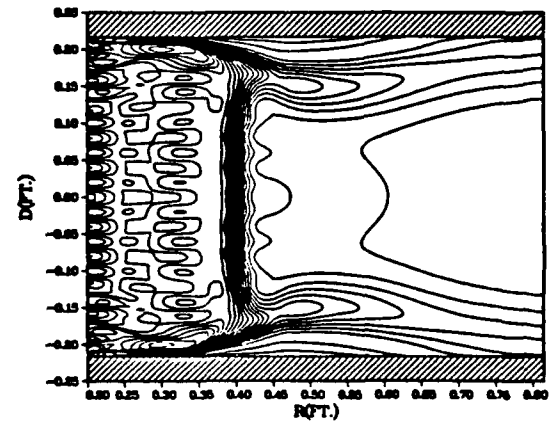
N=195K ACTUAL INFLOW 60%NSR WBB=.195
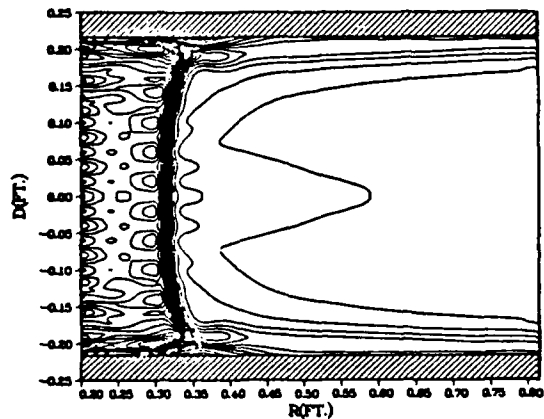
N=200K ACTUAL INFLOW 60%NSR WBB=.195
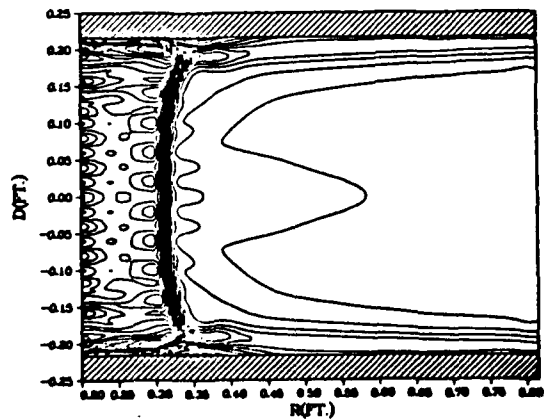
N=205K ACTUAL INFLOW 60%NSR WBB=.195
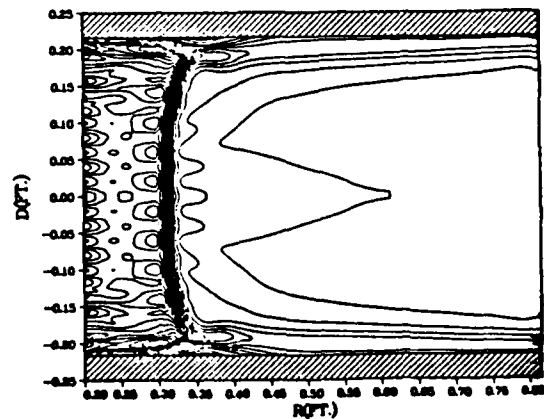
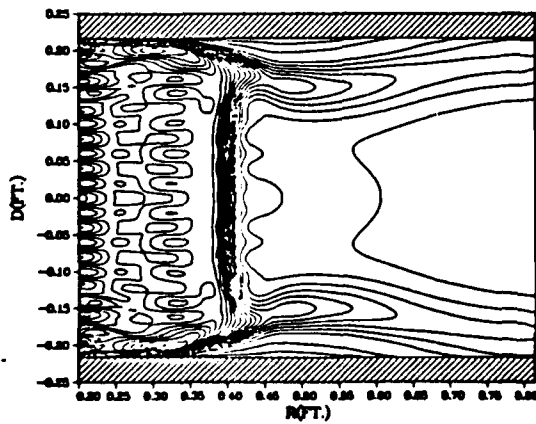N=210K ACTUAL INFLOW 60%NSR WBB=.195
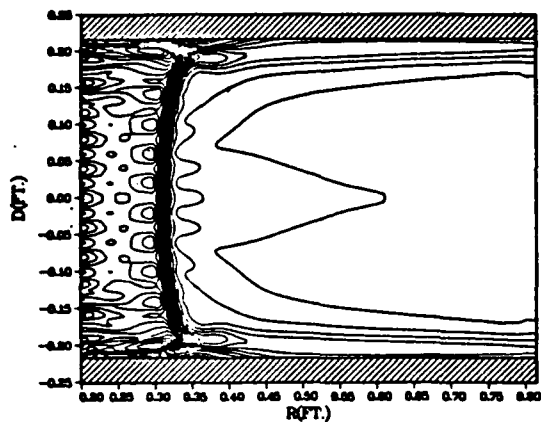
N=215K ACTUAL INFLOW 60%NSR WBB=.195
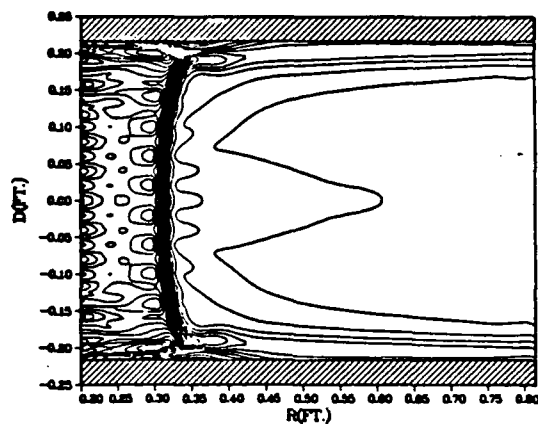
N=220K ACTUAL INFLOW 60%NSR WBB=.195
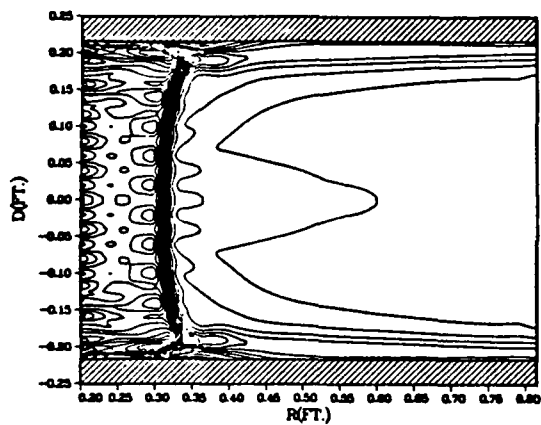
N=225K ACTUAL INFLOW 60%NSR WBB=.195
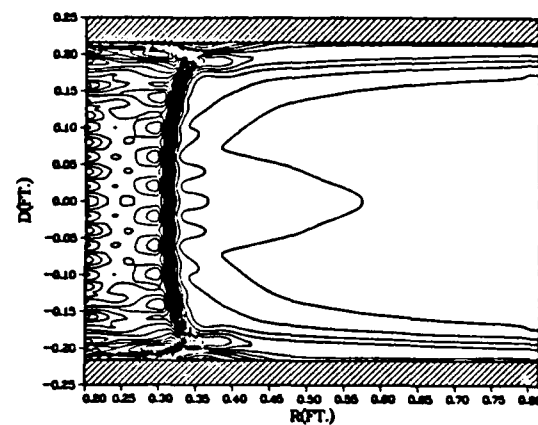
N=230K ACTUAL INFLOW 60%NSR WBB=.195
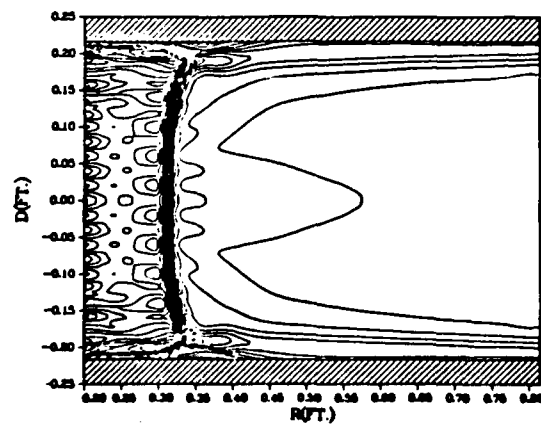
N=235K ACTUAL INFLOW 60%NSR WBB=.195
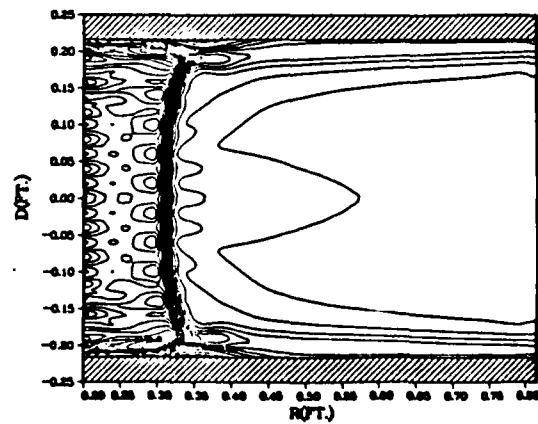
N=240K ACTUAL INFLOW 60%NSR WBB=.195
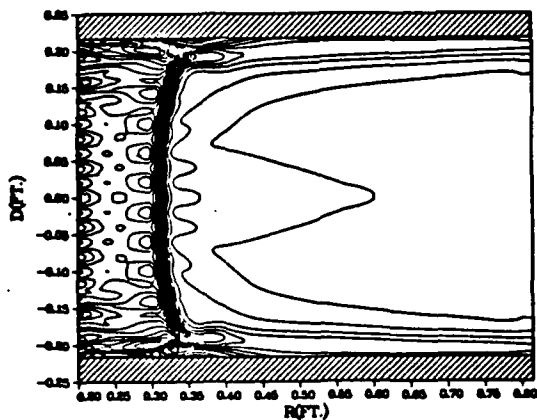
N=245K ACTUAL INFLOW 60%NSR WBB=.195
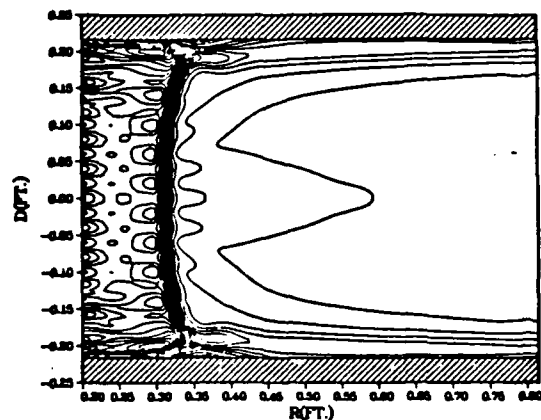
N=250K ACTUAL INFLOW 60%NSR WBB=.195
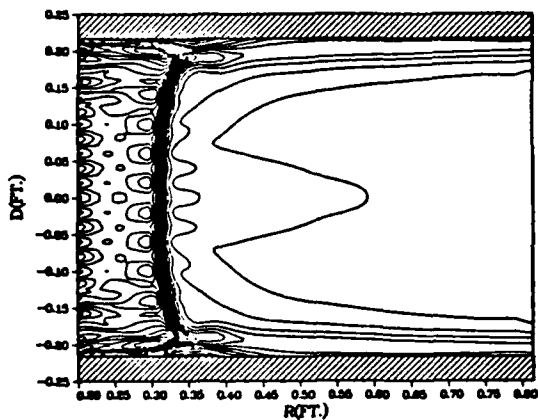
N=255K ACTUAL INFLOW 60%NSR WBB=.195
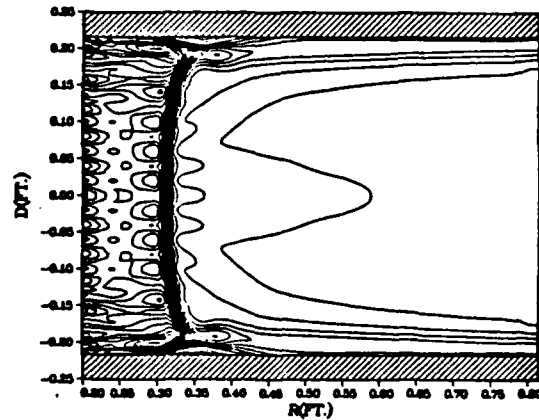
N=260K ACTUAL INFLOW 60%NSR WBB=.195
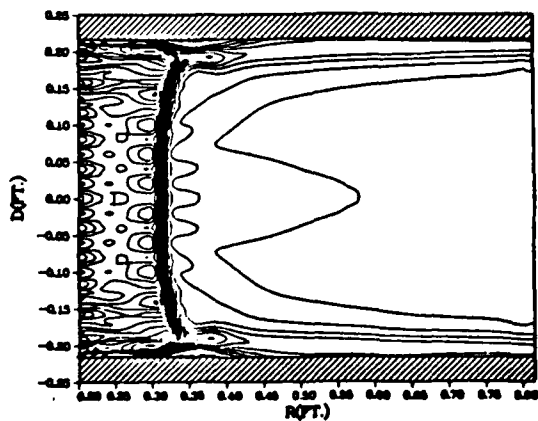
N=265K ACTUAL INFLOW 60%NSR WBB=.195

301
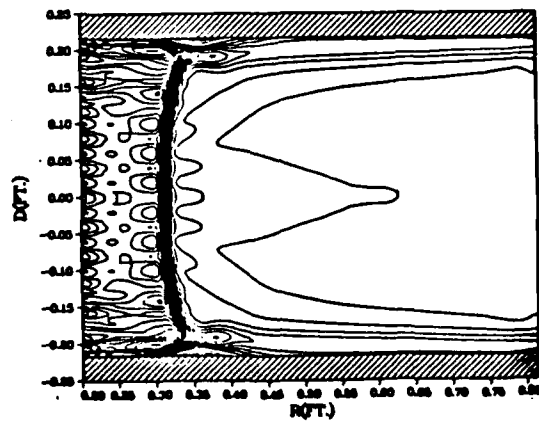
N=270K ACTUAL INFLOW 60%NSR WBB=.195
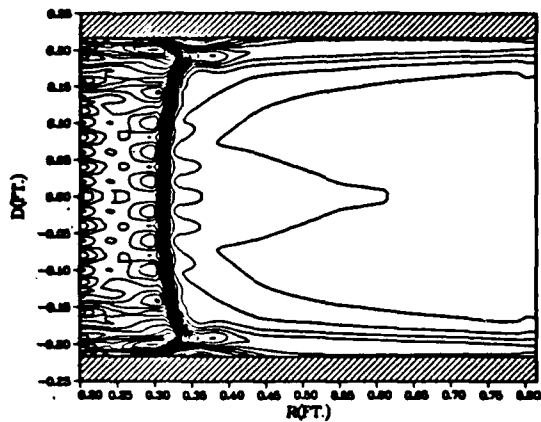
N=275K ACTUAL INFLOW 60%NSR WBB=.195
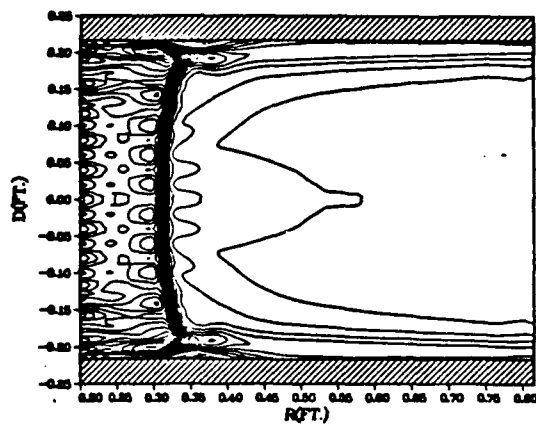
N=280K ACTUAL INFLOW 60%NSR WBB=.195
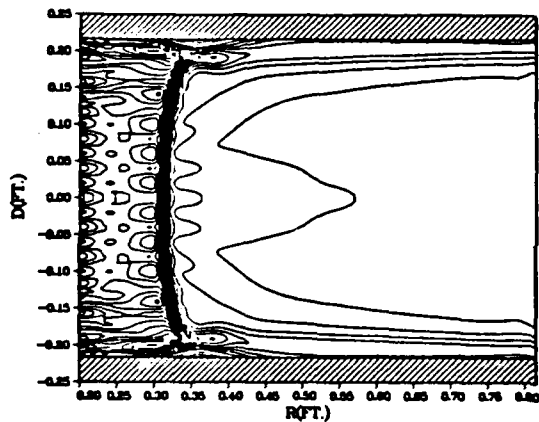
N=285K ACTUAL INFLOW 60%NSR WBB=.195
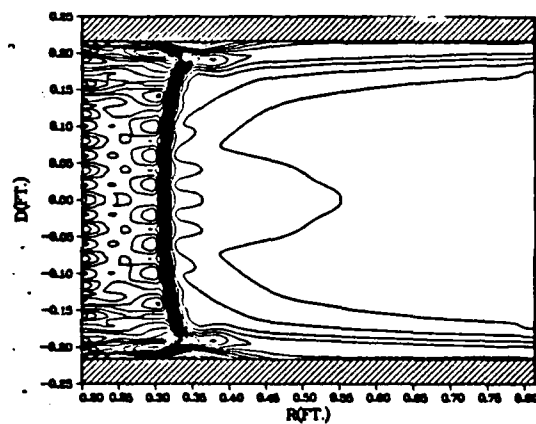
N=290K ACTUAL INFLOW 60%NSR WBB=.195
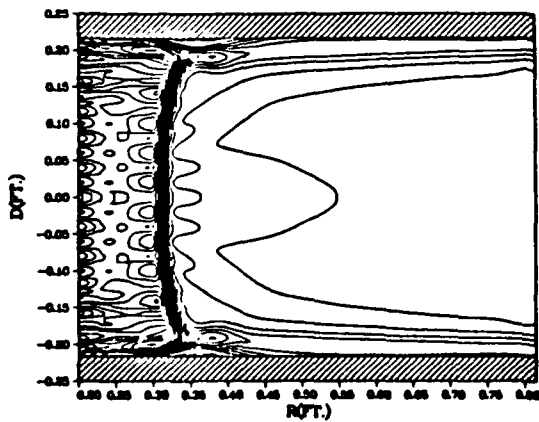
N=295K ACTUAL INFLOW 60%NSR WBB=.195

302
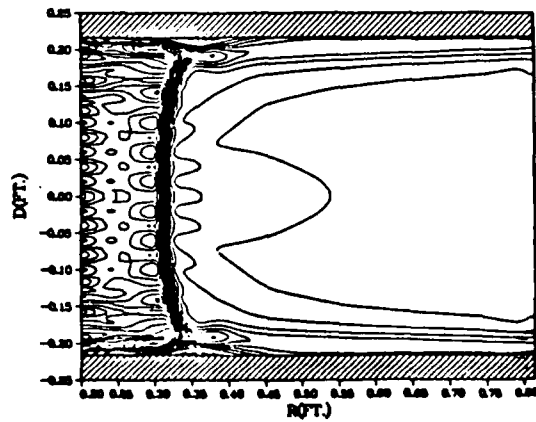
N=300K ACTUAL INFLOW 60%NSR WBB=.195
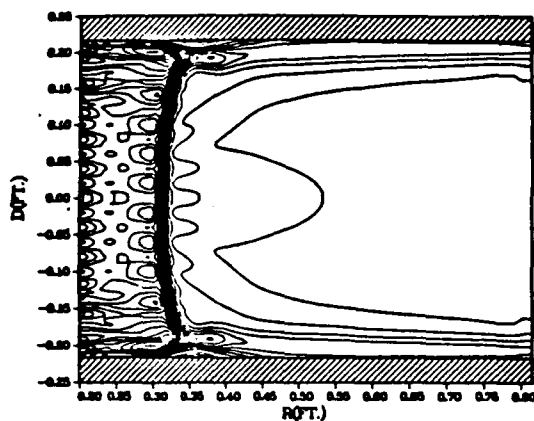
N=305K ACTUAL INFLOW 60%NSR WBB=.195
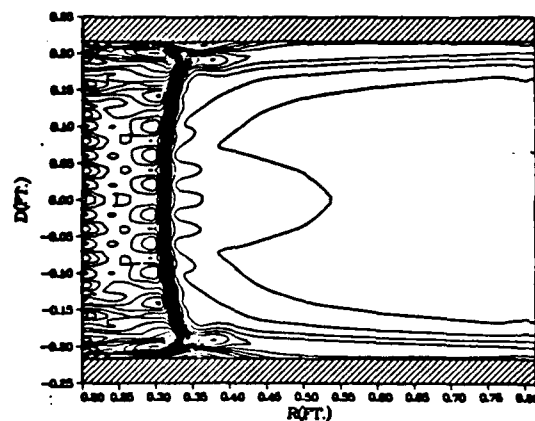
N=310K ACTUAL INFLOIW 60%NSR WBB=.195
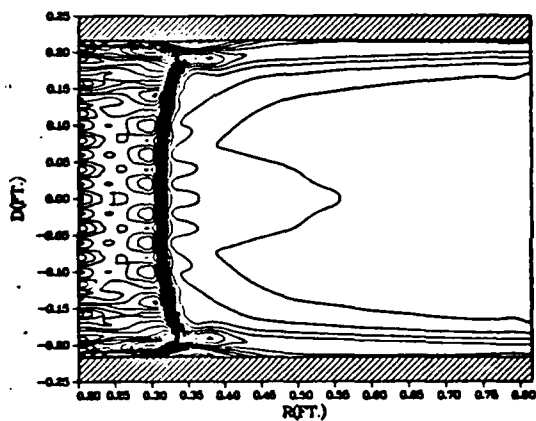
N=315K ACTUAL INFLOW 60%NSR WBB=.195
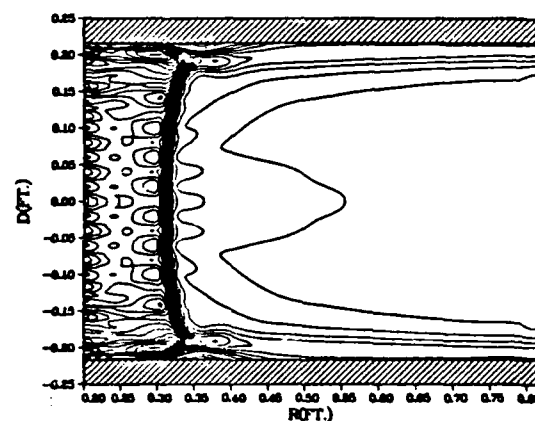
N=320K ACTUAL INFLOW 60%NSR WBB=.195
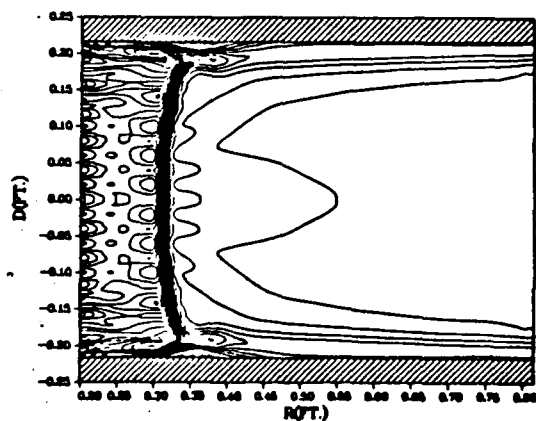
N=325K ACTUAL INFLOW 60%NSR WBB=.195
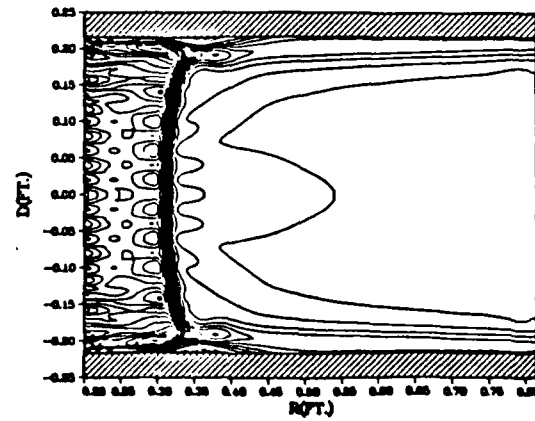
N=330K ACTUAL INFLOW 60%NSR WBB=.195
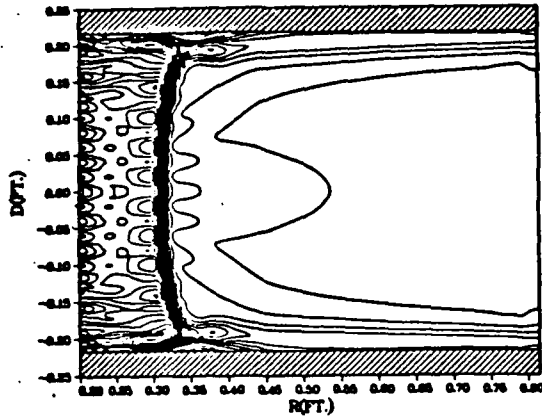
N=335K ACTUAL INFLOW 60%NSR WBB=.195
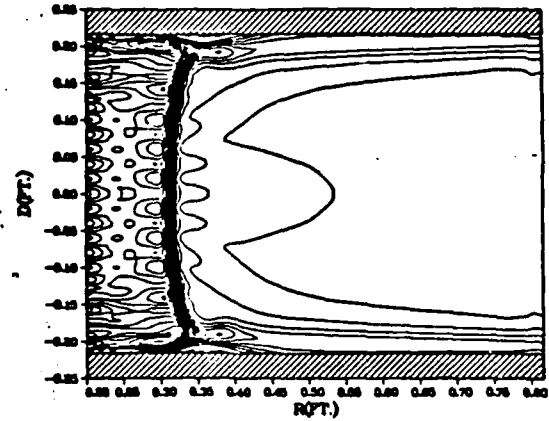
N=340K ACTUAL INFLOW 60%NSR WBB=.195
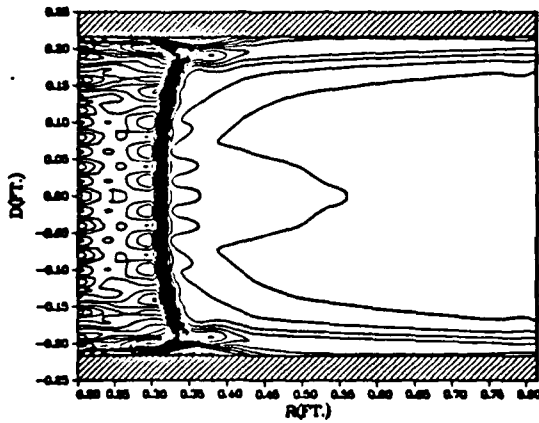
N=345K ACTUAL INFLOW 60%NSR WBB=.195
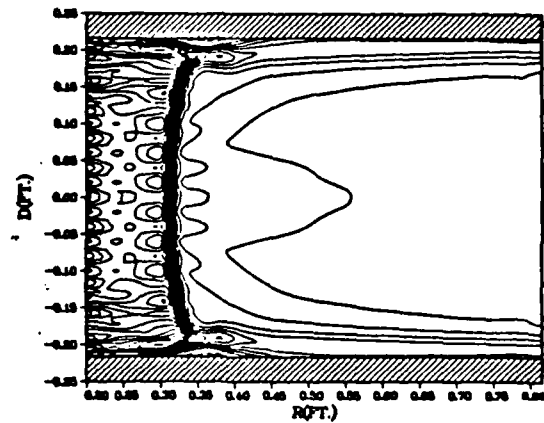
N=350K ACTUAL INFLOW 60%NSR WBB=.195
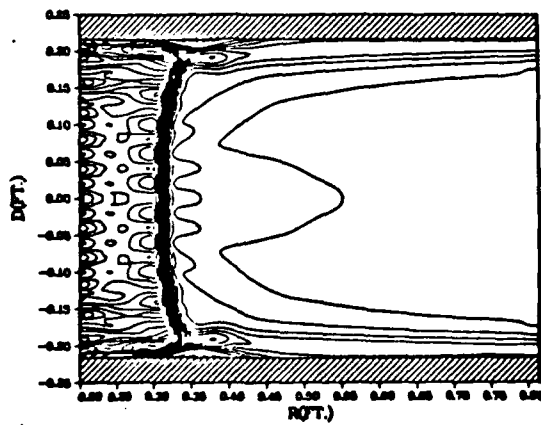
N=355K ACTUAL INFLOW 60%NSR WBB=.195
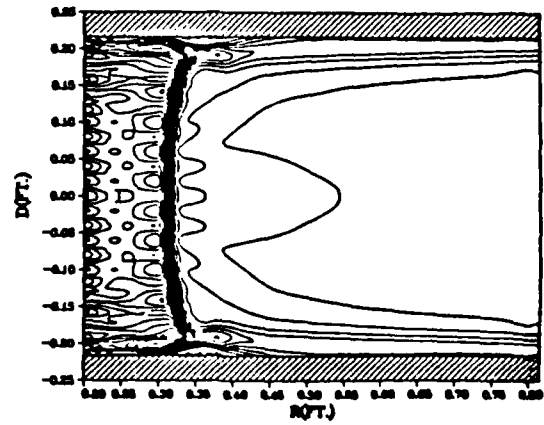
N=360K ACTUAL INFLOW 60%NSR WBB=.195
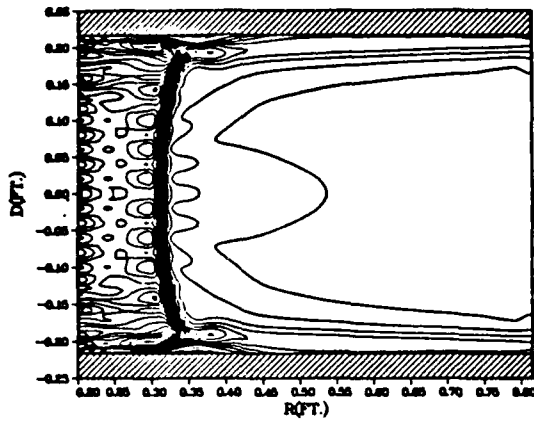
N=365K ACTUAL INFLOW 60%NSR WBB=.195
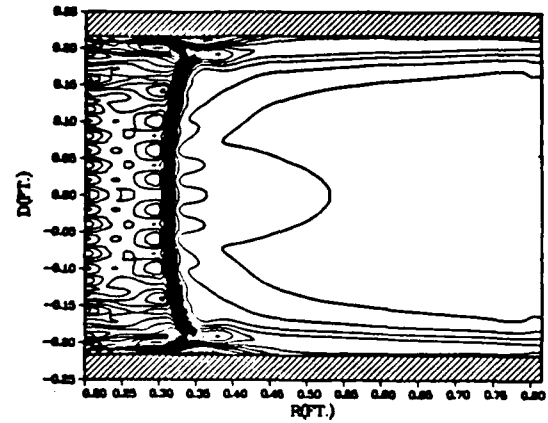
N=370K ACTUAL INFLOW 60%NSR WBB=.195
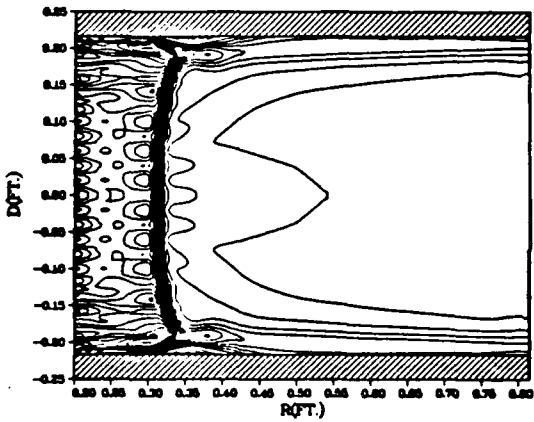
N=375K ACTUAL INFLOW 60%NSR WBB=.195
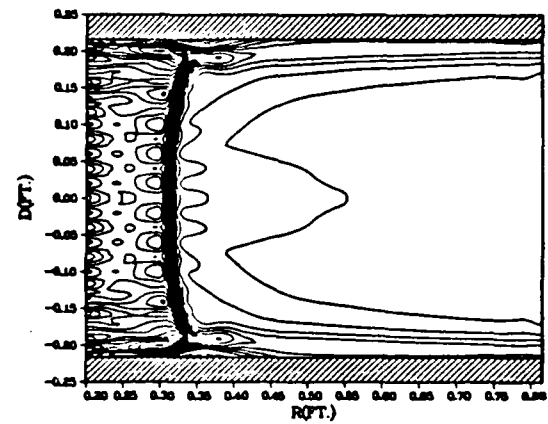
N=380K ACTUAL INFLOW 60%NSR WBB=.195
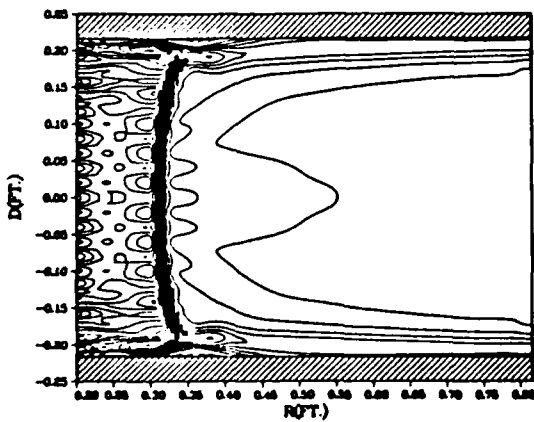
N=385K ACTUAL INFLOW 60%NSR WBB=.195
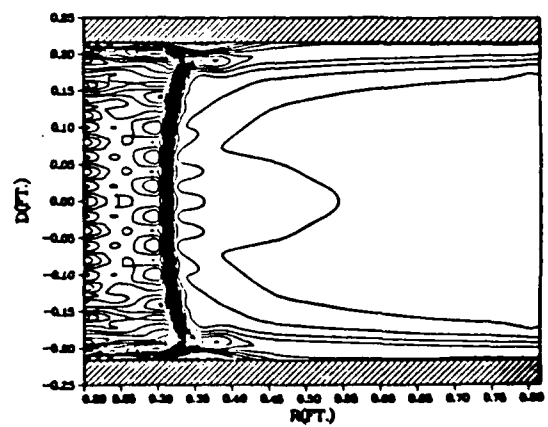
N=390K ACTUAL INFLOW 60%NSR WBB=.195
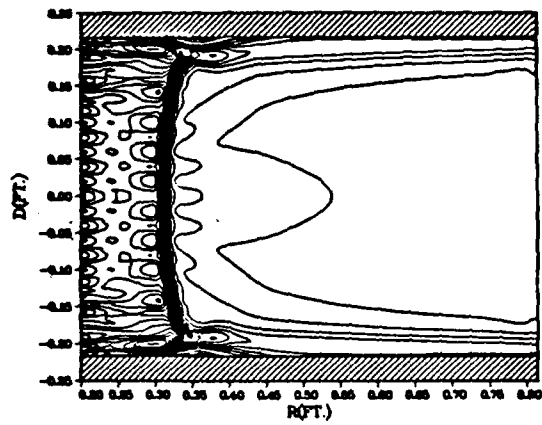
N=395K ACTUAL INFLOW 60%NSR WBB=.195
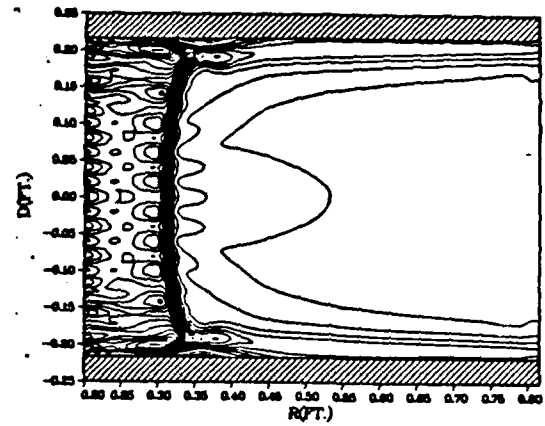
N=400K ACTUAL INFLOW 60%NSR WBB=.195
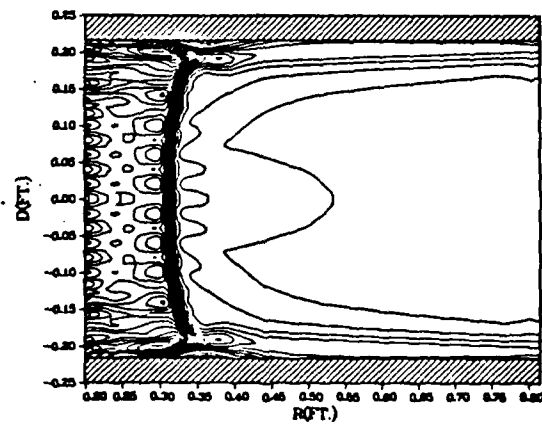
N=1 PW/PPI ACTUAL INFLOW 60%NSR
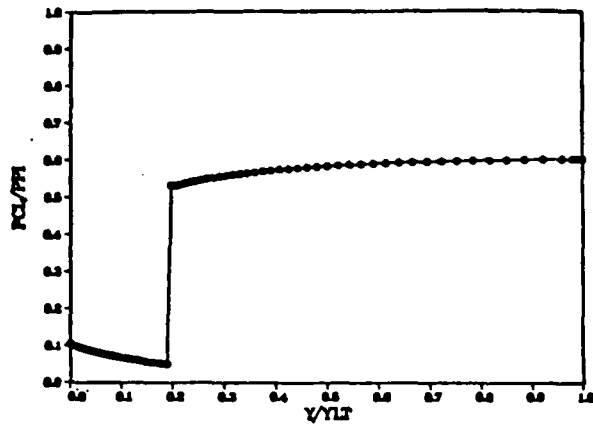
N=25K PW/PPI ACTUAL INFLOW 60%NSR
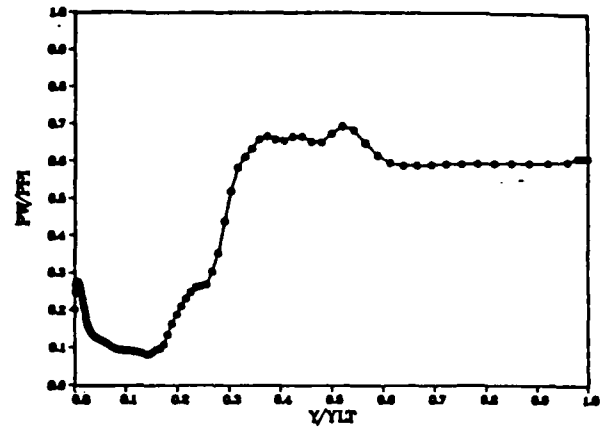
N=1 PCL/PPI ACTUAL INFLOW 60%NSR
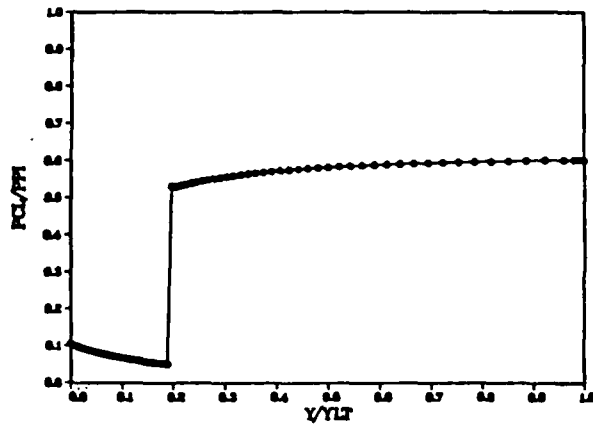
N=25K PCL/PPI ACTUAL INFLOW 60%NSR
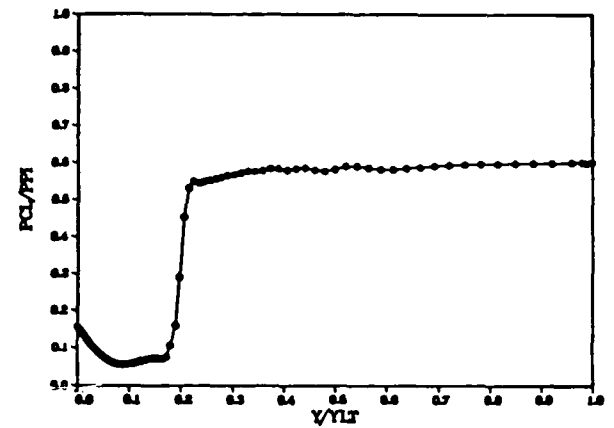
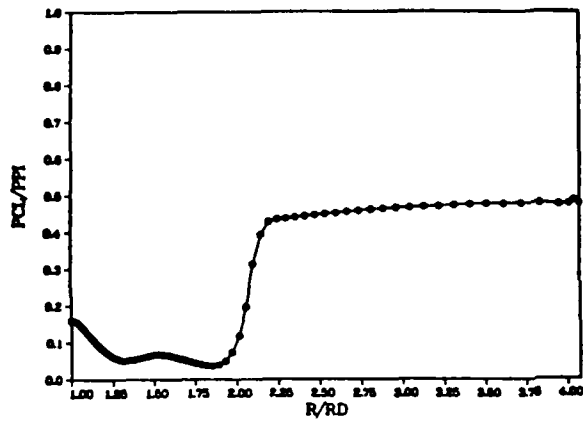# N=1 TCL/TO ACTUAL INFLOW 60%NSR
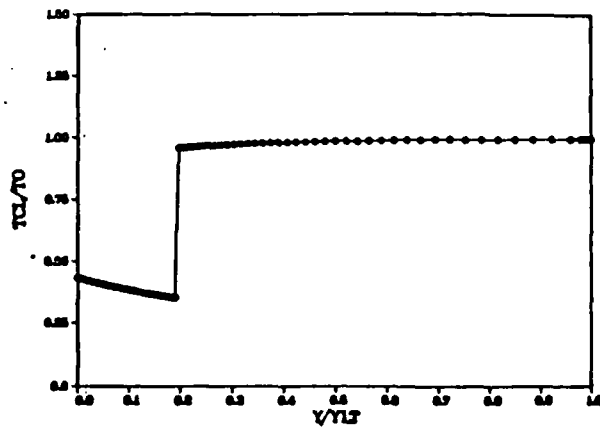
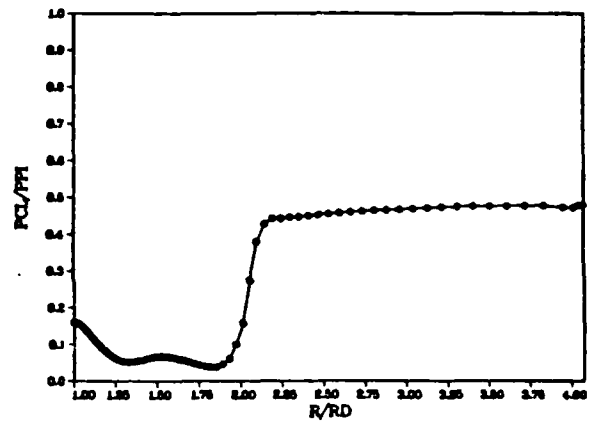# N=25K TCL/TO ACTUAL INFLOW 60%NSR
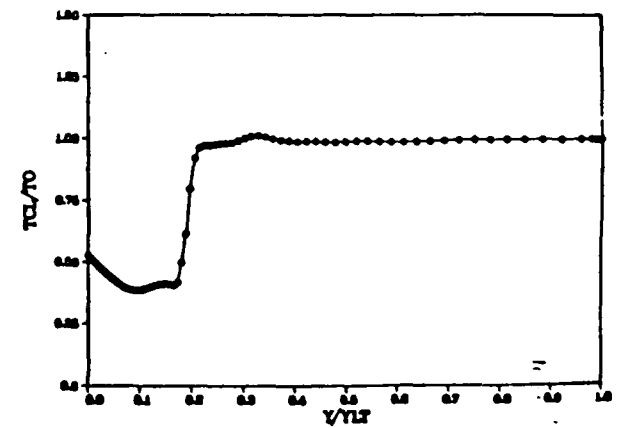
N=50K PW/PPI ACTUAL INFLOW 60%NSR
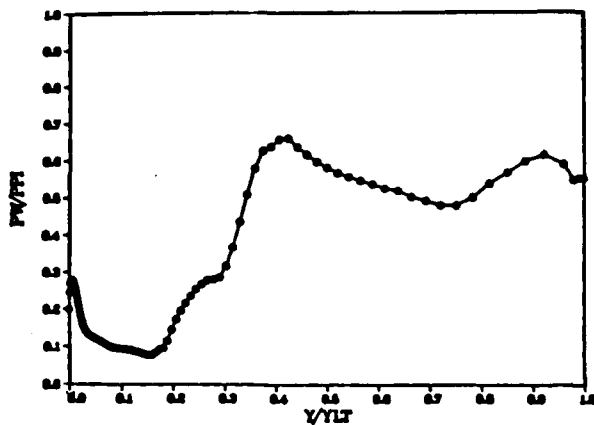
N=75K PW/PPI ACTUAL INFLOW 60%NSR
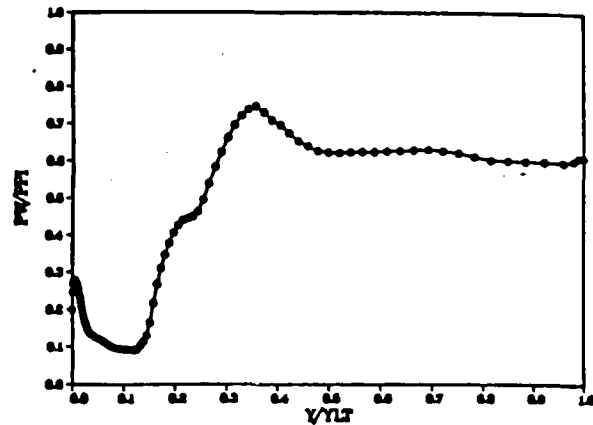
N=50K PCL/PPI ACTUAL INFLOW 60%NSR
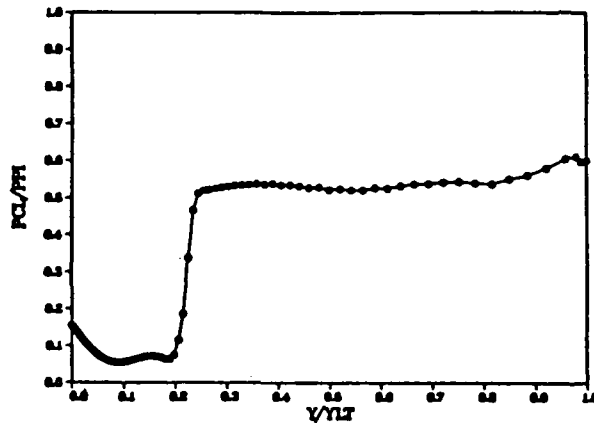
N=75K PCL/PPI ACTUAL INFLOW 60%NSR
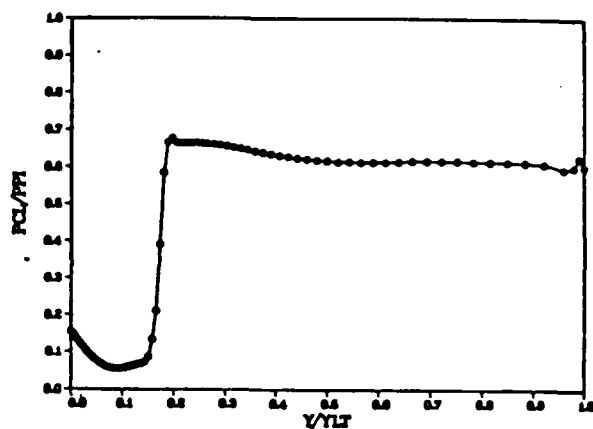
N=50K TCL/TO ACTUAL INFLOW 60%NSR
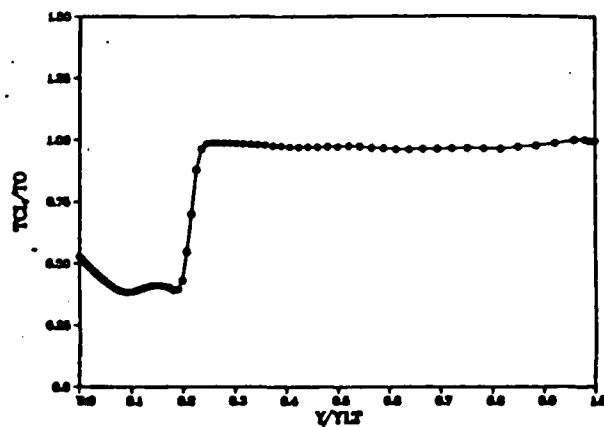
N=75K TCL/TO ACTUAL INFLOW 60%NSR
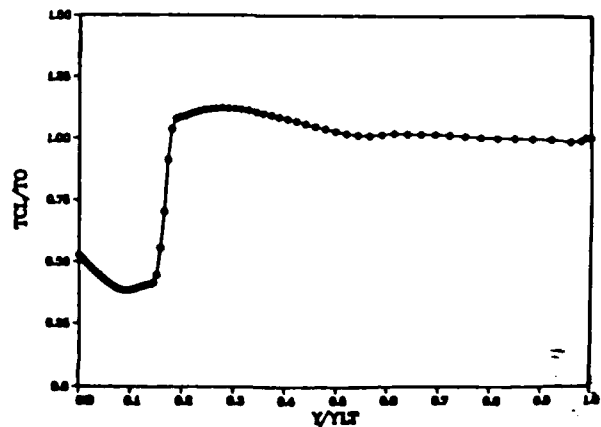
N=100K PW/PPI ACTUAL INFLOW 60%NSR
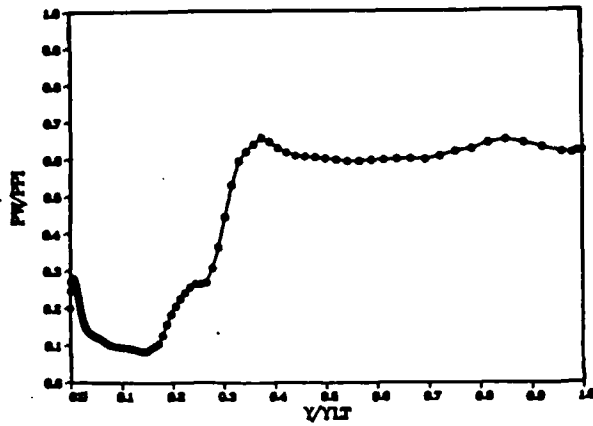
N=125K PW/PPI ACTUAL INFLOW 60%NSR
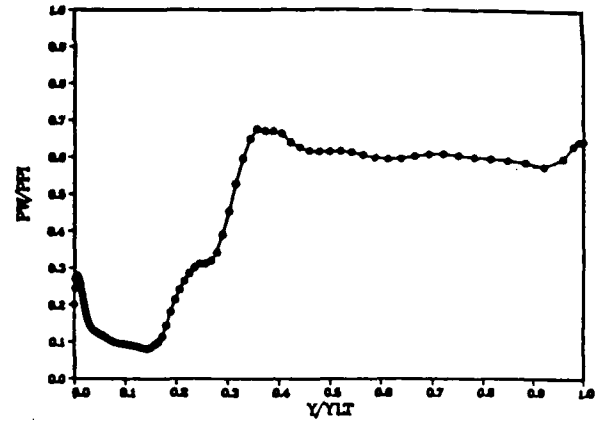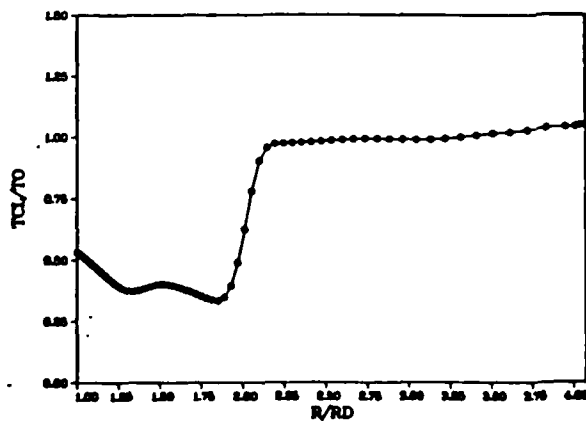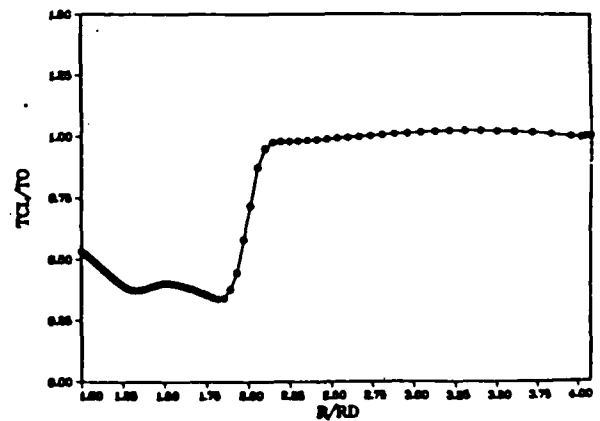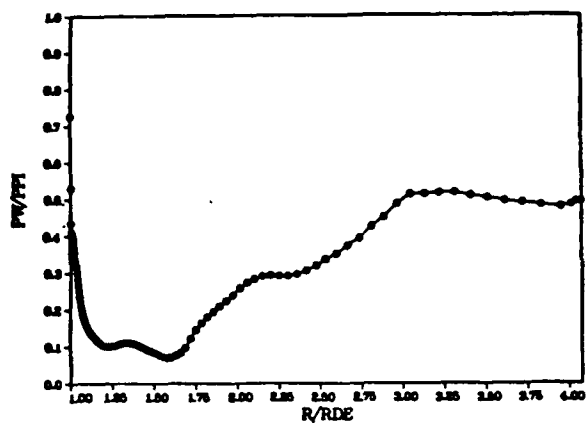
N=100K PCL/PPI ACTUAL INFLOW 60%NSR
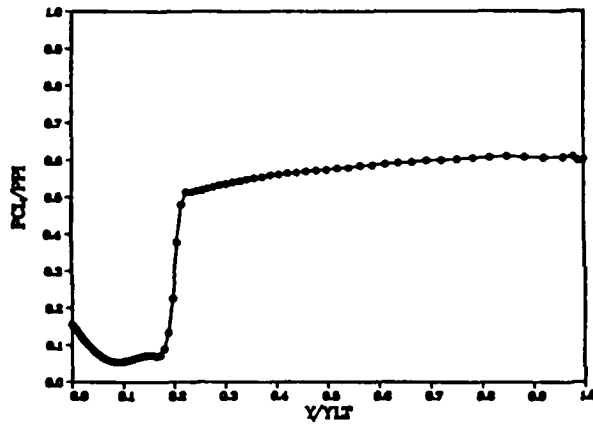
N=125K PCL/PPI ACTUAL INFLOW 60%NSR
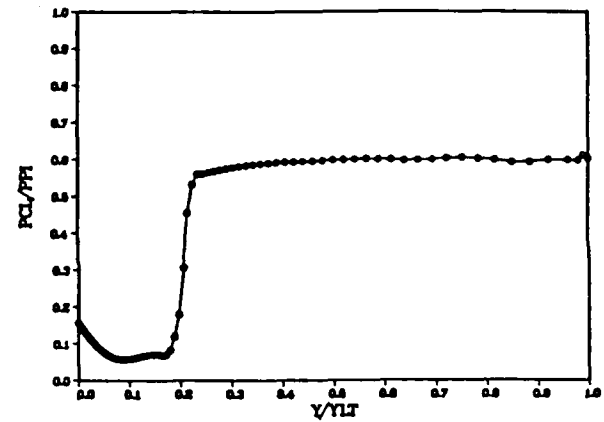
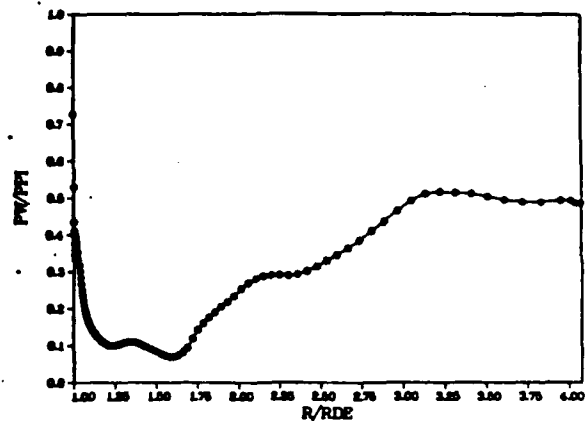N=100K TCL/TO ACTUAL INFLOW 60%NSR
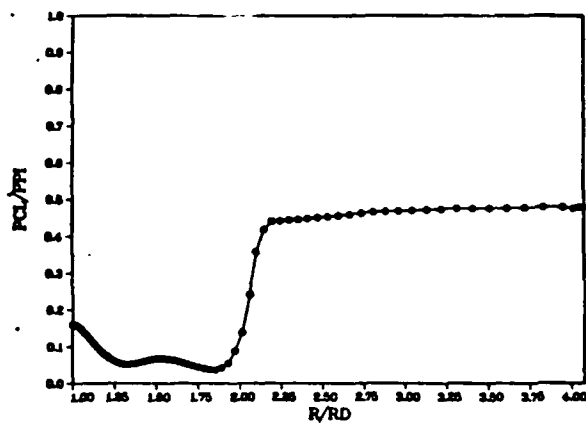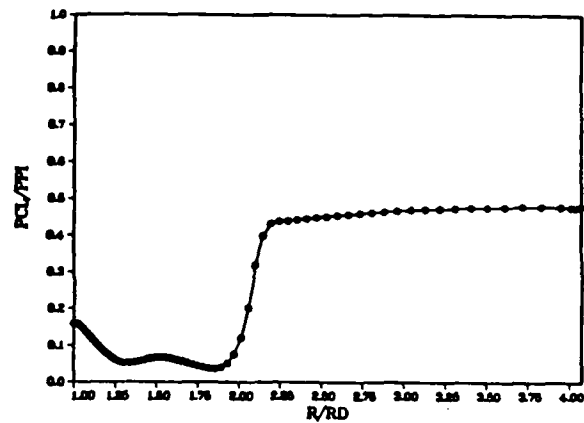
N=125K TCL/TO ACTUAL INFLOW 60%NSR

309
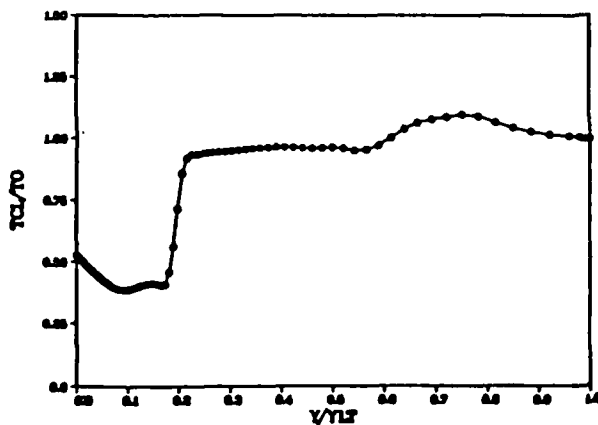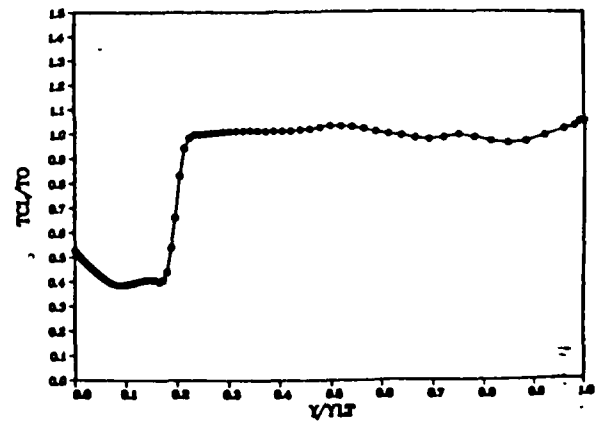
N=150K PW/PPI ACTUAL INFLOW 60%NSR
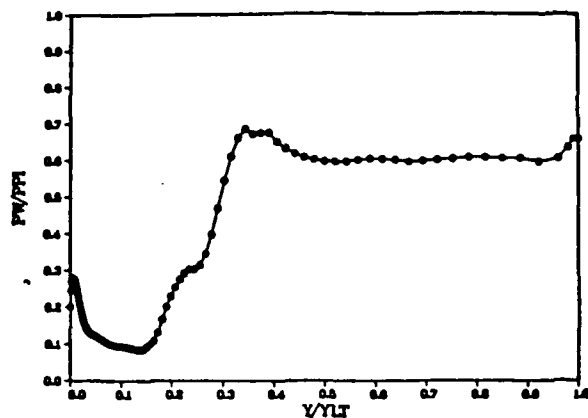
N=175K PW/PPI ACTUAL INFLOW 60%NSR
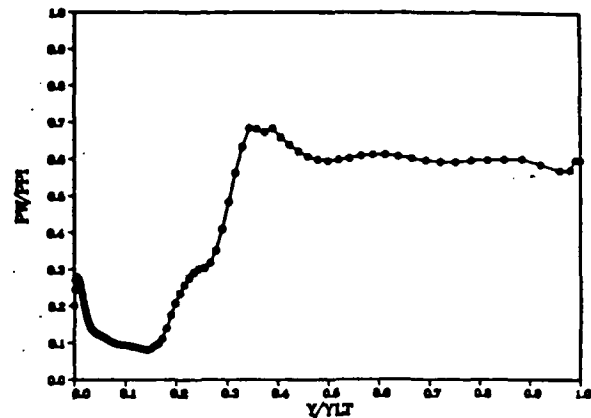
N=150K PCL/PPI ACTUAL INFLOW 60%NSR
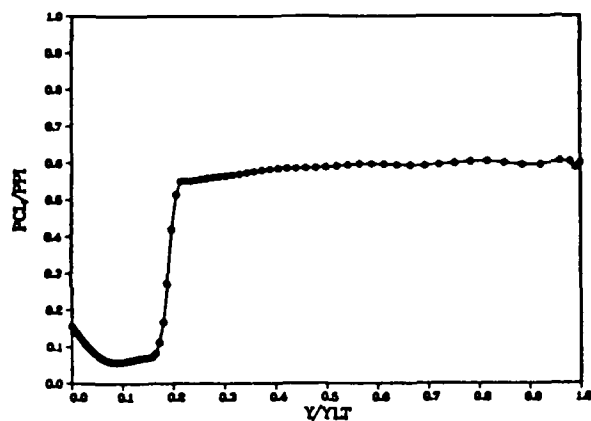
N=175K PCL/PPI ACTUAL INFLOW 60%NSR
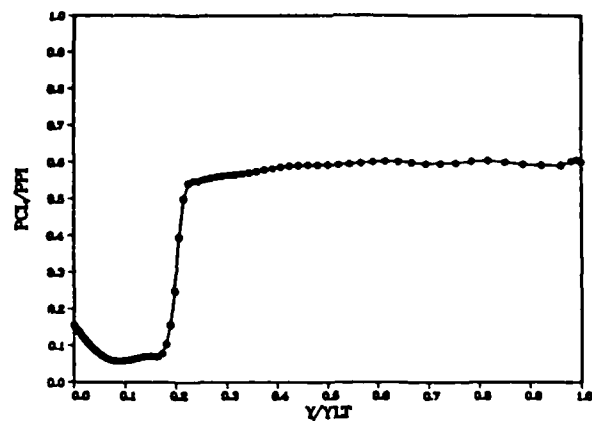
N=150K TCL/TO ACTUAL INFLOW 60%NSR

N=175K TCL/TO ACTUAL INFLOW 60%NSR

310
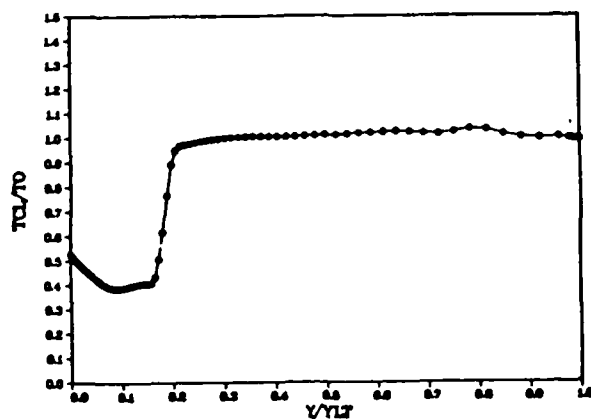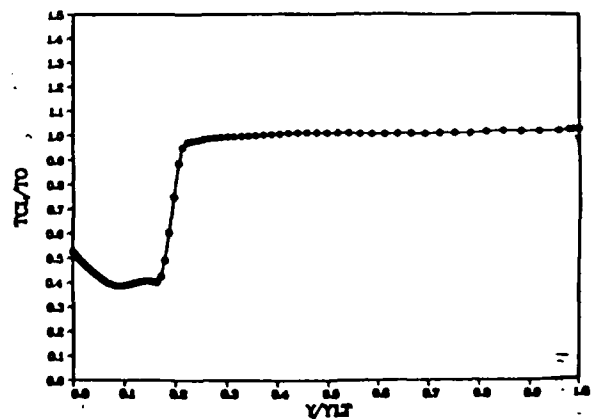
N=200K PW/PPI ACTUAL INFLOW 60%NSR
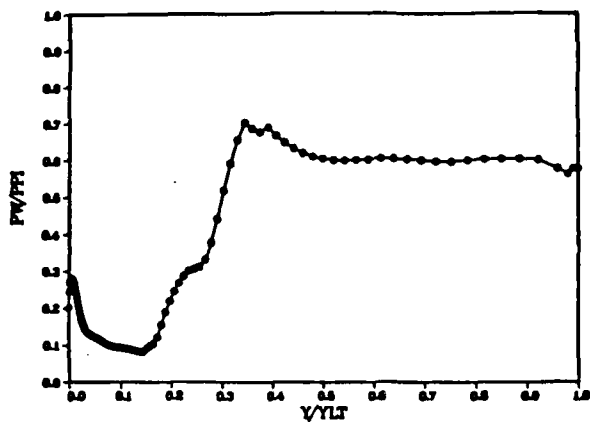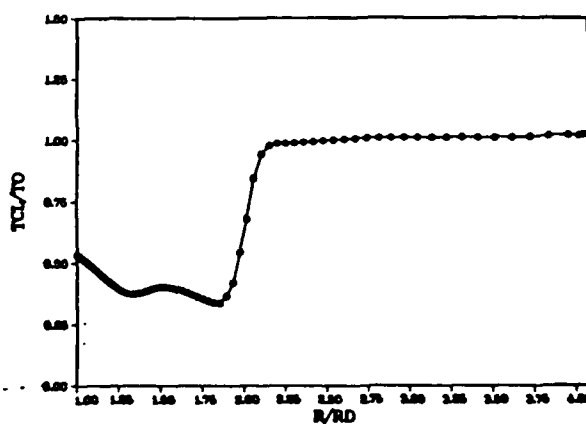
N=225K PW/PPI ACTUAL INFLOW 60%NSR
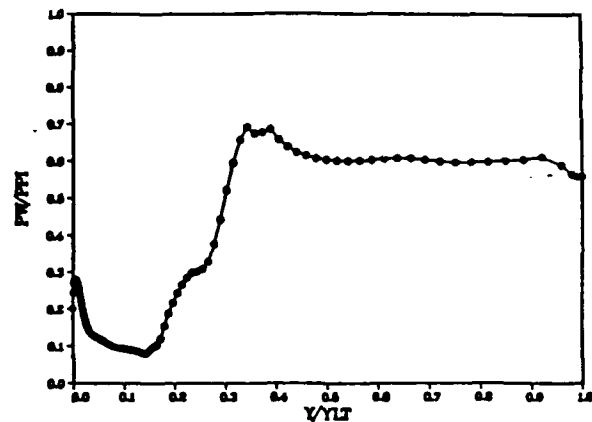
N=200K PCL/PPI ACTUAL INFLOW 60%NSR
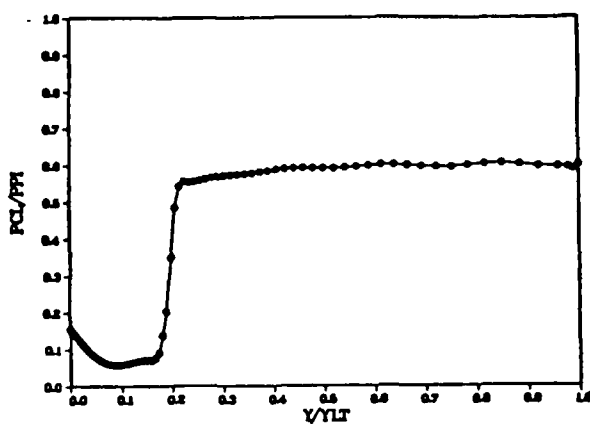
N=225K PCL/PPI ACTUAL INFLOW 60%NSR
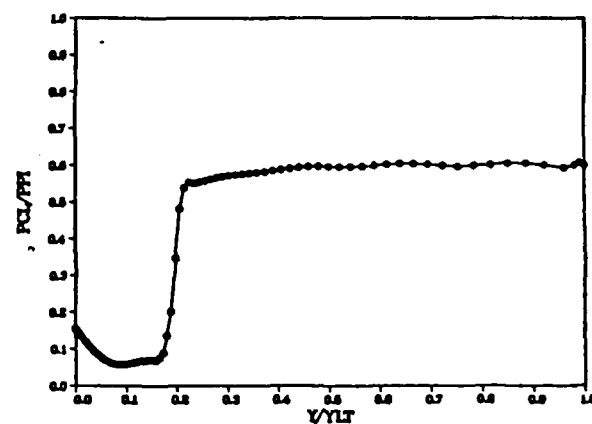
N=200K TCL/TO ACTUAL INFLOW 60%NSR
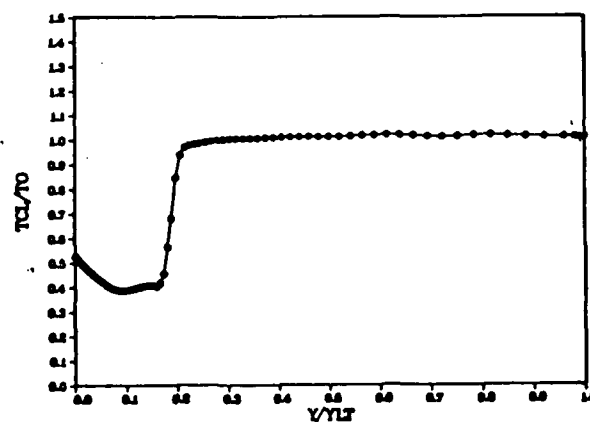
N=225K TCL/TO ACTUAL INFLOW 60%NSR
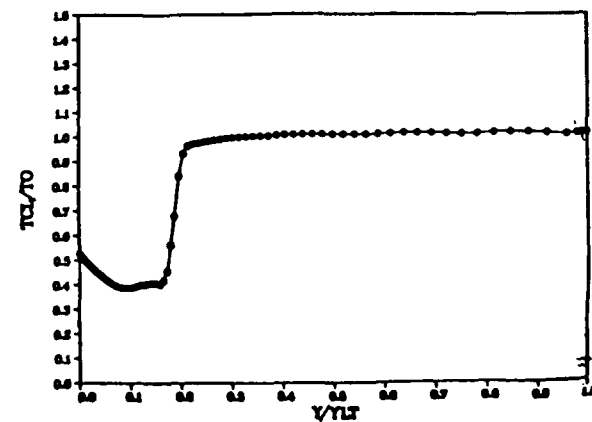
N=250K PW/PPI ACTUAL INFLOW 60%NSR
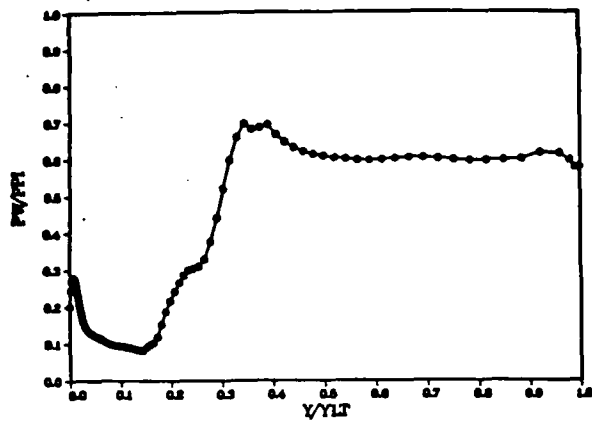
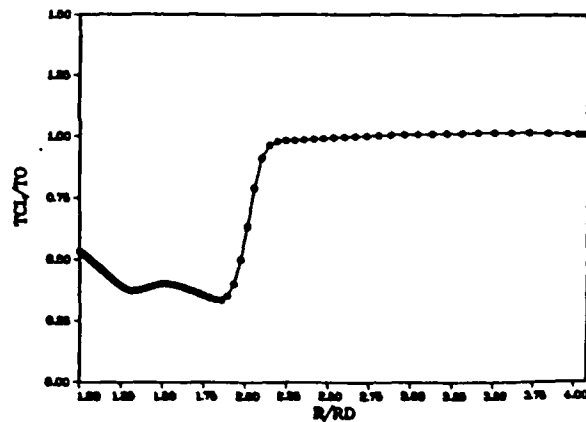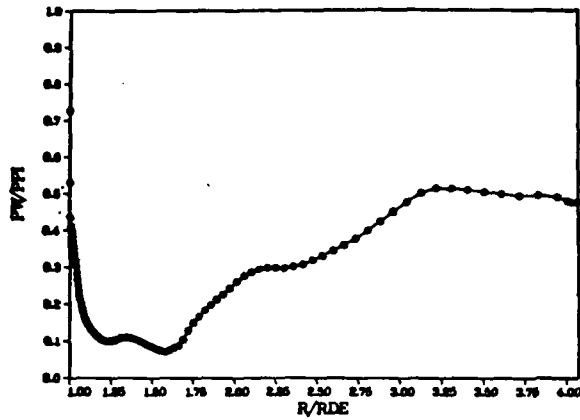N=275K PW/PPI ACTUAL INFLOW 60%NSR
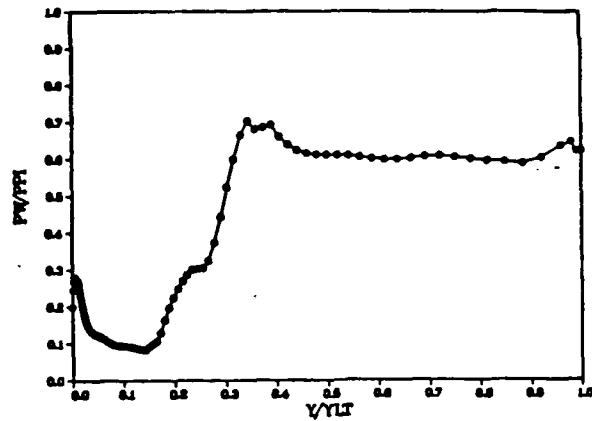
N=250K PCL/PPI ACTUAL INFLOW 60%NSR
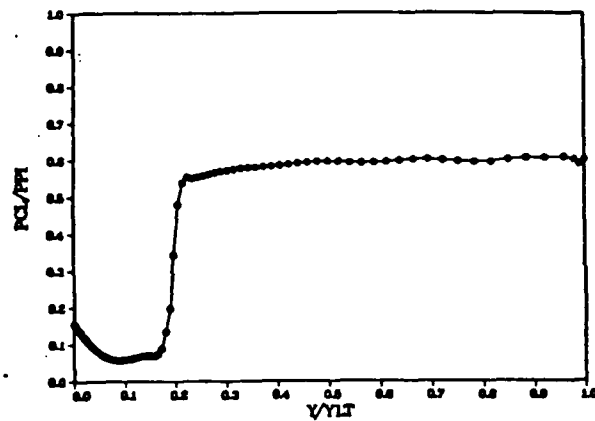
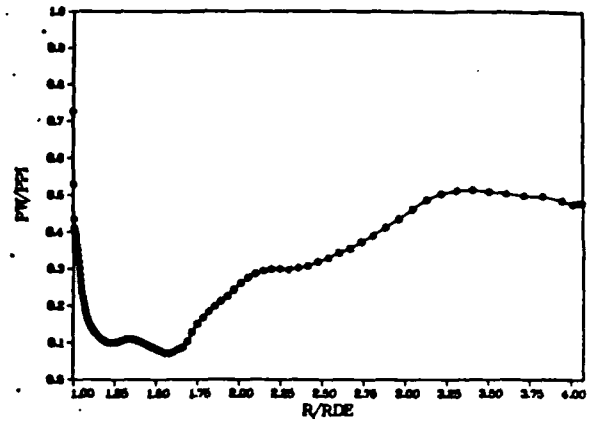N=275K PCL/PPI ACTUAL INFLOW 60%NSR
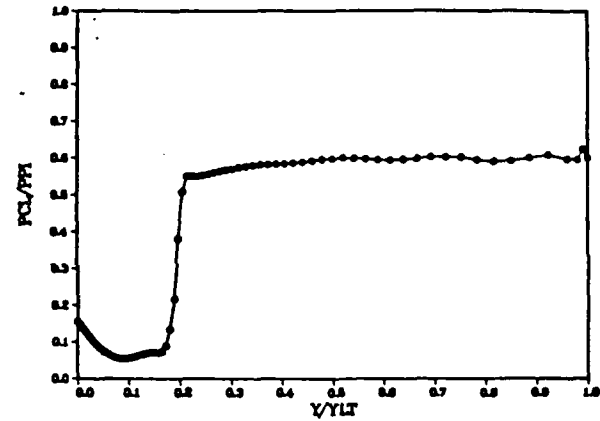
N=250K TCL/TO ACTUAL INFLOW 60%NSR
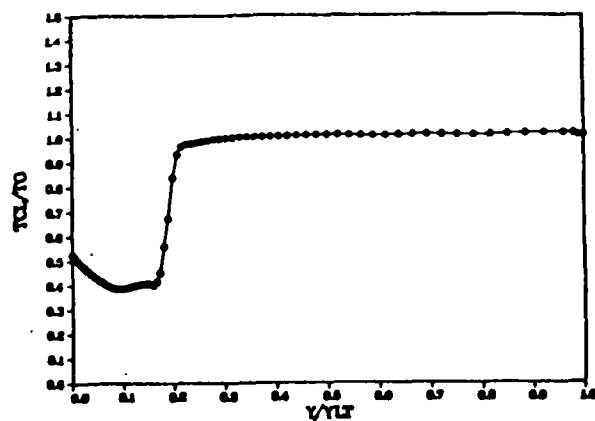
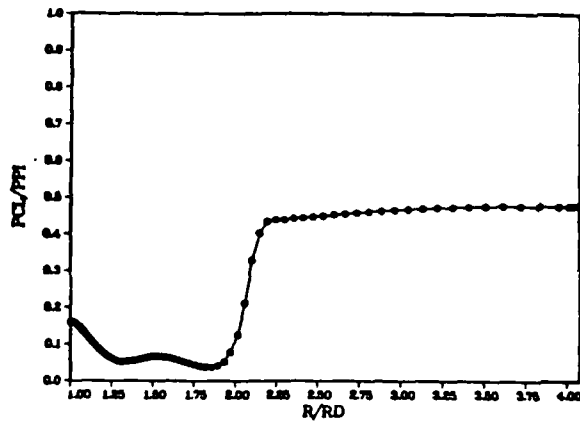N=275K TCL/TO ACTUAL INFLOW 60%NSR
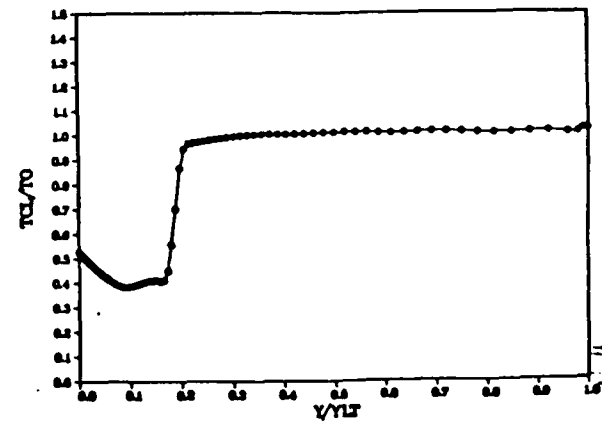
N=300K PW/PPI ACTUAL INFLOW 60%NSR
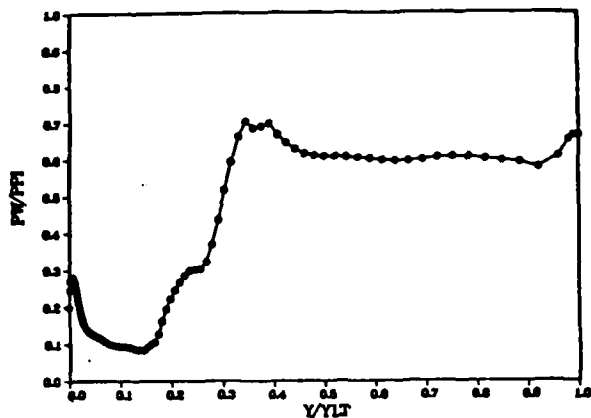
N=325K PW/PPI ACTUAL INFLOW 60%NSR
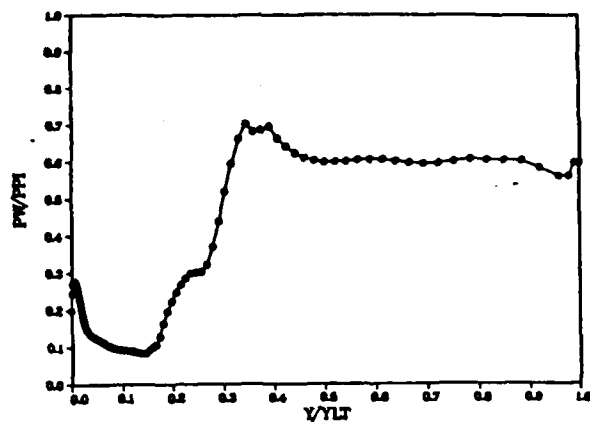
N=300K PCL/PPI ACTUAL INFLOW 60%NSR
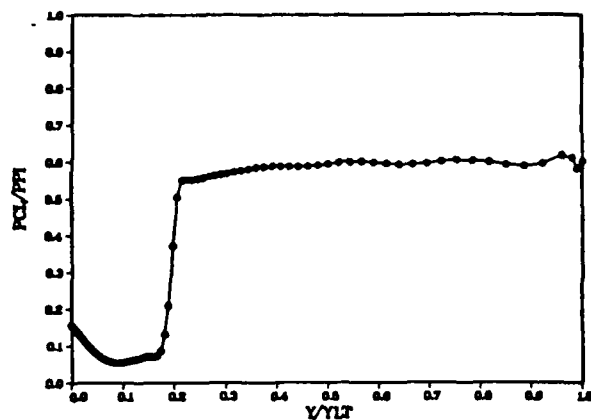
N=325K PCL/PPI ACTUAL INFLOW 60%NSR
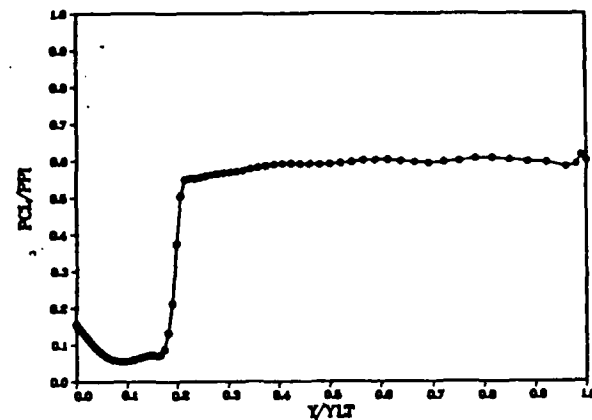
N=300K TCL/TO ACTUAL INFLOW 60%NSR
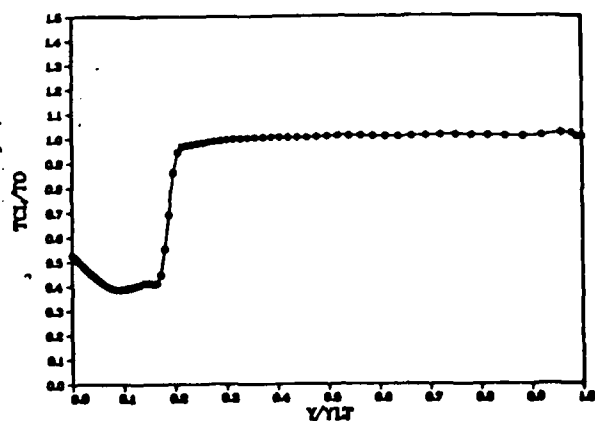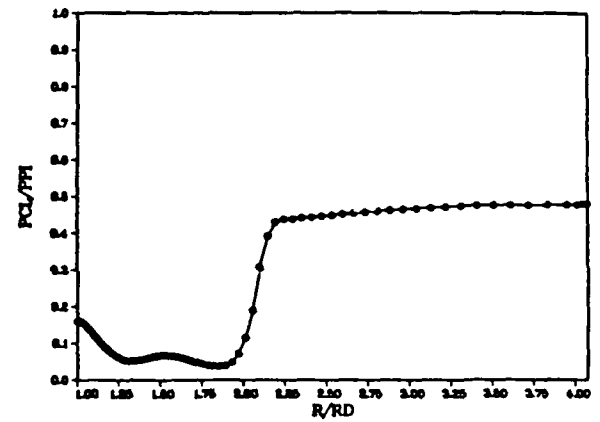
N=325K TCL/TO ACTUAL INFLOW 60%NSR

313
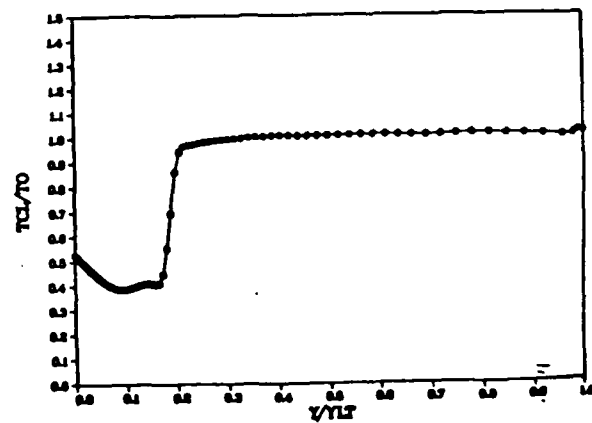
N=350K PW/PPI ACTUAL INFLOW 60%NSR
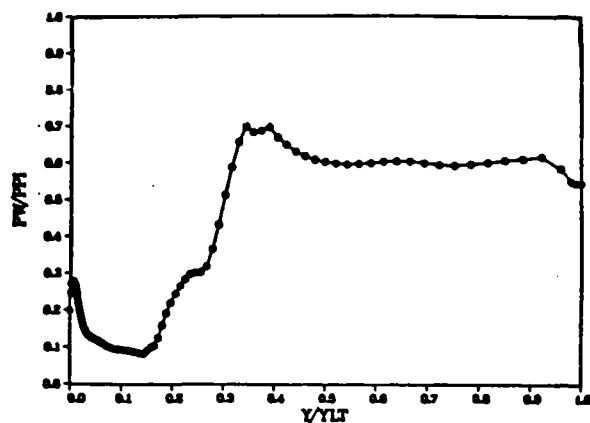
N=375K PW/PPI ACTUAL INFLOW 60%NSR
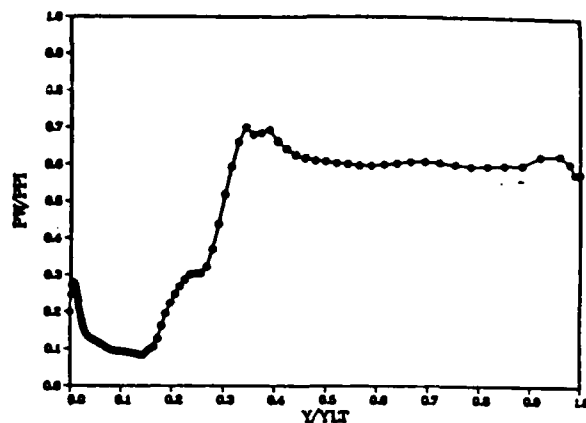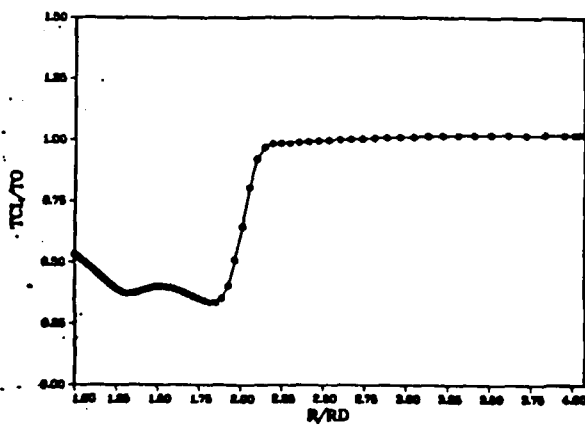
N=350K PCL/PPI ACTUAL INFLOW 60%NSR
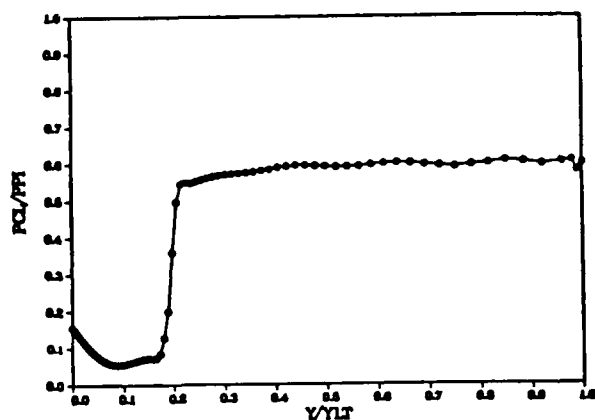
N=375K PCL/PPI ACTUAL INFLOW 60%NSR
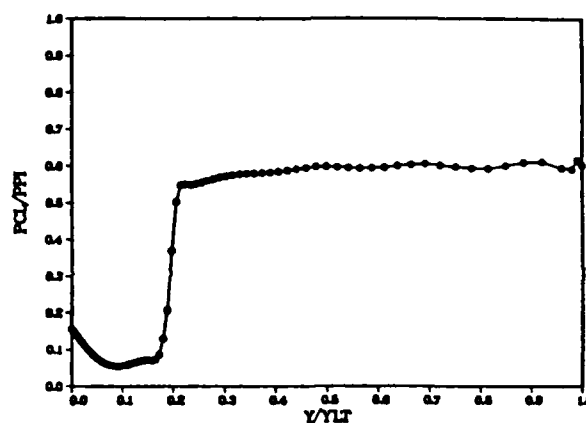
N=350K TCL/TO ACTUAL INFLOW 60%NSR
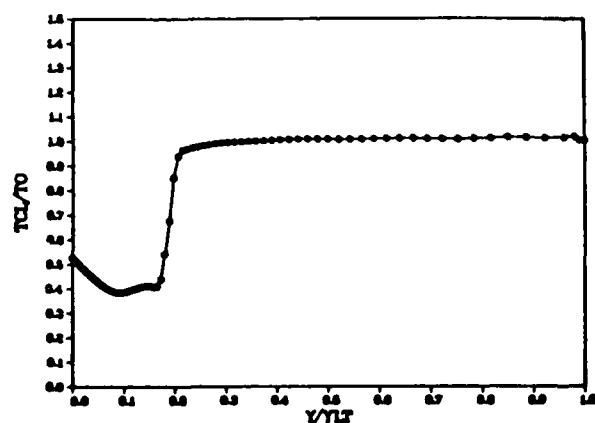
N=375K TCL/TO ACTUAL INFLOW 60%NSR

314
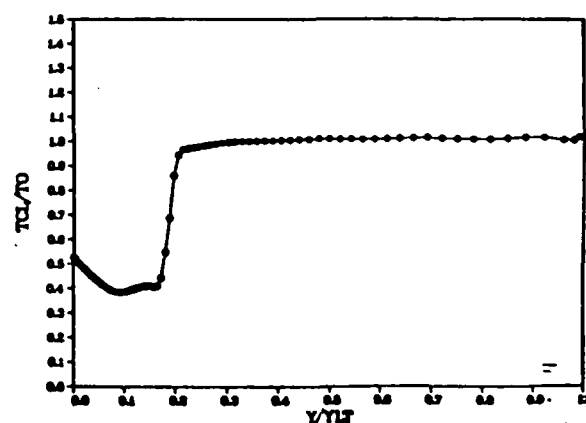
N=400K PW/PPI ACTUAL INFLOW 60%NSR
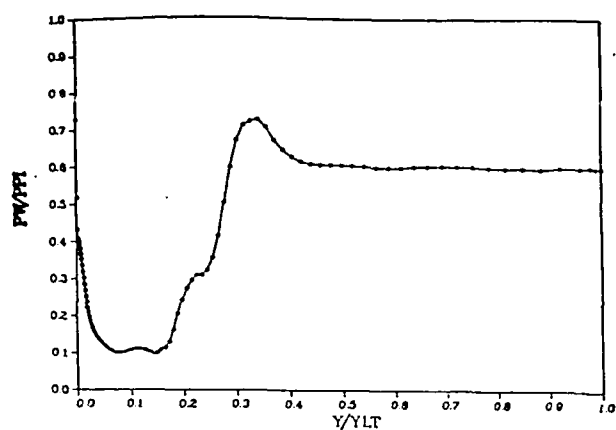
N=425K PW/PPI ACTUAL INFLOW 60%NSR
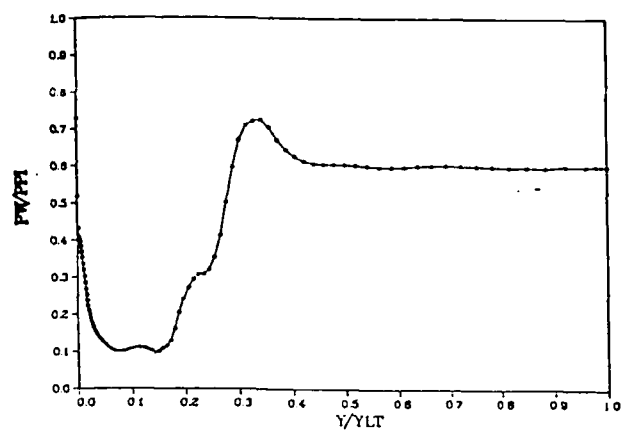
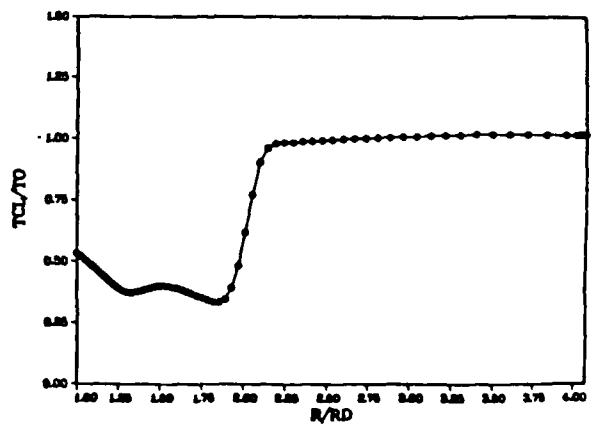N=400K PCL/PPI ACTUAL INFLOW 60%NSR
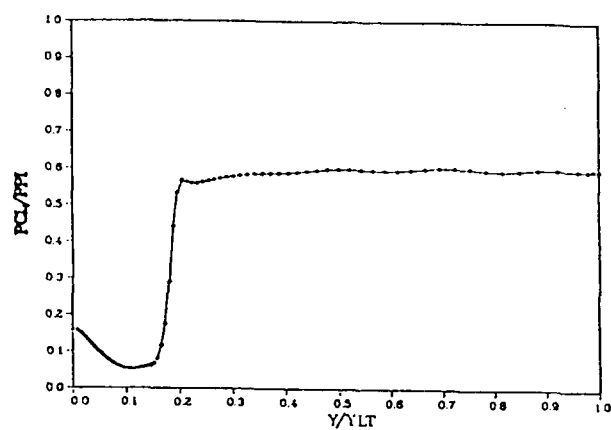
N=425K PCL/PPI ACTUAL INFLOW 60%NSR
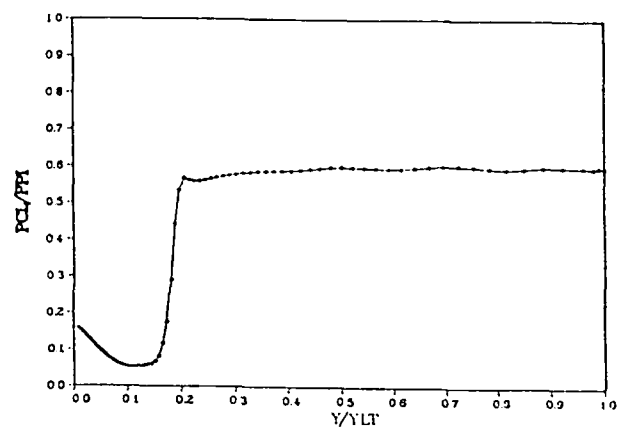
N=400K TCL/TO ACTUAL INFLOW 60%NSR
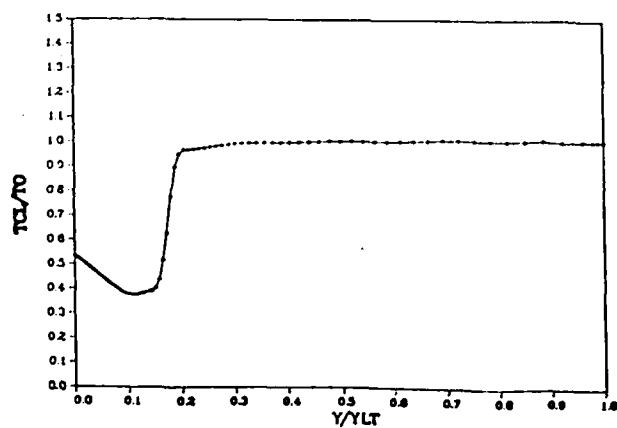
N=425K TCL/TO ACTUAL INFLOW 60%NSR

315
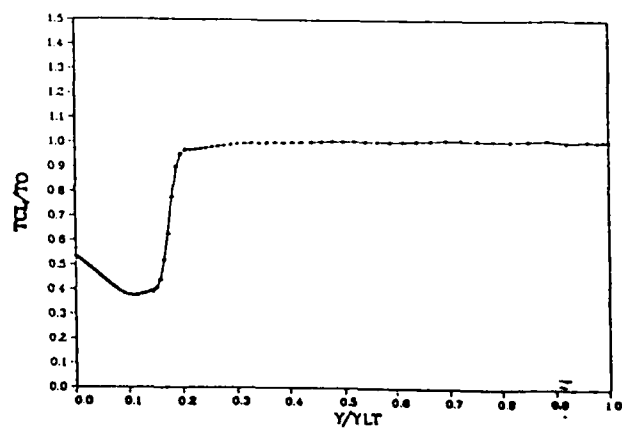
N=450K PW/PPI ACTUAL INFLOW 60%NSR
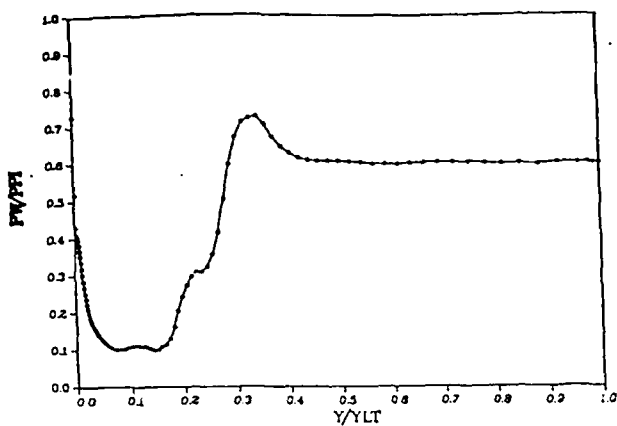
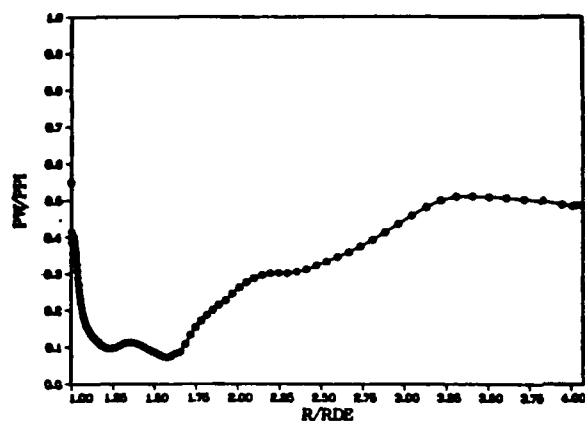N=475K PW/PPI ACTUAL INFLOW 60%NSR
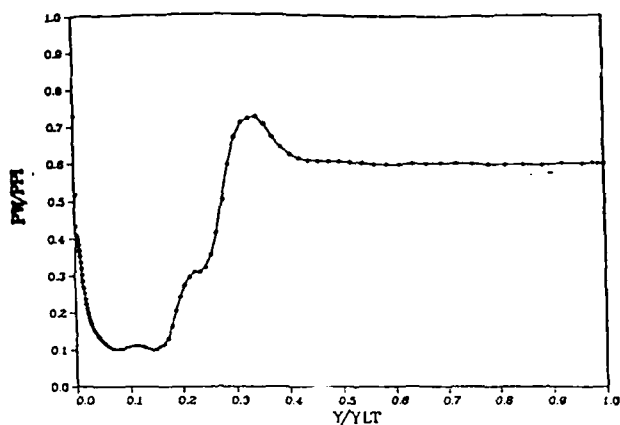
N=450K PCL/PPI ACTUAL INFLOW 60%NSR
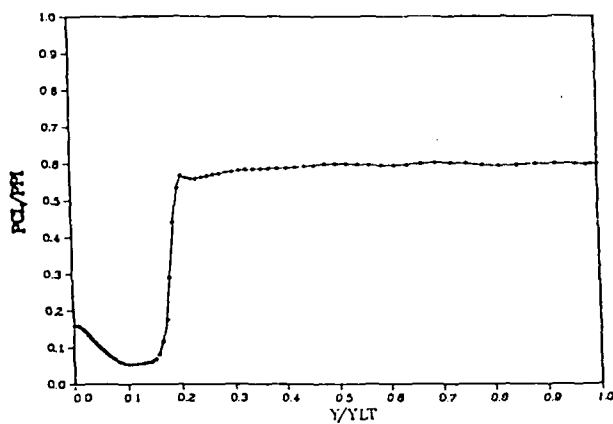
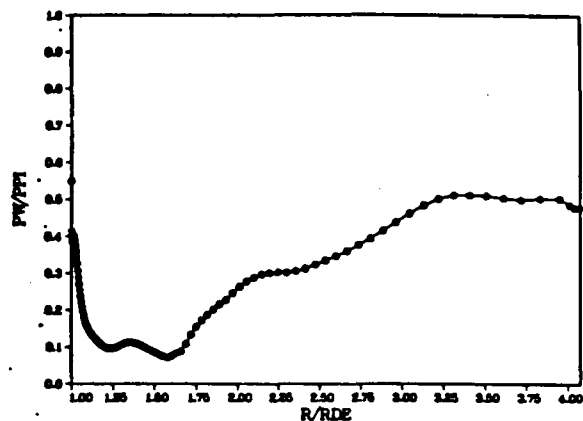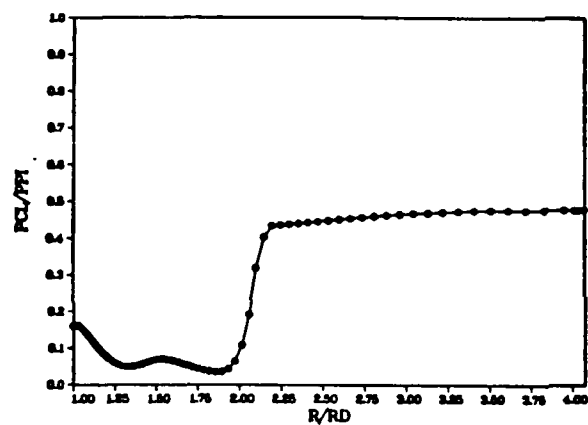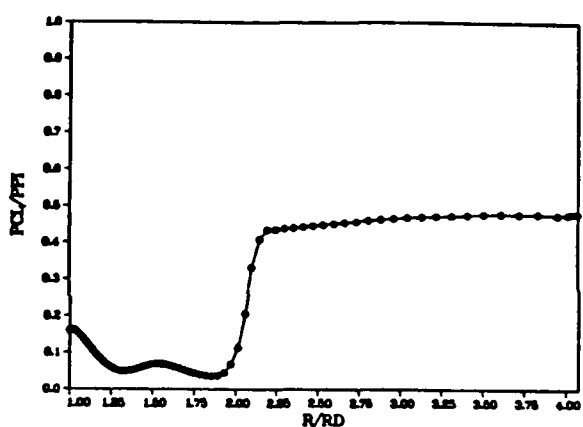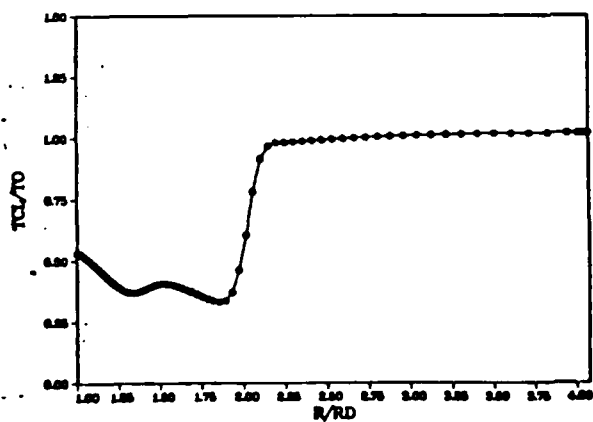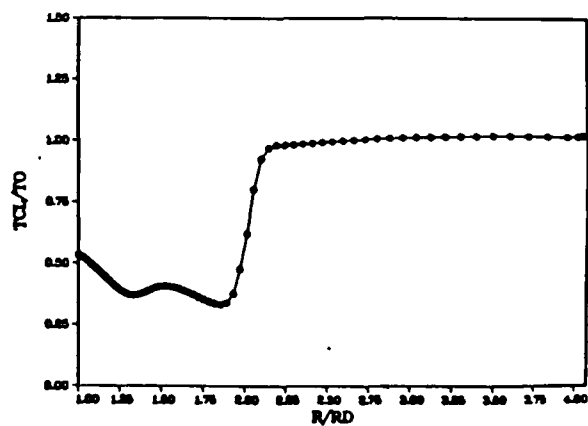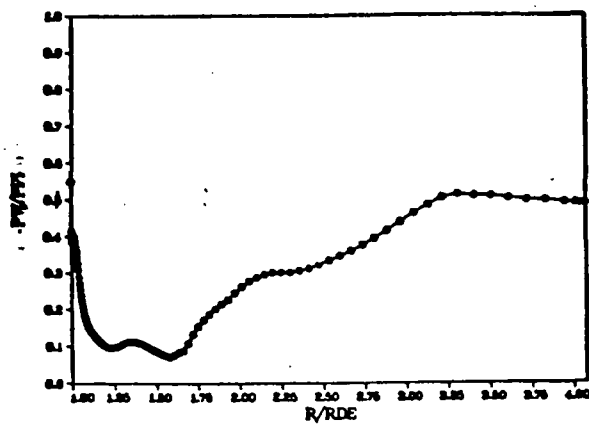N=475K PCL/PPI ACTUAL INFLOW 60%NSR
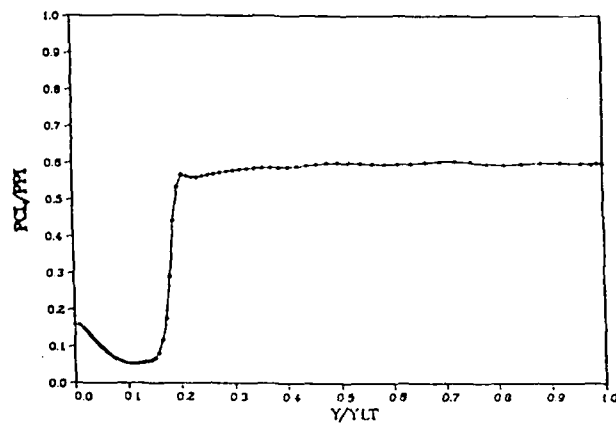
N=450K TCL/TO ACTUAL INFLOW 60%NSR
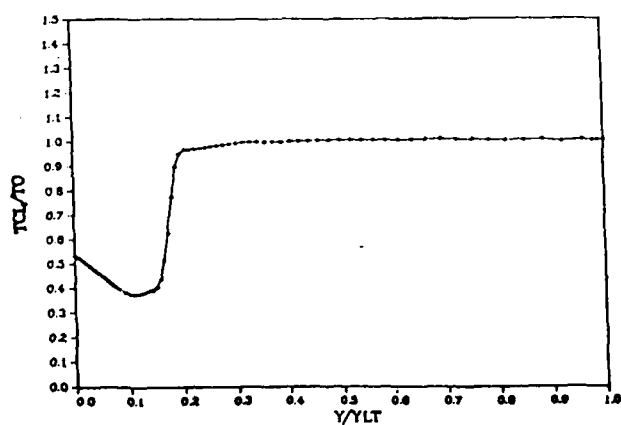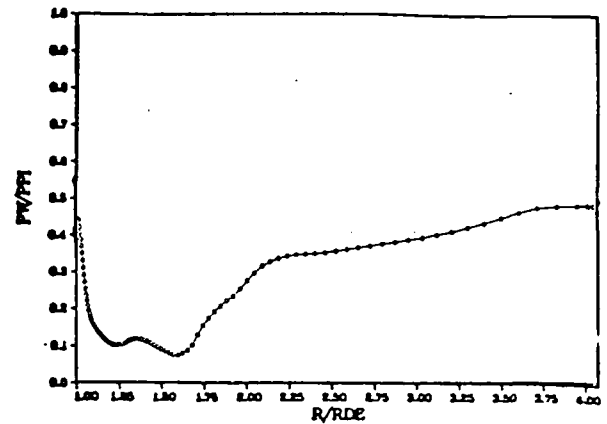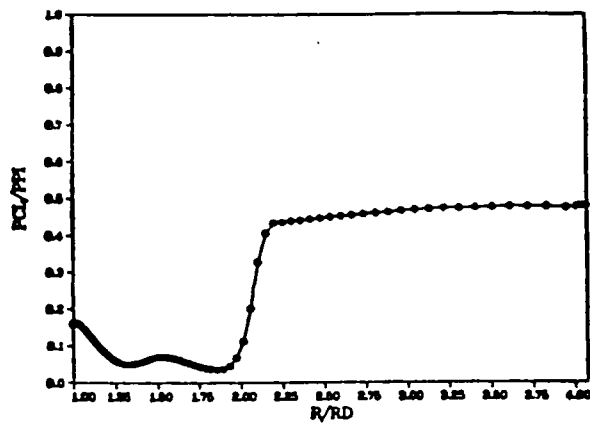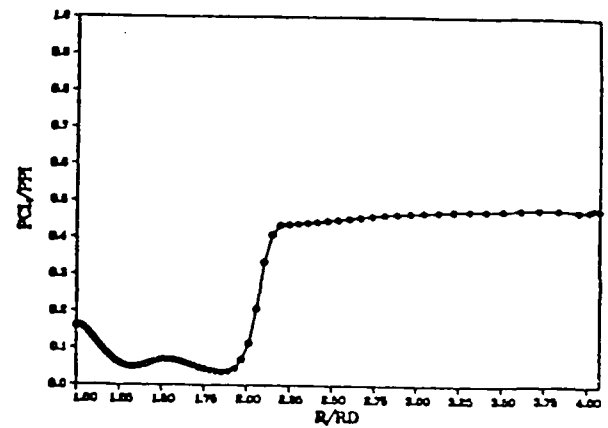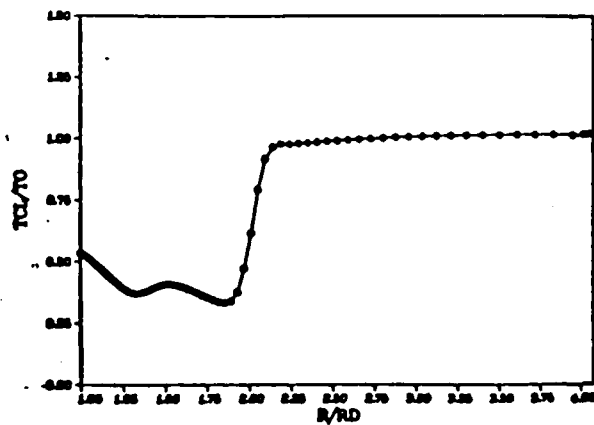
N=475K TCL/TO ACTUAL INFLOW 60%NSR
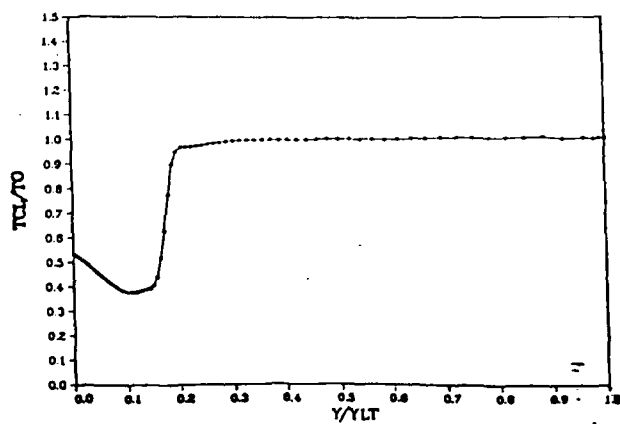
N=500K PW/PPI ACTUAL INFLOW 60%NSR
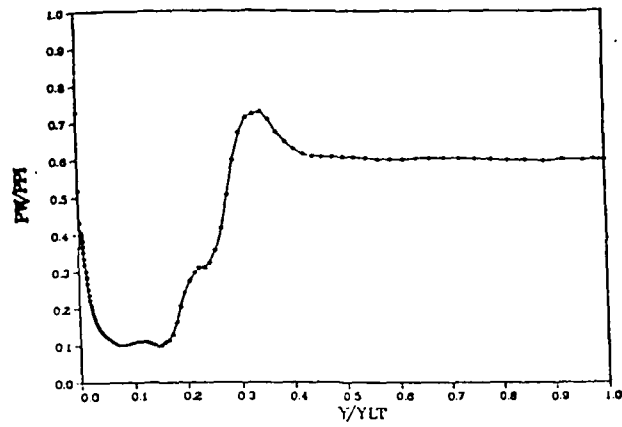
N=500K PCL/PPI ACTUAL INFLOW 60%NSR
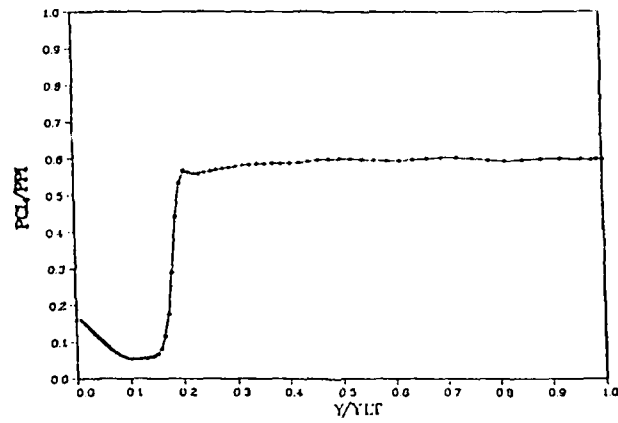
N=500K TCL/TO ACTUAL INFLOW 60%NSR
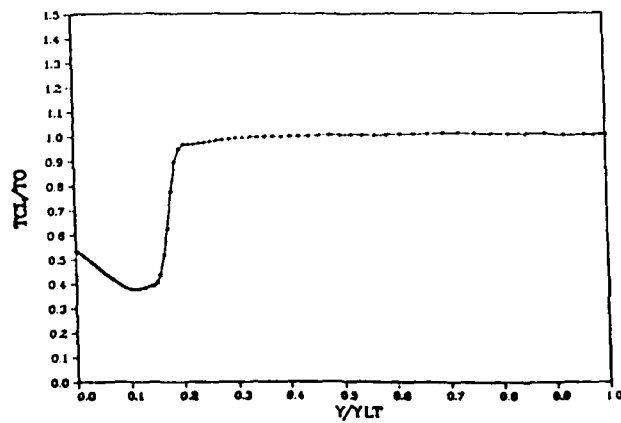
APPENDIX I

NUMERICAL CASE 4B COMPUTATIONAL DETAILS

From the converged solution for case 4a, the exit backpressure was lowered to 47% of normal shock recovery, and the Navier-Stokes computer code employing the adverse pressure gradient modified Cebeci-Smith eddy viscosity turbulence model was applied. Figure 78, repeated, shows the progress of the core flow normal shock to a new stable converged solution for flow conditions representative of the actual UTRC experimental conditions. Selected Mach contour, nondimensionalized wall pressure, line of symmetry pressure, and line of symmetry temperature plots portray the flow behavior. The Mach contour plots again present graphic flow images from M = 0.0 to M = 5.0, in increments of 0.20. Clearly visible are the nozzle profiles and the persistence of the wall bank blower flow energizers to the diffuser exit. From the time history plot it may also be noted that the flow rapidly achieves a new converged solution when the initial conditions start the computations from the previously converged solution. This numerical experiment required 14.5 hours of CRAY 1 CPU time.

CONVERGENCE TIME HISTORY 47%NSR
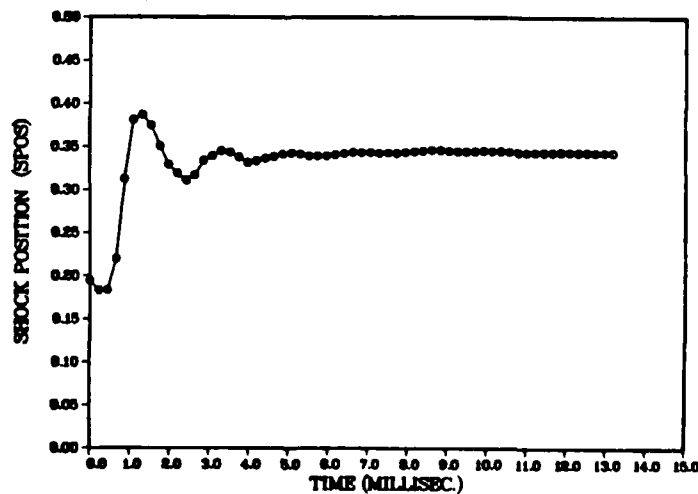
TABLE IX

NUMERICAL CASE 4B COMPUTED SHOCK POSITION VS TIME

N	CFL	TIME	R/R_{de}	SPOS
Number of Iterations		(Milliseconds)		
0		0	1.597675	0.194430
5,000	.50	0.220834	1.562721	0.183059
10,000		0.441668	1.563867	0.183432
15,000		0.662503	1.676240	0.219988
20,000		0.883337	1.960568	0.312483
25,000		1.104171	2.170927	0.380915
30,000		1.325005	2.188937	0.386774
35,000		1.545839	2.151315	0.374535
40,000		1.766673	2.077426	0.350498
45,000		1.987507	2.012340	0.329325
50,000		2.208342	1.981342	0.319241
55,000		2.429176	1.955118	0.310710
60,000		2.650010	1.973851	0.316804
65,000		2.870888	2.025909	0.333739
70,000		3.091722	2.042674	0.339193
75,000		3.312557	2.060008	0.344832
80,000		3.533391	2.055926	0.343504
85,000		3.754225	2.039004	0.337999
90,000		3.975059	2.019266	0.331578
95,000		4.195893	2.024903	0.333412
100,000		4.416727	2.034101	0.336404
105,000		4.637517	2.040018	0.338329
110,000		4.858351	2.049022	0.341258
115,000		5.079186	2.053442	0.342696
120,000		5.300020	2.049784	0.341506
125,000		5.520854	2.043320	0.339403
130,000		5.741688	2.043606	0.339496
135,000		5.962522	2.043578	0.339487
140,000		6.183356	2.048066	0.340947
145,000		6.404191	2.052449	0.342373
150,000		6.625025	2.056851	0.343805
155,000		6.845859	2.056123	0.343568
160,000		7.066693	2.055966	0.343517
165,000		7.287527	2.053565	0.342736
170,000		7.508361	2.054946	0.343185
175,000		7.729195	2.053117	0.342590
180,000		7.950030	2.056246	0.343608
185,000		8.171931	2.059326	0.344610
190,000		8.391698	2.060909	0.345125
195,000		8.612532	2.064214	0.346200
200,000		8.833366	2.063691	0.346030

N	CFL	TIME	R/R_{de}	SPOS
Number of Iterations		(Milliseconds)		
205,000		9.050809	2.060599	0.345024
210,000		9.268102	2.058800	0.344439
215,000		9.485396	2.059234	0.344580
220,000		9.702689	2.059234	0.344580
225,000		9.919982	2.060915	0.345127
230,000		10.137270	2.059664	0.344720
235,000		10.354570	2.059867	0.344786
240,000		10.571860	2.058256	0.344262
245,000		10.789150	2.055610	0.343401
250,000		11.006450	2.054712	0.343109
255,000		11.223740	2.054850	0.343154
260,000		11.441030	2.055314	0.343305
265,000		11.658330	2.054946	0.343185
270,000		11.875620	2.056347	0.343641
275,000		12.092910	2.056230	0.343603
280,000		12.310210	2.055262	0.343288
285,000		12.527500	2.055450	0.343349
290,000		12.744790	2.054063	0.342898
295,000		12.962090	2.053642	0.342761
300,000		13.175030	2.054097	0.342909

N=25K ACTUAL INFLOW 47%NSR WBB=.195
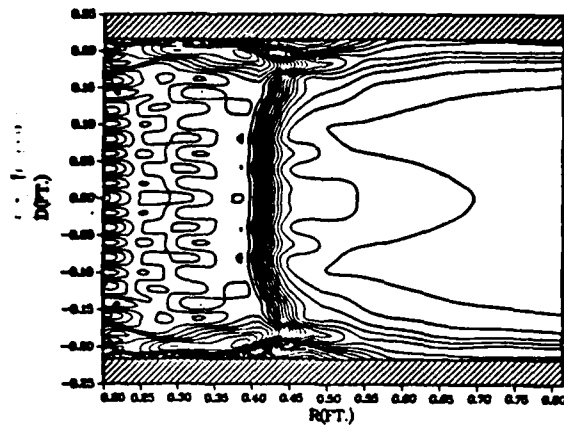
N=50K ACTUAL INFLOW 47%NSR WBB=.195
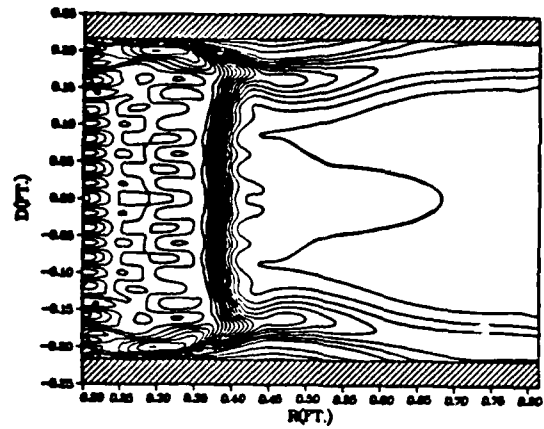
N=75K ACTUAL INFLOW 47%NSR WBB=.195

N=100K ACTUAL INFLOW 47%NSR WBB=.195

N=125K ACTUAL INFLOW 47%NSR WBB=.195

N=150K ACTUAL INFLOW 47%NSR WBB=.195

321
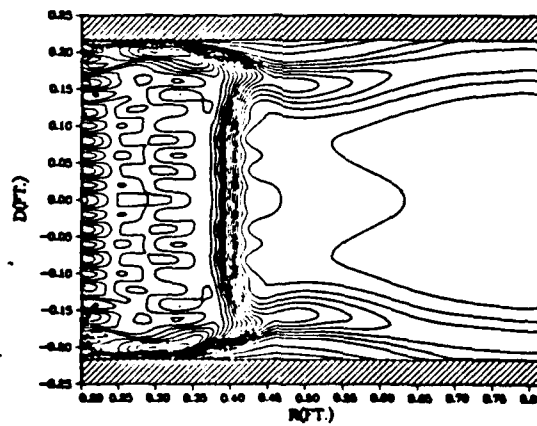
N=175K ACTUAL INFLOW 47%NSR WBB=.195

N=200K ACTUAL INFLOW 47%NSR WBB=.195

N=225K ACTUAL INFLOW 47%NSR WBB=.195

N=250K ACTUAL INFLOW 47%NSR WBB=.195

N=275K ACTUAL INFLOW 47%NSR WBB=.195

N=300K ACTUAL INFLOW 47%NSR WBB=.195
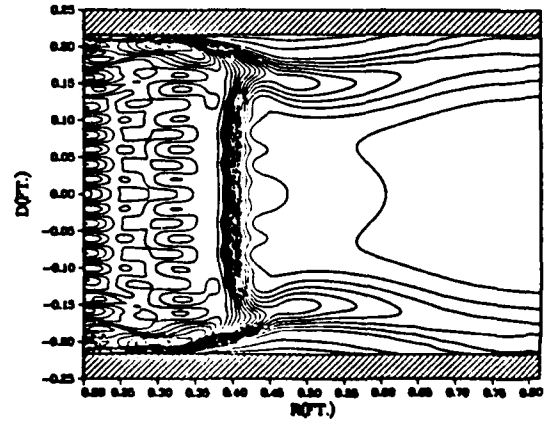
N=25K PW/PPI ACTUAL INFLOW 47%NSR
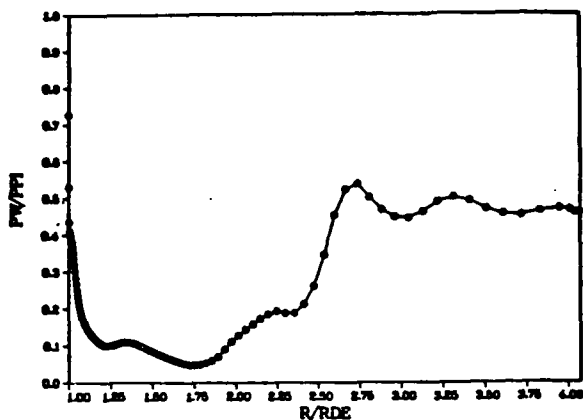
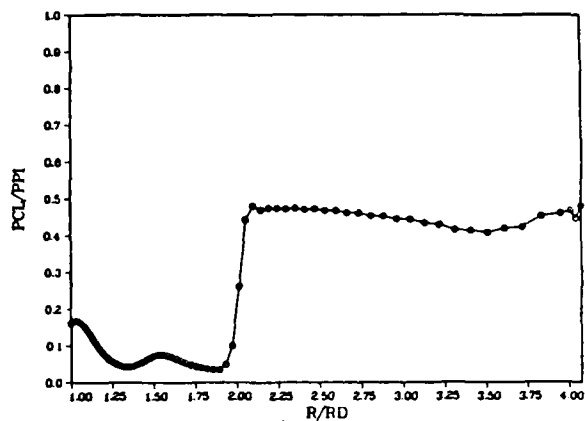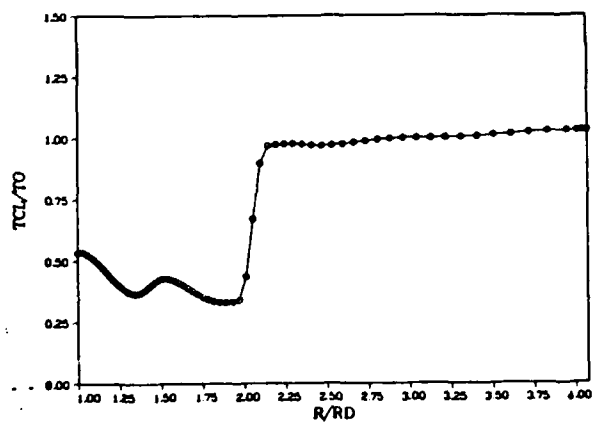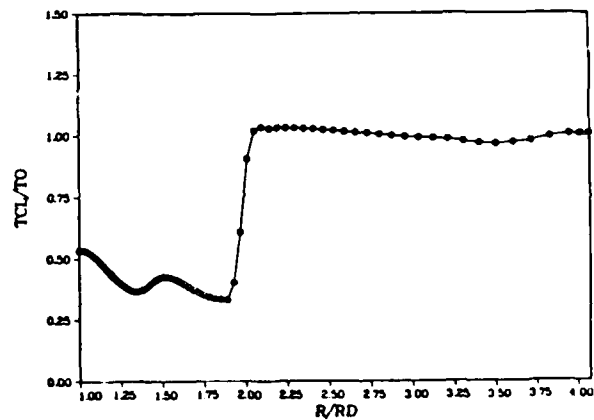N=50K PW/PPI ACTUAL INFLOW 47%NSR
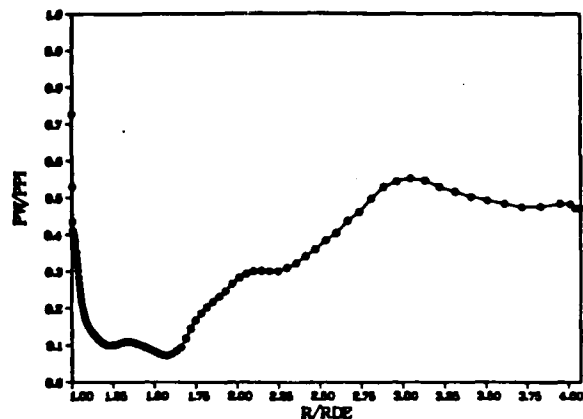
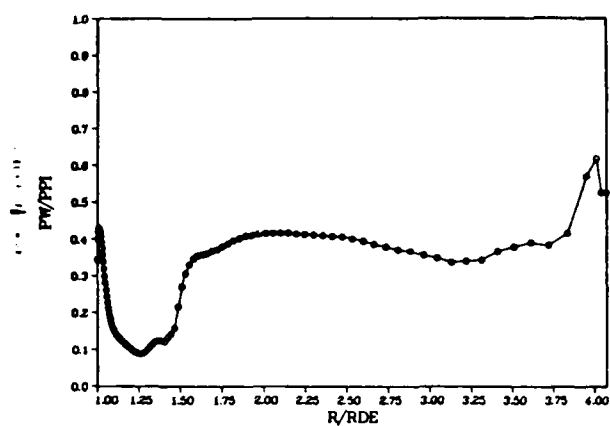N=25K PCL/PPI ACTUAL INFLOW 47%NSR
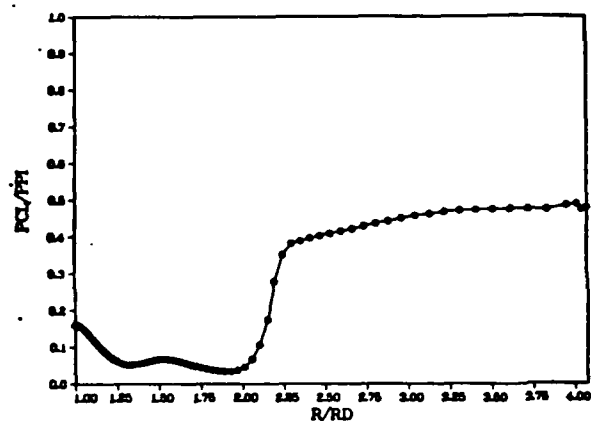
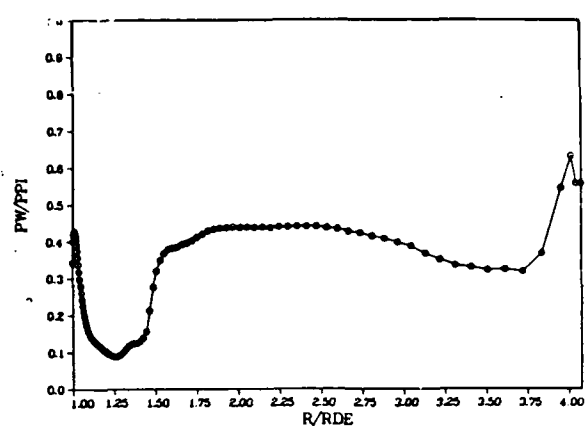N=50K PCL/PPI ACTUAL INFLOW 47%NSR
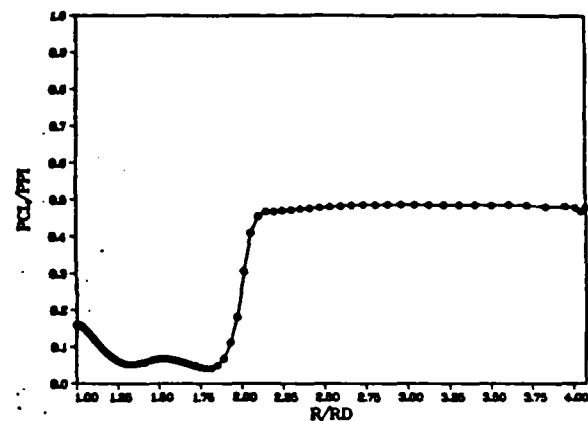
N=25K TCL/TO ACTUAL INFLOW 47%NSR
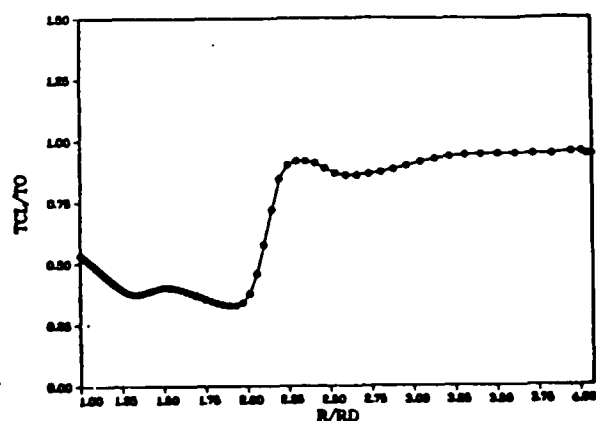
N=50K TCL/TO ACTUAL INFLOW 47%NSR
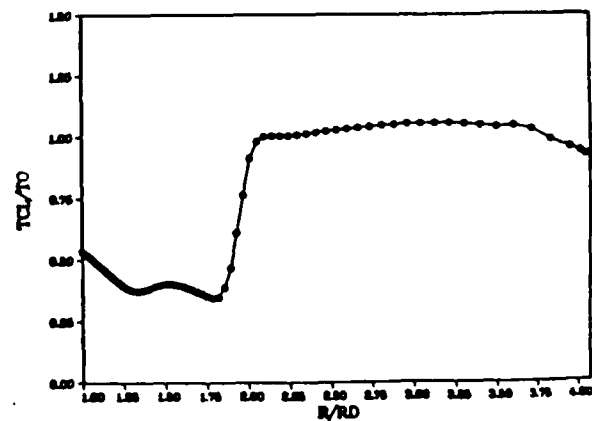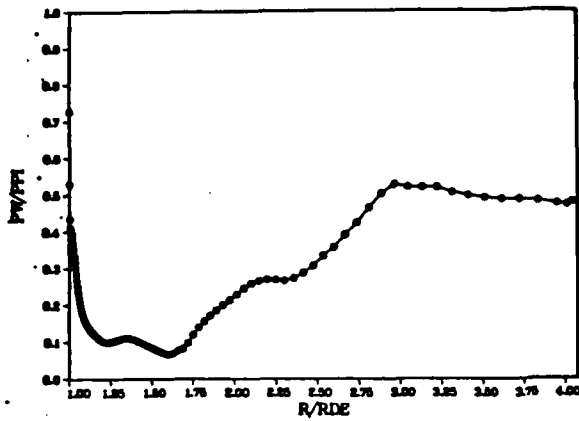
N=75K PW/PPI ACTUAL INFLOW 47%NSR   N=100K PW/PPI ACTUAL INFLOW 47%NSR
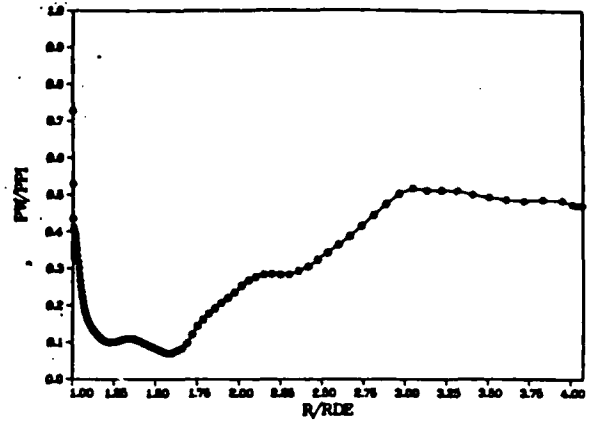
N=75K PCL/PPI ACTUAL INFLOW 47%NSR   N=100K PCL/PPI ACTUAL INFLOW 47%NSR

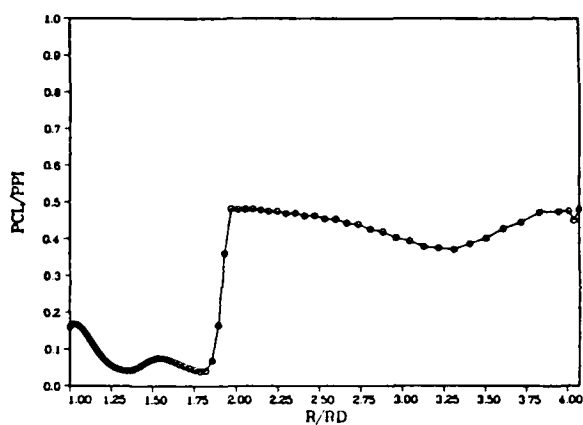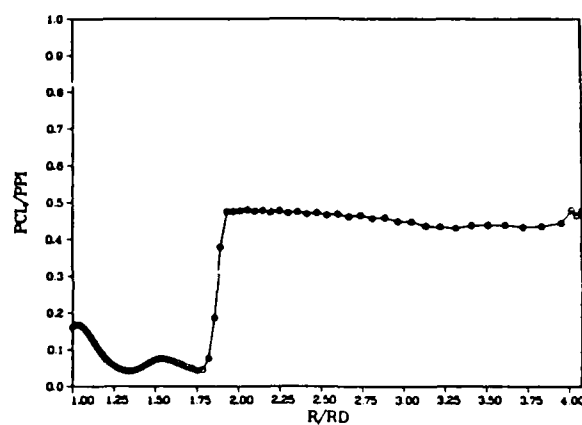N=75K TCL/TO ACTUAL INFLOW 47%NSR   N=100K TCL/TO ACTUAL INFLOW 47%NSR

324

N=125K PW/PPI ACTUAL INFLOW 47%NSR

N=150K PW/PPI ACTUAL INFLOW 47%NSR

N=125K PCL/PPI ACTUAL INFLOW 47%NSR

N=150K PCL/PPI ACTUAL INFLOW 47%NSR

N=125K TCL/TO ACTUAL INFLOW 47%NSR

N=150K TCL/TO ACTUAL INFLOW 47%NSR

N=175K PW/PPI ACTUAL INFLOW 47%NSR

N=200K PW/PPI ACTUAL INFLOW 47%NSR
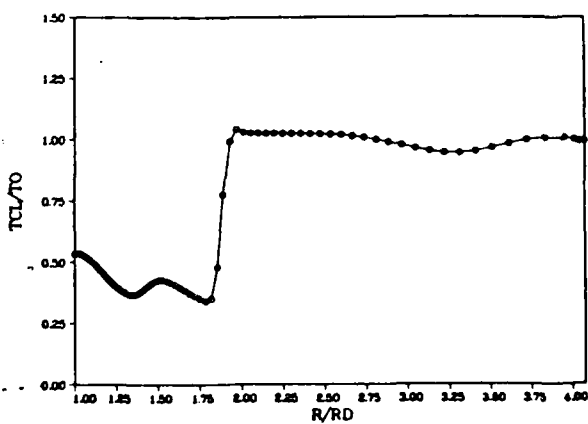

N=175K PCL/PPI ACTUAL INFLOW 47%NSR
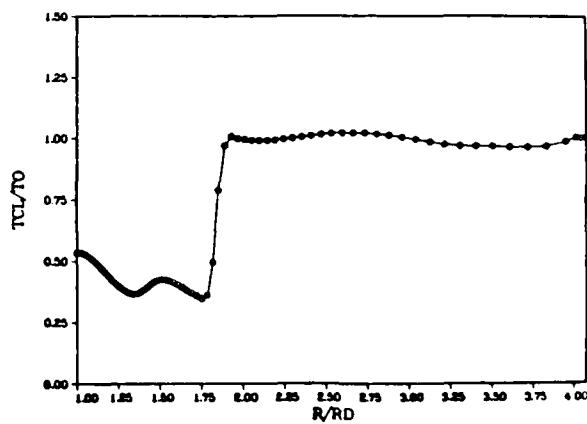

N=200K PCL/PPI ACTUAL INFLOW 47%NSR
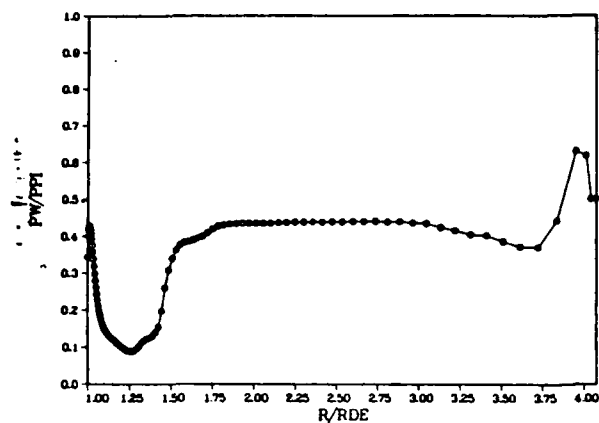

N=175K TCL/TO ACTUAL INFLOW 47%NSR

N=200K TCL/TO ACTUAL INFLOW 47%NSR

N=225K PW/PPI ACTUAL INFLOW 47%NSR

N=250K PW/PPI ACTUAL INFLOW 47%NSR

N=225K PCL/PPI ACTUAL INFLOW 47%NSR

N=250K PCL/PPI ACTUAL INFLOW 47%NSR

N=225K TCL/TO ACTUAL INFLOW 47%NSR
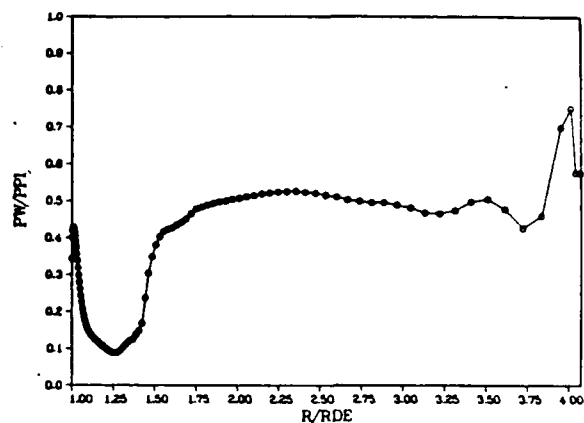
N=250K TCL/TO ACTUAL INFLOW 47%NSR
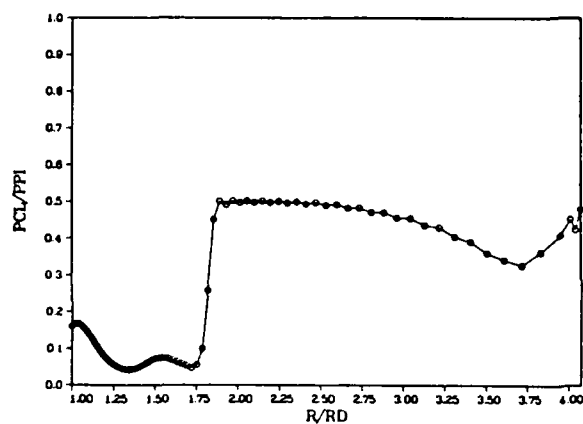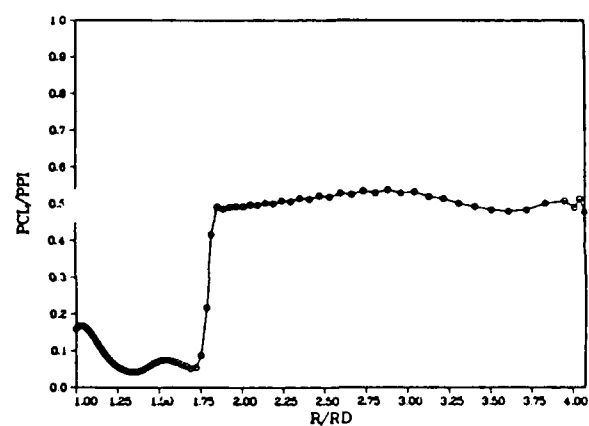
N=275K PW/PPI ACTUAL INFLOW 47%NSR

N=300K PW/PPI ACTUAL INFLOW 47%NSR
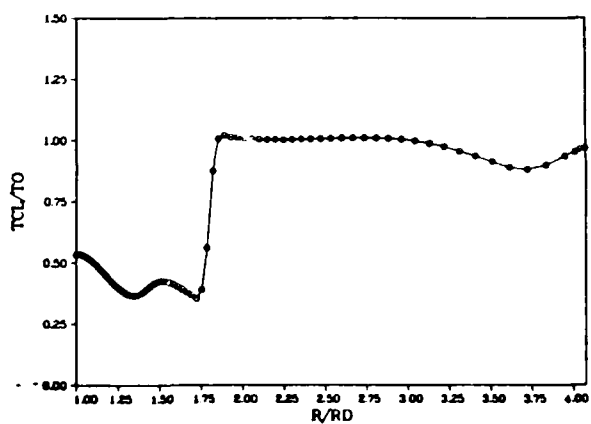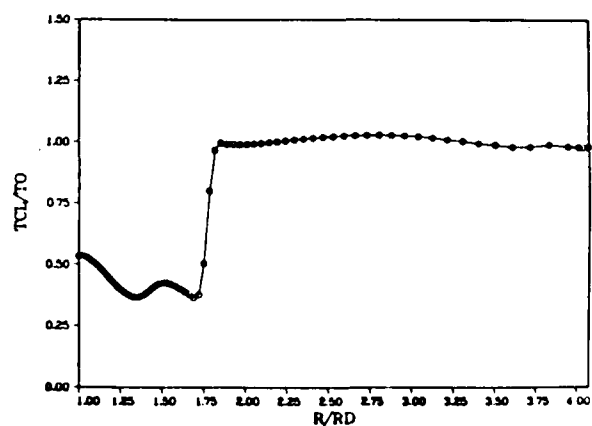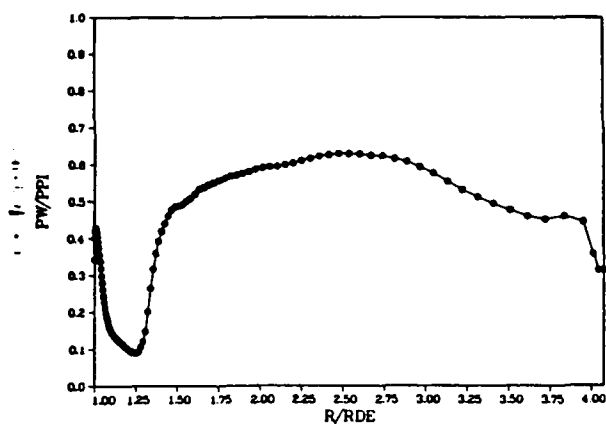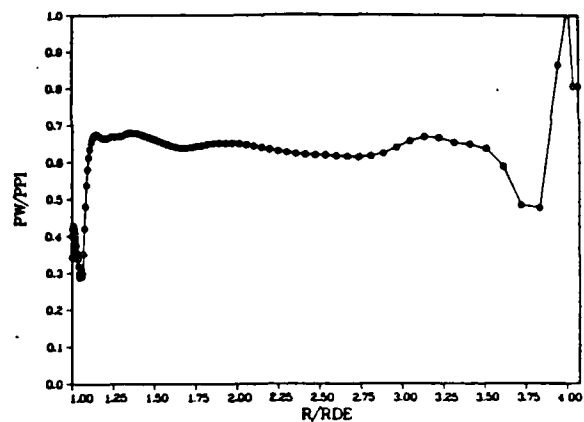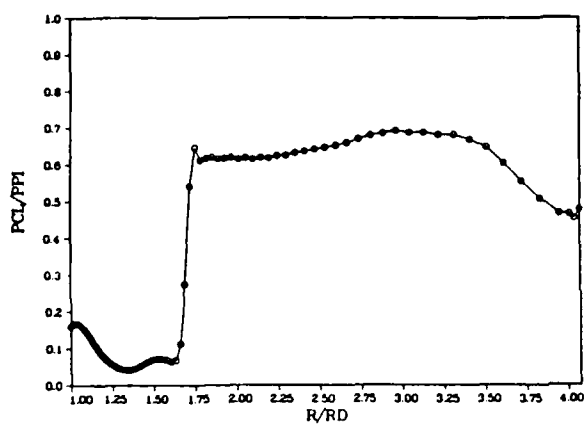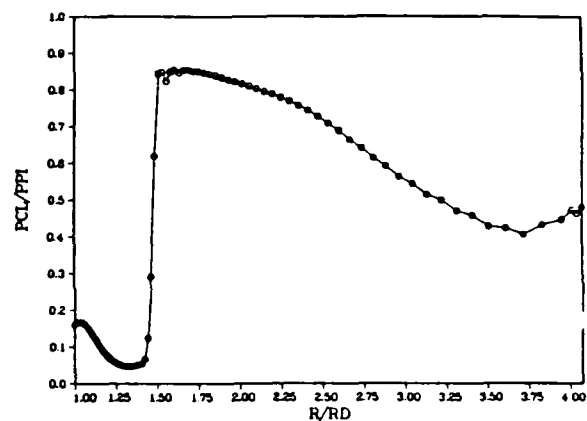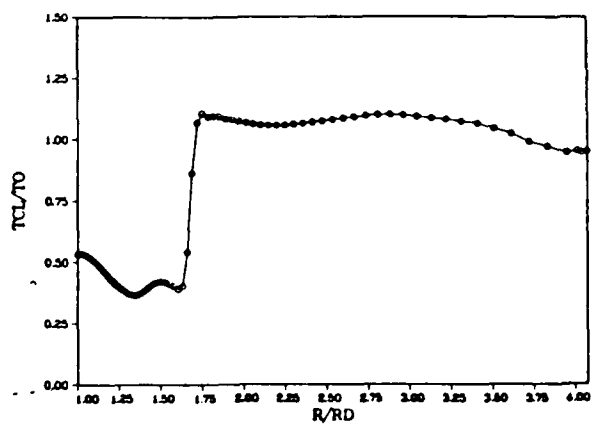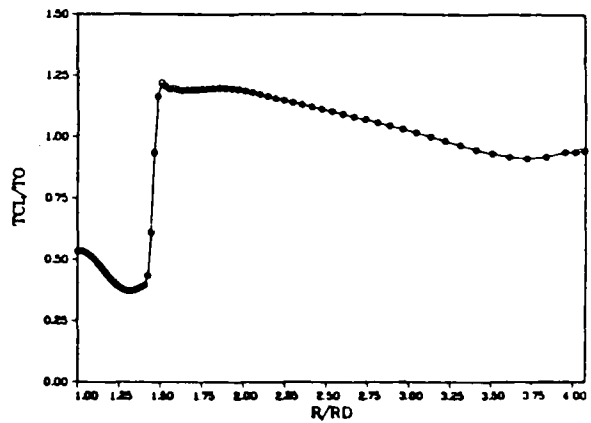
N=275K PCL/PPI ACTUAL INFLOW 47%NSR

N=300K PCL/PPI ACTUAL INFLOW 47%NSR

N=275K TCL/TO ACTUAL INFLOW 47%NSR

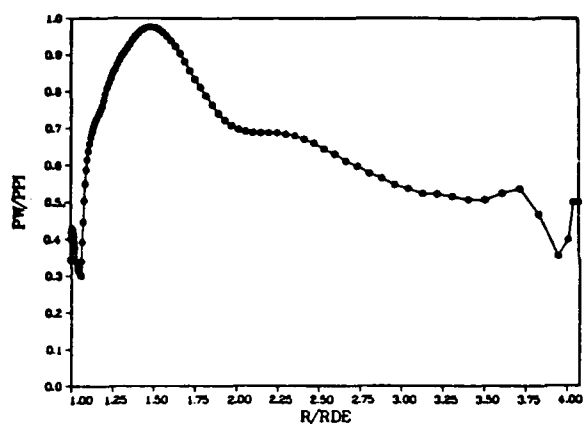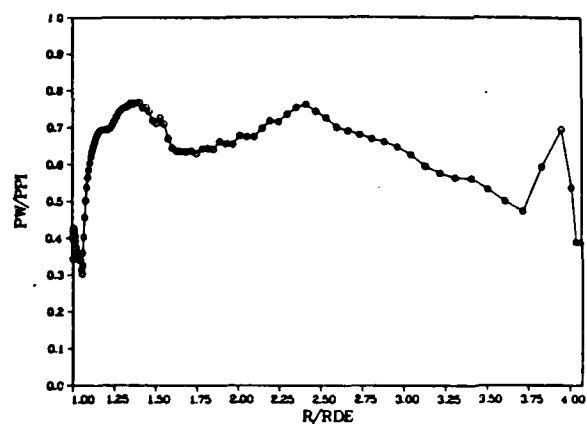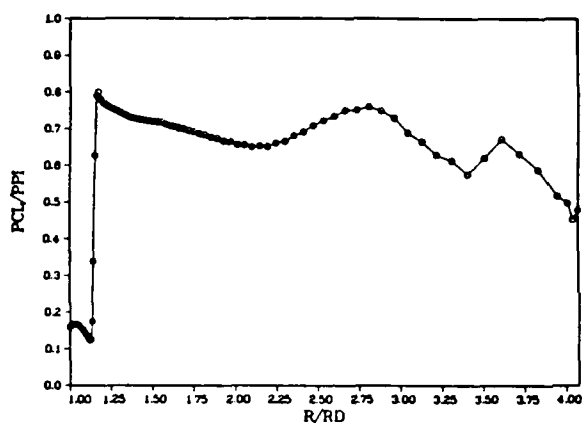N=300K TCL/TO ACTUAL INFLOW 47%NSR

328
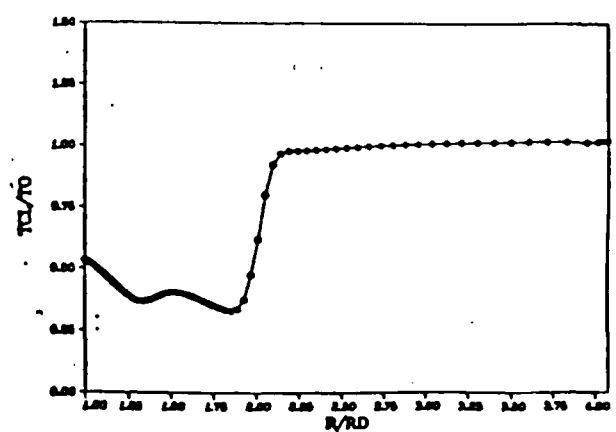
APPENDIX J

NUMERICAL CASE 4C COMPUTATIONAL DETAILS

From the converged solution for case 4b, the adverse pressure gradient modification to the standard Cebeci-Smith eddy viscosity turbulence model in the Navier-Stokes computer code were "turned off," and the algorithm was marched forward in time employing the basic Cebeci-Smith model. The exit backpressure was maintained at 47% of normal shock recovery, and the inflow conditions were again representative of the actual UTRC experimental flow profiles. Figure 90, repeated here, shows the rapid "unstart" of the diffuser flow from the stable, converged, "started" initial condition, in slightly more than 2.0 milliseconds. Selected Mach contour, nondimensionalized wall pressure, line of symmetry pressure, and line of symmetry temperature plots portray the flow behavior, and show the rapid growth of the wall boundary layer separation region and breakdown of the core flow. The Mach contour plots again present graphic flow images from M = 0.0 to M = 5.0, in increments of 0.20. Again, line of symmetry pressure and temperature are seen to significantly lag the wall pressure as indicators of overall diffuser flow behavior. Without the additional "stiffening" of the eddy viscosity turbulence model achieved through incorporation of the modification developed in Chapter V, the wall boundary layer separation grows uncontrollably and causes the core flow to choke, leading to diffuser "unstart." This numerical experiment required 2.4 hours of CRAY 1 CPU time.

TABLE X

NUMERICAL CASE 4C COMPUTED SHOCK POSITION VS TIME

N	CFL	TIME	R/R_{de}	SPOS
Number of Iterations		(Milliseconds)		
0		0	2.054097	0.342909
5,000	.50	0.204322	2.082405	0.352118
10,000		0.408523	2.001089	0.325665
15,000		0.612725	1.900874	0.293064
20,000		0.816926	1.860132	0.279810
25,000		1.021127	1.814080	0.264829
30,000		1.225329	1.787998	0.256344
35,000		1.429530	1.689455	0.224287
40,000		1.633731	1.461307	0.150068
45,000		1.837934	1.143177	0.046577
50,000		2.042141	1.014093	0.0045847

BASIC CEBECI—SMITH TIME HISTORY 47%NSR A.F.

330
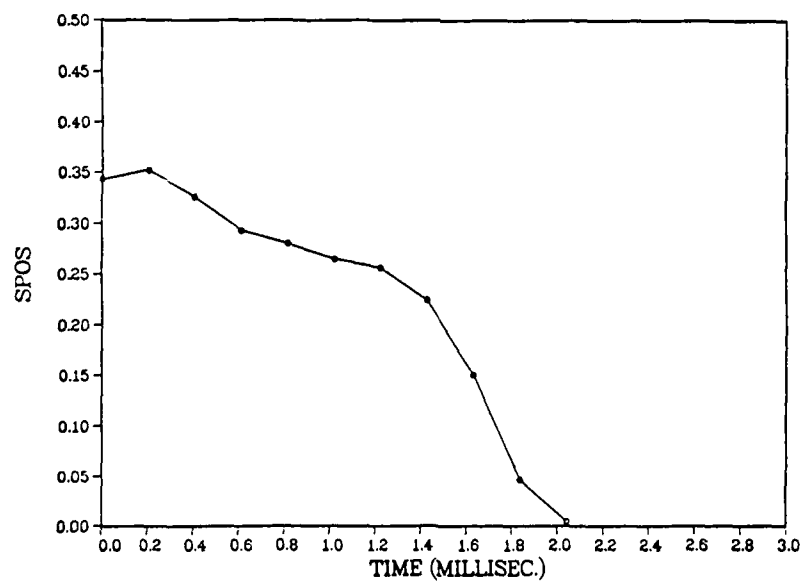
N=5K CSB ACTUAL INFLOW 47%NSR
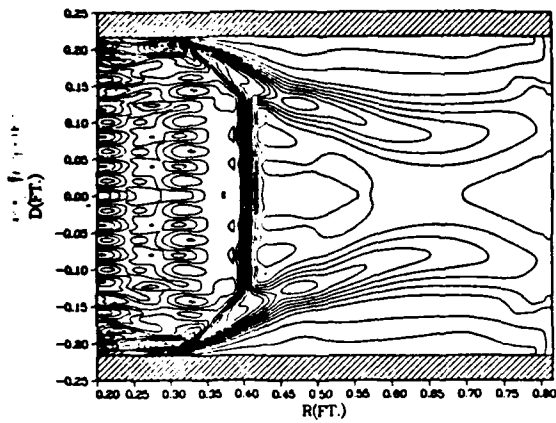
N=10K CSB ACTUAL INFLOW 47%NSR
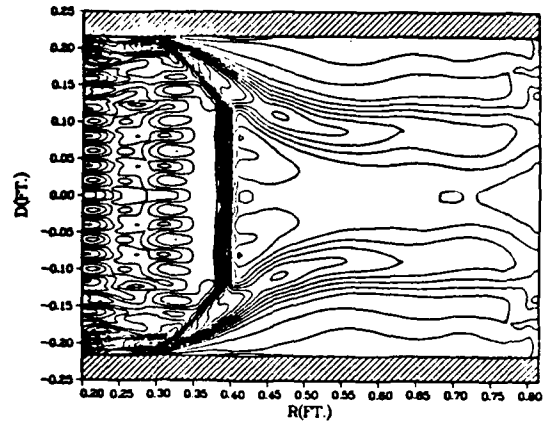
N=15K CSB ACTUAL INFLOW 47%NSR
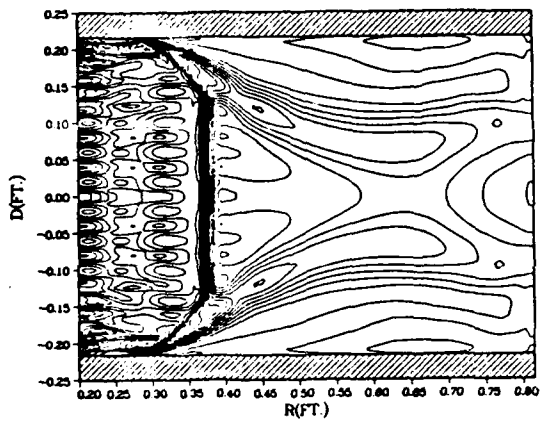
N=20K CSB ACTUAL INFLOW 47%NSR
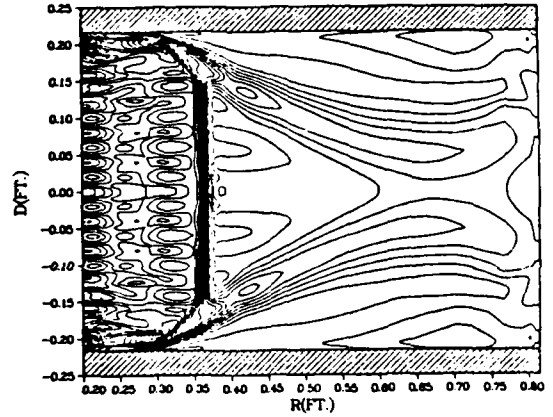
N=25K CSB ACTUAL INFLOW 47%NSR
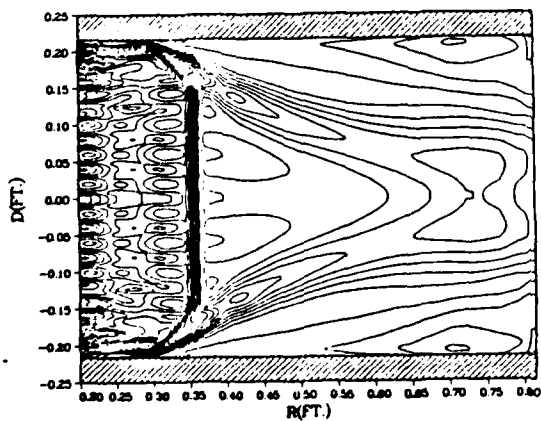
N=30K CSB CATUAL INFLOW 47%NSR
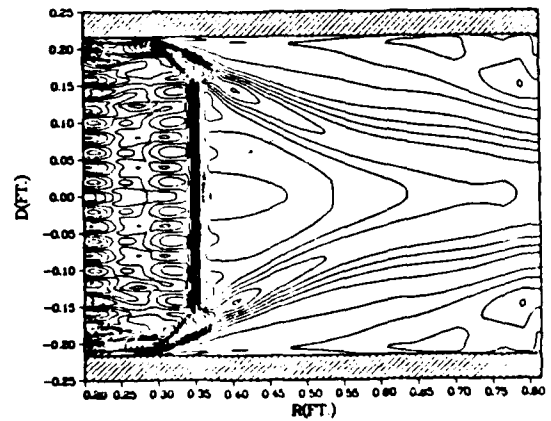
N=35K CSB ACTUAL INFLOW 47%NSR
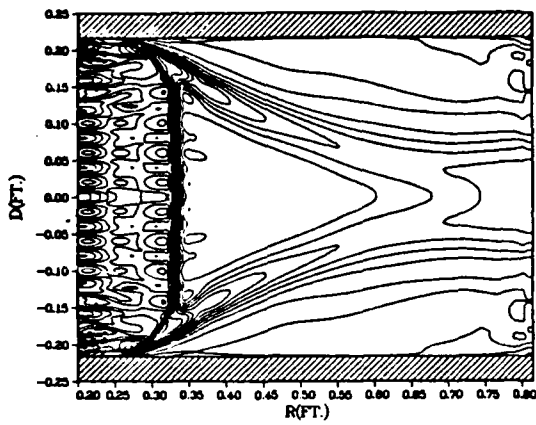
N=40K CSB ACTUAL INFLOW 47%NSR
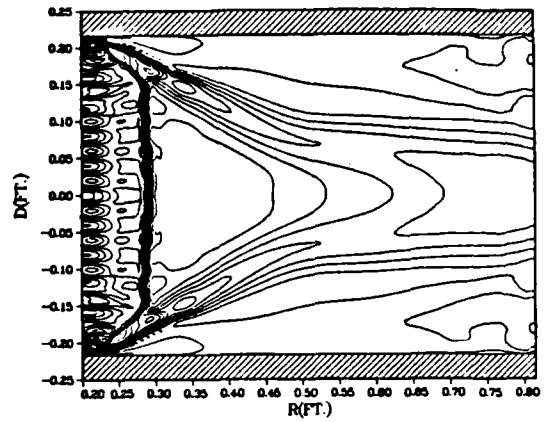
N=45K CSB ACTUAL INFLOW 47%NSR
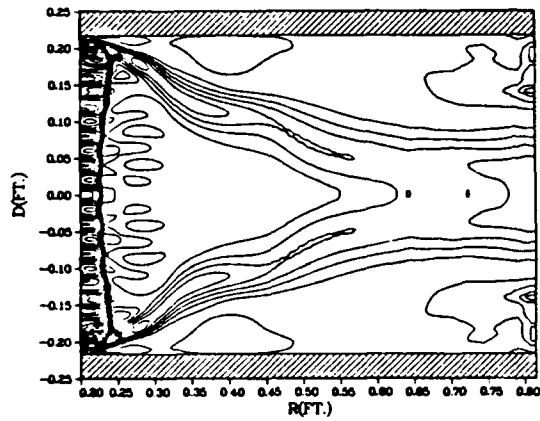
N=50K CSB ACTUAL INFLOW 47%NSR
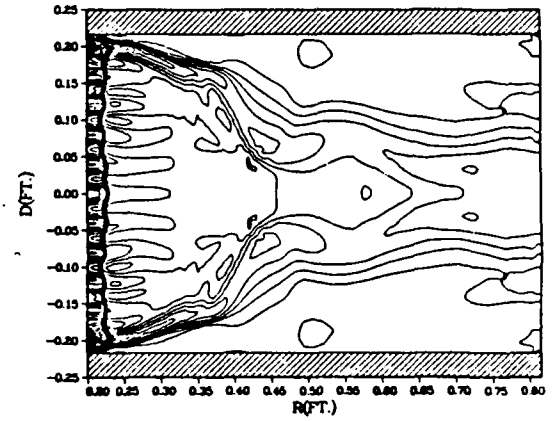
N=5K PW/PPI CSB ACTUAL INFLOW 47%NSR
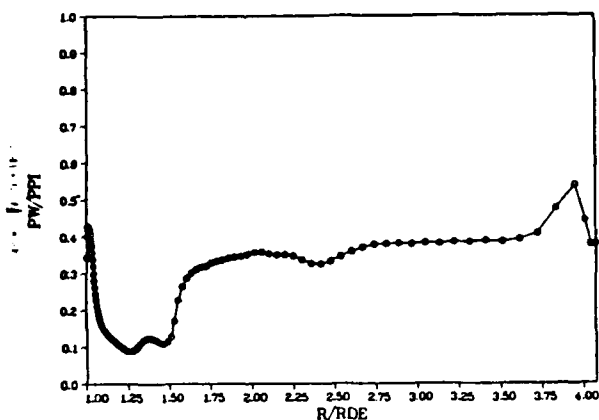
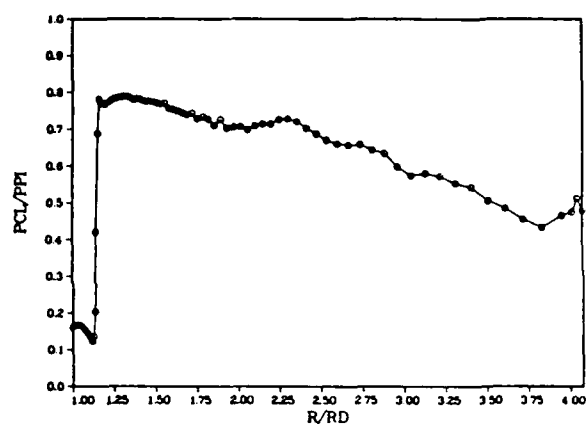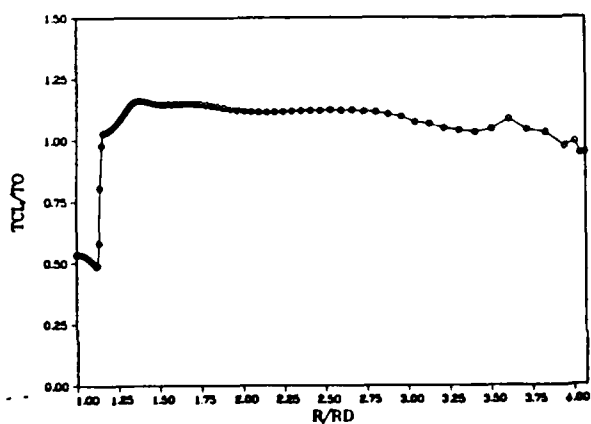N=10K PW/PPI CSB ACTUAL INFLOW 47%NSR
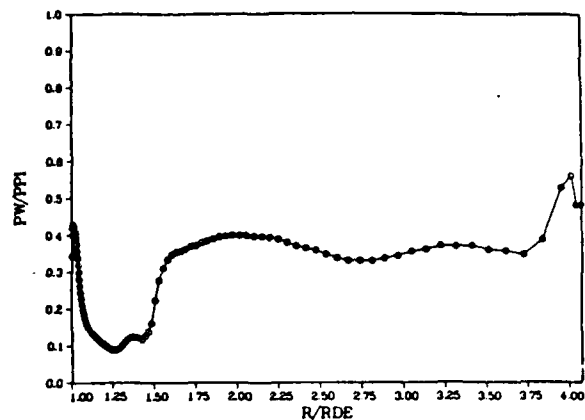
N=5K PCL/PPI CSB ACTUAL INFLOW 47%NSR
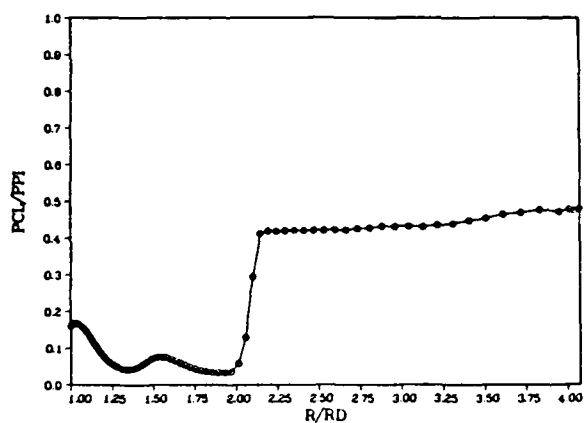
N=10K PCL/PPI CSB ACTUAL INFLOW 47%NSR

N=5K TCL/TO CSB ACTUAL INFLOW 47%NSR

N=10K TCL/TO CSB ACTUAL INFLOW 47%NSR

N=15K PW/PPI CSB ACTUAL INFLOW 47%NSR N=20K PW/PPI CSB ACTUAL INFLOW 47%NSR

N=15K PCL/PPI CSB ACTUAL INFLOW 47%NSR N=20K PCL/PPI CSB ACTUAL INFLOW 47%NSR

N=15K TCL/TO CSB ACTUAL INFLOW 47%NSR N=20K TCL/TO CSB ACTUAL INFLOW 47%NSR

334

N=25K PW/PPI CSB ACTUAL INFLOW 47%NSR

N=30K PW/PPI CSB ACTUAL INFLOW 47%NSR

N=25K PCL/PPI CSB ACTUAL INFLOW 47%NSR

N=30K PCL/PPI CSB ACTUAL INFLOW 47%NSR

N=25K TCL/TO CSB ACTUAL INFLOW 47%NSR

N=30K TCL/TO CSB ACTUAL INFLOW 47%NSR

N=35K PW/PPI CSB ACTUAL INFLOW 47%NSR

N=40K PW/PPI CSB ACTUAL INFLOW 47%NSR

N=35K PCL/PPI CSB ACTUAL INFLOW 47%NSR

N=40K PCL/PPI CSB ACTUAL INFLOW 47%NSR

N=35K TCL/TO CSB ACTUAL INFLOW 47%NSR

N=40K TCL/TO CSB ACTUAL INFLOW 47%NSR

336

N=45K PW/PPI CSB ACTUAL INFLOW 47%NSR   N=50K PW/PPI CSB ACTUAL INFLOW 47%NSR

N=45K PCL/PPI CSB ACTUAL INFLOW 47%NSR   N=50K PCL/PPI CSB ACTUAL INFLOW 47%NSR

N=45K TCL/TO CSB ACTUAL INFLOW 47%NSR   N=50K TCL/TO CSB ACTUAL INFLOW 47%NSR
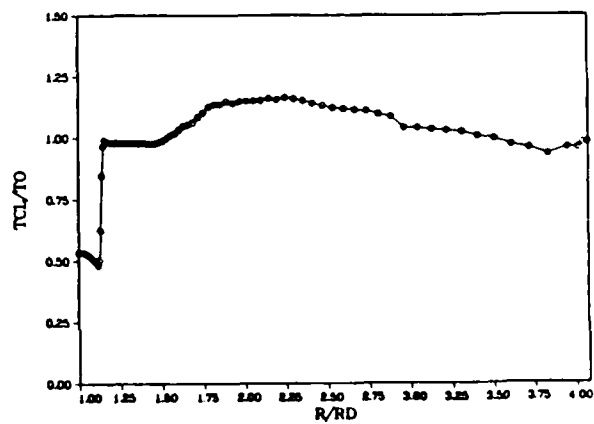
APPENDIX K

NUMERICAL CASE 4D COMPUTATIONAL DETAILS

The adverse pressure gradient modified Cebeci-Smith eddy viscosity turbulence model, applied to the actual UTRC experimental inflow profiles with an exit pressure set at 47% of normal shock recovery, was subjected to a sensitivity analysis where the value of the von Karman (universal mixing length) constant k_1 was increased from its nominal value of 0.40 to 0.50 rather than to 0.65, the value computed by Jobe and Hankey. The immediate response of the sublayer thickness parameter (A^+) from its nominal value of 26 to 65 in the pressence of an adverse pressure gradient was retained, as was the change rate of the Clauser constant k_2 that was employed in the adverse pressure gradient modification developed in Chapter V. The algorithm was marched forward in time from the converged 47% NSR case (Case 4b). Figure 91, repeated here, shows that the core flow normal shock performs a periodic oscillation in the diffuser, but the diffuser does not "unstart." The selected Mach contours show that although the wall boundary layer separation region does grow, it does not do so uncontrollably, and as a result the core flow does not choke but over-responds to the changing wall boundary layer conditions. Each Mach contour plot is again presented from $M = 0.0$ to $M = 5.0$, in increments of 0.20.

This numerical experiment required 19.3 hours of CRAY 1 CPU time.

TABLE XI

NUMERICAL CASE 4D COMPUTED SHOCK POSITION VS TIME

N	CFL	TIME	R/R_{de}	SPOS
Number of Iterations		(Milliseconds)		
0		0	2.054097	0.342909
5,000	.50	0.209000	2.177890	0.383180
10,000		0.418040	2.157410	0.376518
15,000		0.627090	2.133640	0.368786
20,000		0.836130	2.111030	0.361431
25,000		1.045140	2.090350	0.354703
30,000		1.254220	2.081370	0.351780
35,000		1.463270	2.089530	0.354437
40,000		1.672310	2.111700	0.361655
45,000		1.881360	2.138600	0.370411
50,000		2.090400	2.156800	0.376317
55,000		2.299450	2.167700	0.379856
60,000		2.508490	2.153200	0.375152
65,000		2.717530	2.136400	0.369686
70,000		2.926580	2.118000	0.363697
75,000		3.135620	2.094700	0.356124
80,000		3.344670	2.069000	0.347777
85,000		3.553710	2.040000	0.338359
90,000		3.762760	1.981400	0.319271
95,000		3.971800	1.894300	0.290921
100,000		4.180800	1.818200	0.266164
105,000		4.389850	1.793610	0.259390
110,000		4.598890	1.839100	0.272956
115,000		4.807940	1.930100	0.302568
120,000		5.016980	2.032000	0.335719
125,000		5.226030	2.113900	0.362363
130,000		5.434750	2.180300	0.383964
135,000		5.644120	2.228100	0.399514
140,000		5.853160	2.249200	0.406375
145,000		6.062210	2.231800	0.400730
150,000		6.271250	2.169800	0.380552
155,000		6.480300	2.119800	0.364280
160,000		6.689340	2.092300	0.355327
165,000		6.898380	2.086400	0.353409
170,000		7.107430	2.079460	0.351159
175,000		7.316470	2.065200	0.346505
180,000		7.525520	2.036800	0.337297
185,000		7.734560	1.961200	0.312689
190,000		7.943610	1.865400	0.281537
195,000		8.152650	1.801400	0.260705
200,000		8.361660	1.804900	0.261842

N	CFL	TIME	R/R_{de}	SPOS
Number of Iterations		(Milliseconds)		
205,000	.50	8.570740	1.871080	0.283372
210,000		8.779790	1.966755	0.314496
215,000		8.988830	2.054677	0.343097
220,000		9.197880	2.130783	0.367856
225,000		9.406920	2.190111	0.387156
230,000		9.615960	2.234905	0.401728
235,000		9.825010	2.246578	0.405530
240,000		10.034050	2.211652	0.394163
245,000		10.243100	2.151108	0.374468
250,000		10.452140	2.108179	0.360503
255,000		10.661190	2.091507	0.355079
260,000		10.870230	2.083364	0.352430
265,000		11.079280	2.073510	0.349498
270,000		11.288320	2.055014	0.343207
275,000		11.497370	2.013658	0.329754
280,000		11.706410	1.927594	0.301756
285,000		11.915410	1.838404	0.272742
290,000		12.124460	1.793707	0.258201
295,000		12.333500	1.825057	0.266155
300,000		12.542510	1.902331	0.293538
305,000		12.751550	2.001123	0.325676
310,000		12.960550	2.085043	0.352976
315,000		13.169650	2.149332	0.373890
320,000		13.378650	2.206060	0.392344
325,000		13.587750	2.242523	0.404206
330,000		13.796750	2.241075	0.403735
335,000		14.005850	2.188885	0.386757
340,000		14.214850	2.135499	0.369390
345,000		14.423950	2.099226	0.357590
350,000		14.632950	2.088722	0.354173
355,000		14.842050	2.080066	0.351357
360,000		15.051150	2.068496	0.347593
365,000		15.260150	2.046498	0.340437
370,000		15.469250	1.991185	0.322443
375,000		15.678150	1.893149	0.290551
380,000		15.887250	1.813170	0.264533
385,000		16.096250	1.794889	0.258586
390,000		16.305350	1.844092	0.274592
395,000		16.514350	1.936431	0.304631
400,000		16.723350	2.032890	0.336010

XK1 TIME HISTORY 47%NSR
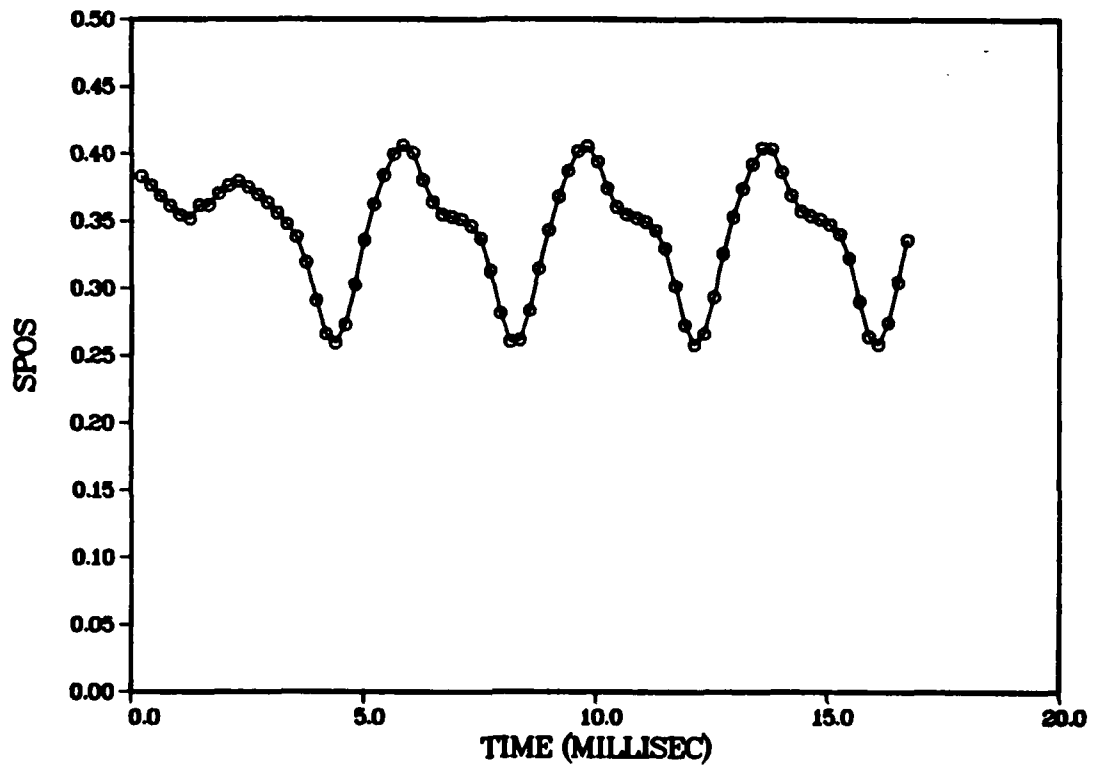
XK1 MACH CONTOURS N=250K 47%NSR
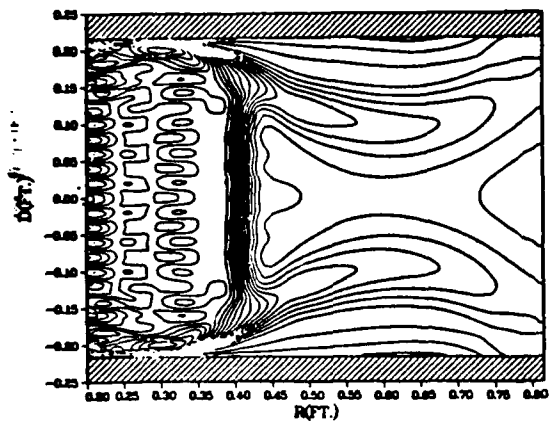
XK1 MACH CONTOURS N=275K 47%NSR
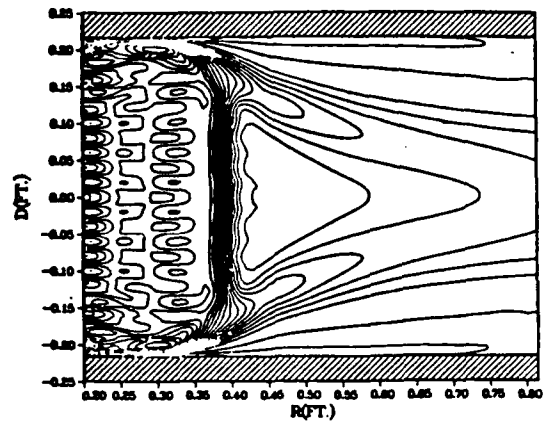
XK1 MACH CONTOURS N=300K 47%NSR
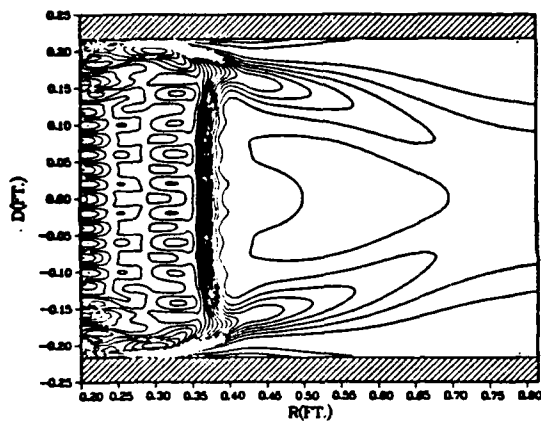
XK1 MACH CONTOURS N=325K 47%NSR
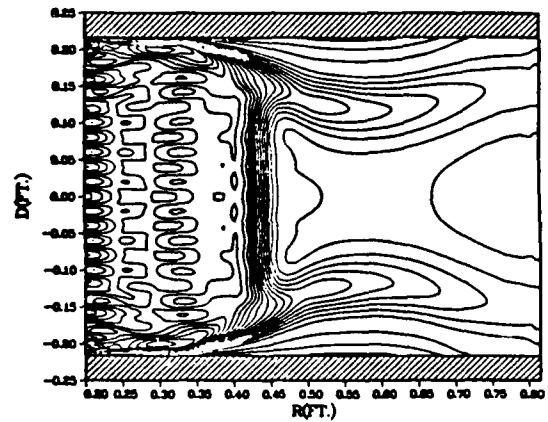
XK1 MACH CONTOURS N=350K 47%NSR
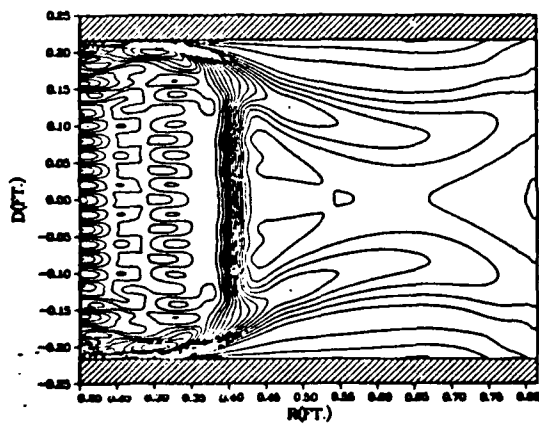
XK1 MACH CONTOURS N=375K 47%NSR

342
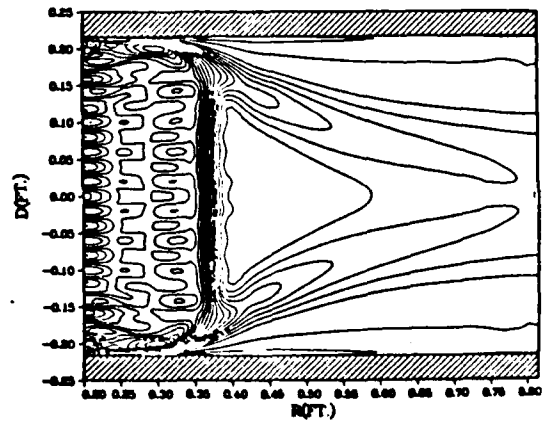
XK1 MACH CONTOURS N=400K 47%NSR
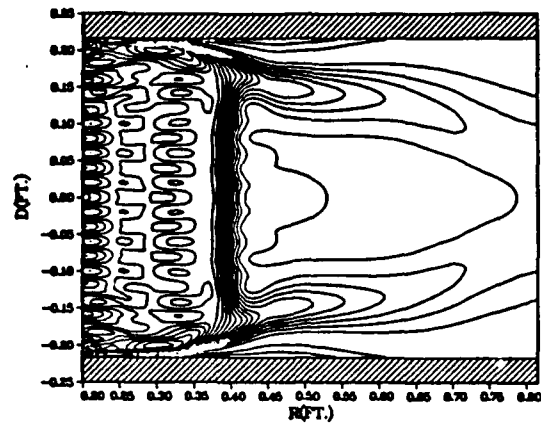
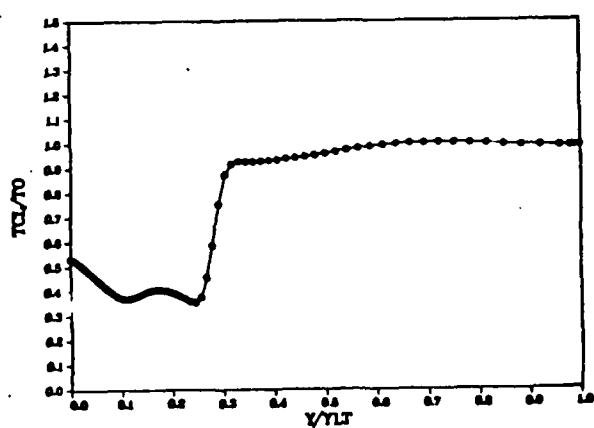N=250K PW/PPI XK1 47%NSR
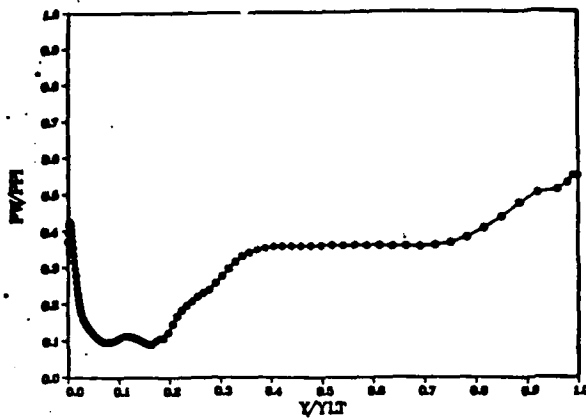
N=275K PW/PPI XK1 47%NSR
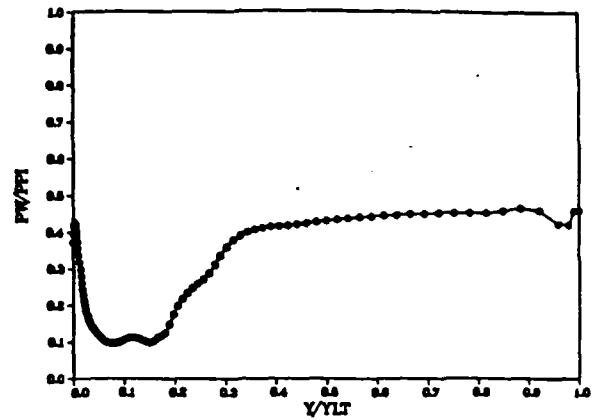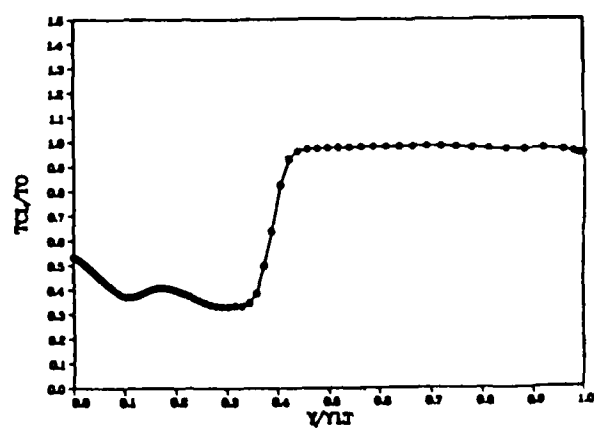
N=250K PCL/PPI XK1 47%NSR
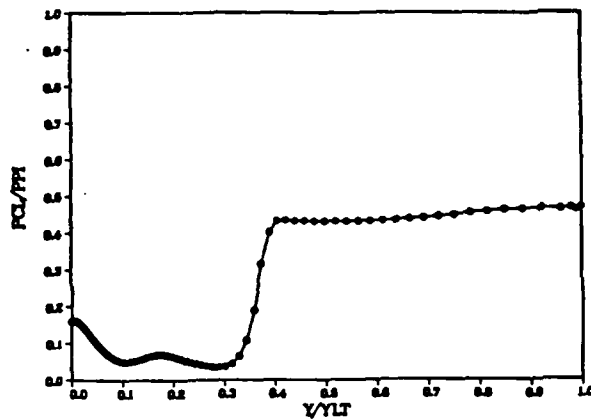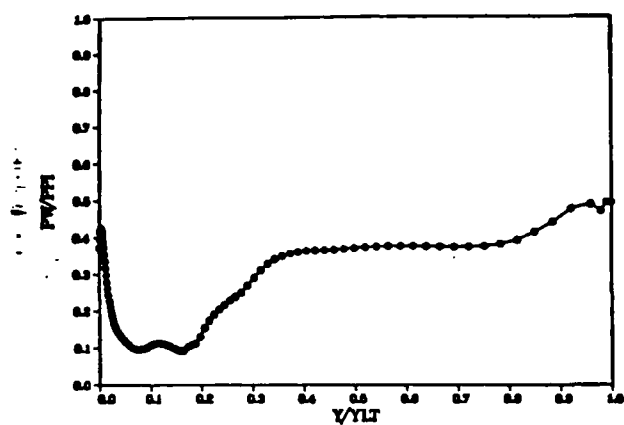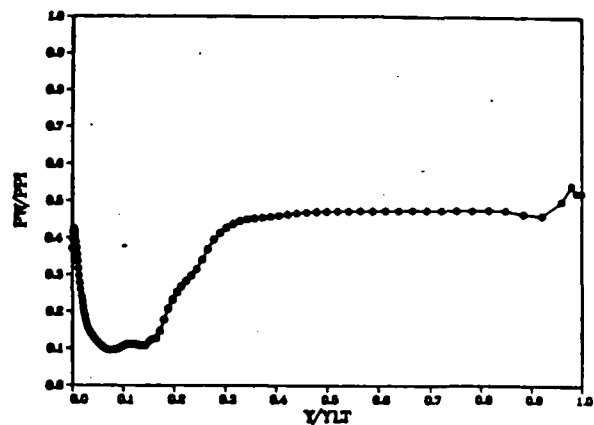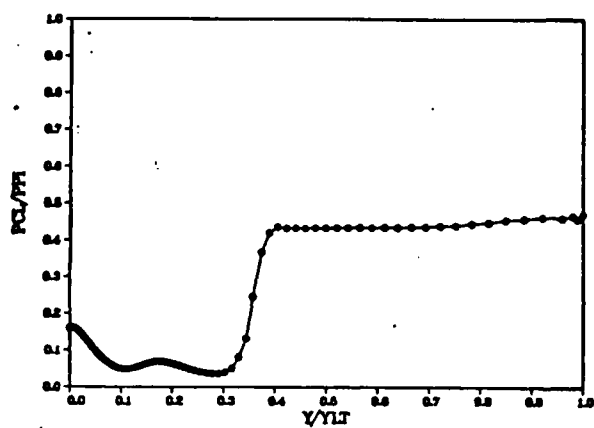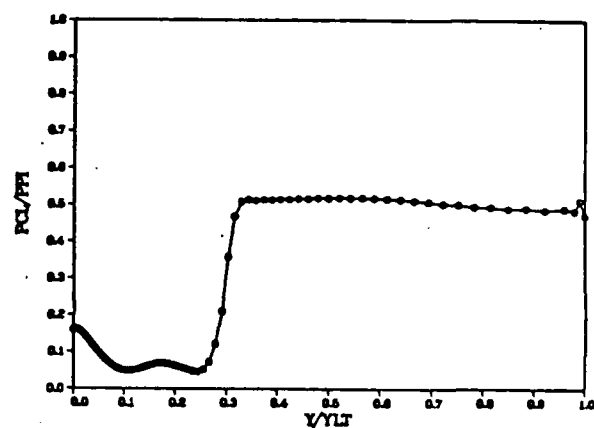
N=275K PCL/PPI XK1 47%NSR
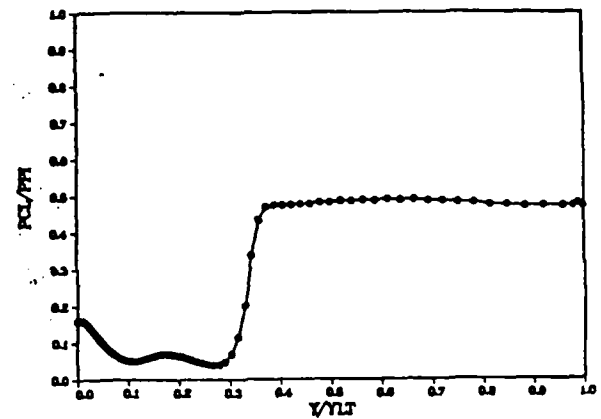
N=250K TCL/TO XK1 47%NSR
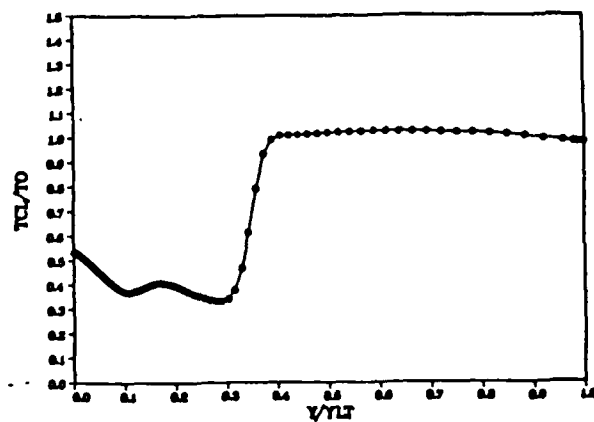
N=275K TCL/TO XK1 47%NSR
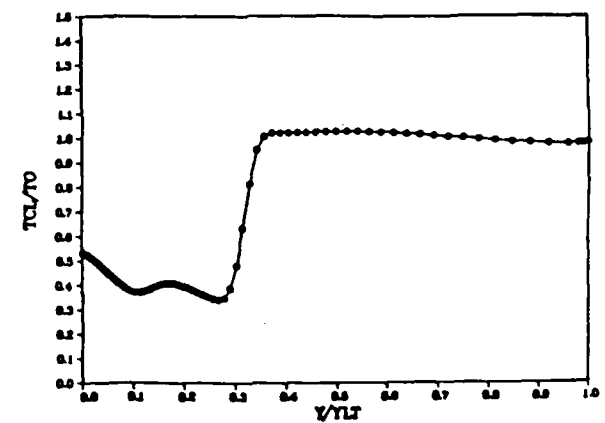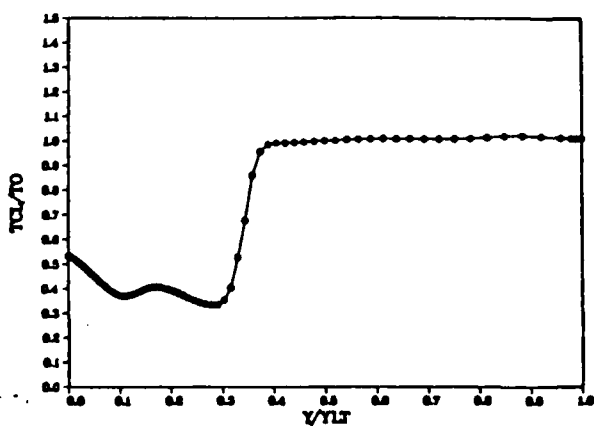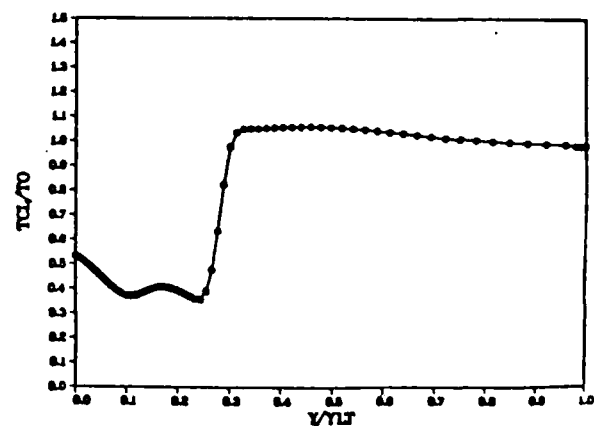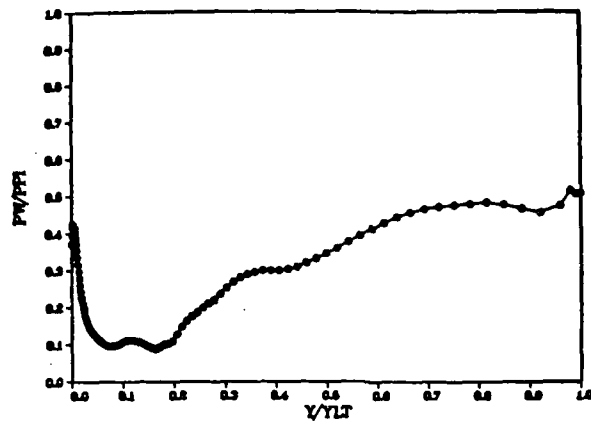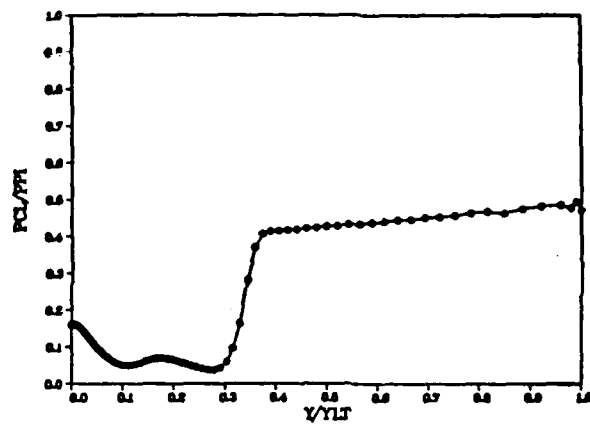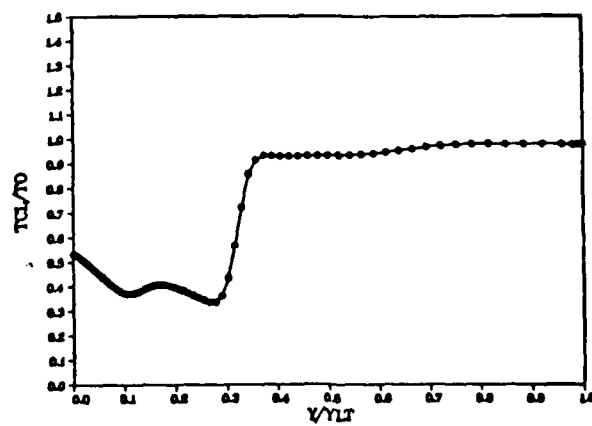
N=300K PW/PPI XK1 47%NSR
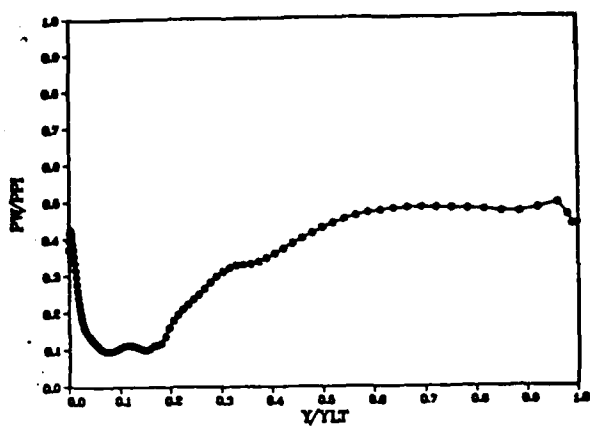
N=325K PW/PPI XK1 47%NSR
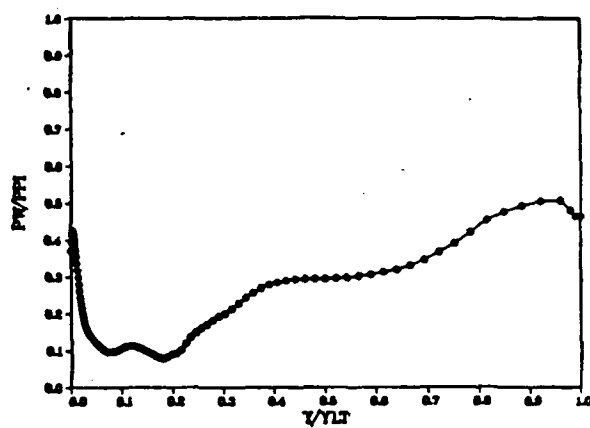
N=300K PCL/PPI XK1 47%NSR
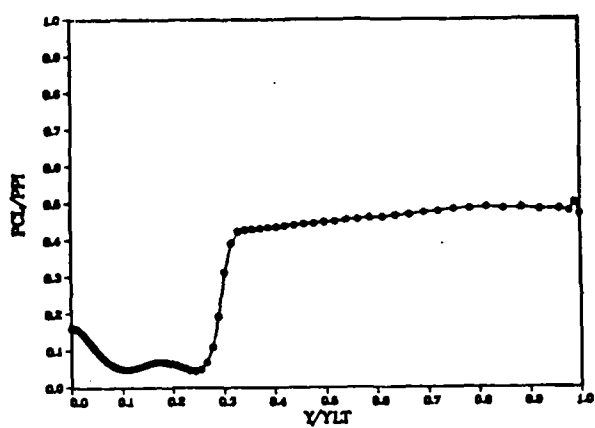
N=325K PCL/PPI XK1 47%NSR
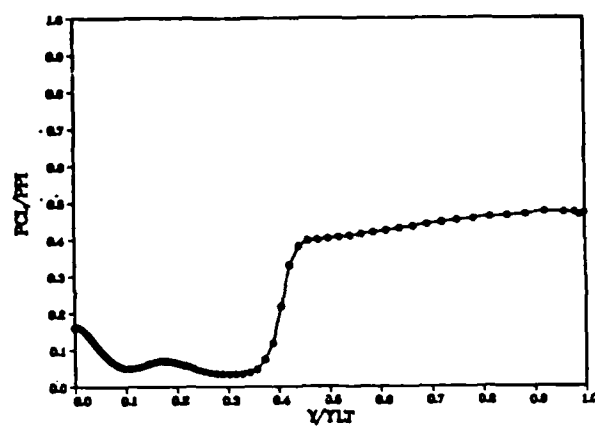
N=300K TCL/TO XK1 47%NSR

N=325K TCL/TO XK1 47%NSR

N=350K PW/PPI XK1 47%NSR

N=375K PW/PPI XK1 47%NSR

N=350K PCL/PPI XK1 47%NSR

N=375K PCL/PPI XK1 47%NSR

N=350K TCL/TO XK1 47%NSR

N=375K TCL/TO XK1 47%NSR

346

N=400K PW/PPI XK1 47%NSR

N=400K PCL/PPI XK1 47%NSR

N=400K TCL/TO XK1 47%NSR

APPENDIX L

NUMERICAL CASE 4E COMPUTATIONAL DETAILS

For this numerical case a second sensitivity analysis of the adverse pressure gradient modification to the basic Cebeci-Smith eddy viscosity turbulence model was accomplished. Flow conditions were again based on the actual UTRC experimental inflow profiles, with exit pressure set at 47% of normal shock recovery. The full inner region modifications were employed, but the change rate in the outer region (Clauser) constant k_2 was relaxed from 0.015 to 0.010. The solution was then marched forward from the case 4b converged solution for these flow conditions with this less stiff eddy viscosty turbulence model. Again, the core flow normal shock is observed to oscillate in the diffuser without "unstarting." Figure 92, repeated here, presents this information. The selected Mach contour plots present this flow behavior graphically, showing the "over-recovery" from the wall boundary layer separation. Each Mach contour plot is again presented from M = 0.0 to M = 5.0, in increments of 0.20.

This numerical experiment required 19.3 hours of CRAY 1 CPU time.

XK2 TIME HISTORY 47%NSR

348
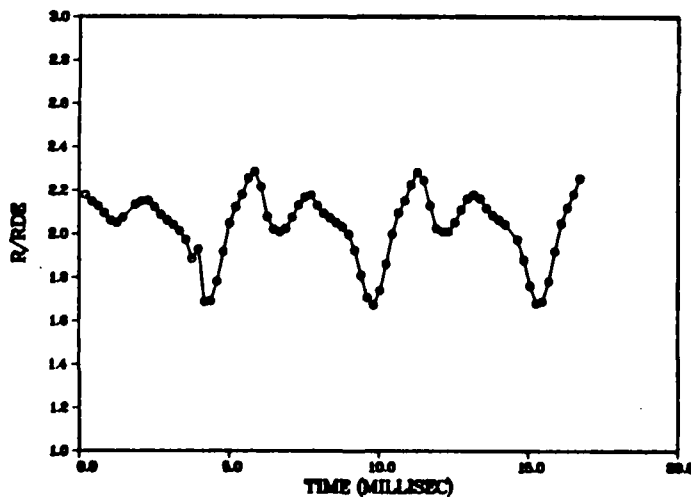
TABLE XII

NUMERICAL CASE 4E COMPUTED SHOCK POSITION VS TIME

N	CFL	TIME	R/R_{de}	SPOS
Number of Iterations		(Milliseconds)		
0		0	2.054097	0.342909
5,000	.50	0.209000	2.179000	0.383541
10,000		0.418040	2.148200	0.373519
15,000		0.627090	2.127600	0.366825
20,000		0.836130	2.096400	0.356675
25,000		1.045180	2.061800	0.345410
30,000		1.254220	2.050500	0.341730
35,000		1.463270	2.074990	0.349706
40,000		1.672310	2.102130	0.358535
45,000		1.881360	2.134600	0.369112
50,000		2.090400	2.150900	0.374402
55,000		2.301450	2.152600	0.374952
60,000		2.508490	2.124000	0.365651
65,000		2.717530	2.088900	0.354235
70,000		2.926580	2.062000	0.345490
75,000		3.135620	2.041700	0.338862
80,000		3.344670	2.014300	0.329966
85,000		3.553710	1.973000	0.316537
90,000		3.762760	1.886100	0.288268
95,000		3.971800	1.930100	0.251116
100,000		4.180800	1.687400	0.223640
105,000		4.389850	1.691395	0.224918
110,000		4.598890	1.782483	0.254550
115,000		4.807940	1.918267	0.298722
120,000		5.016990	2.048549	0.341104
125,000		5.226030	2.123471	0.365477
130,000		5.435070	2.180625	0.384070
135,000		5.644120	2.255495	0.408426
140,000		5.853160	2.286177	0.418407
145,000		6.062210	2.216222	0.395650
150,000		6.271250	2.079187	0.351071
155,000		6.479250	2.021720	0.332376
160,000		6.689340	2.009085	0.328266
165,000		6.898380	2.024656	0.333332
170,000		7.107430	2.075383	0.349833
175,000		7.316470	2.131902	0.368220
180,000		7.525520	2.168335	0.380078
185,000		7.734560	2.178318	0.383319
190,000		7.943610	2.131387	0.368052
195,000		8.152650	2.094292	0.355985
200,000		8.361660	2.073585	0.349249

N	CFL	TIME	R/R_{de}	SPOS
Number of Iterations		(Milliseconds)		
205,000	.50	8.570700	2.051752	0.342146
210,000		8.779740	2.033054	0.336063
215,000		8.988790	1.999435	0.325127
220,000		9.197830	1.925090	0.300942
225,000		9.406880	1.810901	0.263795
230,000		9.615920	1.708070	0.230343
235,000		9.824970	1.673300	0.220017
240,000		10.034010	1.739862	0.240685
245,000		10.243060	1.862145	0.280465
250,000		10.452100	1.998779	0.324913
255,000		10.661150	2.094523	0.356060
260,000		10.870190	2.151935	0.374737
265,000		11.079240	2.224869	0.398463
270,000		11.288280	2.282467	0.417200
275,000		11.497320	2.244293	0.404782
280,000		11.706370	2.130172	0.367657
285,000		11.915410	2.025790	0.333701
290,000		12.124460	2.010736	0.328803
295,000		12.333500	2.011354	0.329004
300,000		12.542510	2.051986	0.342222
305,000		12.751550	2.109980	0.361088
310,000		12.960590	2.160317	0.377463
315,000		13.169640	2.178744	0.383458
320,000		13.378680	2.161871	0.377969
325,000		13.587730	2.117372	0.363493
330,000		13.796770	2.085540	0.353138
335,000		14.005820	2.063735	0.346044
340,000		14.214860	2.043592	0.339492
350,000		14.632950	1.972451	0.316349
355,000		14.842000	1.880451	0.286420
360,000		15.051040	1.762268	0.247974
365,000		15.260090	1.680970	0.221527
370,000		15.469130	1.688610	0.223866
375,000		15.678170	1.782506	0.254558
380,000		15.887220	1.918999	0.298960
385,000		16.096260	2.047002	0.340601
390,000		16.305310	2.119449	0.364169
395,000		16.514350	2.180989	0.384188
400,000		16.723360	2.254392	0.408067

XK2 MACH CONTOURS N=100K 47%NSR
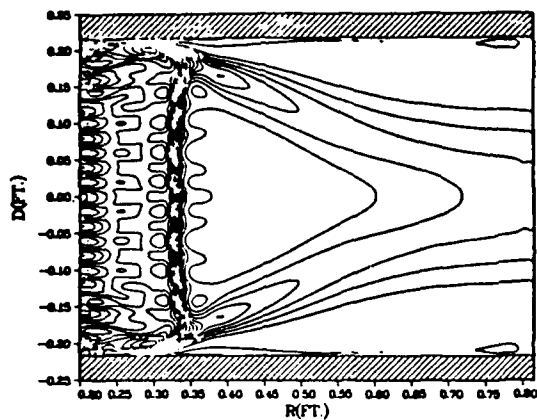
XK2 MACH CONTOURS N=150K 47%NSR
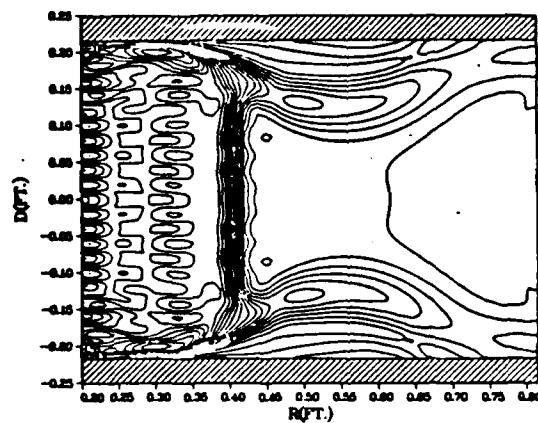
XK2 MACH CONTOURS N=200K 47%NSR
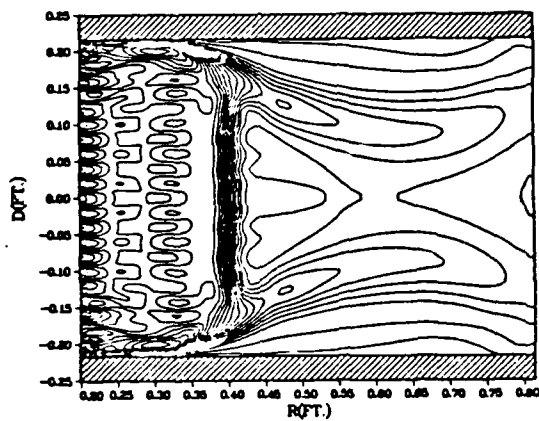
XK2 MACH CONTOURS N=225K 47%NSR
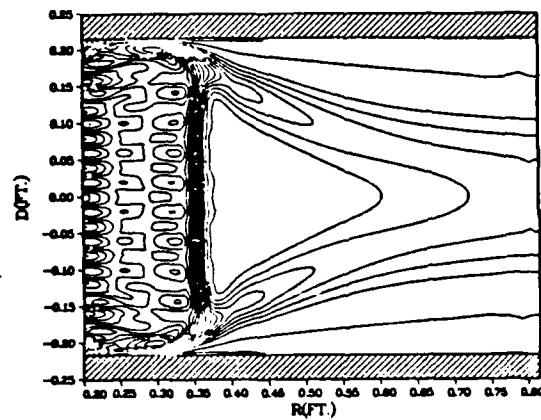
XK2 MACH CONTOURS N=250K 47%NSR
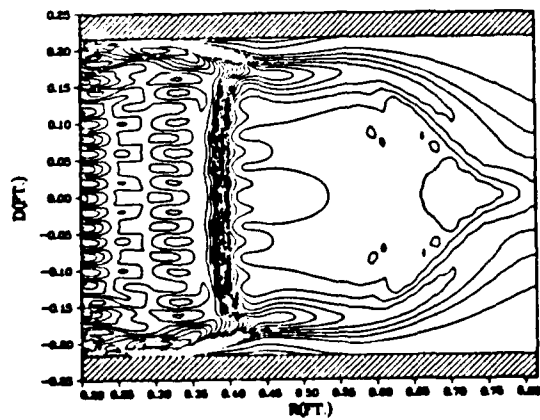
XK2 MACH CONTOURS N=275K 47%NSR

351
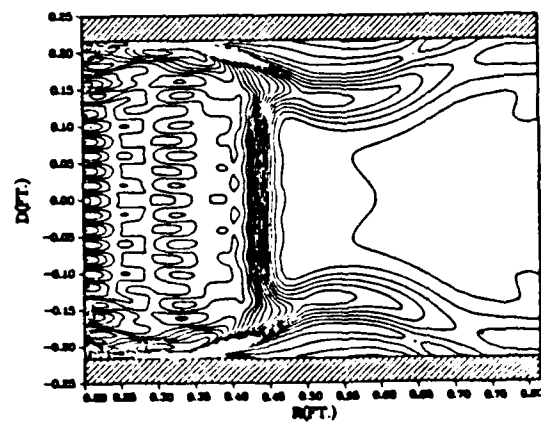
XK2 MACH CONTOURS N=300K 47%NSR
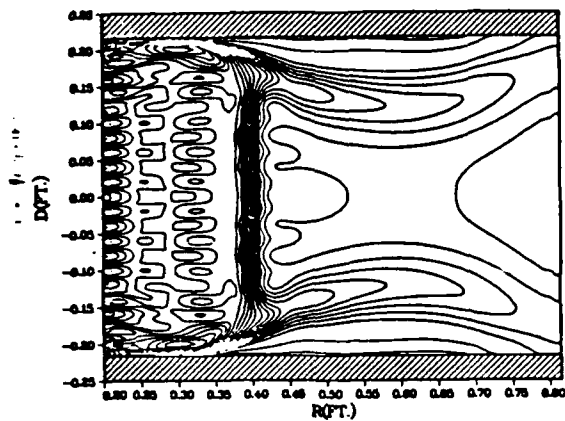
XK2 MACH CONTOURS N=325K 47%NSR
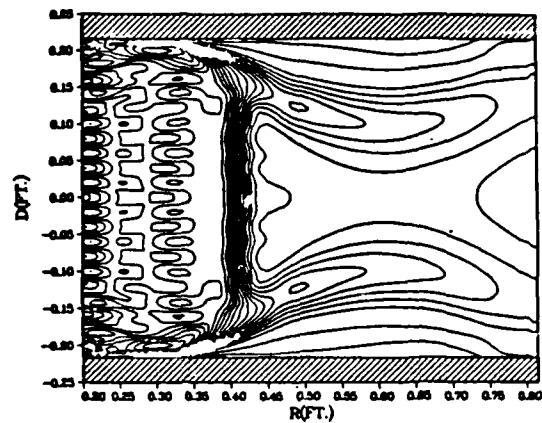
XK2 MACH CONTOURS N=350K 47%NSR
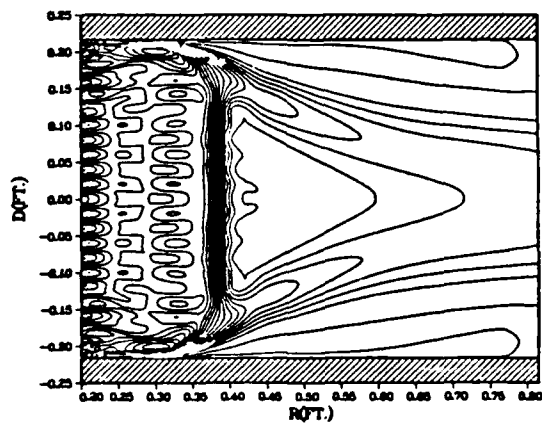
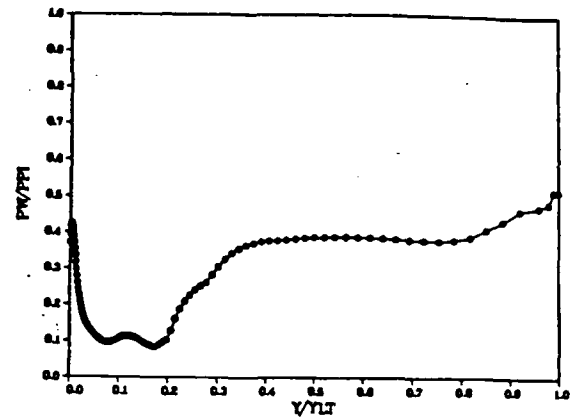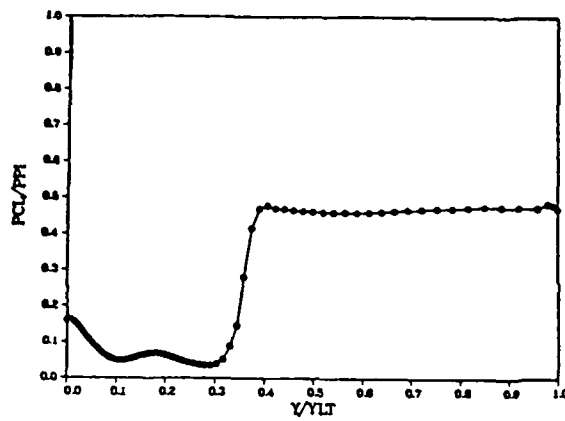XK2 MACH CONTOURS N=375K 47%NSR
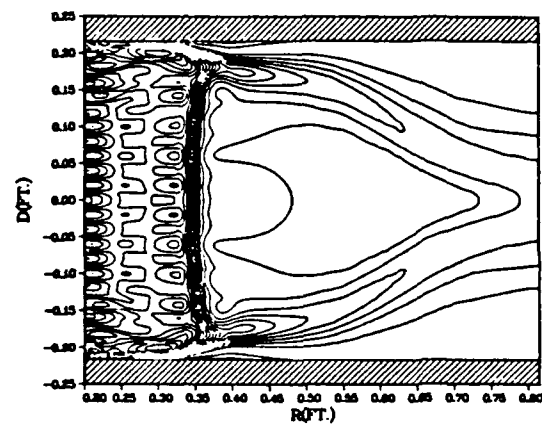
XK2 MACH CONTOURS N=400K 47%NSR
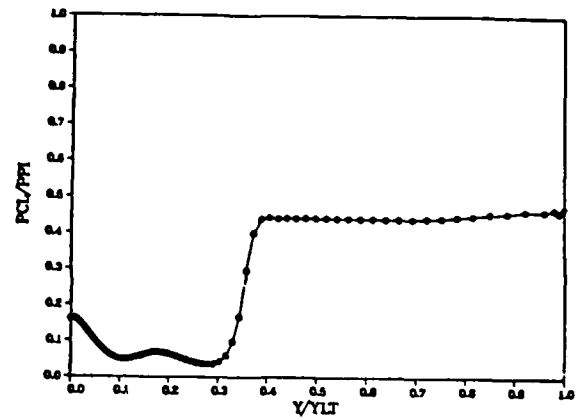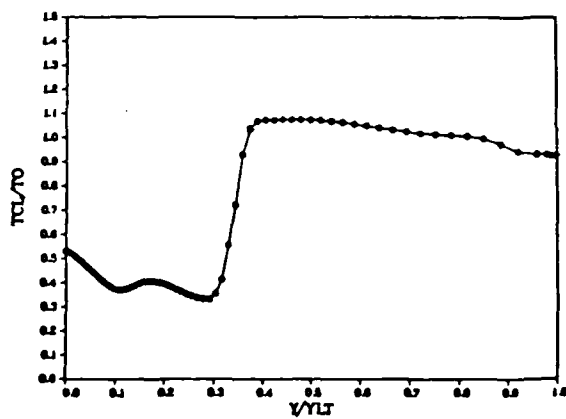
352
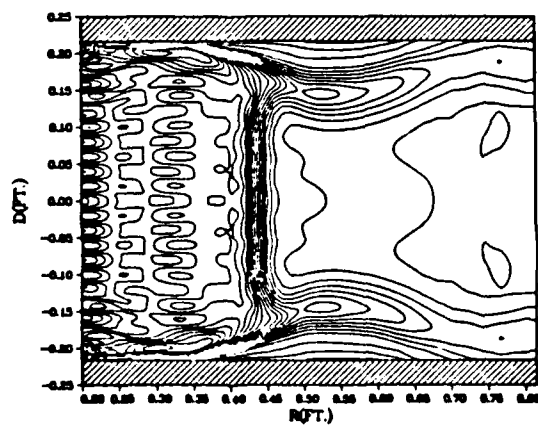
N=150K PW/PPI XK2 47%NSR
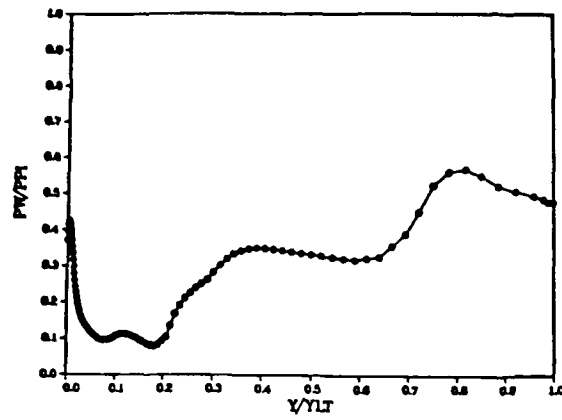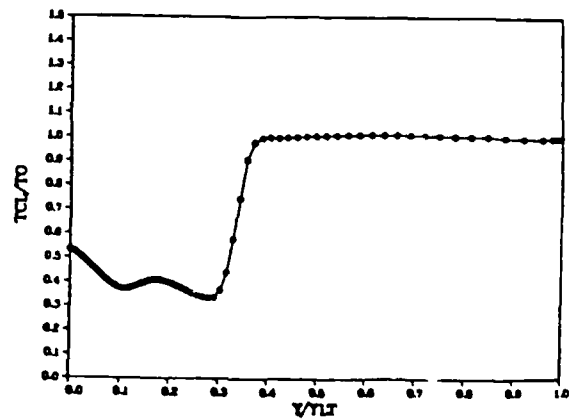
N=200K PW/PPI XK2 47%NSR
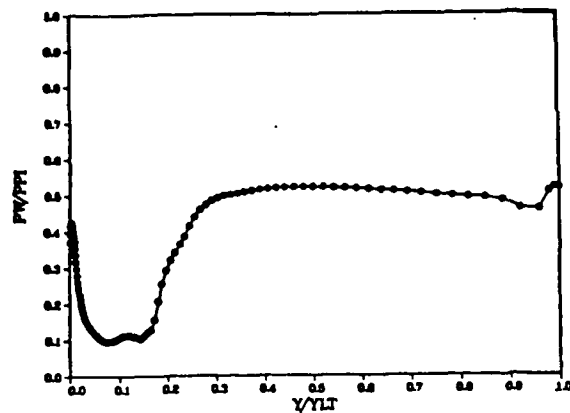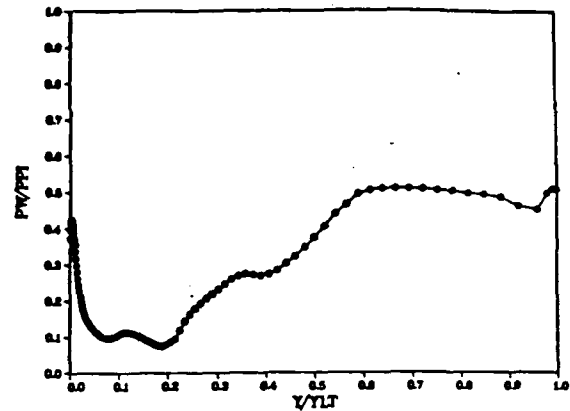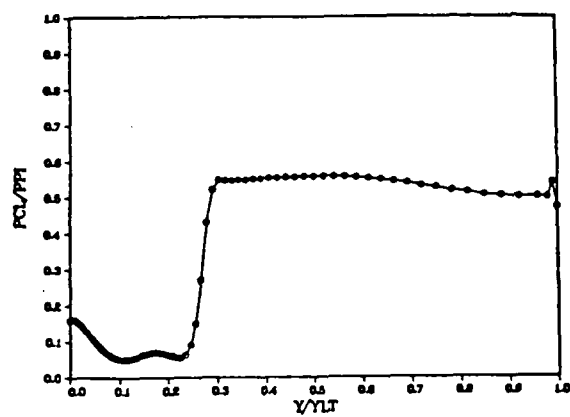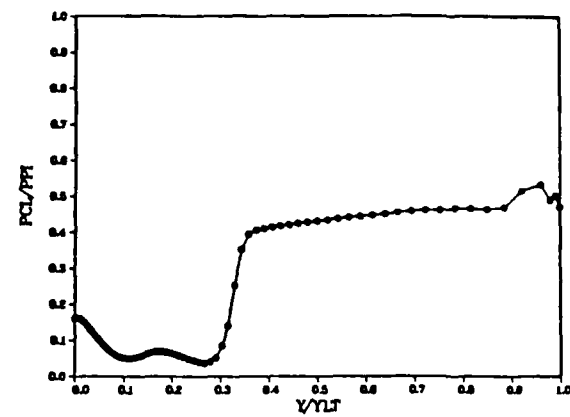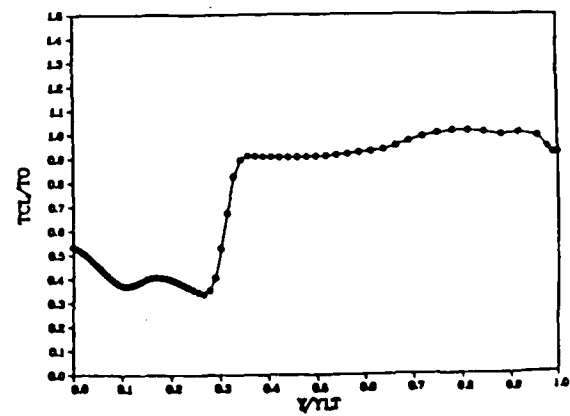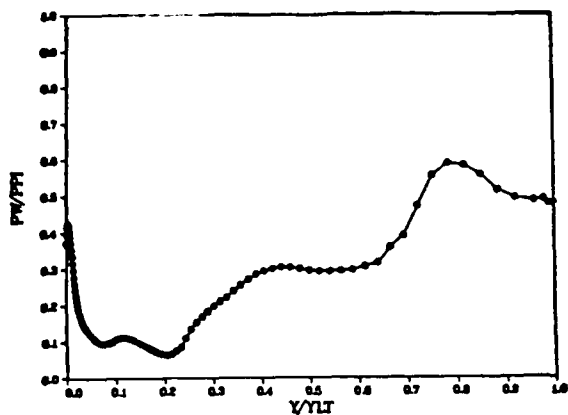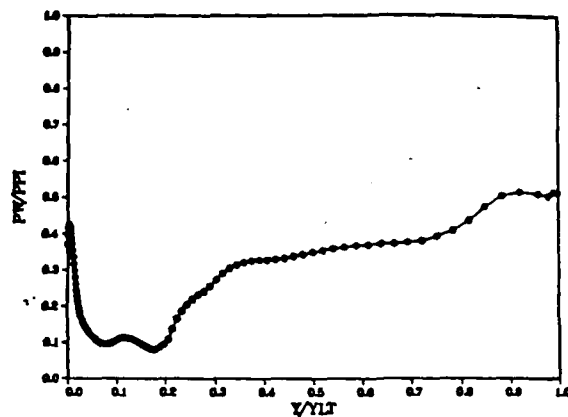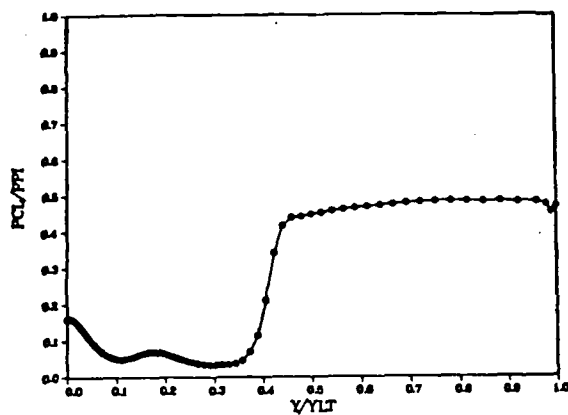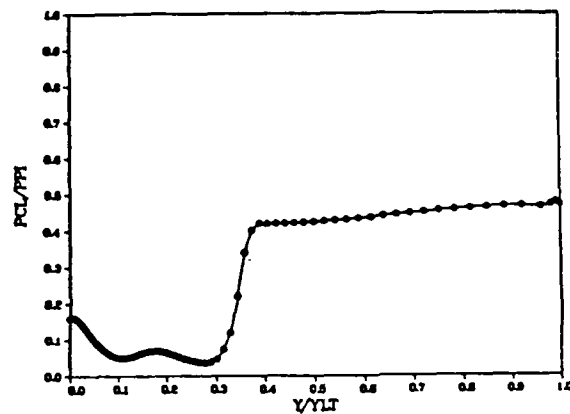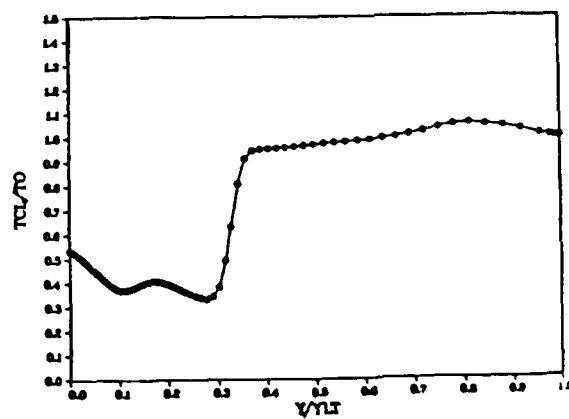
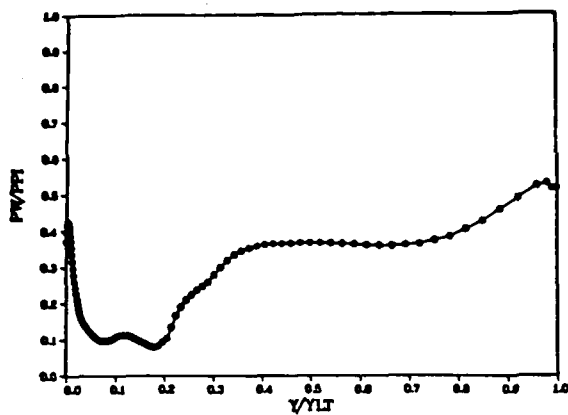N=150K PCL/PPI XK2 47%NSR

N=200K PCL/PPI XK2 47%NSR

N=150K TCL/TO XK2 47%NSR

N=200K TCL/TO XK2 47%NSR

353

N=225K PW/PPI XK2 47%NSR

N=250K PW/PPI XK2 47%NSR

N=225K PCL/PPI XK2 47%NSR

N=250K PCL/PPI XK2 47%NSR
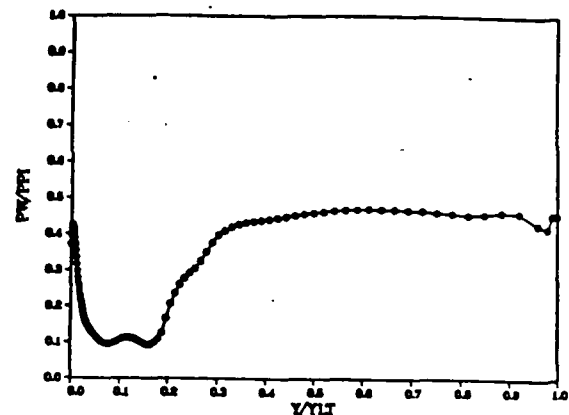
N=225K TCL/TO XK2 47%NSR
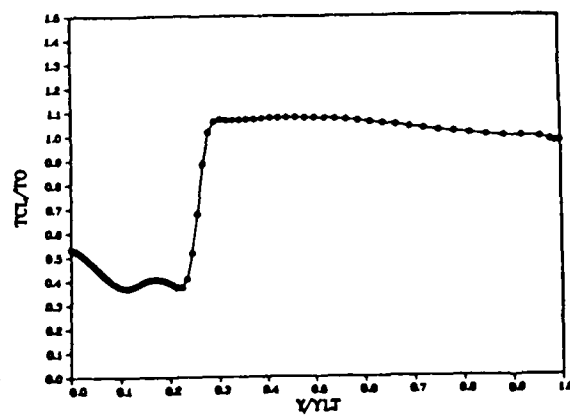
N=250K TCL/TO XK2 47%NSR

354

N=275K PW/PPl XK2 47%NSR

N=300K PW/PPl XK2 47%NSR

N=275K PCL/PPl XK2 47%NSR

N=300K PCL/PPl XK2 47%NSR
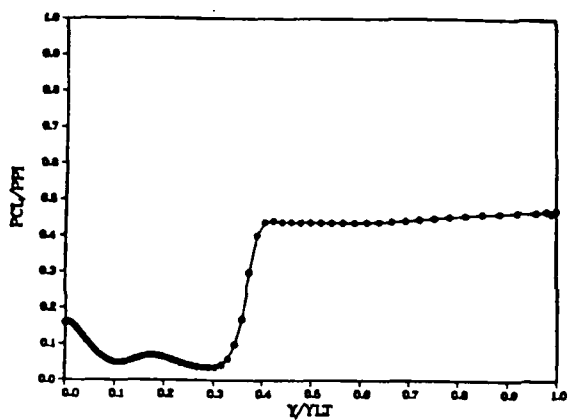
N=275K TCL/TO XK2 47%NSR
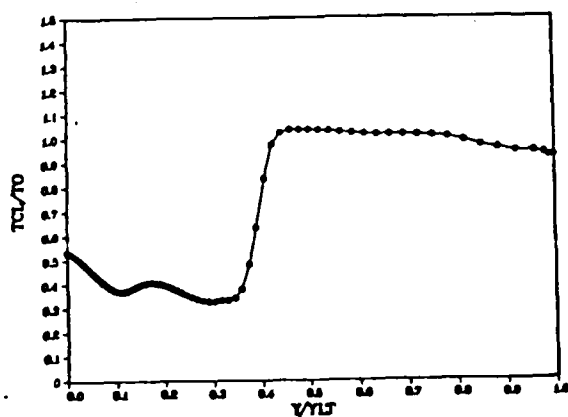
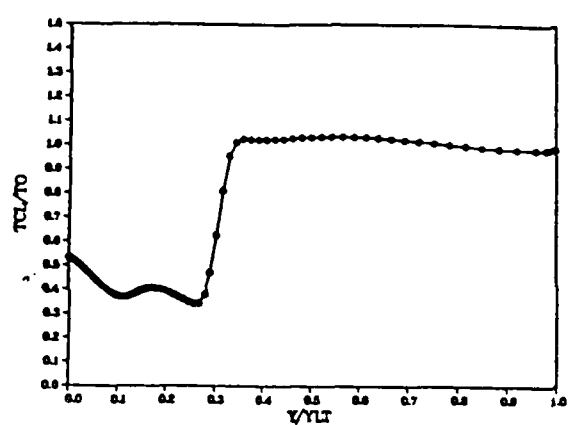N=300K TCL/TO XK2 47%NSR

N=325K PW/PPI XK2 47%NSR
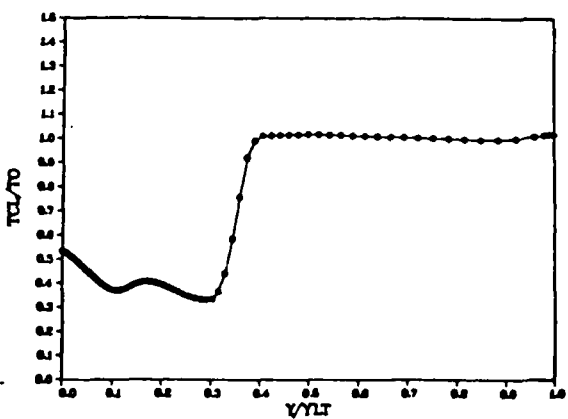
N=350K PW/PPI XK2 47%NSR
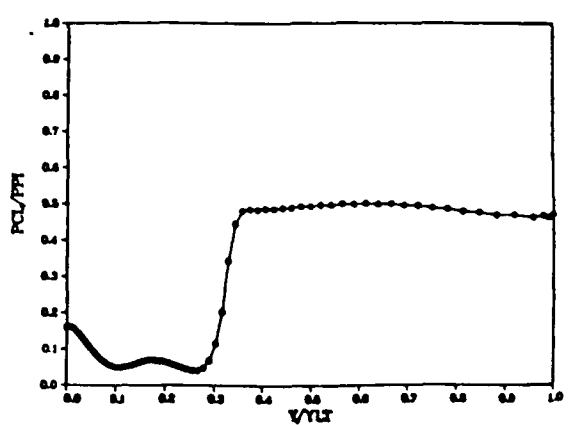
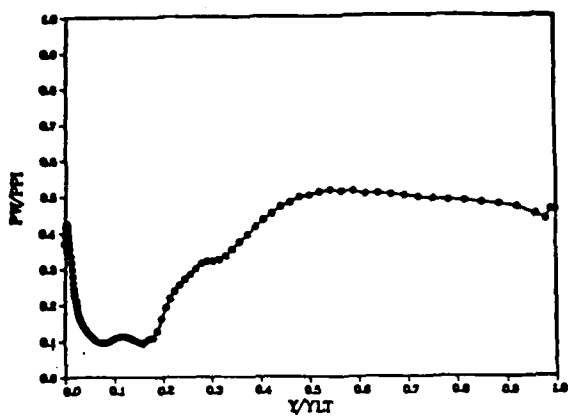N=325K PCL/PPI XK2 47%NSR

N=350K TCL/TO XK2 47%NSR
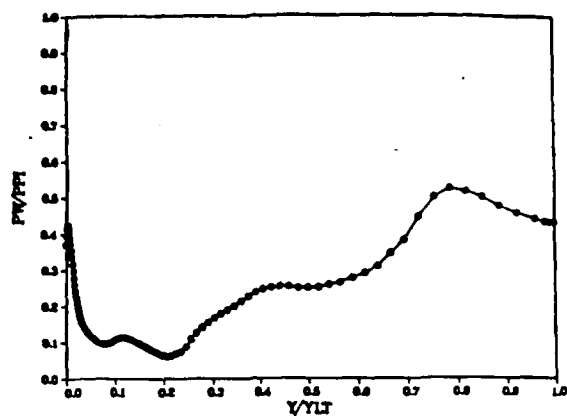
N=325K TCL/TO XK2 47%NSR

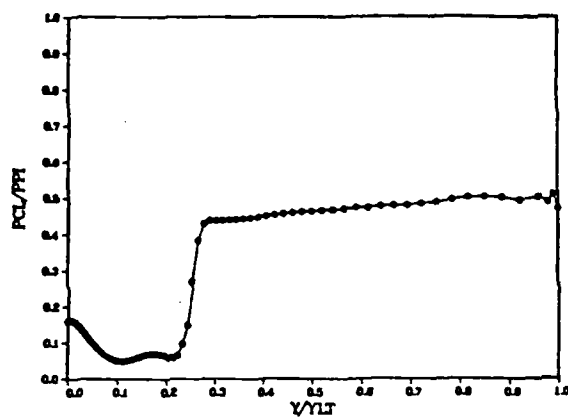N=350K PCL/PPI XK2 47%NSR

356
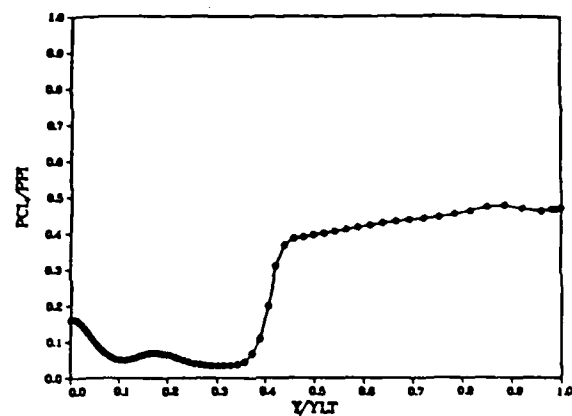
N=375K PW/PPI XK2 47%NSR

N=400K PW/PPI XK2 47%NSR

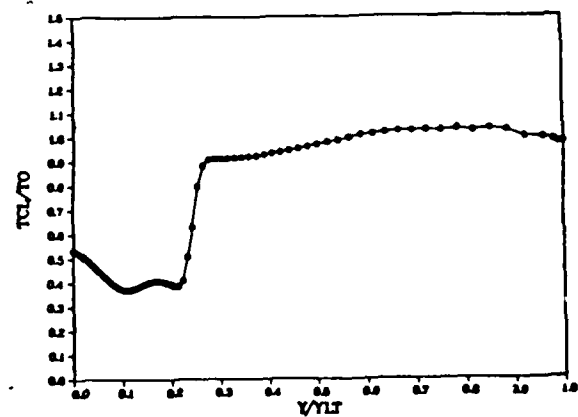N=375K PCL/PPI XK2 47%NSR

N=400K PCL/PPI XK2 47%NSR
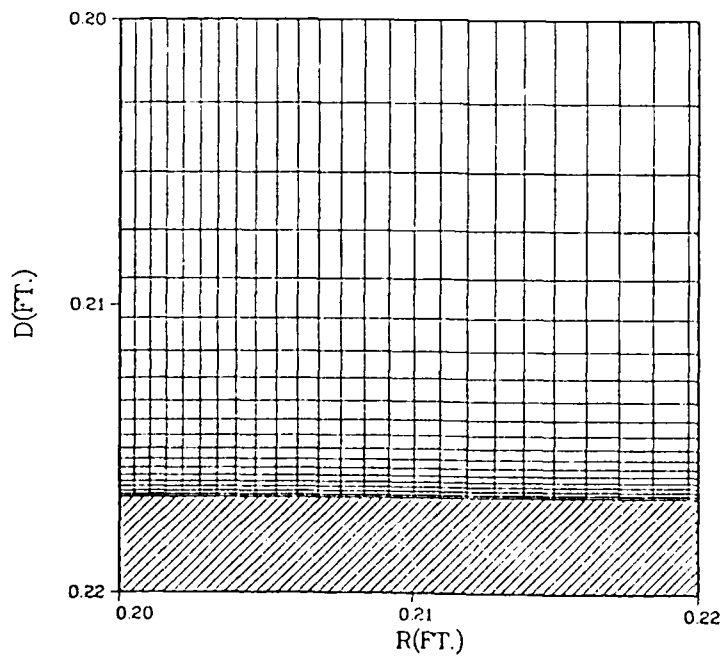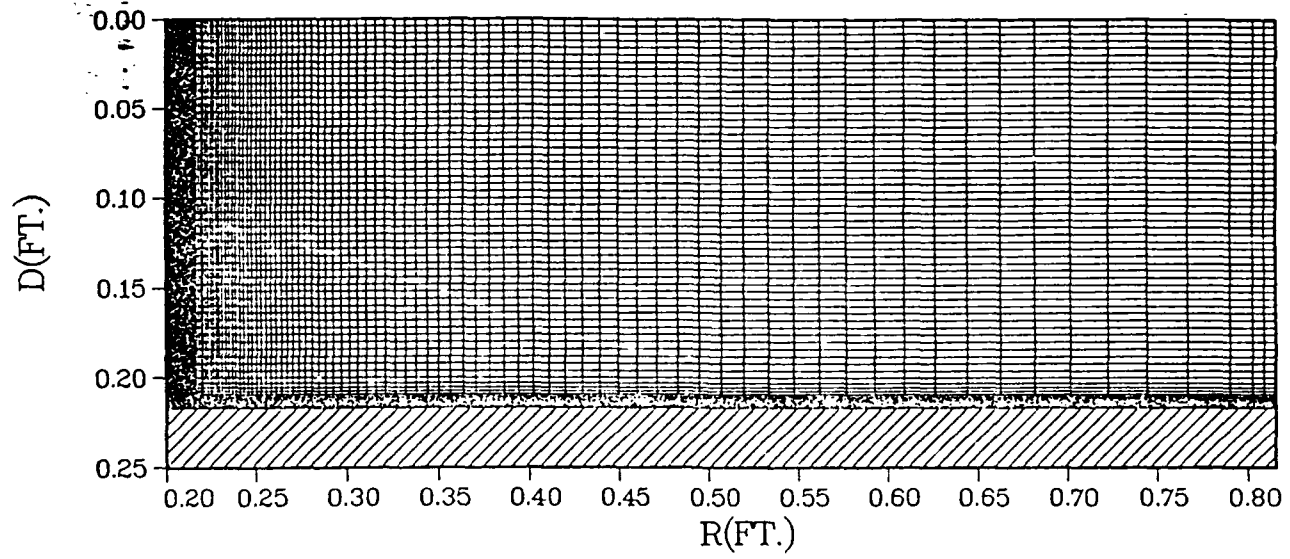
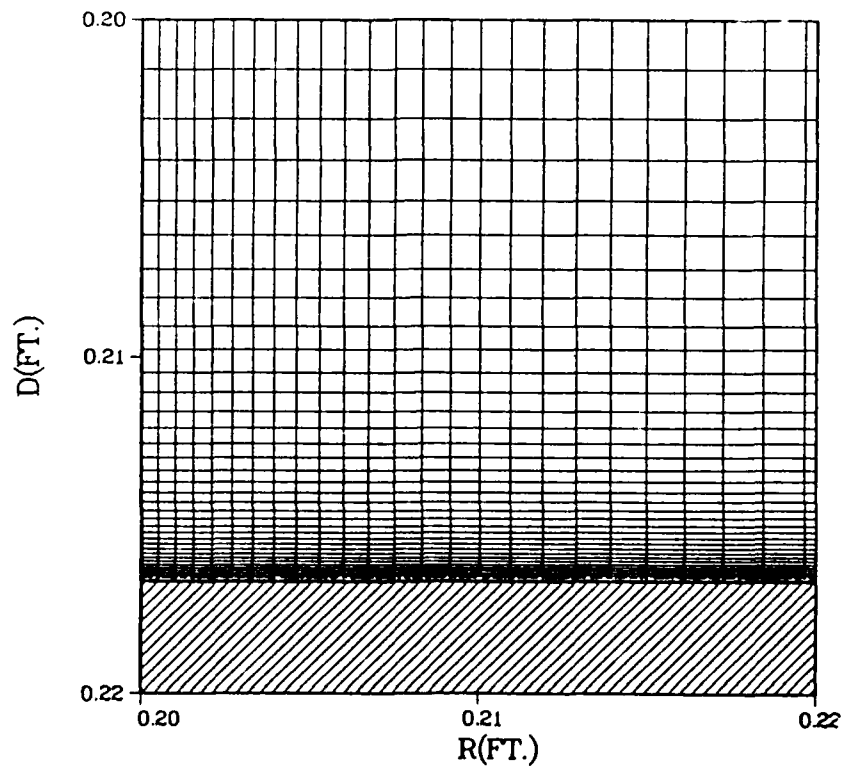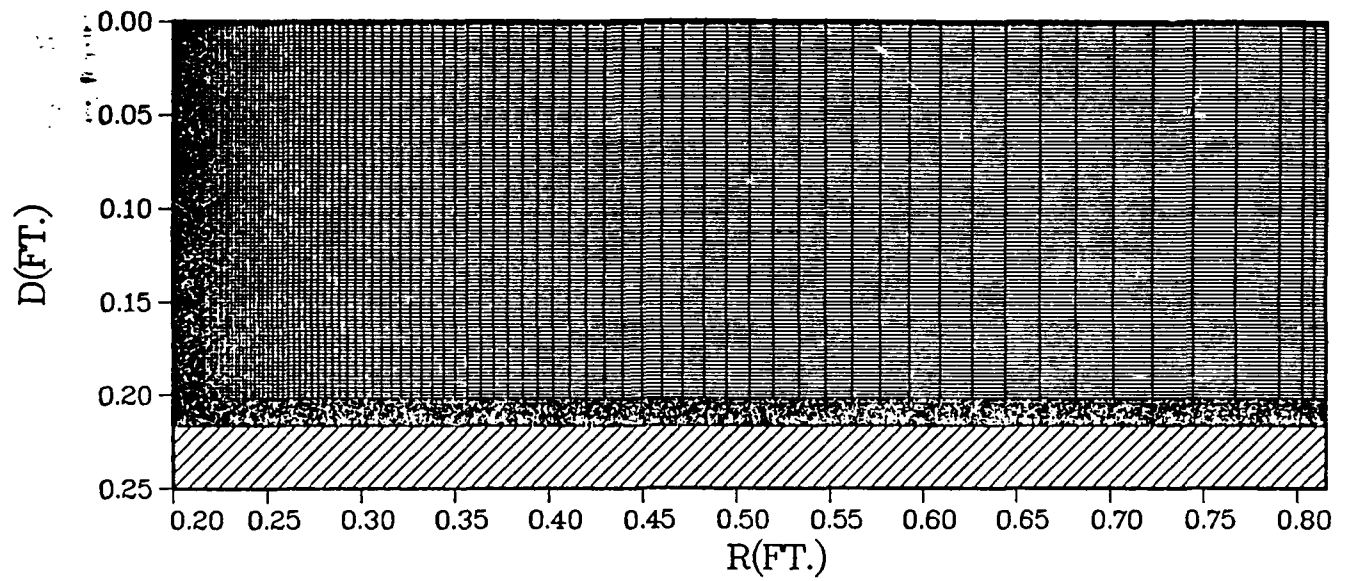N=375K TCL/TO XK2 47%NSR

N=400K TCL/TO XK2 47%NSR
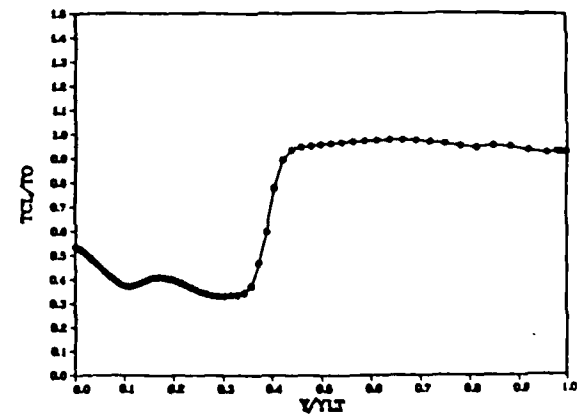
APPENDIX M

COMPUTATIONAL GRIDS

Plots of the key computational grids employed in this investigation are provided on the following pages. All of the grids were purely rectangular and employed exponentially stretched mesh spacing as described in Chapter III.
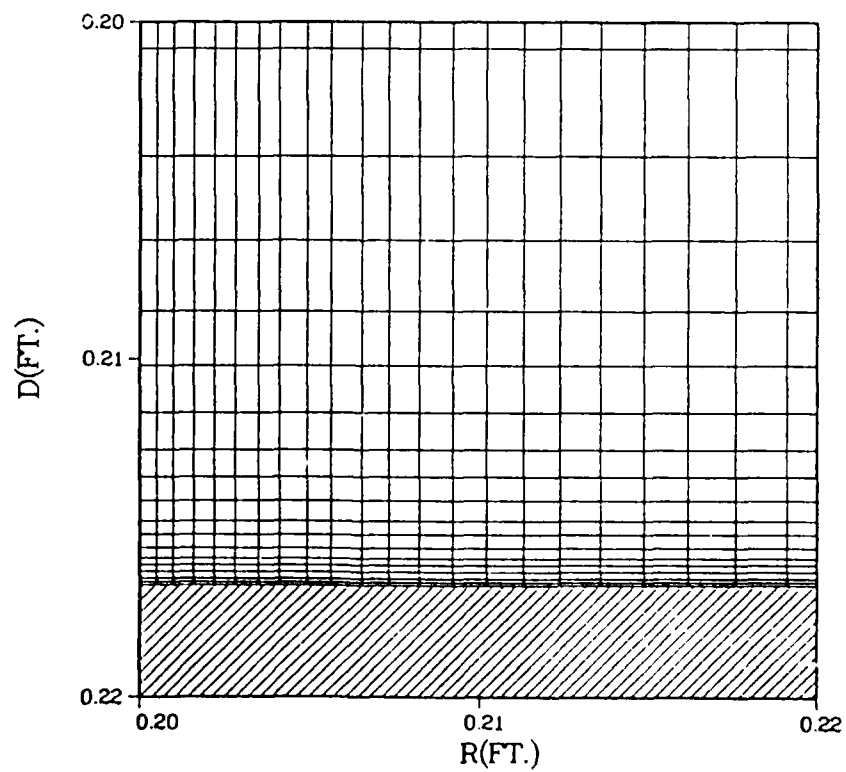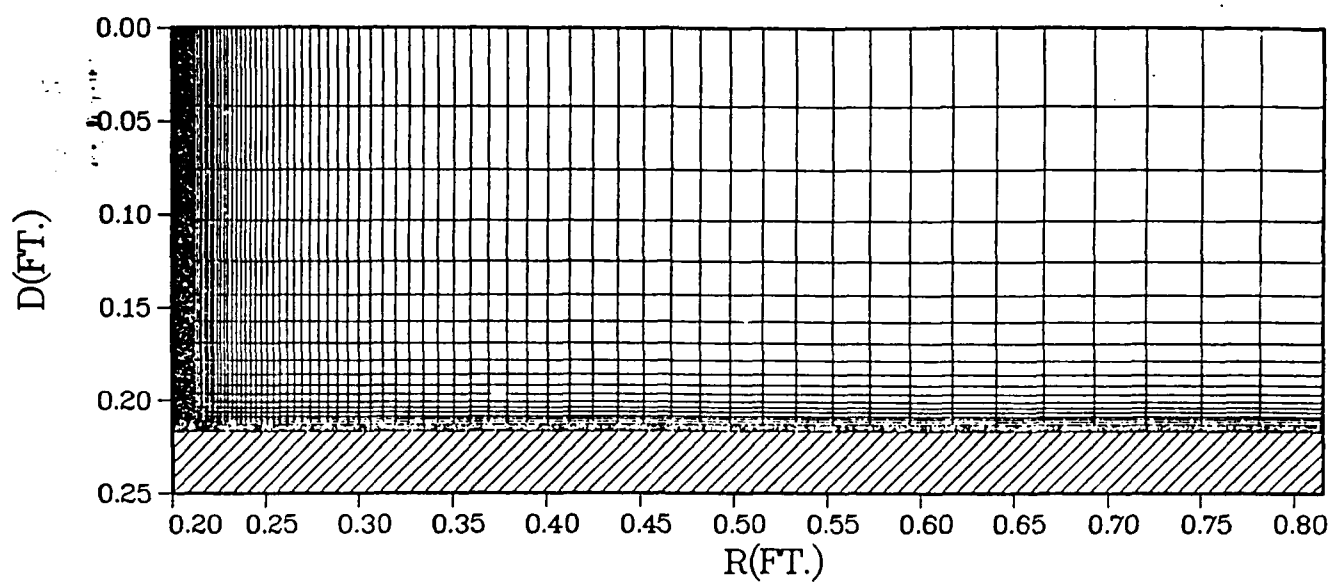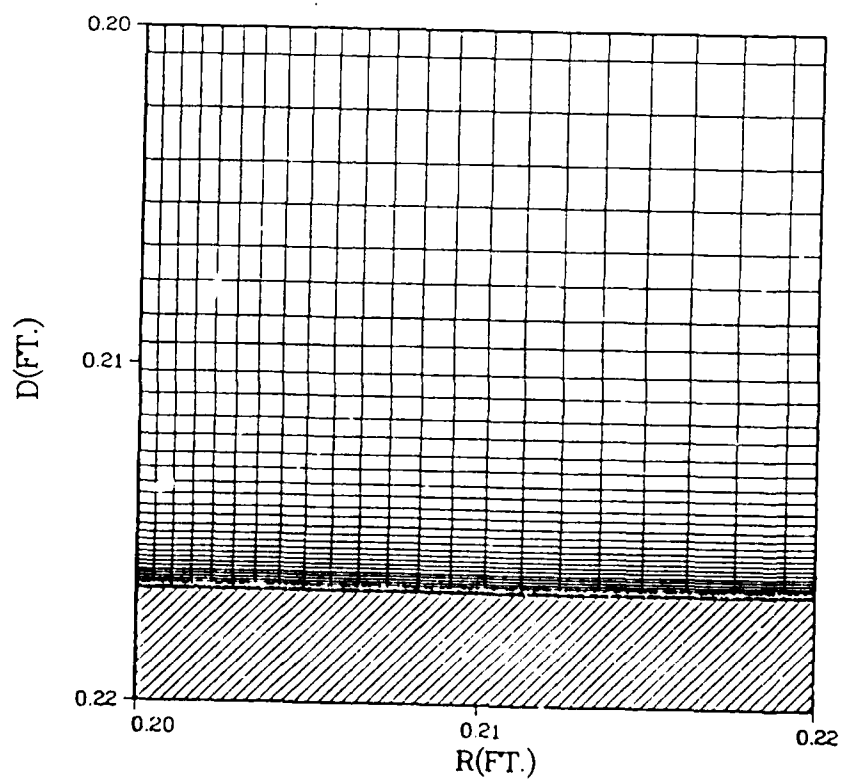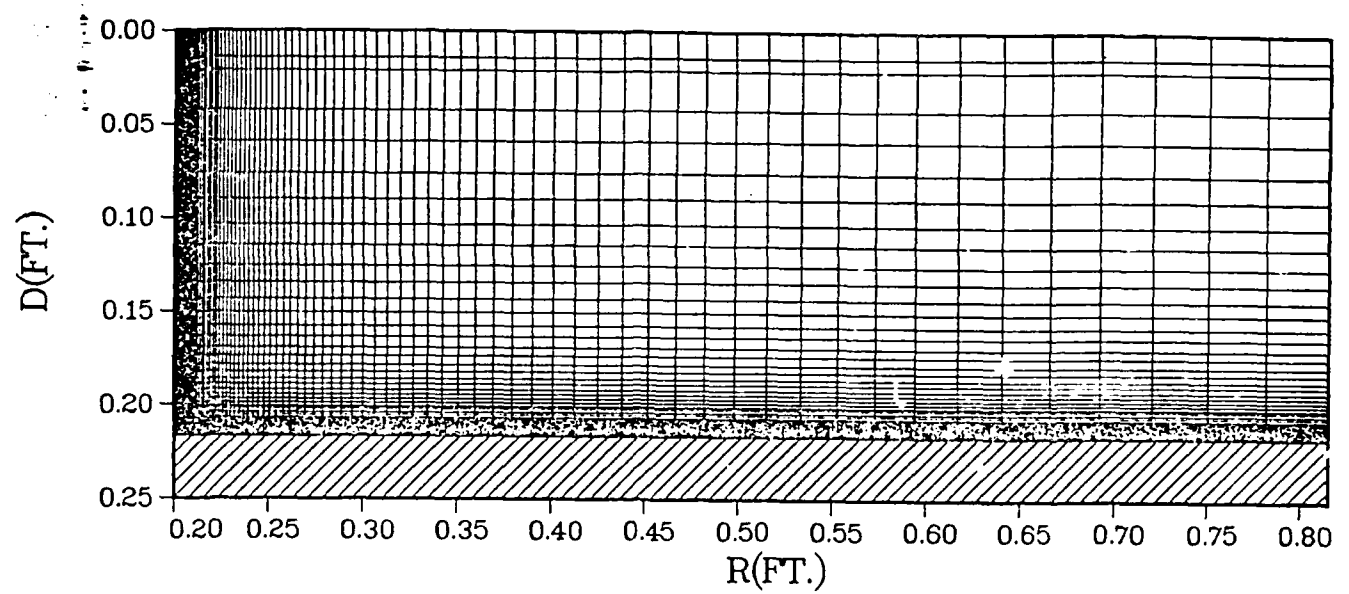
70X103 GRID

140 X 103 GRID

30 X 80 GRID

60X80 GRID

90X80 GRID
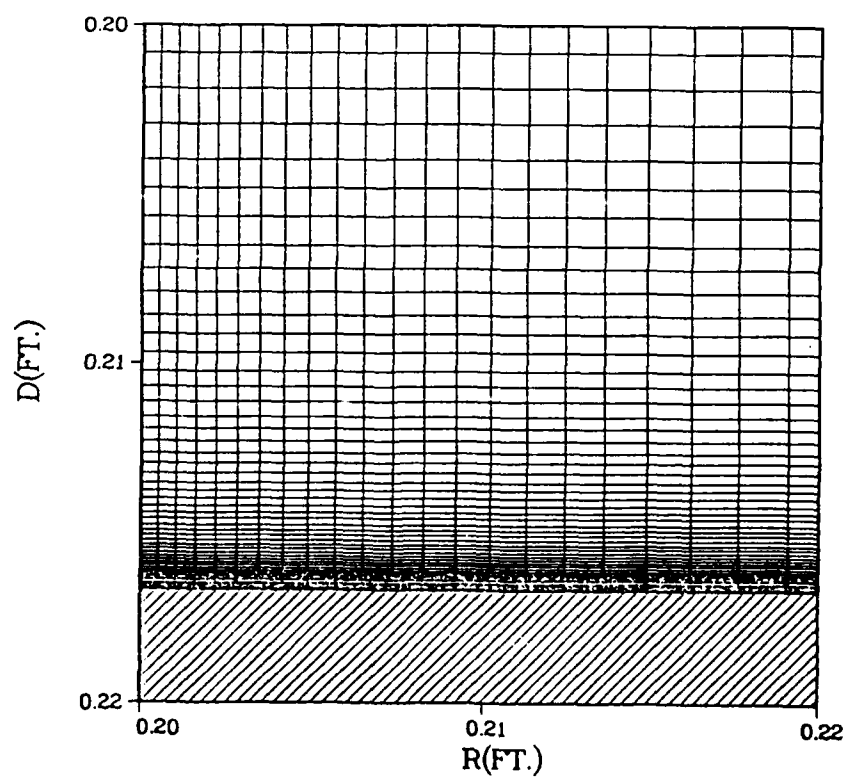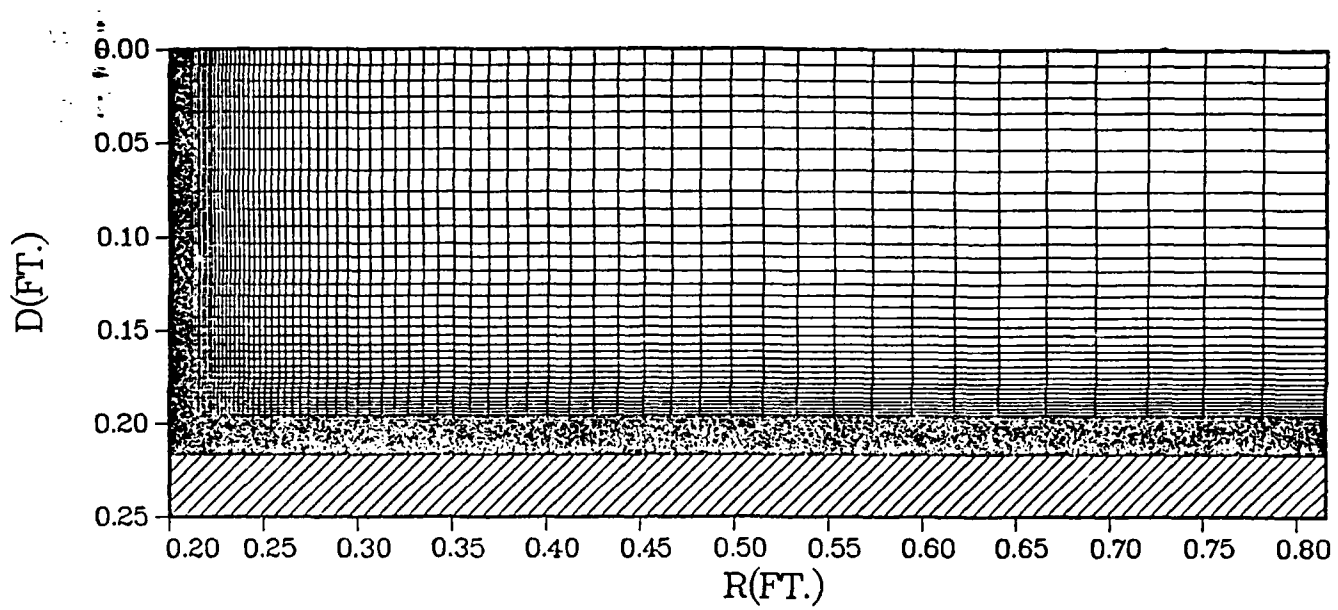
APPENDIX N

RICHARDSON'S EXTRAPOLATION TECHNIQUE

A traditional Richardson's extrapolation technique was applied to the wall pressure solution obtained for the 60% NSR actual inflow solution (numerical case 4a). The basic 70X103 grid was replaced with a 140X103 grid, where the spacing between the grid points normal to the wall was half that of the basic grid. For the 70X103 grid, Δx_{min} = 0.0001 ft. (the spacing for the first grid point away from the wall; i = 1). For the 140X103 grid, Δx_{min} = 0.00005 ft. For each point in the streamwise (j) direction, the extrapolation technique was applied to develop the wall pressure ratio for a theoretical zero grid spacing (an infinite number of grid points). The extrapolations for selected streamwise locations (j = 20, 30, 40, 50, 60, 65, 70, 72, 75, 80, 90, 95) are presented in this appendix, as are the resulting wall pressure ratio plot and a comparison of that plot to the solutions on the two computational grids. Except for the region where separation/recirculation affects the solution, the extrapolation technique shows very little change in the solutions for grid refinement. Even in the separation/recirculation region, the change in the computed wall pressure solution is minor. Thus, the truncation error is demonstrated not to be attributable to grid spacing.

WALL PR RATIO COMPARISON 60%NSR ACTUAL FLOW
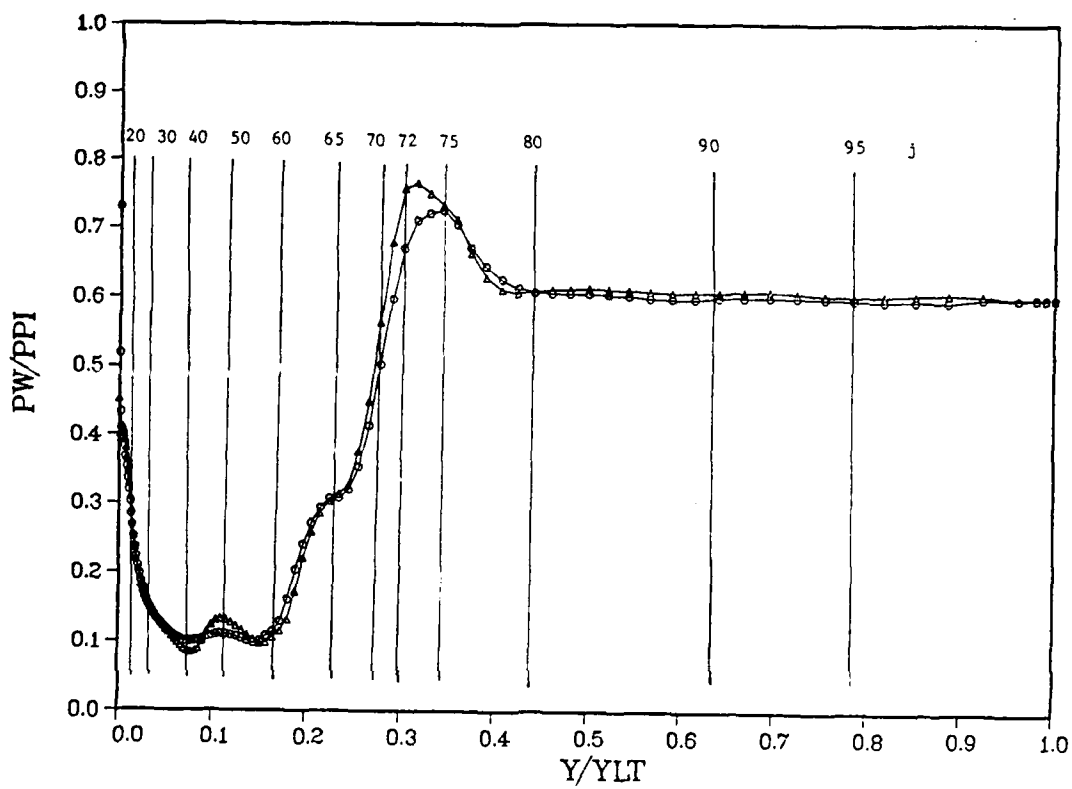
WP Ratio 60%NSR Richardson's Ext. J=20
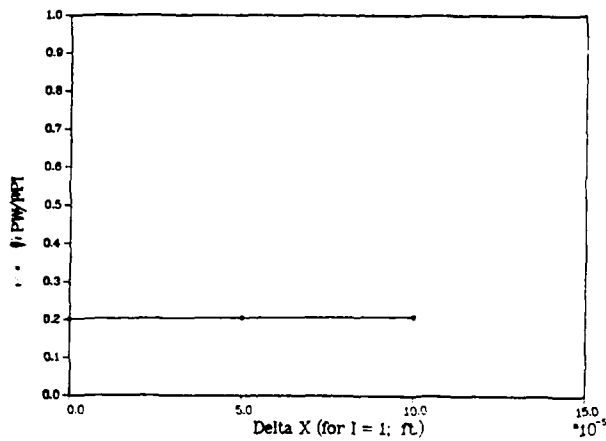
WP Ratio 60%NSR Richardson's Ext. J=30
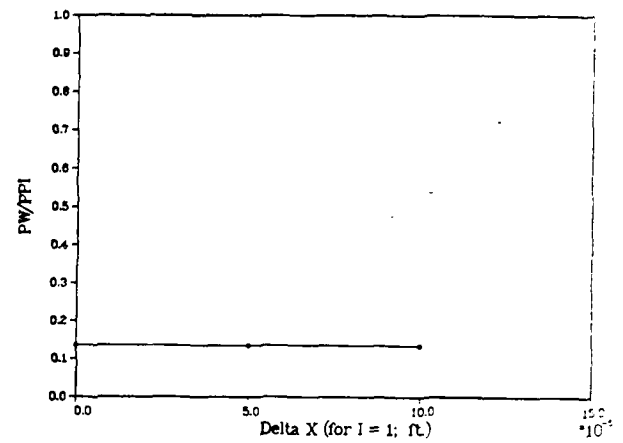
WP Ratio 60%NSR Richardson's Ext. J=40

WP Ratio 60%NSR Richardson's Ext. J=50

WP Ratio 60%NSR Richardson's Ext. J=60

WP Ratio 60%NSR Richardson's Ext. J=65

366

WP Ratio 60%NSR Richardson's Ext. J=70

WP Ratio 60%NSR Richardson's Ext. J=72
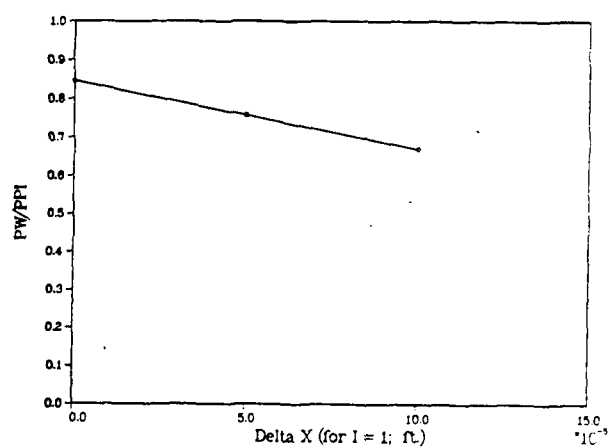
WP Ratio 60%NSR Richardson's Ext. J=75

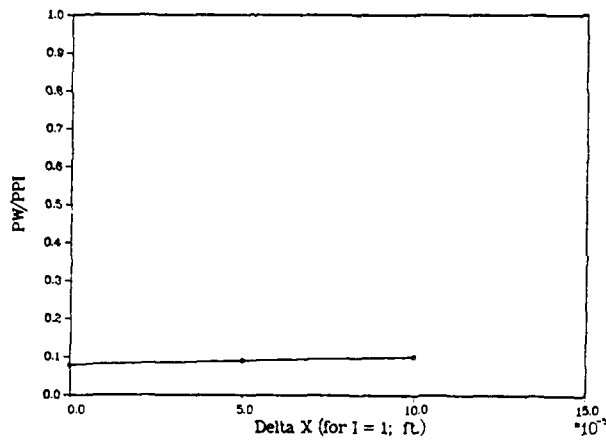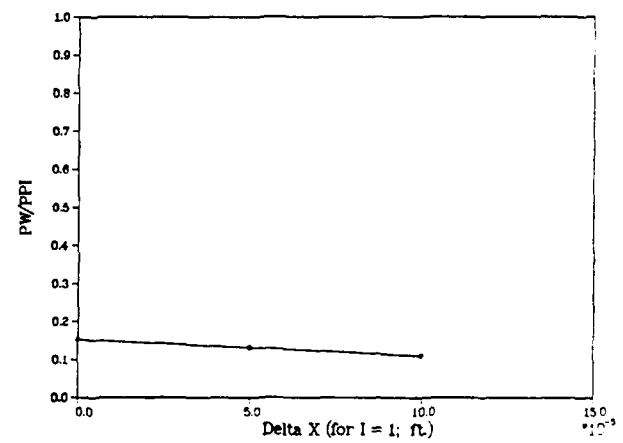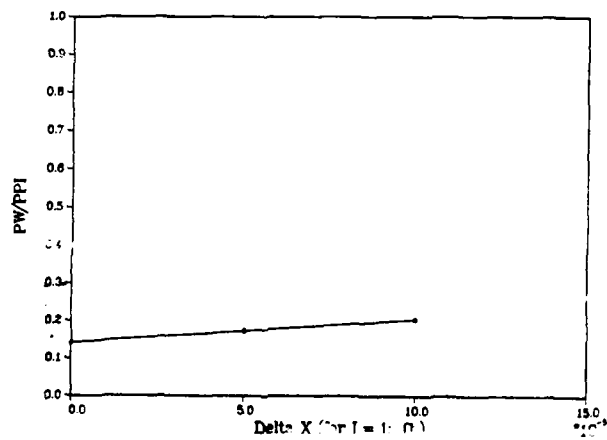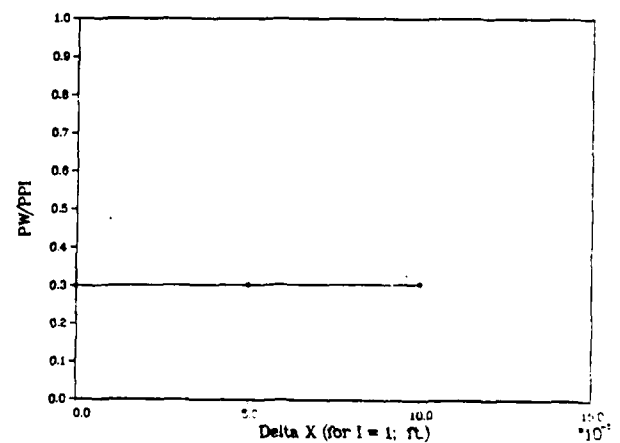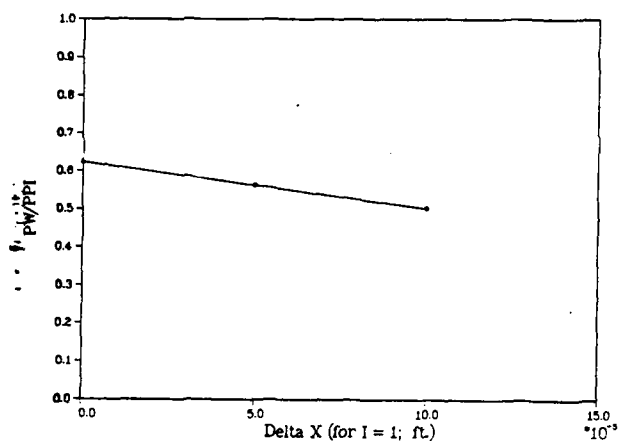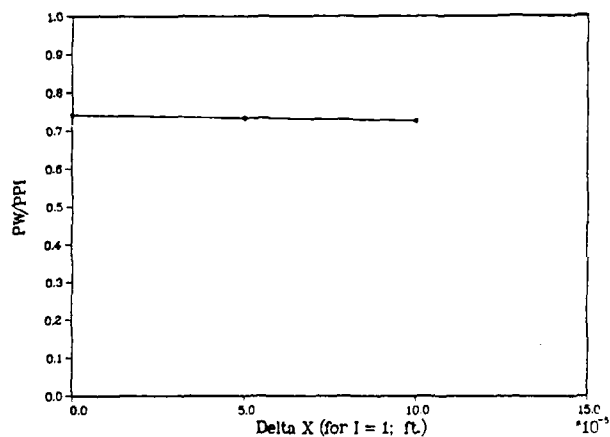## WP Ratio 60%NSR Richardson's Ext. J=80
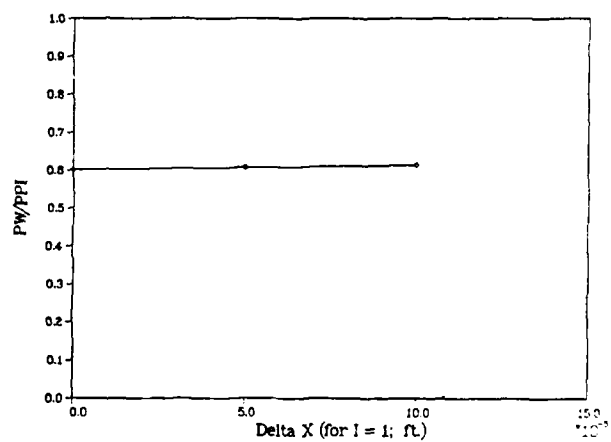
WP Ratio 60%NSR Richardson's Ext. J=90
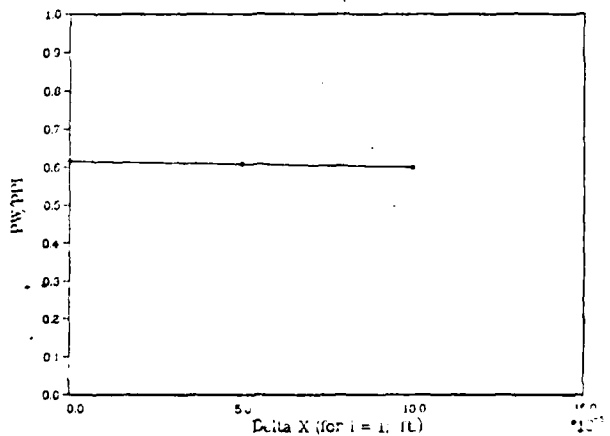
WP Ratio 60%NSR Richardson's Ext. J=95

367
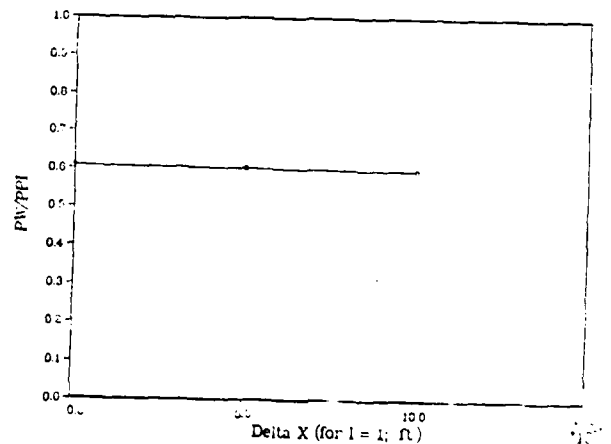
WP Ratio 60%NSR Richardson's Extrapolation
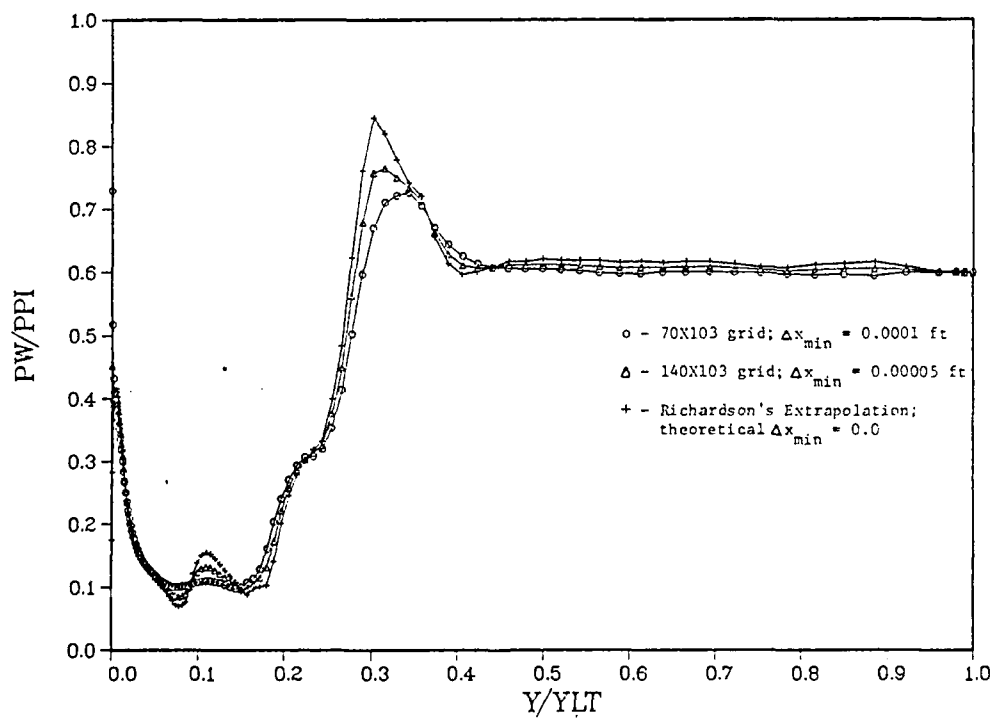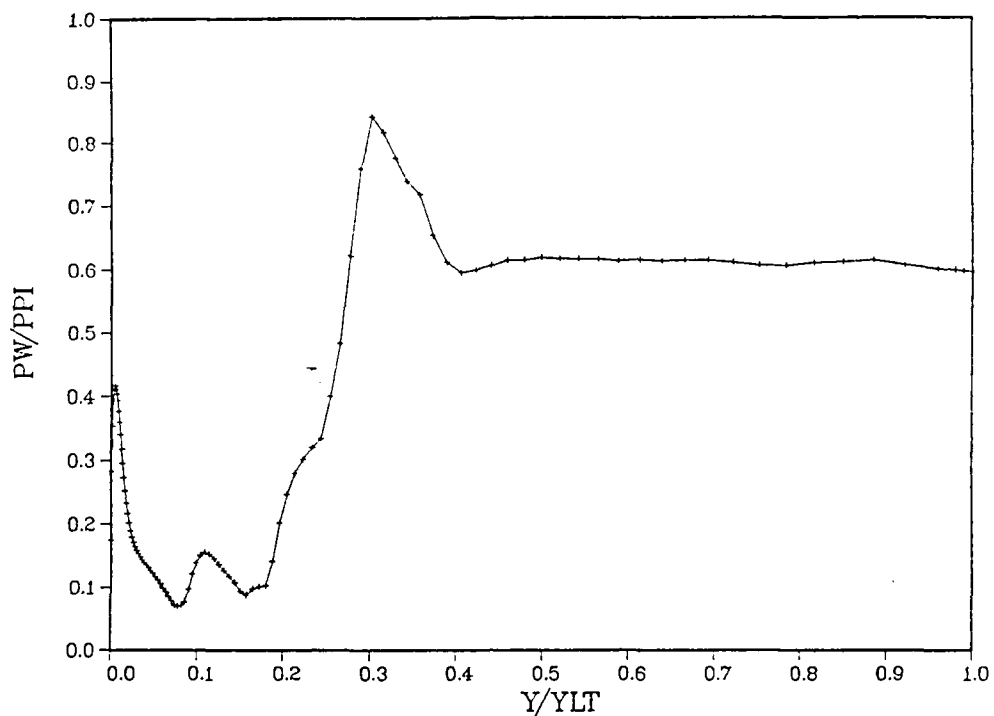
VITA

James Andrew Horkovich ███████████████████████████████████ He
received his Bachelor and Master of Science degrees in Aeronautical
Engineering from Rensselaer Polytechnic Institute in 1969 and 1972,
respectively. He was commissioned in the USAF as a Distinguished Graduate
of the AFROTC program in 1969. After graduate school, his first Air Force
tour was as a Flight Test Engineer with the 3246th Test Wing, Eglin AFB, FL,
where he supervised numerous conventional munition test programs and logged
several hundred hours in the "back seat" of various test aircraft. In 1974
he was assigned to the Faculty of the Department of Aeronautics at the U. S.
Air Force Academy, where he taught and directed the basic aerodynamics and
fluid mechanics courses and served as the Associate Air Officer Commanding
of a cadet squadron. In 1978 he was honored as the Outstanding Military
Educator in Aeronautics. He was reassigned to the Air Force Operational
Test and Evaluation Center in 1979, where he supervised planning and
training in operational suitability for new weapon systems under test. He
entered the School of Engineering, Air Force Institute of Technology, in
1981. In 1984, he was reassigned to the Air Force Weapons Laboratory,
Kirtland AFB, NM, as the Project Officer for the SDIO Alpha Space Based
Laser Program. He is now the Deputy Chief, Program Integration Division,
Advanced Radiation Technology Directorate, Air Force Weapons Laboratory,
where his primary responsibilities are as the program manager for all SDIO
programs involving high power lasers and beam control.

369

Thesis/Dissertation Category and Distribution List

Dissertation Designator: AFIT/DS/ENY/90-3

Title: Numerical Solutions for a Cylindrical Laser Diffuser Flowfield
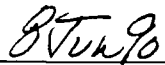
Author: James A. Horkovich, Lt. Colonel, USAF

        Unclassified   Classified

    Approved for public release; distribution unlimited

    _____   _____
    Chairman   Date

COURTESY COPIES

Dr. Joseph Shang
AFWAL/FIMM
Wright-Patterson AFB, OH 45433   _____
                                                    Date Mailed

Colonel Robert C. Bower
AFSTC/SW
Kirtland AFB, NM 87117   _____
                                                    Date Mailed

AUTHOR COPY

James A. Horkovich, Lt. Col. USAF
Star Route Box 521
Placitas, NM 87043   _____
                                                    Date Mailed

ADVISOR COPY

Captain Philip Beran, AFIT/ENY   _____
                                                    Date Mailed

REPORT DOCUMENTATION PAGE

Form Approved
OMB No. 0704-0188

1a REPORT SECURITY CLASSIFICATION UNCLASSIFIED	1b RESTRICTIVE MARKINGS N/A
2a. SECURITY CLASSIFICATION AUTHORITY N/A	3 DISTRIBUTION/AVAILABILITY OF REPORT Approved for public release; distribution unlimited
2b DECLASSIFICATION/DOWNGRADING SCHEDULE N/A	

4 PERFORMING ORGANIZATION REPORT NUMBER(S) AFIT/DS/ENY/90-3	5 MONITORING ORGANIZATION REPORT NUMBER(S)

6a. NAME OF PERFORMING ORGANIZATION School of Engineering Air Force Inst. of Tech.	6b OFFICE SYMBOL (If applicable) AFIT/ENy	7a. NAME OF MONITORING ORGANIZATION

6c. ADDRESS (City, State, and ZIP Code) Wright-Patterson AFB OH 45433	7b ADDRESS (City, State, and ZIP Code)

8a. NAME OF FUNDING/SPONSORING ORGANIZATION	8b. OFFICE SYMBOL (If applicable)	9 PROCUREMENT INSTRUMENT IDENTIFICATION NUMBER

8c. ADDRESS (City, State, and ZIP Code)	10 SOURCE OF FUNDING NUMBERS

PROGRAM ELEMENT NO.	PROJECT NO.	TASK NO	WORK UNIT ACCESSION NO
63221C	F 1302	01	

11. TITLE (Include Security Classification)

Numerical Solutions For A Cylindrical Laser Diffuser FLowfield (Unclassified)

12. PERSONAL AUTHOR(S)
James A. Horkovich, Lt Col, USAF

13a. TYPE OF REPORT PhD Dissertation	13b. TIME COVERED FROM _____ TO _____	14. DATE OF REPORT (Year, Month, Day) June 1990	15. PAGE COUNT 392

16. SUPPLEMENTARY NOTATION

17.	COSATI CODES		18. SUBJECT TERMS (Continue on reverse if necessary and identify by block number)
FIELD	GROUP	SUB-GROUP	Computational Fluid Mechanics Compressible Flow
20	04		Numerical Solution Turbulent Flow
09	03		Navier-Stokes Laser Diffuser MacCormack's Explicit Method

19. ABSTRACT (Continue on reverse if necessary and identify by block number)

Numerical solution to the diffusion of a supersonic flow through a cylindrical laser diffuser is approached by incorporating a modified two-layer Cebici-Smith algebraic eddy viscosity turbulence model into the compressible Navier-Stokes equations. The standard algebraic constants are made functions of the local adverse pressure gradient based on experimental values obtained in the research of Jobe, Hankey, Laderman, Sturek, and Waltrup and Schetz. This modification allows solution of the Navier-Stokes equations by MacCormack's time-splitting explicit numerical scheme for selected experimental flow conditions. This effort represents the first full Navier-Stokes solution that has accurately simulated the viscous-inviscid interactions present in a supersonic axisymmetric diffuser. The experimental tests used as a basis for the computational solutions were conducted at a diffuser entrance unit Reynolds number of 1.6 million per foot. Inflow to the diffuser was provided by ten Mach 2.5 primary nozzles

20. DISTRIBUTION/AVAILABILITY OF ABSTRACT ☒ UNCLASSIFIED/UNLIMITED ☐ SAME AS RPT. ☐ DTIC USERS	21. ABSTRACT SECURITY CLASSIFICATION UNCLASSIFIED
22a. NAME OF RESPONSIBLE INDIVIDUAL Philip Beran, Capt, USAF	22b. TELEPHONE (Include Area Code) 513-255-4476	22c. OFFICE SYMBOL AFIT/ENY

DD Form 1473, JUN 86   Previous editions are obsolete.   SECURITY CLASSIFICATION OF THIS PAGE

plus two Mach 4.0 bank blowers (wall boundary layer flow energizers). Computations were performed for diffuser exit pressures representing 60 percent and 47 percent of normal shock recovery pressure. When the turbulence model was properly modified to accommodate the physics of flows with strong adverse pressure gradients, the numerical solution successfully reproduced all of the essential flow features including boundary layers, location and size of wall separation regions, location of the core flow normal shock, and the persistence of source nozzle flow interactions through several streamwise turnback shocks. Comparison with experimentally obtained wall pressure data is acceptable; the only notable discrepancy occurs in the lambda shock impingement region where the numerical solution fails to accurately reproduce the intrinsic physics of the flowfield. Convergence to stable numerical solutions was not achieved using the basic Cebici-Smith model; eddy viscosity "stiffening" was required in the presence of adverse pressure gradients.